MMNSA

Mathematical Modelling and Numerical Simulation with Applications

ISSN Online : 2791-8564

Year : 2025

Volume : 5

Issue : 1

https://dergipark.org.tr/en/pub/mmnsa

Editor-in-Chief
Mehmet Yavuz, PhD

VOLUME: 5 ISSUE: 1
ISSN ONLINE: 2791-8564

March 2025
https://dergipark.org.tr/en/pub/mmnsa

MATHEMATICAL MODELLING AND NUMERICAL SIMULATION WITH APPLICATIONS

Editor-in-Chief and Publisher

Managing Editors (In Alphabetical Order)

Editorial Board Members (In Alphabetical Order)

Contents

Research Articles

Mathematical Modelling and Numerical Simulation with Applications, 2025, 5(1), 1–17

https://dergipark.org.tr/en/pub/mmnsa

ISSN Online: 2791-8564 / Open Access

https://doi.org/10.53391/mmnsa.1400075

RESEARCH PAPER

Towards a viable control strategy for a model describing the dynamics of corruption

Hassania Abou-nouh [1,*,‡] and **Mohammed El Khomssi** [1,‡]

[1]Department of Mathematics, Laboratory of Modeling and Mathematical Structures, Sidi Mohamed Ben Abdellah University, Route d'Imouzzer, 30000 Fez, Morocco

*Corresponding Author

‡hassania.abounouh@usmba.ac.ma (Hassania Abou-nouh); khomsixmath@yahoo.fr (Mohammed El Khomssi)

Abstract

This paper explores the use of viability theory in the examination of corruption dynamics, using a susceptible-infected-recovered (SIR) model. In order to promote transparency, good governance, and sustainable economic growth, it is crucial to develop effective strategies for controlling corruption in society. Viability theory provides a framework for analyzing the long-term feasibility of different control policies by defining the set of constraints that define acceptable behavior for a given system. We use this framework to study the impact of different anti-corruption measures on the spread of corruption in a population. Our results show that a combination of measures targeting both the susceptible and corrupted populations can lead to significant reductions in corruption levels over time. We also discuss the challenges involved in applying viability theory to the study of corruption dynamics, including the need for reliable data and the limitations of simple models such as the SIR model. Our results highlight the potential of the viability theory as a valuable tool for promoting transparency, good governance, and sustainable development and suggest that further research in this area is needed to refine and improve the methods used. Our research offers a proof-of-concept for applying viability theory to manage the dynamics of corruption, paving the way for potential future research directions.

Keywords: Control theory; viability theory; SIR model; corruption dynamic

AMS 2020 Classification: 37N35; 93A30; 14L24

1 Introduction

Corruption is the improper use of power for individual benefit, eroding trust, weakening democracy, hindering economic development, and further exacerbating inequalities, poverty, social division, and the environmental crisis. [1]. Corruption is a pervasive problem that can have devastating effects on the stability and development of societies. It can undermine public trust, reduce

➤ **Received:** 07.12.2023 ➤ **Revised:** 31.05.2024 ➤ **Accepted:** 02.08.2024 ➤ **Published:** 31.03.2025

economic growth, and lead to political instability. According to Transparency International's 2021 Corruption Perceptions Index [2], more than two-thirds of countries scored below 50 out of 100, indicating a high level of perceived corruption.

Traditionally, bribery or favor is used to distort or destroy integrity in the fulfillment of official obligations. More recently, corruption is defined as an inducement by persons, public or private, to indicate favor or act dishonestly or unfaithfully within the discharge of their duties. It is typically related to public officials, and therefore, the performance of public duties is impacted. However, it's now increasingly accepted that the act of corruption may apply to both public and personal individuals and will extend beyond bribery [3].

In the academic literature, the number of quantitative research studies on corruption is relatively low. Several researchers have explored the conceptual analogy between the spread of infectious diseases [4, 5] and the diffusion of corrupt behavior [6] within social networks. By adapting the epidemiological model to corruption dynamics, these studies aim to understand how corrupt practices propagate through networks of individuals and institutions. Abdulrahman [7] proposed a mathematical model with a constant recruitment rate and standard incidence for corruption as a disease with its transmission dynamics. Distributed numerical simulations showed that corruption can only be lowered to a very low degree, not completely eradicated. In [8], the authors suggested a mathematical model for corruption that took into account the awareness raised by anti-corruption campaigns and in-prison counseling. With the aid of differential equation stability theory, a nonlinear deterministic model illustrates and undergoes qualitative examination for the dynamics of corruption presented in [9]. Employing the next-generation matrix methodology, the basic reproduction number for the corruption-free equilibrium is determined. Additionally, they improved the model by adding one optimal control technique for optimal control. They came to the conclusion that if attempts to control corruption are strengthened and put into practice through the media and punishments, the degree of corruption in society may be lowered.

Efforts to control corruption have been the subject of much research and policy discussion. In recent years, there has been a growing interest in using mathematical modeling to understand the dynamics of corruption and develop effective strategies for controlling it. One such approach is the use of viability theory, or invariance [10].

The viability theory, which examines the evolution of dynamic systems under specified conditions, was formally introduced by Aubin [11]. Research on the efficacy of control systems primarily revolves around two key aspects. Firstly, it involves verifying the system's feasibility within a defined domain [12, 13] or devising an appropriate controller to ensure the closed-loop system's feasibility within that domain [14–16]. Secondly, it entails identifying the viability kernel (the largest controllable invariant manifold) of the system. Additionally, viability theory proves beneficial in addressing other control-related challenges such as the reachability problem [17], stabilization problem [15, 18], differential games [19], and safety behavior problem [20].

The ability to adjust and the multidisciplinary application of viability theory are demonstrated by its use in many domains. In order to assess the resilience and sustainability of economic systems, viability theory has been widely used in financial and economic modeling. Viability analysis has been used by researchers to examine sustainable development, financial stability, and macroeconomic dynamics. Research has, for instance, looked at the sustainability of resource allocation systems [21], the resilience of financial markets [22], and the viability of economic policies [23].

Viability theory has found significant use in ecological and environmental studies. Researchers have applied viability analysis to evaluate the resilience of ecosystems to environmental changes. Viability analysis can identify critical thresholds for biodiversity conservation [24, 25]. In control theory and engineering, viability theory has been employed to design robust control systems and ensure the feasibility of dynamic processes under constraints. Research in this area has focused on

developing viability-based control algorithms [26, 27]. In biology and medicine, viability theory has been used to study the dynamics of biological systems, population viability, and disease control strategies. Researchers have used viability analysis to assess the viability of threatened species, model the spread of infectious diseases, and improve treatment protocols for chronic illnesses [28, 29]. For additional information on viability theory, see [11] or [30].

Motivated by the robust modeling capabilities of the viability theory, this study delves into the application of the SIR model to analyze corruption dynamics. Beginning with an exploration of the theoretical foundations, the research extends to practical investigations, leveraging viability theory to understand the propagation of corrupt behavior within societal frameworks and devise effective strategies for mitigating corruption within complex socio-economic systems.

The main contributions of this research are multifaceted. Firstly, it addresses a crucial challenge in the study of corruption dynamics by applying viability theory within the framework of the SIR model. Traditionally, ensuring the boundedness of trajectories in corruption studies, especially within the context of complex societal systems, poses significant difficulties. However, this paper overcomes this challenge by strategically incorporating viability theory, thus offering a novel avenue to guarantee trajectory boundedness and enhance the robustness of corruption modeling. Additionally, while viability theory inherently ensures constraint avoidance, the integration with the SIR model provides insights into stability aspects, thereby improving the overall understanding of corruption dynamics. This integration represents a theoretical innovation, enabling the analysis of corruption propagation and control in more complex socio-economic environments. Secondly, the study presents a methodological framework for constructing viable strategies to combat corruption using the SIR model, particularly in scenarios where corruption dynamics are influenced by various societal factors and constraints. Thirdly, the proposed approach is applied to real-world cases, such as studying corruption propagation within specific sectors or regions, thereby providing valuable insights for policymakers and practitioners aiming to tackle corruption effectively. The aim of this article is to provide an overview of the viability theory and its application to the control of corruption dynamics. Our approach considers both transient and asymptotic behavior. Rather than aiming for equilibrium or optimization, our goal is to identify policies that can restrict the number of corrupt individuals below a certain threshold at any given point in time. The article will discuss the concept of viability, the methods used to calculate the viability kernel, and the challenges involved in applying viability theory to the study of corruption dynamics. The article will also review recent research in this area and discuss the potential implications of this approach for policymakers and researchers working to address corruption.

2 The viability problem

The viability problem is dependent on the consistency of the acceptability constraints applied to the states and decisions of the system.

The dynamics

To describe the viability property, consider the following non-linear control system:

$$\dot{x}(t) = F(x(t), u(t)),$$

with state $x \in \mathbb{R}^n$, control $u \in \mathcal{U}$ and $F(x, u)$ is a Lipschitz function.

Definition 1 *Let K be a subset of the domain of F. A function $x(.)$ is said to be viable in K if and only if :*

$$\forall t \geq 0, \qquad x(t) \in K.$$

Definition 2 *The tangent cone to K at x denoted by $T_K(x)$, is the closed cone of elements v such that*

$$\liminf_{h \mapsto 0^+} \frac{d(x + hv, K)}{h} = 0.$$

Definition 3 *A subset K is a viability domain of a non-trivial set-valued map F if and only if the following condition is satisfied:*

$$\forall\ x\ \in\ K, \qquad F(x) \cap T_K(x) = \varnothing.$$

It is worth noting that the tangent cone $T_K(x) = \mathbb{R}^n$ for any interior point x within K, thereby satisfying the condition mentioned above. Therefore, it is sufficient to examine only the points on the boundary of set K to verify the condition.

Definition 4 *The viability kernel of K with respect to F, denoted by $Viab_F(K)$, is defined as the largest possible closed subset of K that is viable under F, which could potentially be an empty set.*

Definition 5 ***Viability Kernel*** *is the set of initial states x_0 from which a feasible path $(x(.); u(.))$ respecting the constraints (staying in K) at all times:*

$$Viab_F(K) = \{x_0 \in K \setminus \exists x(t) \quad such\ that \quad x(t) \in K, \quad \forall t \geq 0, \quad x(0) = x_0\}.$$

A set K would be viable for the dynamic (F, u) if the viability kernel $viab_F(K)$ coincides with the set of initial constraints K. Under appropriate assumptions on the dynamics, a closed set K is considered favorable when a control u can initiate a feasible trajectory within K from any state x in K, resulting in velocities $\dot{x} = F(x, u)$ that are either tangent or inward pointing with respect to the domain K.[1] The Hamiltonian formulation can be employed to express this idea. Specifically, we can consider the Hamiltonian function:

$$\mathcal{H}(x, q, u) = \sum_{i=1}^{n} q_i\, F_i(x, u).$$

In this case, the following statements are equivalent:

i K is viable for (F, U),
ii $Viab_F(K) = K$,
iii $\inf_{u \in U(x)} \mathcal{H}(x, q, u) \leq 0, \quad \forall x \in K, \quad \forall q \in N_K(x)$,

with $N_K(x)$ is the cone normal to the set K at x.

3 Mathematical formulation and description of the problem

The SIR model can be adapted to study corruption dynamics by drawing an analogy between the spread of infectious diseases and the diffusion of corrupt behavior within social networks. In this adapted model, we consider a population split into three categories:

1 For example, if U is convex, closed, and bounded with F regular.

S is the number of susceptible,
C is the number of corrupts,
R is the number of individuals to recover,

in which we assume that the whole population: $N = S + C + R$.

We also suppose that:

- The population is fixed: no demographic phenomena (births, deaths, immigration and emigration).
- No longer being honest means necessarily becoming corrupt.
- Corrupt people are all infectious.
- Each person recovered is recovered forever.

The model will have the following system of differential equations:

$$\begin{aligned}\frac{dS_t}{dt} &= \delta N - \frac{\lambda C_t S_t}{N} - \delta S_t,\\ \frac{dC_t}{dt} &= \frac{\lambda C_t S_t}{N} - \nu C_t - \delta C_t,\\ \frac{dR_t}{dt} &= \nu C_t - \delta R_t.\end{aligned}$$

Table 1. Descriptions of the model's parameters

Parameters	Description
λ	Transmission rate of corruption from a corrupter person in a time period
δ	Birth and death rate, which are assumed to be equal
ν	The recovery rate

To simplify matters, we can redefine the occurrence as the proportions:

$$s_t = \frac{S_t}{N}, \qquad c_t = \frac{C_t}{N}, \qquad r_t = \frac{R_t}{N}.$$

We get

$$\begin{aligned}\frac{ds_t}{dt} &= \delta - \lambda c_t s_t - \delta s_t,\\ \frac{dc_t}{dt} &= \lambda c_t s_t - \nu c_t - \delta c_t,\\ \frac{dr_t}{dt} &= \nu c_t - \delta r_t,\end{aligned}$$

with initial conditions:

$$s(0) \geq 0, \qquad c(0) \geq 0, \qquad r(0) \geq 0.$$

Taking into account the overall population density, we have $s(t) + c(t) + r(t) = 1 \Rightarrow r(t) =$

$1 - s(t) - c(t)$. Thus, it is sufficient to consider

$$\begin{aligned} \frac{ds_t}{dt} &= \delta - \lambda c_t s_t - \delta s_t, \\ \frac{dc_t}{dt} &= \lambda c_t s_t - \nu c_t - \delta c_t. \end{aligned} \tag{1}$$

The set $\Delta = \{(s(t), c(t)) \in \mathbb{R}^2_+; \quad s(t) + c(t) \leq 1\}$ is positively invariant for system (1). System (1) has two equilibrium points that are given by the disease-free equilibrium point of the system $E^0 = (1, 0)$ and the endemic equilibrium point

$$E^* = \left(\frac{\nu + \delta}{\lambda}, \frac{\delta(\lambda - \nu - \delta)}{\lambda(\nu + \delta)} \right).$$

The endemic equilibrium point exists only when $\lambda > \nu + \delta$ i.e the transmission of corruption must be greater than the death rate of the corrupt individuals or $R_0 > 1$, where $R_0 = \frac{\lambda}{\nu+\delta}$ is known as reproduction number which determines the asymptotic behavior of the model.

Control problem

We will now introduce our second model, which incorporates honesty as an induced trait. The proposed model is as follows:

$$\begin{aligned} \frac{ds_t}{dt} &= \delta(1-\alpha) - \lambda c_t s_t - \delta s_t, \\ \frac{dc_t}{dt} &= \lambda c_t s_t - \nu c_t - \delta c_t, \\ \frac{dr_t}{dt} &= \nu c_t - \delta r_t, \\ \frac{dh_t}{dt} &= \delta\alpha - \delta h_t. \end{aligned} \tag{2}$$

In this model, h represents the group in which honesty is implemented. Other parameters include α as the rate of honesty,
and: $s(t) + c(t) + r(t) + h(t) = 1 \Rightarrow r(t) = 1 - s(t) - c(t) - h(t)$.
Thus, it suffices to consider

$$\begin{aligned} \frac{ds_t}{dt} &= \delta(1-\alpha) - \lambda c_t s_t - \delta s_t, \\ \frac{dc_t}{dt} &= \lambda c_t s_t - \nu c_t - \delta c_t, \\ \frac{dh_t}{dt} &= \delta\alpha - \delta h_t. \end{aligned} \tag{3}$$

The set $\Delta_1 = \{(s(t), c(t), h(t)) \in \mathbb{R}^3_+; \quad s(t) + c(t) + h(t) \leq 1\}$ is positively invariant for system (3).
System (3) has two equilibrium points that are given by the disease-free equilibrium point $E_1^0 = (1 - \alpha, 0, \alpha)$ and the endemic equilibrium point

$$E_1^* = \left(\frac{\nu + \delta}{\lambda}, \frac{\delta(\lambda(1-\alpha) - \nu - \delta)}{\lambda(\nu + \delta)}, \alpha \right).$$

The impact of honesty on the disease-free equilibrium point and endemic equilibrium point can be readily observed. The susceptible population is reduced by a factor of α (the honesty rate). Additionally, the reproduction number, which represents the number of secondary infections, is greatly affected. Following the introduction of honesty control in the model, the new reproduction number becomes $R_h = R_0(1-\alpha)$. The existence of an endemic equilibrium point is contingent on $R_h > 1$.

4 Viable control of corruption dynamics

Now, applying the viability theory to our dynamic, we focus our study on the following controlled dynamic system:

$$\begin{aligned} \frac{ds_t}{dt} &= \delta(1-\alpha) - \lambda c_t s_t - \delta s_t, \\ \frac{dc_t}{dt} &= \lambda c_t s_t - \nu c_t - \delta c_t, \\ \frac{dh_t}{dt} &= \delta\alpha - \delta h_t. \end{aligned} \tag{4}$$

Viability constraint

The main purpose is to determine the control α that keeps the number of corrupts below the c_m boundary, where the viability constraint expresses the honesty of a community as long as the viability constraint is achieved:

$$c_t < c_m, \quad \forall t \geq t_0, \tag{5}$$

with $0 < c_m \leq N$.
The presence of control essentially relies upon the underlying state $(s_{t_0}, c_{t_0}, h_{t_0})$ at the initial time t_0. We will currently concentrate on these initial states, likewise called the viability kernel [11].

Viability analysis

We may use viability theory methods to analyze our dynamics and, in particular, calculate the viability kernel. This will allow us to see if corruption dynamics (4) are compatible with the viability constraint (5) at any given time t. The viability kernel is formally defined as follows:

Definition 6 *The viability kernel $Viab(c_m)$ is a set of initial states $(s_{t_0}, c_{t_0}, h_{t_0})$ for which an honesty rate $t \mapsto \alpha(t) \in [0,1]$ exists so that the dynamic system (4) solution meets the viability constraint (5).*

$$Viab(c_m) = \left\{ (s_{t_0}, c_{t_0}, h_{t_0}) \mid \begin{array}{c} \text{there exist a control } \alpha_t(.), \text{ so that the solution to (4)} \\ \text{that starts from } (s_{t_0}, c_{t_0}, h_{t_0}) \text{ satisfies the constraint (5)} \end{array} \right\}. \tag{6}$$

Note that our unconstrained domain of research is the positively invariant set

$$\{(s_t, c_t, h_t) \mid 0 \leq s_t,\ 0 \leq c_t\ ,\ s_t + c_t + h_t \leq 1\}.$$

Since the initial point should fulfill the viability constraint (5), The rectangle $[0,1] \times [0, c_m[\times [0,1]$ must contain the viability kernel $Viab(c_m)$.
The constraint set $\mathbb{V}$ is the intersection of the unconstrained domain of study and the cuboid

$[0,1] \times [0, c_m[\times [0,1]$ (see Figure 1)

$$\mathbb{V} := \{(s_t, c_t, h_t) \mid 0 \leq s\,,\, 0 \leq c_t < c_m\,, 0 \leq h\,, s_t + c_t + h_t \leq 1\}. \tag{7}$$

That is,

$$Viab(c_m) \subset \mathbb{V}.$$

As they are a fundamental step in defining the viability kernel, we describe and give a geometrical

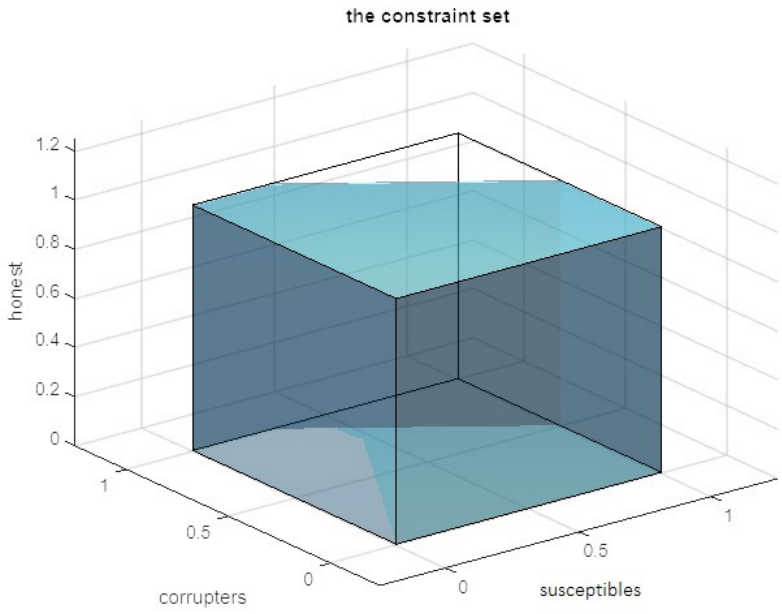

Figure 1. The constraint set $\mathbb{V}$

characterization of the so-called viability domains of system (4).

Definition 7 *A viability domain for the system* (4) *is a subset K of the set of states* $[0;1] \times [0; c_m[\times [0;1]$ *if there exists a control* $\alpha_t(.)$ *such that the solution to* (4)*, which starts from* $(s_{t_0}, c_{t_0}, h_{t_0})$*, remains inside K for every* $t \geq 0$.

The viability kernel is linked to the viability domains in the following way:

Theorem 1 *[11] The viability kernel is the constraint set's largest viability domain.*

We associate the vector field (u_s, u_c, u_h) with system (4):

$$\begin{pmatrix} u_s \\ u_c \\ u_h \end{pmatrix} = \begin{pmatrix} -\lambda c_t s_t + \delta(1-\alpha) - \delta s_t \\ \lambda c_t s_t - \nu c_t + \delta c_t \\ \delta\alpha - \delta h_t \end{pmatrix},$$

the system (4) is equivalent to:

$$\begin{cases} \dot{s} &= u_s(s(t), c(t), \alpha(t)), \\ \dot{c} &= u_c(s(t), c(t)), \\ \dot{h} &= u_h(h(t), \alpha(t)). \end{cases} \tag{8}$$

Using the vector field u, we provide a geometric description of the viability regions of the system with control.

Proposition 1 *[11] For a Marchaud controlled system, a closed subset U is considered viable if the family of vectors formed by the vector field when the control varies is assured to have at least one vector contained within the tangent cone at any point in U.*

In our situation, the geometric characterization of viability domains is as follows:

Proposition 2 *Consider a closed subset K If there is a control* $\alpha_t \in [0;1]$ *such that* (u_s, u_c, u_h) *is an inward-pointing vector, then the set K is a viability domain for the system (4) whenever* (s, c, h) *varies along the frontier* δK *of the set K.*
To be considered a viability domain for system (4), the scalar product of the vector (u_s, u_c, u_h) *and an outward-pointing normal vector (relative to set K) must be less than or equal to zero for a closed subset K with a piecewise smooth boundary* δK.

Viability kernel

Proposition 3 *The viability kernel in (6) is as follows:*

$$Viab\,(c_m) = \mathbb{V} \cap \{(s,c,h) \mid 0 \leq h\,, s_m \leq s \leq 1 \text{ and } c < \mathfrak{C}(s)\}. \tag{9}$$

With $\mathfrak{C}(s)$ *is the set of applications such as s the solution* $s \in [s_m, 1] \mapsto \mathfrak{C}(s)$ *to the differential equation:*

$$\begin{aligned} -u_s(s(t), \mathfrak{C}(s), \alpha(t))\mathfrak{C}'(s) + u_c(s(t), \mathfrak{C}(s)) &= 0, \\ \mathfrak{C}(s_m) &= c_m. \end{aligned} \tag{10}$$

Proof We show that the set $Viab\,(c_m)$ is a viable set. Since $\mathbb{V}$ is an invariant set, we can focus on the boundary of the set: $\{(s,c,h) \mid 0 \leq h,\ s_m \leq s \leq 1 \text{ and } c < \mathfrak{C}(s)\}$.
The boundary can be obtained by considering the conditions where each of the three inequalities in the set definition is satisfied with equality.
First, considering $h = 0$, we get the lower boundary:

$$\partial(\mathbb{V} \cap \{(s,c,h) \mid 0 \leq h,\ s_m \leq s \leq 1 \text{ and } c < \mathfrak{C}(s)\}) = \{(s,c) \mid s_m \leq s \leq 1,\ c < \mathfrak{C}(s),\ s + c < 1\}.$$

Second, for $s = s_m$, we have:

$$\partial(\mathbb{V} \cap \{(s,c,h) \mid 0 \leq h,\ s_m \leq s \leq 1 \text{ and } c < \mathfrak{C}(s)\}) = \{(s_m,c,h) \mid 0 \leq h,\ c < c_m,\ c + h < 1 - s_m\}.$$

Finally, for $c = \mathfrak{C}(s)$, we get the upper boundary:

$$\partial(\mathbb{V} \cap \{(s,c,h) \mid 0 \leq h,\ s_m \leq s \leq 1 \text{ and } c < \mathfrak{C}(s)\}) = \{(s,c,h) \mid s_m \leq s \leq 1,\ c = \mathfrak{C}(s),\ 0 \leq h\}.$$

To examine the scalar product of u with the normal vector to the boundaries of $Viab(c_m)$, we first need to find the normal vectors to each boundary.
Boundary: $h = 0$ The normal vector to this boundary is $\mathbf{n} = (0, 0, 1)$.
Boundary: $s = s_m$ The normal vector to this boundary is $\mathbf{n} = (-1, 0, 0)$.
Boundary: $c = \mathfrak{C}(s)$ The normal vector to this boundary is $\mathbf{n} = \left(-\frac{\partial \mathfrak{C}}{\partial s}, 1, 0\right)$.
Next, we examine the scalar product of u with these normal vectors:

1 Boundary: $h = 0$

$$u.n = u_h(0,0,0).1 = -1 < 0.$$

Since the scalar product is negative, this implies that the vector u points into the domain $Viab(c_m)$.

2 Boundary: $s = s_m$

$$u.n = u_s(s_m, c, h).(-1) < 0.$$

Since the scalar product is negative, this implies that the vector u points into the domain $Viab(c_m)$.

3 Boundary: $c = \mathfrak{C}(s)$
Consider any point (s, c, h) on the boundary with $c = \mathfrak{C}(s)$. Let $u = (u_s, u_c, u_h)$ be any outward pointing normal vector at this point. Since u is outward pointing, we have $u \cdot (-\nabla c, 1, 0) > 0$ where $-\nabla c = (-\frac{\partial \mathfrak{C}}{\partial s}, -\frac{\partial \mathfrak{C}}{\partial c}, 0) = (-\mathfrak{C}'(s)u_s, 1 - u_c, 0)$. This implies that

$$u_s \mathfrak{C}'(s) u_s - (1 - u_c) > 0.$$

Since u is normal to the boundary, we also have $u \cdot (0,0,1) = u_h > 0$. Combining these two inequalities, we get

$$u_s \mathfrak{C}'(s) u_s > 1 - u_c,$$

and hence

$$u_s \mathfrak{C}'(s) u_s - (1 - u_c) + u_h^2 > u_h^2.$$

This can be written as

$$\mathbf{u} \cdot \begin{pmatrix} -\mathfrak{C}'(s)u_s \\ 1 - u_c \\ 2u_h \end{pmatrix} > 0.$$

Since u is outward pointing, we must have

$$-\mathfrak{C}'(s)u_s u_s - (1 - u_c) + 2u_h^2 \leq 0.$$

Using $c = \mathfrak{C}(s)$ and $u_h > 0$, this can be rewritten as $-u_s u_c + u_h^2 \leq 0$. Since u is a unit vector, we have $u_s^2 + u_c^2 + u_h^2 = 1$, which implies $u_h^2 \leq 1 - u_s^2 - u_c^2$. Substituting this inequality in the above expression, we get $u_s^2 + u_c^2 \leq 1$. Therefore, all outward-pointing normal vectors at the boundary satisfy $u_s^2 + u_c^2 \leq 1$, which implies that all inward-pointing vectors satisfy $u_s^2 + u_c^2 \geq 1$.

We have shown that the set $\mathbb{V} \cap \{(s, c, h) \mid 0 \leq h,\ s_m \leq s \leq 1 \text{ and } c < \mathfrak{C}(s)\}$ is forward invariant and that its boundary is also invariant. Moreover, we have shown that there exists a control α such that any vector u in the interior of the set $\mathbb{V} \cap \{(s, c, h) \mid 0 \leq h,\ s_m \leq s \leq 1 \text{ and } c < \mathfrak{C}(s)\}$ satisfies $u \cdot \nu \leq 0$ where ν is the outward normal to the boundary of the set.

Therefore, by definition, this set is viable. This means that starting from any initial condition in

this set, there exists a control strategy $\alpha(t)$ that will keep the system inside the set for all future times. In other words, the set $\mathbb{V} \cap \{(s, c, h) \mid 0 \leq h,\ s_m \leq s \leq 1 \text{ and } c < \mathfrak{C}(s)\}$ represents a region of safe and sustainable operation for the system.

5 Simulation results and discussion

We simulated the corruption dynamic using the constraints $c_m = 0.7$ and the parameters $\lambda = 1.98$, $\delta = 0.5$, and $\nu = 0.5$.

The simulation represents the progression of the corruption dynamic over time with honesty control. The results reveal that corrupts initially rise significantly, but subsequently begin to drop due to the impact of the honesty control. The honest fraction of the population gradually increases, demonstrating that the control technique is effective. Therefore, the simulation shows that the honesty control is successful in reducing corruption in a population.

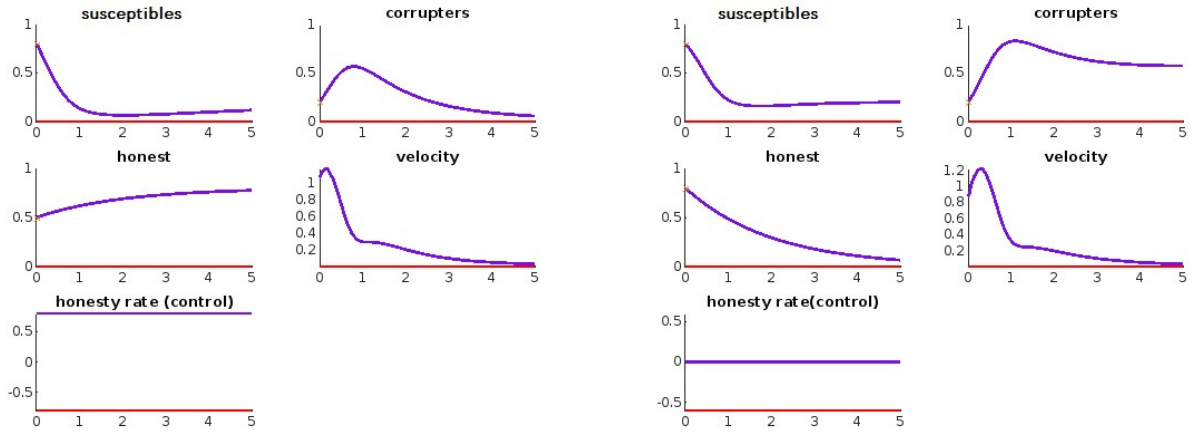

(a) maximum control **(b)** zerocontrol

Figure 2. Time profiles for the dynamics of corruption starting from $x(0) = (0.8, 0.2, 0.5)$

As shown in the Figure 2a, the maximum control method is used, causing the proportion of corrupt persons to climb and peak at a low level before gradually declining to zero over time. On the other hand, the proportion of honest people grows with time and eventually approaches one. This shows that the honesty control technique is effective over time in eliminating corruption in the community.

While in Figure 2b, the honesty control strategy is set to zero, implying that no control is applied to the system. As a result, we see that the proportion of corrupt people increases over time and reaches a high level. At the same time, the proportion of honest people falls to zero. This behavior implies that the corruption dynamic is not viable under this strategy, and the system will eventually collapse due to the significant level of corruption.

Figure 3a shows the viability kernel of the corruption dynamic. The yellow area within the viability kernel shows the initial conditions under which the system can remain viable, whereas the white area outside the viability kernel represents the starting conditions under which the system will eventually collapse into complete corruption.

The figure indicates that, for the given corruption dynamics, the system can stay viable for a limited range of beginning conditions (i.e., within the viability kernel) but will eventually collapse into total corruption for initial conditions outside the viability kernel.

Figure 3b illustrates the trajectory of a system in state space with three variables. The blue zone

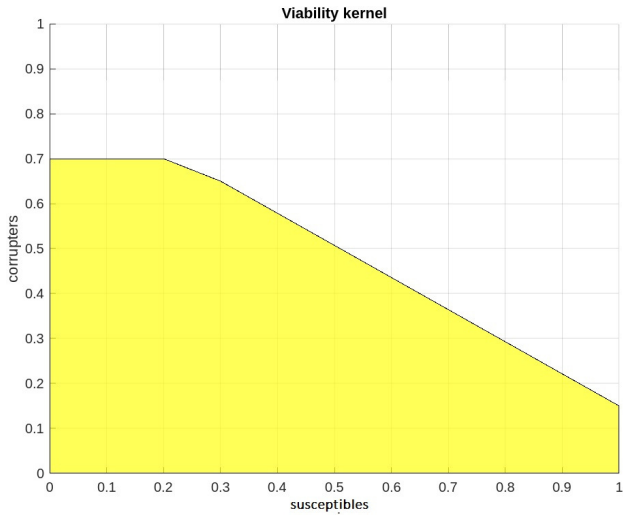

(a) Viability kernel of corruption dynamic

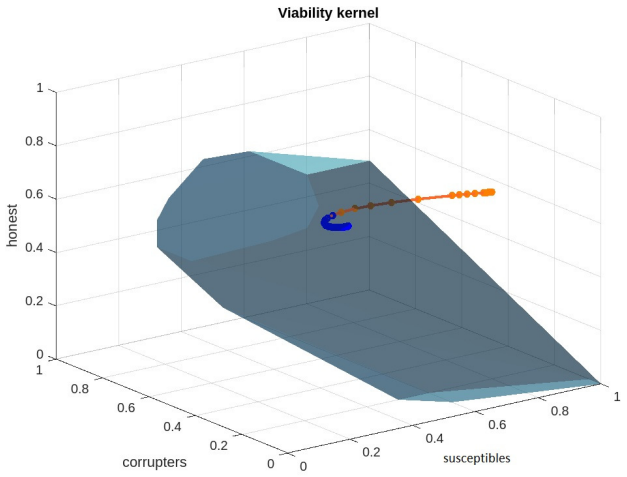

(b) Viability kernel of corruption dynamic with honest people

Figure 3. Viability kernel for the dynamic of corruption with control

represents the initial set of states from which the system can progress to the desired goal set. Because there is a set of initial conditions from which the system can be steered towards the desired goal while avoiding obstacles, the figure shows that the system is controllable. The system's trajectory is determined by its beginning conditions, and the vector field shows how the system will evolve over time. The graphic provides a good visual representation of the system's behavior in state space.

Figure 4a illustrates a slice through the three-dimensional viability kernel of the corruption dynamic with control. The slice is taken at the corrupts value of 0.8, and it indicates that the viability kernel is empty beyond this value of corrupts.

In Figure 4b, we can show the corruption dynamic's viability kernel for different values of susceptible and honest people. The region of initial states where there exists a feasible path that stays inside the constraint set, regardless of the value of control α is shown by the slice through all the values of corrupts. We can observe that with large values of susceptible and honest persons, practically all initial states are viable, showing that controlling corruption in a society with low corruption levels is quite easy. However, as corruption levels rise, the viable zone narrows, and for really high levels of corruption, the viability kernel becomes empty, indicating that controlling corruption from such beginning conditions is impossible. This emphasizes the critical need to prevent corruption from reaching dangerously high levels in the first place.

In Figure 4c, the slice is taken through $h(t) = 0$. The blue zone indicates the corruption dynamic's viability kernel under the stated limitations. In this situation, the viability kernel is a subset of the region with a large number of susceptible and a low number of corrupts. Because there is less pressure on individuals to participate in corrupt activity when the number of susceptible is high. Similarly, when the number of corrupt population is few, corrupt behavior has less of a chance of spreading. The boundary of the viability kernel is represented by the black line within the blue region when the tangent cone condition is satisfied. The tangent cone condition is not satisfied outside of the viability kernel, which means that there are no viable trajectories that remain within the feasible region at all times.

In Figure 4d, we observe a visualization of the corruption dynamic's viability kernel for various values of the honest fraction $h(t)$. The susceptible (non-corrupt persons) are represented by the x-axis, while the corrupts are represented by the y-axis (corrupt individuals). As we slice across $h(t)$, we are simply fixing the value of $h(t)$ and seeing how the viability kernel changes in relation

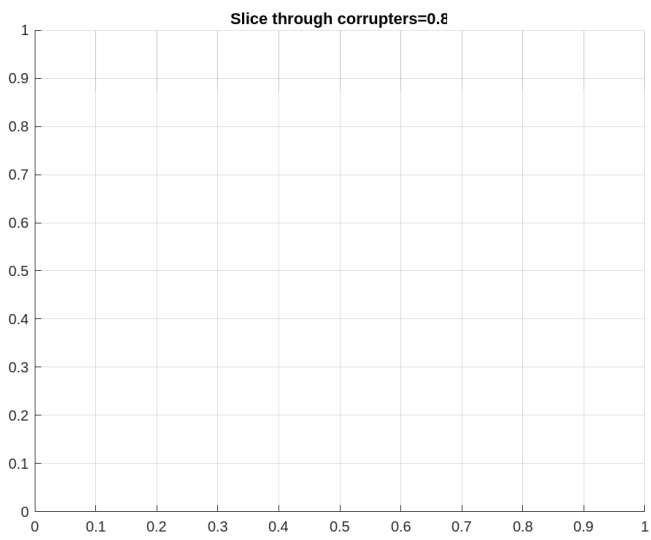

(a) Slice through $c(t) = 0.8$ (no viable points)

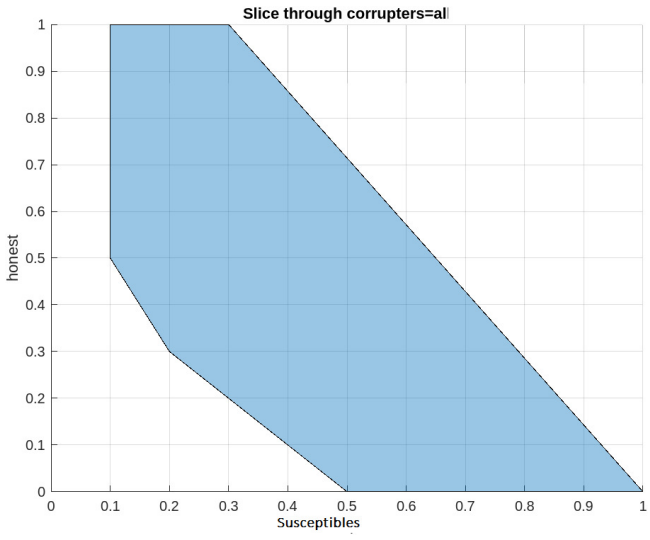

(b) Slice through $c(t)$

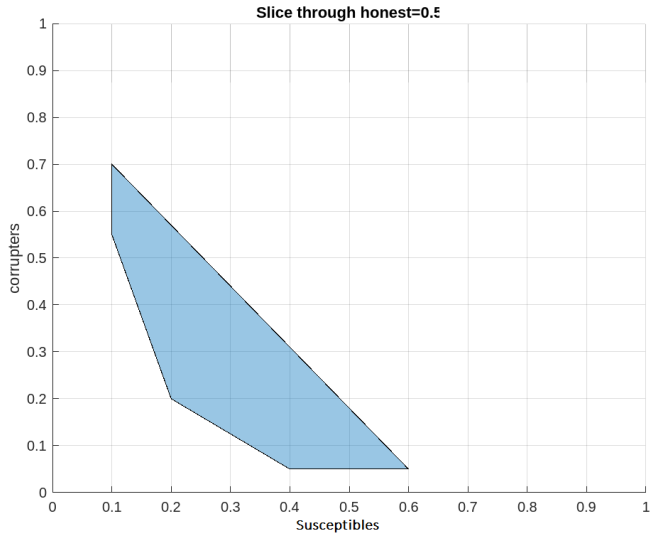

(c) Slice through $h(t) = 0.5$

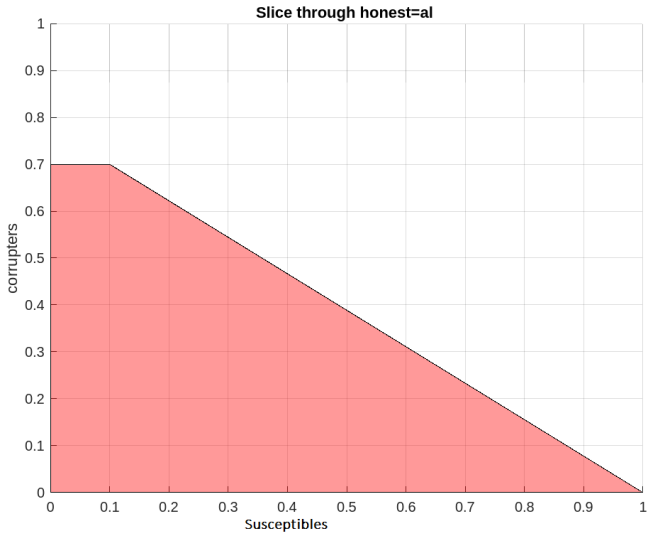

(d) Slice through $h(t)$

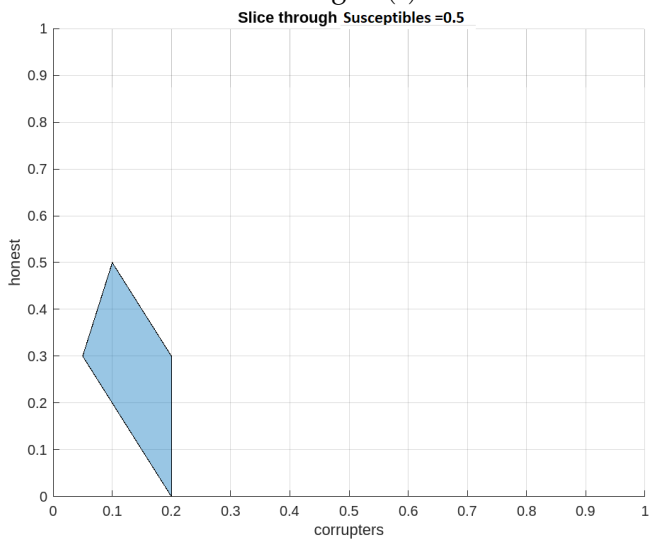

(e) Slice through $s(t) = 0.5$

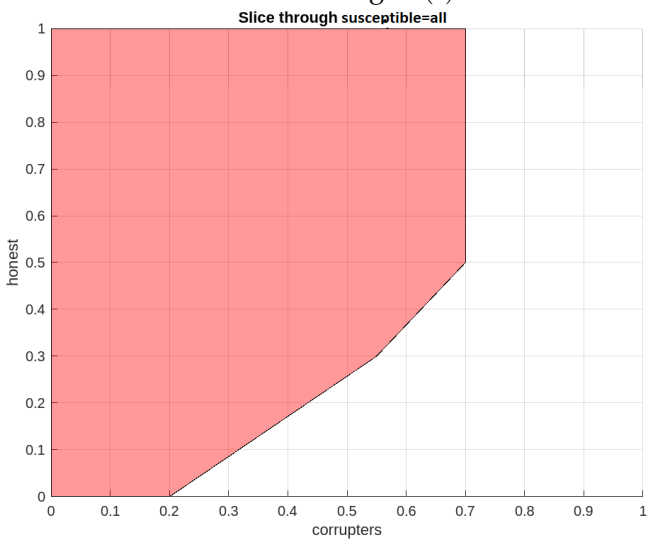

(f) Slice through $s(t)$

Figure 4. Slices of the viability kernel for the corruption problem with honesty as a control

to the other two variables, susceptible and corrupts. For example, if we take a slice across a certain value of $h(t)$ (e.g., $h(t) = 0.6$), we may examine the related viability kernel for that value of $h(t)$ and compare it to the viability kernels for other $h(t)$ values.Thus, the image sheds light on the viability of the corruption dynamic under many situations, emphasizing the relevance of the honest percentage in determining system stability.

This slice of the corrupted dynamic graphic Figure 4e and Figure 4f shows the system's behavior when the susceptible population's initial value is set to 0.5. The color map illustrates the viability kernel. We can see from this slice that for low values of the honest percentage, there is a large region of starting states that are not feasible, as indicated by the white color. This region increases as the honest fraction grows, and more beginning states become viable. Yet, even at high levels of the honest fraction, some initial states are not viable, as seen by the remaining white patches. The corrupt axis depicts the system's level of corruption, and we can see that the viable zone shrinks as the level of corruption increases. The honest axis indicates the system's level of honesty, and we can see that as the level of honesty increases, so does the viable region.

We may say that the viability theory is effective in providing a clear knowledge of the set of initial conditions that lead to a feasible trajectory that respects the restrictions over time in our simulation of the corruption dynamic. It enables us to find the system's viability kernel, which is the biggest closed subset of the state space that is viable under the system's dynamics. We can obtain an understanding of the system's behavior and the impact of different parameters on the dynamics by evaluating distinct slices of the viability kernel.

Furthermore, the viability theory is a powerful tool for developing control mechanisms that ensure the system's viability and adherence to time limits. We can avoid constructing control techniques that lead to such regions of the state space by identifying them. Furthermore, the viability theory can be used to analyze the resilience of control systems by determining if the system remains viable in the presence of uncertainties or disturbances.

To summarize, the viability theory is a useful tool for comprehending and devising control techniques for complicated systems with restrictions, such as the corruption dynamic in our simulation.

6 Conclusion

This study introduces an innovative approach to analyzing corruption dynamics using the SIR model, integrating two innovative methodologies: viability theory and epidemic modeling. Diverging from conventional methods, the proposed approach does not necessitate prior knowledge of specific system dynamics.

The approach we have developed represents, to the best of our knowledge, a novel methodology in the mathematical modeling of corruption dynamics. Unlike traditional approaches focused on achieving equilibrium or optimization, our method prioritizes the design of policies aimed at consistently keeping the number of corrupt individuals below a specified threshold over time.

After first setting a briber's level of C_m, we used a non-stationary technique to find all the starting states where the largest number of bribers at the peak may stay below C_m. We've also found potential answers and offered examples of techniques for managing the highest limit of corrupts at peak and asymptotically reducing the number of corrupts to zero.

The core concept was given using a simple SIR model of corruption dynamics with the honesty rate as a control. On the one hand, our model can be enhanced to be more accurate by defining an upper constraint on the control $\alpha < 1$, preventing a full honesty rate that was either impossible or highly expensive. However, this approach can be utilized in various other models that incorporate different controls.

Inspired by the complexities inherent in corruption studies, the research presents a novel frame-

work for understanding and controlling corruption propagation within societal systems. Initially, a pioneering application of viability theory is demonstrated to ensure the viability of corruption trajectories, addressing challenges of boundedness typically encountered in corruption modeling. Subsequently, the viability-theory-based approach is extended to analyze a broader spectrum of corruption dynamics, encompassing diverse socio-economic contexts and constraints. Furthermore, the practical utility of the proposed methodology is exemplified through its application to real-world scenarios, such as studying corruption within specific sectors or regions. Comparative analyses underscore the effectiveness of the proposed approach in elucidating corruption dynamics and informing evidence-based interventions. Nonetheless, the study acknowledges potential limitations, such as the assumption of viability for certain sets. The accuracy and usefulness of the viability kernel will depend on the quality of the data and models used, and further research is needed to refine the methods and develop more robust approaches. Nevertheless, the viability kernel concept offers a valuable tool for addressing corruption and promoting sustainable development.

Declarations

Use of AI tools

The authors declare that they have not used Artificial Intelligence (AI) tools in the creation of this article.

Data availability statement

No Data associated with the manuscript.

Ethical approval (optional)

The authors state that this research complies with ethical standards. This research does not involve either human participants or animals.

Consent for publication

Not applicable

Conflicts of interest

The authors declare that they have no conflict of interest.

Funding

No funding was received for this research.

Author's contributions

H.A.: Methodology, Conceptualization, Validation, Software, Data Curation, Writing - Original Draft. M.E.K.: Writing-Review Editing, Supervision. All authors have read and agreed to the published version of the manuscript.

Acknowledgements

Not applicable

References

[1] Rodriguez, D. and Ehrichs, L. *Global Corruption Report 2007: Corruption Judicial Systems*. Cambridge University Press: United Kingdom, (2007).

[2] Transparency International. *Corruption Perceptions Index*. (2021). https://www.transparency.org/en/cpi/2020

[3] Adeyeye, A.O. *Corporate Social Responsibility of Multinational Corporations in Developing Countries: Perspectives on Anti-Corruption*. Cambridge University Press: Cambridge, (2012).

[4] Baleanu, D., Hasanabadi, M., Vaziri, A.M. and Jajarmi, A.A new intervention strategy for an HIV/AIDS transmission by a general fractional modeling and an optimal control approach. *Chaos, Solitons & Fractals*, 167, 113078, (2023). [CrossRef]

[5] Baleanu, D., Arshad, S., Jajarmi, A., Shokat, W., Ghassabzade, F.A. and Wali, M. Dynamical behaviours and stability analysis of a generalized fractional model with a real case study. *Journal of Advanced Research*, 48, 157-173, (2023). [CrossRef]

[6] Monteduro, F., D'Onza, G. and Mussari, R. Corruption spreads: understanding interorganizational corruption contagion in municipal governments. *International Journal of Public Sector Management*, 37(1), 108-123, (2024). [CrossRef]

[7] Abdulrahman, S. Stability analysis of the transmission dynamics and control of corruption. *Pacific Journal of Science and Technology*, 15(1), 99-113, (2014).

[8] Lemecha, D.L. Modelling corruption dynamics and its analysis. *Ethiopian Journal of Science and Sustainable Development*, 5(2), 13-27, (2019). [CrossRef]

[9] Alemneh, H.T. Mathematical modeling, analysis, and optimal control of corruption dynamics. *Journal of Applied Mathematics*, 2020(1), 5109841, (2020). [CrossRef]

[10] Blanchini, F. Set invariance in control. *Automatica*, 35(11), 1747-1767, (1999). [CrossRef]

[11] Aubin, J.P. *Viability Theory*. Birkhauser: Berlin, (1991).

[12] Chen, Z. and Gao, Y. Determining the viable unbounded polyhedron under linear control systems. *Asian Journal of Control*, 16(5), 1561-1567, (2014). [CrossRef]

[13] Gao, Y. Viability criteria for differential inclusions. *Journal of Systems Science and Complexity*, 24, 825-834, (2011). [CrossRef]

[14] Panagou, D. and Kyriakopoulos, K.J. Viability control for a class of underactuated systems. *Automatica*, 49(1), 17-29, (2013). [CrossRef]

[15] Gao, Y., Lygeros, J., Quincampoix, M. and Seube, N. On the control of uncertain impulsive systems: approximate stabilization and controlled invariance. *International Journal of Control*, 77(16), 1393-1407, (2004). [CrossRef]

[16] Lou, Z.E. and Gao, Y. The exponential stability for a class of hybrid systems. *Asian Journal of Control*, 15(2), 624-629, (2013). [CrossRef]

[17] Gao, Y., Lygeros, J. and Quincampoix, M. On the reachability problem for uncertain hybrid systems. *IEEE Transactions on Automatic Control*, 52(9), 1572-1586, (2007). [CrossRef]

[18] Quincampoix, M. and Seube, N. Stabilization of uncertain control systems through piecewise constant feedback. *Journal of Mathematical Analysis and Applications*, 218(1), 240-255, (1998). [CrossRef]

[19] Cardaliaguet, P., Quincampoix, M. and Saint-Pierre, P. Differential games through viability theory: Old and recent results. In *Advances in Dynamic Game Theory: Numerical Methods*,

Algorithms, and Applications to Ecology and Economics (pp. 3-35). Boston: Birkhäuser Boston, (2007). [CrossRef]

[20] Kaynama, S., Mitchell, I.M., Oishi, M. and Dumont, G.A. Scalable safety-preserving robust control synthesis for continuous-time linear systems. *IEEE Transactions on Automatic Control*, 60(11), 3065-3070, (2015). [CrossRef]

[21] Ivanov, D. and Keskin, B.B. Post-pandemic adaptation and development of supply chain viability theory. *Omega*, 116, 102806, (2023). [CrossRef]

[22] Karacaoglu, G. and Krawczyk, J.B. Public policy, systemic resilience and viability theory. *Metroeconomica*, 72(4), 826-848, (2021). [CrossRef]

[23] Kregel, J.A. The viability of economic policy and the priorities of economic policy. *Journal of Post Keynesian Economics*, 17(2), 261-277, (1994). [CrossRef]

[24] Mathias, J.D., Bonté, B., Cordonnier, T. and de Morogues, F. Using the viability theory to assess the flexibility of forest managers under ecological intensification. *Environmental Management*, 56, 1170-1183, (2015). [CrossRef]

[25] Béné, C. and Doyen, L. Contribution values of biodiversity to ecosystem performances: A viability perspective. *Ecological Economics*, 68(1-2), 14-23, (2008). [CrossRef]

[26] Bouguerra, M.A., Fraichard, T. and Fezari, M. Viability-based guaranteed safe robot navigation. *Journal of Intelligent & Robotic Systems*, 95, 459-471, (2019). [CrossRef]

[27] Zarch, M.G., Puig, V., Poshtan, J. and Shoorehdeli, M.A. Actuator fault tolerance evaluation approach of nonlinear model predictive control systems using viability theory. *Journal of Process Control*, 71, 35-45, (2018). [CrossRef]

[28] De Lara, M. and Salcedo, L.S.S. Viable control of an epidemiological model. *Mathematical Biosciences*, 280, 24-37, (2016). [CrossRef]

[29] Salcedo, L.S.S. and De Lara, M. Robust viability analysis of a controlled epidemiological model. *Theoretical Population Biology*, 126, 51-58, (2019). [CrossRef]

[30] Aubin, J.P. and Doss, H. A non-stochastic approach for modeling uncertainty in population dynamics. *Stochastic Analysis and Applications*, 21(5), 955-981, (2003). [CrossRef]

Mathematical Modelling and Numerical Simulation with Applications (MMNSA)
(https://dergipark.org.tr/en/pub/mmnsa)

How to cite this article: Abou-nouh, H. & Khomssi, M.E. (2025). Towards a viable control strategy for a model describing the dynamics of corruption. *Mathematical Modelling and Numerical Simulation with Applications*, 5(1), 1-17. https://doi.org/10.53391/mmnsa.1400075

Mathematical Modelling and Numerical Simulation with Applications, 2025, 5(1), 18–37

https://dergipark.org.tr/en/pub/mmnsa
ISSN Online: 2791-8564 / Open Access
https://doi.org/10.53391/mmnsa.1525113

RESEARCH PAPER

Optimizing shellfish aquaculture in nitrogen and fisheries management

Temesgen B. Getahun [1,‡], **Worku T. Bitew** [2,*,‡], **Tsegaye G. Ayele** [3,‡] and **Simon D. Zawka** [1,‡]

[1]Arba Minch University, Department of Mathematics, Arba Minch, Ethiopia, [2]State University of New York, Department of Mathematics, Farmingdale, NY, USA, [3]Addis Ababa University, Department of Mathematics, Addis Ababa, Ethiopia

*Corresponding Author
‡temesgen.berhanu@amu.edu.et (Temesgen B. Getahun); biteww@farmingdale.edu (Worku T. Bitew); tsegaye.ayele@aau.edu.et (Tsegaye G. Ayele); simon.derke@amu.edu.et (Simon D. Zawka)

Abstract

Water quality and the invasion of weeds due to nutrient eutrophication have been a concern in major lakes and coastal areas. Scholars have advocated the cultivation of some species of shellfish as a new potential to facilitate the bioremediation of the polluted environment due to excessive nutrients. In this paper, our objective is to determine the optimal area that must be dedicated to shellfish aquaculture relative to the level of nitrogen pollution, other fisheries activities, and the performance of wild catch. The optimal size also depends on the effort outside the water body to control pollution from the point source. We set up transition equations that describe the system's state based on pollution reduction efforts, nitrogen concentration level, and the size of shellfish cultivation. We show that the impact of the nitrogen concentration level in the habitat can be minimized by allocating optimal management efforts to reduce nitrogen waste from the source and setting aside an area for shellfish cultivation. We found the optimal steady-state solutions and analyzed the optimal solutions based on biological and economic parameters.

Keywords: Nitrogen pollution; shellfish aquaculture; space allocation; fisheries management; optimal effort

AMS 2020 Classification: 49N90; 90C90; 91A80; 93C95

1 Introduction

An aquatic ecosystem enriched with nutrients like nitrogen creates conducive conditions for algae and similar species that utilize these nutrients. Nitrogen pollution has been one of the primary threats to coastal water quality [1]. Deterioration in water quality due to excessive nutrient

➤ **Received:** 31.07.2024 ➤ **Revised:** 12.12.2024 ➤ **Accepted:** 24.01.2025 ➤ **Published:** 31.03.2025

loading from diffuse sources has become a major environmental problem in lakes, reservoirs, and coastlines mainly close to urban areas [2–4]. It is common to observe a substantial increase in the algal population on the surface of eutrophic waters (algal bloom). Algal blooms hinder the flow of sunlight and cause a decline in the dissolved oxygen level in the water. This, in turn, causes many marine animals to suffocate and die, creating "dead zones" [5].

The eutrophication of surface waters due to excessive nitrogen upsets the natural balance of aquatic ecosystems [6, 7]. Eutrophication can also seriously affect our ability to use water for recreation, drinking, agriculture, industry, and other purposes [8]. As part of a water quality management program, governmental regulations and marine policies increasingly require nitrogen remediation practices for industrial and residential wastes. The U.S. Environmental Protection Agency (EPA) developed guidelines to identify at-risk surface water bodies and protect them from eutrophication, stating that nitrogen concentrations should not exceed 0.3 mg per liter in streams and rivers and 0.1 mg per liter in lakes and reservoirs [9]. The public has considered eutrophication through waste management as a worthwhile investment for restoring and preserving freshwater lakes and reservoirs while cleaning coastal areas [10].

Shellfish aquaculture reduces coastal eutrophication by assimilating and storing excess nutrients, facilitating the natural denitrification rates when harvested [11, 12]. The optimizing process involves strategically placing shellfish farms in areas with high nutrient levels to leverage their filter-feeding behavior, thereby improving water quality by removing excess nitrogen and phosphorus while producing farmed seafood products, contributing to overall ecosystem health and sustainable fisheries management goals. In [11–13], the authors studied how excess nutrients can be removed from the marine environment when shellfish cultures are harvested. Mykoniatis and Ready in [14] studied the potential contribution of oysters to water quality goals in the fisheries management of Chesapeake Bay, USA. They developed a bioeconomic model of oysters in the bay area that considers the value of oyster harvests, the cost of fishing effort, and the removal of nitrogen from the bay through harvest and denitrification. In [15], they also studied the effects of oyster aquaculture on local water quality. The study investigated how water quality and hydrodynamics varied among farms and inside versus outside the vicinity of caged grow-out areas in southern Chesapeake Bay.

The development of a model that links water body nutrient concentration to its impact on the environment and water quality is a vital component of the management of fisheries in polluted areas. For our study, in the environment under consideration, we assumed nitrogen is the primary source of nutrient enrichment that affects the livelihood of the fish species, degrades the carrying capacity of the habitat, and affects the growth rate of the fish stock. We mainly focus on nutrient reduction efforts from various external sources and the introduction of shellfish cultivation in polluted areas to facilitate nutrient and fisheries management efforts. Since Shellfish store excess nutrients, we assume that the amount of nitrogen removed by shellfish is proportional to the production function or the size of the aquaculture area [11–13]. Moreover, we assume that the positive impact of shellfish on the fish stock can be measured through the growth rate. In this paper, we determine the optimal efforts and the area that must be dedicated to shellfish aquaculture for sustainable environmental and fisheries management. We also attempt to determine the optimal wild fish harvest dependent on the state of the ecosystem.

In the next section, we presented the model and performed a stability analysis of the steady-state solutions. In Section 3, we set up the control version of the model to determine the best trajectory for the actions and recovery rate of the system so that the overall social return from the aquatic ecosystem is maximum. This enables us to determine the optimal harvesting level, shellfish cultivation volume, and the best practice of the management's nitrogen removal rate from the source. In Section 4, we presented the policy implications of the results and the paper's conclusion.

2 Model formulation

In this section, we will set up the dynamic or transition equations of the fish stocks under different scenarios and analyze the systems at the steady state. In Section 2, we present the transition equation of open-access capture fish stock in the presence of nitrogen pollution before the introduction of shellfish aquaculture. In this case, we assume that the main cause of negative externality to the fishing ground is related to the nitrogen concentration level in the water and harvest. Then, in Section 2, we assume the development of shellfish aquaculture and consider the positive impact of shellfish cultivation on the fishing ground that would be reflected through the growth rate of the fish stock. In Section 2, we present a comparative analysis of the long-run behavior of the two systems.

Open access capture fish and nitrogen dynamics

Nitrogen dynamics

We assume that without effective pollution control actions, a large portion of the nitrogen from the vicinity, W, has the potential of reaching water bodies in the area and polluting the environment [14, 16]. Suppose $L(m, W) = (1-m)W$ is the external rate of nitrogen loading to the water bodies (lakes, reservoirs, or coastal area), where m is a control variable that represents the management's effort to reduce m portion of the nitrogen from the source, where $0 \leq m < 1$. For simplicity, we ignore nitrogen recycling (internal loading) and focus only on elements of nitrogen dynamics because of external sources and internal denitrification [14, 16]. In this case, we describe the dynamics of the nitrogen volume by

$$\frac{dN}{dt} = L(m, W) - \alpha N, \qquad N(0) = N_0 > 0,$$

where α is the natural decay rate.

To align the model to our density-based analysis, we divide both sides of the equation by the total area under consideration, T, and get the concentration of nitrogen equation

$$\frac{dn}{dt} = (1-m)w - \alpha n, \qquad n(0) = n_0 > 0,$$

where $w = \dfrac{W}{T}$ and $n = \dfrac{N}{T}$ are the amounts of nitrogen loading per unit area and surface densities of nitrogen in the area, respectively.

Capture fishery stock dynamics

We assume nitrogen loading is a source of pollution and causes environmental degradation [1, 17]. It damages the habitat and changes the ecological makeup of the system. The improvement or degradation of the habitat directly affects the carrying capacity of the habitat and the growth rate of fish biomass [18]. In a polluted environment of an aquatic ecosystem, the habitat's carrying capacity and the growth rate of fish stock depend on the pollution level [19, 20]. Like [21], we assume that the open-access carrying capacity and growth rate of fish stock depend on the extent of pollution (i.e., the nitrogen concentration level) [18–22]. Therefore, we describe the transition equation of the stock as

$$\frac{dX}{dt} = r(n)\left(1 - \frac{X}{K(n)}\right)X - H(X, E), \qquad X(0) = X_0 > 0,$$

where $H(X,E) = \sigma EX$ is the harvest rate from the capture fishery for stock size X, effort level, E, and catchability coefficient, σ, and $K(n) = K - \Theta n > 0$ and $r(n) = r - \varepsilon_1 n > 0$, where Θ measures the impact of nitrogen on the carrying capacity of the habitat, K, r is the intrinsic growth rate, ε_1 is the measure of the impact of nitrogen on the growth rate. If we scale down the above equation by dividing both sides of the equation by the total carrying capacity, K, we get:

$$\frac{dx}{dt} = (r - \varepsilon_1 n)\left(1 - \frac{x}{1-\theta n}\right)x - \sigma E x, \qquad x(0) = x_0 > 0, \tag{1}$$

where $\theta = \dfrac{\Theta}{K}$, $0 < r - \varepsilon_1 n < r$, provided $r - \varepsilon_1 n - \sigma E > 0$, and $1 - \theta n > 0$.

Thus, the dynamic system of equations of density of fish stock and nitrogen concentration is

$$\begin{aligned} \frac{dn}{dt} &= (1-m)w - \alpha n, \qquad n(0) = n_0 > 0, \\ \frac{dx}{dt} &= (r - \varepsilon_1 n)\left(1 - \frac{x}{1-\theta n}\right)x - \sigma E x, \qquad x(0) = x_0 > 0. \end{aligned} \tag{2}$$

Steady-state solutions and stability

In the steady state $\dfrac{dn}{dt} = \dfrac{dx}{dt} = 0$, this implies the critical points of the above system, Eq. (2), are

$$(n_1^*, x_1^*) = \left(\frac{(1-m)w}{\alpha}, 0\right),$$

and

$$(n_2^*, x_2^*) = \left(\frac{(1-m)w}{\alpha}, \left(1 - \frac{\theta(1-m)w}{\alpha}\right)\left(1 - \frac{\alpha\sigma E}{\alpha r - \varepsilon_1(1-m)w}\right)\right),$$

provided that $\alpha > \theta(1-m)w$, the decay rate of nitrogen concentration in the lake should be greater than θ times the external nitrogen loading rate to the water body, and $\alpha r - \varepsilon_1(1-m)w - \alpha\sigma E > 0$.

To determine the stability of the equilibrium solutions, we first need to derive the Jacobian matrix of the dynamic system in Eq. (2)

$$J(n,x) = \begin{pmatrix} \frac{(r-\varepsilon_1 n)(1-2x-\theta n) - \sigma E(1-\theta n)}{1-\theta n} & -\frac{x\left(rx\theta + \left((1-\theta n)^2 - x\right)\varepsilon_1\right)}{(1-\theta n)^2} \\ 0 & -\alpha \end{pmatrix}.$$

Since the eigenvalues of a triangular matrix equal the values on its diagonal, the eigenvalues of the Jacobian matrix are

$$\lambda_1 = -\alpha,$$

and

$$\lambda_2 = \frac{(1-2x-\theta n)(r-\varepsilon_1 n) - \sigma E(1-\theta n)}{1-\theta n}.$$

The Jacobian matrix at the first critical point, (n_1^*, x_1^*), is

$$J(\cdot) = \begin{pmatrix} r - \varepsilon_1 n - \sigma E & 0 \\ 0 & -\alpha \end{pmatrix}.$$

Observe that $Tr(J) = r - \varepsilon_1 n - \sigma E - \alpha$ and $det(J) = -\alpha(r - \varepsilon_1 n - \sigma E)$. Since $det(J) < 0$, by the Theorem (5.4) in [23], the dynamic system in Eq. (2) is unstable at the critical point

$$(n_1^*, x_1^*) = \left(\frac{(1-m)w}{\alpha}, 0\right).$$

The Jacobian matrix at the second critical point, (n_2^*, x_2^*), is

$$J(\cdot) = \begin{pmatrix} A_{11} & A_{12} \\ 0 & -\alpha \end{pmatrix},$$

where $A_{11} = -(r - \varepsilon_1 n - \sigma E)$, and $A_{12} = -\left(1 - \frac{\sigma E}{r - \varepsilon_1 n}\right)\left[\left(1 - \frac{\sigma E}{r - \varepsilon_1 n}\right)(r\theta - \varepsilon_1) + \varepsilon_1(1 - \theta n)\right]$.

Observe that

$$Tr(J) = -(\alpha + r - \varepsilon_1 n - \sigma E) < 0,$$

and

$$det(J) = \alpha(r - \varepsilon_1 n - \sigma E) > 0,$$

at $n = n_2^*$. This implies that the dynamic system Eq. (2) is locally asymptotically stable at the second critical point [23].

Therefore, the stable steady-state nitrogen concentration level is

$$n_s(m) = \frac{(1-m)w}{\alpha}. \tag{3}$$

It is apparent from Eq. (3) that the nitrogen concentration is the ratio of the amount of nitrogen reaching the water bodies to the natural decay rate. The concentration decreases when the rate of nitrogen reduction efforts from the source increases. It also decreases when the natural decay rate increases.

And the equilibrium stock size, x_s, as a function of wild catch effort, E, and m is

$$x_s(E, m) = \left(1 - \frac{\theta(1-m)w}{\alpha}\right)\left(1 - \frac{\alpha\sigma E}{\alpha r - \varepsilon_1(1-m)w}\right) = (1 - \theta n_s(m))\left(1 - \frac{\sigma E}{r - \varepsilon_1 n_s(m)}\right). \tag{4}$$

The above equation, Eq. (4), implies that capture fish effort and nitrogen concentration negatively impact the stock of captured fish. However, the allocation of management's effort for nitrogen reduction from the source positively impacts the steady state stock size. The corresponding

steady-state or sustainable yield

$$h_s(E,m) = \sigma E(1-\theta n_s(m))\left(1-\frac{\sigma E}{r-\varepsilon_1 n_s(m)}\right). \tag{5}$$

The maximum sustainable yield (MSY) is attained at the effort level E such that $\frac{\partial h_s(E,m)}{\partial E} = 0$. That is at

$$E_{MSY}(m;r,\sigma) = \frac{1}{2\sigma}(r-\varepsilon_1 n_s(m)). \tag{6}$$

From Eq. (6), the critical effort level is negatively impacted by the nitrogen concentration; the higher the impact, the lower the effort. Then, the value of MSY, h_{MSY}, at this effort can be found by substituting $E = E_{MSY}$ into Eq. (5)

$$h_{MSY}(m) = \frac{(1-\theta n_s(m))(1-\varepsilon_1 n_s(m))}{4},$$

and the biomass level at the MSY is

$$x_{MSY}(m) = \frac{(1-\theta n_s(m))}{2}.$$

The steady-state net profit, $P_s(E,m) = ph_s(E,m) - cE$, where p is a competitive market price and c is the cost per unit effort per unit area assumed to be constants, attains its maximum at an effort level E such that

$$\frac{\partial P_s(E,m)}{\partial E} = 0.$$

That is, the sustainable effort that maximizes profit (MSP),

$$E_{MSP}(m;r,\sigma,c,p) = \frac{1}{2\sigma}(r-\varepsilon_1 n_s(m))\left(1-\frac{c}{p\sigma(1-\theta n_s(m))}\right), \tag{7}$$

is positive provided that $c < p\sigma(1-\theta n_s(m))$. Observe that $E_{MSP} < E_{MSY}$. By plugging Eq. (7), with $E = E_{MSP}$, into Eq. (5), the harvest level that maximizes revenue, h_{MSP}, is

$$h_{MSP}(m) = \frac{(1-\theta n_s(m))(1-\varepsilon_1 n_s(m))}{4}\left(1-\frac{c^2}{p^2\sigma^2(1-\theta n_s(m))^2}\right),$$

and the corresponding biomass level is

$$x_{MSP}(m) = \frac{(1-\theta n_s(m))}{2}\left(1+\frac{c}{p\sigma(1-\theta n_s(m))}\right).$$

From Eq. (3), the nitrogen level, $n_s(m)$, decreases with the increment of management's effort, m. The reduction of nitrogen concentration positively impacts the growth rate of the stock, $r-\varepsilon_1 n_s(m)$, and the carrying capacity, $1-\theta n_s(m)$, which in turn results in relaxing the restrictions on the optimal effort (i.e., management's effort allocation is directly related to the effort level that

maximizes the profit). For example, we numerically solve the system for $\theta = 0.10$ and $\varepsilon_1 = 0.085$, and find the stock size and the corresponding effort that maximizes revenue, $x_{MSP} = 0.574167$ and $E_{MSP} = 45.3789$, respectively. Moreover, if we assume that the nitrogen concentration level degrades the environment more than expected, say $\theta = 0.11$ and $\varepsilon_1 = 0.086$, the stock size decreases to $x_{MSP} = 0.571166$, and the optimal catch effort reduces to $E_{MSP} = 45.2804$. The effort level is inversely related to the measures of the impact of nitrogen concentration on the carrying capacity, θ, and on the intrinsic growth rate, ε_1. Moreover, the effort level is determined not only by biological and impact factors but also by the profitability of the shellfish aquaculture, which depends on the cost of production and market price relation, $c < p\sigma(1-\theta n_s(m))$. This condition is hard to achieve, especially at the beginning of the investment. Therefore, private investors would participate in the remediation effort if we subsidized them until their revenue becomes larger than the cost of production. This helps to maintain a sustainable environment and supply of farmed shellfish and, at the same time, supports the economy by creating jobs.

Even though the degradation of the aquatic ecosystem and the decline in water quality from excessive nitrogen can primarily be minimized by reducing external nitrogen loading, it is important to implement an effort-limiting policy that helps the recovery of the environment. In Figure 1, we sketched the effort that maximizes the rent and the corresponding stock size. Both decrease with the increase in pollution.

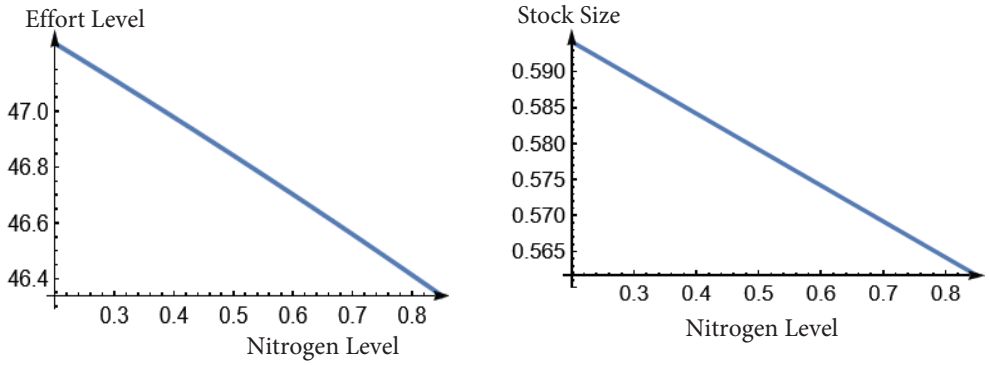

Figure 1. Effort level, E_{MSP}, and the stock size, x_{MSP}, as a function of nitrogen pollution level

Capture fish, nitrogen concentration, and shellfish aquaculture

Regardless of policies and regulatory measures intended to reduce external nitrogen loading, more nitrogen loading from a non-point source is inevitable [1]. Shellfish aquaculture has been considered an alternative to reduce the nitrogen level in water bodies because a significant amount of nitrogen is embedded in shellfish meat and shells. Shellfish also reduce the nitrogen through its denitrification process [14, 24].

Shellfish aquaculture dynamics

Suppose A is the size of the area dedicated to shellfish aquaculture production from the total polluted area under consideration, T. Like [25], we assume the aquaculture expansion rate depends on the relative size of the aquaculture, a, and the magnitude of nitrogen pollution, n,

$$\frac{da}{dt} = \left(v - \rho\frac{a}{n}\right), \qquad a(0) = a_0 \geq 0,$$

where $a = \frac{A}{T}$ is the portion of the area dedicated to aquaculture, v is exogenous control variable determined by the management and ρ is a conversion factor provided $\rho a \leq vn$.

Nitrogen dynamics

Let the amount of nitrogen removed by the shellfish production be proportional to the size of the aquaculture area [21]. Hence, let βan be the reduction rate of the nitrogen concentration due to shellfish, where β is a conversion constant. Let α be the natural rate of nitrogen decay through processes other than the amount removed by shellfish cultivation [14, 16]. Following [14, 16], we extend the dynamic equation of nitrogen from section 2.1 as

$$\frac{dn}{dt} = (1-m)w - \beta an - \alpha n, \qquad n(0) = n_0 > 0.$$

Capture fishery stock dynamics

As mentioned earlier, nitrogen contributes to environmental degradation and reduces the carrying capacity of the habitat as well as the growth rate of the fish stock [18–20]. We assume that its impact depends on the concentration level of nitrogen in the environment, n. Although aquaculture development takes away fishing areas and has some negative externalities on the environment, shellfish farming has a net positive effect. It helps filter the nitrogen and clean the water, improving the stock's growth rate. Therefore, we assume that the per-capita growth rate of the fishery decreases with nitrogen concentration level and increases with shellfish aquaculture size, a. Hence, we set up the transition equation of the stock as

$$\frac{dX}{dt} = r(n,a)\left(1 - \frac{X}{K(n)}\right)X - H(X,E), \qquad X(0) = X_0 > 0,$$

where $H(X,E) = \sigma EX$ is the harvest rate from the capture fishery from a multi-species stock size X, E is the effort level and σ is the catchability coefficient, $r(n,a) = r - \varepsilon_1 n + \varepsilon_2 a$, and $K(n) = K - \Theta n > 0$, where Θ is the measures of the nitrogen level on the environment and ε_2 is the measure of the impact of aquaculture on the growth rate.

If we scale down the above equation by dividing both sides of the equation by the total carrying capacity, K, we get:

$$\frac{dx}{dt} = (r - \varepsilon_1 n + \varepsilon_2 a)\left(1 - \frac{x}{1-\theta n}\right)x - \sigma Ex, \qquad x(0) = x_0 > 0,$$

where $\theta = \frac{\Theta}{K}$, provided $0 < r - \varepsilon_1 n + \varepsilon_2 a \leq r$, $r - \varepsilon_1 n + \varepsilon_2 - \sigma E > 0$, and $1 - \theta n > 0$.

The equations aligned for fish stock, nitrogen concentration, and shellfish aquaculture are

$$\begin{aligned}
\frac{dx}{dt} &= (r - \varepsilon_1 n + \varepsilon_2 a)\left(1 - \frac{x}{1-\theta n}\right)x - \sigma Ex, \qquad x(0) = x_0 > 0,\\
\frac{dn}{dt} &= (1-m)w - \beta an - \alpha n, \qquad n(0) = n_0 > 0,\\
\frac{da}{dt} &= \left(v - \rho\frac{a}{n}\right), \qquad a(0) = a_0 \geq 0.
\end{aligned} \tag{8}$$

Stability of the steady-state solutions

In steady state $\frac{dx}{dt} = \frac{dn}{dt} = \frac{da}{dt} = 0$, implies the critical points of the above system are

$$(x_1^*, n_1^*, a_1^*) = \left(0, \frac{S(v,m) - \alpha\rho}{2v\beta}, \frac{1}{\beta}\left(\frac{2vw\beta(1-m)}{S(v,m) - \alpha\rho} - \alpha\right)\right),$$

and

(x_2^*, n_2^*, a_2^*), where

$$x_2^* = \left(1 - \frac{\theta(S(v,m) - \alpha\rho)}{2v\beta}\right)\left(1 - \frac{E\sigma}{r - \varepsilon_1\left(\frac{S(v,m) - \alpha\rho}{2v\beta}\right) + \varepsilon_2\frac{1}{\beta}\left(\frac{2vw\beta(1-m)}{S(m,v) - \alpha\rho} - \alpha\right)}\right),$$

$$n_2^* = \frac{S(v,m) - \alpha\rho}{2v\beta}, \text{ and } a_2^* = \frac{1}{\beta}\left(\frac{2vw\beta(1-m)}{S(v,m) - \alpha\rho} - \alpha\right),$$

and $S(v,m) = \sqrt{\alpha^2\rho^2 + 4\rho\beta(1-m)wv}$.

To determine the stability of the equilibrium, we derive the Jacobian matrix of the system

$$J(\cdot) = \begin{pmatrix} A_{11} & A_{12} & A_{13} \\ 0 & -(\alpha + \beta a) & -\beta n \\ 0 & \frac{\rho a}{n^2} & -\frac{\rho}{n} \end{pmatrix},$$

where

$$\begin{aligned} A_{11} &= \frac{(1 - \theta\,\mathrm{n} - 2x)(r - \varepsilon_1 n + \varepsilon_2 a)}{1 - \theta\mathrm{n}} - \sigma E, \\ A_{12} &= \frac{x\left(-\theta x(r + \varepsilon_2 a) + \varepsilon_1\left(x - (1 - \theta n)^2\right)\right)}{(1 - \theta n)^2}, \\ A_{13} &= \frac{\varepsilon_2 x(1 - x - \theta n)}{1 - \theta n}. \end{aligned}$$

Then, we evaluate the eigenvalues of the Jacobian matrix at each critical point. The eigenvalues at the first critical point, (x_1^*, n_1^*, a_1^*), are

$$\lambda_1^1 = \frac{-(\alpha n + \beta a n + \rho) - \sqrt{(\alpha n + \beta a n + \rho)^2 - 4n(\alpha\rho + 2\beta\rho a)}}{2n},$$

$$\lambda_2^1 = \frac{-(\alpha n + \beta a n + \rho) + \sqrt{(\alpha n + \beta a n + \rho)^2 - 4n(\alpha\rho + 2\beta\rho a)}}{2n},$$

and

$$\lambda_3^1 = r - \varepsilon_1 n + \varepsilon_2 a - \sigma E.$$

Since $r-\varepsilon_1 n+\varepsilon_2 a-\sigma E$ has to be positive (otherwise the stock become extinct), the trivial equilibrium is not stable [26]. And the eigenvalues of the Jacobian matrix at the second critical point, (x_2^*, n_2^*, a_2^*), are

$$\lambda_1^2=\frac{-(\alpha n+\beta a n+\rho)-\sqrt{(\alpha n+\beta a n+\rho)^2-4n(\alpha\rho+2\beta\rho a)}}{2n},$$

$$\lambda_2^2=\frac{-(\alpha n+\beta a n+\rho)+\sqrt{(\alpha n+\beta a n+\rho)^2-4n(\alpha\rho+2\beta\rho a)}}{2n},$$

and

$$\lambda_3^2=-(r-\varepsilon_1 n+\varepsilon_2 a-\sigma E).$$

In this case, all of the eigenvalues are negative, implying the dynamic system is stable at the critical point (x_2^*, n_2^*, a_2^*) [26].
Therefore, the stable steady-state nitrogen concentration and shellfish aquaculture size in terms of the control variables, m and v, are

$$n_s(m,v)=\frac{\sqrt{4\beta\rho(1-m)wv+\alpha^2\rho^2}-\alpha\rho}{2\beta v}=\frac{(1-m)w}{\alpha+\beta a_s(m,v)}, \tag{9}$$

and

$$a_s(m,v)=\frac{1}{\beta}\left(\frac{2vw\beta(1-m)}{\sqrt{4\beta\rho(1-m)wv+\alpha^2\rho^2}-\alpha\rho}-\alpha\right)=\frac{1}{\beta}\left(\frac{(1-m)w}{n_s(m,v)}-\alpha\right). \tag{10}$$

From Eq. (9), the nitrogen concentration decreases when the production of shellfish or external effort increases. We can also observe from Eq. (10) that shellfish aquaculture size is positive whenever $(1-m)w\geq\alpha n_s(m,v)$.
Then the steady-state stock of fish, x_s, can be written in terms of aquaculture and nitrogen concentration (both depend on m and v) as

$$x_s(m,v,E)=(1-\theta n_s(m,v))\left(1-\frac{\sigma E}{r-\varepsilon_1 n_s(m,v)+\varepsilon_2 a_s(m,v)}\right). \tag{11}$$

From Eq. (11) the equilibrium stock size decreases as the nitrogen concentration or fishing effort increases. However, it increases when the production of shellfish aquaculture or the impact factor, ε_2, on the habitat increases. This implies that even though aquaculture takes away the fishing area and creates pressure in the open-access fishing ground, shellfish aquaculture has a net positive impact on the stock. The corresponding sustainable yield is given by

$$h_s(m,v,E)=\sigma E(1-\theta n_s(m,v))\left(1-\frac{\sigma E}{r-\varepsilon_1 n_s(m,v)+\varepsilon_2 a_s(m,v)}\right),$$

where $n_s(m,v)$ and $a_s(m,v)$ are give by Eqs. (9) and (10).
The maximum sustainable yield (MSY), the largest yield or catch that can be potentially taken

from the stock, is attained at effort level E such that $\frac{\partial h_s}{\partial E}(E, v, m) = 0$. Solving $\frac{\partial h_s}{\partial E}(E, m, v) = 0$ for E, we find the maximum sustainable effort,

$$E_{MSY}(m, v) = \frac{1}{2\sigma}(r - \varepsilon_1 n_s(m, v) + \varepsilon_2 a_s(m, v)). \tag{12}$$

Eq. (12) reveals that if the size of aquaculture farming is fixed and the nitrogen concentration increases, the maximum sustainable effort must be reduced.
We can also solve the equation

$$\frac{\partial(p h_s(m, v, E) - cE)}{\partial E} = 0,$$

to find the effort level that maximizes the net economic rent from wild catch,

$$E_{MSY}(m, v) = \frac{1}{2\sigma}(r - \varepsilon_1 n_s(m, v) + \varepsilon_2 a_s(m, v)) \left(1 - \frac{c}{\sigma p\,(1 - \theta n_s(m, v))}\right). \tag{13}$$

From Eqs. (12) and (13), the optimal effort level is less than the maximum sustainable effort provided $c < \sigma p(1 - \theta n_s)$. Moreover, in Eq. (13), when excessive nitrogen concentration in the aquatic ecosystem, n_s, is reduced, the stock in the fishing ground, x_s, gets better. The increment of fish stock enables us to relax restrictions imposed on the effort, E_{MSY}, and harvest more fish. Observe that E_{MSY} is directly related to the size of the aquaculture. The development of shellfish aquaculture must be encouraged, besides controlling nitrogen loading from the source when the aquatic ecosystem becomes excessively enriched with nitrogen.

Numerical solutions and sensitivity analysis

In this section, we investigate the impact of introducing the shellfish farm in a polluted environment and perform a sensitivity analysis. Like [27], we develop a deterministic bioeconomic model that describes the transition dynamics and interrelationships of the systems using parameters. Then, sensitivity analysis of the optimal solutions is investigated by assigning different values for significant biological parameters and performance measures (in Table 2, the changes in parameter values are highlighted in bold). Some of the values are taken from [28], and we choose reasonable values for the other parameters based on the conditions we impose on the model. Using values from Table 1, we numerically solve for the optimal solutions and report the results in Table 2.

Table 1. Parameters and their values used for the stability of the system

Parameter	Description	Value	Unit
r	Growth rate parameter	1.8	1/year
σ	Catchability coefficient per unit effort	0.015	1/vessel/year
α	The natural decay rate of nitrogen	0.6, 0.65	1/year
β	Conversion factor	3, 4	1/year
ρ	Conversion factor	1	1/year
θ	Measure of the impact of nitrogen on the environment	0.1, 0.11	1/year
ε_1	Measure of the impact of nitrogen on the growth rate	0.085	1/year
ε_2	Measure of the impact of shellfish on the growth rate	.097	1/year
p	Unit price of wild catch in US dollars	15	1/US$

Table 2. Optimal steady-state solutions when nitrogen negatively impacts the environment and shellfish farming benefits the habitat

θ	ε_1	ε_2	β	α	m	a_s	n_s	E_{MSP}	x_{MSP}	h_{MSP}
0.10	0.085	0	0	0.6	0.7	0	0.6000	45.3789	0.574167	0.390826
0.10	0.085	0.097	3	0.6	0.7	0.310366	0.237175	47.4459	0.592308	0.421539
0.10	0.085	0.097	**4**	0.6	0.7	0.27389	0.212319	47.4524	0.593551	0.422481
0.10	0.085	0.097	3	**0.65**	0.7	0.269038	0.208556	47.4534	0.593739	0.422624
0.10	0.085	0.097	3	0.6	**0.75**	0.244961	0.189892	47.4581	0.594672	0.4233

From the steady-state optimal numerical solutions summarized in Table 2:

i) Before the introduction of shellfish aquaculture (when $a = \varepsilon_2 = \beta = 0$), if we manage to reduce the external nitrogen loading by 70%, the nitrogen concentration level in the water would be 0.6 mg.

ii) After the introduction of shellfish aquaculture (when $\varepsilon_2 = 0.097$, $\theta = 0.1$, and $\beta = 3$), the concentration reduces from 0.6 to 0.237175 mg as long as we dedicate 0.31 of the area to the sector and keep the external effort level at $m = 0.70$.

iii) When the conversion constant that determines the reduction rate of nitrogen concentration due to shellfish cultivation, β, increases from 3 to 4, the nitrogen concentration level decreases from .2372 to .2086.

iv) When the natural decay rate, α, increases from 0.6 to 0.65, like the above case, nitrogen concentration decreases while the fish stock size increases.

In general, the development of shellfish aquaculture helps the recovery of the aquatic ecosystem and restores the fish stock. The increment of the fish stock enables us to relax the restriction on the optimal effort. As the rate of nitrogen reduction due to shellfish farming or natural denitrification increases, the optimal aquaculture size reduces, and the fish stock size and the optimal yield increase. In Figure 2, we displayed the state of the stock before and after the introduction of shellfish farming in the environment at any impact level of nitrogen in the area, θ. It shows that the introduction of aquaculture slows the decline of the environment and fish stock.

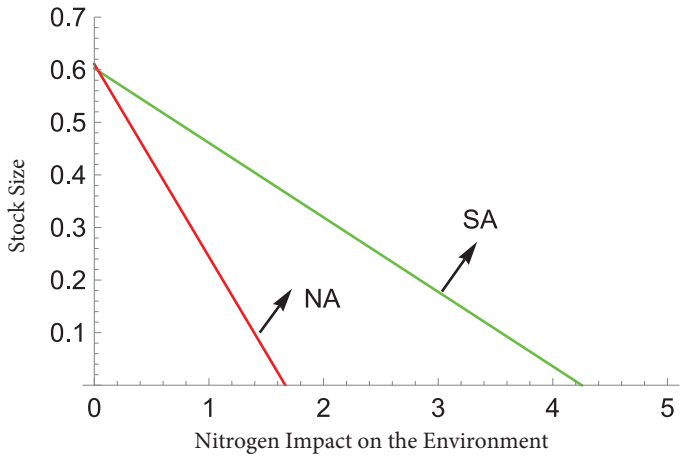

Figure 2. Comparison of stock size of fish (in tonnes), x, at each nitrogen concentration impact level $(1/year)$, θ, before the development of shellfish aquaculture (NA) and after shellfish aquaculture development (SA) for $\sigma = 0.015$, $r = 1.8$, $\alpha = .6$, $\beta = 3$, $m = .7$, $w = 1.2$, and $\theta = .10$

3 Optimized management strategy

In this section, we will consider a control version of the dynamic equations in the previous section, where we determine the asymptotic behavior of the trajectory of the control variables E, m, and v that maximizes the long-run overall benefit from the system. Recent research suggests that improving the quality of water indirectly benefits the community around the coastal line–for example, it appreciates home values near the water bodies [29]. In our optimization model, we only include the economic contributions of shellfish through the supply chain, even though sometimes the net profit may not be positive and needs some type of government subsidy. The primary focus of our research agenda is on the ecological or environmental benefits of shellfish aquaculture.

Let the net profit from capture fishery be $p_1\sigma Ex - cE$, where p_1 is the market price and c is the cost per unit effort per unit area. Suppose the production function for aquaculture is $Z(A) = P_a A$, where P_a is per unit area production of farmed fish in kilograms. We can rewrite the production function in terms of $a = \dfrac{A}{T}$ as $Z(a) = TP_a a$, where T is the surface area of the water under consideration. Let $z(a) = \dfrac{Z(a)}{T}$ and the cost of production is quadratic $c_a(P_a)^2 a$, where c_a is a cost parameter [28]. Then, the net profit from aquaculture is $p_2 Z(a) - C_1(a, v)$, where $C_1(a, v) = c_1\left(v - \rho\frac{a}{n}\right) + c_a(P_a)^2 a$ is a one-time cost of acquiring an extra unit of aquaculture area plus the operation cost for the aquaculture, and p_2 is the competitive market price of a shellfish and c_1 is one time per unit per area leasing cost. If $C_2(m) = c_2 m$ is the cost of removing the pollutant at the source, where c_2 is per unit cost, and all future costs and benefits are discounted at a positive social discount rate of δ, the optimization problem is

$$\max J(E, m, v) = \max_{E,m,v} \int_0^\infty [(p_1\sigma x - c)E + p_2 z(a) - C_1(a, v) - C_2(m)]e^{-\delta t} dt,$$

subject to the dynamic equations in Eq. (8). Thus we seek an optimal control, E^*, v^* , and m^*, and the corresponding states, x^*, a^*, and n^*, that simultaneously solves the equations in Eq. (8) such that

$$J(E^*, m^*, v^*) = \max\{J(E, v, m) |\ (E, v, m) \in U\},$$

where the control set U is compact $U = \{(E(t), v(t), m(t)) |\ 0 \le E(t) \le E_{\max},\ 0 \le m(t) \le m_{\max}, t \in [0, \infty)\}$.

The current-value Hamiltonian corresponding to our problem is

$$\begin{aligned} \mathcal{H}(x, n, a, E, m, v, \lambda_x, \lambda_a, \lambda_n) &= B(x, a, E, v, n, m) + \lambda_x\left[(r - \varepsilon_1 n + \varepsilon_2 a)\left(1 - \frac{x}{1 - \theta n}\right)x - \sigma Ex\right] \\ &+ \lambda_a\left(v - \rho\frac{a}{n}\right) + \lambda_n\Big[(1 - m)w - \beta an - \alpha n\Big], \end{aligned}$$

where $B(x, a, E, v, n, m) = (p_1\sigma x - c)E + p_2 z(a) - C_1(a, v) - C_2(m)$ is the net profit at time t, and λ_x, λ_a and λ_n are the shadow values of the stock, aquaculture, and nitrogen concentration level, respectively.

The optimal control shall be a combination of bang-bang and singular control since the problem under consideration is a linear control problem. Our study focuses on the singular control and the associated optimal singular solutions. The optimality condition for the control variables is to

satisfy

$$\frac{\partial \mathcal{H}(\cdot)}{\partial v} = -c_1 + \lambda_a, \ \frac{\partial \mathcal{H}(\cdot)}{\partial E} = -c + \sigma x(p_1 - \lambda_x), \text{ and } \frac{\partial \mathcal{H}(\cdot)}{\partial m} = -c_3 - w, \tag{14}$$

where the switching functions are

$$\Psi_1(t) = -c_1 + \lambda_a, \ \Psi_2(t) = -c + \sigma x(p - \lambda_x), \text{ and } \Psi_3(t) = -c_3 - w\lambda_n.$$

It is known that in the case of a singular solution, we have

$$\Psi_1(t) = 0, \Psi_2(t) = 0, \text{ and } \Psi_3(t) = 0.$$

That is

$$-c_1 + \lambda_a = 0, \ -c + \sigma x(p - \lambda_x) = 0, \text{ and } -c_3 - w\lambda_n = 0. \tag{15}$$

The adjoint equations corresponding to the states are

$$\begin{aligned}
\frac{d\lambda_a}{dt} - \delta\lambda_a &= -\frac{\partial \mathcal{H}(\cdot)}{\partial a} = -P_a(p_2 - c_a P_a) + \beta\lambda_n n - x\varepsilon_2\left(1 - \frac{x}{1-\theta n}\right)\lambda_x - \frac{(c_1 - \lambda_a)\rho}{n}, \\
\frac{d\lambda_x}{dt} - \delta\lambda_x &= -\frac{\partial \mathcal{H}(\cdot)}{\partial x} = -\frac{(r - \varepsilon_1 n + \varepsilon_2 a)(1 - 2x - \theta n)\lambda_x}{1 - \theta n} - \sigma E(p_1 - \lambda_x), \\
\frac{d\lambda_n}{dt} - \delta\lambda_n &= -\frac{\partial \mathcal{H}(\cdot)}{\partial n} = (\alpha + \beta a)\lambda_n + \frac{x\left(\theta x(r + a\varepsilon_2) + \varepsilon_1\left(-x + (-1 + \theta n)^2\right)\right)\lambda_x}{(-1 + \theta n)^2} + \frac{c_1\rho a}{n^2} - \frac{\rho\lambda_a a}{n^2}.
\end{aligned} \tag{16}$$

In the steady state, $\frac{dx}{dt} = \frac{dn}{dt} = \frac{da}{dt} = \frac{d\lambda_x}{dt} = \frac{d\lambda_n}{dt} = \frac{d\lambda_a}{dt} = 0$, implying the following equations

$$\begin{aligned}
&(1 - m)w - \beta a n - \alpha n = 0, \\
&\left(v - \rho\frac{a}{n}\right) = 0, \\
&(r - \varepsilon_1 n + \varepsilon_2 a)\left(1 - \frac{x}{1 - \theta n}\right)x - \sigma E x = 0, \\
&\delta\lambda_x = \frac{(r - \varepsilon_1 n + \varepsilon_2 a)(1 - 2x - \theta n)\lambda_x}{1 - \theta n} + E(p_1 - \lambda_x)\sigma, \\
&\delta\lambda_a = P_a(p_2 - c_a P_a) - \beta\lambda_n n + \varepsilon_2 x\left(1 - \frac{x}{1 - \theta n}\right)\lambda_x + \frac{(c_1 - \lambda_a)\rho}{n}, \\
&\delta\lambda_n = -(\alpha + \beta a)\lambda_n - \frac{x\left(x(r + a\varepsilon_2)\theta + \varepsilon_1\left(-x + (-1 + \theta n)^2\right)\right)\lambda_x}{(-1 + \theta n)^2} - \frac{ac_1\rho}{n^2} + \frac{a\lambda_a\rho}{n^2}.
\end{aligned} \tag{17}$$

The interior optimal solutions for the state and control variables can be found by solving the system of equations in Eq. (15) and Eq. (17).

Numerical solutions and sensitivity analysis

In this section, we find numerical solutions to the above system, Eq. (15) and Eq. (17), by specifying aquaculture's per-unit production and operation costs, unit market price, and assigning appropriate parameter values given in Table 1 and Table 3. Sensitivity analysis is also performed for the conversion factors, the measures of the negative impacts of nitrogen, and the positive

benefits of shellfish aquaculture. The results are summarized in Table 4.

Table 3. Parameters and their values used for numerical solutions

Parameter	Description	Value	Unit
P_a	Aquaculture production per unit square meter in kg	0.446	m^2/Kg
c_a	Cost parameter for aquaculture	0.1682	$1/US\$$
c_1	Cost of acquiring a square meter of aquaculture area in US dollars	1	$1/m^2/US\$$
c_2	The cost of removing the pollutant at the source in US dollars	0.135	1/US$
c	Cost per unit effort per unit carrying capacity for wild-catch	0.05	1/US$
δ	Positive social discount rate	0.05	1/year
θ	Measure of the impact of nitrogen on the environment	0.1, 0.11	1/vessel/year
ε_1	Measure of the impact of nitrogen on the growth rate	0.085, 0.086	1/year
ε_2	Measure of the impact of shellfish on the growth rate	0.097, 0.098	1/year
p_1	Unit price of wild catch in US dollars	15	1/US$
p_2	Unit price of farmed shellfish in US dollars	3	1/US$

Table 4. Steady-state optimal solutions for the state and control variables

ε_1	ε_2	θ	E^*	x^*	n^*	a^*	m^*	h^*
0.085	0.097	0.1	48.5255	0.584869	0.211729	0.273105	0.701388	0.425716
0.086	0.097	0.1	48.523	0.584869	0.211729	0.274299	0.700546	0.425694
0.085	**0.098**	0.1	48.5373	0.584931	0.210493	0.273202	0.703063	0.4258647
0.085	0.097	**0.11**	48.5804	0.583832	0.212129	0.306619	0.678127	0.425069

The numerical solutions in Table 4 show that

- As the impact of nitrogen concentration level on the habitat or the growth rate, θ or ε_1, increases, the optimal stock size, x^*, decreases, and consequently optimal harvest, h^*, declines. This shows a need to increase the optimal size of shellfish aquaculture since a significant amount of nitrogen can be removed through shellfish harvest and denitrification. This, in turn, allows us to reduce external effort.
- If the effectiveness of shellfish cultivation on the environment, ε_2, increases, we can observe that the nitrogen concentration level tends to approach a lower level. As a result of this, we can relax the optimal effort limits on the fishing ground.

Like the previous section, the control version reflects the positive contributions of shellfish aquaculture toward protecting aquatic ecosystems from eutrophication while increasing the supply of shellfish to the market and improving capture fish.

Transition dynamics

Following the computation of the optimal steady-state solution of the state, co-state, and control variables, it is natural to determine the trajectories of the states toward close-to-equilibrium solutions over a finite but large time. Because of the non-linear nature of the functional forms of the equations used in the dynamic analysis and the number of equations, it is not easy to find analytic solutions. Therefore, we use the fourth-order Runge–Kutta forward-backward sweep numerical method to solve the system of Eqs. (8) and (16). First, we approximate the state equations in Eq. (8), by first-order forward difference, and the corresponding co-state equations

in Eq. (16), by first-order backward difference equations. Then by substituting the values of the parameters given in Table 3, using initial values, $x(0) = 0.27$, $n(0) = 0.6$, and $a(0) = 0$, and a guess for optimal control, say the steady-state values, we solve the state equations forward for the discrete-time interval of $[0, t_f]$ partitioned into k parts using a time step h such that $t_f = kh$. Then, using the state values at t_f and the transversality condition at t_f, we find the values of the co-state at t_f and solve the co-state equations backward. After each forward-backward computation, we update the control values using the state and co-state values and repeat the process until the control values become sufficiently close. The accuracy or convergence of the iterative method is based on Hackbusch [30]. Figure 3 displays the trajectories of the numerical solutions generated using Hermite interpolation of order 3. Note that for all combinations of the conversion factors, decay rates, and other parameter values given in Table 3, the trend is the same (i.e., as the aquaculture increases, the nitrogen level decreases while the fish stock increases) except they converge to different terminal points.

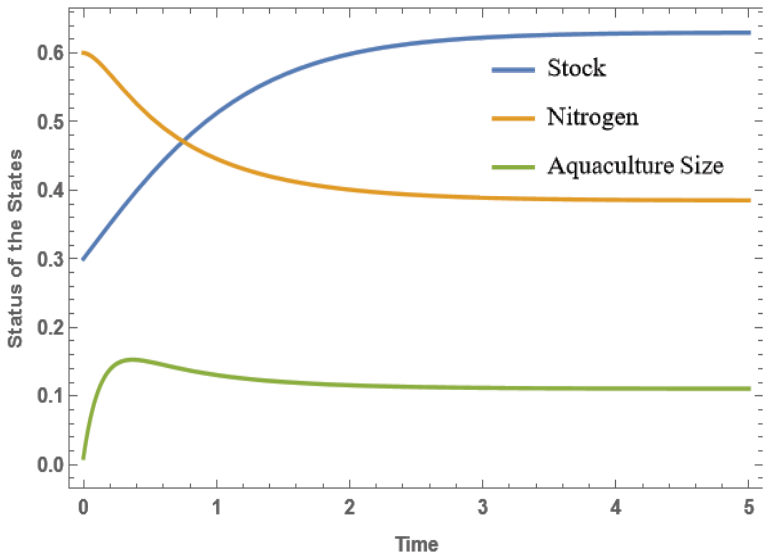

Figure 3. The trajectories of the optimal fish stock size and nitrogen level relative to the aquaculture expansion rate

4 Conclusion

This study assumes that shellfish aquaculture helps remediate nitrogen in an eutrophic aquatic ecosystem. We also attempted to determine the optimal sizes of shellfish aquaculture and the optimal capture fish effort before and after introducing shellfish aquaculture into the system. This ties in with our finding of the optimal nitrogen reduction effort needed to sustain the ecosystem. We reviewed various models related to our research and set up our model based on recent developments in the field and our intended research objectives. The system was analyzed in two scenarios to evaluate the effects of shellfish aquaculture.

In the first scenario, we defined the transition equation of open-access capture fish stock in an environment polluted by excessive nitrogen before the introduction of shellfish aquaculture. Excessive nitrogen contributes to environmental degradation, impacts the carrying capacity, and affects the growth rate of the fish stock. Our analysis shows a positive impact of nitrogen pollution reduction practices on the stock size and sustainable harvest. In addition, we show that the effort level that maximizes profit and optimal effort is inversely related to nitrogen concentration.

In the second scenario, we extended the model by considering the development of shellfish

aquaculture and including the positive impacts of shellfish cultivation on fishing grounds, the environment, and fish stock. We assume that the effect on the fish stock is measured through growth rate, and the amount of nitrogen removed by shellfish production is proportional to the size of the aquaculture area. Even though aquaculture takes away the fishing area and creates pressure in the open access fishing ground, we show that the development of shellfish aquaculture helps the recovery of polluted aquatic ecosystems and restocks the fishing ground. In this case, we can increase the optimal effort and harvest more captured shellfish, reducing the scarcity of shellfish in the market.

Eutrophication management and control is based primarily on the restriction of nutrient inputs in bodies of water and nutrient reduction strategies at the point source. Then, it requires collaborating with fisheries managers to integrate shellfish aquaculture into broader ecosystem management plans. This approach can limit nitrogen loading and remove excessive nitrogen through shellfish harvest. This study compares the impact of nitrogen eutrophication on the fish stock before and after the development of shellfish cultivation. We show that shellfish aquaculture can be considered as an alternative option to reduce nitrogen accumulation in aquatic ecosystems. It supports the economy by creating jobs and supplying more farmed shellfish. It also indirectly improves the performance of wild catches.

Declarations

Use of AI tools

The authors declare that they have not used Artificial Intelligence (AI) tools in the creation of this article.

Data availability statement

No Data associated with the manuscript.

Ethical approval (optional)

The authors state that the research does not involve either human participants or animals.

Consent for publication

Not applicable

Conflicts of interest

The authors declare that they have no conflict of interest.

Funding

No funding was received for this research.

Author's contributions

T.B.G.: Conceptualization, Methodology, Investigation, Formal analysis, Writing – original draft, Writing – Reviewing and Editing. W.T.B.: Conceptualization, Methodology, Formal analysis, Supervision, Writing – Reviewing and Editing. T.G.A.: Conceptualization, Supervision, Writing – Reviewing and editing. S.D.Z.: Conceptualization, Supervision, Writing – Reviewing and editing. All authors discussed the results and agreed to publish the manuscript.

Acknowledgements

We wish to express our profound gratitude to the editors and reviewers for their very thoughtful comments, which have helped us to improve the manuscript substantially.

References

[1] Rose, J.M., Gosnell, J.S., Bricker, S., Brush, M.J., Colden, A., Harris, L. et al. Opportunities and challenges for including oyster-mediated denitrification in nitrogen management plans. *Estuaries and Coasts*, 44, 2041-2055, (2021). [CrossRef]

[2] Wang, D., Gan, X., Wang, Z., Jiang, S., Zheng, X., Zhao, M. et al. Research status on remediation of eutrophic water by submerged macrophytes: A review. *Process Safety and Environmental Protection*, 169, 671-684, (2023). [CrossRef]

[3] Boopathy, R. Factors limiting bioremediation technologies. *Bioresource Technology*, 74(1), 63-67, (2000). [CrossRef]

[4] Fetahi, T. Eutrophication of Ethiopian water bodies: a serious threat to water quality, biodiversity and public health. *African Journal of Aquatic Science*, 44(4), 303-312, (2019). [CrossRef]

[5] Liu, C., Zhang, F., Ge, X., Zhang, X., Chan, N.W. and Qi, Y. Measurement of total nitrogen concentration in surface water using hyperspectral band observation method. *Water*, 12(7), 1842, (2020). [CrossRef]

[6] United Nations Environment Programme: Mediterranean Action Plan. Approaches for Eutrophication assessment of Mediterranean coastal waters. UNEP(DEPI)/MED WG.321/Inf.6, (2007).

[7] Caspers, H. OECD: Eutrophication of Waters. Monitoring, Assessment and Control.—154 pp. Paris: Organisation for Economic Co-Operation and Development 1982. (Publié en français sous le titre» Eutrophication des Eaux. Méthodes de Surveillance, d'Evaluation et de Lutte «). *nternationale Revue der gesamten Hydrobiologie und Hydrographie*, 69(2), 200, (1984). [CrossRef]

[8] Xuan, B.B. and Armstrong, C.W. Marine reserve creation and interactions between fisheries and capture-based aquaculture: A bioeconomic model analysis. *Natural Resource Modeling*, 30, 1–16, (2016). [CrossRef]

[9] US Environmental Protection Agency (EPA), National Recommended Water Quality Criteria, (2002). https://www.epa.gov/sites/default/files/2018-12/documents/national-recommended-hh-criteria-2002.pdf

[10] Smith, V.H. Cultural eutrophication of inland, estuarine, and coastal waters. In *Successes, Limitations, and Frontiers in Ecosystem Science* (pp. 7-49). New York, NY: Springer New York, (1998). [CrossRef]

[11] Humphries, A.T., Ayvazian, S.G., Carey, J.C., Hancock, B.T., Grabbert, S., Cobb, D. et al. Directly measured denitrification reveals oyster aquaculture and restored oyster reefs remove nitrogen at comparable high rates. *Frontiers in Marine Science*, 3, 74, (2016). [CrossRef]

[12] Ray, N.E., Hancock, B., Brush, M.J., Colden, A., Cornwell, J., Labrie, M.S. et al. A review of how we assess denitrification in oyster habitats and proposed guidelines for future studies. *Limnology and Oceanography: Methods*, 19(10), 714-731, (2021). [CrossRef]

[13] Petersen, J.K., Saurel, C., Nielsen, P. and Timmermann, K. The use of shellfish for eutrophication control. *Aquaculture International*, 24, 857-878, (2016). [CrossRef]

[14] Mykoniatis, N. and Ready, R. The potential contribution of oyster management to water quality goals in the Chesapeake Bay. *Water Resources and Economics*, 32, 100167, (2020). [CrossRef]

[15] Turner, J.S., Kellogg, M.L., Massey, G.M. and Friedrichs, C.T. Minimal effects of oyster aquaculture on local water quality: Examples from southern Chesapeake Bay. *PLoS One*, 14(11), e0224768, (2019). [CrossRef]

[16] Mykoniatis, N. and Ready, R. Spatial harvest regimes for a sedentary fishery. *Environmental and Resource Economics*, 65, 357-387, (2016). [CrossRef]

[17] Ngatia, L., Grace III, J.M. and Moriasi, D. Nitrogen and phosphorus eutrophication in marine. In *Monitoring of Marine Pollution* (pp. 77-93). IntechOpen: London, (2019). [CrossRef]

[18] Foley, N.S., Armstrong, C.W., Kahui, V., Mikkelsen, E. and Reithe, S. A review of bioeconomic modelling of habitat-fisheries interactions. *International Journal of Ecology*, 2012(1), 861635, (2012). [CrossRef]

[19] Pichika, S.D.N. and Zawka, S.D. Optimal harvesting of a renewable resource in a polluted environment: An allocation problem of the sole owner. *Natural Resource Modeling*, 32(2), e12206, (2019). [CrossRef]

[20] Tahvonen, O. On the dynamics of renewable resource harvesting and pollution control. *Environmental and Resource Economics*, 1, 97-117, (1991). [CrossRef]

[21] Akpalu, W. and Bitew, W.T. Externalities and foreign capital in aquaculture production in developing countries. *Environment and Development Economics*, 23(2), 198-215, (2018). [CrossRef]

[22] Chatterjee, A. and Pal, S. A predator-prey model for the optimal control of fish harvesting through the imposition of a tax. *An International Journal of Optimization and Control: Theories & Applications*, 13(1), 68-80, (2023). [CrossRef]

[23] Allen, L.J.S. *An Introduction to Mathematical Biology*. Pearson Prentice Hall: Italy, (2007).

[24] Smith, V.H., Tilman, G.D. and Nekola, J.C. Eutrophication: impacts of excess nutrient inputs on freshwater, marine, and terrestrial ecosystems. *Environmental Pollution*, 100(1-3), 179-196, (1999). [CrossRef]

[25] Hailu, F.F., Bitew, W.T., Ayele, T.G. and Zawka, S.D. Marine protected areas for resilience and economic development. *Aquatic Living Resources*, 36, 22, (2023). [CrossRef]

[26] Wirkus, S.A., Swift, R.J. and Szypowski, R. *A Course in Differential Equations with Boundary Value Problems*. Chapman and Hall/CRC: New York, (2017). [CrossRef]

[27] Soulaimani, S., Kaddar, A. and Rihan, F.A. Stochastic stability and global dynamics of a mathematical model for drug use: Statistical sensitivity analysis via PRCC. *Partial Differential Equations in Applied Mathematics*, 12, 100964, (2024). [CrossRef]

[28] Getahun, T.B., Bitew, W.T., Ayele, T.G. and Zawka, S.D. Optimal effort, fish farming, and marine reserve in fisheries management. *Aquaculture and Fisheries*, 9(6), 975-980, (2024). [CrossRef]

[29] Nepf, M., Dvarskas, A. and Walsh, P.J. Economic valuation for coastal water infrastructure planning: Analysis of the housing market and nutrient pollution in Suffolk County, NY. *Marine Resource Economics*, 37(4), 369-386, (2022). [CrossRef]

[30] Hackbusch, W. A numerical method for solving parabolic equations with opposite orientations. *Computing*, 20(3), 229-240, (1978).

Mathematical Modelling and Numerical Simulation with Applications (MMNSA)
(https://dergipark.org.tr/en/pub/mmnsa)

How to cite this article: Getahun, T.B., Bitew, W.T., Ayele, T.G. & Zawka, S.D. (2025). Optimizing shellfish aquaculture in nitrogen and fisheries management. *Mathematical Modelling and Numerical Simulation with Applications*, 5(1), 18-37. https://doi.org/10.53391/mmnsa.1525113

Mathematical Modelling and Numerical Simulation with Applications, 2025, 5(1), 38–64

https://dergipark.org.tr/en/pub/mmnsa

ISSN Online: 2791-8564 / Open Access

https://doi.org/10.53391/mmnsa.1496827

RESEARCH PAPER

Bifurcation analysis of an additional food-provided predator-prey system with anti-predator behavior

Manoj Kumar Singh [1,*,‡] and **Poonam Poonam** [1,‡]

[1]Department of Mathematics and Statistics, Banasthali Vidyapith, Rajasthan-304022, India

*Corresponding Author

‡ s.manojbbau@gmail.com (Manoj Kumar Singh); poonambanasthali91@gmail.com (Poonam)

Abstract

This article analyzes the qualitative behavior of a predator-prey system where the predator receives extra food and the prey engages in anti-predator behavior to defend itself against attacks by the predator. The positivity and the boundedness of solutions to the system have been examined. The biologically well-posed equilibrium points of the proposed system are derived, and an analysis of their local stability is conducted. In specific situations, it is observed that the solutions of the proposed system are significantly dependent on the initial values. The emergence of several bifurcations in the system, including the saddle-node, Bogdanov-Takens, and Hopf-Andronov, is also shown. Through numerical simulation, the rise of a homoclinic loop is shown. The analytic results are verified by numerical simulations and phase portrait sketches.

Keywords: Additional food; anti-predator behavior; stability; bifurcation

AMS 2020 Classification: 37G10; 34C23; 93D20

1 Introduction

The fragile equilibrium of life on Earth relies on ecological systems, the complex webs of interactions between species and their surroundings. These networks extend from local to global levels, including everything from small ecosystems such as oceans, forests, and wetlands to the entire biosphere. Preserving biodiversity, managing natural resources, and reducing the effects of environmental changes all require an understanding of the dynamics of ecological systems. The dynamics between predators and their prey are one of the fundamental ecological phenomena that have a significant impact on biodiversity. The strong intuition to be alive in predators and prey has led to the development of remarkable strategies in these species. For example, predator species do not rely on a single prey species but rather on a varied range of prey species [1], while prey species exhibit anti-predator behavior [2]. In this article, the impacts of these strategies on a predator-prey system are analyzed.

➤ **Received:** 06.06.2024 ➤ **Revised:** 27.12.2024 ➤ **Accepted:** 12.02.2025 ➤ **Published:** 31.03.2025

Researchers are aware that predators exhibit a behavioral adaptation whereby they shift their feeding preferences to alternate food sources in response to decreasing densities of their preferred prey [3]. To develop a comprehensive predator-prey model for such species, it is essential to take into account the inclusion of alternative prey species. The inclusion of supplementary food in a predator-prey system may have a substantial impact on the ecological dynamics and overall stability of ecosystems. For instance, the presence of scavenging possibilities or the introduction of non-native prey species can perturb the ecological balance of the whole system [4]. Moreover, the introduction of this surplus food may have a cascading effect on the ecosystem, impacting not just the populations of prey species and competitors but also those at higher trophic levels [5]. Hence, it is essential to comprehend the ramifications of additional food within predator-prey systems to manage ecosystems and advance conservation initiatives effectively.

The empirical study indicates that the provision of supplementary food to predators does not always result in an increase in predation on target species. Sometimes, it may lead to a reduction in the population density of prey species [3]. This phenomenon is often referred to as "apparent competition" [6]. In addition, the predator population may have short-term advantages via an additional food supply. For instance, using supplementary resources may lead to overexploitation, increasing the likelihood of population collapses or fluctuations [7]. This discrepancy between theory and observations prompted a thorough mathematical investigation of predator-prey systems that include provisions to supply additional food.

Srinivasu et al. [8] developed a predation model including two species to examine the effects of supplementary food provided to the predator species. The researchers noted that manipulating additional food, in terms of quality and quantity, can manage and constrain prey numbers and restrict and eradicate predator populations. The aforementioned theoretical results are consistent with the facts documented in a recent literature review [9] that examines the impact of artificial food sprays on conservation biological control. Prasad et al. [10] created and analyzed an additional food-provided predator-prey system with a Beddington-DeAngelis functional response (a way to incorporate mutual interference between predators). They observed the possibility of the coexistence of predator species with a low density of prey species. This phenomenon contrasts with classical predator-prey models, where the coexistence of predators and prey at low population densities is not attainable. The ramifications of providing alternative food sources to predators in a predator-prey paradigm with harvesting have been studied by Sahoo and Poria [11]. Chakraborty and Das [12] conducted an analysis of the variability of a predator-prey system. They specifically investigated the impact of constant prey refuge and alternative food provided to the predator. The global dynamics of a predator-prey system have been investigated by Sen et al. [13], where the predator is subjected to alternative food as well as harvesting at a constant rate. This work offers valuable methodologies for examining the controllability of systems, which have significant relevance in real-world applications. Shome [14] examined the effects of additional food in a predator-prey model incorporating intraspecific competition among prey species and the theta-logistic prey growth rate. They found that when alternative food sources are limited and intraspecific competition is intense, prey species experience extinction. Consequently, the predator species also face extinction, resulting in the collapse of the whole system. In continuation, they observed that the potential occurrence of this collapse may be averted with the provision of a sufficient amount of alternate sustenance to predatory organisms. This finding suggests that including alternative food sources significantly affects regulating the dynamics of the proposed system. Ghosh et al. [15] studied the dynamics of a predator-prey system with prey refuge and additional food for the predator. Singh et al. [16] performed a qualitative inquiry into a predator-prey model, whereby it was assumed that a continual extra food supply is provided to the predator species and the growth of the predator is regulated by the Allee effect.

Several researchers have recently explored the influence of additional food delivered to predators in predator-prey systems that incorporate various real-life phenomena. For instance, Das et al. [17] used a predator-prey model with prey refuge; Thirthar et al. [18] used a predator-prey model with fear effects, prey refuge, and harvesting; Debnath et al. [19] used a predator-prey system with fear effects and anti-predator behavior; Ananth et al. [20] used a predator-prey model involving Holling-type III functional response; Das et al. [21] used a predator-prey model with fear effects; and Umaroh and Savitri [22] used a predator-prey model with Holling-type III functional response and anti-predator behavior.

Prey species have evolved a variety of strategies to avoid their natural predators. When preys are threatened, they sometimes display a peculiar defensive behavior in which they sacrifice specific body parts. Lizards, for instance, can release their tails to protect themselves from predators. Adult prey kill juvenile predators to reduce the pressure of future predation and increase population density [23–27]. These kinds of prey behaviors are known as anti-predator behaviors. Zanette et al. [28] performed experiments to demonstrate anti-predator behavior's impact on song sparrows' reproductive rates. The results indicated that implementing such efforts led to a significant reduction of 40% in the song sparrow's reproductive output whenever direct predation was effectively mitigated. As a result, the presence of anti-predator behavior among prey species plays a crucial role in maintaining the intricate equilibrium of predator-prey ecosystems.

Several researchers have examined anti-predator behavior in the context of analyzing nonlinear ecological systems [29–31]. Samanta et al. [31] conducted an analysis of a modified Leslie-Gower model using a Beddington-DeAngelis functional response in order to categorize an anti-predator behavior. Tang and Xiao [32] modified a predator-prey system equipped with a non-monotonic functional response by utilizing anti-predator behavior. The saddle-node, the homoclinic, the Hopf bifurcation, and the Bogdanov-Takens bifurcation of co-dimension two were the bifurcations the authors examined as possible system outcomes. Mortoja et al. [33] presented a stage-structure predator-prey model including anti-predator behavior and group defense. The researchers investigated the system's stability and examined the occurrence of the Hopf bifurcation in the suggested system. A dynamical study is carried out by Savitri [2] on a predator-prey model that is endowed with ratio-dependent functional responses and anti-predator behavior. Recently, Prasad et al. [34] explored the influence of anti-predator behavior on predator-prey dynamics where additional food is provided to predators. They observed that several kinds of bifurcations occur, such as saddle-node bifurcation, Hopf bifurcation, homoclinic bifurcation, and a Bogdanov-Takens bifurcation of co-dimension 2. They concluded that successful implementation of biological control might be achieved by taking the anti-predator behavior as a control parameter. This article employed the Holling type IV functional response (Monod-Haldane), often used in models with predator interference, where high prey density leads to reduced predation rates owing to defensive behaviors shown by prey species. The Holling type II functional response, which is more commonly used, is more suitable for modeling predator-prey interactions where there is a limitation on predator efficiency due to handling time and prey saturation. This research examines the effects of supplementary food in the predator-prey system, including Holling type II functional response and anti-predator behavior. It is observed that the anti-predator behavior enhances the dynamical complexities and can be used as a controlling parameter.

2 The basic mathematical model

Srinivasu et al. [8] proposed a bi-dimensional system of equations to represent a predator-prey dynamic, whereby the predator species are provided with a constant supply of supplementary food distributed equally across the environment. If we assume that the prey species exhibits anti-predator behavior, the model takes the following form:

$$\begin{cases} \frac{du}{dt} = r\,u(1-\frac{u}{K}) - \frac{e_1uv}{1+e_1h_1u+e_2h_2A}, \\ \frac{dv}{dt} = \frac{n_1e_1uv+n_2e_2Av}{1+e_1h_1u+e_2h_2A} - mv - nuv, \end{cases} \tag{1}$$

where $u = u(t)$ and $v = v(t)$ represent the prey and predator populations at time t, respectively. To provide an ecologically appropriate interpretation of the proposed model, it is necessary to assume that $u(0) \geq 0$ and $v(0) \geq 0$. The positive parameters A, r, K, m, $h_1(h_2)$, $n_1(n_2)$ and $e_1(e_2)$ are the amount of additional food, the intrinsic growth rate of prey, the carrying capacity of the environment, the predator's mortality rate, the handling time of the predator per unit quantity of prey (additional food), the nutritional value of the prey (additional food), and the ability of the predator to detect the prey (additional food), respectively. The term nuv represents anti-predator behavior, and the parameter n is the rate of anti-predator behavior of prey for the predator population. Ecologically, it can be interpreted that this form of anti-predator behavior does not directly benefit the prey population but reduces the growth of the predator population, and in this way, it helps the prey population.
Defining $c = \frac{1}{h_1}$, $b = n_1c$, $a = \frac{1}{e_1h_1}$, $\eta = \frac{n_2e_2}{n_1e_1}$, $\alpha = \frac{n_1h_2}{n_2h_1}$, the system (1) can be expressed as

$$\begin{cases} \frac{du}{dt} = r\,u(1-\frac{u}{K}) - \frac{c\,uv}{a+\alpha\eta A+u}, \\ \frac{dv}{dt} = \frac{b(u+\eta A)v}{a+\alpha\eta A+u} - mv - nuv. \end{cases} \tag{2}$$

The ecological interpretation of the parameters a, b, and c in the above model aligns with the conventional predator-prey model. The parameter α is inversely proportional to the additional food quality, and ηA refers to the amount of additional food perceptible to the predator relative to the prey.
Employing the transformations $u = ax$, $v = \frac{ary}{c}$, $t = \frac{\hat{t}}{r}$ and dropping the hat, system (2) becomes

$$\begin{cases} \frac{dx}{dt} = x(1-\frac{x}{\gamma}) - \frac{xy}{1+\alpha\xi+x}, \\ \frac{dy}{dt} = \frac{\beta(x+\xi)y}{1+\alpha\xi+x} - \delta y - \theta xy, \end{cases} \tag{3}$$

where $\gamma = \frac{K}{a}$, $\beta = \frac{b}{r}$, $\xi = \frac{\eta A}{a}$, $\delta = \frac{m}{r}$ and $\theta = \frac{na}{r}$. From an ecological perspective, our focus is only on the dynamics of system (3) inside the first quadrant $\mathbb{R}_0^+ \times \mathbb{R}_0^+ = \{(x,y) \in \mathbb{R}^2 : x \geq 0, y \geq 0\}$.

Lemma 1 (i) *All solutions of the system* (3) *initiating in the interior of the positive quadrant of the state space are positive for all* $t \geq 0$.
(ii) *All solutions of the system* (3) *initiating in the interior of the positive quadrant of the state space are bounded for all* $t \geq 0$.

Proof

(i) The two Eqs. of the system (3) yield

$$x(t) = x(0)\exp\left[\int_0^t \left(1 - \frac{x(\tau)}{\gamma} - \frac{v(\tau)}{1+\alpha\xi+u(\tau)}\right)d\tau\right],$$

and

$$y(t) = y(0)\exp\left[\int_0^t \left(\frac{\beta(x(\tau)+\xi)}{1+\alpha\xi+x(\tau)} - \delta - \theta x(\tau)\right)d\tau\right],$$

respectively. The conditions $x(0) \geq 0$ and $y(0) \geq 0$ imply $x(t) \geq 0$ and $y(t) \geq 0$, respectively. Therefore, it can be deduced that a solution originating in the positive quadrant of the xy-plane stays positive throughout.

(ii) The first Eq. of the system (3) yields the following result:

$$\frac{dx}{dt} < x\left(1 - \frac{x}{\gamma}\right).$$

It can be inferred that every solution of the system (3) satisfies $x(t) \leq \gamma$ for all $t > 0$.
Define $\Phi(t) = x(t) + \frac{y(t)}{\beta}$. Then

$$\frac{d\Phi}{dt} = x\left(1 - \frac{x}{\gamma}\right) + \frac{\xi y}{1 + \alpha\xi + x} - \frac{(\delta + \theta x)y}{\beta}.$$

For $\lambda > 0$, we have

$$\frac{d\Phi}{dt} + \lambda\Phi(t) = x\left(1 - \frac{x}{\gamma} + \lambda\right) - \left(\frac{\delta - \lambda}{\beta} - \frac{\xi}{1 + \alpha\xi}\right) y,$$

$$\frac{d\Phi}{dt} + \lambda\Phi(t) \leq \frac{\gamma(1+\lambda)^2}{4} - \left(\frac{\delta - \lambda}{\beta} - \frac{\xi}{1 + \alpha\xi}\right) y.$$

By selecting a suitably small $(\lambda < \delta)$, above inequality can be written as

$$\frac{d\Phi}{dt} + \lambda\Phi(t) < \frac{\gamma(1+\lambda)^2}{4} + \frac{\xi y}{1 + \alpha\xi}.$$

Thus,

$$\frac{d\Phi}{dt} + \lambda\Phi(t) < \mu,$$

where $\mu = \frac{\gamma(1+\lambda)^2}{4} + \frac{\xi y}{1+\alpha\xi}$.
Employing Gronwall's inequality, we get

$$0 < \Phi(t) \leq \frac{\mu}{\lambda}\left(1 - e^{-\lambda t}\right) + \Phi(0)\, e^{-\lambda t}.$$

The above inequality implies, $0 < \Phi(t) \leq \frac{\mu}{\lambda}$, as $t \to \infty$. Thus, every solution of the system (3) originating in the positive quadrant of the xy-plane is bounded for all future time.

The above lemma ensures that the system (3) is ecologically well-posed.

3 Existence of equilibrium points

The non-negative solutions of the system $\frac{dx}{dt} = 0$, $\frac{dy}{dt} = 0$ are the constant solutions of the system (3) and are called equilibrium points of the system. It is easy to see that the system (3) has a trivial equilibrium point $E_0(0, 0)$, a predator-free equilibrium point $E_\gamma(\gamma, 0)$, and interior equilibrium

points $E^*(x^*, y^*)$. The abscissa x^* is the root of the quadratic equation

$$\theta x^2 + (\delta + \theta(1+\alpha\xi) - \beta)x + \delta(1+\alpha\xi) - \beta\xi = 0. \tag{4}$$

The roots of Eq. (4) are $x^* = \frac{\beta - (\delta+\theta(1+\alpha\xi)) \mp \sqrt{(\delta+\theta(1+\alpha\xi)-\beta)^2 - 4\theta(\delta(1+\alpha\xi)-\beta\xi)}}{2\theta}$. For the sake of clarity, consider $\Delta_1 = \delta(1+\alpha\xi) - \beta\xi$, $\Delta_2 = \beta - (\delta + \theta(1+\alpha\xi))$, and $\Delta_3 = 4\theta\Delta_1$.
To find the equilibrium points of the system (3), we consider the following cases:

Case I: $\Delta_1 > 0$ and $\Delta_2 > 0$.
In this case, if $\Delta_2^2 > \Delta_3$ holds, then the system (3) has two interior equilibrium points $E_1^*(x_1^*, y_1^*)$ and $E_2^*(x_2^*, y_2^*)$, where $x_{1,2}^* = \frac{\Delta_2 \mp \sqrt{\Delta_2^2 - \Delta_3}}{2\theta}$ and $y_{1,2}^* = (1 - \frac{x_{1,2}^*}{\gamma})(1 + \alpha\xi + x_{1,2}^*)$, provided $\gamma > x_{1,2}^*$; if $\Delta_2^2 = \Delta_3$ holds, then the system (3) has a unique interior equilibrium point $E_3^*(x_3^*, y_3^*)$, where $x_3^* = \frac{\Delta_2}{2\theta}$ and $y_3^* = (1 - \frac{x_3^*}{\gamma})(1 + \alpha\xi + x_3^*)$, provided $\gamma > x_3^*$; if $\Delta_2^2 < \Delta_3$ holds, then the system (3) has no interior equilibrium point.

Case II: $\Delta_1 < 0$.
In this case, the system (3) has a unique interior equilibrium point $E_4^*(x_4^*, y_4^*)$, where $x_4^* = \frac{\Delta_2 + \sqrt{\Delta_2^2 - \Delta_3}}{2\theta}$ and $y_4^* = (1 - \frac{x_4^*}{\gamma})(1 + \alpha\xi + x_4^*)$, provided $\gamma > x_4^*$.

Case III: $\Delta_1 = 0$.
In this case, if $\Delta_2 > 0$ holds, the system (3) has an interior equilibrium point $E_5^*(x_5^*, y_5^*)$ and a prey-free equilibrium point $E_6^*(x_6^*, y_6^*) = (0, 1+\alpha\xi)$, where $x_5^* = \frac{\Delta_2}{\theta}$ and $y_5^* = (1 - \frac{x_5^*}{\gamma})(1 + \alpha\xi + x_5^*)$, provided $\gamma > x_5^*$, if $\Delta_2 < 0$ holds, the system (3) has no interior equilibrium point, but a unique prey-free equilibrium point $E_6^*(x_6^*, y_6^*) = (0, 1+\alpha\xi)$ occurs.

4 Stability analysis

This section performs an analysis to derive the stability conditions around the equilibrium points determined in the previous section using the linearization technique.

Theorem 1 *(i) The equilibrium point $E_0 = (0,0)$ of system (3) is unstable if $\frac{\beta\xi}{1+\alpha\xi} > \delta$ and saddle if $\frac{\beta\xi}{1+\alpha\xi} < \delta$.*
(ii) The equilibrium point $E_\gamma = (\gamma, 0)$ of system (3) is saddle if $\frac{\beta(\gamma+\xi)}{1+\alpha\xi+\gamma} > (\delta + \theta\gamma)$ and asymptotically stable if $\frac{\beta(\gamma+\xi)}{1+\alpha\xi+\gamma} < (\delta + \theta\gamma)$.

Proof

(i) At $E_0(0,0)$, the Jacobian matrix of the system (3) is

$$J_{E_0} = \begin{pmatrix} 1 & 0 \\ 0 & \frac{\beta\xi}{1+\alpha\xi} - \delta \end{pmatrix}.$$

The eigenvalues of the matrix J_{E_0} are $\lambda_1 = 1 > 0$ and $\lambda_2 = \frac{\beta\xi}{1+\alpha\xi} - \delta$. If $\frac{\beta\xi}{1+\alpha\xi} > \delta$ ($\lambda_2 > 0$), the trivial equilibrium point E_0 is unstable. If $\frac{\beta\xi}{1+\alpha\xi} < \delta$ ($\lambda_2 < 0$), the trivial equilibrium point E_0 is saddle.

(ii) At $E_\gamma(\gamma,0)$, the Jacobian matrix of the system (3) is

$$J_{E_\gamma}=\begin{pmatrix} -1 & -\frac{\gamma}{1+\alpha\xi+\gamma} \\ 0 & \frac{\beta(\gamma+\xi)}{1+\alpha\xi+\gamma}-(\delta+\theta\gamma) \end{pmatrix}.$$

The eigenvalues of the above matrix are $\lambda_1=-1<0$ and $\lambda_2=\frac{\beta(\gamma+\xi)}{1+\alpha\xi+\gamma}-(\delta+\theta\gamma)$. If $\frac{\beta(\gamma+\xi)}{1+\alpha\xi+\gamma}>(\delta+\theta\gamma)$ $(\lambda_2>0)$, the point E_γ is saddle. If $\frac{\beta(\gamma+\xi)}{1+\alpha\xi+\gamma}<(\delta+\theta\gamma)$ $(\lambda_2<0)$, the point E_γ is stable.

Theorem 2 (i) *The equilibrium point $E_1^*(x_1^*,y_1^*)$ of system (3), if it exists, is stable if $\gamma<1+\alpha\xi+2x_1^*$ and unstable if $\gamma>1+\alpha\xi+2x_1^*$.*

(ii) *The equilibrium points $E_2^*(x_2^*,y_2^*)$, $E_4^*(x_4^*,y_4^*)$ and $E_5^*(x_5^*,y_5^*)$ of system (3), if they exist, are always saddle.*

(iii) *The equilibrium point $E_3^*(x_3^*,y_3^*)$ of system (3), if it exists, is a degenerate singularity.*

Proof At $E_i^*(x_i^*,y_i^*)$, $i=1,2,3,4,5$, the Jacobian matrix of the system (3) is

$$J_{E_i^*}=\begin{pmatrix} x_i^*(-\frac{1}{\gamma}+(1-\frac{x_i^*}{\gamma})\frac{1}{1+\alpha\xi+x_i^*}) & -\frac{x_i^*}{1+\alpha\xi+x_i^*} \\ \Big((\beta-\delta)-2\theta x_i^*-\theta(1+\alpha\xi)\Big)(1-\frac{x_i^*}{\gamma}) & 0 \end{pmatrix}.$$

The determinant and trace of the matrix $J_{E_i^*}$ are $\det J_{E_i^*}=\frac{x_i^*y_i^*}{(1+\alpha\xi+x_i^*)^2}\Big(\Delta_2-2\theta x_i^*\Big)$ and $\operatorname{trace} J_{E_i^*}=\frac{x_i^*}{\gamma(1+\alpha\xi+x_i^*)}\Big(\gamma-(1+\alpha\xi+2x_i^*)\Big)$, respectively.

(i) It is easy to show that $\det J_{E_1^*}=\frac{x_1^*y_1^*}{(1+\alpha\xi+x_1^*)^2}(\sqrt{(\Delta_2^2-\Delta_3)}>0$ and $\operatorname{tr} J_{E_1^*}=\frac{x_1^*}{\gamma(1+\alpha\xi+x_1^*)}\Big(\gamma-(1+\alpha\xi+2x_1^*)\Big)$. The Routh-Hurwitz criteria confirm the result.

(ii) A simple calculation may provide $\det J_{E_2^*}=-\frac{x_2^*y_2^*}{(1+\alpha\xi+x_2^*)^2}(\sqrt{(\Delta_2^2-\Delta_3)}<0$, $\det J_{E_4^*}=-\frac{x_4^*y_4^*}{(1+\alpha\xi+x_4^*)^2}(\sqrt{(\Delta_2^2-\Delta_3)}<0$, and $\det J_{E_5^*}=-\frac{x_5^*y_5^*\sqrt{\Delta_2}}{(1+\alpha\xi+x_5^*)^2}<0$. Thus, the result follows.

(iii) It is easy to show that $\det J_{E_3^*}=0$. Thus, the equilibrium point E_3^* is a degenerate singularity.

Theorem 3 *The equilibrium point E_3^* of system (3), if exists, then it is*

(i) *a stable saddle-node if $\gamma<1+\alpha\xi+2x_3^*$ and an unstable saddle-node if $\gamma>1+\alpha\xi+2x_3^*$.*

(ii) *a cusp of codimension 2 if $\gamma=1+\alpha\xi+2x_3^*$ and $\eta_1\eta_2\neq 0$.*

Proof

(i) Firstly, we employ the transformations $\check{x}=x-x_3^*$, $\check{y}=y-y_3^*$, the equilibrium point E_3^* shifts to the origin $(0,0)$. Using Taylor series expansion centered at $(0,0)$, the system (3) reduces to

$$\begin{cases} \frac{d\check{x}}{dt}=a_{10}\check{x}+a_{01}\check{y}+a_{20}\check{x}^2+a_{11}\check{x}\check{y}+o|(\check{x},\check{y})^3|, \\ \frac{d\check{y}}{dt}=b_{10}\check{x}+b_{01}\check{y}+b_{20}\check{x}^2+b_{11}\check{x}\check{y}+b_{02}\check{y}^2+o|\check{x},\check{y})^3|, \end{cases} \tag{5}$$

where $a_{10}=\frac{x_3^*}{\gamma(1+\alpha\xi+x_3^*)}\Big(\gamma-(1+\alpha\xi+2x_3^*)\Big)$, $a_{01}=-\frac{x_3^*}{1+\alpha\xi+x_3^*)}$, $a_{20}=-\frac{1}{\gamma}+\frac{(1+\alpha\xi)y_3^*}{(1+\alpha\xi+x_3^*)^3}$, $a_{11}=-\frac{(1+\alpha\xi)}{(1+\alpha\xi+x_3^*)^2}$, $b_{10}=\Big(\frac{\beta(1+\alpha\xi-\xi)}{(1+\alpha\xi+x_3^*)^2}-\theta\Big)y_3^*$, $b_{01}=0$, $b_{20}=-\frac{\beta(1+\alpha\xi-\xi)y_3^*}{(1+\alpha\xi+x_3^*)^3}$, $b_{11}=\frac{\beta(1+\alpha\xi-\xi)}{(1+\alpha\xi+x_3^*)^2}-\theta$, $b_{02}=0$.

It is simple to check if $a_{10} \neq 0$, i.e., $\gamma \neq 1+\alpha\xi+2x_3^*$, then the $\text{tr}(J_{E_3^*}) \neq 0$ but $\det(J_{E_3^*}) = 0$. Thus, the equilibrium point E_3^* is a saddle node. Furthermore, if $\gamma < 1+\alpha\xi+2x_3^*$, i.e., $\text{tr}(J_{E_3^*}) < 0$, the equilibrium point E_3^* is a stable saddle node. If $\gamma > 1+\alpha\xi+2x_3^*$, i.e., $\text{tr}(J_{E_3^*}) > 0$, the equilibrium point E_3^* is an unstable saddle node.

(ii) If $\gamma = 1+\alpha\xi+2x_3^*$, then $\text{tr}(J_{E_3^*}) = 0$ and $\det(J_{E_3^*}) = 0$. By applying the transformation $\tilde{x} = \check{x}$, $\tilde{y} = a_{10}\check{x} + a_{01}\check{y}$, the system (5) reduces to

$$\begin{cases} \frac{d\tilde{x}}{dt} = \tilde{y} + \overline{a_{20}}\tilde{x}^2 + \overline{a_{11}}\tilde{x}\tilde{y} + o|(\tilde{x},\tilde{y})^3|, \\ \frac{d\tilde{y}}{dt} = \overline{b_{20}}\tilde{x}^2 + \overline{b_{11}}\tilde{x}\tilde{y} + o|(\tilde{x},\tilde{y})^3|, \end{cases} \tag{6}$$

where $\overline{a_{20}} = a_{20} - \frac{a_{11}a_{10}}{a_{01}}$, $\overline{a_{11}} = \frac{a_{11}}{a_{01}}$, $\overline{b_{20}} = a_{10}a_{20} + a_{01}b_{20} - b_{11}a_{10} - \frac{a_{11}a_{10}^2}{a_{01}}$, $\overline{b_{11}} = \frac{a_{11}a_{10}}{a_{01}} + b_{11}$. By applying the transformations $w_1 = \tilde{x} - \frac{1}{2}\overline{a_{11}}\tilde{x}^2$, $w_2 = \tilde{y} + \overline{a_{20}}\tilde{x}^2$, the system (6) reduces to

$$\begin{cases} \frac{dw_1}{dt} = w_2 + o|(w_1,w_2)^3|, \\ \frac{dw_2}{dt} = \eta_1 w_1^2 + \eta_2 w_1 w_2 + o|(w_1,w_2)^3|, \end{cases} \tag{7}$$

where $\eta_1 = \overline{b_{20}}$ and $\eta_2 = 2\overline{a_{20}} + \overline{b_{11}}$.
Finally, applying the transformations $z_1 = w_1$, $z_2 = w_2 + o|(w_1,w_2)^3|$, the system (7) reduces to

$$\begin{cases} \frac{dz_1}{dt} = z_2, \\ \frac{dz_2}{dt} = \eta_1 z_1^2 + \eta_2 z_1 z_2 + o|(z_1,z_2)^3|. \end{cases}$$

The non-degeneracy condition $\eta_1\eta_2 = \overline{b_{20}}(2\overline{a_{20}} + \overline{b_{11}}) \neq 0$ for a cusp with co-dimension 2 is satisfied in the z_1z_2. Consequently, the point E_3^* is a cusp of co-dimension 2.

Theorem 4 *The equilibrium point $E_6^*(u_6^*, v_6^*)$ of the system (3) is a cusp of co-dimension 2 if $\gamma \neq 1+\alpha\xi$.*

Proof At $E_6^*(x_6^*, y_6^*)$, the Jacobian matrix of the system (3) is

$$J_{E_6^*} = \begin{pmatrix} 0 & 0 \\ \frac{\beta(1+\alpha\xi-\xi)}{1+\alpha\xi} - \theta(1+\alpha\xi) & 0 \end{pmatrix}.$$

The determinant and trace of the above matrix are zero. To relocate the equilibrium point E_6^* to the origin, we consider transformations $X = x - x_6^*, Y = y - y_6^*$. The Taylor series expansion centered at $(0,0)$ reduces the system (3) as follows:

$$\begin{cases} \frac{dX}{dt} = \alpha_{20}X^2 + \alpha_{11}XY + o|(X,Y)^3|, \\ \frac{dY}{dt} = \beta_{10}X + \beta_{20}X^2 + \beta_{11}XY + o|(X,Y)^3|, \end{cases} \tag{8}$$

where $\alpha_{20} = \left(-\frac{1}{\gamma} + \frac{1}{1+\alpha\xi}\right)$, $\alpha_{11} = -\frac{1}{1+\alpha\xi}$, $\beta_{10} = \frac{\beta(1+\alpha\xi-\xi)}{1+\alpha\xi} - \theta(1+\alpha\xi)$, $\beta_{20} = -\frac{\beta(1+\alpha\xi-\xi)}{(1+\alpha\xi)^2}$, $\beta_{11} = \frac{\beta(1+\alpha\xi-\xi)}{(1+\alpha\xi)^2} - \theta$. Introduce a new time variable T by $T = \beta_{10}t$, the system (8) reduced to

$$\begin{cases} \frac{dX}{dT} = \bar{\alpha_{20}}X^2 + \bar{\alpha_{11}}XY + o|(X,Y)^3|, \\ \frac{dY}{dT} = X + \bar{\beta_{20}}X^2 + \bar{\beta_{11}}XY + o|(X,Y)^3|, \end{cases} \tag{9}$$

where $\bar{\alpha_{20}} = \frac{\alpha_{20}}{\beta_{10}}$, $\bar{\alpha_{11}} = \frac{\alpha_{11}}{\beta_{10}}$, $\bar{\beta_{20}} = \frac{\beta_{20}}{\beta_{10}}$, $\bar{\beta_{11}} = \frac{\beta_{11}}{\beta_{10}}$.
By applying the transformations $Y_1 = Y - \frac{1}{2}\bar{\beta_{11}}Y^2$, $X_1 = X + \bar{\beta_{20}}X^2$, system (9) reduces to

$$\begin{cases} \frac{dX_1}{dT} = \vartheta_1 X_1^2 + \vartheta_2 X_1 Y_1 + o|(X_1, Y_1)^3|, \\ \frac{dY_1}{dT} = X_1 + o|(X_1, Y_1)^3|, \end{cases} \tag{10}$$

where $\vartheta_1 = \bar{\alpha_{20}}$, $\vartheta_2 = \bar{\alpha_{11}}$.
Finally, applying the transformations $Y_2 = Y_1$, $X_2 = X_1 + o|(X_2, Y_2)^3|$, the system (10) reduces to

$$\begin{cases} \frac{dX_2}{dT} = \vartheta_1 X_2^2 + \vartheta_2 X_2 Y_2 + o|(X_2, Y_2)^3|, \\ \frac{dY_2}{dT} = X_2. \end{cases}$$

The non-degeneracy condition $\vartheta_1\vartheta_2 \neq 0$, i.e., $\frac{1}{1+\alpha\xi}\left(-\frac{1}{\gamma} + \frac{1}{1+\alpha\xi}\right) \neq 0$ for cusp of co-dimension 2 can be satisfied in the X_2Y_2 plane, if $\gamma \neq 1 + \alpha\xi$. As a result, the equilibrium point E_6^* is a cusp of co-dimension 2.

5 Bifurcation analysis

In this section of the article, we are interested in a variety of distinct bifurcations that might take place in the system (3), such as saddle-node, Bogdanov-Takens, and Hopf bifurcations.

Saddle-node bifurcation

In Section 3, the requirements necessary for the existence of two interior equilibrium points $E_1^*(x_1^*, y_1^*)$ and $E_2^*(x_2^*, y_2^*)$ have been achieved that were based on many constraints. The distinguishable features of these equilibrium points persist until $\Delta_1 > 0$, $\Delta_2 > 0$ and $\Delta_2^2 > \Delta_3$; afterward, they have a chance of converging to $E_3^*(x_3^*, y_3^*)$ if $\Delta_1 > 0$, $\Delta_2 > 0$ and $\Delta_2^2 = \Delta_3$ and vanishing if $\Delta_1 > 0$, $\Delta_2 > 0$ and $\Delta_2^2 < \Delta_3$. This kind of annihilation of equilibrium points may be due to the saddle-node bifurcation for interior equilibrium points, which transpires when the bifurcation parameter θ satisfies $\theta = \theta^* = \frac{((\delta+\beta)(1+\alpha\xi)-2\beta\xi)-2\sqrt{\Delta_4}}{(1+\alpha\xi)^2}$, provided $(\delta+\beta)(1+\alpha\xi) > 2\beta\xi$ and $\delta(1+\alpha\xi) > \xi(\delta+\beta)$, where $\Delta_4 = (\delta(1+\alpha\xi) - \xi(\delta+\beta))\beta(1+\alpha\xi) + \beta^2\xi^2$. Here, θ^* is known as the saddle-node bifurcation threshold. Sotomayor's theorem [38] has been applied to ascertain the occurrence of the bifurcation.

Theorem 5 *System (3) exhibits a saddle-node bifurcation at the equilibrium point $E_3^* = (x_3^*, y_3^*)$ with respect to the parameter θ if $\theta = \theta^* = \frac{((\delta+\beta)(1+\alpha\xi)-2\beta\xi)-2\sqrt{\Delta_4}}{(1+\alpha\xi)^2}$, provided, $(\delta+\beta)(1+\alpha\xi) > 2\beta\xi$ and $\delta(1+\alpha\xi) > \xi(\delta+\beta)$, where $\Delta_4 = (\delta(1+\alpha\xi) - \xi(\delta+\beta))\beta(1+\alpha\xi) + \beta^2\xi^2$.*

Proof The Jacobian matrix for system (3) at interior equilibrium point E_3^* is

$$J_{E_3^*} = \begin{bmatrix} \frac{(\beta-\delta-\theta(1+\alpha\xi))(\gamma\theta+\delta-\beta)}{\gamma\theta(\beta-\delta+\theta(1+\alpha\xi))} & \frac{-(\beta-\delta-\theta(1+\alpha\xi))}{\beta-\delta+\theta(1+\alpha\xi)} \\ 0 & 0 \end{bmatrix}.$$

The eigenvalues of the above matrix are $\lambda_1 = \frac{(\beta-\delta-\theta(1+\alpha\xi))(\gamma\theta+\delta-\beta)}{\gamma\theta(\beta-\delta+\theta(1+\alpha\xi))} \neq 0$ and $\lambda_2 = 0$. Let P and Q be the eigenvectors corresponding to $\lambda_2 = 0$ for the matrices $J_{E_3^*}$ and $J_{E_3^*}^T$, respectively.

A straightforward calculation implies

$$P = \begin{bmatrix} 1 \\ \frac{\gamma\theta+\delta-\beta}{\gamma\theta} \end{bmatrix}, \quad Q = \begin{bmatrix} 0 \\ 1 \end{bmatrix}.$$

Consider

$$\psi(x, y, \theta) = \begin{bmatrix} 1 - \frac{x}{\gamma} - \frac{y}{1+\alpha\xi+x} \\ \frac{\beta(x+\xi)}{1+\alpha\xi+x} - \delta - \theta x \end{bmatrix}.$$

One can easily find,

$$\psi_\theta\left(E_3^*, \theta^*\right) = \begin{bmatrix} 0 \\ \frac{-(\beta-\delta-\theta(1+\alpha\xi))}{2\theta} \end{bmatrix},$$

and

$$D^2\psi\left(E_3^*, \theta^*\right)(P, P) = \begin{bmatrix} \frac{-4\theta(2\theta\gamma-(\beta-\delta-\theta(1+\alpha\xi)))}{\gamma(\beta-\delta+\theta(1+\alpha\xi))^2} + \frac{8\theta(\gamma\theta+\delta-\beta)}{\gamma(\beta-\delta+\theta(1+\alpha\xi))} \\ \frac{-16\beta\theta^3(1+\alpha\xi-\xi)}{(\beta-\delta+\theta(1+\alpha\xi))^3} \end{bmatrix}.$$

We have

$$Q^T.\psi_\theta\left(E_3^*, \theta^*\right) = \frac{-(\beta-\delta-\theta(1+\alpha\xi))}{2\theta} \neq 0,$$

and

$$Q^T.D^2\psi\left(E_3^*, \theta^*\right)(P, P) = \frac{-16\beta\theta^3(1+\alpha\xi-\xi)}{(\beta-\delta+\theta(1+\alpha\xi))^3} \neq 0.$$

Therefore, the transversality conditions necessary for the appearance of the saddle-node bifurcation are satisfied, thereby confirming the presence of a saddle-node bifurcation.

Hopf bifurcation

Theorem 2 concludes that the equilibrium point $E_1^* = (x_1^*, y_1^*)$ is unstable if $1 + \alpha\xi + 2x_1^* < \gamma$ and stable if $1 + \alpha\xi + 2x_1^* > \gamma$. It is interesting to investigate the nature of the point E_1^* whenever $\gamma - (1 + \alpha\xi + 2x_1^*) = 0$.

Theorem 6 *Assume that the equilibrium point $E_1^* = (x_1^*, y_1^*)$ exists. For the parametric condition, $\gamma - (1 + \alpha\xi + 2x_1^*) = 0$, system (3) undergoes a Hopf bifurcation around the equilibrium point E_1^* with respect to the parameter γ.*

Proof We have $det\left(J_{E_1^*}\right) > 0$. The parametric condition $\gamma = \gamma^{[hf]} = 1 + \alpha\xi + 2x_1^*$ implies $tr\left(J_{E_1^*}\right) = 0$. Further, at $\gamma = \gamma^{[hf]} = 1 + \alpha\xi + 2x_1^*$

$$\frac{d}{d\gamma}\left(tr\left(J_{E_1^*}\right)\right)\Big|_{\gamma=\gamma^{[hf]}} = \frac{x_1^*(1+\xi+2x_1^*)}{\gamma^2(1+\alpha\xi+x_1^*)} \neq 0.$$

Thus, the transversality requirement necessary for the appearance of the Hopf bifurcation is satisfied, thereby confirming the presence of a Hopf bifurcation.
The aforementioned theorem is sure enough for the emergence of the limit cycle around the point E_1^*. However, it provides no insight into the stability of the limit cycle. In this continuation, we will proceed with the computation of the first Lyapunov number for the system (3) at the point E_1^*. This calculation will enable us to ascertain the stability of the limit cycle.
To relocate the point E_1^*, to the origin $(0,0)$, we substitute $x = \bar{x} - x_1^*$ and $y = \bar{y} - y_1^*$. The system (3) reduces to

$$\begin{cases} \frac{d\bar{x}}{dt} = \alpha_{10}\bar{x} + \alpha_{01}\bar{y} + \alpha_{20}\bar{x}^2 + \alpha_{11}\bar{x}\bar{y} + \alpha_{02}\bar{y}^2 + \alpha_{30}\bar{x}^3 + \alpha_{21}\bar{x}^2\bar{y} + \alpha_{12}\bar{x}\bar{y}^2 + \alpha_{03}\bar{y}^3 + g_1(\bar{x},\bar{y}), \\ \frac{d\bar{y}}{dt} = \beta_{10}\bar{x} + \beta_{01}\bar{y} + \beta_{20}\bar{x}^2 + \beta_{11}\bar{x}\bar{y} + \beta_{02}\bar{y}^2 + \beta_{30}\bar{x}^3 + \beta_{21}\bar{x}^2\bar{y} + \beta_{12}\bar{x}\bar{y}^2 + \beta_{03}\bar{y}^3 + g_2(\bar{x},\bar{y}), \end{cases} \tag{11}$$

where $\alpha_{10} = x_1^*(\frac{-1}{\gamma} + \frac{y_1^*}{(1+\alpha\xi+x_1^*)^2})$, $\alpha_{01} = \frac{-x_1^*}{1+\alpha\xi+x_1^*}$, $\alpha_{20} = (\frac{-1}{\gamma} + \frac{y_1^*(1+\alpha\xi)}{(1+\alpha\xi+x_1^*)^3})$, $\alpha_{11} = \frac{-(1+\alpha\xi)}{(1+\alpha\xi+x_1^*)^2}$, $\alpha_{02} = 0$, $\alpha_{30} = \frac{-y_1^*(1+\alpha\xi)}{(1+\alpha\xi+x_1^*)^4}$, $\alpha_{21} = \frac{1+\alpha\xi}{(1+\alpha\xi+x_1^*)^3}$, $\alpha_{12} = 0$, $\alpha_{03} = 0$, $\beta_{10} = y_1^*\Big(\frac{(\beta(1+\alpha\xi-\xi))}{(1+\alpha\xi+x_1^*)^2} - \theta\Big)$, $\beta_{01} = 0$, $\beta_{20} = \frac{-y_1^*\beta(1+\alpha\xi-\xi)}{1+\alpha\xi+x_1^*)^3}$, $\beta_{11} = \frac{\beta(1+\alpha\xi-\xi)}{(1+\alpha\xi+x_1^*)^2} - \theta$, $\beta_{02} = 0$, $\beta_{30} = \frac{y_1^*\beta(1+\alpha\xi-\xi)}{(1+\alpha\xi+x_1^*)^4}$, $\beta_{21} = \frac{-\beta(1+\alpha\xi-\xi)}{(1+\alpha\xi+x_1^*)^3}$, $\beta_{12} = 0$, $\beta_{03} = 0$, and $g_1(\bar{x},\bar{y}) = \sum_{i+j=4}^{\infty}\alpha_{ij}\bar{x}\bar{y}$, $g_2(\bar{x},\bar{y}) = \sum_{i+j=4}^{\infty}\beta_{ij}\bar{x}\bar{y}$.
The first Lyapunov number [38] at the origin is

$$\begin{aligned} \sigma = \frac{-3\pi}{2\alpha_{01}\Delta^{3/2}}\{&[\alpha_{10}\beta_{10}M_1 + \alpha_{10}\alpha_{01}M_2 + \beta_{10}^2M_3 + 2\alpha_{10}\beta_{10}(\alpha_{20}\alpha_{02} - \beta_{02}^2) \\ &+ 2\alpha_{10}\alpha_{01}(\beta_{20}\beta_{02} - \alpha_{20}^2) - \alpha_{01}^2(\beta 11\beta_{20} + 2\alpha_{20}\beta_{20}) + (2\alpha_{10}^2 - \alpha_{01}\beta_{10})(\alpha_{11}\alpha_{20} - \beta_{11}\beta_{02})] \\ &- (\alpha_{10}^2 + \alpha_{01}\beta_{10})M_4\}, \end{aligned} \tag{12}$$

where, $M_1 = \alpha_{02}\beta_{11} + \alpha_{11}\beta_{02} + \alpha_{11}^2$, $M_2 = \alpha_{11}\beta_{02} + \alpha_{20}\beta_{11} + \beta_{11}^2$, $M_3 = 2\alpha_{02}\beta_{02} + \alpha_{11}\alpha_{02}$, $M_4 = \alpha_{12}\beta_{10} - \beta_{21}\alpha_{01} + 2\alpha_{10}(\beta_{12} + \alpha_{21}) + 3(\beta_{03}\beta_{10} - \alpha_{30}\alpha_{01})$, and $\Delta = \frac{x_1^*y_1^*}{(1+\alpha\xi+x_1^*)^2}\sqrt{\Delta_2{}^2 - \Delta_3}$. If $\sigma > 0$, then a subcritical Hopf-bifurcation appears around the point E_1^* and the limit cycle will be unstable. If $\sigma < 0$, then a supercritical Hopf-bifurcation appears around the point E_1^*, and the limit cycle will be stable.

Bogdanove-taken bifurcation

In addition to the codimension one bifurcations that have been studied up to this point, it is also conceivable for the system (3) to experience a codimension two bifurcation, such as a Bogdanov-Takens (BT) bifurcation. This bifurcation is expected to take place in the vicinity of the point E_3^*, which is identified as a cusp of co-dimension two under certain parametric constraints.

Theorem 7 *Assume that the point E_3^* exists and that it is a cusp of codimension two. If γ and θ are the bifurcation parameters, the system (3) experiences the Bogdanov-Takens bifurcation of codimension 2 in the vicinity of E_3^*.*

Proof Here, our objective is to provide analytical expressions for the saddle-node bifurcation curve, Hopf bifurcation curve, and homoclinic bifurcation curve in the vicinity of the Bogdanov-Takens (BT) point. To accomplish our objective, we use the approach defined in the works [36, 37]. Let γ_{BT} and θ_{BT} represent the threshold values of the bifurcation parameters γ and θ that satisfy $\det J_{E_3} = 0, \mathrm{tr} J_{E_3} = 0$. Consider a perturbation to the parameters γ and θ in the vicinity of BT

bifurcation values provided by $\gamma = \gamma_{BT} + \lambda_1$ and $\theta = \theta_{BT} + \lambda_2$, respectively, where $\lambda = (\lambda_1, \lambda_2)$ is a parameter vector in the vicinity of $(0,0)$.

When we substitute these perturbations into system (3), we obtain

$$\begin{cases} \frac{dx}{dt} = x(1 - \frac{x}{\gamma_{BT}+\lambda_1}) - \frac{xy}{1+\alpha\xi+x} = f_1(x,y,\lambda_1), \\ \frac{dy}{dt} = \frac{\beta(x+\xi)y}{1+\alpha\xi+x} - \delta y - (\theta_{BT}+\lambda_2)xy = f_2(x,y,\lambda_2). \end{cases} \tag{13}$$

The transformations $U = x - x_3^*$, $V = y - y_3^*$ are taken into consideration to relocate the point E_3^* to the origin $(0,0)$. After applying Taylor's series expansion centered at $(0,0)$, the system (13) becomes

$$\begin{cases} \frac{dU}{dt} = \alpha_{00} + \alpha_{10}U + \alpha_{01}V + \alpha_{20}U^2 + \alpha_{11}UV + P_1(U,V), \\ \frac{dV}{dt} = \beta_{00} + \beta_{10}U + \beta_{01}V + \beta_{20}U^2 + \beta_{11}UV + P_2(U,V), \end{cases} \tag{14}$$

where $\alpha_{00} = f_1(U,V,\lambda_1)$, $\alpha_{10} = 1 - \frac{2x_3^*}{\gamma_{BT}+\lambda_1} - \frac{(1+\alpha\xi)y_3^*}{(1+\alpha\xi+x_3^*)^2}$, $\alpha_{01} = -\frac{x_3^*}{1+\alpha\xi+x_3^*}$, $\alpha_{20} = -\frac{1}{\gamma_{BT}+\lambda_1} + \frac{(1+\alpha\xi)y_3^*}{(1+\alpha\xi+x_3^*)^3}$, $\alpha_{11} = -\frac{(1+\alpha\xi)}{(1+\alpha\xi+x_3^*)^2}$, $\alpha_{02} = 0$, $\beta_{00} = -\lambda_2 x_3^* y_3^*$, $\beta_{10} = \frac{\beta(1+\alpha\xi-\xi)y_3^*}{(1+\alpha\xi+x_3^*)^2} - (\theta_{BT}+\lambda_2)y_3^*$,

$\beta_{01} = -\lambda_2 x_3^*$, $\beta_{11} = \frac{\beta(1+\alpha\xi-\xi)}{(1+\alpha\xi+x_3^*)^2} - (\theta_{BT}+\lambda_2)$, $\beta_{02} = 0$, and P_1, P_2 is power series in (U,V) with powers $x^i y^j$ satisfying $i+j \geq 3$, and the coefficients smoothly depend upon λ_1 and λ_2.

After using the affine transformation $U_1 = U$, $U_2 = \alpha_{10}U + \alpha_{01}V$, the system (14) simplifies to

$$\begin{cases} \frac{dU_1}{dt} = \xi_{00} + U_2 + \xi_{20}U_1^2 + \xi_{11}U_1U_2 + \tilde{P}_1(U_1,U_2), \\ \frac{dU_2}{dt} = \mu_{00} + \mu_{10}U_1 + \mu_{01}U_2 + \mu_{20}U_1^2 + \mu_{11}U_1U_2 + \tilde{P}_2(U_1,U_2), \end{cases} \tag{15}$$

where $\xi_{00} = \alpha_{00}$, $\xi_{20} = \alpha_{20} - \frac{\alpha_{11}\alpha_{10}}{\alpha_{01}}$, $\xi_{11} = \frac{\alpha_{11}}{\alpha_{01}}$, $\mu_{00} = \alpha_{00}\alpha_{10} + \beta_{00}\alpha_{01}$, $\mu_{10} = \alpha_{10}\beta_{10} - \beta_{01}\alpha_{10}$, $\mu_{01} = \alpha_{10} + \beta_{01}$, $\mu_{20} = \alpha_{10}\alpha_{20} + \alpha_{01}\beta_{20} - \beta_{11}\alpha_{10} - \frac{\alpha_{11}\alpha_{10}^2}{\alpha_{01}}$, $\mu_{11} = \beta_{11} + \frac{\alpha_{10}\alpha_{11}}{\alpha_{01}}$, and $\tilde{P}_1$, $\tilde{P}_2$ are the power series in (U_1,U_2) with powers U_1^i, U_2^j satisfying $i+j \geq 3$.

Next, under the following C^∞ change of coordinates in the close vicinity of $(0,0)$.

Define $V_1 = U_1$, $V_2 = \xi_{00} + U_2 + \xi_{20}U_1^2 + \xi_{11}U_1U_2$, system (15) reduced to

$$\begin{cases} \frac{dV_1}{dt} = V_2 + \check{P}_1(V_1,V_2), \\ \frac{dV_2}{dt} = \gamma_{00} + \gamma_{10}V_1 + \gamma_{01}V_2 + \gamma_{20}V_1^2 + \gamma_{11}V_1V_2 + \gamma_{02}V_2^2 + \check{P}_2(V_1,V_2), \end{cases} \tag{16}$$

where $\gamma_{00} = \mu_{00} - \mu_{01}\xi_{00}$, $\gamma_{10} = \mu_{10} - \mu_{11}\xi_{00} + \xi_{11}\mu_{00} - \mu_{01}\xi_{00}\xi_{11}$, $\gamma_{01} = \mu_{01} - \xi_{11}\xi_{00}$, $\gamma_{20} = \mu_{20} - \mu_{01}\xi_{20} + \xi_{11}\mu_{10} - \mu_{11}\xi_{00}\xi_{11}$, $\gamma_{11} = 2\xi_{20} + \mu_{11} - \mu_{01}\xi_{11} + \xi_{11}\mu_{01}$, $\gamma_{02} = \xi_{11}$, and $\check{P}_1, \check{P}_2$ are the power series in (V_1,V_2) with powers V_1^i, V_2^j satisfying $i+j \geq 3$.

Let us introduce a new time variable T by $dt = (1 - \gamma_{02}V_1)dT$. Rewriting T as t, the system (16) can be rewritten as

$$\begin{cases} \frac{dV_1}{dt} = V_2(1 - \gamma_{02}V_1) + \check{P}_1(V_1,V_2), \\ \frac{dV_2}{dt} = (1 - \gamma_{02}V_1)[\gamma_{00} + \gamma_{10}V_1 + \gamma_{01}V_2 + \gamma_{20}V_1^2 + \gamma_{11}V_1V_2 + \gamma_{02}V_2^2 + \check{P}_2(V_1,V_2)], \end{cases} \tag{17}$$

$Z_1 = V_1, Z_2 = V_2(1-\gamma_{02}V_1) + \check{P}_1(V_1, V_2)$, then system (17) reduced to

$$\begin{cases} \frac{dZ_1}{dt} = Z_2, \\ \frac{dZ_2}{dt} = \delta_{00} + \delta_{10}Z_1 + \delta_{01}Z_2 + \delta_{20}Z_1^2 + \delta_{11}Z_1Z_2 + \bar{P}_2(Z_1, Z_2), \end{cases} \tag{18}$$

where $\delta_{00} = \gamma_{00}$, $\delta_{10} = \gamma_{10} - 2\gamma_{02}\gamma_{00}$, $\delta_{01} = \gamma_{01}, \delta_{20} = \gamma_{20} + \gamma_{00}\gamma_{02}^2 - 2\gamma_{02}\gamma_{10}$, $\delta_{11} = \gamma_{11} - \gamma_{02}\gamma_{01}$, and $\bar{P}_2$ are the power series in (Z_1, Z_2) with powers Z_1^i, Z_2^j satisfying $i + j \geq 3$.

One can not determine the sign of δ_{20} whenever $\lambda_1 \to 0$ and $\lambda_2 \to 0$. Consequently, it is essential to consider the following two cases:

Case 1: $\delta_{20} > 0$, Consider $u_1 = Z_1, \quad u_2 = \frac{Z_2}{\sqrt{\delta_{20}}}, \quad d\tau = \sqrt{\delta_{20}}dt$, then system (18) becomes

$$\begin{cases} \frac{du_1}{d\tau} = u_2, \\ \frac{du_2}{d\tau} = \frac{\delta_{00}}{\delta_{20}} + \frac{\delta_{10}}{\delta_{20}}u_1 + \frac{\delta_{01}}{\sqrt{\delta_{20}}}u_2 + u_1^2 + \frac{\delta_{11}}{\sqrt{\delta_{20}}}u_1u_2 + P(u_1, u_2, \lambda), \end{cases} \tag{19}$$

where $P(u_1, u_2, 0)$ is a power series in (u_1, u_2) with powers u_1^i, u_2^j satisfying $i + j \geq 3$.

Using the affine transformation $v_1 = u_1 + \frac{\delta_{10}}{2\delta_{20}}, \quad v_2 = u_2$, then system (19) becomes

$$\begin{cases} \frac{dv_1}{d\tau} = v_2, \\ \frac{dv_2}{d\tau} = \frac{\delta_{00}}{\delta_{20}} - \frac{\delta_{10}^2}{4\delta_{20}^2} + \left(\frac{\delta_{01}}{\sqrt{\delta_{20}}} - \frac{\delta_{11}\delta_{10}}{2\delta_{20}\sqrt{\delta_{20}}}\right)v_2 + v_1^2 + \frac{\delta_{11}}{\sqrt{\delta_{20}}}v_1v_2 + Q(v_1, v_2, \lambda), \end{cases} \tag{20}$$

where $Q(v_1, v_2, 0)$ is a power series in (v_1, v_2) with powers v_1^i, v_2^j satisfying $i + j \geq 3$.

Consider $w_1 = \frac{\delta_{11}^2}{\delta_{20}}v_1, \quad w_2 = \frac{\delta_{11}^3}{\delta_{20}\sqrt{\delta_{20}}}v_2, \quad t = \frac{\sqrt{\delta_{20}}}{\delta_{11}}\tau$, then the system (20) becomes

$$\begin{cases} \frac{dw_1}{dt} = w_2, \\ \frac{dw_2}{dt} = v_1(\lambda_1, \lambda_2) + v_2(\lambda_1, \lambda_2)w_2 + w_1^2 + w_1w_2 + R(w_1, w_2, \lambda), \end{cases}$$

where $v_1(\lambda_1, \lambda_2) = \frac{\delta_{00}\delta_{11}^4}{\delta_{20}^3} - \frac{\delta_{10}^2\delta_{11}^4}{4\delta_{20}^4}, \quad v_2(\lambda_1, \lambda_2) = \frac{\delta_{01}\delta_{11}}{\delta_{20}} - \frac{\delta_{11}^2\delta_{10}}{2\delta_{20}^2}$, and $R(w_1, w_2, 0)$ is a power series in (w_1, w_2) with powers w_1^i, w_2^j satisfying $i + j \geq 3$.

Case 2: $\delta_{20} < 0$, Consider $\imath\bar{1} = z_1, \quad \imath\bar{2} = \frac{z_2}{\sqrt{-\delta_{20}}}, \quad d\tau = \sqrt{-\delta_{20}}dt$, then system (18) becomes

$$\begin{cases} \frac{d\imath\bar{1}}{d\tau} = \imath\bar{2}, \\ \frac{d\imath\bar{2}}{d\tau} = \frac{-\delta_{00}}{\delta_{20}} - \frac{\delta_{10}}{\delta_{20}}\imath\bar{1} + \frac{\delta_{01}}{\sqrt{-\delta_{20}}}\imath\bar{2} - \imath\bar{1}^2 + \frac{\delta_{11}}{\sqrt{-\delta_{20}}}\imath\bar{1}\imath\bar{2} + \bar{P}(\imath\bar{1}, \imath\bar{2}, \lambda), \end{cases} \tag{21}$$

where $\bar{P}(\imath\bar{1}, \imath\bar{2}, 0)$ is a power series in $(\imath\bar{1}, \imath\bar{2})$ with powers $\imath\bar{1}^i, \imath\bar{2}^j$ satisfying $i + j \geq 3$.

Using the affine transformation $\bar{v_1} = \imath\bar{1} + \frac{\delta_{10}}{2\delta_{20}}, \quad \bar{v_2} = \imath\bar{2}$, then system (21) becomes

$$\begin{cases} \frac{d\bar{v_1}}{d\tau} = \bar{v_2}, \\ \frac{d\bar{v_2}}{d\tau} = -\frac{\delta_{00}}{\delta_{20}} + \frac{\delta_{10}^2}{4\delta_{20}^2} + \left(\frac{\delta_{01}}{\sqrt{-\delta_{20}}} - \frac{\delta_{11}\delta_{10}}{2\delta_{20}\sqrt{-\delta_{20}}}\right)\bar{v_2} + \bar{v_1}^2 + \frac{\delta_{11}}{\sqrt{-\delta_{20}}}\bar{v_1}\bar{v_2} + \bar{Q}(\bar{v_1}, \bar{v_2}, \lambda), \end{cases} \tag{22}$$

where $Q(\bar{v_1}, \bar{v_2}, 0)$ is a power series in $(\bar{v_1}, \bar{v_2})$ with powers $\bar{v_1}^i, \bar{v_2}^j$ satisfying $i + j \geq 3$.

Consider $\bar{w_1} = \frac{\delta_{11}^2}{\delta_{20}}\bar{v_1}$, $\bar{w_2} = -\frac{\delta_{11}^3}{\delta_{20}\sqrt{-\delta_{20}}}\bar{v_2}$, $t = -\frac{\sqrt{-\delta_{20}}}{\delta_{11}}\tau$, then system (22) becomes

$$\begin{cases} \frac{d\bar{w_1}}{dt} = \bar{w_2}, \\ \frac{d\bar{w_2}}{dt} = \bar{v_1}(\lambda_1,\lambda_2) + \bar{v_2}(\lambda_1,\lambda_2)\bar{w_2} + \bar{w_1}^2 + \bar{w_1}\bar{w_2} + \bar{R}(\bar{w_1},\bar{w_2},\lambda), \end{cases} \tag{23}$$

where $\bar{v_1}(\lambda_1,\lambda_2) = \frac{\delta_{00}\delta_{11}^4}{\delta_{20}^3} - \frac{\delta_{10}^2\delta_{11}^4}{4\delta_{20}^4}$, $\bar{v_2}(\lambda_1,\lambda_2) = \frac{\delta_{01}\delta_{11}}{\delta_{20}} - \frac{\delta_{11}^2\delta_{10}}{2\delta_{20}^2}$, and $\bar{R}(\bar{w_1},\bar{w_2},0)$ is a power series in $(\bar{w_1},\bar{w_2})$ with powers $\bar{w_1}^i,\bar{w_2}^j$ satisfying $i+j \geq 3$.

In order to minimize the number of cases, it is advisable to retain $v_1(\lambda)$ and $v_2(\lambda)$ to denote $\bar{v_1}(\lambda)$, and $\bar{v_2}(\lambda)$ in system (23). Moreover, if $\left|\frac{\partial(v_1,v_2)}{\partial(\lambda_1,\lambda_2)}\right|_{\lambda_1=\lambda_2=0} \neq 0$, then the parameter transformations

$$v_1(\lambda_1,\lambda_2) = \frac{\delta_{00}\delta_{11}^4}{\delta_{20}^3} - \frac{\delta_{10}^2\delta_{11}^4}{4\delta_{20}^4}, \quad v_2(\lambda_1,\lambda_2) = \frac{\delta_{01}\delta_{11}}{\delta_{20}} - \frac{\delta_{11}^2\delta_{10}}{2\delta_{20}^2},$$

and

$$\bar{v_1}(\lambda_1,\lambda_2) = \frac{\delta_{00}\delta_{11}^4}{\delta_{20}^3} - \frac{\delta_{10}^2\delta_{11}^4}{4\delta_{20}^4}, \quad \bar{v_2}(\lambda_1,\lambda_2) = \frac{\delta_{01}\delta_{11}}{\delta_{20}} - \frac{\delta_{11}^2\delta_{10}}{2\delta_{20}^2},$$

are topologically equivalent in the vicinity of the origin and v_1, v_2 are independent parameters. As a result, it can be inferred that the system (13) experiences the Bogdanov-Takens bifurcation when the values of (λ_1,λ_2) are within closed proximity to the origin $(0,0)$, [38]. The following are the local representations of the bifurcation curves:

1 The Saddle-node bifurcation curve $SN = \{(v_1,v_2) : v_1 = 0, v_2 \neq 0\}$.
2 The Hopf bifurcation curve $H = \{(v_1,v_2) : v_2 = \pm\sqrt{-v_1}, v_1 < 0\}$.
3 The Homoclinic bifurcation curve $HL = \{(v_1,v_2) : v_2 = \pm\frac{5}{7}\sqrt{-v_1}, v_1 < 0\}$.

6 Numerical simulation

In this section, numerical simulations are provided to validate our analytical findings. We benefited from MATHEMATICA 10.0 software to draw the phase portrait diagrams for the computations. We provide a total of six numerical examples, each carefully selected to demonstrate the implications of our analytical results. For these examples, we have chosen specific values for the ecosystem parameters γ, β, ξ, δ, and θ to ensure that they align with the theoretical findings and enhance the understanding of the dynamics of the systems.

(1)

$$\begin{cases} \frac{dx}{dt} = x\left((1-\frac{x}{5}) - \frac{y}{1+2.8\times0.35+x}\right), \\ \frac{dy}{dt} = y\left(\frac{0.9(x+0.35)}{1+2.8\times0.35+x} - 0.3 - \theta x\right). \end{cases} \tag{24}$$

System (24) exhibits several equilibrium points depending on parametric conditions. The nature of these points is explained in Table 1 and is also depicted in Figure 1. A threshold value of the anti-predator behavior parameter $\theta = 0.118988$ is obtained in Figure 1a and Figure 1b.

Table 1. Number and nature of equilibrium points (Eps) of the system (24)

Value of θ	Conditions	Number of Eps	Existence of Eps	Nature of Eps	Figure
$0 < \theta < 0.118988$	$\Delta_2^2 > \Delta_3$	4	$E_0 = (0,0)$ $E_\gamma = (5,0)$ $E_1^* = (1.04319, 2.39244)$ $E_2^* = (2.43136, 2.26624)$	Saddle Stable Unstable Saddle	1c
$\theta = 0.11898$	$\Delta_2^2 = \Delta_3$	3	$E_0 = (0,0)$ $E_\gamma = (5,0)$ $E_3^* = (1.53127, 2.43593)$	Saddle Stable Unstable saddle-node	1d
$\theta > 0.11898$	$\Delta_2^2 < \Delta_3$	2	$E_0 = (0,0)$ $E_\gamma = (5,0)$	Saddle Globally Stable	1e

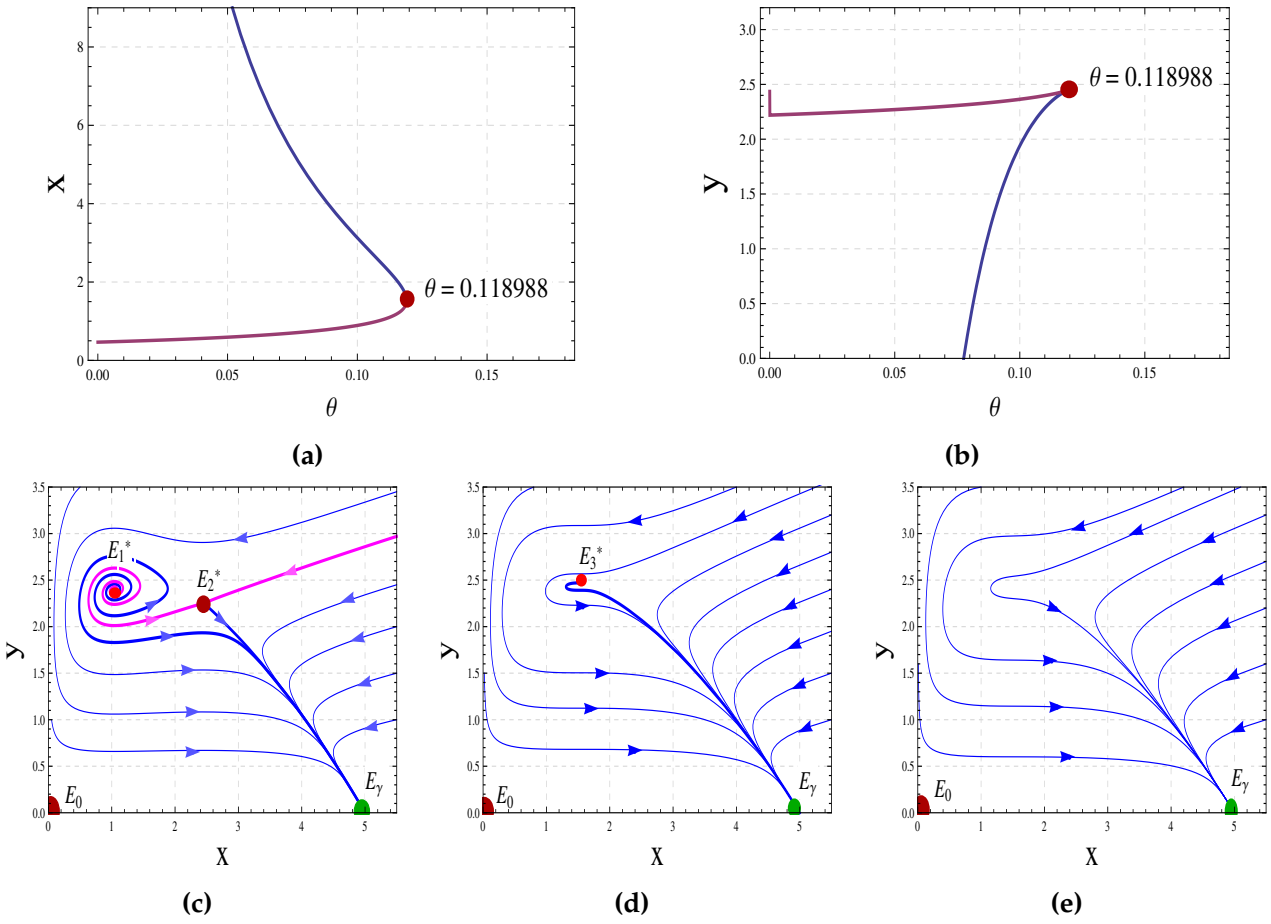

Figure 1. (a)-(b) Saddle-node bifurcation diagram. (c) $\theta = 0.11$. The equilibrium point E_1^* is unstable, and E_2^* is a saddle. (d) $\theta = 0.118988$. The equilibrium point E_3^* is an unstable saddle node. (e) $\theta = 0.12$. The predator-free equilibrium point is globally stable. Ecologically, there is a threshold value of the anti-predator parameter θ below which species may coexist and above which the predator species go extinct, leading to the collapse of the system

(2)

$$\begin{cases} \frac{dx}{dt} = x\left((1-\frac{x}{2}) - \frac{y}{1+0.001\times 0.8+x}\right), \\ \frac{dy}{dt} = y\left(\frac{0.4(x+0.8)}{1+0.001\times 0.8+x} - 0.3 - 0.11x\right). \end{cases} \tag{25}$$

Table 2. Number and nature of equilibrium points (Eqs) of the system (25)

Condition	Number of Eqs	Existence of Eqs	Nature of Eqs	Figure
$\Delta_1 < 0$	3	$E_0 = (0,0)$ $E_\gamma = (2,0)$ $E_4^* = (0.380454, 1.1185)$	Unstable Stable Saddle	2

Table 3. Number and nature of equilibrium points (Eqs) of the system (26)

Value of θ	Conditions	Number of Eqs	Existence of Eqs	Nature of Eqs	Figure
$\theta = 0.2$	$\Delta_1 = 0,\ \Delta_2 > 0,$	4	$E_0 = (0,0)$ $E_\gamma = (3,0)$ $E_5^* = (1.992, 1.008)$ $E_6^* = (0, 1.02)$	Unstable Stable Saddle Unstable saddle node	3a
$\theta = 0.8$	$\Delta_1 = 0,\ \Delta_2 < 0,$	3	$E_0 = (0,0)$ $E_\gamma = (3,0)$ $E_6^* = (0, 1.008)$	Unstable Stable Cusp	3b

System (25) exhibits several equilibrium points depending on the parametric condition. The nature of these points is explained in Table 2 and is also shown graphically in Figure 2.

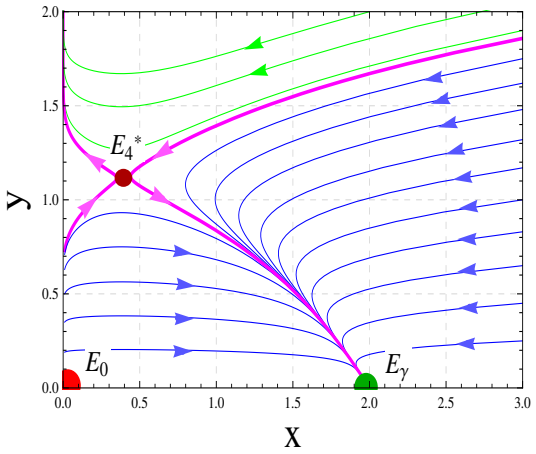

Figure 2. The equilibrium point E_0 is unstable, E_γ is stable, and E_4^* is saddle. Ecologically, the system will collapse due to the extinction of either the prey or the predator

(3)

$$\begin{cases} \frac{dx}{dt} = x\left((1-\frac{x}{3}) - \frac{y}{1+0.02381\times 0.336+x}\right), \\ \frac{dy}{dt} = y\left(\frac{0.9(x+0.336)}{1+0.02381\times 0.336+x} - 0.3 - \theta x\right). \end{cases} \tag{26}$$

System (26) exhibits several equilibrium points depending on certain parametric conditions. The nature of these points is explained in Table 3 and is also shown graphically in Figure 3.

(4)

$$\begin{cases} \frac{dx}{dt} = x\left((1-\frac{x}{\gamma}) - \frac{y}{1+2.8\times 0.35+x}\right), \\ \frac{dy}{dt} = y\left(\frac{0.9(x+0.35)}{1+2.8\times 0.35+x} - 0.3 - 0.11x\right), \end{cases} \tag{27}$$

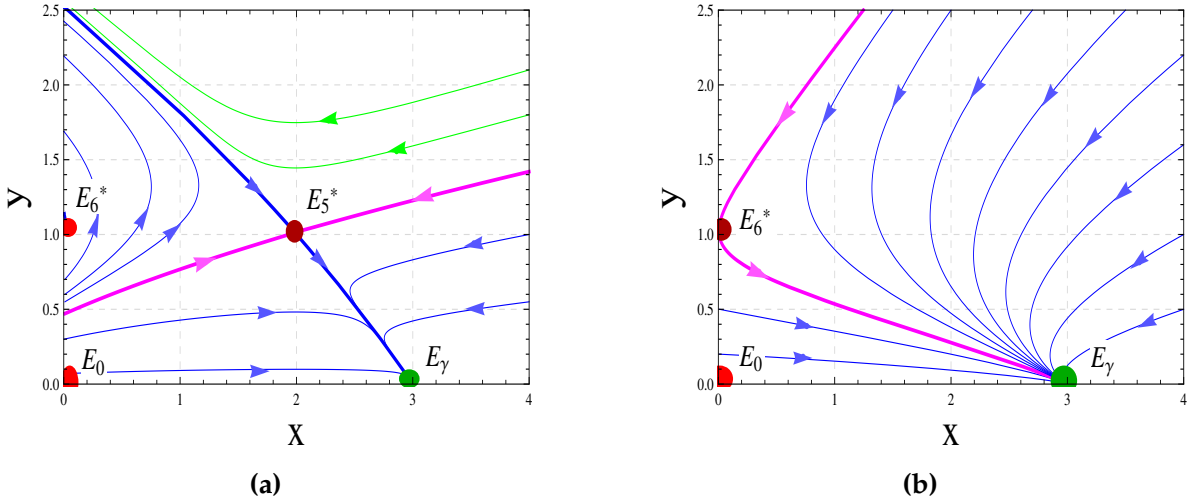

Figure 3. (a) $\theta = 0.2$. The equilibrium point E_0 is unstable, E_γ is globally stable, E_5^* is a saddle point, and E_6^* is an unstable saddle node. (b) $\theta = 0.8$. The equilibrium point E_0 is unstable, E_γ is globally stable, and E_6^* forms a cusp of co-dimension 2. Ecologically, the system will collapse

Table 4. Number and nature of feasible equilibrium points (Eqs) of the system (27)

Value of γ	Existence of Eqs	Nature of Eqs	Figure
$\gamma = 3.5$	$E_0 = (0,0)$ $E_\gamma = (3.5,0)$ $E_1^*(1.04319, 2.12212)$ $E_2^*(2.43136, 1.3469)$	Saddle Stable Stable Saddle	4a
$\gamma = 4.06638$	$E_0 = (0,0)$ $E_\gamma = (4.06638,0)$ $E_1^*(1.04319, 2.24762)$ $E_2^*(2.43136, 1.77373)$	Saddle Stable Stable limit cycle Saddle	4b
$\gamma = 4.61$	$E_0 = (0,0)$ $E_\gamma = (4.61,0)$ $E_1^*(1.04319, 2.33908)$ $E_2^*(2.43136, 2.08477)$	Saddle Stable Homoclinic loop Saddle	4c
$\gamma = 5$	$E_0 = (0,0)$ $E_\gamma = (5,0)$ $E_1^*(1.04319, 2.39244)$ $E_2^*(2.43136, 2.26624)$	Saddle Stable Unstable Saddle	4d

The system (27) exhibits several equilibrium points depending on the value of γ. The nature of these points is explained in Table 4 and is also shown graphically in Figure 4.

(5)

$$\begin{cases} \frac{dx}{dt} = x\left((1-\frac{x}{\gamma}) - \frac{y}{1+2.8\times0.35+x}\right), \\ \frac{dy}{dt} = y\left(\frac{0.9(x+0.35)}{1+2.8\times0.35+x} - 0.3 - 0.118988x\right). \end{cases} \tag{28}$$

System (28) exhibits several equilibrium points depending on certain parametric conditions. The nature of these points is explained in Table 5 and is also shown graphically in Figure 5.

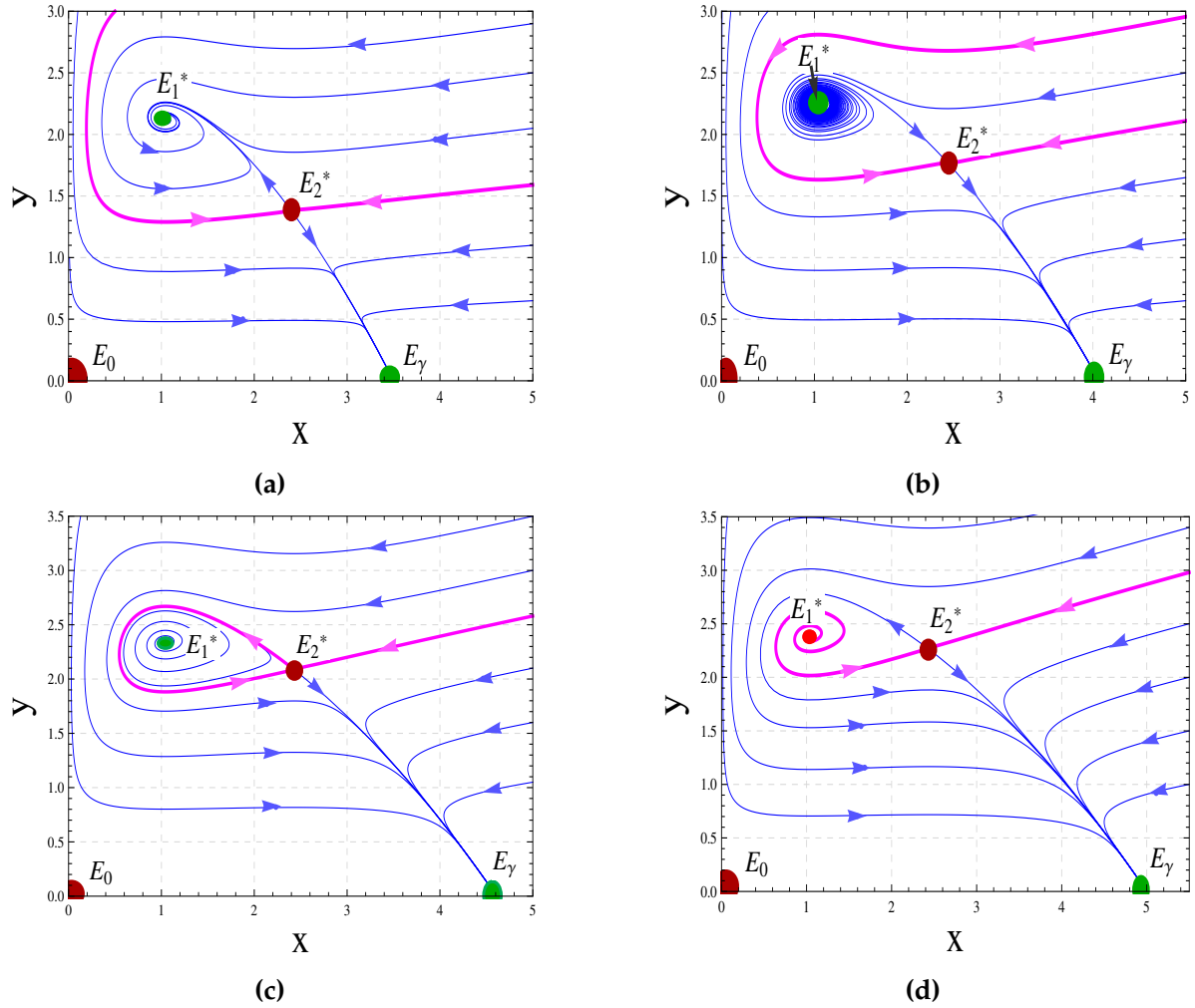

Figure 4. (a) $\gamma = 3.5$. The equilibrium point $E_1^* = (1.04319, 2.12212)$ is a stable point. (b) $\gamma = \gamma^{[hf]} = 4.06638$. A stable limit cycle arises around the point $E_1^*(1.04319, 2.24762)$. (c) $\gamma = 4.61$. The limit cycle collides with the saddle point, $E_2^* = (2.43136, 2.08477)$ and consequently a homoclinic loop arises around the point $E_1^*(1.04319, 2.33908)$. (d) $\gamma = 5$. The equilibrium $E_1^* = (1.04319, 2.39244)$ is an unstable point. Ecologically, the system will either stabilise or collapse, contingent upon the parameteric conditions and the initial population of the species

Table 5. Nature of equilibrium points of the system (28)

Value of γ |	Conditions	Existence of Eqs	Nature of Eqs	Figure
$\gamma = 3$	$\gamma < 1 + \alpha\xi + 2u_1^*$	$E_0 = (0,0)$ $E_\gamma = (3,0)$ $E_3^*(1.53127, 1.71904)$	Saddle Stable Stable saddle-node	5a
$\gamma = 5.04253$	$\gamma = 1 + \alpha\xi + 2u_1^*$	$E_0 = (0,0)$ $E_\gamma = (5.04253,0)$ $E_3^*(1.53127, 2.445)$	Saddle Stable Cusp	5b
$\gamma = 5.2$	$\gamma > 1 + \alpha\xi + 2u_1^*$	$E_0 = (0,0)$ $E_\gamma = (5.2,0)$ $E_3^* E_3^*(1.53127, 2.47729)$	Saddle Stable Unstable saddle-node	5c

(6)

$$\begin{cases} \frac{dx}{dt} = x\left((1 - \frac{x}{3.2777+\lambda_1}) - \frac{y}{1+2.5\times0.25+x}\right) = f_1(x, y, \lambda_1), \\ \frac{dy}{dt} = y\left(\frac{0.8(x+0.25)y}{1+2.5\times0.25+x} - 0.2 - (0.183055 + \lambda_2)x\right) = f_2(x, v, \lambda_2). \end{cases} \tag{29}$$

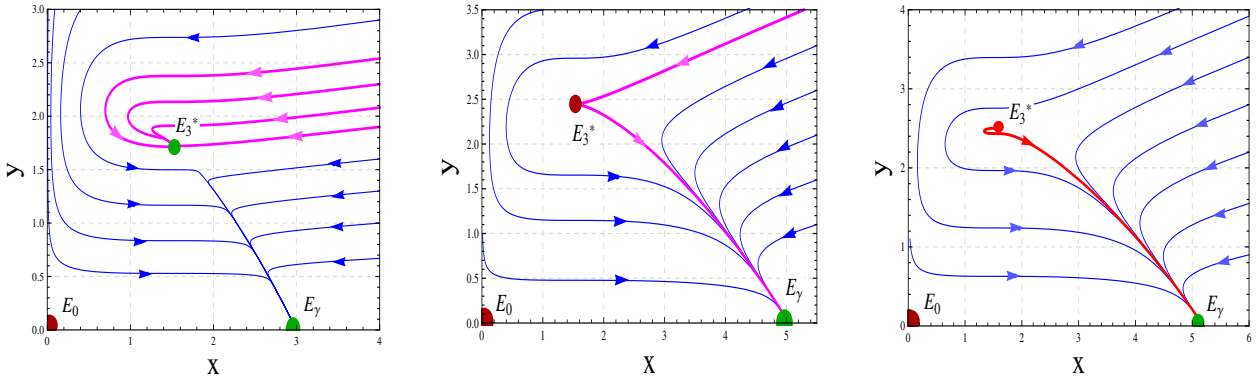

Figure 5. (a) $\gamma = 3$. The equilibrium point $E_3^*(1.53127, 1.71904)$ is a stable saddle-node. (b) $\gamma = 5.04253$. The equilibrium point $E_3^*(1.53127, 2.445)$ is a cusp of co-dimension 2. (c) $\gamma = 5.2$. The equilibrium point $E_3^*(1.53127, 2.47729)$ is an unstable saddle-node. Ecologically, the system will either stabilise or collapse, contingent upon the parametric conditions and the initial population of the species

The system (29) has a unique interior equilibrium point $E_3^* = (0.82635, 1.83333)$. The transformations $U = x - 0.82635$, $V = y - 1.83333$ are used to move the point $E_3^* = (0.82635, 1.83333)$ to the origin and next, the affine transformation $U_1 = U$, $U_2 = \alpha_{10}U + \alpha_{01}V$ is introduced. The system (29) shrinks to

$$\begin{cases} \frac{dU_1}{dt} = \xi_{00} + U_2 + \xi_{20}U_1^2 + \xi_{11}U_1U_2 + \tilde{P}_1(U_1, U_2), \\ \frac{dU_2}{dt} = \mu_{00} + \mu_{10}U_1 + \mu_{01}U_2 + \mu_{20}U_1^2 + \mu_{11}U_1U_2 + \tilde{P}_2(U_1, U_2), \end{cases} \tag{30}$$

where $\xi_{00} = 0.82635\left(0.252113 - \frac{0.82635}{3.2777+\lambda_1}\right)$, $\xi_{20} = 0.202246 - \frac{1}{3.2777+\lambda_1} - 0.802203\left(0.504225 - \frac{1.6527}{3.2777+\lambda_1}\right)$, $\xi_{11} = 0.802203$, $\mu_{00} = 0.82635\left(0.504225 - \frac{1.6527}{3.2777+\lambda_1}\right)\left(0.252113 - \frac{0.82635}{3.2777+\lambda_1}\right) + 0.510698\lambda_2$, $\mu_{10} = 1.833330\left(0.504225 - \frac{1.6527}{3.2777+\lambda_1}\right)\lambda_2 - 0.3371\Big(0.335601 - 1.83333(0.183055 + \lambda_2)\Big)$, $\mu_{01} = 0.504225 - \frac{1}{3.2777+\lambda_1} - 1.83333\lambda_2$, $\mu_{20} = 0.0461505 - 0.802203\left(0.504225 - \frac{1.6527}{3.2777+\lambda_1}\right)^2 + \left(0.504225 - \frac{1.6527}{3.2777+\lambda_1}\right)\left(0.202246 - \frac{1}{3.2777+\lambda_1}\right) - \left(0.504225 - \frac{1.6527}{3.2777+\lambda_1}\right)\left(-8.32667 \times 10^{-17} - \lambda_2\right)$, $\mu_{11} = -8.32667 \times 10^{-17} + 0.802203\left(0.504225 - \frac{1.6527}{3.2777+\lambda_1}\right) - \lambda_2$, and $\tilde{P}_1$, $\tilde{P}_2$ are the power series in (x_1, x_2) with powers x_1^i, x_2^j satisfying $i + j \geq 3$.
Consider the C^∞ change of co-ordinates in the close vicinity of $(0, 0)$: $V_1 = U_1$, $V_2 = \xi_{00} + U_2 + \xi_{20}U_1^2 + \xi_{11}U_1U_2$, $dt = (1 - \gamma_{02}V_1)dT$ and $Z_1 = V_1, Z_2 = V_2(1 - \gamma_{02}V_1) + \check{P}_1(V_1, V_2)$ respectively. The system (30) shrinks to

$$\begin{cases} \frac{dZ_1}{dt} = Z_2, \\ \frac{dZ_2}{dt} = \delta_{00} + \delta_{10}Z_1 + \delta_{01}Z_2 + \delta_{20}Z_1^2 + \delta_{11}Z_1Z_2 + \bar{P}_2(Z_1, Z_2), \end{cases} \tag{31}$$

where $\delta_{00} = \frac{5.48659\lambda_2 + 4.59973\lambda_1\lambda_2 + 0.892642\lambda_1^2\lambda_2}{(3.2777+\lambda_1)^2}$,
$\delta_{10} = \frac{6.0311\times10^{-16} + 3.5065\times10^{-16}\lambda_1 - 0.084269\lambda_1^2 + 2.23819\lambda_2 + 4.07424\lambda_1\lambda_2 + 1.03468\lambda_1^2\lambda_2}{(3.2777+\lambda_1)^2}$,
$\delta_{01} = \frac{-4.42835\times10^{-16} + 0.3371\lambda_1 - 6.00912\lambda_2 - 1.83333\lambda_1\lambda_2}{3.2777+\lambda_1}$,

Table 6. Nature of equilibrium points

Region	Behavior of the region
Region I	Number interior points
Region II	Two interior points, one is saddle and the other is stable
Region III	Two interior points, one is saddle and the other is stable enclosed by a limit cycle
Region IV	Two interior points, one is saddle and the other is unstable

$\delta_{11} = \frac{-0.6742-0.270422\lambda_1+1.54283\lambda_2+0.470705\lambda_1\lambda_2}{3.2777+\lambda_1}$,
$\delta_{20} = \frac{0.49581+0.302535\lambda_1+0.113751\lambda_1^2-10.8827\lambda_2-9.36911\lambda_1\lambda_2-1.84547\lambda_1^2\lambda_2}{(3.2777+\lambda_1)^2}$ and $\bar{P}_2$ are the power series in (z_1, z_2) with powers z_1^i, z_2^j satisfying $i + j \geq 3$. Thus $\delta_{20} = 0.0461505 > 0$. By using the following three transformations:

$$
\begin{aligned}
&(i)\ \ u_1 = Z_1,\ \ u_2 = \frac{Z_2}{\sqrt{\delta_{20}}},\ \ d\tau = \sqrt{\delta_{20}}dt,\\
&(ii)\ \ v_1 = u_1 + \frac{\delta_{10}}{2\delta_{20}},\ \ v_2 = u_2,\\
&(iii)\ \ w_1 = \frac{\delta_{11}^2}{\delta_{20}}v_1,\ \ w_2 = \frac{\delta_{11}^3}{\delta_{20}\sqrt{\delta_{20}}}v_2,\ \ t = \frac{\sqrt{\delta_{20}}}{\delta_{11}}\tau,
\end{aligned}
$$

system (31) shrinks to

$$
\begin{cases}
\frac{dw_1}{dt} = w_2,\\
\frac{dw_2}{dt} = v_1(\lambda_1,\lambda_2) + v_2(\lambda_1,\lambda_2)w_2 + w_1^2 + w_1w_2 + R(w_1, w_2, \lambda),
\end{cases}
$$

where $v_1(\lambda_1,\lambda_2) = \frac{\delta_{00}\delta_{11}^4}{\delta_{20}^3} - \frac{\delta_{10}^2\delta_{11}^4}{4\delta_{20}^4}$ and $v_2(\lambda_1,\lambda_2) = \frac{\delta_{01}\delta_{11}}{\delta_{20}} - \frac{\delta_{11}^2\delta_{10}}{2\delta_{20}^2}$. The determinant of the matrix $\left[\frac{\partial(v_1,v_2)}{\partial(\lambda_1,\lambda_2)}\right] = -5.35162 \times 10^{-6} \neq 0$. The rank of matrix $\left[\frac{\partial(v_1,v_2)}{\partial(\lambda_1,\lambda_2)}\right]_{\lambda_1=\lambda_2=0}$ is 2 as a result, $v_1(\lambda_1,\lambda_2) = \frac{\delta_{00}\delta_{11}^4}{\delta_{20}^3} - \frac{\delta_{10}^2\delta_{11}^4}{4\delta_{20}^4}$, $v_2(\lambda_1,\lambda_2) = \frac{\delta_{01}\delta_{11}}{\delta_{20}} - \frac{\delta_{11}^2\delta_{10}}{2\delta_{20}^2}$ are non-singular parameter transformations. In the $\lambda_1\lambda_2$ plane, the three bifurcation curves separate the local neighborhood of the BT-bifurcation point $(0, 0)$ into four distinct regions: Region I, Region II, Region III, and Region IV, as illustrated in Figure 6a. The saddle-node bifurcation curve is represented in red, the Hopf bifurcation curve in blue, and the homoclinic bifurcation curve in green. The system (29) has a unique interior equilibrium point that is a cusp of co-dimension 2 when $\lambda_1 = 0 = \lambda_2$, as seen in Figure 6b. When the values of λ_1 and λ_2 vary and they belong to region I, the predator species in this region are likely to face extinction due to the absence of an interior equilibrium point, as seen in Figure 6c. When the values of λ_1 and λ_2 belong to region II, there are two interior equilibrium points. Among these equilibrium points, one exhibits the characteristics of a saddle, while the other demonstrates stability. Therefore, it can be inferred that the initial population size will play a crucial role in determining the possibility of the coexistence of the two species or the ultimate extinction of the predator species, as seen in Figure 6d. When the values of λ_1 and λ_2 belong to the region III, the stable equilibrium point loses its stability, and a stable limit cycle emerges around this point. Therefore, it can be inferred that the initial population size will play a crucial role in determining the possibility of oscillation, or the predator species tends to become extinct as seen in Figure 6e . When the values of λ_1 and λ_2 belong to the region IV, the limit cycle will disappear and there will be an unstable focus and saddle point. Therefore, it can be inferred that the predator species go extinct, as seen in Figure 6f.

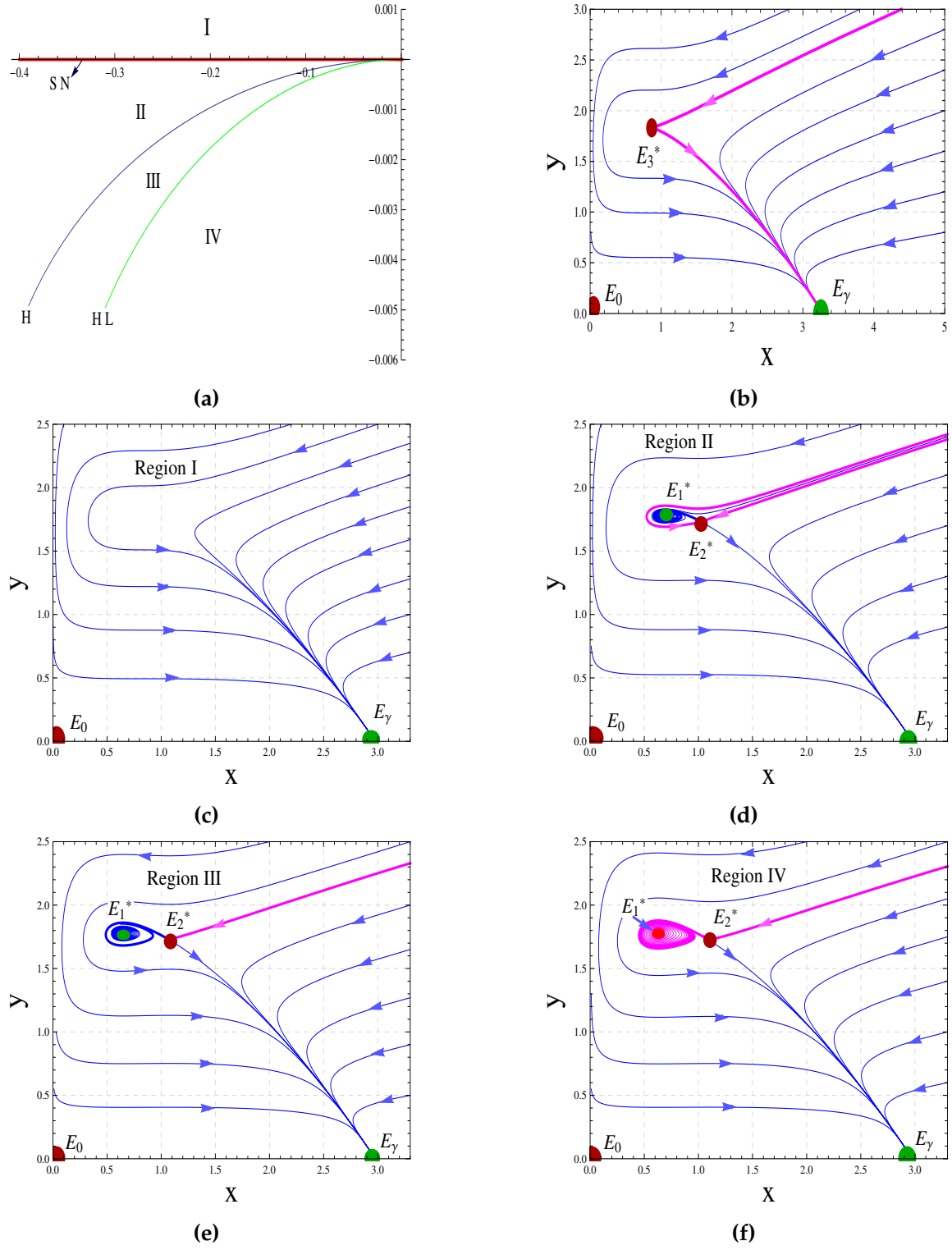

Figure 6. (a) Bifurcation diagram of the model (3). The saddle-node bifurcation curve is shown in red, the Hopf bifurcation curve in blue, and the homoclinic bifurcation curve in green. (b) The unique interior equilibrium point E_3^*, when $\lambda_1 = \lambda_2 = 0$ is a cusp of co-dimension 2. (c) When $(\lambda_1, \lambda_2) = (-0.3,\ 0.0003)$ lies in region I, the system (3) has no interior equilibrium point and the equilibrium point E_γ is globally asymptotically stable. (d) When $(\lambda_1, \lambda_2) = (-0.3, -0.002)$ lies in the region II, system (3) has two interior equilibrium points. One is a saddle, while the other is stable. (e) When $(\lambda_1, \lambda_2) = (-0.3, -0.004)$ lies in the region III, a stable limit cycle enclosing an interior point, and the other interior point is a saddle, system (3) has two interior equilibrium points. (f) When $(\lambda_1, \lambda_2) = (-0.3, -0.0048)$ lies in the region IV, system (3) has two interior equilibrium points: one is a saddle, while the other is an unstable one. Ecologically, system (3) is highly sensitive to the parameters θ and γ. A slight variation in these parameters can lead to significant changes in the system's dynamics, such as species coexistence, coexistence through oscillations, or the extinction of the predator species

7 Impact of Anti-predator behavior

The proposed model (3) without anti-predator behavior has been analyzed by Srinivasu et al. [8]. The authors observed some interesting results, which are very important from an ecological point of view. In this section, we aim to discuss how the anti-predator parameter θ affects the dynamics of the proposed system. In Figure 7a, Figure 7b, Figure 7c and Figure 7d we have depicted the region of coexistence. In Figure 7a, only parameters θ (anti-predator) and ξ (quantity of additional food) are allowed to vary. In Figure 7b, only parameters θ (anti-predator) and α (quality of additional food) are allowed to vary. In Figure 7c, only parameters θ (anti-predator) and δ (ratio of the predator's mortality rate and prey growth rate) are allowed to vary. In Figure 7d, only parameters θ (anti-predator) and parameter β (ratio of nutritional value of prey to the product of prey's handling time and prey growth rate) are allowed to vary. These graphs play a vital role in examining the range of parameter θ as the other parameters vary. In Figure 8, we have plotted the time series solution graphs where all the parameters of the model are fixed except θ. It can be observed that as θ increases, the periodicity of solutions decreases, and eventually, the solutions become non-periodic solutions.

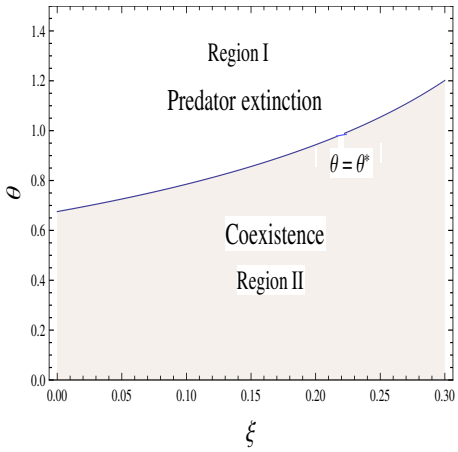

(a)

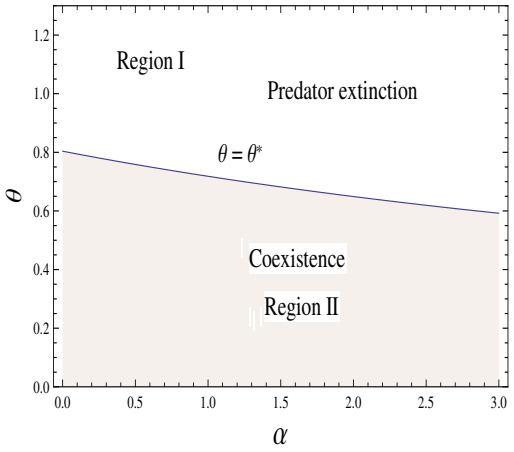

(b)

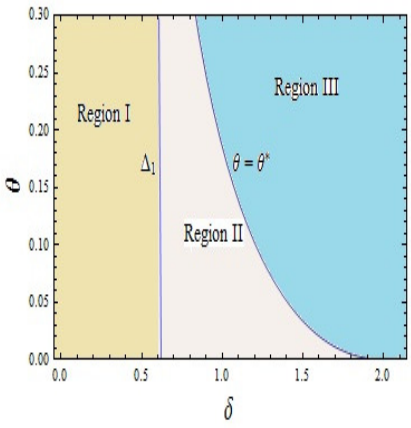

(c)

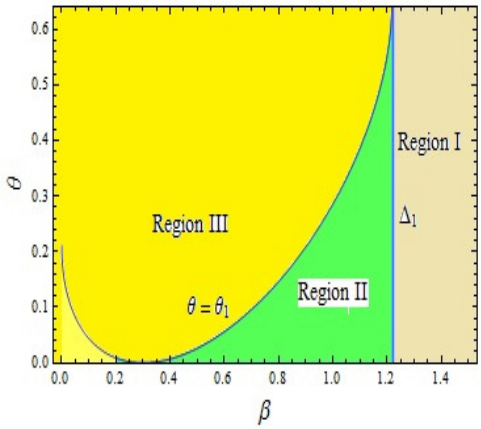

(d)

Figure 7. $(a) - (b)$ In region I, predator extinction will occur, while in region II prey and predator will coexist. (c) In region I, either one interior equilibrium point or two axial equilibrium points will exist, while in the region II, two interior and two axial equilibrium points will exist. In region III, only one axial equilibrium point will exist. (d) In region I, one interior and two axial equilibrium points will exist. There are two interiors and two axial equilibrium points on the boundary of regions I and II. In region II, there are two interior and two axial equilibrium points. One interior and two axial equilibrium points will exist on the boundary of II and III regions

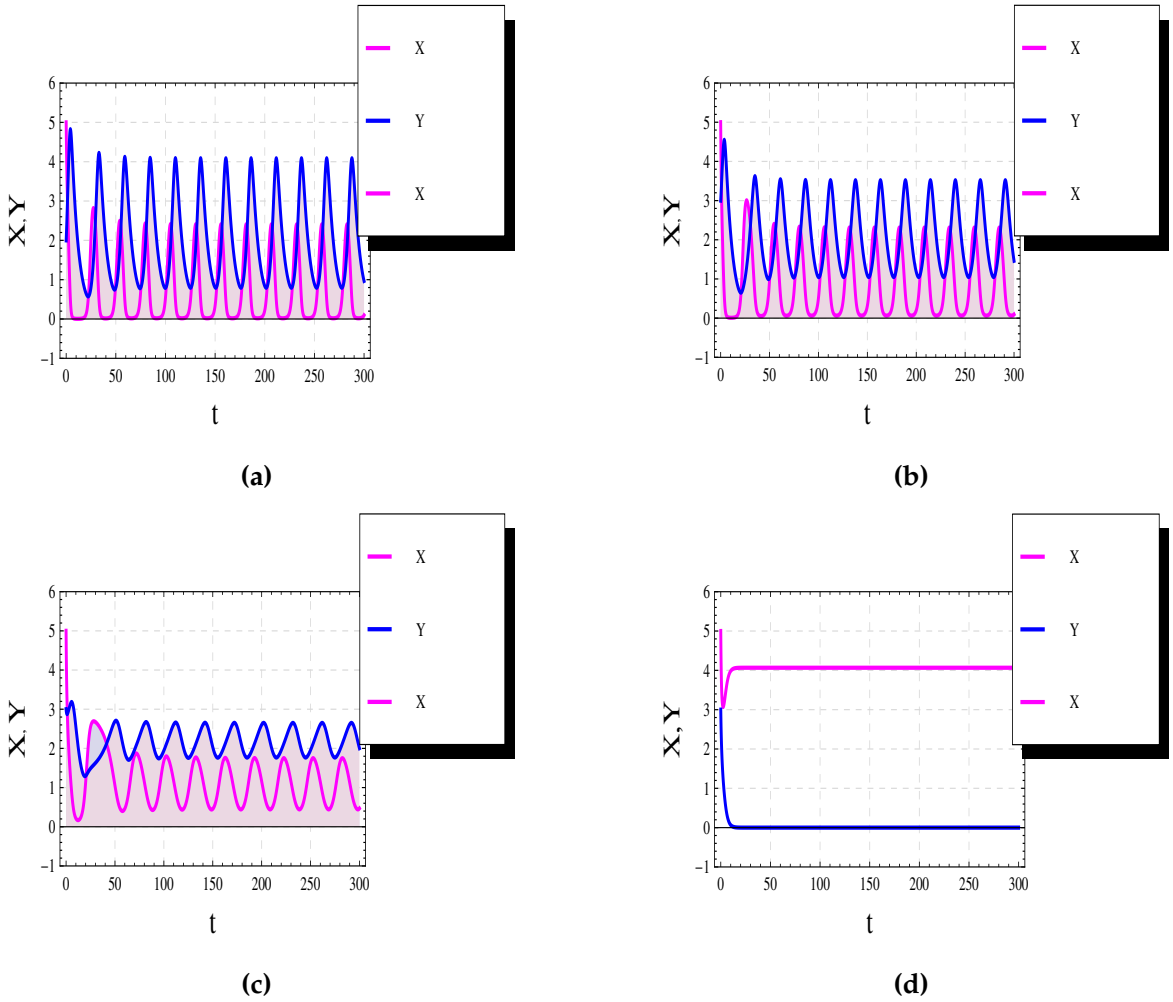

Figure 8. Consider $\alpha = 2.8$, $\beta = 0.9$, $\gamma = 4.06638$, $\delta = 0.3$. Time series solution graph fo the system (3) for different values of rate of anti-predator behavior parameter θ (a) $\theta = 0.01$. (b) $\theta = 0.05$. (c) $\theta = 0.1$. (d) $\theta = 0.11$. For small values of θ, the solutions are periodic; however, as θ grows, the period of the solutions diminishes, ultimately leading to the collapse of the periodic solution. Ecologically, both species coexist when θ is small, as θ increases, the predator species will face extinction

8 Conclusion

A qualitative study that considers all factors reveals the model's intriguing, complicated, and diverse dynamics. This manuscript has studied the qualitative analysis of an additional food-provided predator-prey system in the presence of an anti-predator behavior. After developing the model equations and establishing the positivity and boundedness of its solution, we have discussed both theoretically and numerically the local stability of the system around various equilibrium points. It is observed that the system (3) with an anti-predator behavior has at most four equilibrium points, consisting of trivial, predator-free, and interior equilibrium points. It is observed that the trivial equilibrium point will never be stable. Ecologically, it can be stated that the two species cannot go extinct together. Depending on parametric restrictions, the predator-free equilibrium point can be asymptotically stable, or it shows a saddle point. Ecologically, it can be stated that prey species will never go extinct, regardless of the initial population density, but predator species can go extinct under some restrictions. If there are two interior equilibrium points, one will be a saddle point, and the other will be asymptotically stable, unstable, or a stable limit cycle will appear around it, depending on some restrictions. Ecologically, it can be stated that

there is the possibility of coexistence of the species, prey extinction, or oscillation. The system depicts a threatening behavior, bistability, under certain parametric conditions, which indicates the system's sensitivity to initial populations. From an ecological perspective, it may be argued that the long-term survival of a species is contingent upon the size of its original population.

The model displays numerous types of bifurcations, such as saddle-node, Hopf, and BT bifurcations. These bifurcations are an essential part of qualitative analysis and have several ecological consequences. It is observed that the parameters representing the rate of anti-predator behavior of adult prey to predators and the quality and quantity of supplementary food significantly impact the emergence of these bifurcations. If the parameter θ surpasses a specific critical value, model (3) experiences a saddle-node bifurcation, leading to the possibility of zero, one, or two positive interior equilibrium points. As a result, a critical threshold value of θ emerges, below which the coexistence of both populations is possible and beyond which the predator species becomes extinct. Moreover, the manifestation of a limit cycle through Hopf bifurcation has been shown, and the first Lyapunov number can establish the stability of this limit cycle. We have used numerical simulation to indicate that the convergence of a saddle point and a limit cycle might potentially lead to the emergence of homoclinic loops. The system (3) is shown to undergo Bogdanov-Takens bifurcation by selecting the parameters that represent the carrying capacity and the adult prey's anti-predator behavior. Ecologically, it can be stated that certain regions will emerge that exhibit unique qualitative behavior, such as the coexistence of predators and prey in a positive equilibrium state, their coexistence by oscillations, or the eventual extinction of predator species. This study posits that the presence of anti-predator behavior plays a pivotal role in influencing the interactions within a predator-prey system with access to additional food supplies.

This study examined the effects of anti-predator behavior within a two-species predator-prey model. Future research could explore the implications of anti-predator behaviour in ecological systems comprising three or more species, where investigations may assess how anti-predator strategies affect the stability and dynamics of multi-species ecosystems, potentially leading to more complex interactions and behaviours.

Declarations

Use of AI tools

The authors declare that they have not used Artificial Intelligence (AI) tools in the creation of this article.

Data availability statement

There are no external data associated with the manuscript.

Ethical approval (optional)

The authors state that this research complies with ethical standards. This research does not involve either human participants or animals.

Consent for publication

Not applicable

Conflicts of interest

The authors declare that they have no conflict of interest.

Funding

No funding was received for this research.

Author's contributions

M.K.S.: Conceptualization, Methodology, Validation, Writing-Original draft preparation, Software, Supervision, Validation, Formal Analysis. P.P.: Methodology, Writing-Original draft preparation, Data Curation, Software, Writing - Review & Editing. All authors have read and agreed to the published version of the manuscript.

Acknowledgements

Not applicable

References

[1] Strauss, S.Y. Indirect effects in community ecology: their definition, study and importance. *Trends in Ecology & Evolution*, 6(7), 206-210, (1991). [CrossRef]

[2] Savitri, D. Dynamics analysis of anti-predator model on intermediate predator with ratio dependent functional responses. In Proceedings, *The 2nd International Joint Conference on Science and Technology (IJCST)*, pp. 012201-012206, Bali, Indonesia, (2017, September). [CrossRef]

[3] Murdoch, W.W., Chesson, J. and Chesson, P.L. Biological control in theory and practice. *The American Naturalist*, 125(3), 344-366, (1985). [CrossRef]

[4] Haque, M. and Greenhalgh, D. When a predator avoids infected prey: a model-based theoretical study. *Mathematical Medicine and Biology*, 27(1), 75-94, (2010). [CrossRef]

[5] Holt, R.D. and Lawton, J.H. The ecological consequences of shared natural enemies. *Annual Review of Ecology, Evolution, and Systematics*, 25, 495-520, (1994). [CrossRef]

[6] Holt, R.D. Predation, apparent competition, and the structure of prey communities. *Theoretical Population Biology*, 12(2), 197-229, (1977). [CrossRef]

[7] Sahoo, B. and Poria, S. Disease control in a food chain model supplying alternative food. *Applied Mathematical Modelling*, 37(8), 5653-5663, (2013). [CrossRef]

[8] Srinivasu, P.D.N., Prasad, B.S.R.V. and Venkatesulu, M. Biological control through provision of additional food to predators: a theoretical study. *Theoretical Population Biology*, 72(1), 111-120, (2007). [CrossRef]

[9] Wade, M.R., Zalucki, M.P., Wratten, S.D. and Robinson, K.A. Conservation biological control of arthropods using artificial food sprays: current status and future challenges. *Biological Control*, 45(2), 185-199, (2008). [CrossRef]

[10] Prasad, B.S.R.V., Banerjee, M. and Srinivasu, P.D.N. Dynamics of additional food provided predator–prey system with mutually interfering predators. *Mathematical Biosciences*, 246(1), 176-190, (2013). [CrossRef]

[11] Sahoo, B. and Poria, S. Effects of supplying alternative food in a predator–prey model with harvesting. *Applied Mathematics and Computation*, 234, 150-166, (2014). [CrossRef]

[12] Chakraborty, K. and Das, S.S. Biological conservation of a prey-predator system incorporating constant prey refuge through provision of alternative food to predators: a theoretical study. *Acta Biotheoretica*, 62, 183-205, (2014). [CrossRef]

[13] Sen, M., Srinivasu, P.D.N. and Banerjee, M. Global dynamics of an additional food provided

predator-prey system with constant harvest in predators. *Applied Mathematics and Computation*, 250, 193-211, (2015). [CrossRef]

[14] Shome, P., Maiti, A. and Poria, S. Effects of intraspecific competition of prey in the dynamics of a food chain model. *Modeling Earth Systems and Environment*, 2, 1-11, (2016). [CrossRef]

[15] Ghosh, J., Sahoo, B. and Poria, S. Prey-predator dynamics with prey refuge providing additional food to predator. *Chaos, Solitons & Fractals*, 96, 110-119, (2017). [CrossRef]

[16] Singh, M.K. and Bhadauria, B.S. Qualitative analysis of an additional food provided predator–prey model in the presence of Allee effect. *International Journal of Applied and Computational Mathematics*, 3(Suppl 1), 1173-1195, (2017). [CrossRef]

[17] Das, A. and Samanta, G.P. A prey–predator model with refuge for prey and additional food for predator in a fluctuating environment. *Physica A: Statistical Mechanics and its Applications*, 538, 122844, (2020). [CrossRef]

[18] Thirthar, A.A., Majeed, S.J., Alqudah, M.A., Panja, P. and Abdeljawad, T. Fear effect in a predator-prey model with additional food, prey refuge and harvesting on super predator. *Chaos, Solitons & Fractals*, 159, 112091, (2022). [CrossRef]

[19] Debnath, S., Majumdar, P., Sarkar, S. and Ghosh, U. Memory effect on prey–predator dynamics: Exploring the role of fear effect, additional food and anti-predator behaviour of prey. *Journal of Computational Science*, 66, 101929, (2023). [CrossRef]

[20] Ananth, V.S. and Vamsi, D.K.K. Time optimal control studies and sensitivity analysis of additional food provided prey-predator systems involving Holling type III functional response based on quality of additional food. *Journal of Biological Systems*, 31(01), 271-308, (2023). [CrossRef]

[21] Das, B.K., Sahoo, D. and Samanta, G. Fear and its carry-over effects in a delay-induced predator-prey model with additional food to predator. *Filomat*, 37(18), 6059-6088, (2023). [CrossRef]

[22] Umaroh, S.Z. and Savitri, D. Dynamic analysis of a prey predator model with Holling-type III functional response and anti-predator behavior. *Jurnal Sains, Teknologi dan Industri*, 21(1), 51-57, (2023). [CrossRef]

[23] Berryman, A.A. The origins and evolution of predator-prey theory. *Ecology*, 73(5), 1530-1535, (1992). [CrossRef]

[24] Ford, J.K. and Reeves, R.R. Fight or flight: antipredator strategies of baleen whales. *Mammal Review*, 38(1), 50-86, (2008). [CrossRef]

[25] Ge, D., Chesters, D., Gomez-Zurita, J., Zhang, L., Yang, X. and Vogler, A.P. Anti-predator defence drives parallel morphological evolution in flea beetles. *Proceedings of the Royal Society B: Biological Sciences*, 278(1715), 2133-2141, (2011). [CrossRef]

[26] Lima, S.L. Nonlethal effects in the ecology of predator-prey interactions. *Bioscience*, 48(1), 25-34, (1998). [CrossRef]

[27] Matassa, C.M., Donelan, S.C., Luttbeg, B. and Trussell, G.C. Resource levels and prey state influence antipredator behavior and the strength of nonconsumptive predator effects. *Oikos*, 125(10), 1478-1488, (2016). [CrossRef]

[28] Zanette, L.Y., White, A.F., Allen, M.C. and Clinchy, M. Perceived predation risk reduces the number of offspring songbirds produce per year. *Science*, 334(6061), 1398-1401, (2011). [CrossRef]

[29] Panja, P., Mondal, S.K. and Chattopadyay, J. Dynamical effects of anti-predator behavior of adult prey in a predator-prey model with ratio-dependent functional response. *Asian Journal of Mathematics and Physics*, 1(1), 19-32, (2017).

[30] Khater, M., Murariu, D. and Gras, R. Predation risk tradeoffs in prey: effects on energy and behaviour. *Theoretical Ecology*, 9, 251-268, (2016). [CrossRef]

[31] Samanta, S., Mandal, A.K., Kundu, K. and Chattopadhyay, J. Control of disease in prey population by supplying alternative food to predator. *Journal of Biological Systems*, 22(04), 677-690, (2014). [CrossRef]

[32] Tang, B. and Xiao, Y. Bifurcation analysis of a predator-prey model with anti-predator behaviour. *Chaos, Solitons & Fractals*, 70, 58-68, (2015). [CrossRef]

[33] Mortoja, S.G., Panja, P. and Mondal, S.K. Dynamics of a predator-prey model with stage-structure on both species and anti-predator behavior. *Informatics in Medicine Unlocked*, 10, 50-57, (2018). [CrossRef]

[34] Prasad, K.D. and Prasad, B.S.R.V. Qualitative analysis of additional food provided predator-prey system with anti-predator behaviour in prey. *Nonlinear Dynamics*, 96, 1765-1793, (2019). [CrossRef]

[35] Sahoo, B., Das, B. and Samanta, S. Dynamics of harvested-predator–prey model: role of alternative resources. *Modeling Earth Systems and Environment*, 2, 140, (2016). [CrossRef]

[36] Chen, J., Huang, J., Ruan, S. and Wang, J. Bifurcations of invariant tori in predator-prey models with seasonal prey harvesting. *SIAM Journal on Applied Mathematics*, 73(5), 1876-1905, (2013). [CrossRef]

[37] Huang, J., Gong, Y. and Chen, J. Multiple bifurcations in a predator-prey system of Holling and Leslie type with constant-yield prey harvesting. *International Journal of Bifurcation and Chaos*, 23(10), 1350164, (2013). [CrossRef]

[38] Perko, L. *Differential Equations and Dynamical Systems* (Vol. 7). Springer: New York, (2001).

Mathematical Modelling and Numerical Simulation with Applications (MMNSA)
(https://dergipark.org.tr/en/pub/mmnsa)

How to cite this article: Singh, M.K. & Poonam, P. (2025). Bifurcation analysis of an additional food-provided predator-prey system with anti-predator behavior. *Mathematical Modelling and Numerical Simulation with Applications*, 5(1), 38-64. https://doi.org/10.53391/mmnsa.1496827

Mathematical Modelling and Numerical Simulation with Applications, 2025, 5(1), 65–96

https://dergipark.org.tr/en/pub/mmnsa

ISSN Online: 2791-8564 / Open Access

https://doi.org/10.53391/mmnsa.1571609

RESEARCH PAPER

A comprehensive study of monkeypox disease through fractional mathematical modeling

M. Manivel [1,‡], **A. Venkatesh** [1,*,‡] **and Shyamsunder Kumawat** [2,‡]

[1]Department of Mathematics, AVVM Sri Pushpam College (Affiliated to Bharathidasan University, Tiruchirappalli), Poondi, Thanjavur 613503, Tamilnadu, India, [2]Department of Mathematics, SRM University Delhi-NCR, Sonepat 131029, Haryana, India

*Corresponding Author

‡manivelmani718@gmail.com (M. Manivel); avenkateshmaths@gmail.com (A. Venkatesh); skumawatmath@gmail.com (Shyamsunder Kumawat)

Abstract

This research investigates a fractional-order mathematical model for analyzing the dynamics of Monkeypox (Mpox) disease using the Caputo-Fabrizio derivative. The model incorporates both human and rodent populations, aiming to elucidate the disease's transmission mechanics, which is demonstrated to be more effective than integer-order models in capturing the complex nature of disease spread. The study determines the fundamental reproduction number (R_0) while assessing the existence and uniqueness of the solutions. Numerical simulations are conducted to validate the model using Adams-Bashforth technique and illustrate the influence of different factors on the progression of the disease. The findings shed light on Mpox control and prevention, emphasizing the importance of fractional calculus in epidemiological modeling.

Keywords: Adams-Bashforth technique; Caputo-Fabrizio derivative; existence and uniqueness; fixed point theorem; monkeypox virus

AMS 2020 Classification: 26A33; 92B05; 92D30; 92C50

1 Introduction

Monkeypox (Mpox) is a viral zoonotic disease that is transmitted between animals and humans, caused by the Mpox virus. This infection mostly occurs in Central and West Africa. Mpox became a significant orthopoxvirus for human health in 1980, after the eradication of smallpox infection. The first occurrence of this virus outside African nations was documented in 2003 in the United States. Afterwards, several instances of Mpox infection were recorded in countries across Africa and Europe [1]. In May 2022, the presence of the pathogen was verified in other nonendemic regions. The World Health Organization (WHO) received reports of about 3413 confirmed cases

➤ **Received:** 22.10.2024 ➤ **Revised:** 20.12.2024 ➤ **Accepted:** 12.02.2025 ➤ **Published:** 31.03.2025

and 1 fatality case from 50 countries/territories. Mpox is transmitted zoonotically from animals to humans [2]. Typically, the hosts in animals include a variety of rodents and non-human primates. The transmission of the virus may occur via interpersonal contact, particularly by droplets emitted during conversation, respiration, or sneezing. Additionally, it may be transferred by sexual contact with an individual who is contagious. Mpox may potentially be transmitted via the environment [3]. Wild animals, such as African rats and monkeys, are the primary sources of viral transmission to humans. Nevertheless, there is a high occurrence of human-to-human transmissions in the majority of the documented instances. Spreading diseases from animals to humans can occur through various mechanisms, including bites or scuffs the handling and consumption of bush meat, direct contact with body fluids, or the ingestion of food contaminated by rodents. The illness may be transmitted by direct contact with lesions and body fluids of infected individuals. Smallpox vaccination, antivirals, and vaccine immune globulin may serve as alternatives for preventing the transmission of Mpox. However, there is presently no established and reliable therapy for Mpox virus infection [4]. Mathematical models are crucial and have been widely used to examine the dynamics and provide effective ways to eliminate infectious illnesses from society [5, 6]. Those frameworks analyze quantitative aspects of the circumstance. Several epidemiological characteristics of Mpox infection are currently being studied [7, 8]. Ongoing research is being conducted to further investigate the transmission and treatment of this virus. Venkatesh et al. [9] established numerical method using new time fractional model for the Mpox. Also, Manivel et al. [10] developed a fractional mathematical modeling in humans and rodents for the Mpox disease. The numerical simulation indicates that individuals' immunological state has a significant role in their recovery process after orthopoxvirus infection. Several mathematical models [11] have been examined to enhance comprehension of the transmission dynamics and various strategies for managing endemic diseases.

The fractional modeling works synthesizes advanced mathematical modeling approaches to address epidemiological challenges by integrating key concepts from fractional-order models and stability analysis [12]. A mathematical model of mobility-related infection and vaccination is extended to consider the dynamics of SARS-CoV-2 through a Fractional SIQRV framework, emphasizing the role of fractional derivatives in capturing memory effects and complex dynamics [13]. Simultaneously, insights from a fractional-order model designed to analyze stability and propose sterilization strategies for the habitat of stray dogs are leveraged to develop holistic and adaptive intervention strategies [14]. Meanwhile, the SIR model with constrained medical resources and time delay examines the dynamics of healthcare system capacity and the impact of delayed interventions on disease progression [15]. This unified approach underscores the utility of fractional-order systems in understanding infection dynamics, vaccination impact, and the stability of populations, offering innovative solutions to pressing public health issues.

The primary motivation for this study arises from the increasing prevalence of Mpox infections outside traditionally endemic regions, underscoring the need for advanced mathematical tools to understand and predict the dynamics of its spread. Unlike classical integer-order models, fractional-order models can capture the memory effects and complex dynamics intrinsic to biological processes. This unique advantage provides a more accurate representation of Mpox's epidemiological patterns, which is crucial for effective disease control and prevention.

To enhance comprehension of the dynamics of Mpox, [16] formulated a mathematical model. The results indicate that Mpox may be effectively managed and eliminated by using vaccination strategies, even in regions where the disease is moderately prevalent. However, vaccination alone is insufficient to completely eliminate Mpox in a population that is already totally endemic [17]. In addition, the research conducted by [18] found that the recommended treatments resulted to the eradication of infected individuals in both human and non-human primate populations over the

study period, as shown by numerical simulations done on the model. Scientists and engineers from several fields have lately shown interest in using fractional differential equations for mathematical modeling, especially in the field of epidemiology. The memory effect is a fascinating characteristic of fractional-order framework that is absent in classical differential equations because of the diverse features of equations with fractions.

All Mpox transmission models currently in use solely account for transfer from animals to humans. There have been recent reports of transfer from humans to rodents. Based on the recent facts, in this paper, we develop the Mpox transmission model with animal-to-human transmission of infection. The aim of this research is to examine the spread and management of Mpox in the population by employing a classical and fractional-order model. Additionally, the study aims to examine the impact of the memory index or fractional order element on the dynamics of Mpox disease and determine whether it can be utilized as a control parameter.

The subsequent sections of the paper are structured as follows: Section 2 discusses model formulations and analyses of the Mpox model. Findings on the existence and uniqueness of the model variable are elaborated in Section 3. Section 4 delineates the equilibrium and reproduction number with the parameters affecting R_0. Section 5 illustrates a numerical technique using the Adams-Bashforth method. Section 6 includes the quantitative simulations and discussions pertaining to the model. Section 7 presents a succinct conclusion.

Preliminaries

This section presents the essential foundational materials concerning fractional order operators.

Definition 1 *[19] The fractional derivative in the Caputo-Fabrizio (CF) sense for the function* $H \in M^1(a,b), b > a, \delta \in [0,1]$ *is characterized as*

$$D_t^{\delta}\{H(t)\} = \frac{M(\delta)}{1-\delta}\int_a^t H'(s)\exp\Big(-\frac{\delta(t-s)}{1-\delta}\Big)ds. \tag{1}$$

$M(\delta)$ *is the normalized function that meets the criteria* $M(0) = M(1) = 1$ *[19]. In the scenario where* $H \notin M^1(a,b)$ *the aforementioned CF derivative can be articulated as*

$$D_t^{\delta}\{H(t)\} = \frac{\delta M(\delta)}{1-\delta}\int_a^t (H(t)-H(s))\exp\Big(-\frac{\delta(t-s)}{1-\delta}\Big)ds. \tag{2}$$

Remark 1 *If* $\alpha = \frac{1-\delta}{\delta} \in [0,\infty)$, $\delta = \frac{1}{1+\alpha} \in [0,1]$, *then Eq. (2) this can be written:*

$$D_t^{\alpha}\{H(t)\} = \frac{N\alpha}{\delta}\int_a^t H'(s)\exp\Big[-\frac{t-s}{\alpha}\Big]ds, N(0) = N(\infty) = 1. \tag{3}$$

Moreover,

$$\lim_{\alpha\to 0}\frac{1}{\alpha}\exp\Big[-\frac{t-s}{\alpha}\Big] = \tau(s-t).$$

The integral that is related to the CF derivative is described as follows [20]. The initial function $H(t)$ *is assumed to satisfy the regularity conditions required for the application of the CF derivative. Specifically,* $H(t)$ *is considered to be a member of* $M_1(a,b)$, *ensuring it possesses the necessary smoothness and*

boundedness over the interval of interest. Moreover, the model presumes that the initial conditions $H(t_0) = H_0$ *align with the physical or epidemiological study.*

Definition 2 *While* $t > 0$ *and* $M(\delta)$ *indicates the normalization function, In such a way that* $M(1) = 0 = M(0)$*. It is presumed that* $0 < \delta < 1$ *and* $H(t)$*, is dependent on* t*, then the Riemann-Liouville fractional crucial of order* δ *is characterized as*

$$^{RL}I^{\delta}_{0,t}\{H(t)\} = \frac{1}{\Gamma(\delta)}\int_0^t (t-s)^{\delta-1}H(s)ds,$$

the Caputo-Fabrizio integral of order δ *is expressed as*

$$^{CF}I^{\delta}_{0,t}\{H(t)\} = \frac{2(1-\delta)H(t)}{(2-\delta)M(\delta)} + \frac{2\delta}{(2-\delta)M(\delta)}\int_0^t H(s)ds, \tag{4}$$

where $t \geq 0$*.*

2 Mpox model formulation

In order to create the model, the complete human population N_m divided into six distinct categories, namely susceptible S_m, exposed E_m, infected I_m, asymptomatically-ill A_m, vaccinated V_m, and recovered humans R_m. Likewise, the total rodent population is N_a. It is further separated into three distinct categories, namely susceptible S_a, exposed E_a, and infected rodent I_a groups.

The initiation of the susceptible human class occurs through two mechanisms: either by birth or through the immigration of susceptible individuals at a specified rate Π_m and from the vaccinated population following the decline of the induced immunity at a specified rate τ. The natural death rate declines throughout human classes μ_1. The group of individuals susceptible to infection is diminished as a result of vaccination at the specified rate α_m and as a result of the interaction with infected humans and animals. Consequently, the individuals who are susceptible transition to the exposed category at the rate of infection force λ_1 depicts as: $\lambda_1 = \left(\frac{\beta_1 I_m + \beta_2 I_a + \beta_3 A_m}{N_m}\right)$.

The interaction terms in the model are derived from fundamental epidemiological principles. These terms capture the probabilistic nature of contacts leading to disease transmission. The force of infection for the human population λ_1 includes $\frac{\beta_1 I_m + \beta_2 I_a + \beta_3 A_m}{N_m}$, where the numerators represent interactions between susceptible and infectious individuals across compartments, scaled by their respective contact rates. These interactions reflect real-world dynamics, where direct or indirect contacts between infected and susceptible humans lead to new exposures.

The choice to multiply these variables ensures that the rate of new infections is proportional to the number of infectious individuals, their contact rates, and the availability of susceptible individuals. Exposed individuals transition to either asymptomatic or symptomatic infectious states ($E_m \rightarrow A_m, I_m$) based on progression rates ($k(1-\rho)$ and $k\rho$ respectively). It is emphasized that the interactions in the model occur via rates that represent indirect effects (e.g., disease transmission or recovery) rather than direct inter-compartmental mixing. This separation ensures that the model accurately depicts real-world disease transmission while maintaining mathematical and conceptual simplicity. The parameters β_1, β_2, and β_3 are the effective contact rates. The group of susceptible animals, which includes primates or rodents, is established through the incorporation of newly enlisted animals Π_a. The number of individuals in the susceptible class decreases as a result of two key factors: The phrase $\lambda_2 = \frac{\beta_4 I_a}{N_a}$, it considers the connection among vulnerable animals (primates or rats) and infected ones, as well as the natural mortality rate μ_2.

Consequently, the system illustrating the spreading processes of Mpox in both populations is as described below:

$$\begin{aligned}
\frac{dS_m}{dt} &= \Pi_m - \lambda_1 S_m - (\mu_1 + \alpha_m) S_m + \tau V_m, \\
\frac{dE_m}{dt} &= \lambda_1 S_m - (k + \mu_1) E_m, \\
\frac{dA_m}{dt} &= k(1-\rho) E_m - (\gamma_1 + \mu_1 + \eta_1) A_m, \\
\frac{dI_m}{dt} &= k\rho E_m - (\gamma_2 + \mu_1 + \eta_2) I_m, \\
\frac{dV_m}{dt} &= \alpha_m S_m - (\tau + \mu_1) V_m, \\
\frac{dR_m}{dt} &= \gamma_1 A_m + \gamma_2 I_m - \mu_1 R_m, \\
\frac{dS_a}{dt} &= \Pi_a - \lambda_2 S_a - \mu_2 S_a, \\
\frac{dE_a}{dt} &= \lambda_2 S_a - (\pi + \mu_2) E_a, \\
\frac{dI_a}{dt} &= \pi E_a - (\mu_2 + \eta_3) I_a.
\end{aligned} \tag{5}$$

The flowchart of the problem explained in system (5) is given in the following Figure 1.

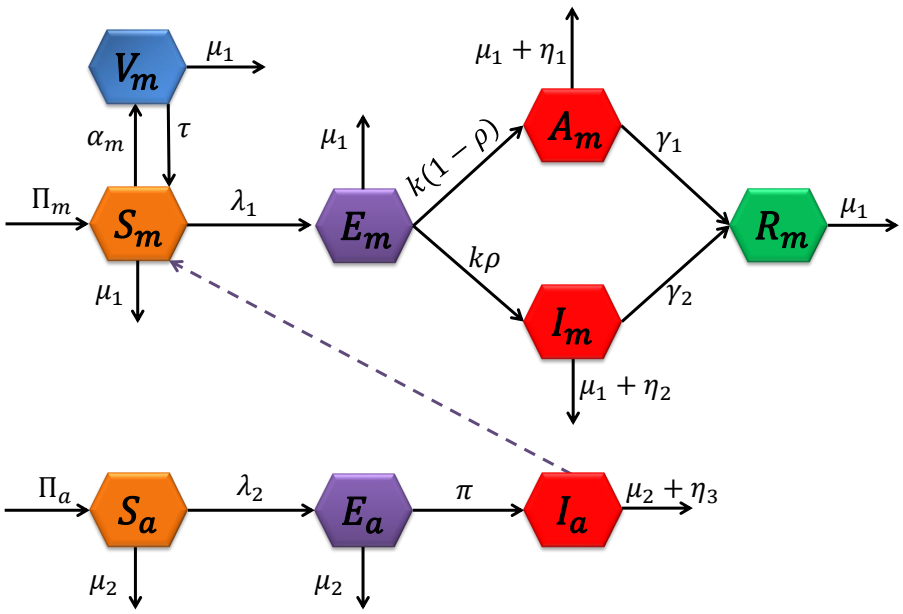

Figure 1. Graphical representation of Mpox model

The Caputo fractional derivative was used for this investigation because it accommodates initial conditions articulated in integer-order derivatives, which is consistent with the majority of physical and epidemiological issues. In contrast to Riemann-Liouville derivatives, the Caputo derivative

permits the direct integration of real-world initial conditions, hence enhancing the intuitive and practical use of fractional calculus in modeling infectious disease dynamics. The Caputo operator is well suited for numerical approaches, guaranteeing stability and precision in simulations, which is essential for accurately portraying the intricate memory effects of Mpox transmission. The memory effects, characterized by the non-local properties of the Caputo derivative, provide a more thorough comprehension of disease dynamics compared to integer-order models. In addition, unlike the CF derivative, which emphasizes exponential decay, the classical Caputo derivative provides versatility in characterizing long-range temporal interactions inherent to epidemiological phenomena. Replacing the integer order model (5) with non-integer order in CF operator with each differential equation's dimension maintained as stated:

$$\begin{aligned}
{}^{CF}D^{\delta}_{0,t}(S_m(t)) &= \Pi_m - \lambda_1 S_m - (\mu_1 + \alpha_m)S_m + \tau V_m,\\
{}^{CF}D^{\delta}_{0,t}(E_m(t)) &= \lambda_1 S_m - (k + \mu_1)E_m,\\
{}^{CF}D^{\delta}_{0,t}(A_m(t)) &= k(1-\rho)E_m - (\gamma_1 + \mu_1 + \eta_1)A_m,\\
{}^{CF}D^{\delta}_{0,t}(I_m(t)) &= k\rho E_m - (\gamma_2 + \mu_1 + \eta_2)I_m,\\
{}^{CF}D^{\delta}_{0,t}(V_m(t)) &= \alpha_m S_m - (\tau + \mu_1)V_m,\\
{}^{CF}D^{\delta}_{0,t}(R_m(t)) &= \gamma_1 A_m + \gamma_2 I_m - \mu_1 R_m,\\
{}^{CF}D^{\delta}_{0,t}(S_a(t)) &= \Pi_a - \lambda_2 S_a - \mu_2 S_a,\\
{}^{CF}D^{\delta}_{0,t}(E_a(t)) &= \lambda_2 S_a - (\pi + \mu_2)E_a,\\
{}^{CF}D^{\delta}_{0,t}(I_a(t)) &= \pi E_a - (\mu_2 + \eta_3)I_a,
\end{aligned} \tag{6}$$

with regard to the initial conditions involved in system (6) are $S_m(0) = S_{m0}$, $E_m(0) = E_{m0}$, $A_m(0) = A_{m0}$, $I_m(0) = I_{m0}, V_m(0) = V_{m0}$, $R_m(0) = R_{m0}$, $S_a(0) = S_{a0}$, $E_a(0) = E_{a0}$, $I_a(0) = I_{a0}$.

3 Model analysis in the fractional case

We will examine fundamental mathematical elements of the Mpox compartmental epidemiological model in fractional form as outlined in (6).

Existence and uniqueness

This section will demonstrate the outcome of the fractional-order model (6) through an analysis of fixed point hypothesis. This is achieved by reformulating the fractional-order differential equations as integral equations and verifying the Lipschitz conditions for all model kernels. We will additionally demonstrate the uniqueness of the remedy. To achieve this, the initial step involves converting the proposed fractional order system into a corresponding integral equation structure as follows:

$$\begin{aligned}
S_m(t) - S_m(0) &= {}^{CF}I^{\delta}_{0,t}\{\Pi_m - \lambda_1 S_m - (\mu_1 + \alpha_m)S_m + \tau V_m\},\\
E_m(t) - E_m(0) &= {}^{CF}I^{\delta}_{0,t}\{\lambda_1 S_m - (k + \mu_1)E_m\},\\
A_m(t) - A_m(0) &= {}^{CF}I^{\delta}_{0,t}\{k(1-\rho)E_m - (\gamma_1 + \mu_1 + \eta_1)A_m\},\\
I_m(t) - I_m(0) &= {}^{CF}I^{\delta}_{0,t}\{k\rho E_m - (\gamma_2 + \mu_1 + \eta_2)I_m\},\\
V_m(t) - V_m(0) &= {}^{CF}I^{\delta}_{0,t}\{\alpha_m S_m - (\tau + \mu_1)V_m\},\\
R_m(t) - R_m(0) &= {}^{CF}I^{\delta}_{0,t}\{\gamma_1 A_m + \gamma_2 I_m - \mu_1 R_m\},\\
S_a(t) - S_a(0) &= {}^{CF}I^{\delta}_{0,t}\{\Pi_a - \lambda_2 S_a - \mu_2 S_a\},
\end{aligned} \tag{7}$$

$$\begin{aligned} E_a(t) - E_a(0) &= {}^{CF}I^{\delta}_{0,t}\{\lambda_2 S_a - (\pi + \mu_2)E_a\}, \\ I_a(t) - I_a(0) &= {}^{CF}I^{\delta}_{0,t}\{\pi E_a - (\mu_2 + \eta_3)I_a\}. \end{aligned}$$

Through the implementation of CF fractional order integrating [20], one can acquire

$$\begin{aligned} S_m(t) - S_m(0) &= \frac{2(1-\delta)}{(2-\delta)M(\delta)}J_1(t, S_m) + \frac{2\delta}{(2-\delta)M(\delta)}\int_0^t J_1(x, S_m)dx, \\ E_m(t) - E_m(0) &= \frac{2(1-\delta)}{(2-\delta)M(\delta)}J_2(t, E_m) + \frac{2\delta}{(2-\delta)M(\delta)}\int_0^t J_2(x, E_m)dx, \\ A_m(t) - A_m(0) &= \frac{2(1-\delta)}{(2-\delta)M(\delta)}J_3(t, A_m) + \frac{2\delta}{(2-\delta)M(\delta)}\int_0^t J_3(x, A_m)dx, \\ I_m(t) - I_m(0) &= \frac{2(1-\delta)}{(2-\delta)M(\delta)}J_4(t, I_m) + \frac{2\delta}{(2-\delta)M(\delta)}\int_0^t J_4(x, I_m)dx, \\ V_m(t) - V_m(0) &= \frac{2(1-\delta)}{(2-\delta)M(\delta)}J_5(t, V_m) + \frac{2\delta}{(2-\delta)M(\delta)}\int_0^t J_5(x, V_m)dx, \\ R_m(t) - R_m(0) &= \frac{2(1-\delta)}{(2-\delta)M(\delta)}J_6(t, R_m) + \frac{2\delta}{(2-\delta)M(\delta)}\int_0^t J_6(x, R_m)dx, \\ S_a(t) - S_a(0) &= \frac{2(1-\delta)}{(2-\delta)M(\delta)}J_7(t, S_a) + \frac{2\delta}{(2-\delta)M(\delta)}\int_0^t J_7(x, S_a)dx, \\ E_a(t) - E_a(0) &= \frac{2(1-\delta)}{(2-\delta)M(\delta)}J_8(t, E_a) + \frac{2\delta}{(2-\delta)M(\delta)}\int_0^t J_8(x, E_a)dx, \\ I_a(t) - I_a(0) &= \frac{2(1-\delta)}{(2-\delta)M(\delta)}J_9(t, I_a) + \frac{2\delta}{(2-\delta)M(\delta)}\int_0^t J_9(x, I_a)dx. \end{aligned}$$

We assume kernels as determined by

$$\begin{aligned} J_1(S_m(t), t) &= \Pi_m - \lambda_1 S_m - (\mu_1 + \alpha_m)S_m + \tau V_m, \\ J_2(E_m(t), t) &= \lambda_1 S_m - (k + \mu_1)E_m, \\ J_3(A_m(t), t) &= k(1-\rho)E_m - (\gamma_1 + \mu_1 + \eta_1)A_m, \\ J_4(I_m(t), t) &= k\rho E_m - (\gamma_2 + \mu_1 + \eta_2)I_m, \\ J_5(V_m(t), t) &= \alpha_m S_m - (\tau + \mu_1)V_m, \\ J_6(R_m(t), t) &= \gamma_1 A_m + \gamma_2 I_m - \mu_1 R_m, \\ J_7(S_a(t), t) &= \Pi_a - \lambda_2 S_a - \mu_2 S_a, \\ J_8(E_a(t), t) &= \lambda_2 S_a - (\pi + \mu_2)E_a, \\ J_9(I_a(t), t) &= \pi E_a - (\mu_2 + \eta_3)I_a. \end{aligned} \tag{8}$$

Theorem 1 *The kernels J_1, J_2, J_3, J_4, J_5, J_6, J_7, J_8, and J_9 meet the Lipschitz criteria.*

Proof Let us imagine that S_m and S_{m_1}, E_m and E_{m_1}, A_m and A_{m_1}, I_m and I_{m_1}, V_m and V_{m_1}, R_m and R_{m_1}, S_a and S_{a_1}, E_a and E_{a_1}, I_a and I_{a_1}, represents the two functions corresponding to the

aforementioned kernels $J_1, J_2, J_3, J_4, J_5, J_6, J_7, J_8$, and J_9. Thus, we set up the subsequent system

$$\begin{aligned}
J_1(S_m(t),t) - J_1(S_{m_1}(t),t) =& -\lambda_1(S_m(t) - S_{m_1}(t)) - (\mu_1 + \alpha_m)(S_m(t) - S_{m_1}(t)) \\
&+ \tau(V_m(t) - V_{m_1}(t)), \\
J_2(E_m(t),t) - J_2(E_{m_1}(t),t) =& \lambda_1(S_m(t) - S_{m_1}(t)) - (k + \mu_1)(E_m(t) - E_{m_1}(t)), \\
J_3(A_m(t),t) - J_3(A_{m_1}(t),t) =& k(1-\rho)(E_m(t) - E_{m_1}(t)) - (\gamma_1 + \mu_1 + \eta_1)(A_m(t) - A_{m_1}(t)), \\
J_4(I_m(t),t) - J_4(I_{m_1}(t),t) =& k\rho(E_m(t) - E_{m_1}(t)) - (\gamma_2 + \mu_1 + \eta_2)(I_m(t) - I_{m_1}(t)), \\
J_5(V_m(t),t) - J_5(V_{m_1}(t),t) =& \alpha_m(S_m(t) - S_{m_1}(t)) - (\tau + \mu_1)(V_m(t) - V_{m_1}(t)), \\
J_6(R_m(t),t) - J_6(R_{m_1}(t),t) =& \gamma_1(A_m(t) - A_{m_1}(t)) + \gamma_2(I_m(t) - I_{m_1}(t)) \\
&- \mu_1(R_m(t) - R_{m_1}(t)), \\
J_7(S_a(t),t) - J_7(S_{a_1}(t),t) =& -(\lambda_2 + \mu_2)(S_a(t) - S_{a_1}(t)), \\
J_8(E_a(t),t) - J_8(E_{a_1}(t),t) =& \lambda_2 S_a(t) - S_{a_1}(t)) - (\pi + \mu_2)(E_a(t) - E_{a_1}(t)), \\
J_9(I_a(t),t) - J_9(I_{a_1}(t),t) =& \pi(E_a(t) - E_{a_1}(t)) - (\mu_2 + \eta_3)(I_a(t) - I_{a_1}(t)).
\end{aligned}$$

By applying Cauchy's inequality to the aforementioned system, it is possible to derive

$$\begin{aligned}
\|J_1(S_m(t),t) - J_1(S_{m_1}(t),t)\| &= \| -\lambda_1(S_m(t) - S_{m_1}(t)) - (\mu_1 + \alpha_m)(S_m(t) - S_{m_1}(t)) \\
&\quad + \tau(V_m(t) - V_{m_1}(t))\| \\
&\leq \|\lambda_1 + \mu_1 + \alpha_m\|\|(S_m(t) - S_{m_1}(t))\|, \\
\|J_2(E_m(t),t) - J_2(E_{m_1}(t),t)\| &= \|\lambda_1(S_m(t) - S_{m_1}(t)) - (k + \mu_1)(E_m(t) - E_{m_1}(t))\| \\
&\leq \|\lambda_1 + k + \mu_1\|\|E_m(t) - E_{m_1}(t))\|, \\
\|J_3(A_m(t),t) - J_3(A_{m_1}(t),t)\| &= \|k(1-\rho)(E_m(t) - E_{m_1}(t)) - (\gamma_1 + \mu_1 + \eta_1)(A_m(t) - A_{m_1}(t))\| \\
&\leq \|k(1-\rho) + \gamma_1 + \mu_1 + \eta_1\|\|(A_m(t) - A_{m_1}(t))\|, \\
\|J_4(I_m(t),t) - J_4(I_{m_1}(t),t)\| &= \|k\rho(E_m(t) - E_{m_1}(t)) - (\gamma_2 + \mu_1 + \eta_2)(I_m(t) - I_{m_1}(t))\| \\
&\leq \|k\rho + \gamma_2 + \mu_1 + \eta_2\|\|(I_m(t) - I_{m_1}(t))\|,
\end{aligned}$$

$$\begin{aligned}
\|J_5(V_m(t),t) - J_5(V_{m_1}(t),t)\| &= \|\alpha_m(S_m(t) - S_{m_1}(t)) - (\tau + \mu_1)(V_m(t) - V_{m_1}(t))\| \\
&\leq \|\alpha_m + \tau + \mu_1\|\|(V_m(t) - V_{m_1}(t))\|, \\
\|J_6(R_m(t),t) - J_6(R_{m_1}(t),t)\| &= \|\gamma_1(A_m(t) - A_{m_1}(t)) + \gamma_2(I_m(t) - I_{m_1}(t)) \\
&\quad - \mu_1(R_m(t) - R_{m_1}(t))\| \\
&\leq \|\gamma_1 + \gamma_2 + \mu_1\|\|(R_m(t) - R_{m_1}(t))\|, \\
\|J_7(S_a(t),t) - J_7(S_{a_1}(t),t)\| &= \| -(\lambda_2 + \mu_2)(S_a(t) - S_{a_1}(t))\| \\
&\leq \|\lambda_2 + \mu_2\|\|S_a(t) - S_{a_1}(t))\|, \\
\|J_8(E_a(t),t) - J_8(E_{a_1}(t),t)\| &= \|\lambda_2 S_a(t) - S_{a_1}(t)) - (\pi + \mu_2)(E_a(t) - E_{a_1}(t))\| \\
&\leq \|\lambda_2 + \pi + \mu_2\|\|(E_a(t) - E_{a_1}(t))\|, \\
\|J_9(I_a(t),t) - J_9(I_{a_1}(t),t)\| &= \|\pi(E_a(t) - E_{a_1}(t)) - (\mu_2 + \eta_3)(I_a(t) - I_{a_1}(t))\| \\
&\leq \|\pi + \mu_2 + \eta_3\|\|(I_a(t) - I_{a_1}(t))\|.
\end{aligned}$$

Employing the definition of the CF fractional integral, recursively, one may obtain

$$
\begin{aligned}
S_m(t) &= \frac{2(1-\delta)J_1(S_{m_{n-1}}(t),t)}{(2-\delta)M(\delta)} + \frac{2\delta}{(2-\delta)M(\delta)}\int_0^t J_1(S_{m_{n-1}}(s),s)ds,\\
E_m(t) &= \frac{2(1-\delta)J_2(E_{m_{n-1}}(t),t)}{(2-\delta)M(\delta)} + \frac{2\delta}{(2-\delta)M(\delta)}\int_0^t J_2(E_{m_{n-1}}(s),s)ds,\\
A_m(t) &= \frac{2(1-\delta)J_3(A_{m_{n-1}}(t),t)}{(2-\delta)M(\delta)} + \frac{2\delta}{(2-\delta)M(\delta)}\int_0^t J_3(A_{m_{n-1}}(s),s)ds,\\
I_m(t) &= \frac{2(1-\delta)J_4(I_{m_{n-1}}(t),t)}{(2-\delta)M(\delta)} + \frac{2\delta}{(2-\delta)M(\delta)}\int_0^t J_4(I_{m_{n-1}}(s),s)ds,\\
V_m(t) &= \frac{2(1-\delta)J_5(V_{m_{n-1}}(t),t)}{(2-\delta)M(\delta)} + \frac{2\delta}{(2-\delta)M(\delta)}\int_0^t J_5(V_{m_{n-1}}(s),s)ds,\\
R_m(t) &= \frac{2(1-\delta)J_6(R_{m_{n-1}}(t),t)}{(2-\delta)M(\delta)} + \frac{2\delta}{(2-\delta)M(\delta)}\int_0^t J_6(R_{m_{n-1}}(s),s)ds,\\
S_a(t) &= \frac{2(1-\delta)J_7(S_{a_{n-1}}(t),t)}{(2-\delta)M(\delta)} + \frac{2\delta}{(2-\delta)M(\delta)}\int_0^t J_7(S_{a_{n-1}}(s),s)ds,\\
E_a(t) &= \frac{2(1-\delta)J_8(E_{a_{n-1}}(t),t)}{(2-\delta)M(\delta)} + \frac{2\delta}{(2-\delta)M(\delta)}\int_0^t J_8(E_{a_{n-1}}(s),s)ds,\\
I_a(t) &= \frac{2(1-\delta)J_9(E_{a_{n-1}}(t),t)}{(2-\delta)M(\delta)} + \frac{2\delta}{(2-\delta)M(\delta)}\int_0^t J_9(I_{a_{n-1}}(s),s)ds.
\end{aligned}
\tag{9}
$$

The utilization of norms the concept of majorizing indicates that the variance among successive terms suggests

$$
\begin{aligned}
\|\mathcal{K}_n(t)\| = \|S_{m_n}(t) - S_{m_{1,n-1}}\| &\le \frac{2(1-\delta)}{(2-\delta)M(\delta)}\|J_1(S_{m_{n-1}}(t),t) - J_1(S_{m_{1,n-2}}(t),t)\|\\
&+ \frac{2\delta}{(2-\delta)M(\delta)}\left\|\int_0^t [J_1(S_{m_{n-1}}(s),s) - J_1(S_{m_{1,n-2}}(s),s)]ds\right\|,
\end{aligned}
$$

$$
\begin{aligned}
\|\mathcal{L}_n(t)\| = \|E_{m_n}(t) - E_{m_{1,n-1}}\| &\le \frac{2(1-\delta)}{(2-\delta)M(\delta)}\|J_2(E_{m_{n-1}}(t),t) - J_2(E_{m_{1,n-2}}(t),t)\|\\
&+ \frac{2\delta}{(2-\delta)M(\delta)}\left\|\int_0^t [J_2(E_{m_{n-1}}(s),s) - J_2(E_{m_{1,n-2}}(s),s)]ds\right\|,
\end{aligned}
$$

$$
\begin{aligned}
\|\mathcal{M}_n(t)\| = \|A_{m_n}(t) - A_{m_{1,n-1}}\| &\le \frac{2(1-\delta)}{(2-\delta)M(\delta)}\|J_3(A_{m_{n-1}}(t),t) - J_3(A_{m_{1,n-2}}(t),t)\|\\
&+ \frac{2\delta}{(2-\delta)M(\delta)}\left\|\int_0^t [J_3(A_{m_{n-1}}(s),s) - J_3(A_{m_{1,n-2}}(s),s)]ds\right\|,
\end{aligned}
$$

$$\|\mathcal{N}_n(t)\| = \|I_{m_n}(t) - I_{m_{1,n-1}}\| \leq \frac{2(1-\delta)}{(2-\delta)M(\delta)}\|J_4(I_{m_{n-1}}(t),t) - J_4(I_{m_{1,n-2}}(t),t)\| + \frac{2\delta}{(2-\delta)M(\delta)}\left\|\int_0^t [J_4(I_{m_{n-1}}(s),s) - J_4(I_{m_{1,n-2}}(s),s)]ds\right\|,$$

$$\|\mathcal{O}_n(t)\| = \|V_{m_n}(t) - V_{m_{1,n-1}}\| \leq \frac{2(1-\delta)}{(2-\delta)M(\delta)}\|J_5(V_{m_{n-1}}(t),t) - J_5(V_{m_{1,n-2}}(t),t)\| + \frac{2\delta}{(2-\delta)M(\delta)}\left\|\int_0^t [J_5(V_{m_{n-1}}(s),s) - J_5(V_{m_{1,n-2}}(s),s)]ds\right\|,$$

$$\|\mathcal{P}_n(t)\| = \|R_{m_n}(t) - R_{m_{1,n-1}}\| \leq \frac{2(1-\delta)}{(2-\delta)M(\delta)}\|J_6(R_{m_{n-1}}(t),t) - J_6(R_{m_{1,n-2}}(t),t)\| + \frac{2\delta}{(2-\delta)M(\delta)}\left\|\int_0^t [J_6(R_{m_{n-1}}(s),s) - J_6(R_{m_{1,n-2}}(s),s)]ds\right\|,$$

$$\|\mathcal{X}_n(t)\| = \|S_{a_n}(t) - S_{a_{1,n-1}}\| \leq \frac{2(1-\delta)}{(2-\delta)M(\delta)}\|J_7(S_{a_{n-1}}(t),t) - J_7(S_{a_{1,n-2}}(t),t)\| + \frac{2\delta}{(2-\delta)M(\delta)}\left\|\int_0^t [J_7(S_{a_{n-1}}(s),s) - J_7(S_{a_{1,n-2}}(s),s)]ds\right\|,$$

$$\|\mathcal{Y}_n(t)\| = \|E_{a_n}(t) - E_{a_{1,n-1}}\| \leq \frac{2(1-\delta)}{(2-\delta)M(\delta)}\|J_8(E_{a_{n-1}}(t),t) - J_8(E_{a_{1,n-2}}(t),t)\| + \frac{2\delta}{(2-\delta)M(\delta)}\left\|\int_0^t [J_8(S_{a_{n-1}}(s),s) - J_8(E_{a_{1,n-2}}(s),s)]ds\right\|,$$

$$\|\mathcal{Z}_n(t)\| = \|I_{a_n}(t) - I_{a_{1,n-1}}\| \leq \frac{2(1-\delta)}{(2-\delta)M(\delta)}\|J_9(I_{a_{n-1}}(t),t) - J_9(I_{a_{1,n-2}}(t),t)\| + \frac{2\delta}{(2-\delta)M(\delta)}\left\|\int_0^t [J_9(I_{a_{n-1}}(s),s) - J_9(I_{a_{1,n-2}}(s),s)]ds\right\|,$$

where

$$\begin{aligned}
&\sum_{i=0}^{\infty}\mathcal{K}_i(t) = S_{m_n}(t),\ \sum_{i=0}^{\infty}\mathcal{L}_i(t) = E_{m_n}(t),\ \sum_{i=0}^{\infty}\mathcal{M}_i(t) = A_{m_n}(t),\ \sum_{i=0}^{\infty}\mathcal{N}_i(t) = I_{m_n}(t),\\
&\sum_{i=0}^{\infty}\mathcal{O}_i(t) = V_{h_n}(t),\ \sum_{i=0}^{\infty}\mathcal{P}_i(t) = R_{m_n}(t),\ \sum_{i=0}^{\infty}\mathcal{X}_i(t) = S_{a_n}(t),\ \sum_{i=0}^{\infty}\mathcal{Y}_i(t) = E_{a_n}(t),\\
&\sum_{i=0}^{\infty}\mathcal{Z}_i(t) = I_{a_n}(t).
\end{aligned} \tag{10}$$

Moreover, the kernels $J_1, \ldots, J_9$ fulfill the Lipschitz condition, allowing one to express

$$\|\mathcal{K}_n(t)\| = \|S_{m_n}(t) - S_{m_{1,n-1}}\| \leq \frac{2(1-\delta)}{(2-\delta)M(\delta)}\xi_1\|S_{m_{n-1}}(t) - S_{m_{1,n-2}}(t)\| + \frac{2\delta}{(2-\delta)M(\delta)}\xi_2\left\|\int_0^t S_{m_{n-1}}(s) - S_{m_{1,n-2}}(s)ds\right\|,$$

$$\|\mathcal{L}_n(t)\| = \|E_{m_n}(t) - E_{m_{1,n-1}}\| \leq \frac{2(1-\delta)}{(2-\delta)M(\delta)}\xi_3\|E_{m_{n-1}}(t) - E_{m_{1,n-2}}(t)\| + \frac{2\delta}{(2-\delta)M(\delta)}\xi_4\left\|\int_0^t E_{m_{n-1}}(s) - E_{m_{1,n-2}}(s)ds\right\|,$$

$$\|\mathcal{M}_n(t)\| = \|A_{m_n}(t) - A_{m_{1,n-1}}\| \leq \frac{2(1-\delta)}{(2-\delta)M(\delta)}\xi_5\|A_{m_{n-1}}(t) - A_{m_{1,n-2}}(t)\| + \frac{2\delta}{(2-\delta)M(\delta)}\xi_6\left\|\int_0^t A_{m_{n-1}}(s) - A_{m_{1,n-2}}(s)ds\right\|,$$

$$\|\mathcal{N}_n(t)\| = \|I_{m_n}(t) - I_{m_{1,n-1}}\| \leq \frac{2(1-\delta)}{(2-\delta)M(\delta)}\xi_7\|I_{m_{n-1}}(t) - I_{m_{1,n-2}}(t)\| + \frac{2\delta}{(2-\delta)M(\delta)}\xi_8\left\|\int_0^t I_{m_{n-1}}(s) - I_{m_{1,n-2}}(s)ds\right\|,$$

$$\|\mathcal{O}_n(t)\| = \|V_{m_n}(t) - V_{m_{1,n-1}}\| \leq \frac{2(1-\delta)}{(2-\delta)M(\delta)}\xi_9\|V_{m_{n-1}}(t) - V_{m_{1,n-2}}(t)\| + \frac{2\delta}{(2-\delta)M(\delta)}\xi_{10}\left\|\int_0^t V_{m_{n-1}}(s) - V_{m_{1,n-2}}(s)ds\right\|,$$

$$\|\mathcal{P}_n(t)\| = \|R_{m_n}(t) - R_{m_{1,n-1}}\| \leq \frac{2(1-\delta)}{(2-\delta)M(\delta)}\xi_{11}\|R_{m_{n-1}}(t) - R_{m_{1,n-2}}(t)\| + \frac{2\delta}{(2-\delta)M(\delta)}\xi_{12}\left\|\int_0^t R_{m_{n-1}}(s) - R_{m_{1,n-2}}(s)ds\right\|,$$

$$\|\mathcal{X}_n(t)\| = \|S_{a_n}(t) - S_{a_{1,n-1}}\| \leq \frac{2(1-\delta)}{(2-\delta)M(\delta)}\xi_{13}\|S_{a_{n-1}}(t) - S_{a_{1,n-2}}(t)\| + \frac{2\delta}{(2-\delta)M(\delta)}\xi_{14}\left\|\int_0^t S_{a_{n-1}}(s) - S_{a_{1,n-2}}(s)ds\right\|,$$

$$\|\mathcal{Y}_n(t)\| = \|E_{a_n}(t) - E_{a_{1,n-1}}\| \leq \frac{2(1-\delta)}{(2-\delta)M(\delta)}\xi_{15}\|E_{a_{n-1}}(t) - E_{a_{1,n-2}}(t)\| + \frac{2\delta}{(2-\delta)M(\delta)}\xi_{16}\left\|\int_0^t E_{a_{n-1}}(s) - E_{a_{1,n-2}}(s)ds\right\|,$$

$$\|\mathcal{Z}_n(t)\| = \|I_{a_n}(t) - I_{a_{1,n-1}}\| \leq \frac{2(1-\delta)}{(2-\delta)M(\delta)}\xi_{17}\|I_{a_{n-1}}(t) - I_{m_{1,n-2}}(t)\| + \frac{2\delta}{(2-\delta)M(\delta)}\xi_{18}\left\|\int_0^t I_{a_{n-1}}(s) - I_{a_{1,n-2}}(s)ds\right\|.$$

Theorem 2 *The existence of the solution for the introduced fractional order model (6) is established based on the CF operator.*

Proof The utilization of Eq. (10) along with the implementation of a recursive scheme results in the subsequent system

$$\begin{aligned}
\|\mathcal{K}_n(t)\| &\leq \|S_m(0)\| + \left\{\left(\frac{2\xi_1(1-\delta)}{M(\delta)(2-\delta)}\right)^n\right\} + \left\{\left(\frac{2\xi_2\delta t}{M(\delta)(2-\delta)}\right)^n\right\},\\
\|\mathcal{L}_n(t)\| &\leq \|E_m(0)\| + \left\{\left(\frac{2\xi_3(1-\delta)}{M(\delta)(2-\delta)}\right)^n\right\} + \left\{\left(\frac{2\xi_4\delta t}{M(\delta)(2-\delta)}\right)^n\right\},\\
\|\mathcal{M}_n(t)\| &\leq \|A_m(0)\| + \left\{\left(\frac{2\xi_5(1-\delta)}{M(\delta)(2-\delta)}\right)^n\right\} + \left\{\left(\frac{2\xi_6\delta t}{M(\delta)(2-\delta)}\right)^n\right\},\\
\|\mathcal{N}_n(t)\| &\leq \|I_m(0)\| + \left\{\left(\frac{2\xi_7(1-\delta)}{M(\delta)(2-\delta)}\right)^n\right\} + \left\{\left(\frac{2\xi_8\delta t}{M(\delta)(2-\delta)}\right)^n\right\},\\
\|\mathcal{O}_n(t)\| &\leq \|V_m(0)\| + \left\{\left(\frac{2\xi_9(1-\delta)}{M(\delta)(2-\delta)}\right)^n\right\} + \left\{\left(\frac{2\xi_{10}\delta t}{M(\delta)(2-\delta)}\right)^n\right\},\\
\|\mathcal{P}_n(t)\| &\leq \|R_m(0)\| + \left\{\left(\frac{2\xi_{11}(1-\delta)}{M(\delta)(2-\delta)}\right)^n\right\} + \left\{\left(\frac{2\xi_{12}\delta t}{M(\delta)(2-\delta)}\right)^n\right\},\\
\|\mathcal{X}_n(t)\| &\leq \|S_a(0)\| + \left\{\left(\frac{2\xi_{13}(1-\delta)}{M(\delta)(2-\delta)}\right)^n\right\} + \left\{\left(\frac{2\xi_{14}\delta t}{M(\delta)(2-\delta)}\right)^n\right\},\\
\|\mathcal{Y}_n(t)\| &\leq \|E_a(0)\| + \left\{\left(\frac{2\xi_{15}(1-\delta)}{M(\delta)(2-\delta)}\right)^n\right\} + \left\{\left(\frac{2\xi_{16}\delta t}{M(\delta)(2-\delta)}\right)^n\right\},\\
\|\mathcal{Z}_n(t)\| &\leq \|I_a(0)\| + \left\{\left(\frac{2\xi_{17}(1-\delta)}{M(\delta)(2-\delta)}\right)^n\right\} + \left\{\left(\frac{2\xi_{18}\delta t}{M(\delta)(2-\delta)}\right)^n\right\}.
\end{aligned} \tag{11}$$

To examine whether the functions in Eq. (11) serve as solutions to the model (6), we will employ

the subsequent replacements

$$\begin{aligned} &S_m(t) = S_{m_n}(t) - \Upsilon_{1,n}(t), \;\; E_m(t) = E_{m_n}(t) - \Upsilon_{2,n}(t), \;\; A_m(t) = A_{m_n}(t) - \Upsilon_{3,n}(t), \\ &I_m(t) = I_{m_n}(t) - \Upsilon_{4,n}(t), \;\; V_m(t) = V_{m_n}(t) - \Upsilon_{5,n}(t), \;\; R_m(t) = R_{m_n}(t) - \Upsilon_{6,n}(t), \\ &S_a(t) = S_{a_n}(t) - \Upsilon_{7,n}(t), \;\; E_a(t) = E_{a_n}(t) - \Upsilon_{8,n}(t), \;\; I_a(t) = I_{a_n}(t) - \Upsilon_{9,n}(t), \end{aligned} \tag{12}$$

where $\Upsilon_{1,n}(t), \Upsilon_{2,n}(t), \Upsilon_{3,n}(t), \Upsilon_{4,n}(t), \Upsilon_{5,n}(t), \Upsilon_{6,n}(t), \Upsilon_{7,n}(t), \Upsilon_{8,n}(t), \Upsilon_{9,n}(t)$, illustrate the residual components of the series solutions. Therefore,

$$\begin{aligned} S_m(t) - S_{m_{n-1}}(t) &= \frac{2(1-\delta)J_1(S_m(t) - \Upsilon_{1,n}(t))}{M(\delta)(2-\delta)} + \frac{2\delta}{M(\delta)(2-\delta)}\int_0^t J_1(S_m(s) - \Upsilon_{1,n}(s))ds, \\ E_m(t) - E_{m_{n-1}}(t) &= \frac{2(1-\delta)J_2(E_m(t) - \Upsilon_{2,n}(t))}{M(\delta)(2-\delta)} + \frac{2\delta}{M(\delta)(2-\delta)}\int_0^t J_2(E_m(s) - \Upsilon_{2,n}(s))ds, \\ A_m(t) - A_{m_{n-1}}(t) &= \frac{2(1-\delta)J_3(A_m(t) - \Upsilon_{3,n}(t))}{M(\delta)(2-\delta)} + \frac{2\delta}{M(\delta)(2-\delta)}\int_0^t J_3(A_m(s) - \Upsilon_{3,n}(s))ds, \\ I_m(t) - I_{m_{n-1}}(t) &= \frac{2(1-\delta)J_4(I_m(t) - \Upsilon_{4,n}(t))}{M(\delta)(2-\delta)} + \frac{2\delta}{M(\delta)(2-\delta)}\int_0^t J_4(I_m(s) - \Upsilon_{4,n}(s))ds, \\ V_m(t) - V_{m_{n-1}}(t) &= \frac{2(1-\delta)J_5(V_m(t) - \Upsilon_{5,n}(t))}{M(\delta)(2-\delta)} + \frac{2\delta}{M(\delta)(2-\delta)}\int_0^t J_5(V_m(s) - \Upsilon_{5,n}(s))ds, \\ R_m(t) - R_{m_{n-1}}(t) &= \frac{2(1-\delta)J_6(R_m(t) - \Upsilon_{6,n}(t))}{M(\delta)(2-\delta)} + \frac{2\delta}{M(\delta)(2-\delta)}\int_0^t J_6(R_m(s) - \Upsilon_{6,n}(s))ds, \\ S_a(t) - S_{a_{n-1}}(t) &= \frac{2(1-\delta)J_7(S_a(t) - \Upsilon_{7,n}(t))}{M(\delta)(2-\delta)} + \frac{2\delta}{M(\delta)(2-\delta)}\int_0^t J_7(S_a(s) - \Upsilon_{7,n}(s))ds, \\ E_a(t) - E_{a_{n-1}}(t) &= \frac{2(1-\delta)J_8(E_a(t) - \Upsilon_{8,n}(t))}{M(\delta)(2-\delta)} + \frac{2\delta}{M(\delta)(2-\delta)}\int_0^t J_8(E_a(s) - \Upsilon_{8,n}(s))ds, \\ I_a(t) - I_{a_{n-1}}(t) &= \frac{2(1-\delta)J_9(I_a(t) - \Upsilon_{9,n}(t))}{M(\delta)(2-\delta)} + \frac{2\delta}{M(\delta)(2-\delta)}\int_0^t J_9(I_a(s) - \Upsilon_{9,n}(s))ds. \end{aligned} \tag{13}$$

By utilizing the norm on both sides and utilizing the Lipschitz principle, the preceding assertion results in

$$\begin{aligned} &\left\| S_m(t) - \frac{2(1-\delta)J_1(S_m(t),t)}{(2-\delta)M(\delta)} - S_m(0) - \frac{2\delta}{(2-\delta)M(\delta)}\int_0^t J_1(S_m(s),s)ds \right\| \\ &\leq \|\Upsilon_{1,n}(t)\| \left\{ 1 + \left(\frac{2(1-\delta)\xi_1}{(2-\delta)M(\delta)} + \frac{2\delta\xi_2 t}{(2-\delta)M(\delta)} \right) \right\}, \end{aligned}$$

$$\begin{aligned} &\left\| E_m(t) - \frac{2(1-\delta)J_2(E_m(t),t)}{(2-\delta)M(\delta)} - E_m(0) - \frac{2\delta}{(2-\delta)M(\delta)}\int_0^t J_2(E_m(s),s)ds \right\| \\ &\leq \|\Upsilon_{2,n}(t)\| \left\{ 1 + \left(\frac{2(1-\delta)\xi_2}{(2-\delta)M(\delta)} + \frac{2\delta\xi_4 t}{(2-\delta)M(\delta)} \right) \right\}, \end{aligned}$$

$$\left\| A_m(t) - \frac{2(1-\delta)J_3(A_m(t),t)}{(2-\delta)M(\delta)} - A_m(0) - \frac{2\delta}{(2-\delta)M(\delta)}\int_0^t J_3(E_m(s),s)ds \right\|$$
$$\leq \|\Upsilon_{3,n}(t)\|\left\{1 + \left(\frac{2(1-\delta)\xi_5}{(2-\delta)M(\delta)} + \frac{2\delta\xi_6 t}{(2-\delta)M(\delta)}\right)\right\},$$

$$\left\| I_m(t) - \frac{2(1-\delta)J_4(I_m(t),t)}{(2-\delta)M(\delta)} - I_m(0) - \frac{2\delta}{(2-\delta)M(\delta)}\int_0^t J_4(I_m(s),s)ds \right\|$$
$$\leq \|\Upsilon_{4,n}(t)\|\left\{1 + \left(\frac{2(1-\delta)\xi_7}{(2-\delta)M(\delta)} + \frac{2\delta\xi_8 t}{(2-\delta)M(\delta)}\right)\right\},$$

$$\left\| V_m(t) - \frac{2(1-\delta)J_5(V_m(t),t)}{(2-\delta)M(\delta)} - V_m(0) - \frac{2\delta}{(2-\delta)M(\delta)}\int_0^t J_5(V_m(s),s)ds \right\|$$
$$\leq \|\Upsilon_{5,n}(t)\|\left\{1 + \left(\frac{2(1-\delta)\xi_9}{(2-\delta)M(\delta)} + \frac{2\delta\xi_{10} t}{(2-\delta)M(\delta)}\right)\right\},$$

$$\left\| R_m(t) - \frac{2(1-\delta)J_6(R_m(t),t)}{(2-\delta)M(\delta)} - R_m(0) - \frac{2\delta}{(2-\delta)M(\delta)}\int_0^t J_6(R_m(s),s)ds \right\|$$
$$\leq \|\Upsilon_{6,n}(t)\|\left\{1 + \left(\frac{2(1-\delta)\xi_{11}}{(2-\delta)M(\delta)} + \frac{2\delta\xi_{12} t}{(2-\delta)M(\delta)}\right)\right\},$$

$$\left\| S_a(t) - \frac{2(1-\delta)J_7(S_a(t),t)}{(2-\delta)M(\delta)} - S_a(0) - \frac{2\delta}{(2-\delta)M(\delta)}\int_0^t J_7(S_a(s),s)ds \right\|$$
$$\leq \|\Upsilon_{7,n}(t)\|\left\{1 + \left(\frac{2(1-\delta)\xi_{13}}{(2-\delta)M(\delta)} + \frac{2\delta\xi_{14} t}{(2-\delta)M(\delta)}\right)\right\},$$

$$\left\| E_a(t) - \frac{2(1-\delta)J_8(E_a(t),t)}{(2-\delta)M(\delta)} - E_a(0) - \frac{2\delta}{(2-\delta)M(\delta)}\int_0^t J_8(E_a(s),s)ds \right\|$$
$$\leq \|\Upsilon_{8,n}(t)\|\left\{1 + \left(\frac{2(1-\delta)\xi_{15}}{(2-\delta)M(\delta)} + \frac{2\delta\xi_{16} t}{(2-\delta)M(\delta)}\right)\right\},$$

$$\left\| I_a(t) - \frac{2(1-\delta)J_9(I_a(t),t)}{(2-\delta)M(\delta)} - I_a(0) - \frac{2\delta}{(2-\delta)M(\delta)}\int_0^t J_9(I_a(s),s)ds \right\|$$
$$\leq \|\Upsilon_{9,n}(t)\|\left\{1 + \left(\frac{2(1-\delta)\xi_{17}}{(2-\delta)M(\delta)} + \frac{2\delta\xi_{18}t}{(2-\delta)M(\delta)}\right)\right\}.$$

Following the implementation of *limit* as t procedures ∞ indicates that

$$\begin{aligned}
S_m(t) &= \frac{2(1-\delta)J_1(S_m(t),t)}{M(\delta)(2-\delta)} + \frac{2\delta}{M(\delta)(2-\delta)}\int_0^t J_1(S_m(s),s)ds + S_m(0),\\
E_m(t) &= \frac{2(1-\delta)J_2(E_m(t),t)}{M(\delta)(2-\delta)} + \frac{2\delta}{M(\delta)(2-\delta)}\int_0^t J_2(E_m(s),s)ds + E_m(0),\\
A_m(t) &= \frac{2(1-\delta)J_3(A_m(t),t)}{M(\delta)(2-\delta)} + \frac{2\delta}{M(\delta)(2-\delta)}\int_0^t J_3(A_m(s),s)ds + A_m(0),\\
I_m(t) &= \frac{2(1-\delta)J_4(I_m(t),t)}{M(\delta)(2-\delta)} + \frac{2\delta}{M(\delta)(2-\delta)}\int_0^t J_4(I_m(s),s)ds + I_m(0),\\
V_m(t) &= \frac{2(1-\delta)J_5(V_m(t),t)}{M(\delta)(2-\delta)} + \frac{2\delta}{M(\delta)(2-\delta)}\int_0^t J_5(V_m(s),s)ds + V_m(0),\\
R_m(t) &= \frac{2(1-\delta)J_6(R_m(t),t)}{M(\delta)(2-\delta)} + \frac{2\delta}{M(\delta)(2-\delta)}\int_0^t J_6(R_m(s),s)ds + R_m(0),\\
S_a(t) &= \frac{2(1-\delta)J_7(S_a(t),t)}{M(\delta)(2-\delta)} + \frac{2\delta}{M(\delta)(2-\delta)}\int_0^t J_7(S_a(s),s)ds + S_a(0),\\
E_a(t) &= \frac{2(1-\delta)J_8(E_a(t),t)}{M(\delta)(2-\delta)} + \frac{2\delta}{M(\delta)(2-\delta)}\int_0^t J_8(E_a(s),s)ds + E_a(0),\\
I_a(t) &= \frac{2(1-\delta)J_9(I_a(t),t)}{M(\delta)(2-\delta)} + \frac{2\delta}{M(\delta)(2-\delta)}\int_0^t J_9(I_a(s),s)ds + I_a(0).
\end{aligned}$$

This demonstrates the conclusion, indicating that the aforementioned are solutions of the model as specified by system (6).

Theorem 3 *The fractional order infectious disease model, as indicated by system (6), exhibits a unique solution.*

Proof Based on the principle of contradiction, we posit that $\left(S_m'(t), E_m'(t), A_m'(t), I_m'(t), V_m'(t), R_m'(t), S_a'(t), E_a'(t), I_a'(t)\right)$ it's additionally the solution to the developed fractional infectious disease model (6), consequently

$$\begin{aligned}
S_m(t) - S_m'(t) &= \frac{2(1-\delta)\{J_1(S_m(t),t) - J_1(S_m'(t),t)\}}{(2-\delta)M(\delta)}\\
&\quad + \frac{2\delta}{(2-\delta)M(\delta)}\int_0^t \left\{J_1(S_m(s),s) - J_1(S_m'(s),s)\right\}ds,
\end{aligned}$$

$$
\begin{aligned}
E_m(t)-E_m^{'}(t) &= \frac{2(1-\delta)\{J_2(E_m(t),t)-J_2(E_m^{'}(t),t)\}}{(2-\delta)M(\delta)} \\
&+\frac{2\delta}{(2-\delta)M(\delta)}\int_0^t\Big\{J_2(E_m(s),s)-J_2(E_m^{'}(s),s)\Big\}ds, \\
A_m(t)-A_m^{'}(t) &= \frac{2(1-\delta)\{J_3(A_m(t),t)-J_3(A_m^{'}(t),t)\}}{(2-\delta)M(\delta)} \\
&+\frac{2\delta}{(2-\delta)M(\delta)}\int_0^t\Big\{J_3(A_m(s),s)-J_3(A_m^{'}(s),s)\Big\}ds, \\
I_m(t)-I_m^{'}(t) &= \frac{2(1-\delta)\{J_4(I_m(t),t)-J_4(I_m^{'}(t),t)\}}{(2-\delta)M(\delta)} \\
&+\frac{2\delta}{(2-\delta)M(\delta)}\int_0^t\Big\{J_4(I_m(s),s)-J_4(I_m^{'}(s),s)\Big\}ds, \\
V_m(t)-V_m^{'}(t) &= \frac{2(1-\delta)\{J_5(V_m(t),t)-J_5(V_m^{'}(t),t)\}}{(2-\delta)M(\delta)} \\
&+\frac{2\delta}{(2-\delta)M(\delta)}\int_0^t\Big\{J_5(V_m(s),s)-J_5(V_m^{'}(s),s)\Big\}ds, \\
R_m(t)-R_m^{'}(t) &= \frac{2(1-\delta)\{J_6(R_m(t),t)-J_6(R_m^{'}(t),t)\}}{(2-\delta)M(\delta)} \\
&+\frac{2\delta}{(2-\delta)M(\delta)}\int_0^t\Big\{J_6(R_m(s),s)-J_6(R_m^{'}(s),s)\Big\}ds, \\
S_a(t)-S_a^{'}(t) &= \frac{2(1-\delta)\{J_7(S_a(t),t)-J_7(S_a^{'}(t),t)\}}{(2-\delta)M(\delta)} \\
&+\frac{2\delta}{(2-\delta)M(\delta)}\int_0^t\Big\{J_7(S_a(s),s)-J_7(S_a^{'}(s),s)\Big\}ds, \\
E_a(t)-E_a^{'}(t) &= \frac{2(1-\delta)\{J_8(E_a(t),t)-J_8(E_a^{'}(t),t)\}}{(2-\delta)M(\delta)} \\
&+\frac{2\delta}{(2-\delta)M(\delta)}\int_0^t\Big\{J_8(E_a(s),s)-J_8(E_a^{'}(s),s)\Big\}ds, \\
I_a(t)-I_a^{'}(t) &= \frac{2(1-\delta)\{J_9(I_a(t),t)-J_9(I_a^{'}(t),t)\}}{(2-\delta)M(\delta)} \\
&+\frac{2\delta}{(2-\delta)M(\delta)}\int_0^t\Big\{J_9(I_a(s),s)-J_9(I_a^{'}(s),s)\Big\}ds.
\end{aligned}
$$

Based on the property of majorizing, we can express the aforementioned system as

$$
\begin{aligned}
\|S_m(t)-S_m^{'}(t)\| &\leq \frac{2(1-\delta)\|J_1(S_m(t),t)-J_1(S_m^{'}(t),t)\|}{(2-\delta)M(\delta)} \\
&+\frac{2\delta}{(2-\delta)M(\delta)}\int_0^t\Big\|J_1(S_m(s),s)-J_1(S_m^{'}(s),s)\Big\|ds, \\
\|E_m(t)-E_m^{'}(t)\| &\leq \frac{2(1-\delta)\|J_2(E_m(t),t)-J_2(E_m^{'}(t),t)\|}{(2-\delta)M(\delta)} \\
&+\frac{2\delta}{(2-\delta)M(\delta)}\int_0^t\Big\|J_2(E_m(s),s)-J_2(E_m^{'}(s),s)\Big\|ds,
\end{aligned}
$$

$$
\begin{aligned}
\|A_m(t)-A_m^{'}(t)\| &\leq \frac{2(1-\delta)\|J_3(A_m(t),t)-J_3(A_m^{'}(t),t)\|}{(2-\delta)M(\delta)} \\
&\quad +\frac{2\delta}{(2-\delta)M(\delta)}\int_0^t \left\|J_3(A_m(s),s)-J_3(A_m^{'}(s),s)\right\|ds, \\
\|I_m(t)-I_m^{'}(t)\| &\leq \frac{2(1-\delta)\|J_4(I_m(t),t)-J_4(I_m^{'}(t),t)\|}{(2-\delta)M(\delta)} \\
&\quad +\frac{2\delta}{(2-\delta)M(\delta)}\int_0^t \left\|J_4(I_m(s),s)-J_4(I_m^{'}(s),s)\right\|ds, \\
\|V_m(t)-V_m^{'}(t)\| &\leq \frac{2(1-\delta)\|J_5(V_m(t),t)-J_5(V_m^{'}(t),t)\|}{(2-\delta)M(\delta)} \\
&\quad +\frac{2\delta}{(2-\delta)M(\delta)}\int_0^t \left\|J_5(V_m(s),s)-J_5(V_m^{'}(s),s)\right\|ds, \\
\|R_m(t)-R_m^{'}(t)\| &\leq \frac{2(1-\delta)\|J_6(R_m(t),t)-J_6(R_m^{'}(t),t)\|}{(2-\delta)M(\delta)} \\
&\quad +\frac{2\delta}{(2-\delta)M(\delta)}\int_0^t \left\|J_6(R_m(s),s)-J_6(R_m^{'}(s),s)\right\|ds, \\
\|S_a(t)-S_a^{'}(t)\| &\leq \frac{2(1-\delta)\|J_7(S_a(t),t)-J_7(S_a^{'}(t),t)\|}{(2-\delta)M(\delta)} \\
&\quad +\frac{2\delta}{(2-\delta)M(\delta)}\int_0^t \left\|J_7(S_a(s),s)-J_7(S_a^{'}(s),s)\right\|ds, \\
\|E_a(t)-E_a^{'}(t)\| &\leq \frac{2(1-\delta)\|J_8(E_a(t),t)-J_8(E_a^{'}(t),t)\|}{(2-\delta)M(\delta)} \\
&\quad +\frac{2\delta}{(2-\delta)M(\delta)}\int_0^t \left\|J_8(E_a(s),s)-J_8(E_a^{'}(s),s)\right\|ds, \\
\|I_a(t)-I_a^{'}(t)\| &\leq \frac{2(1-\delta)\|J_9(I_a(t),t)-J_9(I_a^{'}(t),t)\|}{(2-\delta)M(\delta)} \\
&\quad +\frac{2\delta}{(2-\delta)M(\delta)}\int_0^t \left\|J_9(I_a(s),s)-J_9(I_a^{'}(s),s)\right\|ds.
\end{aligned}
$$

By applying the findings established in (1) and (2), we achieve

$$
\begin{aligned}
\|S_m(t)-S_m^{'}\| &\leq \frac{2\xi_1\zeta_1(1-\delta)}{(2-\delta)M(\delta)}+\left(\frac{2\xi_2\delta\zeta_2 t}{M(\delta)(2-\delta)}\right)^n, \\
\|E_m(t)-E_m^{'}\| &\leq \frac{2\xi_3\zeta_3(1-\delta)}{(2-\delta)M(\delta)}+\left(\frac{2\xi_4\delta\zeta_4 t}{M(\delta)(2-\delta)}\right)^n, \\
\|A_m(t)-A_m^{'}\| &\leq \frac{2\xi_5\zeta_5(1-\delta)}{(2-\delta)M(\delta)}+\left(\frac{2\xi_6\delta\zeta_6 t}{M(\delta)(2-\delta)}\right)^n, \\
\|I_m(t)-I_m^{'}\| &\leq \frac{2\xi_7\zeta_7(1-\delta)}{(2-\delta)M(\delta)}+\left(\frac{2\xi_8\delta\zeta_8 t}{M(\delta)(2-\delta)}\right)^n, \\
\|V_m(t)-V_m^{'}\| &\leq \frac{2\xi_9\zeta_9(1-\delta)}{(2-\delta)M(\delta)}+\left(\frac{2\xi_{10}\delta\zeta_{10} t}{M(\delta)(2-\delta)}\right)^n,
\end{aligned} \tag{14}
$$

$$
\begin{aligned}
\|R_m(t) - R_m^{'}\| &\leq \frac{2\xi_{11}\zeta_{11}(1-\delta)}{(2-\delta)M(\delta)} + \left(\frac{2\xi_{12}\delta\zeta_{12}t}{M(\delta)(2-\delta)}\right)^n, \\
\|S_a(t) - S_a^{'}\| &\leq \frac{2\xi_{13}\zeta_{13}(1-\delta)}{(2-\delta)M(\delta)} + \left(\frac{2\xi_{14}\delta\zeta_{14}t}{M(\delta)(2-\delta)}\right)^n, \\
\|E_a(t) - E_a^{'}\| &\leq \frac{2\xi_{15}\zeta_{15}(1-\delta)}{(2-\delta)M(\delta)} + \left(\frac{2\xi_{16}\delta\zeta_{17}t}{M(\delta)(2-\delta)}\right)^n, \\
\|I_a(t) - I_a^{'}\| &\leq \frac{2\xi_{17}\zeta_{17}(1-\delta)}{(2-\delta)M(\delta)} + \left(\frac{2\xi_{18}\delta\zeta_{18}t}{M(\delta)(2-\delta)}\right)^n.
\end{aligned}
$$

The inequalities presented in Eq. (14) are valid for all values of n, leading us to the conclusion

$$
\begin{aligned}
&S_m(t) = S_m^{'}(t),\ \ E_m(t) = E_m^{'}(t),\ \ A_m(t) = A_m^{'}(t),\ \ I_m(t) = I_m^{'}(t),\ \ V_m(t) = V_m^{'}(t), \\
&R_m(t) = R_m^{'}(t),\ \ S_a(t) = S_a^{'}(t),\ \ E_a(t) = E_a^{'}(t),\ \ I_a(t) = I_a^{'}(t).
\end{aligned} \tag{15}
$$

The Lipschitz condition is pivotal in ensuring the uniqueness of the solution by guaranteeing that small variations in the initial conditions or parameters lead to proportionally small changes in the solution. Intuitively, this condition prevents the system from exhibiting erratic or unpredictable behavior, which is critical when modeling real-world disease dynamics. In this work, the context of Mpox transmission, the Lipschitz condition ensures that the predicted number of infections remains stable and consistent under slight perturbations in the transmission or recovery rates. This stability is vital for reliable disease modeling and control strategies. By enforcing a bounded rate of change, the Lipschitz condition acts as a safeguard against anomalies, ensuring the mathematical and practical robustness of the model.

4 Equilibra and fundamental reproduction number

The Mpox-free equilibrium corresponds to the case when no infections exist within the population. The derivations of the equilibrium points Ψ^0 and Ψ^*, it is important to note their practical implications in understanding disease dynamics. The disease-free equilibrium Ψ^0 represents a scenario where the disease is eradicated from the population, with all infected compartments at zero. This presents the critical role of intervention strategies, such as vaccination and public health measures, in achieving and maintaining a disease-free state. In contrast, the endemic equilibrium Ψ^* corresponds to a persistent state of the disease within the population. The proportions of infected individuals at Ψ^* depend on parameters such as contact rates, recovery rates, and vaccination efficacy. This underscores the significance of controlling the reproduction number R_0 and modifying key parameters to shift the system toward the disease-free equilibrium. These insights provide actionable guidance for policymakers and public health officials in formulating strategies to manage and potentially eliminate Mpox outbreaks.
Hence, the Mpox free equilibrium point

$$
\begin{aligned}
\Psi^0 &= (S_m^0, E_m^0, A_m^0, I_m^0, V_m^0, R_m^0, S_a^0, E_a^0, I_a^0) \\
&= \left(\frac{c_5\Pi_m}{(c_1c_5 - \alpha_m\tau) + c_5\lambda_m}, 0, 0, 0, \frac{\alpha_m\Pi_m}{(c_1c_5 - \alpha_m\tau) + c_5\lambda_m}, 0, \frac{\Pi_a}{\mu_2}, 0, 0\right).
\end{aligned}
$$

The endemic equilibrium of Mpox is $\Psi^* = (S_m^*, E_m^*, A_m^*, I_m^*, V_m^*, R_m^*, S_a^*, E_a^*, I_a^*)$. Then, from system (6) the endemic equilibrium points are

$$S_m^* = \frac{c_5\Pi_m}{(c_1c_5 - \alpha_m\tau) + c_5\lambda_m}, \quad E_m^* = \frac{\lambda_m^* S_m^*}{c_2}, \quad A_m^* = \frac{k(1-\rho)E_m^*}{c_4}, \quad I_m^* = \frac{k\rho E_h^*}{c_3},$$
$$V_m^* = \frac{\alpha_m\Pi_m}{(c_1c_5 - \alpha_m\tau) + c_5\lambda_m}, \quad R_h^* = \frac{k(1-\rho)c_5\gamma_1\lambda_m\Pi_m}{c_2c_4\big((c_1c_5 - \alpha_m\tau) + c_5\lambda_m\big)} + \frac{k\rho c_5\gamma_2\lambda_m\Pi_m}{c_2c_3\Big((c_1c_5 - \alpha_m\tau) + c_5\lambda_m\Big)},$$
$$S_a^* = \frac{\Pi_a(\pi + c_7)}{(c_6c_7(\frac{\beta_4\pi}{C_6c_7} - 1) + \mu_2(\pi + c_7))}, \quad E_a^* = \frac{\Pi_a c_7(\frac{\beta_4\pi}{C_6c_7} - 1)}{(c_6c_7(\frac{\beta_4\pi}{C_6c_7} - 1) + \mu_2(\pi + c_7))},$$
$$I_a^* = \frac{\pi\Pi_a(\frac{\beta_4\pi}{C_6c_7} - 1)}{(c_6c_7(\frac{\beta_4\pi}{C_6c_7} - 1) + \mu_2(\pi + c_7))},$$

where

$$c_1 = (\mu_1 + \alpha_m), \ c_2 = (\mu_1 + k), \ c_3 = (\gamma_2 + \mu_1 + \eta_1), \ c_4 = (\gamma_1 + \mu_1 + \eta_2),$$
$$c_5 = (\tau + \mu_1), \ c_6 = (\pi + \mu_2), \ c_7 = (\mu_2 + \eta_3), \ \lambda_m = \Big(\frac{\beta_1 I_m^* + \beta_2 I_a^* + \beta_3 A_m^m}{N_m}\Big).$$

The fundamental reproduction number of the human and rodent population Mpox model (6) is computed via the next-generation matrix. Using this technique [21], we have

$$F = \begin{bmatrix} 0 & \frac{S_m^0\beta_1}{N_m^0} & \frac{S_m^0\beta_3}{N_m^0} & 0 & 0 & \frac{S_m^0\beta_2}{N_m^0} \\ 0 & 0 & 0 & 0 & 0 & 0 \\ 0 & 0 & 0 & 0 & 0 & 0 \\ 0 & 0 & 0 & 0 & 0 & 0 \\ 0 & 0 & 0 & 0 & 0 & \beta_4 \\ 0 & 0 & 0 & 0 & 0 & 0 \end{bmatrix}, \quad V = \begin{bmatrix} c_2 & 0 & 0 & 0 & 0 & 0 \\ -k\rho & c_3 & 0 & 0 & 0 & 0 \\ -k(1-\rho) & 0 & c_4 & 0 & 0 & 0 \\ 0 & 0 & 0 & c_5 & 0 & 0 \\ 0 & 0 & 0 & 0 & c_6 & 0 \\ 0 & 0 & 0 & 0 & -\pi & c_7 \end{bmatrix}.$$

The reproduction number is the dominant eigenvalue of FV^{-1}. Thus,

$$R_0 = \max\{R_{m_0}, R_{a_0}\} = \max\left\{\frac{kc_5(\beta_1\rho c_4 + \beta_3(1-\rho)c_3)}{c_2c_3c_4(\alpha_m + c_5)}, \frac{\beta_4\pi}{c_6c_7}\right\}. \tag{16}$$

The fundamental reproduction number R_0 is a pivotal metric in understanding the spread of infectious diseases. The Mpox model's R_0 depends on several parameters, such as contact rates, transmission probabilities, recovery rates, and others as outlined in Eq. (16). Additionally, these Figure 2 and Figure 3 illustrate the effect of different parameter combinations of the examining the influencing the fundamental reproduction numbers of humans R_{m_0} and rodent R_{a_0}. The interplay of these factors determines whether the disease will spread $(R_0 > 1)$ or decline $(R_0 < 1)$. To ensure effective control, policies should target reducing R_0 to below 1. Vaccinating a substantial fraction of the population is estimated to be at least 75% of the total susceptible individuals based on model outputs. Implementing social distancing and minimizing inter-species transmission pathways to reduce contact rates. Also, enhancing recovery rates through early diagnosis and treatment programs. This analysis underlines the importance of targeted interventions on specific

parameters to control the spread of Mpox.

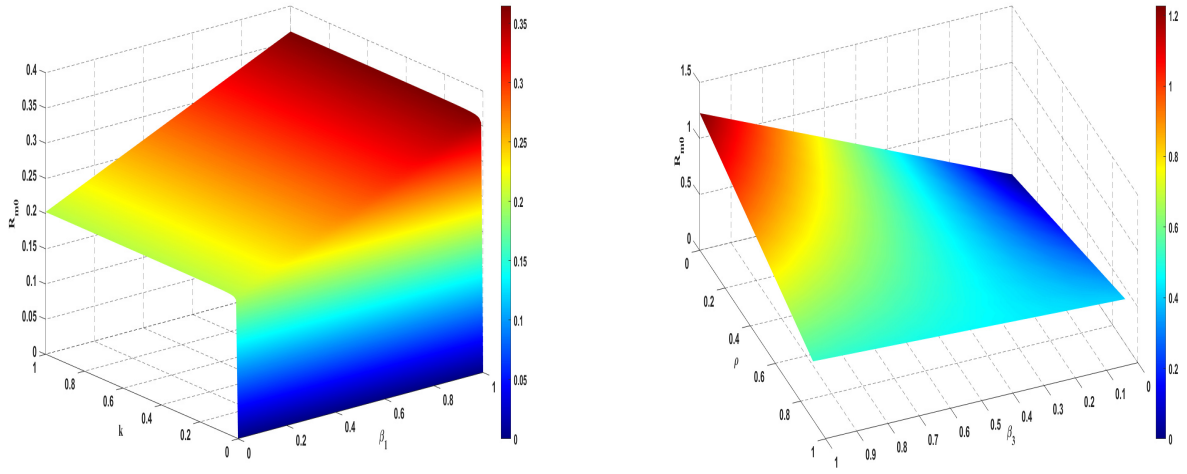

(a) Dynamical behaviour of R_{m_0} for β_1 and k values **(b)** Dynamical behaviour of R_{m_0} for β_3 and ρ values

Figure 2. Dynamical behaviour of R_{m_0} for different variables

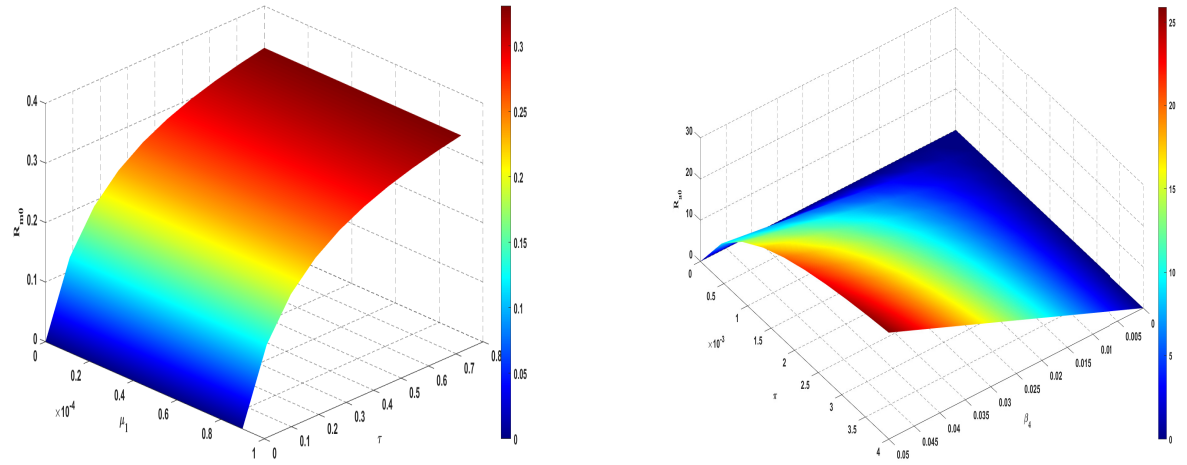

(a) Dynamical behaviour of R_{m_0} for μ_1 and τ values **(b)** Dynamical behaviour of R_{a_0} for β_4 and π values

Figure 3. Dynamical behaviour of R_{m_0} and R_{a_0} for different variables

5 Numerical simulations

Numerical method

This section of the study presents an estimated approach to addressing the fractional order Mpox model (6) utilizing the two-step fractional Adams-Bashforth approach for the CF fractional derivative [22]. The structure is implemented using the fractional Volterra model, which is based on the basic theorem of integration. This method offers a balance between computational efficiency and accuracy, making it well-suited for iterative simulations involving fractional derivatives. The choice of the Adams-Bashforth method is rooted in its ability to handle the memory effect inherent

in fractional models, as it builds on previous computational steps to predict future values. This iterative approach aligns well with the characteristics of the Caputo-Fabrizio derivative used in our model, ensuring stability and precision in the simulations. Specifically, the method's compatibility with non-local properties of fractional calculus enhances its capability to simulate long-term interactions and dynamic responses. In order to achieve the required iterative strategy, we first focus just on the first equation of system (6) and follow the steps shown below. Utilizing the basic concept of integration, we derive the subsequent outcome from the initial equation of the system (7).

$$S_m(t) - S_m(0) = \frac{(1-\delta)}{M(\delta)} J_1(t, S_m) + \frac{\delta}{M(\delta)} \int_0^t J_1(x, S_m) dx. \tag{17}$$

For $t = t_{n+1}, n = 0, 1, 2, \ldots,$ we acquire

$$S_m(t_{n+1}) - S_{m_0} = \frac{(1-\delta)}{M(\delta)} J_1(t, S_m) + \frac{\delta}{M(\delta)} \int_0^{t_{n+1}} J_1(x, S_m) dx. \tag{18}$$

The difference between each consecutive term is shown as follows:

$$S_{m_{n+1}} - S_{m_n} = \frac{1-\delta}{M(\delta)} \{J_1(t_n, S_{m_n}) - J_1(t_{n-1}, S_{m_{n-1}})\} + \frac{\delta}{M(\delta)} \int_{t_n}^{t_{n+1}} J_1(t, S_m) dt. \tag{19}$$

Over the close interval $[t_k, t_{(k+1)}]$, the function $J_1(t, S_m)$ is able to estimated using the interpolation polynomial

$$\mathcal{H}_k \cong \frac{f(t_k, y_k)}{h}(t - t_{k-1}) - \frac{f(t_{k-1}, y_{k-1})}{h}(t - t_k),$$

where $h = t_n - t_{n-1}$. The integral in (19) is computed using the polynomial estimation outlined above, resulting in

$$\begin{aligned} \int_{t_n}^{t_{n+1}} J_1(t, S_m) dt &= \int_{t_n}^{t_{n+1}} \left(\frac{J_1(t_n, S_{m_n})}{h} - \frac{J_1(t_{n-1}, S_{m_{n-1}})}{h}(t - t_n) \right) dt \\ &= \frac{3h}{2} J_1(t_n, S_{m_n}) - \frac{n}{2} J_1(t_{n-1}, S_{m_{n-1}}). \end{aligned} \tag{20}$$

Putting (20) in (19) and after simplification we acquire

$$S_{m_{n+1}} = S_{m_n} + \left(\frac{1-\delta}{M(\delta)} + \frac{3h}{2M(\delta)} \right) J_1(t_n, S_{m_n}) - \left(\frac{1-\delta}{M(\delta)} + \frac{\delta h}{2M(\delta)} \right) J_1(t_{n+1}, S_{m_{n-1}}). \tag{21}$$

Similar to this, we were able to derive the recursive formulas for the other equations in system (7) as follows

$$\begin{aligned} E_{m_{n+1}} &= E_{m_n} + \left(\frac{1-\delta}{M(\delta)} + \frac{3h}{2M(\delta)} \right) J_2(t_n, E_{m_n}) - \left(\frac{1-\delta}{M(\delta)} + \frac{\delta h}{2M(\delta)} \right) J_2(t_{n+1}, E_{m_{n-1}}), \\ A_{m_{n+1}} &= A_{m_n} + \left(\frac{1-\delta}{M(\delta)} + \frac{3h}{2M(\delta)} \right) J_3(t_n, A_{m_n}) - \left(\frac{1-\delta}{M(\delta)} + \frac{\delta h}{2M(\delta)} \right) J_3(t_{n+1}, A_{m_{n-1}}), \end{aligned}$$

$$
\begin{aligned}
I_{m_{n+1}} &= I_{m_n} + \left(\frac{1-\delta}{M(\delta)} + \frac{3h}{2M(\delta)}\right) J_4(t_n, I_{m_n}) - \left(\frac{1-\delta}{M(\delta)} + \frac{\delta h}{2M(\delta)}\right) J_4(t_{n+1}, I_{m_{n-1}}),\\
V_{m_{n+1}} &= V_{m_n} + \left(\frac{1-\delta}{M(\delta)} + \frac{3h}{2M(\delta)}\right) J_5(t_n, V_{m_n}) - \left(\frac{1-\delta}{M(\delta)} + \frac{\delta h}{2M(\delta)}\right) J_5(t_{n+1}, V_{m_{n-1}}),\\
R_{m_{n+1}} &= R_{m_n} + \left(\frac{1-\delta}{M(\delta)} + \frac{3h}{2M(\delta)}\right) J_6(t_n, R_{m_n}) - \left(\frac{1-\delta}{M(\delta)} + \frac{\delta h}{2M(\delta)}\right) J_6(t_{n+1}, R_{m_{n-1}}),\\
S_{a_{n+1}} &= S_{a_n} + \left(\frac{1-\delta}{M(\delta)} + \frac{3h}{2M(\delta)}\right) J_7(t_n, S_{a_n}) - \left(\frac{1-\delta}{M(\delta)} + \frac{\delta h}{2M(\delta)}\right) J_7(t_{n+1}, S_{a_{n-1}}),\\
E_{a_{n+1}} &= E_{a_n} + \left(\frac{1-\delta}{M(\delta)} + \frac{3h}{2M(\delta)}\right) J_8(t_n, E_{a_n}) - \left(\frac{1-\delta}{M(\delta)} + \frac{\delta h}{2M(\delta)}\right) J_8(t_{n+1}, E_{a_{n-1}}),\\
I_{a_{n+1}} &= I_{a_n} + \left(\frac{1-\delta}{M(\delta)} + \frac{3h}{2M(\delta)}\right) J_9(t_n, I_{a_n}) - \left(\frac{1-\delta}{M(\delta)} + \frac{\delta h}{2M(\delta)}\right) J_9(t_{n+1}, I_{a_{n-1}}).
\end{aligned} \tag{22}
$$

Furthermore, we present the numerical simulations conducted to examine the interactions of the proposed model, as indicated in system (6), for different values of δ, random sequence of CF derivative throughout the range of $[0, 1]$, as well as for other model relevant factors.

6 Discussion

The objective of the numerical simulation is to examine the effects of changes in order and parameters are shown in the Table 1 on the dynamic behavior of the system. To create Figure 4-Figure 14, we use the utilizing two-step fractional Adams-Bashforth technique [22] of the CF derivative.

Table 1. The values of the model parameters

Parameter	Explanation	Values	Source
Π_m	Recruitment into susceptible humans	64850	[1]
Π_a	Recruitment into susceptible rodent	0.2	[8]
β_1	Rate of S_m and contagious rodent	0.3632	$0 < \beta_1 \leq 1$
β_2	Rate of S_m and contagious humans	0.4192	$0 < \beta_2 \leq 1$
β_3	Rate of A_m from susceptible humans	0.1900	[23]
β_4	Rate of S_a and contagious rodent	0.1802	[23]
α_m	Vaccination rate from the susceptible humans	0.2104	Fitted
τ	Waning rate of induced immunity	0.3525	[23]
k	Rate of transition of E_m to infected human	0.3966	$0 < k \leq 1$
ρ	Exposure-related infection rate	0.132	$0 < \rho \leq 1$
γ_1	Recovery rate from A_m	0.5093	Assumed
γ_2	Recovery rate from infected humans	0.5093	Fitted
π	Infected rodent to exposed rodents rate	0.5410	$0 < \pi \leq 1$
μ_1	Natural morality rate of humans	0.000303	[1]
μ_2	Natural morality rate of rodetns	0.0012	Assumed
η_1	Death rate of A_m due to Mpox	4.1187×10^{-4}	Fitted
η_2	Death rate of I_m due to Mpox	0.0012	[23]
η_3	Death rate of I_a due to Mpox	2.8532×10^{-4}	Fitted

Figure 4 shows the density of susceptible human populations over time (t) at various values of the fractional order δ. The values of δ likely represent different scenarios in the model, affecting how the susceptible population changes over time. Figure 5 represents the population density of individuals who have been exposed to the illness but have not yet become contagious. The numerous graphs represent different values of δ, illustrating the temporal fluctuations in exposure levels.

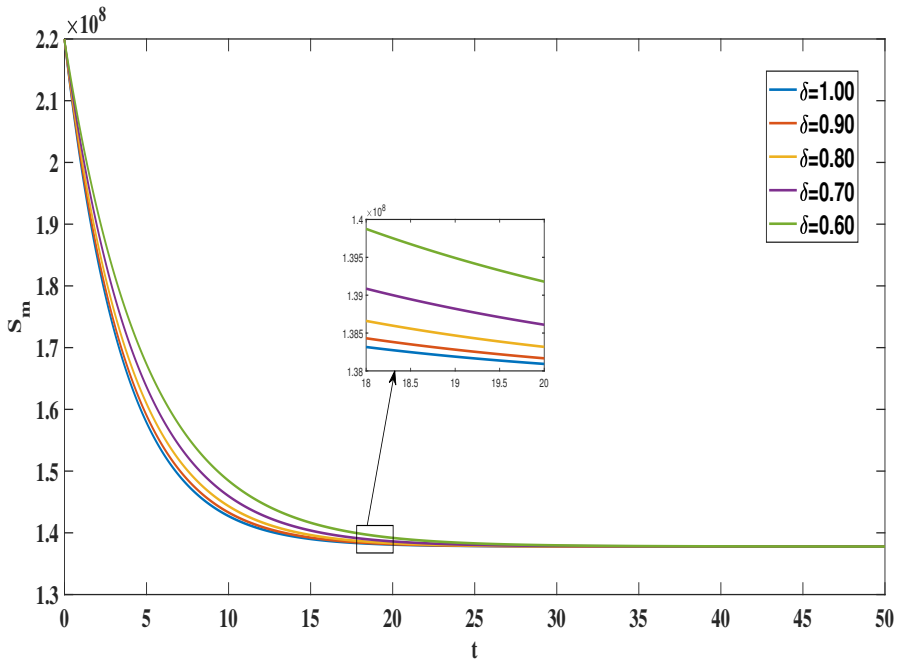

Figure 4. Population density of suspected human populations at different values δ

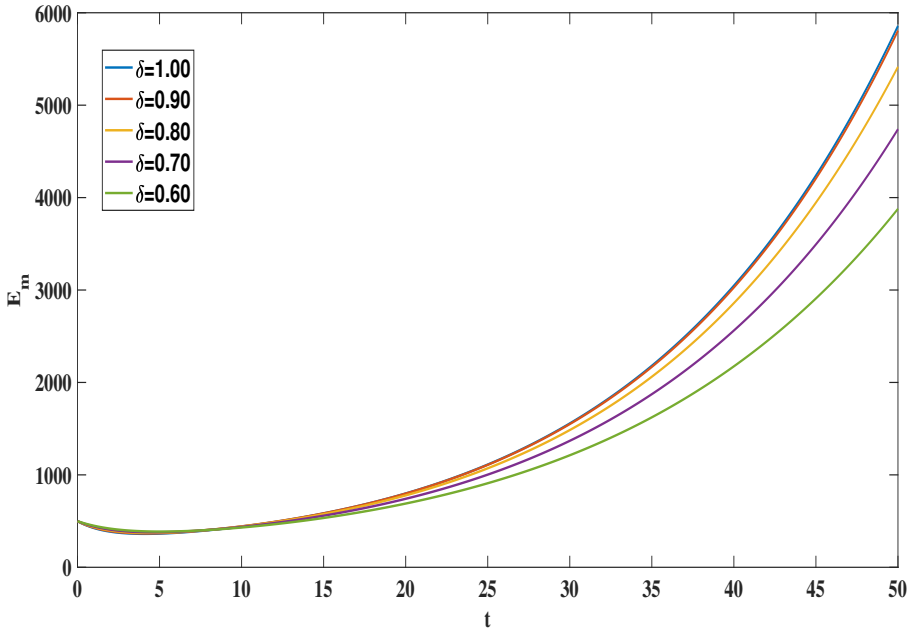

Figure 5. Population density of exposed humans populations at different values δ

Figure 6 focuses on the asymptomatic but infected human population. The different δ values show how this segment of the population varies over time t, indicating the impact of different model parameters on asymptomatic infection rates. Figure 7 shows the density of humans who are actively infected. The variation in δ values allows for the comparison of infection trends under different fractional orders as represented by δ.

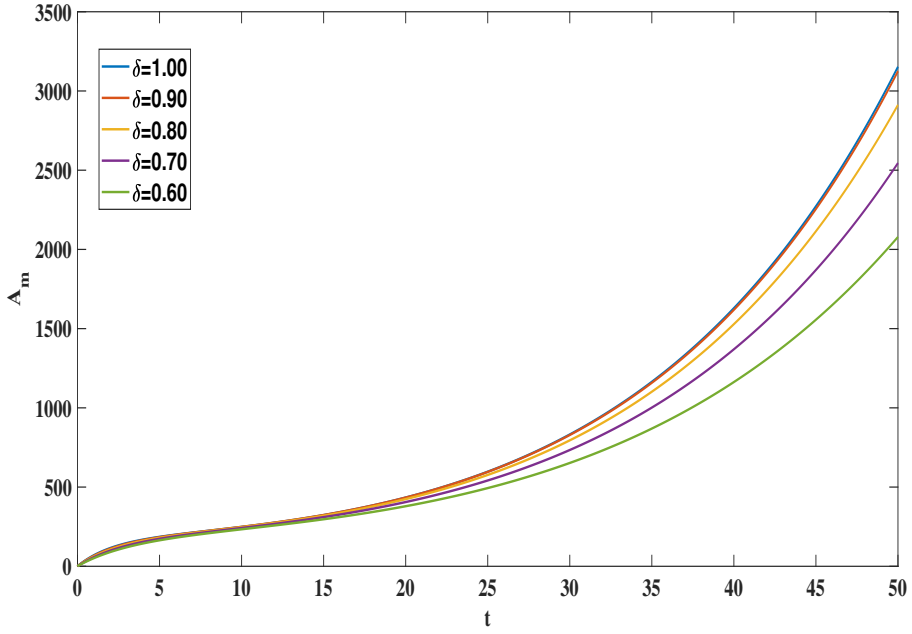

Figure 6. Population density of asymptotically-ill human populations at different values δ

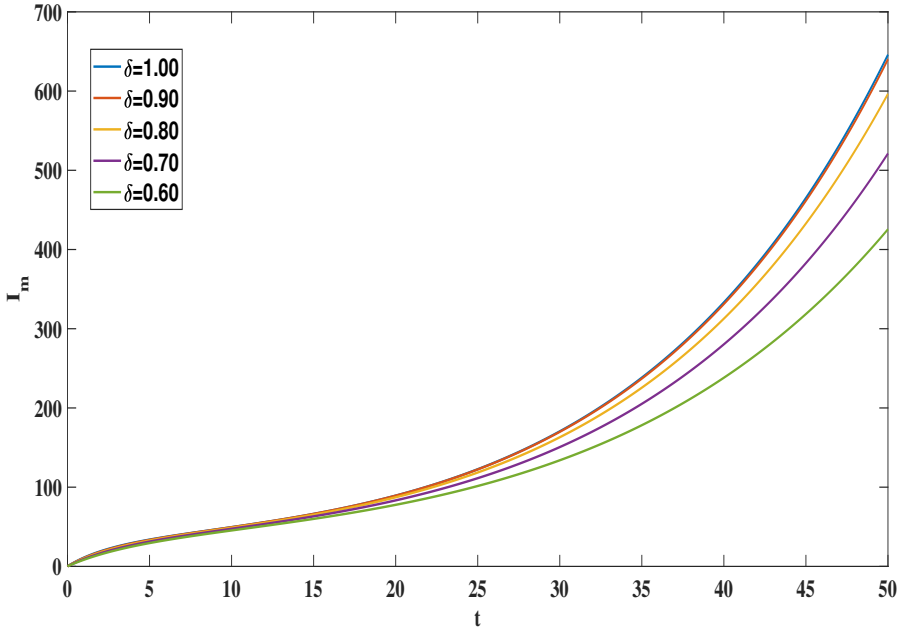

Figure 7. Population density of infected human populations at different values δ

The Figure 8 illustrates the population density of humans who have been vaccinated. The various δ values likely represent different vaccination rates or efficacies, showing how vaccination impacts the population over time t. Figure 9 presents the density of humans who have recovered from the infection. The different δ values depict how recovery rates and the number of recovered individuals evolve under different scenarios.

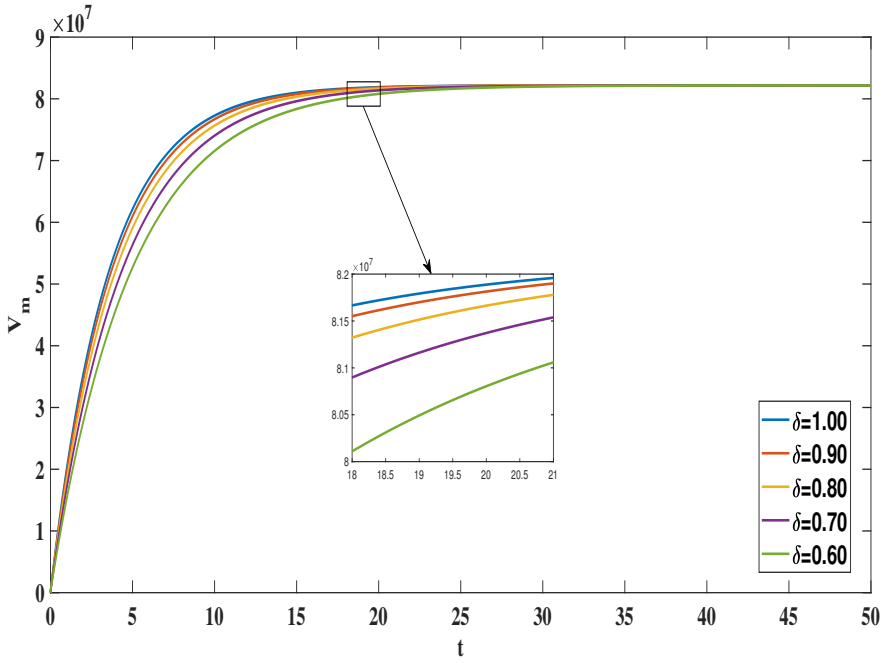

Figure 8. Population density of vaccinated human populations at different values δ

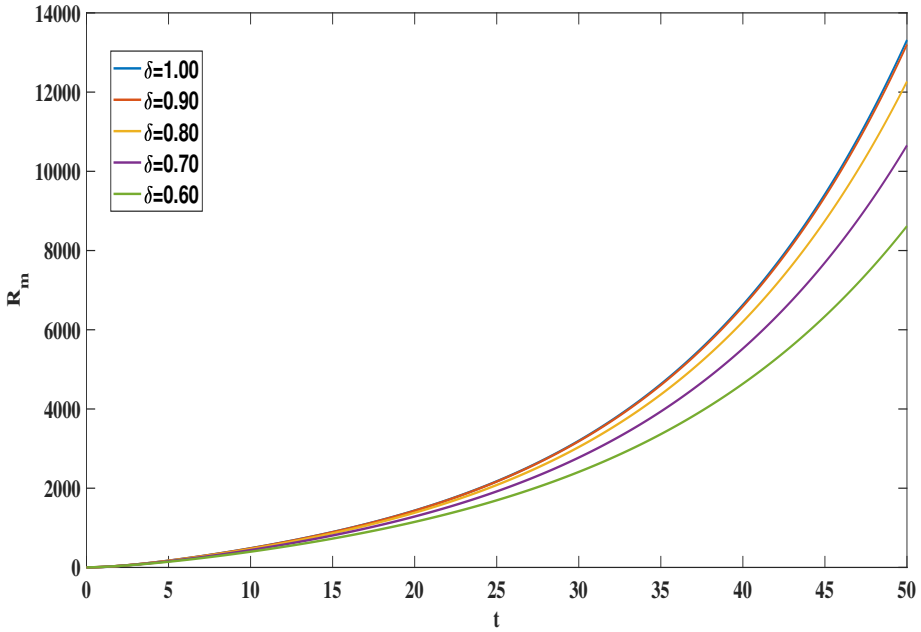

Figure 9. Population density of recovered human populations at different values δ

Figure 10 shows the population density of rodents suspected to be susceptible to the disease. The fractional order δ indicates different scenarios or intervention strategies affecting this population over time. Figure 11 illustrates the population density of exposed rodent populations. The different δ values demonstrate how exposure among rodents changes over time under various conditions. Figure 12 depicts the density of actively infected rodent populations. The variations in δ values show how infection spreads within the rodent population.

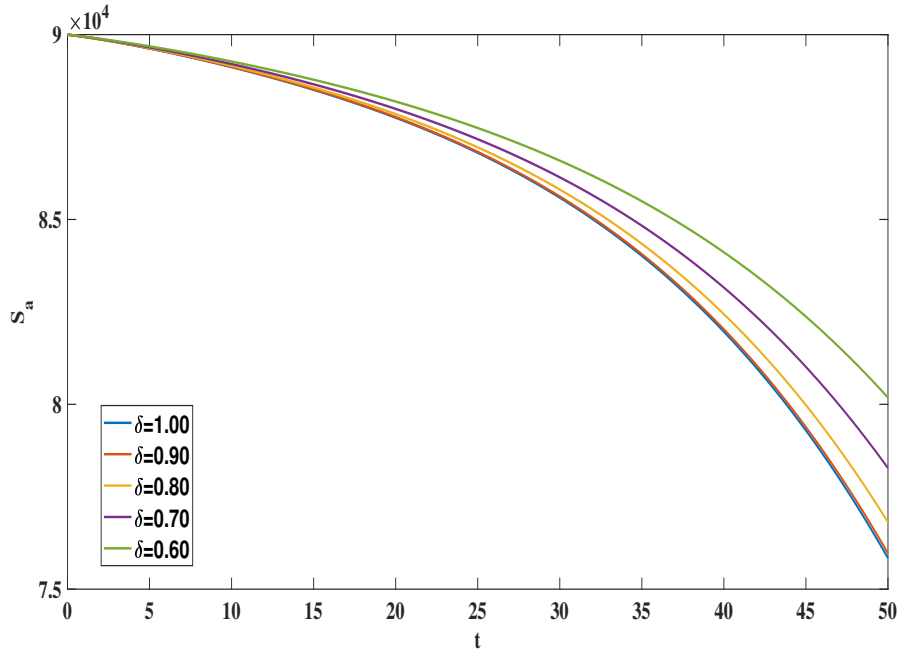

Figure 10. Population density of suspected rodent populations at different values δ

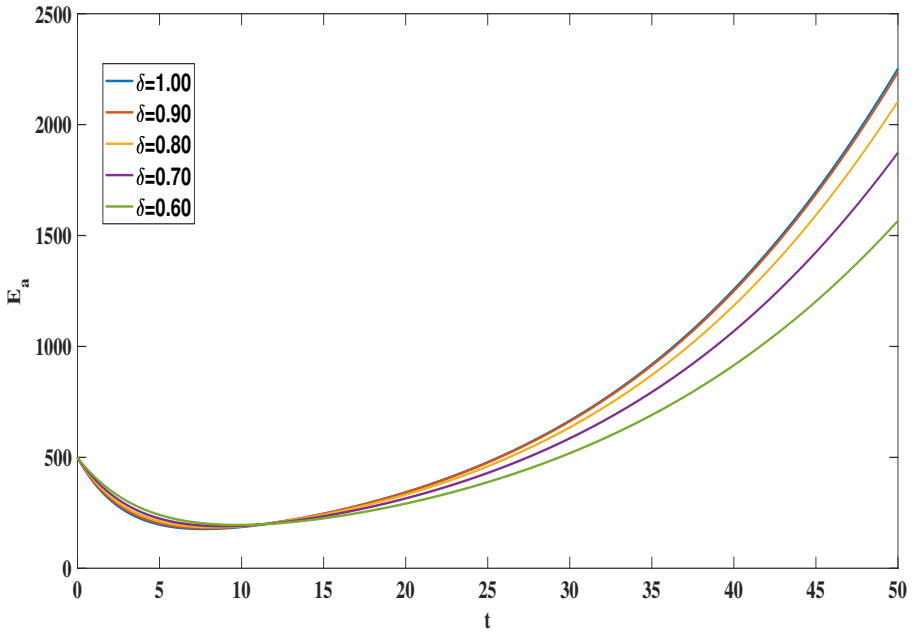

Figure 11. Population density of exposed rodent populations at different values δ

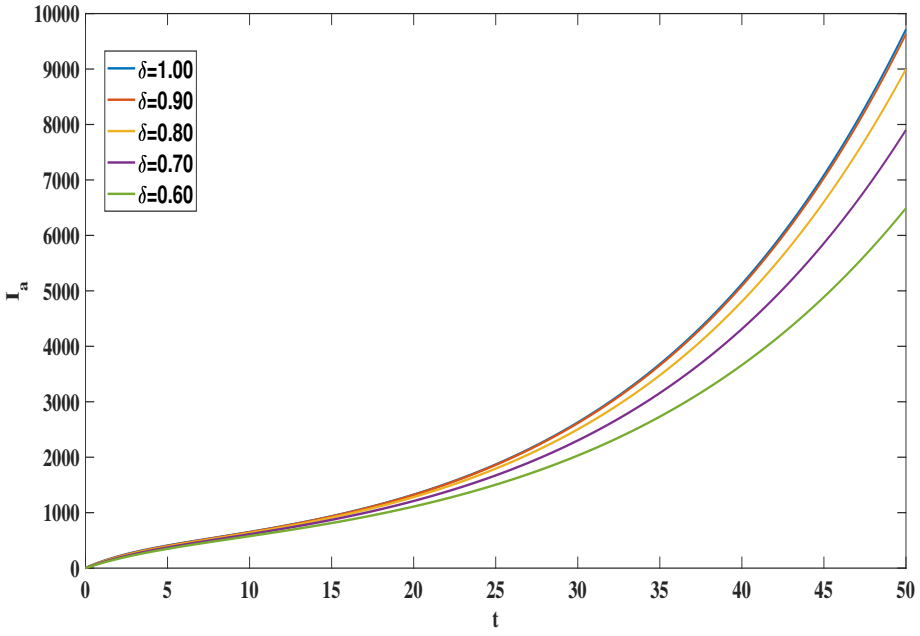

Figure 12. Population density of infected rodent populations at different values δ

From Figure 13 to Figure 16 appear to show the results of numerical simulations that explore the dynamics of a proposed model asymptomatically-ill A_m humans and infected I_m humans for Mpox transmission. Specifically, this figure likely illustrates how varying a key parameter, denoted respectively $\beta_1, \beta_3, \beta_4$ affects certain population densities or infection rates over time t.

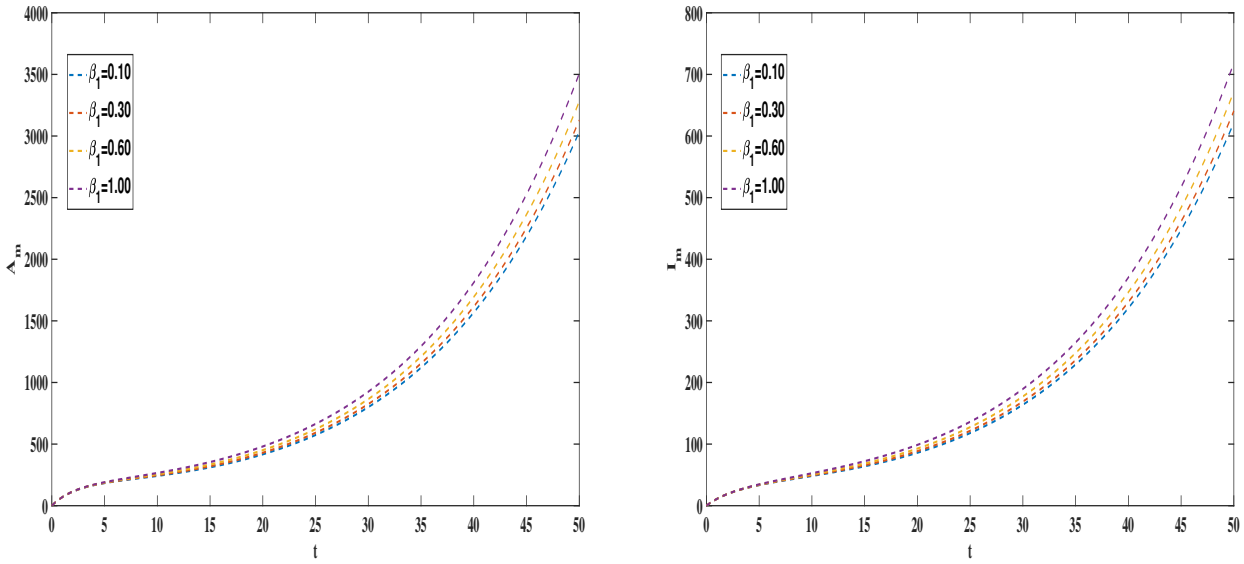

(a) Dynamical behavior of A_m at different values of β_1

(b) Dynamical behaviour of I_m at different values of β_1

Figure 13. Graphical representations of A_m and I_m for β_1

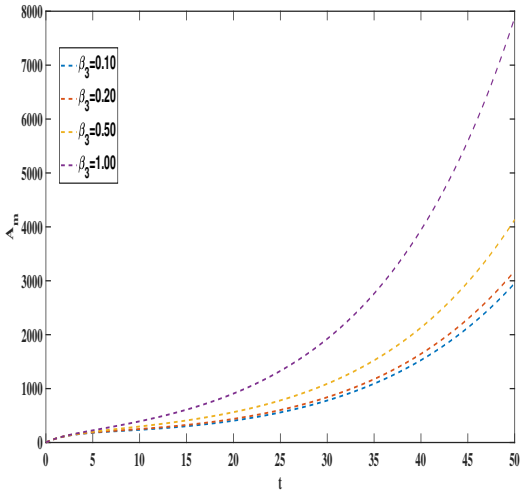

(a) Dynamical behavior of A_m at different values of β_3

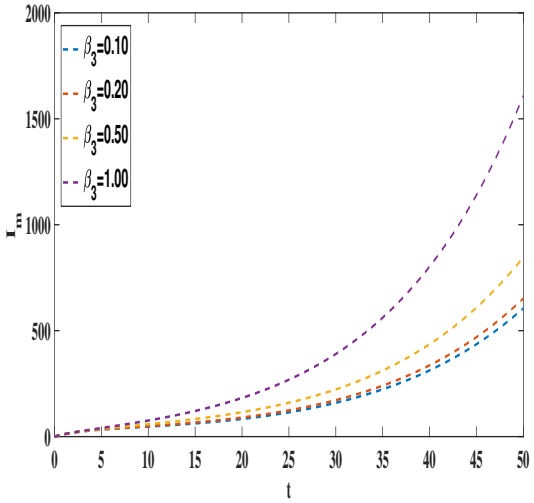

(b) Dynamical behaviour of I_m at different values of β_3

Figure 14. Graphical representations of A_m and I_m for β_3

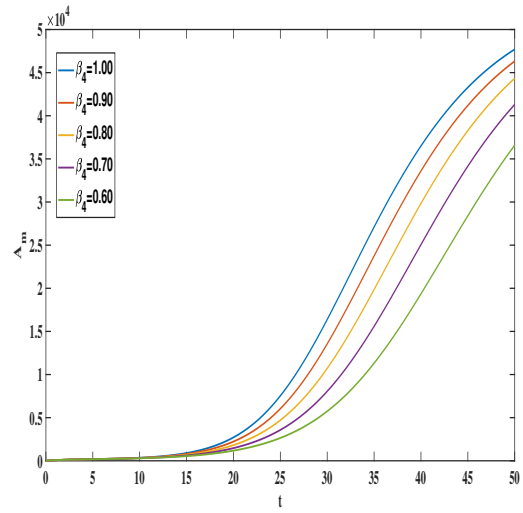

(a) Dynamical behavior of A_m at different values of β_4

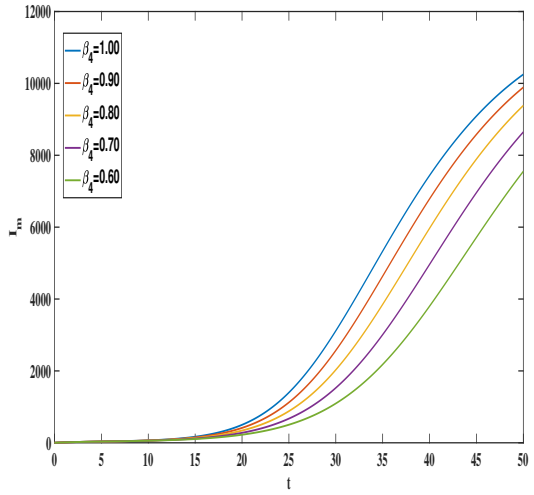

(b) Dynamical behaviour of I_m at different values of β_4

Figure 15. Graphical representations of A_m and I_m for β_4

Figure 16 presents the outcomes of numerical simulations that investigate the dynamics of a proposed model involving asymptomatically-ill A_m and infected I_m in the context of Mpox transmission. This figure likely demonstrates the impact of altering a key parameter, represented by π, on specific population densities or infection rates as time t progresses.

The model employs the CF fractional derivative, which is a mathematical tool used to describe processes with memory or hereditary properties. Simulations using numerical methods are conducted to analyze the dynamics of the model as outlined in system (6). The iterative technique of the CF derivative is used to generate the data for these figures.

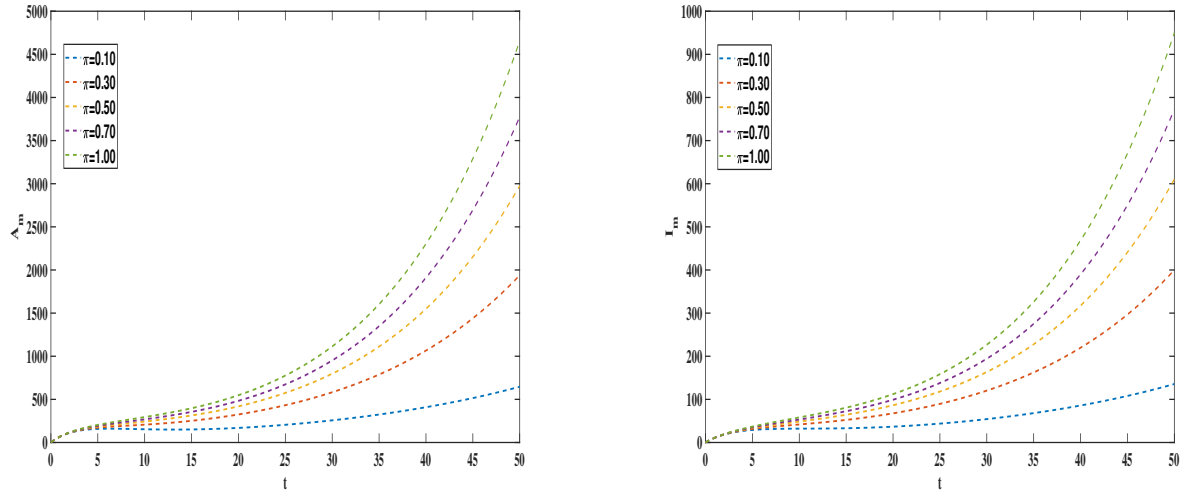

(a) Dynamical behavior of A_m at different values of π **(b)** Dynamical behaviour of I_m at different values of π

Figure 16. Graphical representations of A_m and I_m for π

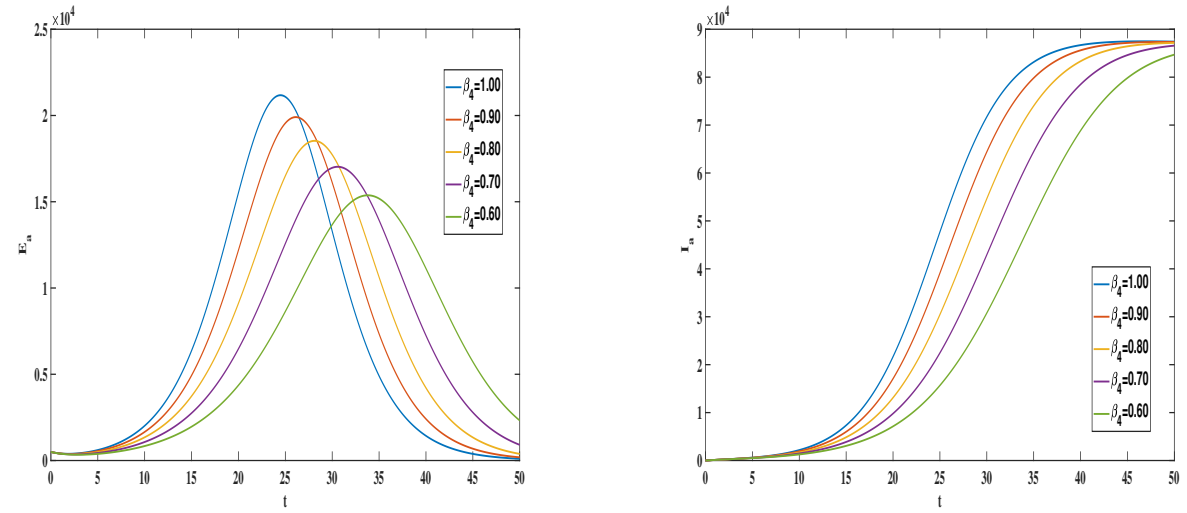

(a) Dynamical behaviour of E_a for β_4 values **(b)** Dynamical behavior of I_a at different values of β_4

Figure 17. Graphical representations of E_a and I_a for β_4

Figure 17 continues from Figure 15 by showing additional or comparative results of the numerical simulations under different β_4 values. This figure might depict another aspect of the model's behavior, such as the transition rates between different compartments of the model (e.g., susceptible, exposed, infected) over time t. The focus on different β_4 values helps in understanding the sensitivity of the model to changes in this fractional order, which is crucial for validating the model's robustness and reliability in predicting Mpox dynamics under varying conditions.

The CF fractional model captures memory and hereditary properties in epidemiological systems. This feature aligns well with the observed transmission dynamics of Mpox, which may involve delayed responses in immunity and disease progression. The solutions demonstrate consistency across a range of fractional orders δ. Notably, the choice of $\delta = 0.60, 0.70, 0.80, 0.90, 1.00$ appeared to yield slightly more accurate alignment with empirical data. The value of δ significantly impacts

the rate of infection spread and recovery, as it controls the degree of memory effect incorporated into the model.

7 Conclusion

In this investigation, we formulated a fractional-order epidemiological framework to examine the dynamics of the Mpox virus transmission, incorporating both symptomatic and asymptomatic infections. The model was rigorously analyzed for the existence and uniqueness of solutions, demonstrating that it possesses a unique solution under certain conditions. The key findings demonstrate the impact of vaccination rates, contact rates, and immunity waning on the basic reproduction number (R_0) and the disease's spread within human and rodent populations. The synergistic effect of the human-to-human transmission rate (β_1) and the progression rate of exposed individuals (k) significantly elevates the human reproduction number (R_{m_0}), while increased vaccination rates (α_m) and reduced immunity waning (τ) contribute to a decline in R_{m_0}. Similarly, in rodents, the interaction between the infected-to-susceptible contact rate (β_4) and the progression rate of exposed rodents (π) critically affects the rodent reproduction number R_{a_0}. Numerical simulations were conducted to validate the theoretical findings, showing that the model accurately captures the spread of the virus and the impact of various parameters on the infection dynamics. The results highlight the critical role of asymptomatic individuals in the transmission of Mpox and underscore the importance of targeted control measures. This work provides a valuable framework for understanding the complex dynamics of Mpox and can inform public health strategies for managing outbreaks. Future studies could benefit from localized modeling efforts. Also, the model has been validated using simulated datasets, but the incorporation of real epidemiological data could improve the robustness of our findings and validate assumptions made regarding disease progression and intervention strategies.

Declarations

Use of AI tools

The authors declare that they have not used Artificial Intelligence (AI) tools in the creation of this article.

Data availability statement

There are no data associated with this article

Ethical approval (optional)

The authors state that this research complies with ethical standards. This research does not involve either human participants or animals.

Consent for publication

Not applicable

Conflicts of interest

The authors declare that they have no conflict of interest.

Funding

No funding was received for this research.

Author's contributions

M.M.: Conceptualization, Writing-Original draft preparation, Investigation, Methodology, Software, Visualization. A.V.: Writing - Review & Editing, Formal Analysis, Supervision. S.K.: Software, Validation, Writing-Reviewing and Editing. All authors discussed the results and contributed to the final manuscript.

Acknowledgements

Not applicable

References

[1] Worldometer, United States Population, (2022). https://www.worldometers.info/world-population/us-population/

[2] Centers for Disease Control and Prevention (CDC), What You Should Know About Monkeypox, (2022). https://www.cdc.gov/poxvirus/monkeypox/

[3] World Health Organization (WHO), Monkeypox, (2022). https://www.who.int/news-room/factsheets/detail/Mpox

[4] Bunge, E.M., Hoet, B., Chen, L., Lienert, F., Weidenthaler, H., Baer, L.R. and Steffen, R. The changing epidemiology of human monkeypox-A potential threat? A systematic review. *PLoS Neglected Tropical Diseases*, 16(2), e0010141, (2022). [CrossRef]

[5] Bhatter, S., Jangid, K., Abidemi, A., Owolabi, K.M. and Purohit, S.D. A new fractional mathematical model to study the impact of vaccination on COVID-19 outbreaks. *Decision Analytics Journal*, 6, 100156, (2023). [CrossRef]

[6] Jose, S.A., Yaagoub, Z., Joseph, D., Ramachandran, R. and Jirawattanapanit, A. Computational dynamics of a fractional order model of chickenpox spread in Phuket province. *Biomedical Signal Processing and Control*, 91, 105994, (2024). [CrossRef]

[7] Okyere, S. and Ackora-Prah, J. Modeling and analysis of monkeypox disease using fractional derivatives. *Results in Engineering*, 17, 100786, (2023). [CrossRef]

[8] Peter, O.J., Kumar, S., Kumari, N., Oguntolu, F.A., Oshinubi, K. and Musa, R. Transmission dynamics of Monkeypox virus: a mathematical modelling approach. *Modeling Earth Systems and Environment*, 8, 3423–3434, (2022). [CrossRef]

[9] Venkatesh, A., Manivel, M. and Baranidharan, B. Numerical study of a new time-fractional Mpox model using Caputo fractional derivatives. *Physica Scripta*, 99(2), 025226, (2024). [CrossRef]

[10] Manivel, M., Venkatesh, A., Arunkumar, K., Prakash Raj, M. and Shyamsunder. A mathematical model of the dynamics of the transmission of monkeypox disease using fractional differential equations. *Advanced Theory and Simulations*, 7(9), 2400330, (2024). [CrossRef]

[11] Venkatesh, A., Manivel, M., Arunkumar, K., Prakash Raj, M., Shyamsunder and Purohit, S.D. A fractional mathematical model for vaccinated humans with the impairment of Monkeypox transmission. *European Physical Journal Special Topics*, (2024). [CrossRef]

[12] Bozkurt, F., Baleanu, D. and Bilgil, H. A mathematical model of mobility-related infection and vaccination in an epidemiological case. *Computer Methods in Biomechanics and Biomedical Engineering*, 1-21, (2024). [CrossRef]

[13] Öztürk, Z., Bilgil, H. and Sorgun, S. Application of fractional SIQRV model for SARS-CoV-2 and stability analysis. *Symmetry*, 15(5), 1048, (2023). [CrossRef]

[14] Öztürk, Z., Yousef, A., Bilgil, H. and Sorgun, S. A Fractional-order mathematical model to analyze the stability and develop a sterilization strategy for the habitat of stray dogs. *An International Journal of Optimization and Control: Theories & Applications*, 14(2), 134-146, (2024). [CrossRef]

[15] Jothika, S. and Radhakrishnan, M. Dynamics of an SIR pandemic model using constrained medical resources with time delay. *Communications in Mathematical Biology and Neuroscience*, 2023, 90, (2023). [CrossRef]

[16] Bankuru, S.V., Kossol, S., Hou, W., Mahmoudi, P., Rychtář, J. and Taylor, D. A game-theoretic model of Monkeypox to assess vaccination strategies. *PeerJ*, 8, e9272, (2020). [CrossRef]

[17] Manivel, M., Venkatesh, A., Kumar, K.A., Raj, M.P., Fadugba, S.E. and Kekana, M. Quantitative modeling of monkeypox viral transmission using Caputo fractional variational iteration method. *Partial Differential Equations in Applied Mathematics*, 13, 101026, (2025). [CrossRef]

[18] Usman, S. and Adamu, I.I. Modeling the transmission dynamics of the monkeypox virus infection with treatment and vaccination interventions. *Journal of Applied Mathematics and Physics*, 5(12), 2335-2353, (2017). [CrossRef]

[19] Caputo, M. and Fabrizio, M. A new definition of fractional derivative without singular kernel. *Progress in Fractional Differentiation & Applications*, 1(2), 73-85, (2015). [CrossRef]

[20] Losada, J. and Nieto, J.J. Properties of a new fractional derivative without singular kernel. *Progress in Fractional Differentiation and Applications*, 1(2), 87-92, (2015). [CrossRef]

[21] Van den Driessche, P. and Watmough, J. Reproduction numbers and sub-threshold endemic equilibria for compartmental models of disease transmission. *Mathematical Biosciences*, 180(1-2), 29-48, (2002). [CrossRef]

[22] Atangana, A. and Owolabi, K.M. New numerical approach for fractional differential equations. *Mathematical Modelling of Natural Phenomena*, 13(1), 3, (2018). [CrossRef]

[23] Li, S., Ullah, S., AlQahtani, S.A., Tag, S.M. and Akgül, A. Mathematical assessment of Monkeypox with asymptomatic infection: Prediction and optimal control analysis with real data application. *Results in Physics*, 51, 106726, (2023). [CrossRef]

Mathematical Modelling and Numerical Simulation with Applications (MMNSA)
(https://dergipark.org.tr/en/pub/mmnsa)

How to cite this article: Manivel, M., Venkatesh, A. & Kumawat, S. (2025). A comprehensive study of monkeypox disease through fractional mathematical modeling. *Mathematical Modelling and Numerical Simulation with Applications*, 5(1), 65-96. https://doi.org/10.53391/mmnsa.1571609

Mathematical Modelling and Numerical Simulation with Applications, 2025, 5(1), 97–116

https://dergipark.org.tr/en/pub/mmnsa
ISSN Online: 2791-8564 / Open Access
https://doi.org/10.53391/mmnsa.1522021

RESEARCH PAPER

Numerical analysis of the three-dimensional model of pulsatile and non-Newtonian blood flow in a carotid artery with local occlusion

Mansur Mustafaoğlu [1,‡], **İsak Kotçioğlu** [1,‡] **and Muhammet Kaan Yeşilyurt** [1,*,‡]

[1]Department of Mechanical Engineering, Faculty of Engineering, Ataturk University, 25240 Erzurum, Türkiye

*Corresponding Author
‡mansour@atauni.edu.tr (Mansur Mustafaoğlu); ikotcioglu@atauni.edu.tr (İsak Kotçioğlu); kaan.yesilyurt@atauni.edu.tr (Muhammet Kaan Yeşilyurt)

Abstract

The analysis of blood flow in blood vessels, particularly in arteries, is a topic with important clinical applications. The blood can undergo a reduction in its viscosity under shear stress, which is called shear thinning. In this study, the effect of the shear thinning of blood is simulated using the Carreau-Yasuda model, neglecting the viscoelastic effects. The purpose of this investigation is to analyze the pulsatile blood flow in a three-dimensional model of the carotid artery and the effects of occlusion using Ansys Fluent. The results obtained in this study show that, compared to Newtonian fluids, non-Newtonian fluids exhibit significant differences in secondary flow patterns and shear flow behavior. Additionally, the axial velocity in the non-planar branch decreases with obstruction. The maximum shear stress of the walls with Newtonian fluid viscosity exhibits a significant error, and the values are lower than those of walls with non-Newtonian viscosity in most cases. In continuation of this research, vessel occlusion models with different occlusion sizes are analyzed. In the case where the outlet of the vessel is narrowed, an increase in velocity is observed in the furcation area. Although the software cannot simulate rupture, occlusion of the vessel at 80% and 50% of the internal diameter is analyzed.

Keywords: Non-Newtonian fluid; shear thinning; Carreau-Yasuda model; blood flow; CFD analysis

AMS 2020 Classification: 65N12; 76A05; 92C35

1 Introduction

Cardiovascular diseases (CVDs) account for approximately 17.9 million deaths annually, which corresponds to 32% of all global deaths. Including coronary artery disease, stroke, and hypertension, CVDs are often linked to abnormalities in blood flow and vessel occlusion. Besides being the

➤ **Received:** 25.07.2024 ➤ **Revised:** 11.02.2025 ➤ **Accepted:** 16.02.2025 ➤ **Published:** 31.03.2025

leading cause of death globally, CVDs also create a significant economic burden, with healthcare costs and productivity losses estimated to exceed one trillion US dollars annually worldwide. Understanding the hemodynamics of blood flow, particularly in occluded vessels, is therefore critical for developing effective diagnostic and therapeutic strategies against CVDs.

With the increasing number of CVDs during the last few decades, the study of blood flow in vessels and its behavior has been of particular importance and interest. Through a review of the literature, it has become clear that there is still much to investigate regarding the shear stress on the walls of the vessels, the effects of the hyperelasticity of the blood vessels, and how blood interacts with the vessel structure under different gravity conditions. Another CVD, carotid artery disease, is a condition characterized by the narrowing of the carotid arteries, the primary vessels supplying oxygenated blood to the brain. This narrowing, or stenosis, is typically caused by the accumulation of atherosclerotic plaque within the arterial walls. The primary objective of treatment is to mitigate the risk of ischemic stroke by reducing plaque burden, preventing thrombus formation, and maintaining adequate cerebral blood flow. Currently, it has been proven that the occurrence of many CVDs is linked to blood flow characteristics [1].

Blood is a concentrated suspension of red blood cells (RBCs) in plasma, with these cells constituting nearly 45% of the total blood volume. At normal temperatures, blood behaves as non-Newtonian in the form of shear liquefaction [2]. A cramp is an abnormal swelling in a vein or other organs with tubular structures in the body. Sometimes, it is also called stenosis [3] and [4]. From the point of view of fluid mechanics, constriction indicates the presence of an obstacle to blood flow inside the vessel [5]. Vascular branches in areas that have abnormal fluid dynamics are known to be prone to atherosclerosis. Fluid mechanics studies have shown that atherosclerosis occurs at bifurcations that have a complex geometry, i.e., in areas with a high Reynolds number and where the shear stress is lower than the average of wall shear stress (WSS). The curvature of the wall is related; in addition, local disturbances and areas of circulation play important roles in the initiation and development of atherosclerosis. It is thought that the complexity of the blood flow dynamics downstream of the occlusion will cause further development of the occlusion or cause the plaque to be vulnerable to failure and thrombosis. It is almost universally accepted that blood vessels that have curves or bifurcations are prone to constriction due to the complexity of the flow in these areas [6]. Because the blood flow is pulsatile, these complicated flow patterns cause constrictions in certain periods within the geometries that feature high shear stress, separation, circulation, and turbulent flow.

Various studies have been conducted in this field. The investigation of blood flow in narrowed vessels is an interesting topic that has attracted the attention of many researchers. This issue is particularly important because the blood flow in constricted vessels and channels has a crucial impact on the development of vascular obstruction [7]. Examining the mechanism of blood flow and the distribution of blood flow in these stages leads to determining the dependence of blood flow on various physical and physiological factors and to a correct understanding of this phenomenon. As a result, it is possible to solve this problem or prevent it from an engineering point of view. As a result of the clogging and narrowing (obstruction) that occur in the vein, the normal flow of blood is disrupted. This disturbance in normal blood flow plays an important role in vascular diseases. For this reason, to determine how constriction affects blood flow and analyze blood flow in the parts of vessels that are clogged or blocked, much research has been performed, including laboratory investigations as well as numerical studies.

Having started approximately 25 years ago, several experimental research studies have been conducted using different laboratory models to study how unstable flow affects the blood flow at occlusion sites. With the advancement of computational methods in recent years, later studies featuring numerical simulations of this physiological phenomenon have been performed by

numerous researchers [8, 9]. Many researchers have studied pulsatile blood flow in healthy and blocked vessels using computational fluid dynamics (CFD) and compared the results using MRI techniques [7, 10, 11].

Clogged or engorged blood vessels face various hemodynamic consequences of pressure drop, which lead to the development of clots. The pressure drop depends on the flow velocity and the geometry of the constriction, but the properties of fluid, such as density and apparent viscosity, are relatively constant. Multiple constrictions in the arteries are the result of plaque growth in atherosclerosis, which can collapse under certain physiological conditions [5].

Vascular narrowing is often accompanied by an unusual sound of blood flow, which results from the disturbance of flow in the narrowed channel, and in this way, the location of the constriction can be recognized. These sounds can be heard using a medical stethoscope, but disease diagnosis with medical imaging refers to the set of methods and techniques that can be used to obtain visual images of the parts of the human body [12].

Seo [13] investigated blood flow in the human carotid artery using ANSYS software. He investigated the effect of the interaction between fluid and solid on the flow characteristics and shear stress of the wall. He investigated two flow models, one of which considered the interaction between solid and fluid, while the other did not. The results showed that the shear stress values for these two models differ between 5% and 11%.

The collapse of the inner wall of the vessel is a process in which the bending of the artery is under certain pressure and tension, and under these conditions, the collapse of the inner wall of the vessel occurs. The result of the compression resulting from this collapse is to speed up the process of fatigue and rupture. If plaque detachment occurs in the coronary and cerebral arteries, it directly leads to a heart attack or stroke. The activity of blood plaques in certain cases, such as cramps and, in particular, when thrombosis occurs, is of great interest [6]. Upon plaques sticking together, congestion develops, and once the flow becomes sufficiently constricted, turbulence may increase, bringing on an increase in the shear stress of the flow and the walls. Studies in the computer environment show that flow transitions into turbulent and back into laminar in pulsatile flow; therefore, it is very important to predict transient and turbulent flow in flows with low Reynolds numbers when simulating blood flow within blood vessels with occlusion [14]. Another factor that affects blood viscosity is the concentration and type of proteins in plasma, but these effects are so small that they are not considered important in most hemodynamic studies [15].

Using Ansys software, Dong et al. [16] conducted a numerical study to explore the relationship between mechanical forces that are exerted at the coronary branching (furcation) sites and the angle of furcation, considering the division angles to be between 75 and 120 degrees. The results revealed a relationship between environmental stress and left coronary artery diseases. In addition, they considered two elastic and nonelastic assumptions for the blood vessel [16]. On the other hand, Leeuwen et al. [17] investigated the diameter of the vessel and the RBC velocity in the vessel and reported that vessel constriction induces a large change in the RBC velocity [17].

Botti et al. [18] conducted a CFD study modeling the blood hemodynamics of a specific patient with an intracranial aneurysm by using two different CFD solvers, i.e., the finite element method and the finite volume method, in order to compare their performances. They reported that the finite element model provided better accuracy in high-order analysis for every degree of freedom [18].

The particle hydrodynamic method has always been developed as a meshless Lagrange method for simulating fluid-structure interactions. This algorithm, which involves the two-dimensional simulation of blood flow, provides new support for the application of the SPH method. This method is used to simulate the opening of the elastic valve due to the force of the fluid column behind it, which, compared to the experimental results, proves the ability of this method to solve

fluid and structural problems [19].

Many of the studies reported in the literature have focused on Newtonian fluid models or simplified geometries. While some have incorporated non-Newtonian models, they often neglect the effects of pulsatile flow or fail to analyze the impact of varying occlusion sizes on flow patterns and wall shear stress. This study aims to address these gaps by employing a non-Newtonian Carreau-Yasuda model to simulate pulsatile blood flow in a three-dimensional model of the carotid artery with varying degrees of occlusion. By incorporating realistic vessel geometry and pulsatile flow conditions, this study provides a more accurate representation of the hemodynamics in stenotic vessels. Furthermore, the analysis of different occlusion sizes (50% and 80% of the internal diameter) is important to address in more detail the hemodynamic risks associated with high occlusion levels and their implications for CVDs.

The purpose of this study was to analyze the pulsatile flow inside vessels with non-Newtonian blood fluid. In the present study, the flow is unsteady and fully developed before entry. The Carreau model is considered for the simulation of non-Newtonian blood fluid. Additionally, the values of velocity and pressure are defined the same as real values and with pulses.

2 Materials and methods

This section presents the governing flow equations and the corresponding boundary conditions. Homogeneous fluid motion equations are derived from the conservation principles of mass, momentum, and energy. To facilitate engineering analysis, a continuum assumption is employed, averaging the fluid properties over a representative elementary volume. This assumption is called continuous media, and as long as the smallest physical dimension is much larger than the free distance of molecules, this assumption is true.

Another assumption made in this study is that the blood was an incompressible fluid. This assumption is justified by the fact that the density of blood remains nearly constant under physiological conditions. The compressibility of blood is negligible due to the fact that the greatest part of the blood plasma, as high as 90%, consists of water and that the pressure variations in the cardiovascular system is relatively low. This assumption simplifies the continuity equation and is consistent with the majority of blood flow models in the literature.

Governing equations

The governing equations are for the solid wall that interacts with the fluid. The equations solved in the ANSYS software include the equations of conservation of mass Eq. (1) and momentum Eq. (2).

$$\frac{\partial p}{\partial t} + \nabla \cdot (\rho V) = 0. \tag{1}$$

The momentum equations, also known as the Navier–Stokes equations, govern viscous flow of Newtonian fluids and can be written as in Eq. (2) in the general form:

$$\rho \left(\frac{\partial u_i}{\partial t} + \mathbf{u_j} \frac{\partial u_i}{\partial x_j} \right) = \frac{\partial P}{\partial x_j} + \mathbf{B_i} + \frac{\partial}{\partial x_i} \left[\mu \left(\frac{\partial u_i}{\partial x_j} + \frac{\partial u_j}{\partial x_i} - \frac{2}{3} \mathbf{‹_{ij}} \frac{\partial u_k}{\partial x_k} \right) \right], \tag{2}$$

where B_i represents the body forces that include primarily the gravitational forces, which are relevant in hemodynamic studies. Other body forces, such as electromagnetic forces, are mostly irrelevant and, therefore, negligible in this context.

This method can usually remove the viscosity of the fluid from inside the derivative, and in the

Table 1. Constant values of the k-ω turbulence model

σ_ω	σ_k	$'\beta$	β	α
2.0	2.0	0.09	0.075	5.9

meantime, only a small and negligible error occurs. For an incompressible flow, Eq. (3) can be shown as the following vector:

$$\rho \frac{D\vec{D}}{Dt} = -\nabla P + B + \mu \nabla^2 \mathbf{U}. \tag{3}$$

For turbulent flows, the velocity and pressure variables are completely dependent on time; now, if we want to use them as two average and fluctuating components in the Navier-Stokes equations, a series of unknown parameters appear in the equation, which are called Reynolds stresses. By substituting the separated velocity and pressure in the Navier-Stokes equation and simplifying it, Eq. (3) becomes:

$$\rho \left(\frac{\partial \bar{u}_i}{\partial t} + \bar{u}_j \frac{\partial \bar{u}_i}{\partial x_j} \right) = \bar{B}_i - \frac{\partial \bar{P}}{\partial x_i} + \frac{\partial}{\partial x_j} \left[\mu \left(\frac{\partial \bar{u}_i}{\partial x_j} - \rho \overline{u_i' u_j'} \right) \right]. \tag{4}$$

The difference between the resulting momentum equation and the instantaneous momentum equation is the last term on the right side of Eq. (4), which is called the Reynolds stress or disturbance stress. It is more suitable for simulating the flow behavior near the wall at low Reynolds numbers and separating the flows caused by the reverse pressure gradient compared to the k-ϵ model. Unlike the k-ϵ model, which incorporates nonlinear and complex damping functions, the k-ω model offers a simplified approach by neglecting these terms. The k-ω turbulence model posits a direct relationship between turbulent viscosity, turbulent kinetic energy, and turbulence frequency. In the k-ω model, the turbulence viscosity is obtained from the following Eq. (5):

$$\mu_t = \frac{\rho k}{\omega}. \tag{5}$$

The two transfer equations of this model, the turbulent kinetic energy equation (k) and the specific dissipation rate equation (ω) are as given in Eqs. (6) and (7), respectively.

$$\frac{\partial(\rho k)}{\partial t} + \nabla \cdot (\rho U k) = \nabla \cdot \left[\left(\mu + \frac{\mu_t}{\sigma_k} \right) \nabla k \right] + P_k + P_{kb} - Y_k, \tag{6}$$

$$\frac{\partial(\rho \omega)}{\partial t} + \nabla \cdot (\rho U \omega) = \nabla \cdot \left[\left(\mu + \frac{\mu_t}{\sigma_\omega} \right) \nabla \omega \right] + \alpha \frac{\omega}{k} P_k + P_{\omega b} - Y_\omega. \tag{7}$$

The constants of this equation are shown in Table 1.

The constants in the k-ω turbulence model (Table 1) were validated through comparison with experimental data and established benchmarks for turbulent flows. These constants were derived from extensive empirical studies and are widely accepted in the literature for simulating wall-bounded flows with adverse pressure gradients. The model's accuracy was further verified by comparing simulation results with experimental measurements of velocity profiles and turbulence statistics in similar geometries.

The capacity of standard two-equation turbulence models to accurately predict the inception and extent of flow separation from smooth surfaces under adverse pressure gradients is limited. The starting point for the development of the shear stress transfer turbulence model was the need for accurate calculations of flows with separation phenomena and reverse pressure gradients. For a long time, turbulence models were unable to account for these flows.

The k-ϵ turbulence model exhibits limitations in accurately capturing near-wall turbulent boundary layer behavior. In this region, the k-ω model offers superior performance and is more suitable for flows with adverse pressure gradients. On the other hand, the k-ω model's sensitivity to free-stream conditions outside the boundary layer can hinder its application in flows involving separation induced by pressure gradients. This sensitivity in the free stream in turbulence modeling prevents the wide substitution of ω equations in place of standard ϵ equations. This is the basis for the development of the k-ω SST (Shear Stress Transport) model, which is given in Eqs. (8) and (9) below [20].

$$\frac{\partial}{\partial t}(\rho k) + \frac{\partial}{\partial x_i}(\rho k u_i) = \frac{\partial}{\partial x_i}\left(\Gamma_k \frac{\partial k}{\partial x_j}\right) + G_k - Y_k + S_k, \tag{8}$$

$$\frac{\partial}{\partial t}(\rho \omega) + \frac{\partial}{\partial x_i}(\rho \omega u_i) = \frac{\partial}{\partial x_i}\left(\Gamma_\omega \frac{\partial \omega}{\partial x_j}\right) + G_\omega - Y_\omega + D_\omega + S_\omega. \tag{9}$$

In the standard k-ω and SST k-ω models, the production terms of the k and ω equations are dissected presented in tabular form in Table 2 below.

Table 2. Terms in the $k-\omega$ turbulence model

Term	**Standard k-ω equation**	**SST k-ω equation**
Production of k	$P_k = \tau_{ij}\frac{\partial U_i}{\partial x_j} = \nu_t S_{ij} S_{ij}$	$G_k = \tau_{ij}\frac{\partial U_i}{\partial x_j}$
Buoyancy production of k	$P_{kb} = -\frac{g_i}{\rho}\frac{\partial \rho}{\partial x_i}$	
Production of ω	$P_\omega = \alpha \frac{\omega}{k} P_k$	$G_\omega = \frac{\gamma}{\nu_t} G_k$
Buoyancy production of ω	$P_{\omega b} = C_{\omega b}\frac{\omega}{k} P_{kb}$	
Dissipation of k	$Y_k = \beta^* \rho k \omega$	
Dissipation of ω	$Y_\omega = \beta \rho \omega^2$	
Cross-diffusion	Not present	$D_\omega = 2(1-F_1)\rho\sigma_{\omega 2}\frac{1}{\omega}\frac{\partial k}{\partial x_i}\frac{\partial \omega}{\partial x_i}$
Source terms	Not present	$S_k = C_k \rho \frac{\lvert S\rvert^3}{\omega}$ $S_\omega = C_\omega \rho \lvert S\rvert^2$

Turbulence models such as k-ϵ or LES are less accurate for near-wall flow behavior and need more computation workload, but the k-ω SST model combines the strengths of the k-ϵ model for free shear flows and the k-ω model for near-wall flows and thus strikes a balance between accuracy and computational efficiency. The k-ω SST turbulence model is well-known for its success in simulating turbulent flows in structures containing complex geometries and boundary layers by accurately resolving the boundary layer and near-wall flow behavior, which is essential for calculating WSS and other hemodynamic parameters [21, 22].

Studies have shown that the k-ω SST model provides accurate estimates of wall shear stress and flow separation, which are critical parameters in cardiovascular health assessment [22]. The application of these models in pulsatile flow simulations has also been validated through comparisons with experimental data. For example, the k-ω SST model has been shown to provide

highly accurate results, usually within 5% error, when compared to experimental measurements [23]. As a result, the k-ω SST turbulence model was chosen for this study due to its superior performance and for being a validated and reliable choice for simulating blood flow in stenotic vessels. The Carreau-Yasuda model, which takes into account the shear thinning properties of blood that become important under variable flow conditions [22, 24], has been widely used for simulating pulsating blood flow, and has been supported by studies to be an effective model in capturing the complex flow properties observed in biological systems [21, 22]. Furthermore, integrating the Carreau-Yasuda model with the k-ω SST turbulence model provides a more comprehensive understanding of flow dynamics in occluded arteries because it effectively captures both the non-Newtonian properties of blood and the turbulent flow characteristics [22–24].

In the present study, blood has a profile similar to that in the study of Chen and Lu [25] and enters the inlet branch at a Reynolds number equal to 270 (or an average velocity of 0.0694 m/s). As for the output boundary conditions, zero relative pressure at the outlet of the two branches is used, as per the above study, and due to the incompressibility of blood in this problem, the amount of working pressure does not affect the results. Additionally, the axial flow velocity gradients at the exits of both branches are considered to be zero. The boundary condition of the wall is assumed to be non-slip. In the present study, blood flow in a bifurcating blood vessel has been numerically

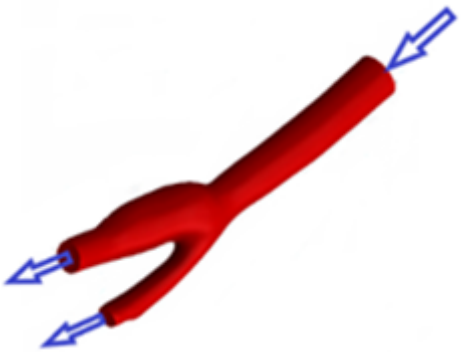

Figure 1. Blood vessel geometry

simulated in a three-dimensional model for Newtonian and non-Newtonian Carreau–Yasuda viscosity conditions. The desired geometry is drawn in the design software. Figure 1 shows the geometry drawn in SOLIDWORKS software. The Carreau-Yasuda model has been chosen for this study due to its ability to accurately describe the shear-thinning behavior of blood across a wide range of shear rates. Unlike the power-law model, which is limited to intermediate shear rates, and the Casson model, which does not account for the gradual transition between Newtonian and non-Newtonian behavior, the Carreau-Yasuda model captures the viscosity variation of blood more comprehensively. This makes it particularly suitable for simulating blood flow in vessels with complex geometries and varying shear conditions.

The shear thinning behavior of blood is described by the Carreau-Yasuda model using:

$$\mu(\dot{\gamma}) = \mu_\infty + (\mu_0 - \mu_\infty)\left[1 + (\lambda\dot{\gamma})^a\right]^{\frac{n-1}{a}},$$

where $\mu(\dot{\gamma})$ is the dynamic viscosity as a function of shear rate (γ), μ_0 is the zero-shear viscosity, μ_∞ is the infinite-shear viscosity, λ is the relaxation time, n is the power-law index that describes the degree of shear thinning, and a is the Yasuda parameter that controls the transition between Newtonian and shear-thinning regions. Values of these model parameters are presented in Table 3.

The heartbeat pattern has been selected as the pulse function, and because the Fluent software is not able to define this type of pulse, the custom codes have been defined to induce the pulse for the simulation and have been incorporated into the solver through the use of UDFs. To simulate pulsatile blood flow in a CFD model, a physiological waveform that represents the heartbeat has been obtained by using a Fourier series to approximate the periodic nature of the arterial pulse. The blood flow rate calculated based on the waveform derived from experimental data or idealized representations of the cardiac cycle has been represented by the following formula:

$$Q(t) = Q_{\text{mean}} + \sum_{n=1}^{N} \left[A_n \cos\left(\frac{2\pi nt}{T}\right) + B_n \sin\left(\frac{2\pi nt}{T}\right) \right]. \tag{10}$$

In Eq. (10), the wave function can also be converted into a single sinusoidal form by using amplitudes and phase-shift:

$$A_n \cos\left(\frac{2\pi nt}{T}\right) + B_n \sin\left(\frac{2\pi nt}{T}\right) = C_n \sin\left(\frac{2\pi nt}{T} + \phi_n\right),$$

where the amplitude $\mathbf{C_n}$ is:

$$C_n = \sqrt{A_n^2 + B_n^2}.$$

And the phase angle ϕ_n is:

$$\phi_n = \tan^{-1}\left(\frac{A_n}{B_n}\right).$$

Eq. (10), then becomes:

$$Q(t) = Q_{\text{mean}} + \sum_{n=1}^{N} C_n \sin\left(\frac{2\pi nt}{T} + \phi_n\right),$$

where T is the period of the cardiac cycle (typically 0.8–1.0 s for a heart rate of 60–75 bpm), ϕ_n are the phase angles for each harmonic, N is the number of harmonics (typically 4–10 for a realistic waveform). The parameters and respective values used to simulate the pulse are presented in Table 3 below.

With the given parameters, the pulsatile blood flow has been simulated in the modeled vessel. The Womersley number, which characterizes the pulsatile blood flow, has been calculated for the non-stenotic and stenotic (%50 and %80 constricted) cases using:

$$\alpha = \frac{r\sqrt{\omega\rho}}{\mu},$$

and respective α numbers were found to be 52.46, 26.23, and 10.49, respectively.

The solution domain is organized and discretized using the so-called O-shaped mesh, except near the tip of the bifurcation and that part of the outlet branch that includes the constriction. Additionally, the unorganized mesh adapts better to the mix of the flow (caused by the presence of bifurcations and obstructions). Therefore, in this area, an unorganized mesh has been used in a

Table 3. Parameters used to simulate the pulsatile blood flow

Property	Value(s)
Vessel diamater	0.0045 m
Density	1060 kg/m3
Zero-shear viscosity	0.056 Pa.s
Infinite-shear Viscosity	0.0035 Pa.s
Temperature	37 C
Mean velocity	0.0694 m/s (Re=270)
Period of cardiac cycle	1 s
Number of harmonics	5
Cosine coefficients (B_n)	0.2, 0.15, 0.1, 0.05, 0.02
Sine coefficients (A_n)	0.3, -0.1, 0.08, -0.03, 0.015
Amplitudes (C_n)	0.36, 0.18, 0.13, 0.058, 0.025
Phase Angles (ϕ_n, radian)	0.59, -0.59, 0.67, -0.54, 0.64
Power-law index (n)	0.03568
Yasuda parameter (a)	2
Relaxation time (λ)	3.313 s

small enough way. Ansys Fluent software, which can create unorganized and organized meshes, was used to create the mesh, which can be seen in Figure 2 below. The number of generated mesh was 122540 elements. To determine the correct number of elements to build the mesh, a mesh independence analysis was made, and convergence was established.

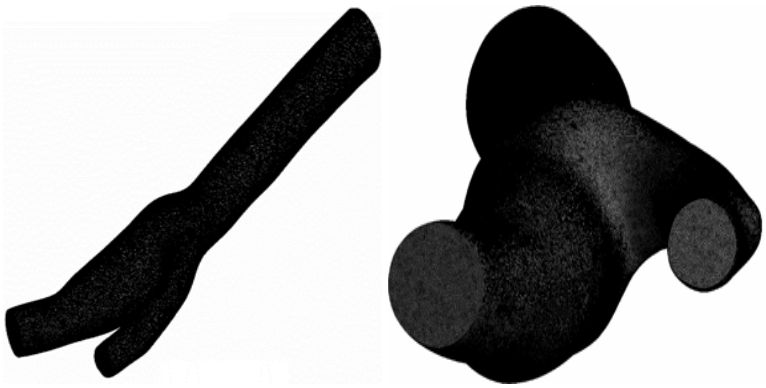

Figure 2. Side and front views of the meshed model

For numerical analysis in the ANSYS Fluent software, it is necessary to provide boundary conditions. To model the inlet flow, the mass flow rate values given in the reference study have been used. The outlet pressure boundary condition has been used for both of the two outlets of the artery division. Since the solution is unsteady, a user-defined function is used to provide the input and output boundary conditions. Figure 3 shows a view of the desired geometry along with the boundary conditions, and Figure 4 shows the values for the input and output blood pressure as given by the reference study.

In order to ensure that the number of elements that constitute the mesh have no or negligible impact on the solution, a mesh independence test is always carried out. In this study, mesh independence was demonstrated using WSS values. WSS is a critical parameter in hemodynamic simulations and is highly sensitive to mesh resolution. Therefore, it is often the primary metric for mesh independence. Once WSS converges with mesh refinement, it implicitly means that the mesh is also validated for the accuracy of velocity and pressure fields, as these are the underlying

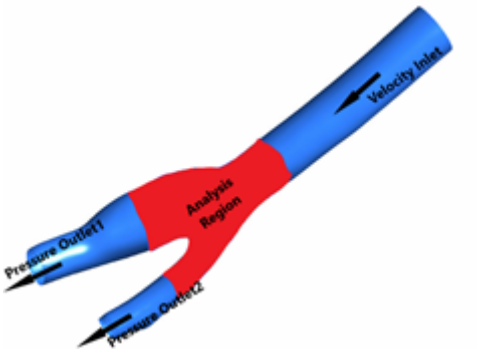

Figure 3. Boundary conditions of blood vessel geometry

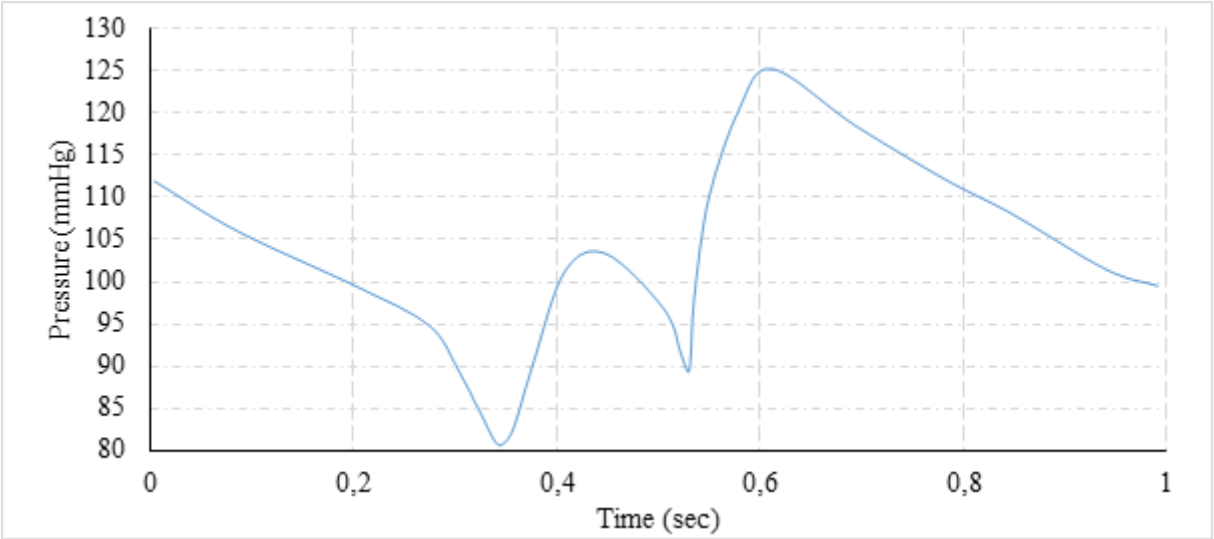

Figure 4. Input and output values of blood flow according to time

quantities used to compute WSS. In this regard, the WSS parameter in a section near the wall has been investigated in meshes with different numbers of elements. As shown in Figure 5, a number of elements greater than 1350,000 inside the geometry indicates the independence of the mesh.

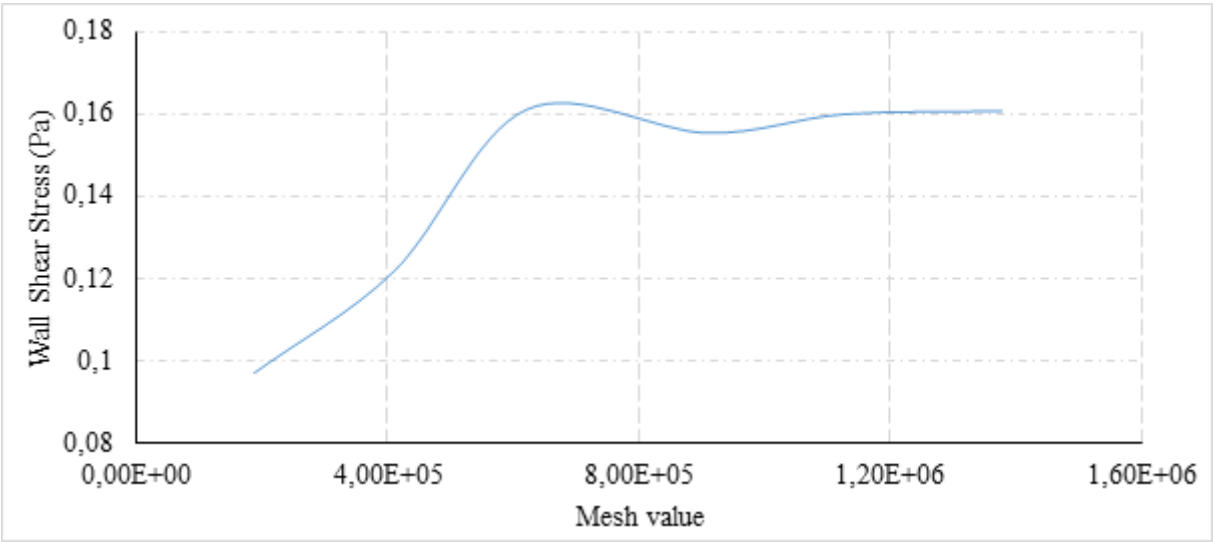

Figure 5. Shear stress according to the number of elements

One of the critical aspects of turbulence modeling is the accurate representation of near-wall flow physics, i.e., reflecting real-world conditions accurately. The performance of turbulence models is significantly influenced by their ability to capture wall-bounded flow characteristics. In this regard, the y+ parameter, a non-dimensional wall distance, serves as a crucial metric for evaluating the adequacy of near-wall mesh resolution. The logarithmic law of the wall provides theoretical guidelines for the appropriate range of y+ values to ensure accurate representation of the boundary layer. Ansys-Fluent software can be used to solve flow models that include moving cells. Depending on the complexity of movement and physics, the flow of one of the mesh movement models can be suitable for modeling. One of the most common models in Fluent for simulating streams that have a moving and variable mesh is the dynamic mesh model. To use the dynamic mesh model, we need to start with a mesh volume and describe each moving area in the model. Fluent can describe motion under a boundary profile based on functions defined by the user, known as user-defined functions (UDFs). For dynamic meshes, remeshing and smoothing techniques were employed to maintain mesh quality during deformation. Remeshing involves locally refining or coarsening the mesh in response to changes in geometry, whereas smoothing is the adjustment of nodes' positions to reduce distortion. These techniques ensure accurate simulation of fluid-structure interactions and moving boundaries.

3 Results and discussion

Many models have been presented to simulate non-Newtonian blood fluid in vessels, but none of them have been able to analyze the elastic behavior of vessel walls due to the pulse pressure of the blood, as in real samples, to minimize deviation. This problem has become one of the reasons for the failure of researchers. Computer simulation can solve the most complex problems of engineering sciences; therefore, in such problems, all required algorithms are simulated according to real vessel samples. The geometry of the vessel, which includes a two-way vessel with a diameter of the outlet different from the diameter of the inlet, is drawn, tested, and compared in the region before the constriction with different percentages. To create more tension in the vessel and complicate the problem, the diameter of one of the outlets is reduced by half, and the results are compared with each other. This complexity enables us to solve similar problems and analyze the output information. Different models are available to define blood fluid in the software. The selected models include three models: a non-Newtonian power law, a Newtonian power law, and the Carreau model, which has the least error compared to the analytical solution.

WSS (τ_w) is calculated from the velocity gradients on the wall of the vessel using the following relationship:

$$\tau_w = \mu \left(\frac{\partial u}{\partial y} \right)_{y=0},$$

where μ is the dynamic viscosity of blood, u is the velocity parallel to the wall, and y is the distance perpendicular to the wall. ANSYS uses the same formulation to calculate the wall stress based on the velocity gradients obtained during the numerical solution of the governing Navier-Stokes equations at the wall (y=0). In this study, the contour plots for WSS were obtained directly in CFD post and presented in Figure 6 for different conditions.

The shear stress values obtained in this simulation were validated against those of another study conducted using a similar bifurcation vessel model. The values are presented in Table 4. The range of the errors is from approximately 2 to 13%, and the average error is approximately 7%, which is acceptable. Figure 6 shows the distribution of inner-wall shear stress.

The results of the analysis are given as shear stress values near the vessel wall. Figure 6 shows

Table 4. Inner wall shear stress

X/C Time (s)	Shear Stress (Pas) CFD (A)	Shear Stress (Pas) [16] (B)	Error (%) (B-A)/A*100
0.0	0.123	0.12	−2.5
0.2	0.174	0.18	3.4
0.4	0.280	0.26	−7.1
0.6	0.355	0.38	7.0
0.8	0.220	0.24	9.0
1.0	0.150	0.13	−13.3

the values of shear stress inside the vessel resulting from the analysis with the Carreau model. The average value near the vessel wall is approximately 0.3 Pascal. In the case of constriction, the region behind the constriction experiences the highest shear stress. The flow output also has shear stress values, and this stress increases with the narrowing of the outlet of the vessel.

Figure 6 show shear stress values on walls of the vessel with 80% and 50% constriction. The shear stress is highest in the region near the branch and near the constriction because of the increase in pressure in these areas. With the narrowing of the constriction due to a sudden change in diameter, the velocity in the narrowed channel increases greatly, which in turn increases the pressure on the wall, and with the narrowing of the outlet, this pressure increases. The tension at these points increases due to the increase in pressure. The concentration of greatest stress occurs after constriction and in the furcation area.

The velocity streamlines in Figure 7 show that the flow characteristics in normal and stenotic arteries change significantly. While the velocity distribution in the normal artery is relatively balanced, the flow lines progress smoothly, and no significant recirculation or turbulence is observed. With the increase of constriction, a significant increase in the flow velocity and the formation of turbulence in the region after the constriction are observed with the expansion of backflow areas. This supports the formation of high shear stresses in the arterial wall seen in Figure 6.

Figure 8 shows the values of the velocity inside the vessel for different modes of analysis. As it approaches the area before the constriction, due to the increase in pressure, the flow experiences a sharp drop in velocity, which acts like the flow inside the nozzle in the constriction area, and a higher velocity is observed in the flow of the constriction area. This increase in velocity continues to the furcation area, which induces an increase in friction and shear stress. In the case where the outlet of the vessel is narrowed, the increase in velocity increases, and up to 17% greater velocity is observed in the furcation area. With increasing velocity, the amount of pressure and shear stress increases, and the vessel is unable to bear this pressure and is on the threshold of rupture.

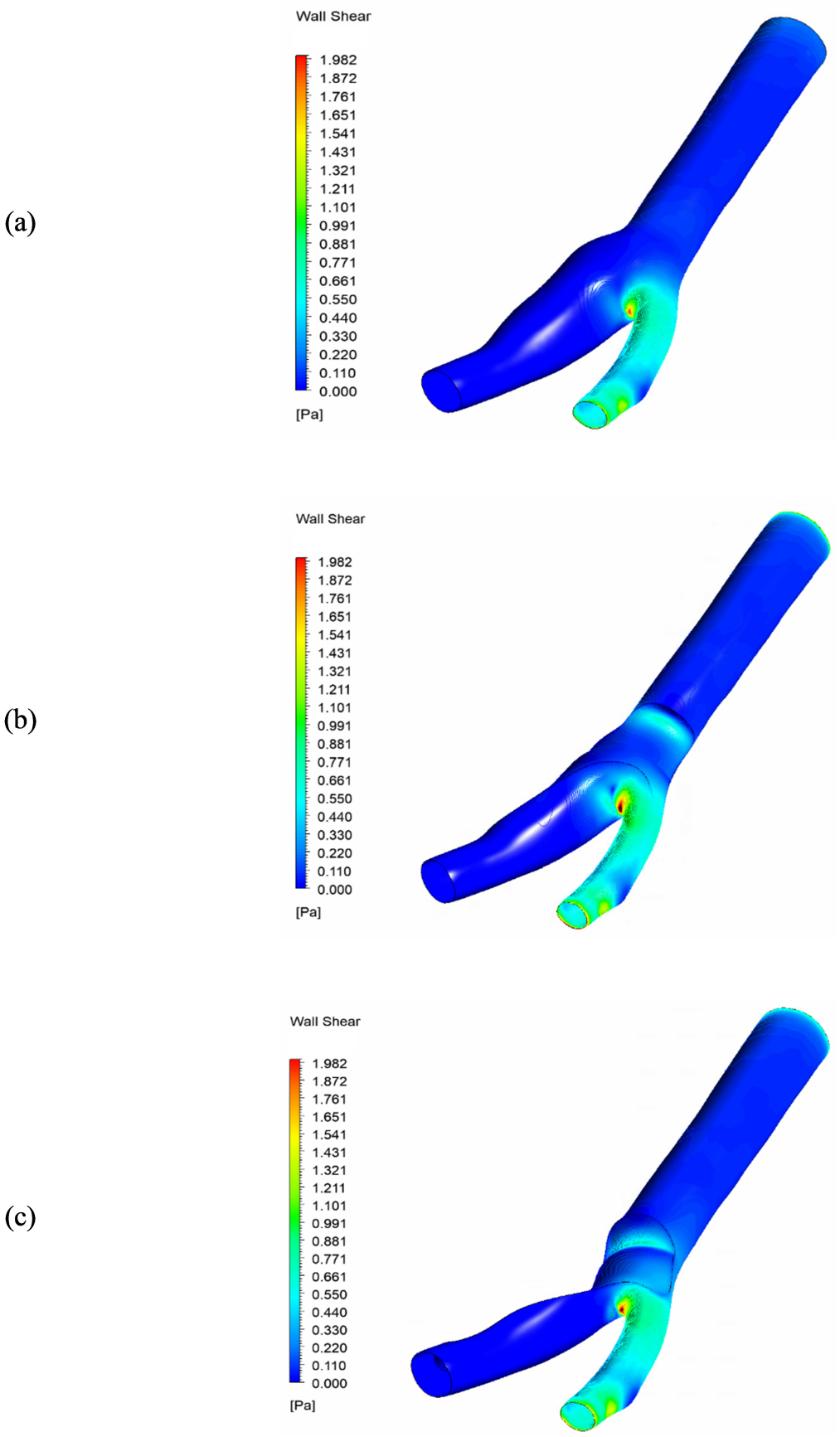

Figure 6. Shear stress contours on (a) normal (b) 50% and (c) 80% constricted vessel

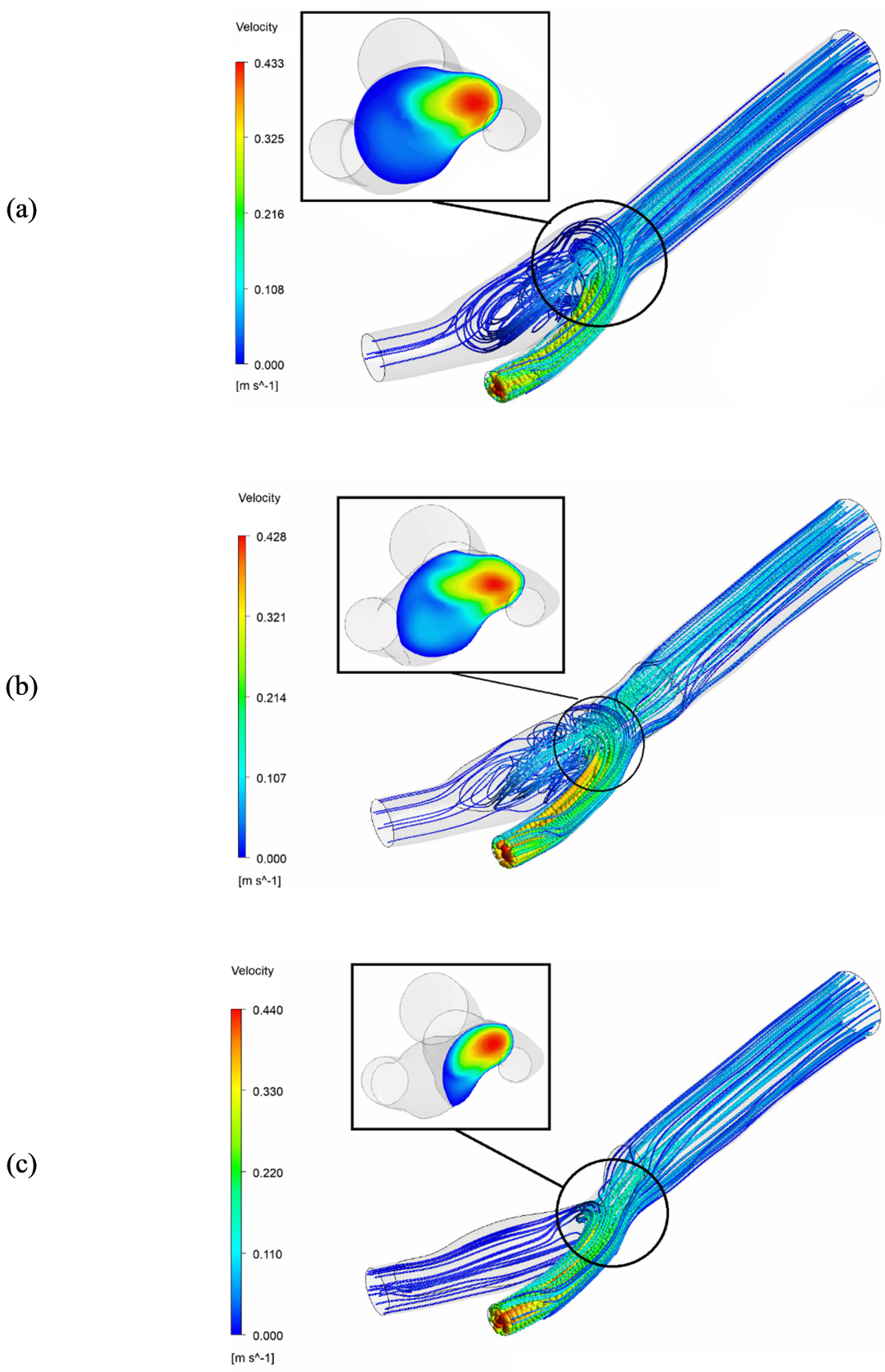

Figure 7. Velocity values of vessel geometry (a) normal (b) 50% and (c) 80% constricted vessel

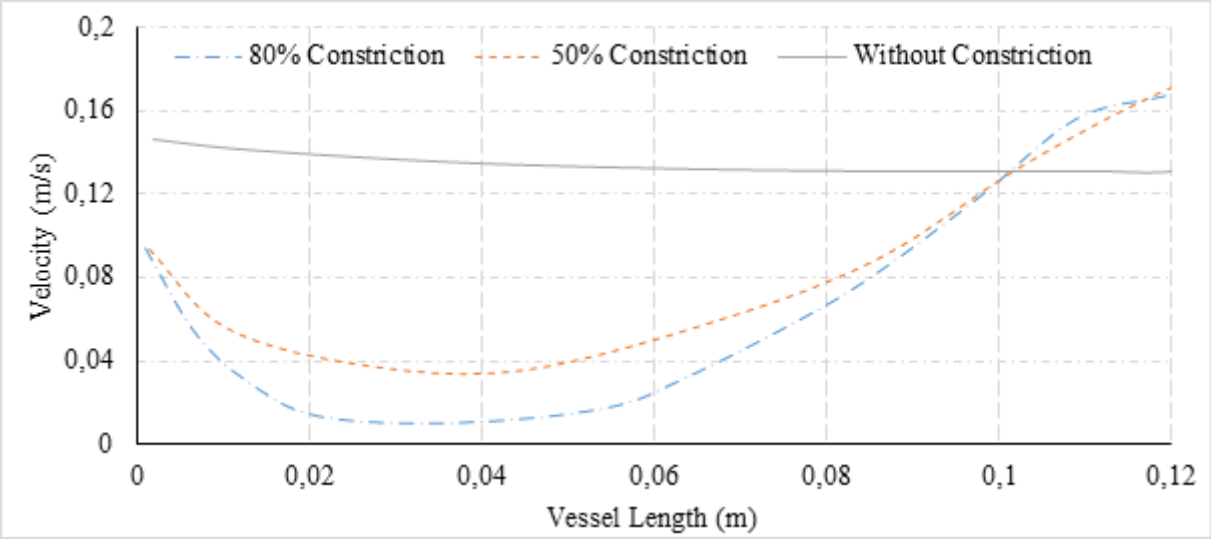

Figure 8. Velocity values before the furcation for different conditions

As seen from the pressure values, the effect of pressure is also evident within the entire tissue of the vessel wall. The shear stress values of the wall grid due to this pressure are given in Figure 9. In this case, the wall tissue will not bear this pressure and will be on the verge of tearing. As seen from the deformation values, the effect of pressure inside the tissue of the vessel wall is also evident; with the increase in the amount of relaxation, the pressure increases. In Figure 10,

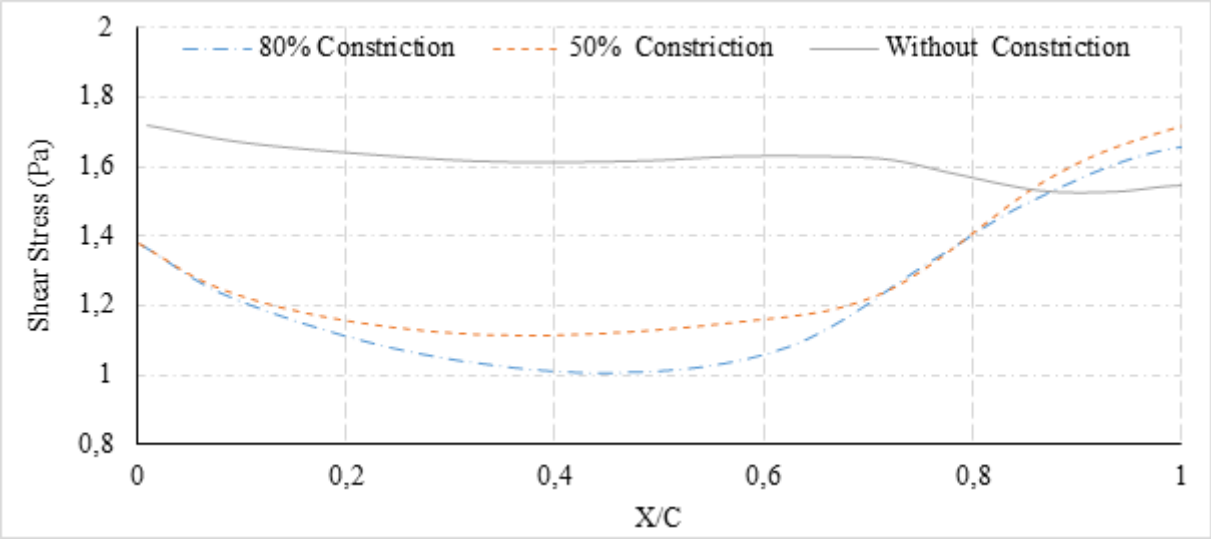

Figure 9. Shear stress values before the flow crossroads on the wall for different

the pressure values inside the vessel are analyzed for different states. By approaching the area before the constriction, due to the increase in pressure, the flow encounters an increase in pressure, which acts like the flow inside the nozzle in the constriction area, and more pressure is observed in the flow of the constriction area. This increase in pressure continues to the furcation area, which causes an increase in friction and shear stress. In the case where the outlet of the vessel is narrowed, this increase in pressure is greater. Shear stress is a critical factor in the development of thrombosis. Low shear stress (< 0.4 Pa) promotes platelet adhesion, whereas high shear stress (> 1.0 Pa) potentially causes endothelial damage. The shear stress values observed in this study, particularly near occlusions, fall within these clinically relevant ranges.

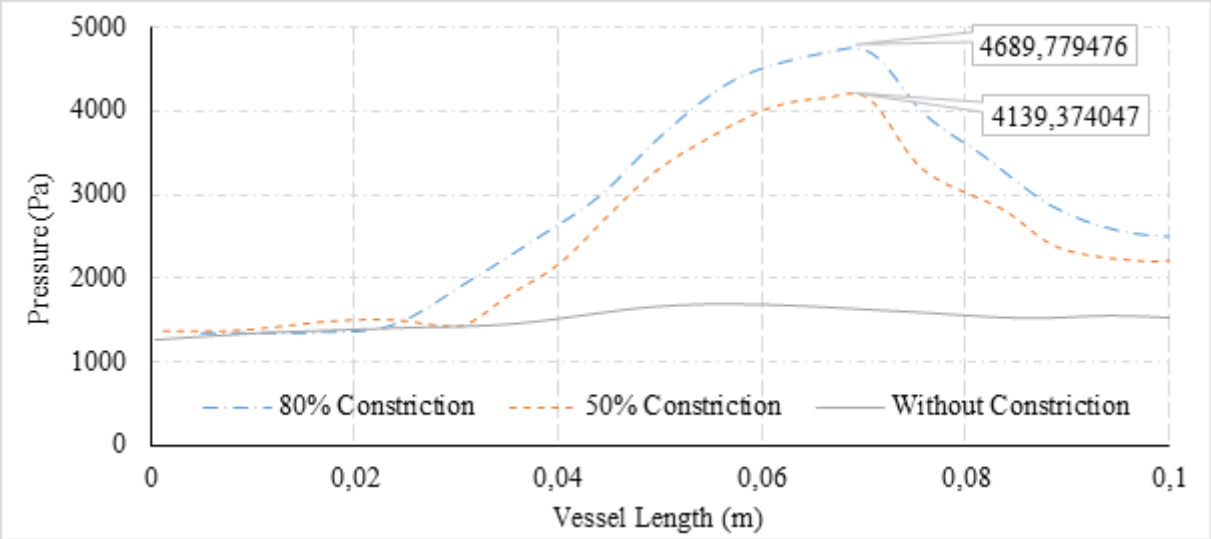

Figure 10. Velocity values before the furcation for different conditions

When the highest pressure values near the occlusions are concerned, the maximum pressure was found to be 4139,37 Pa for the 50% constriction case, it reached 4689,78 Pa for the 80% constriction case. These elevated pressure values highlight the increased risk of vessel wall damage in highly occluded vessels. The pressure values suggest that the occlusion exerts pressure on the entire vessel wall, clearly indicating that clogging causes a sharp pressure increase in the vessel just before the stenosis.

4 Conclusion

The stress–strain relationship in the blood does not follow a single relationship. This analysis depends on the dimensions of the vessel compared to the dimensions of the particles present in plasma (red and white blood cells, and platelets). The behavior of blood flow in vessels with a large internal diameter adheres to well-established hemodynamic principles, where inertial forces dominate viscous forces, and the continuum assumption remains valid. To achieve the objectives of the research, the numerical studies carried out in this field are first discussed, and in this part, the main focus has been on the research carried out using Ansys software. In the second part, the computational studies performed on the blood flow are discussed, and then the governing equations are explained. Furthermore, the vessel model was selected from reliable sources to ensure the validity of the simulation data. The results indicate the approximate accuracy of the non-Newtonian model used. Continuing this research, vessel occlusion models with varying occlusion sizes have been analyzed. The effect of pressure on the vessel wall tissue is evident. For small occlusions, large vessels can withstand the pressure. Although the software cannot simulate rupture, the vessel wall tissue appears capable of tolerating up to 50% stenosis.

In a vessel with 80% constriction of the internal diameter and a narrowed outlet, pressure values indicate high pressure intensity and velocity heterogeneity. This leads to a significant increase in shear stress near the constriction while the vessel flow exerts pressure on the wall. Wall mesh deformation due to this pressure suggests that the wall tissue would not withstand this level of pressure and would be at the threshold of tearing.

Velocity values within the vessel are analyzed under different conditions. As the flow approaches the constricted area, velocity sharply decreases due to increased pressure. Within the constriction, the flow behaves similarly to that inside a nozzle, resulting in higher fluid velocity in the narrowed region of the vessel.

This study highlights the importance of accurately modeling non-Newtonian blood behavior and vessel occlusion to understand the hemodynamic risk factors associated with CVDs.
The main findings of the study can be summarized as follows:

- It was observed that blood modeled as a non-Newtonian fluid exhibited significant differences in flow patterns compared to the Newtonian assumption and that the Carreau-Yasuda model played a critical role in determining the flow dynamics in high shear stress regions near the stenosis.
- The fact that the maximum WSS values were significantly higher in non-Newtonian flows indicated the importance of using the Carreau-Yasuda model to consider the shear thinning behavior of blood in hemodynamic studies.
- It was observed that the narrowing of the vessel significantly changed the flow characteristics of the blood. In the case of 50% and 80% constrictions, the axial velocity in the non-planar branch decreased, while the velocity and, hence, the pressure increased in the furcation region, which led to an increase in the critical factor of wall shear stress.
- When the velocity distributions within the vessel were evaluated, it showed significant heterogeneity, especially in the regions downstream of the occlusion, which could worsen the vascular damage due to hemodynamic risk factors such as flow separation, recirculation, and turbulence.
  - The use of the k-ω SST turbulence model has been shown to provide accurate resolution of near-wall flow physics and adverse pressure gradients, which are critical for capturing complex flow patterns in narrow vessels

5 Limitations

Although this study provides valuable information on the hemodynamics of the constricted vessels, the study is limited by the fact that the viscoelastic effects of blood and vessel walls are neglected, which may affect the flow dynamics, especially in highly stenotic regions. Another limitation is that the study does not include experimental validation.

6 Future Research

To take this research further, future studies can use viscoelastic models that take into account the elastic behavior of blood and vessel walls. Numerical results can be validated with experimental data obtained by techniques such as MRI or ultrasound. The effects of different turbulence models, such as Large Eddy Simulations and Reynold Stress Model on the accuracy of hemodynamic predictions can be investigated.

Declarations

Use of AI tools

The authors declare that they have not used Artificial Intelligence (AI) tools in the creation of this article.

Data availability statement

No Data associated with the manuscript.

Ethical approval (optional)

The authors state that this research complies with ethical standards. This research does not involve either human participants or animals.

Consent for publication

Not applicable

Conflicts of interest

The authors declare that they have no conflict of interest.

Funding

No funding was received for this research.

Author's contributions

M.M.: Conceptualization, Methodology, Investigation, Data Curation, Formal Analysis, Writing-Original draft, Software, Visualization, Validation. İ.K.: Resources, Supervision, Writing-Reviewing and Editing. M.K.Y.: Methodology, Investigation, Data Curation, Formal Analysis, Validation, Writing-Original Draft, Writing-Reviewing and Editing. All authors discussed the results and contributed to the final manuscript.

Acknowledgements

Not applicable

References

[1] Pontrelli, G. Pulsatile blood flow in a pipe. *Computers & Fluids*, 27(3), 367-380, (1998). [CrossRef]

[2] Gijsen, F.J.H. *Modeling of Wall Shear Stress in Large Arteries.* Ph.D. Thesis, Technische Universiteit Eindhoven, (1998). [https://doi.org/10.6100/IR510253]

[3] Nathan, D.M. Long-term complications of diabetes mellitus. *New England Journal of Medicine*, 328(23), 1676-1685, (1993). [CrossRef]

[4] Kannel, W.B. and McGee, D.L. Diabetes and cardiovascular disease: the Framingham study. *Jama*, 241(19), 2035-2038, (1979). [CrossRef]

[5] Ishikawa, T., Guimaraes, L.F., Oshima, S. and Yamane, R. Effect of non-Newtonian property of blood on flow through a stenosed tube. *Fluid Dynamics Research*, 22, 251, (1998). [CrossRef]

[6] Nichols, W.W., O'Rourke, M., Edelman, E.R. and Vlachopoulos, C. *McDonald's Blood Flow in Arteries: Theoretical, Experimental and Clinical Principles*. CRC Press: USA, (2022). [CrossRef]

[7] Kumar, G., Kumar, H., Mandia, K., Zunaid, M., Ansari, N.A. and Husain, A. Non-Newtonian pulsatile flow through an artery with two stenosis. *Materials Today: Proceedings*, 46(20), 10793-10798, (2021). [CrossRef]

[8] Ahmed, S.A. and Giddens, D.P. Pulsatile poststenotic flow studies with laser Doppler anemometry. *Journal of Biomechanics*, 17(9), 695-705, (1984). [CrossRef]

[9] Siouffi, M., Peronneau, P., Wildt, E. and Pelissier, R. Modifications of flow patterns induced by a vascular stenosis. In Proceedings, *of Euromech*, pp. 73-88, Paris, France, (1977, November).

[10] Tu, C., Deville, M., Dheur, L. and Vanderschuren, L. Finite element simulation of pulsatile flow through arterial stenosis. *Journal of Biomechanics*, 25(10), 1141-1152, (1992). [CrossRef]

[11] Marshall, I., Zhao, S., Papathanasopoulou, P., Hoskins, P. and Xu, X.Y. MRI and CFD studies of pulsatile flow in healthy and stenosed carotid bifurcation models. *Journal of Biomechanics*, 37(5), 679-687, (2004). [CrossRef]

[12] Steinman, D.A., Thomas, J.B., Ladak, H.M., Milner, J.S., Rutt, B.K. and Spence, J.D. Reconstruction of carotid bifurcation hemodynamics and wall thickness using computational fluid dynamics and MRI. *Magnetic Resonance in Medicine*, 47(1), 149-159, (2002). [CrossRef]

[13] Seo, T. Hemodynamic characteristics in the human Carreautid artery model induced by blood-arterial wall interactions. *International Journal of Biomedical and Biological Engineering*, 7(5), 153-158, (2013).

[14] Biswas, D. and Laskar, R.B. Steady flow of blood through a stenosed artery: A non-Newtonian fluid model. *Assam University Journal of Science & Technology: Physical Sciences and Technology*, 7(2), 144-153, (2011).

[15] Chaichana, T., Sun, Z. and Jewkes, J. Computation of hemodynamics in the left coronary artery with variable angulations. *Journal of Biomechanics*, 44(10), 1869-1878, (2011). [CrossRef]

[16] Dong, J., Sun, Z., Inthavong, K. and Tu, J. Fluid-structure interaction analysis of representative left coronary artery models with different angulations. In Proceedings, *Computing in Cardiology 2013*, pp. 5-8, Zaragoza, Spain, (2013, September).

[17] Van Leeuwen-van Zaane, F., de Bruijn, H.S., Sterenborg, H.J.M.C. and Robinson, D.J. The effect of fluence rate on the acute response of vessel diameter and red blood cell velocity during topical 5-aminolevulinic acid photodynamic therapy. *Photodiagnosis and Photodynamic Therapy*, 11(2), 71-81, (2014). [CrossRef]

[18] Botti, L., Paliwal, N., Conti, P., Antiga, L. and Meng, H. Modeling hemodynamics in intracranial aneurysms: Comparing accuracy of CFD solvers based on finite element and finite volume schemes. *International Journal for Numerical Methods in Biomedical Engineering*, 34(9), e3111, (2018). [CrossRef]

[19] Eum, T.S., Seo, I.W., Shin, E.T. and Song, C.G. Development and application of a user-friendly general-purpose predictive simulation tool for two-dimensional flow analysis. *Environmental Modelling & Software*, 163, 105665, (2023). [CrossRef]

[20] La Porta, G., Leonardi, A., Pirulli, M., Cafaro, F. and Castelli, F. Time-resolved triggering and runout analysis of rainfall-induced shallow landslides. *Acta Geotechnica*, 19, 1873-1889, (2024). [CrossRef]

[21] Tabe, R., Ghalichi, F., Hossainpour, S. and Ghasemzadeh, K. Laminar-to-turbulence and relaminarization zones detection by simulation of low Reynolds number turbulent blood flow in large stenosed arteries. *Bio-medical Materials and Engineering*, 27(2-3), 119-129, (2016). [CrossRef]

[22] Mahalingam, A., Gawandalkar, U.U., Kini, G., Buradi, A., Araki, T., Ikeda, N. et al. Numerical analysis of the effect of turbulence transition on the hemodynamic parameters in human coronary arteries. *Cardiovascular Diagnosis and Therapy*, 6(3), 208-220, (2016). [CrossRef]

[23] Mohd Saat, F.A. and Jaworski, A.J. Numerical predictions of early stage turbulence in oscillatory flow across parallel-plate heat exchangers of a thermoacoustic system. *Applied Sciences*, 7(7), 673, (2017). [CrossRef]

[24] Carvalho, V., Rodrigues, N., Lima, R.A. and Teixeira, S.F.C.F. Modeling blood pulsatile turbulent flow in stenotic coronary arteries. *International Journal of Biology and Biomedical Engineering*, 14(22), 160-168, (2020). [CrossRef]

[25] Chen, J. and Lu, X.Y. Numerical investigation of the non-Newtonian pulsatile blood flow in a bifurcation model with a non-planar branch. *Journal of Biomechanics*, 39(5), 818-832, (2006). [CrossRef]

Mathematical Modelling and Numerical Simulation with Applications (MMNSA)
(https://dergipark.org.tr/en/pub/mmnsa)

How to cite this article: Mustafaoğlu, M., Kotçioğlu, İ. & Yeşilyurt, M.K. (2025). Numerical analysis of the three-dimensional model of pulsatile and non-Newtonian blood flow in a carotid artery with local occlusion. *Mathematical Modelling and Numerical Simulation with Applications*, 5(1), 97-116. https://doi.org/10.53391/mmnsa.1522021

Mathematical Modelling and Numerical Simulation with Applications, 2025, 5(1), 117–142

https://dergipark.org.tr/en/pub/mmnsa
ISSN Online: 2791-8564 / Open Access
https://doi.org/10.53391/mmnsa.1503311

RESEARCH PAPER

Fractional-order model of the post-disaster period: study on the earthquakes in Türkiye

Teslima Daşbaşı [1,‡] and **Bahatdin Daşbaşı** [2,*,‡]

[1]Kayseri University, Bünyan Vocational School, Department of Property Protection and Security, 38600 Kayseri, Türkiye, [2]Kayseri University, Faculty of Engineering, Architecture and Design, Department of Engineering Basic Sciences, 38280 Kayseri, Türkiye

*Corresponding Author
‡teslimadasbasi@kayseri.edu.tr (Teslima Daşbaşı); bdasbasi@kayseri.edu.tr (Bahatdin Daşbaşı)

Abstract

In this study, the mathematical model that examined the relationships between the variables of the population that continued to live in the disaster area, the population that migrated to another region, the number of newly built independent sections in the disaster area the post-disaster, and the socio-economic development index (SEDI) of the disaster area is expressed through fractional-order differential equations (FODEs) and qualitative analysis of the model is carried out. Furthermore, the relationship between migrated and non-migrated populations is presented in the model with four different functional responses. In real-world applications of the model, some earthquakes in Türkiye, which are similar to each other in many ways, are taken into account. Therefore, data after the Gölcük earthquake in 1999 are used, and parameters, derivative order, and functional response are determined by considering the minimum root mean squared error (RMSE). Then, the performance of the proposed model with these values is shown in the Elbistan earthquake in 2023. Finally, the 5-year and 10-year estimates of the non-migratory population, the migrated population, the number of newly built independent sections, and the SEDI index values are presented for Elbistan.

Keywords: Fractional-order differential equation; functional response; earthquakes; socio-economic development index; root mean squared error

AMS 2020 Classification: 26A33; 34A08; 92D25

1 Introduction

It is known that disasters have occurred in every period of history. Disasters can be defined as ecological events that suddenly change the normal life order of the society, result in loss of life and property, and create a need for external assistance depending on their size and speed of occurrence. They, which cannot be determined exactly where, when and how they will occur, have

➤ **Received:** 24.06.2024 ➤ **Revised:** 27.01.2025 ➤ **Accepted:** 12.03.2025 ➤ **Published:** 31.03.2025

similar following effects in terms of their consequences: economic losses and social psychological destruction, especially physical losses [1]. Disaster types, whether natural or not, are given in Table 1. There has been an increasing trend in disaster events globally from 1900 to 2022. In this context, the number of disasters averaged 56 events per year in the 1960s (reached 81 in 1966), while the average number of disasters in the last decade (2012-2022) reached 363 events per year. In addition, a total of 30748 deaths were recorded, an estimated 186 million people were negatively affected, and according to available data, these disasters caused damage worth USD 223.84 billion due to 388 disasters recorded worldwide in 2022 which are extreme heat, flood, storm, drought, forest fire, landslide, earthquake, extreme temperature and volcanic activities [2].

Table 1. Types of disasters [3]

Natural disasters		**Human-Made Disasters**
Slow-developing natural disasters	*Sudden Natural Disasters*	
-Severe cold -Drought -Famine etc.	-Earthquake -Floods -Landslides, rock falls -Avalache -Storms, tornadoes -Volcanoes -Fires etc.	-Nuclear, biological, chemical accidents -Terrorism -Transportation accidents -Industrial accidents -Accidents caused by overcrowding -Migrants and displaced persons etc.

Today, disaster management has become an important issue due to the loss of life and large financial burden. In fact, our societies, regardless of their level of development, are still not adequately prepared for a natural or human disaster and its possible domino effects [4]. Therefore, the necessary precautions to be taken disaster-before in order to minimize the loss of life and property, as well as the necessary measures to be taken for the society to return to its normal life disaster-after, are of vital importance.

Disasters such as earthquakes and nuclear explosions or acts of terrorism in another area also occur suddenly and surprisingly. In such events, due to the effect of surprise and fear, reactions are more instinctive and individuals often tend to leave the area they are in. Migration is often considered one of the primary responses to natural disasters. Existing literature broadly recognizes the fact that disaster victims migrate from affected areas [5]. In this context, the return of individuals, who survived and migrated the post-disaster to the same region, is possible by meaning of socio-economic development of the disaster area and by building enough settlements to meet the needs. Socio-economic development involves parameters such as demography, technology, health, education, economic development, financial capacity, competitive structure and quality of life, and the data on these parameters can provide information at the regional level about what social needs are and to what extent they are met [6].

Although an earthquake is a natural event, it is inevitable that it will turn into a disaster, especially considering its duration and magnitude and the precautions taken in advance. When disasters are mentioned in Türkiye, the first thing that comes to mind is earthquakes due to its location in an earthquake zone. In this region, major earthquakes have occurred in almost every period of history, resulting in many deaths and a wave of migration. In the last 100 years, 16 earthquakes of magnitude 7 Mw and above have occurred in Türkiye, as seen Figure 1. 124558 people lost their lives in these earthquakes, and the number of buildings with moderate and more damage is about 1037108 [7]. Reverse migration after a disaster is possible with the development of the disaster area in many areas. SEDI focusing on 12 basic indicators of economic development and 12 basic indicators of social development in terms of evaluation is one of the measurable parameters

in terms of the development level of a region. Socio-Economic Development Ranking Studies are analysis studies that objectively measure and compare the socio-economic development of regions, provinces and districts in Türkiye in order to provide input to policies, strategies and public practices [8]. District SEDI studies conducted to date have been published seven times between 1966-2022. In this study, changes in the populations of individuals who survived the disaster and some of whom migrated to other regions were mathematically modeled through FODEs according to the SEDI and the independent section numbers.

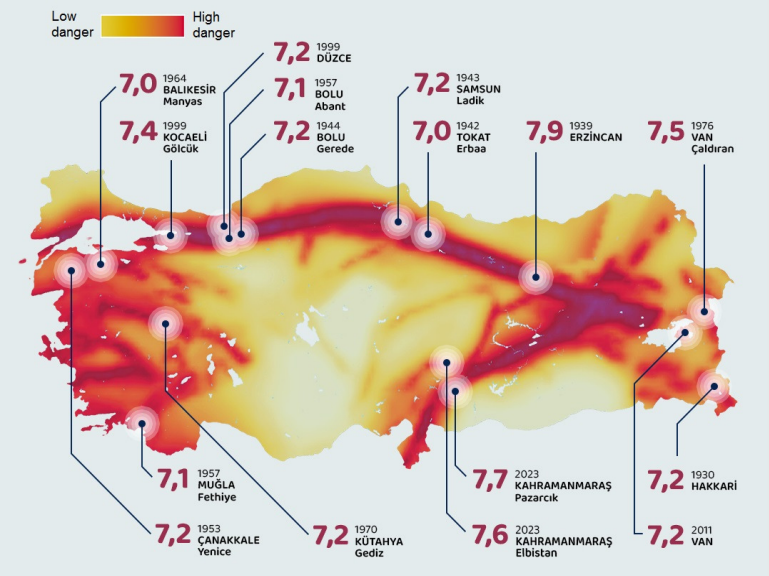

Figure 1. Earthquakes of magnitude 7 Mw and above in the last 100 years in Türkiye [7]

In a scientific investigation, we explore and therefore understand our real world by observing, collecting data, finding rules within or among them, then we discover the truth behind this phenomenon and want to apply it to predict the future. This process is mostly through mathematical modeling. Such modeling is differential equations, which are well known for describing relationships between variables and their derivatives, and so usually used for planning, prevention and control scenarios.

Fractional calculus has been an old but increasingly important subject of mathematics since the 17th century. Fractional integral and differential operators can be thought of as generalized forms of integer order integral and derivative operators. The concept of memory is important for fractional calculation. In a memory system, the input must remember its previous values in order to indicate the current value of the output. When considering the modeling of various memory events, it is often stated that a memory process consists of two stages; It is a short-term state that can be presented through fractional derivation with permanent retention [9, 10]. Recently, an increasing number of studies and applications of fractional order systems have been presented in many fields of science and engineering [11–17]. Many various descriptions of fractional derivatives are encountered in the literature, such as Riemann-Liouville, Caputo, Caputo-Fabrizio and Atangana-Baleanu [18]. Caputo's fractional operator is possibly the most significant in fractional analysis since its derivative is the most appropriate fractional operator to use in modeling a real-world problem. Talking about real problems, the Caputo derivative is considerable practical because it allows conventional initial and boundary conditions to be involved in the derivation and the derivative of a constant is zero, which is not the circumstance with the Riemann-Liouville fractional derivative [19]. In the manuscript, Caputo's fractional

definition is considered.

In the mathematical and computer literature, scholars have mainly focused on modeling crowd dynamics and collective panic in the event of a catastrophic event [20, 21] or simulating movements to model pedestrian evacuation inside buildings [22]. Let's consider a sudden disaster that causes loss of life and property, such as an earthquake, nuclear explosion, or flood. There are few mathematical modeling studies in the literature that examine the return of individuals living in a region to their normal lives in the disaster area according to their behavior and housing needs. In addition, when looking at the studies on this subject in the literature, the number of mathematical models with ordinary differential equations (ODEs)is very low, and no mathematical model with FODEs was found.

Kumar et al. [23] examined the population in a region after a flood disaster through the ODE model, based on the classical SIR model, in which individuals are divided into susceptible, affected, survivor, or deceased compartments. They only presented a qualitative analysis of this model, which is widely used in different fields, without developing it.

Verdière et al. [24] modeled by ODE the temporal dynamics of human behavior during a catastrophic event. They proposed so-called PCR mathematical models that simulate sequences of individual behaviors called as Panic, Controlled, and Reflex according to the type of threat, domino effects, and the local environment. In their model, the population that continues its normal daily life is denoted by Q, individuals with uncontrolled behavior are denoted by r and p, and individuals with controlled behavior are denoted by c. At the beginning, the total population N is in Q_1, subpopulation of Q. A post-disaster occurs, all individuals move to compartment r at a certain rate, individuals in r, those showing panic behavior at certain rates, move to compartment p, and those showing controlled behavior move to compartment c. Finally, at a certain rate, there is a transition from c to the Q_2 compartment in which individuals continue their daily life. Furthermore, the authors assumed reciprocal transition between r, c, and p compartments. They numerically illustrated their model for the earthquake in Haiti and Japan in 2010.

In our proposed model, the interaction between the population that migrated and those that did not migrate post-disaster was expressed with different functional responses, and then the functional response closest to the real data was determined. Therefore, the reason for using four responses, which are frequently mentioned in the literature, is to increase the performance of the model by determining the response that gives the minimum RMSE value. In fact, four different mathematical models are presented as a single model in the manuscript.

Earthquakes, landslides, floods, volcanic eruptions, hurricanes, and tornadoes, which have been repeated countless times since the world was formed 4.6 billion years ago, are actually ordinary events that give our planet its current appearance. Therefore, disasters are intertwined with humanity and are inevitable. Many researchers around the world have carried out many studies on the effects of disasters. However, there are very few studies in the literature on post-disaster migration mobility and changes in population projection, which aim to determine in advance the size of the workforce that will be needed in the future and to prepare the infrastructure and opportunities accordingly.

In this study, the scenario immediately after a disaster, such as an earthquake or flood, that causes a sudden loss of life and property is discussed. All individuals living in the region naturally exhibit reflexive behavior. Some of them migrate to another region due to a lack of shelter or panic behavior, and their population size is shown as M in the model. The rest of them continue to live in the disaster area by exhibiting controlled behavior, and their population size in the model is denoted by S. The number of new buildings built to replace independent sections that were demolished or decided to be demolished after the disaster is also indicated by R. Moreover, the SEDI of the region is presented with I. In this sense, the relationship among the dimensions of the

variables S, M, R, and I has been modeled mathematically through FODEs in the Caputo meaning. In this way, due to the definition of fractional derivative, the natural delay in the relevant disaster scenario was also taken into account.
Therefore, the differences in the presented study from the literature can be listed as follows:

- FODEs are used in the model.
- The different functional responses are used in the model.
- According to the real values, the parameter values and the derivative-order with minimum RMSE have been obtained.
- Predictions are made for future population projection, SEDI, and independent section numbers.

The remainder of the study is organized as follows.

- Some basic definitions and theorems used in the definition and analysis of the model are given in Section 2.
- The proposed mathematical model is formulated in Section 3. It was also presented respectively in:
  - The positivity, boundedness, and non-negative of solutions of the model,
  - Different possible equilibrium points of the model and,
  - Stability analysis of the equilibrium points.
- The estimation of the parameters of the proposed model is given in Section 4. Therefore, the data set was created, parameters with minimum RMSE were obtained, the fractional order was determined to obtain lower RMSE, and numerically simulated results for Elbistan of our proposed model have been presented.
- Finally, in Section 5, we have presented some of the main outcomes of the present work.

2 Preliminaries and definitions

In this section, we have discussed some functional answers for the Lotka-Volterra system. Later, we present some useful definitions and properties of fractional derivatives. In addition, some properties regarding the existence and signs of the roots of the polynomials used in the study are given.

Definition 1 *The Lotka-Volterra predator-prey model consists of two differential equations, the first equation for the prey and the second equation for the predator, and is as follows:*

$$\frac{dx}{dt} = ax - \gamma xy \ \text{ and } \ \frac{dy}{dt} = -cy + exy,$$

where $a, \gamma, c, e > 0$. *The terms* $\gamma xy = F(x,y)$ *and* $exy = G(x,y)$ *in this system are called functional and numerical responses, respectively [25].*
Some functional responses are Holling Type I for $F(x,y) = \gamma xy, \gamma > 0$, *Holling Type II for* $F(x,y) = \frac{\gamma xy}{x+b}\ \gamma, b > 0$, *Holling Type III for* $F(x,y) = \frac{\gamma x^2 y}{x^2+b}\ \gamma, b > 0$ *and Ivlev for* $F(x,y) = \gamma y\left(1 - e^{bx}\right)\ \gamma, b > 0$ *[26, 27].*

In this study, the above-mentioned functional responses were used for the relationship between post-disaster migratory and non-migratory populations. The functional responses used in the manuscript can be briefly explained as follows. Let us consider two species that have certain sizes at reference time t and, moreover, interact with each other. Functions describing their varying population sizes are modeled in a continuous framework. Changes depending on the relationship between these functions can be explained by functional response. Functional response [28] is one

of the oldest and most common mathematical constructs used to describe and make prospective predictions about the nutritional interaction between a consumer and a resource. This response describes the feeding rate of a consumer based on its density in its environment. The most common of these are Holling type I-III responses [27] and Ivlev response [29].

Type I functional response supposes a linear increase in intake rate with food density, either for all food densities or only for maximum food densities, beyond which the intake rate is constant. Linear increase reckons for the following: the time a consumer needs to process a food item is neglectable or that consuming food does not prevent foraging.

Type II functional response is qualified by a slowing rate of intake, following from the presumption that the consumer is restricted by his or her food processing capacity. Also, the functional response is commonly modeled through a rectangular hyperbola.

Type III functional response is alike to type II in that at high levels of prey density, saturation occurs. At low prey density levels, the graphical connection of the number of prey consumed and the density of the prey population is a super linearly increasing function of prey consumed by predators.

In Ivlev's functional response, the maximal rate of predation and decline in hunting drive are represented by the positive constant γ and b, respectively [30].

Definition 2 *(Caputo Fractional Derivative) [31]* $0 < \phi \leq 1$ *for the function* $u: C^n[0,\infty] \to \mathbb{R}$ *is defined as*

$$ {}^{C}D_t^{\phi}(u(t)) = \frac{1}{\Gamma(n-\phi)} \int_0^t \frac{1}{(t-z)^{\phi+1-n}} \frac{d^n}{dz^n} u(z)dz, \tag{1} $$

where $C^n[0,\infty]$ *is a* n *times continuously differentiable function and Gamma function is defined by* $\Gamma()$ *such that* $n-1 < \phi < n$.

Lemma 1 *[32] Let* $0 < \phi \leq 1$. *Suppose that* $u(t) \in C[a,b]$ *and* ${}_{t_0}^{C}D_t^{\phi} u(t) \in C[a,b]$.

- *If* ${}_{t_0}^{C}D_t^{\phi} u(t) \geq 0, \forall t \in (a,b)$, *then* $u(t)$ *is a non-decreasing function.*
- *If* ${}_{t_0}^{C}D_t^{\phi} u(t) \geq 0, \forall t \in (a,b)$, *then* $u(t)$ *is a non-increasing function.*

Theorem 1 *[33, 34] Consider the following fractional-order system:*

$$ \begin{aligned} {}^{C}D_t^{\phi}(u(t)) &= f(t,u(t)), \\ u(t_0) &= u_0, \end{aligned} \tag{2} $$

where ${}^{C}D_t^{\phi}$ *is Caputo's derivative of the order* $0 < \phi \leq 1$ *and* $f(t,u(t)) : \mathbb{R}^+ \times \mathbb{R}^n \to \mathbb{R}^n$ *is a vector field. The equilibrium points of this system are locally asymptotically stable (LAS) if all eigenvalues* λ_i *of the Jacobian matrix* $\frac{\partial f(t,u)}{\partial u}$ *evaluated at the equilibrium points satisfy the following condition:*

$$ |arg\lambda_i| > \frac{\phi\pi}{2}. \tag{3} $$

Let's consider system (2) *for* $u = (u_1\ u_2)^T$. *In this case, the characteristic equation is*

$$ p(\lambda) = \lambda^2 + a_1\lambda + a_2 = 0. \tag{4} $$

The conditions for LAS of the equilibrium point are either Routh–Hurwitz conditions given as

$$a_1, a_2 > 0, \tag{5}$$

or:

$$a_1 < 0,\ 4a_2 > (a_1)^2,\ \left| tan^{-1}\left(\frac{\sqrt{4a_2-(a_1)^2}}{a_1}\right)\right| > \frac{\alpha\pi}{2}, \tag{6}$$

[35].

Theorem 2 *(Descartes's Rule of Signs) [36] "Let*

$$p(x) = a_0x^{b_0} + a_1x^{b_1} + \cdots + a_nx^{b_n}, \tag{7}$$

denote a polynomial with nonzero real coefficient a_i, where b_i are integers satisfying $0 \leq b_0 < b_1 < b_2 < \cdots < b_n$. Then the number of positive real zeros of $p(x)$ (counted with multiplicities) is either equal to the number of variations in sign in the sequence $a_0, a_1, \ldots, a_n$ of the coefficients or less than that by an even whole number. The number of negative zeros of $p(x)$ (counted with multiplicities) is either equal to the number of variations in sign in the sequence of the coefficients of $p(-x)$ or less than that by an even whole number."

3 Methodology

Fractional-order model

Let t denote the time parameter and the independent variable. The dependent variables whose changes are being examined post-disaster in the proposed model consisting of FODEs in the Caputo meaning are given in Table 2. In addition, the parameters used in the model and whose

Table 2. State variables in the proposed mathematical model

Variable	Definition	Explanation
$S(t)$	The population number at time t who continues to live the post-disaster in the region where they lived before the disaster	These are people who, the post-disaster, continue to live in their pre-disaster residence or a temporary place in the same area
$M(t)$	The population number at time t migrating to another region the post-disaster	These are people settled another region by leaving the area they were in before the disaster, temporarily or permanently, the post-disaster
$R(t)$	The number at time t of newly built independent sections	These are the number of newly built independent sections to replace buildings that were demolished or decided to be demolished post-disaster
$I(t)$	The SEDI at time t	Socio-Economic Performance Index, which is a measurable indicator of the development of the disaster area

approximate values will be estimated later in numerical studies by using the actual values of the variables are given in Table 3.

Table 3. Parameters used in the mathematical model and their meanings

Parameter	Definition
θ_S	Constant increase rate of the population living in the region where they lived before the disaster,
η	The return rate to the disaster area with respect to SEDI with controlled behavior of individuals who migrated with panic behavior,
μ	The return rate of individuals to the region where they were before the disaster, thanks to the newly built independent sections,
$f_i(M)$	Functions for $i = 1, 2, 3, 4$, which represent the functional and numerical responses, are Holling Type 1-3 and Ivlev functions, respectively,
γ	As a result of the contact between migrated and non-migrated populations, the rate of return of the migrated population to the region where they were before the disaster,
ε	Migration rate to the region the post-disaster according to the SEDI,
v_S	Natural mortality rate of the population living in the destruction zone the post-disaster,
θ_M	Constant increase rate of the migrated population,
v_M	Natural mortality rate of the migrated population the post-disaster,
r_R	The increase rate of newly built independent sections,
C_R	Carrying capacity of the newly built independent section,
σ	The rate of independent sections built in proportion to SEDI,
β	Decrease rate of newly built independent sections,
θ	Constant rate of SEDI,
ω	Decrease rate of SEDI.

Thus, the proposed fractional-order model in the Caputo meaning is

$$\begin{aligned}
&{}_{t_0}^{C}D_t^{\phi} S = \theta_S + \eta MI + \mu MR + \gamma S f_i(M) + \varepsilon I - v_S S,\\
&{}_{t_0}^{C}D_t^{\phi} M = \theta_M - \eta MI - \mu MR - \gamma S f_i(M) - v_M M,\\
&{}_{t_0}^{C}D_t^{\phi} R = r_R R\left(1-\frac{R}{C_R}\right) + \sigma RI - \beta R,\\
&{}_{t_0}^{C}D_t^{\phi} I = \theta_I - \omega I,\\
&S \equiv S(t),\ M \equiv M(t),\ R \equiv R(t),\ I \equiv I(t),\\
&S(t_0) = S_0,\ R(t_0) = R_0,\ M(t_0) = M_0, I(t_0) = I_0 \text{ such that } S_0,\ R_0, M_0, I_0 > 0,
\end{aligned} \tag{8}$$

where $t \geq t_0 \geq 0, \phi \in (.0, 1|$. and ${}_{t_0}^{C}D_t^{\phi}$ denotes the Caputo operator. The parameters in system (8) satisfy

$$\theta_S, \eta, \mu, \gamma, \varepsilon, v_S,\ \theta_M, v_M, r_R, C_R, \sigma, \beta, \theta, \omega > 0. \tag{9}$$

Additionally, mathematical expressions of the functions $f_i(M)$ for $i = 1, 2, 3, 4$ are shown in Table 4.

Table 4. Functional responses used in Eqs. (8) for $b>0$

Response Type	Function $(f_i(M))$
Holling Type-1	$f_1(M) = M$
Holling Type-2	$f_2(M) = \frac{M}{M+b}$
Holling Type-3	$f_3(M) = \frac{M^2}{M^2+b}$
Ivlev Type	$f_4(M) = 1 - e^{-bM}$

Theorem 3 *There is one solution of the equation in* (8) *with non-negative initial conditions.*

Proof Existence and uniqueness of system (8) will be displayed in the map $\Omega \times (0;\ T]$ where

$$\Omega = \{(S, M, R, I) \in \mathbb{R}^4_+ : \max(|S|, |M|, |R|, |I|) \leq \zeta\}. \tag{10}$$

Reference [37] is taken into account for the proof. We express $X = (S, M, R, I)$ and $\overline{X} = (\overline{S},\ \overline{M}, \overline{R}, \overline{I})$. Consider a mapping

$$G(X) = (G_1(X), G_2(X), G_3(X), G_4(X)), \tag{11}$$

and

$$\begin{aligned} G_1(X) &= \theta_S + \eta MI + \mu MR + \gamma S f_i(M) + \varepsilon I - v_S S, \\ G_2(X) &= \theta_M - \eta MI - \mu MR - \gamma S f_i(M) - v_M M, \\ G_3(X) &= r_R R(1 - \tfrac{R}{C_R}) + \sigma RI - \beta R, \\ G_4(X) &= \theta - \omega I. \end{aligned} \tag{12}$$

First, consider the functions in (12). For any X, $\overline{X}$, one can find the followings by:

$$\|G(X) - G(\overline{X})\| = |(\theta_S + \eta MI + \mu MR + \gamma S f_i(M) + \varepsilon I - v_S S) - (\theta_S + \eta \overline{MI} + \mu \overline{MR} + \gamma \overline{S} f_i(\overline{M}) + \varepsilon \overline{I} - v_S \overline{S})| + |(\theta_M - \eta MI - \mu MR - \gamma S f_i(M) - v_M M) - (\theta_M - \eta \overline{MI} - \mu \overline{MR} - \gamma \overline{S} f_i(\overline{M}) - v_M \overline{M})| + |(r_R R(1 - \tfrac{R}{C_R}) + \sigma RI - \beta R) - (r_R \overline{R}(1 - \tfrac{\overline{R}}{C_R}) + \sigma \overline{RI} - \beta \overline{R})| + |(\theta - \omega I) - (\theta - \omega \overline{I})|,$$

$$\|G(X) - G(\overline{X})\| = |\eta MI - \eta \overbrace{(M\overline{I} - M\overline{I})}^{=0} - \eta \overline{MI} + \mu MR - \mu \overbrace{(M\overline{R} - M\overline{R})}^{=0} - \mu \overline{MR} + \gamma S f_i(M) - \gamma \overbrace{(\overline{S} f_i(M) - \overline{S} f_i(M))}^{=0} - \gamma \overline{S} f_i(\overline{M}) + \varepsilon I - \varepsilon \overline{I} - v_S S + v_S \overline{S}| + |-\eta MI - \eta \overbrace{(M\overline{I} - M\overline{I})}^{=0} + \eta \overline{MI} - \mu MR - \mu \overbrace{(\overline{R}M - \overline{R}M)}^{=0} + \mu \overline{MR} - \gamma S f_i(M) - \gamma \overbrace{(\overline{S} f_i(M) - \overline{S} f_i(M))}^{=0} + \gamma \overline{S} f_i(\overline{M}) - v_M M + v_M \overline{M}| + |r_R R - r_R \overline{R} - \tfrac{r_R}{C_R} R^2 + \tfrac{r_R}{C_R} \overline{R}^2 + \sigma RI - \sigma \overbrace{(R\overline{I} - R\overline{I})}^{=0} - \sigma \overline{RI} - \beta R + \beta \overline{R}| + |-\omega(I - \overline{I})|,$$

$$\|G(X) - G(\overline{X})\| = |+\eta M(I - \overline{I}) + \eta \overline{I}(M - \overline{M}) + \mu M(R - \overline{R}) + \mu \overline{R}(M - \overline{M}) + \gamma f_i(M)(S - \overline{S}) + \gamma \overline{S}(f_i(M) - f_i(\overline{M})) + \varepsilon(I - \overline{I}) - v_S(S - \overline{S})| + |-\eta M(I - \overline{I}) - \eta \overline{I}(M - \overline{M}) - \mu M(R - \overline{R}) - \mu \overline{R}(M - \overline{M}) - \gamma f_i(M)(S - \overline{S}) - \gamma \overline{S}(f_i(M) - f_i(\overline{M})) - v_M(M - \overline{M})| + |r_R(R - \overline{R}) - \tfrac{r_R}{C_R}(R - \overline{R})(R + \overline{R}) + \sigma R(I - \overline{I}) - \sigma \overline{I}(R - \overline{R}) - \beta(R - \overline{R})| + \omega |I - \overline{I}|,$$

and

$$\begin{aligned} \|G(X) - G(\overline{X})\| &\leq (v_S + 2\gamma f_i(M))|S - \overline{S}| + (2\mu \overline{R} + 2\eta \overline{I} + v_M)|M - \overline{M}| \\ &+ (2\mu M + r_R + \beta + \sigma \overline{I} + \tfrac{r_R}{C_R}(R + \overline{R}))|R - \overline{R}| \\ &+ (2\eta M + \varepsilon + \sigma R + \omega)|I - \overline{I}| + 2\gamma \overline{S} \overbrace{|f_i(M) - f_i(\overline{M})|}^{*}. \end{aligned} \tag{13}$$

If the expression marked * in Ineq. (13) is taken into account throughout Table 4, then we have

$$|f_i(M)-f_i(\overline{M})| = \left\{ \begin{array}{l} |M-\overline{M}| \text{ for } i=1, \\ \frac{b|M-\overline{M}|}{(M+b)(\overline{M}+b)} \leq \frac{|M-\overline{M}|}{b} \text{ for } i=2, \\ \frac{b(M+\overline{M})|M-\overline{M}|}{(M^2+b)(\overline{M}^2+b)} \leq \frac{2\zeta|M-\overline{M}|}{b} \text{ for } i=3, \\ \left\{ \begin{array}{l} \overbrace{|b(\overline{M}-M)+\frac{b^2(\overline{M}^2-M^2)}{2!}+\cdots+\frac{b^n(\overline{M}^n-M^n)}{n!}|}^{\text{by Taylor Expansion}} \\ |M-\overline{M}||b+\frac{b^2(\overline{M}+M)}{2!}+\cdots+\frac{b^n(\sum_{j=1}^{n}\overline{M}^{n-j}M^{j-1})}{n!}| \\ \leq |M-\overline{M}|(b+\frac{\zeta b^2}{1!}+\frac{\zeta^2 b^3}{2!}+\cdots+\frac{\zeta^{n-1}b^n}{(n-1)!}) \end{array} \right\} \text{for } i=4, \end{array} \right\},$$

and so,

$$|f_i(M)-f_i(\overline{M})| \leq \xi_M|M-\overline{M}|, \tag{14}$$

where

$$\xi_M = \max\left\{1, \frac{1}{b}, \frac{2\zeta}{b}, (b+\frac{\zeta b^2}{1!}+\frac{\zeta^2 b^3}{2!}+\cdots+\frac{\zeta^{n-1}b^n}{(n-1)!})\right\}.$$

In this case, Ineq. (14) is obtained as follows:

$$\|G(X)-G(\overline{X})\| \leq \varphi_1|S-\overline{S}|+\varphi_2|M-\overline{M}|+\varphi_3|R-\overline{R}|+\varphi_4|I-\overline{I}|,$$

where

$$\begin{array}{l} \varphi_1 = (v_S+2\gamma f_i(\zeta)\xi_S), \\ \varphi_2 = (2\mu\zeta+2\eta\zeta+v_M+2\gamma(\zeta)\xi_M), \\ \varphi_3 = (2\mu\zeta+r_R+\beta+\sigma\zeta+2\frac{r_R}{C_R}\zeta), \\ \varphi_4 = (2\eta\zeta+\varepsilon+\sigma\zeta+\omega). \end{array} \tag{15}$$

Consequently, it is acquired $\|G(X)-G(\overline{X})\| \leq L\|X-\overline{X}\|$ where $L=\max(\varphi_1,\varphi_2,\varphi_3,\varphi_4)$, and so, $G(X)$ met the Lipschitz condition. In summary, the existence and uniqueness of solutions of (8) is demonstrated.

Theorem 4 *The FOS's solutions in* (8)*, starting in* $\mathbb{R}^4_+$ *are uniformly bounded.*

Proof The approach used in [38] was considered.

i. Consider the fourth equation in (8). Therefore, we have ${}^{C}_{t_0}D^{\phi}_{t} I+\omega I=\theta_I$. Considering the standard comparison theorem for fractional-order, it is obtained as follows:

$$I(t) = (I(0)-\frac{\theta_I}{\omega})E_{\phi,1}(-\omega t^{\phi})+\frac{\theta_I}{\omega},$$

and so,

$$\lim_{t\to\infty} I(t) = \frac{\theta_I}{\omega}, \tag{16}$$

where E_α is the Mittag–Leffler function.

ii. From the third equation in (8), we have the followings:

$$ {}_{t_0}^{C}D_t^{\phi}R + \beta R = \frac{r_R}{C_R}\left(\frac{(r_R+\sigma I)}{2\frac{r_R}{C_R}}\right)^2 - \frac{r_R}{C_R}\left(R - \left(\frac{(r_R+\sigma I)}{2\frac{r_R}{C_R}}\right)\right)^2 \leq \frac{r_R}{C_R}\left(\frac{(r_R+\sigma I)}{2\frac{r_R}{C_R}}\right)^2, $$

$$ R(t) \leq \left(R(0) - \frac{1}{\beta}\frac{r_R}{C_R}\left(\frac{(r_R+\sigma I)}{2\frac{r_R}{C_R}}\right)^2\right)E_{\phi,1}(-\beta t^{\phi}) + \frac{1}{\beta}\frac{r_R}{C_R}\left(\frac{(r_R+\sigma I)}{2\frac{r_R}{C_R}}\right)^2, $$

and

$$ \lim_{t\to\infty} R(t) = \frac{1}{\beta}\frac{r_R}{C_R}\left(\frac{(r_R+\sigma\frac{\theta_I}{\omega})}{2\frac{r_R}{C_R}}\right)^2. \tag{17} $$

iii. Now let's consider the first and second equations of the system (8) for $N(t) = S(t) + M(t)$. In this case, we have the following:

$$ {}_{t_0}^{C}D_t^{\phi}S(t) + {}_{t_0}^{C}D_t^{\phi}M(t) = {}_{t_0}^{C}D_t^{\phi}N(t) = \theta_S + \theta_M + \varepsilon I - v_S S - v_M M, $$

$$ {}_{t_0}^{C}D_t^{\phi}N(t) + v_S S + v_M M = (\theta_S + \theta_M + \varepsilon I), $$

and

$$ {}_{t_0}^{C}D_t^{\phi}N(t) + v_N N \leq (\theta_S + \theta_M + \varepsilon I), $$

where $\min\{v_S, v_M\} = v_N$. Therefore, it is found that

$$ N(t) \leq \left(N(0) - \frac{\theta_S + \theta_M + \varepsilon I}{v_N}\right)E_{\phi,1}(-v_N t^{\phi}) + \frac{\theta_S + \theta_M + \varepsilon I}{v_N}, $$

and

$$ \lim_{t\to\infty} N(t) = \frac{\theta_S+\theta_M+\varepsilon\frac{\theta_I}{\omega}}{v_N}. \tag{18} $$

As a result, the solutions starting in $\mathbb{R}_+^4$ of system (8) are uniformly bounded to the region Ω, in which $\Omega := \{(S, M, R, I) \in \mathbb{R}_+^4 : S + M \leq \frac{\theta_S+\theta_M+\varepsilon\frac{\theta_I}{\omega}}{v_N} + \in_1, R(t) \leq \frac{1}{\beta}\frac{r_R}{C_R}\left(\frac{(r_R+\sigma\frac{\theta_I}{\omega})}{2\frac{r_R}{C_R}}\right)^2 + \in_2, I(t) \leq \frac{\theta_I}{\omega} + \in_3, \ \in_1, \in_2, \in_3 > 0\}$.

Theorem 5 *The FOS's solutions in* (8) *starting in* $\mathbb{R}_+^4$ *are non-negative.*

Proof For proof, the approach used in [38] was taken into account. From the first and second equations of Eqs. (8), it has been assumed that $N(t) = S(t) + M(t)$ where $N(t) \to 0$ means $S(t) \to 0$ and $M(t) \to 0$. Therefore, the followings ${}_{t_0}^{C}D_t^{\phi}I(t)|_{I=0} = \theta_I > 0, {}_{t_0}^{C}D_t^{\phi}N(t)|_{N=0} =$

$\theta_S + \theta_M + \varepsilon I > 0$, ${}^{C}_{t_0}D^{\phi}_{t} R(t)|_{R=0} = 0$ are found. In this sense, the solutions are non-negative.

Equilibrium points of proposed model

$E(\overline{S}, \overline{M}, \overline{R}, \overline{I})$ points found by solving the equation system ${}^{C}_{t_0}D^{\phi}_{t} S(t) = 0, {}^{C}_{t_0}D^{\phi}_{t} M(t) = 0, {}^{C}_{t_0}D^{\phi}_{t} R(t) = 0, {}^{C}_{t_0}D^{\phi}_{t} I(t) = 0$ obtained from the system (8) are the equilibrium points. In this case,

$$\begin{aligned} &\theta_S + \eta\overline{MI} + \mu\overline{MR} + \gamma\overline{S}f_i(\overline{M}) + \varepsilon\overline{I} - v_S\overline{S} = 0, && (a)\\ &\theta_M - \eta\overline{MI} - \mu\overline{MR} - \gamma\overline{S}f_i(\overline{M}) - v_M\overline{M} = 0, && (b)\\ &r_R\overline{R}(1-\tfrac{\overline{R}}{C_R}) + \sigma\overline{RI} - \beta\overline{R} = 0, && (c)\\ &\theta_I - \omega\overline{I} = 0, && (d) \end{aligned} \tag{19}$$

is obtained. From Eqs. (19), it is found as

$$\begin{aligned} &\overline{S} = \tfrac{(\theta_S+\theta_M+\varepsilon\overline{I}-v_M\overline{M})}{v_S} \text{ when } \overline{I} > \tfrac{v_M\overline{M}-(\theta_S+\theta_M)}{\varepsilon}, && (a)\\ &\overline{R}_1 = 0 \text{ or } \overline{R}_2 = \tfrac{r_R+\sigma\overline{I}-\beta}{\frac{r_R}{C_R}} \text{ when } \overline{I} > \tfrac{\beta-r_R}{\sigma}, && (b)\\ &\overline{I} = \tfrac{\theta_I}{\omega}. && (c) \end{aligned} \tag{20}$$

In addition, the equations for $\overline{M}$ from Eq. (19) -(b) according to each function in Table 4 are as follows:

$$\begin{aligned} &\overline{M} = \tfrac{\theta_M}{(\gamma\overline{S}+(\eta\overline{I}+\mu\overline{R}+v_M))}, && \text{for } i=1, && (a)\\ &\overline{M}^2 + [b + \tfrac{(\gamma\overline{S}-\theta_M)}{(\eta\overline{I}+\mu\overline{R}+v_M)}]\overline{M} - \tfrac{b\theta_M}{(\eta\overline{I}+\mu\overline{R}+v_M)} = 0, && \text{for } i=2, && (b)\\ &\overline{M}^3 + \tfrac{(\gamma\overline{S}-\theta_M)}{(\eta\overline{I}+\mu\overline{R}+v_M)}\overline{M}^2 + b\overline{M} - \tfrac{b\theta_M}{(\eta\overline{I}+\mu\overline{R}+v_M)} = 0, && \text{for } i=3, && (c)\\ &(1-e^{-b\overline{M}})\tfrac{\gamma\overline{S}}{(\eta\overline{I}+\mu\overline{R}+v_M)} = (\tfrac{\theta_M}{(\eta\overline{I}+\mu\overline{R}+v_M)} - \overline{M}), && \text{for } i=4, && (d) \end{aligned} \tag{21}$$

where $\overline{S}$, $\overline{R}$ and $\overline{I}$ are shown in Eqs. (20). Let us consider Ineqs. in (20). If at least one value $\overline{M}$ can be obtained from the Eqs. (21), when

$$\tfrac{v_M\overline{M}-(\theta_S+\theta_M)}{\varepsilon} < \overline{I}, \tag{22}$$

for $\overline{R}_1$, and when

$$\max\{\tfrac{\beta-r_R}{\sigma}, \tfrac{v_M\overline{M}-(\theta_S+\theta_M)}{\varepsilon}\} < \overline{I}, \tag{23}$$

for $\overline{R}_2$. Therefore, the existence of an equilibrium point can be said. In this case, let us show the existence of the component $\overline{M}$ of the equilibrium point from the Eqs. (21).

i. Consider the Eq. (21)-(a). It is clear that $\overline{M} > 0$ due to Ineqs. (9), (22) and (23). Thus, the equilibrium points $E_1^{(1)}(\overline{S}, \overline{M}, \overline{R}_1, \overline{I})$ or $E_1^{(1)}(\overline{S}, \overline{M}, \overline{R}_2, \overline{I})$ are obtained.
ii. Now let us consider equation (21)-(b). In this case, the equation for $\overline{M}$ is

$$\overline{M}^2 + \xi_1\overline{M} + \xi_2 = 0, \tag{24}$$

where

$$\xi_1 = \left(b + \frac{(\gamma\overline{S}-\theta_M)}{(\eta\overline{I}+\mu\overline{R}+\upsilon_M)}\right), \text{ and } \xi_2 = -\frac{b\theta_M}{(\eta\overline{I}+\mu\overline{R}+\upsilon_M)}. \tag{25}$$

From the Ineqs. (9), (22) and (23), it can be seen that $\xi_2 < 0$. This shows that Eq. (24) has one positive $\overline{M}$ value. In this case, there is the equilibrium points $E_2^{(1)}(\overline{S}, \overline{M}, \overline{R}_1, \overline{I})$ or $E_2^{(1)}(\overline{S}, \overline{M}, \overline{R}_2, \overline{I})$.

iii. Considering (21)-(c), the equation for $\overline{M}$ is the following:

$$\overline{M}^3 + \vartheta_1\overline{M}^2 + \vartheta_2\overline{M} + \vartheta_3 = 0, \tag{26}$$

where $\vartheta_1 = \frac{(\gamma\overline{S}-\theta_M)}{(\eta\overline{I}+\mu\overline{R}+\upsilon_M)}, \vartheta_2 = b, \vartheta_3 = -\frac{b\theta_M}{(\eta\overline{I}+\mu\overline{R}+\upsilon_M)}$. Due to the Ineqs. (9), (22) and (23), it is obvious that $\vartheta_2 > 0$, $\vartheta_3 < 0$. According to Descartes' rule of signs in Theorem 2, one can reach the following conclusions for the $\overline{M}$ roots of Eq. (26):

- If $\vartheta_1 \geq 0$,

$$\overline{I} \geq \frac{\upsilon_M\overline{M}+\frac{\theta_M}{\gamma}\upsilon_S-(\theta_S+\theta_M)}{\varepsilon}, \tag{27}$$

  then Eq. (26) has one positive root, denoted by $E_3^{(1)}(\overline{S}, \overline{M}, \overline{R}_1, \overline{I})$ or $E_3^{(1)}(\overline{S}, \overline{M}, \overline{R}_2, \overline{I})$.
- If $\vartheta_1 < 0$,

$$\overline{I} < \frac{\upsilon_M\overline{M}+\frac{\theta_M}{\gamma}\upsilon_S-(\theta_S+\theta_M)}{\varepsilon}, \tag{28}$$

  then Eq. (26) has one or three positive roots denoted by $E_3^{(i)}(\overline{S}, \overline{M}, \overline{R}_1, \overline{I})$ or $E_3^{(i)}(\overline{S}, \overline{M}, \overline{R}_2, \overline{I})$ for $i = 1, 2, 3$. Consequently, when the discriminant of Eq. (26) denoted by

$$\Delta_{f_3} = 18\vartheta_1\vartheta_2\vartheta_3 - 27{\vartheta_3}^2 + {\vartheta_1}^2{\vartheta_2}^2 - 4{\vartheta_2}^3 - 4{\vartheta_1}^3\vartheta_3,$$

  is taken into consideration, Eq. (26) has one positive root if

$$\Delta_{f_3} \leq 0, \tag{29}$$

  and three positive roots if

$$\Delta_{f_3} > 0. \tag{30}$$

iv. When $\overline{M}$ is evaluated for equation (21)-(d), the equation $\Psi_1(\overline{M}) = \Psi_2(\overline{M})$ is reached such that $\Psi = \Psi_1(\overline{M}) = (1 - e^{-b\overline{M}})\frac{\gamma\overline{S}}{(\eta\overline{I}+\mu\overline{R}+\upsilon_M)}$ and $\Psi = \Psi_2(\overline{M}) = (\frac{\theta_M}{(\eta\overline{I}+\mu\overline{R}+\upsilon_M)} - \overline{M})$. In this case, the existence of a positive $\overline{M}$ value can be proven using the graphical method in the $\overline{M} - \Psi$ coordinate plane. The graph showing the positive $\overline{M}$ value is shown in Figure 2. Therefore, there is a positive equilibrium point $E_4^{(1)}(\overline{S}, \overline{M}, \overline{R}_1, \overline{I})$ or $E_4^{(1)}(\overline{S}, \overline{M}, \overline{R}_2, \overline{I})$.

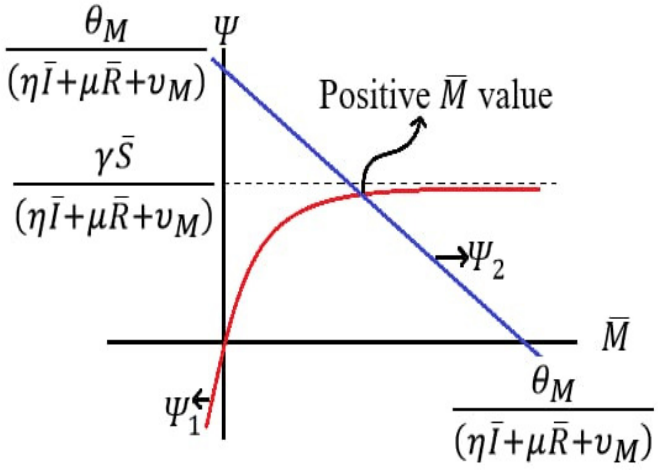

Figure 2. Graphical representation of the existence of a positive $\overline{M}$ value for Eq. (21)-(d)

Local stability analysis

In this section, the LAS equilibrium points of the system (8) for each function shown in Table 4 have been examined. For this, the Jacobian matrix is calculated as

$$J = \begin{pmatrix} \gamma f_i(M) - \upsilon_S & (\eta I + \mu R + \gamma S \frac{df_i(M)}{dM}) & \mu M & \varepsilon \\ -\gamma f_i(M) & (-\eta I - \mu R - \gamma S \frac{df_i(M)}{dM} - \upsilon_M) & -\mu M & -\eta M \\ 0 & 0 & (r_R - 2R\frac{r_R}{C_R} + \sigma I - \beta)) & \sigma R \\ 0 & 0 & 0 & -\omega \end{pmatrix}.$$

The equation of the eigenvalues for any the equilibrium point $(\bar{S}, \overline{M}, \bar{R}, \bar{I})$ from this matrix is

$$\begin{aligned}&(\lambda^2 + (-\gamma f_i(\overline{M}) - \upsilon_S + \upsilon_M + \eta\bar{I} + \mu\bar{R} + \gamma\bar{S}\tfrac{df_i(M)}{dM}|_{M=\overline{M}})\lambda \\ &+\upsilon_S(\eta\bar{I} + \mu\bar{R} + \gamma S\tfrac{df_i(M)}{dM}|_{M=\overline{M}} + \upsilon_M - \tfrac{\upsilon_M}{\upsilon_S}\gamma f_i(M)))(\lambda - (r_R - 2\bar{R}\tfrac{r_R}{C_R} + \sigma\bar{I} - \beta))(\lambda+\omega) = 0.\end{aligned} \tag{31}$$

From the second and third factor of Eq. (31), it is clear that $\lambda_3 = -\bar{R}\frac{r_R}{C_R} \in \mathbb{R}^-$ by (19)-(c) and $\lambda_4 = -\omega \in \mathbb{R}^-$ due to Ineq. (9). In this case, the eigenvalues λ_3 and λ_4 satisfies Ineq. (5).

Lastly, when the first factor of Eq. (31), in which the eigenvalues λ_1 and λ_2 are obtained, is taken into consideration, the characteristic equation is

$$\lambda^2 + \varkappa_1\lambda + \varkappa_2 = 0, \tag{32}$$

where

$$\left\{ \begin{array}{l} \varkappa_1 = (-\gamma f_i(\overline{M}) - \upsilon_S + \upsilon_M + \eta\bar{I} + \mu\bar{R} + \gamma\bar{S}\frac{df_i(M)}{dM}|_{M=\overline{M}}) \\ \varkappa_2 = \upsilon_S(\eta\bar{I} + \mu\bar{R} + \gamma\bar{S}\frac{df_i(M)}{dM}|_{M=\overline{M}} + \upsilon_M - \frac{\upsilon_M}{\upsilon_S}\gamma f_i(\overline{M})) \end{array} \right\} \quad \text{for } i = 1, 2, 3, 4. \tag{33}$$

Thus, if the coefficients of Eq. (32) satisfy Ineqs. (5) and (6), the eigenvalues λ_1 and λ_2 satisfy the stability conditions for equilibrium point. Therefore, we have

$$\varkappa_1, \varkappa_2 > 0, \tag{34}$$

or:

$$\varkappa_1 < 0,\ 4\varkappa_2 > {\varkappa_1}^2,\ |tan^{-1}(\frac{\sqrt{4\varkappa_2 - {\varkappa_1}^2}}{\varkappa_1})| > \frac{\phi\pi}{2}. \tag{35}$$

As a result, Table 5 regarding the equilibrium points can be accessed.

Table 5. Stability of equilibrium points obtained according to each functional response (for $i = 1, 2, 3$)

Response Type	Point	Existence Condition	LAS Condition
Holling Type 1	$E_1^{(1)}(\overline{S}, \overline{M}, \overline{R}_1, \overline{I})$	$\frac{\upsilon_M \overline{M} - (\theta_S + \theta_M)}{\varepsilon} < \overline{I}$	If $\overline{I} < \frac{\beta - r_R}{\sigma}$ and *
Holling Type 1	$E_1^{(1)}(\overline{S}, \overline{M}, \overline{R}_2, \overline{I})$	$\max\{\frac{\beta - r_R}{\sigma}, \frac{\upsilon_M \overline{M} - (\theta_S + \theta_M)}{\varepsilon}\} < \overline{I}$	If *
Holling Type 2	$E_2^{(1)}(\overline{S}, \overline{M}, \overline{R}_1, \overline{I})$	$\frac{\upsilon_M \overline{M} - (\theta_S + \theta_M)}{\varepsilon} < \overline{I}$	If $\overline{I} < \frac{\beta - r_R}{\sigma}$ and *
Holling Type 2	$E_2^{(1)}(\overline{S}, \overline{M}, \overline{R}_2, \overline{I})$	$\max\{\frac{\beta - r_R}{\sigma}, \frac{\upsilon_M \overline{M} - (\theta_S + \theta_M)}{\varepsilon}\} < \overline{I}$	If *
Holling Type 3	$E_3^{(1)}(\overline{S}, \overline{M}, \overline{R}_1, \overline{I})$	$\frac{\upsilon_M \overline{M} - (\theta_S + \theta_M)}{\varepsilon} < \overline{I}$	$\overline{I} \geq \frac{\upsilon_M \overline{M} + \frac{\theta_M}{\gamma} \upsilon_S - (\theta_S + \theta_M)}{\varepsilon}$ If $\overline{I} < \frac{\beta - r_R}{\sigma}$ and *
Holling Type 3	$E_3^{(1)}(\overline{S}, \overline{M}, \overline{R}_2, \overline{I})$	$\max\{\frac{\beta - r_R}{\sigma}, \frac{\upsilon_M \overline{M} - (\theta_S + \theta_M)}{\varepsilon}\} < \overline{I}$	If *
Holling Type 3	$E_3^{(i)}(\overline{S}, \overline{M}, \overline{R}_1, \overline{I})$	$\frac{\upsilon_M \overline{M} - (\theta_S + \theta_M)}{\varepsilon} < \overline{I}$	$\overline{I} < \frac{\upsilon_M \overline{M} + \frac{\theta_M}{\gamma} \upsilon_S - (\theta_S + \theta_M)}{\varepsilon}$ and $\Delta_{f_3} > 0$ If $\overline{I} < \frac{\beta - r_R}{\sigma}$ and *
Holling Type 3	$E_3^{(i)}(\overline{S}, \overline{M}, \overline{R}_2, \overline{I})$	$\max\{\frac{\beta - r_R}{\sigma}, \frac{\upsilon_M \overline{M} - (\theta_S + \theta_M)}{\varepsilon}\} < \overline{I}$	If *
Ivlev Type	$E_4^{(1)}(\overline{S}, \overline{M}, \overline{R}_1, \overline{I})$	$\frac{\upsilon_M \overline{M} - (\theta_S + \theta_M)}{\varepsilon} < \overline{I}$	If $\overline{I} < \frac{\beta - r_R}{\sigma}$ and *
Ivlev Type	$E_4^{(1)}(\overline{S}, \overline{M}, \overline{R}_2, \overline{I})$	$\max\{\frac{\beta - r_R}{\sigma}, \frac{\upsilon_M \overline{M} - (\theta_S + \theta_M)}{\varepsilon}\} < \overline{I}$	If *

*: Ineqs. (34) or (35) are satisfied

4 Estimation of derivative-order and parameters of the proposed model

The situation after the two major earthquakes with magnitudes (Kandilli Observatory) of Mw=7.7 in Kahramanmaraş, Pazarcık and Mw=7.6 in Kahramanmaraş, Elbistan, that occurred on 06.02.2023 was discussed in numerical studies. Therefore, the model in (8) was applied according to the parameters and derivative order determined for the Elbistan district. For this purpose, the following were done in order.

- In parameter estimations, time-dependent values of variables used in the system in (8) are needed. For this reason, in parameter estimation, data from the 1999 Gölcük earthquake in Türkiye were used in terms of its historical proximity, intensity, affected area, and results. The data set was determined accordingly.
- The model proposed in (8) was expressed through the ODE, and the parameters for each functional response were estimated with respect to real values by using the lsqcurvefit function of the Matlab R2024b software. In this way, the model parameters were found by determining the functional response that gave the minimum RMSE.
- Then, the derivative-order of the model with determined parameters was reduced by a precision of 0.01 and the most appropriate derivative-order was determined. The model with the parameters and derivative order that gave the minimum RMSE was determined as the best model.
- Finally, the results of the scenario with the relevant initial conditions for Elbistan after the Kahramanmaraş Elbistan earthquakes were presented.

Dataset

Türkiye is located in an earthquake zone and has witnessed many devastating earthquakes in history. In this sense, the largest earthquakes that have occurred here since the Republic period (1923-) are shown in Table 6. The Kocaeli/Gölcük and Kahramanmaraş/Elbistan earthquakes

Table 6. Three major earthquakes experienced in Türkiye [39]

Date	*Location*	*Magnitude*	*Deaths*	*Damaged Building*
26.12.1939	Erzincan	7.9	32962	116720
17.08.1999	Kocaeli (Gölcük)	7.4	17479	43953
06.02.2023	Kahramanmaraş(Pazarcık-Elbistan)	7.7 and 7.6	50783	227027

are similar to each other in terms of the intensity of the earthquake, the number of deaths, the size of the affected area, and the closeness of their dates. In addition, the Gölcük earthquake was accepted as a reference for the Elbistan earthquake in terms of the accessibility of the variables (S, M, R and I in (8)) used in this study.

For parameter estimation, data following a 7.4 magnitude earthquake that hit the Kocaeli province of Türkiye on August 17, 1999, and whose epicenter was Gölcük, were used. Approximately 17479 people died in this earthquake and caused an estimated US$6.5 billion in damage. The values used for parameter estimation are given in Table 7.

The explanation of the variables in Table 7 is as follows:

- $\boldsymbol{P_1}$: Total population for Kocaeli/Türkiye,
- $\boldsymbol{P_2}$: Migration population due to disaster for Kocaeli/Türkiye,
- Ratio: Population ratio (Gölcük Population/Kocaeli Population),
- $\boldsymbol{S(t)}$: Total population for Gölcük district,
- $\boldsymbol{M(t)}$: Migration population due to disaster according to population ratio for Gölcük district,
- $\boldsymbol{R(t)}$: Number of flats according to building occupancy permit (for Residence Purposes) for Gölcük district,
- $\boldsymbol{I(t)}$: SEDI for Gölcük district,
- $\frac{x}{\|x\|}$ for $x = t, S, M, R, I$: Vector normalization Values for Gölcük district.

Consider Table 7. It is clear that $\|t\| = 9854.35559$, $\|S(t)\| = 710389.87055$, $\|M(t)\| = 8349.39620$, $\|R(t)\| = 118274.57312$ and $\|I(t)\| = 5.93951$. Data colored green are accepted as hypotheses. Data colored blue are data added according to the trend of the column data. Data colored in red were obtained according to population ratio (Gölcük/Kocaeli). In addition, the data colored yellow are the data augmented with ARIMA. Time data provides information for forecasting models. For this reason, the evaluation of these values in the model is useful for prediction. For forecasting using time data, along with classic ARIMA models, Prophet or LSTM models can be used with powerful recurrent neural network models [40, 41]. In this study, the ARIMA model was used to estimate the missing data.

ARIMA has a structure that uses a linear regression model to make forecasts on time series data in order to examine time-varying situations in patterns. The model automatically has regressive and moving average components, and its basic equation is as shown below.

$$Y_t = \partial_1 Y_{t-1} + \partial_1 Y_{t-2} + \cdots + \partial_1 Y_{t-p} + \gamma_1 - \theta_1 \gamma_{t-1} - \gamma_2 - \theta_2 \gamma_{t-2} - \cdots - \gamma_q - \theta_q \gamma_{t-q}, \tag{36}$$

∂_p, the parameter of the AR model, γ_q, error term coefficient, θ_q, the parameter value of the MA model and Y_t, shows the degree to which the data differs from the original data. In order to

Table 7. Time-dependent values of S, M, R and I variables after the Gölcük earthquake on 17 August 1999

t (Year)	P_1	P_2	$S(t)$	Ratio	$M(t)$	$R(t)$	$I(t)$	$\frac{t}{\|t\|}$	$\frac{S(t)}{\|S(t)\|}$	$\frac{M(t)}{\|M(t)\|}$	$\frac{R(t)}{\|R(t)\|}$	$\frac{I(t)}{\|I(t)\|}$
1996	-	-	-	-	-	-	1.725715 [42]					
2000	1206085 [43]	25000 [44]	107341 [44]	0.08900	2224.98829	1514	1.584858	0.202956	0.151102	0.266485	0.012801	0.266833
2001	1226460 [45]	24500	110862.6	0.09039	2214.61254	3099	1.549643	0.203057	0.156059	0.265242	0.026202	0.260904
2002	1259932 [45]	23510	114384.1	0.09079	2134.37724	4760	1.514429	0.203159	0.161016	0.255633	0.040245	0.254975
2003	1293594 [45]	22550	117905.7	0.09115	2055.33849	6373	1.479214	0.20326	0.165973	0.246166	0.053883	0.249046
2004	1328481 [45]	22250	121427.3	0.09140	2033.71928	7930	1.444 [42]	0.203362	0.170931	0.243577	0.067047	0.243118
2005	1364317 [45]	21400	124948.9	0.09158	1959.88649	9409	1.408154	0.203463	0.175888	0.234734	0.079552	0.237083
2006	1401013 [45]	20500	128470.4	0.09170	1879.81353	11009	1.372308	0.203565	0.180845	0.225144	0.09308	0.231047
2007	1437926 [46]	20000	131992 [46]	0.09179	1835.86638	12782	1.336462	0.203666	0.185802	0.21988	0.108071	0.225012
2008	1490358 [46]	19500	136513 [46]	0.09160	1786.15037	14791	1.300616	0.203768	0.192166	0.213926	0.125056	0.218977
2009	1522408 [46]	19300	136035 [46]	0.08936	1724.55446	16728	1.26477	0.203869	0.191493	0.206548	0.141434	0.212942
2010	1560138 [46]	18900	137637 [46]	0.08822	1667.37769	18450 [46]	1.228924	0.203971	0.193749	0.1997	0.155993	0.206907
2011	1601720 [46]	18000	141926 [46]	0.08861	1594.95293	19797 [46]	1.193078	0.204072	0.199786	0.191026	0.167382	0.200871
2012	1634691 [46]	17900	143867 [46]	0.08801	1575.35540	21231 [46]	1.157232	0.204174	0.202518	0.188679	0.179506	0.194836
2013	1676202 [46]	17750	145805 [46]	0.08699	1543.98978	23066 [46]	1.121386	0.204275	0.205246	0.184922	0.195021	0.188801
2014	1722795 [46]	17500	149238 [46]	0.08663	1515.94647	24816 [46]	1.08554	0.204377	0.210079	0.181564	0.209817	0.182766
2015	1780055 [46]	17480	152607 [46]	0.08573	1498.58873	26593 [46]	1.049694	0.204478	0.214821	0.179485	0.224841	0.176731
2016	1830772 [46]	17300	156901 [46]	0.08570	1482.64628	27807 [46]	1.013848	0.20458	0.220866	0.177575	0.235105	0.170696
2017	1883270 [46]	17100	161117 [46]	0.08555	1462.93452	29034 [46]	0.978002 [42]	0.204681	0.226801	0.175214	0.24548	0.16466
2018	1906391 [46]	16500	162584 [46]	0.08528	1407.18037	30635 [46]	0.960802	0.204783	0.228866	0.168537	0.259016	0.161765
2019	1953035 [46]	16000	165663 [46]	0.08482	1357.17383	33288 [46]	0.943602	0.204884	0.2332	0.162548	0.281447	0.158869
2020	1997258 [46]	15800	170503 [46]	0.08537	1348.82294	35738 [46]	0.926402	0.204985	0.240013	0.161547	0.302161	0.155973
2021	2033441 [46]	15750	172802 [46]	0.08498	1338.43642	38810 [46]	0.909202	0.205087	0.24325	0.160303	0.328135	0.153077
2022	2079072 [46]	15730	175940 [46]	0.08462	1331.14014	40897 [46]	0.892002 [42]	0.205188	0.247667	0.15943	0.34578	0.150181
2023	2102907 [46]	15700	177441 [46]	0.08438	1324.74888	42675.13044	0.874802	0.20529	0.24978	0.158664	0.360916	0.147285

make forecasting, the time-varying series must be stationary, and the simplest method for this is to observe the change based on the difference. The ARIMA equation $(p,\ d,\ q)$ is obtained by performing a difference operation of degree d on the nonstationary ARMA model $(p,\ q)$. p is the degree of the AR model, d is the number of differences to make the data stationary, and q is the degree of the MA model.

Parameter estimation with minimum RMSE

The ODE form of (8) is

$$\begin{aligned}
&\tfrac{dS(t)}{dt} = \theta_S + \eta MI + \mu MR + \gamma S f_i(M) + \varepsilon I - v_S S,\\
&\tfrac{dM(t)}{dt} = \theta_M - \eta MI - \mu MR - \gamma S f_i(M) - v_M M,\\
&\tfrac{dR(t)}{dt} = r_R R(1-\tfrac{R}{C_R}) + \sigma RI - \beta R,\\
&\tfrac{dI(t)}{dt} = \theta_I - \omega I,\\
&S(t_0) = S_0,\ M(t_0) = M_0,\ R(t_0) = R_0,\ I(t_0) = I_0 \text{ such that } S_0, M_0, R_0, I_0 > 0.
\end{aligned} \tag{37}$$

By using the data in the last five columns of Table 7, the parameter values obtained for each functional response of the (37) system are shown in Table 8. In addition, RMSE was used to

Table 8. Parameter values for each functional response of the Eqs. (37) and their RMSEs with respect to real values

Parameter	Holling Type-1	Holling Type-2	Holling Type-3	Ivlev Type
θ_S	41.75284	36.01879	31.54418	38.10101
η	112.49679	84.30196	170.74247	114.54013
μ	2.154	1.02587	0.1561	0.1561
γ	54.46518	1.9227	0.01217	0.01217
ε	0.0125891	15.27381	18.08166	0.0125891
v_S	30.7521	0.9157	1.02787	0.9157
θ_M	68.34056	1.2135	38.8599	44.87356
v_M	544.44999	240.7555	400.28472	441.69912
r_R	0.05191	2626.72693	2615.04485	0.05191
C_R	0.8752	0.32068	0.32034	0.08752
σ	29323.25997	642.82021	661.18863	22649.37148
β	4334.17795	3.5924	0.2324	2989.99665
θ_I	95.71375	0.2183	0.9715	17.13876
ω	733.45629	260.88913	266.48972	368.17729
b	Not available	36.13035	0.9965	0.24649
RMSE	0.100637153	0.121708496	0.120707238	0.116430262

compare the performances of functional responses with respect to real values. Accordingly, the function that gives the minimum RMSE compared to the others is the Holling Type-1 and the relevant graph can be seen in Figure 3.

Determining of the derivative-order to get lower RMSE

Here, the most appropriate derivative parameter has been investigated to take into account the delay in the model. The model giving the minimum RMSE was determined as for $i = 1$ (Holling Type-1). Now, the fractional model with first column parameters in Eq. (8) as regards Holling

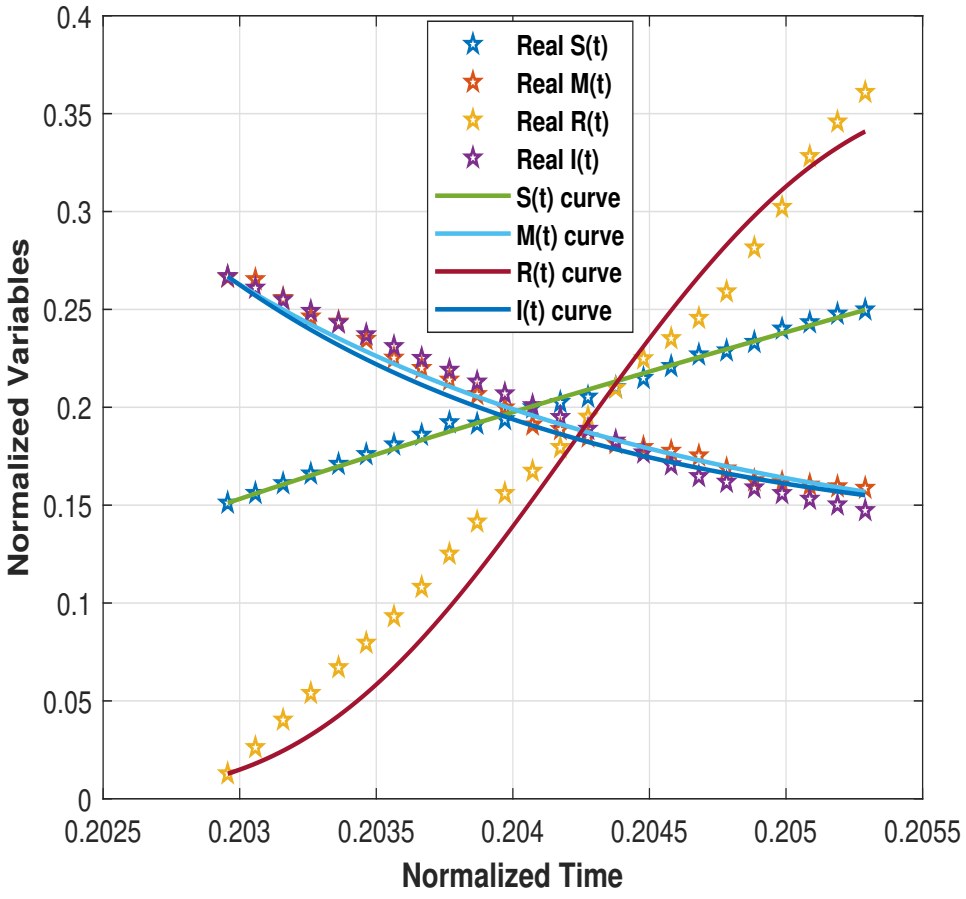

Figure 3. Graphical representation of the performance of system in (37) for Holling Type-1 functional response

Type-1 is as follows:

$$\begin{aligned}
&{}_{t_0}^{C}D_t^{\phi} S = \theta_S + \eta MI + \mu MR + \gamma SM + \varepsilon I - v_S S,\\
&{}_{t_0}^{C}D_t^{\phi} M = \theta_M - \eta MI - \mu MR - \gamma SM - v_M M,\\
&{}_{t_0}^{C}D_t^{\phi} R = r_R R(1-\tfrac{R}{C_R}) + \sigma RI - \beta R,\\
&{}_{t_0}^{C}D_t^{\phi} I = \theta_I - \omega I,
\end{aligned} \tag{38}$$

where $S(t_0) = S_0,\ R(t_0) = R_0,\ M(t_0) = M_0, I(t_0) = I_0$ such that $S_0,\ R_0, M_0, I_0 > 0$. In addition, the equilibrium points and their stabilities are calculated as follows. The equilibrium points are found as $E_1^{(1)}(1.72787, 0.10462, 0, 0.1305)$ and $E_1^{(2)}(1.72787, 0.67744, 0, 0.1305)$. Additionally, the coefficients of Eq. (32) are $\varkappa_1 = 616.7893, \varkappa_2 = 16986.19$ for $E_1^{(1)}$ and $\varkappa_1 = 33.23197, \varkappa_2 = -16986.2$ for $E_1^{(2)}$. Since these coefficients only for $E_1^{(1)}$ satisfy the equality in (34), the equilibrium point $E_1^{(1)}$ is LAS. The denormalized point corresponding to the LAS equilibrium point is $E_1^{(1)}(17027, 74319, 0, 0.775087)$.

By solving the system (38) with the Matlab R2023b software, the RMSE values corresponding to

different derivative orders are found as follows:

$$\begin{aligned}
&0.143743817 \text{ for } \phi = 1.004,\\
&0.124240729 \text{ for } \phi = 1.003,\\
&0.110412390 \text{ for } \phi = 1.002,\\
&0.103947676 \text{ for } \phi = 1.001,\\
&0.105643008 \text{ for } \phi = 1.000,\\
&0.114644800 \text{ for } \phi = 0.999,\\
&0.129015936 \text{ for } \phi = 0.998,\\
&0.146836443 \text{ for } \phi = 0.997,\\
&0.166705461 \text{ for } \phi = 0.996.
\end{aligned} \tag{39}$$

As can be clearly seen here, the derivative-order showing the best performance is determined as $\phi = 1.001$.

Numerical simulations of the model for Elbistan district after the earthquakes on 06.02.2023

The most recent earthquakes that caused major destruction in Türkiye are the following: Mw 7.7 (focal depth = 8.6 km) and Mw 7.6 (focal depth = 7km) with the epicenter in Pazarcık and Elbistan districts of Kahramanmaraş at 04:17 and 13:24 Türkiye time on February 6, 2023. These earthquakes are unprecedented disasters in recent history in terms of intensity and area covered. On the 51st day of the earthquakes, the death toll was announced as 50096. According to the report of the Ministry of Environment, Urbanization and Climate Change, it was determined that 224923 independent units in 50576 buildings, for which the damage assessment study was completed, were heavily damaged and collapsed, requiring urgent demolition. Especially severe consequences occurred in the Elbistan district of Kahramanmaraş, which was one of the epicenters of the earthquake. According to this report, 4943 houses were destroyed in Elbistan and the number of houses seriously damaged was 7238 [47]. In addition, the death toll from the earthquake was announced as 924.

For Elbistan, Figure 4 shows the time-dependent changes of the examined variables for three different derivative orders. The derivative order with minimum RMSE for model (38) has already been shown in (39). Here, graphs of the variables for Elbistan district are presented for three different values of ϕ: 0.901, 1.001 and 1.101. For $\phi = 1.001$, The model's 5-year forecast indicates: $S(t) \approx 150810$, $M(t) \approx 9473$, $R(t) \approx 620$ and $I(t) \approx 0.35$. Similarly, the model prediction for 10 years is the following: $S(t) \approx 173196$, $M(t) \approx 7131$, $R(t) \approx 166$ and $I(t) \approx 0.5$. According to the proposed model, it is estimated that Elbistan district will reach its pre-earthquake population size (141307) at the beginning of 2026.

According to Turkish Statistical Institute (TSI), the population data for Elbistan district decreased from 141307 for 2022 to 127755 ($S_0(t)$) for 2023 (after the earthquake) [46]. Therefore, it can be concluded that the number of population migrating after the earthquake in Elbistan district is approximately 12628 ($M_0(t)$). According to the statement of Elbistan Municipality, it was stated that most of the construction works of 4 thousand 12 houses ($R_0(t)$) created in the first stage have been completed. Considering the SEDI value of the Gölcük district between 1996 and 2000, there was an annual downward trend of 2.04%. SEDI-2022 for Elbistan was announced as 0.13 [42]. When the same trend is applied for Elbistan, the SEDI value will be 0.127348 for 2023 and 0.12475 for 2024.

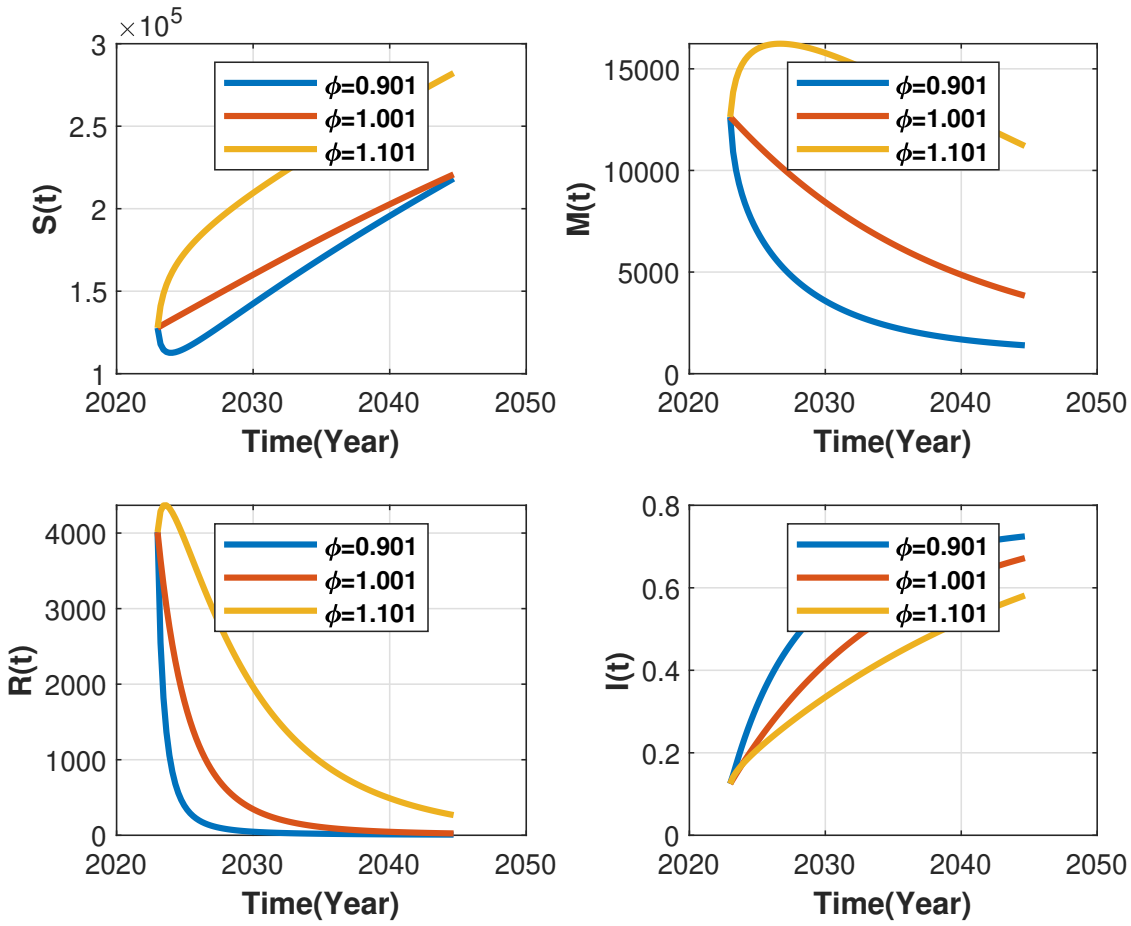

Figure 4. Time-dependent changes of S, M, R and I variables for Elbistan district

5 Conclusions

In the event of a disaster, different situations such as evacuation, leakage, containment, shelter, aid search, looting, theft, etc. may occur. Human nature tends to return to normal life after a disaster. For the surviving population post-disaster, there is a certain interaction between individuals who showed short-term panic behavior against such situations and migrated to a different region and individuals who continue to live in the disaster area within the means with controlled behavior. Thanks to this interaction, it is inevitable for the migrated population to exhibit controlled behavior and to have a tendency to return to the region when suitable conditions occur in the disaster area. In the model we proposed, we aimed to investigate the relationship between these two populations using different functional responses. Thus, it was aimed to find the functional response that gives the minimum RMSE by comparing the results of the proposed model with real data. Of course, the most important factors affecting the population after the disaster are whether the region has enough independent sections for settlement and socio-economic development of the region. Therefore, the effect of these variables on the population was also examined. The relationship between these variables is mathematically modeled using fractional order differential equations. In the model, there are four different functional responses. In numerical studies, parameter values were estimated using data from the 1999 Gölcük earthquake. Then, by changing the derivative order, the RMSE value was further reduced, and thus, the performance of the proposed model was increased. Lastly, the prediction results for Elbistan of FOS in (8) with Holling Type-1 functional response and derivative orders $\phi = 1.001$, is given in Table 9.

Table 9. The prediction results for Elbistan

Time (Year)	*S(t)*	*M(t)*	*R(t)*	*I(t)*	*Time (Year)*	*S(t)*	*M(t)*	*R(t)*	*I(t)*
2023	127755	12628	4012	0.12475	2034	177919	6712	131	0.520727
2024	132890	11877	2521	0.181987	2035	182580	6321	106	0.543116
2025	136879	11294	1782	0.224046	2036	186263	6027	90	0.559603
2026	141860	10606	1190	0.272454	2037	190807	5682	74	0.578579
2027	146836	9960	819	0.316618	2038	194395	5423	64	0.592552
2028	150808	9473	620	0.349146	2039	198820	5118	53	0.608633
2029	155749	8900	448	0.386588	2040	203178	4834	45	0.623302
2030	160656	8365	331	0.420747	2041	206618	4621	40	0.634103
2031	164551	7961	264	0.445904	2042	210859	4370	34	0.646533
2032	169376	7488	203	0.474859	2043	215037	4137	30	0.657871
2033	173196	7131	166	0.496184	2044	218334	3962	27	0.666219

The purpose of population forecasts is to determine the size of workforce that will be needed in the future and to prepare the infrastructure and facilities accordingly. Population projections help identify future risks and opportunities, make plans, and take precautions. Thus, it is important to estimate the future population in a region after a disaster in the light of certain parameters, and mathematical methods are used for this. Public institutions and organizations aim to achieve their social and economic target plans within the stipulated time in order for a region to reach its pre-disaster population structure. Thanks to the results of the model we propose, predictions are made about whether they will achieve these goals in the specified time period. It adds innovation to the literature in terms of the structure of the mathematical model used, its analysis, and adaptation of the results to the real world example.

The model and analysis proposed in this study are extremely useful in terms of their applicability to natural disasters such as tsunamis and landslides occurring in different parts of the world.

Declarations

Use of AI tools

The authors declare that they have not used Artificial Intelligence (AI) tools in the creation of this article.

Data availability statement

No Data associated with the manuscript.

Ethical approval (optional)

The authors state that this research complies with ethical standards. This research does not involve either human participants or animals.

Consent for publication

Not applicable

Conflicts of interest

The authors declare that they have no conflict of interest.

Funding

This study was supported by Scientific and Technological Research Council of Türkiye (TUBITAK) under the Grant Number 123F220 (TUBITAK 1002).

Author's contributions

T.D.: Writing - Original Draft Preparation – Review & Editing, Validation. B.D.: Conceptualization, Methodology, Data Curation, Writing-Original Draft Preparation, Formal Analysis, Validation, Software. All authors have read and agreed to the published version of the manuscript.

Acknowledgements

The authors thank to TUBITAK for their support.

References

[1] Chaudhary, M.T. and Piracha, A. Natural disasters-origins, impacts, management. *Encyclopedia*, 1(4), 1101-1131, (2021). [CrossRef]

[2] Asian Disaster Reduction Center. Natural disaster data book 2022 (an analytical overview). (2022). https://www.adrc.asia/publications/databook/ORG/databook_2022/pdf/DataBook2022.pdf

[3] AFAD, Afet Türleri, (2023). https://www.afad.gov.tr/afet-turleri

[4] Verdière, N., Lanza, V., Charrier, R., Provitolo, D., Dubos-Paillard, E., Bertelle, C. and Alaoui, A. Mathematical modeling of human behaviors during catastrophic events. In Proceedings, *4th International Conference on Complex Systems and Applications (ICCSA)*, pp. 67-74, Le Havre, France, (2014, June).

[5] Paul, B.K. Evidence against disaster-induced migration: the 2004 tornado in north-central Bangladesh. *Disasters*, 29(4), 370-385, (2005). [CrossRef]

[6] Tuncer, G. Türkiye'de sosyo-ekonomik gelişmişliğin mekânsal eşitsizliği. *Journal of Economics Public Finance Business*, 2(2), 69-80, (2019).

[7] Boğaziçi University, Kandilli Observatory and Earthquake Research Institute, Regional Earthquake-Tsunami Monitoring and Evaluation Center, (2024). http://udim.koeri.boun.edu.tr/zeqmap/hgmmap.asp

[8] Ozaslan, M., Dincer, B. and Ozgur, H. Regional disparities and territorial indicators in Turkey: Socio-economic development index (SEDI). In Proceedings, *46th Congress of the European Regional Science Association: "Enlargement, Southern Europe and the Mediterranean" (ERSA)*, pp. 1-34, Volos, Greece, (2006, August).

[9] Du, M., Wang, Z. and Hu, H. Measuring memory with the order of fractional derivative. *Scientific Report*, 3, 3431, (2013). [CrossRef]

[10] Avci, D., Ozdemir, N. and Yavuz, M. Fractional optimal control of diffusive transport acting on a spherical region. In *Methods of Mathematical Modelling* (pp. 63-82). Boca Raton, USA: CRC Press, (2019).

[11] Paul, S., Mahata, A., Mukherjee, S., Mali, P. and Roy, B. Fractional order SEIQRD epidemic model of COVID-19: A case study of Italy. *PLoS One*, 18(3), e0278880, (2023). [CrossRef]

[12] Husnain, S. and Abdulkader, R. Fractional order modeling and control of an articulated robotic arm. *Engineering, Technology & Applied Science Research*, 13(6), 12026-12032, (2023). [CrossRef]

[13] Joshi, H. and Yavuz, M. Transition dynamics between a novel coinfection model of fractional-order for COVID-19 and tuberculosis via a treatment mechanism. *The European Physical Journal Plus*, 138(5), 468, (2023). [CrossRef]

[14] Ersoy, B., Daşbaşı, B. and Aslan, E. Mathematical modelling of fiber optic cable with an electro-optical cladding by incommensurate fractional-order differential equations. *An International Journal of Optimization and Control: Theories & Applications (IJOCTA)*, 14(1), 50-61, (2024). [CrossRef]

[15] Kumar, D., Nama, H. and Baleanu, D. Dynamical and computational analysis of fractional order mathematical model for oscillatory chemical reaction in closed vessels. *Chaos, Solitons & Fractal*, 180, 114560, (2024). [CrossRef]

[16] Moya, E.M.D., Rodriguez, R.A., Pietrus, A. and Bernard, S. A study of fractional optimal control of overweight and obesity in a community and its impact on the diagnosis of diabetes. *Mathematical Modelling and Numerical Simulation with Applications*, 4(4), 514-543, (2024). [CrossRef]

[17] Iwa, L.L., Omame, A. and Inyama, S.C. A fractional-order model of COVID-19 and Malaria co-infection. *Bulletin of Biomathematics*, 2(2), 133-161, (2024). [CrossRef]

[18] Adu, I.K., Wireko, F.A., Adarkwa, S.A. and Agyekum, G. O. Mathematical analysis of Ebola considering transmission at treatment centres and survivor relapse using fractal-fractional Caputo derivatives in Uganda. *Mathematical Modelling and Numerical Simulation with Applications*, 4(3), 296-334, (2024). [CrossRef]

[19] Daşbaşı, B. Fractional order bacterial infection model with effects of anti-virulence drug and antibiotic. *Chaos, Solitons & Fractals*, 170, 113331, (2023). [CrossRef]

[20] Helbing, D., Farkas, I. and Vicsek, T. Simulating dynamical features of escape panic. *Nature*, 407, 487-490, (2000). [CrossRef]

[21] Provitolo, D. A new classification of catastrophes based on "Complexity Criteria". In *From System Complexity to Emergent Properties* (pp. 179-194). Berlin, Heidelberg: Springer, (2009). [CrossRef]

[22] Yang, J., Yokoo, M., Ito, T., Jin, Z. and Scerri, P. *Principles of Practice in Multi-Agent Systems*. Springer: Berlin, (2009).

[23] Kumar, S., Singh, R., Singh, B.K. and Garg, R. Mathematical model for estimating flood disaster effect on a population by using differential equation. *International Journal of Computational Modeling and Physical Sciences*, 1(2), 14-18, (2021).

[24] Verdière, N., Cantin, G., Provitolo, D., Lanza, V., Dubos-Paillard, E., Charrier, R. et al. Understanding and simulation of human behaviors in areas affected by disasters: From the observation to the conception of a mathematical model. *Global Journal of Human Social Science: H Interdisciplinary*, 15(10-H), (2015).

[25] Hassell, M.P. *The Dynamics of Arthropod Predator-Prey Systems*. Princeton University Press: New Jersey, (1978).

[26] Xu, H. and Zou, S. A diffusive Monod-Haldane predator-prey system with Smith growth and a protection zone. *Nonlinear Analysis: Real World Applications*, 76, 104018, (2024). [CrossRef]

[27] Allen, L.J.S. *An Introduction to Mathematical Biology*. Pearson Prentice Hall: Italy, (2007).

[28] Holling, C.S. Some characteristics of simple types of predation and parasitism. *The Canadian Entomologist*, 91(7), 385-398, (1959). [CrossRef]

[29] Kooij, R.E. and Zegeling, A. A predator-prey model with Ivlev's functional response. *Journal of Mathematical Analysis and Applications*, 198(2), 473-489, (1996). [CrossRef]

[30] Uddin, M.J., Santra, P.K., Rana, S.M.S. and Mahapatra, G. Chaotic dynamics of the fractional order predator-prey model incorporating Gompertz growth on prey with Ivlev functional response. *Chaos Theory and Applications*, 6(3), 192-204, (2024). [CrossRef]

[31] Caputo, M. and Fabrizio, M. A new definition of fractional derivative without singular kernel. *Progress in Fractional Differentiation & Applications*, 1(2), 73-85, (2015). [CrossRef]

[32] Odibat, Z.M. and Shawagfeh, N.T. Generalized Taylor's formula. *Applied Mathematics and Computation*, 186(1), 286-293, (2007). [CrossRef]

[33] Matignon, D. Stability results for fractional differential equations with applications to control processing. In Proceedings, *Computational Engineering in Systems Applications*, pp. 963-968, Paris, France, (1996, July).

[34] Rostamy, D. and Mottaghi, E. Stability analysis of a fractional-order epidemics model with multiple equilibriums. *Advances in Difference Equations*, 2016, 170, (2016). [CrossRef]

[35] Daşbaşı, B. The Fractional-Order mathematical modeling of bacterial resistance against multiple antibiotics in case of local bacterial infection. *Sakarya University Journal of Science*, 21(3), 442-453, (2017). [CrossRef]

[36] Wang, X. A simple proof of Descartes's rule of signs. *The American Mathematical Monthly*, 111(6), 525-526, (2004). [CrossRef]

[37] Li, Y., Chen, Y. and Podlubny, I. Stability of fractional-order nonlinear dynamic systems: Lyapunov direct method and generalized Mittag-Leffler stability. *Computers & Mathematics with Applications*, 59(5), 1810-1821, (2010). [CrossRef]

[38] Li, H.L., Zhang, L., Hu, C., Jiang, Y.L. and Teng, Z. Dynamical analysis of a fractional-order predator-prey model incorporating a prey refuge. *Journal of Applied Mathematics and Computing*, 54, 435-449, (2017). [CrossRef]

[39] Peker, A.E. and Şanlı, İ. Deprem ve göç ilişkisi: 24 Ocak 2020 Elazığ deprem örneği. *Firat University International Journal of Economics and Administrative Sciences*, 6(1), 125-154, (2022).

[40] Box, G.E. and Jenkins, G.M. Time series analysis, control, and forecasting. *San Francisco, CA: Holden Day*, 3226(3228), 10, (1976).

[41] Arslan, R.S., Barışcı, N., Arici, N. and Kocer, S. Detecting and correcting automatic speech recognition errors with a new model. *Turkish Journal of Electrical Engineering and Computer Sciences*, 29(5), 2298-2311, (2021). [CrossRef]

[42] Republic of Türkiye Ministry of Industry and Trade, Socio-Economic Development Ranking Research Reports, (2024). https://www.sanayi.gov.tr/merkez-birimi/b94224510b7b/sege/ilce-sege-raporlari

[43] Turkish Statistical Institute, 2000 General Population Census, (2000). https://biruni.tuik.gov.tr/nufusapp/idari.zul

[44] Sudaş. İ. 17 Ağustos 1999 Marmara depreminin nüfus ve yerleşme üzerindeki etkileri: Gölcük (Kocaeli) örneği. *Aegean Geographical Journal*, 13, 73-91, (2004).

[45] Wikipedia, Kocaeli/ (province), (2023). https://fr.wikipedia.org/wiki/Kocaeli_(province)

[46] Turkish Statistical Institute, Address-Based Population Registration System Results, (2024). https://biruni.tuik.gov.tr/medas/?locale=tr

[47] Presidency of the Republic of Turkey, Strategy and Budget Directorate, 2023 Kahramanmaraş and Hatay Earthquakes Report, (2023). https://www.sbb.gov.tr/wp-content/uploads/2023/03/2023-Kahramanmaras-ve-Hatay-Depremleri-Raporu.pdf

Mathematical Modelling and Numerical Simulation with Applications (MMNSA)
(https://dergipark.org.tr/en/pub/mmnsa)

How to cite this article: Daşbaşı, T. & Daşbaşı, B. (2025). Fractional-order model of the post-disaster period: study on the earthquakes in Türkiye. *Mathematical Modelling and Numerical Simulation with Applications*, 5(1), 117-142. https://doi.org/10.53391/mmnsa.1503311

Mathematical Modelling and Numerical Simulation with Applications, 2025, 5(1), 143–171

https://dergipark.org.tr/en/pub/mmnsa
ISSN Online: 2791-8564 / Open Access
https://doi.org/10.53391/mmnsa.1571964

RESEARCH PAPER

Effect of chaos on the performance of spider wasp meta-heuristic optimization algorithm for high-dimensional optimization problems

Haneche Nabil [1,*,‡] and **Hamaizia Tayeb** [2,‡]

[1]Applied Mathematics & Modeling Laboratory, Department of Mathematics, University of Mentouri Brothers, 25000 Constantine, Algeria, [2]Mathematical Modeling & Simulation Laboratory, Department of Mathematics, University of Mentouri Brothers, 25000 Constantine, Algeria

*Corresponding Author
‡nabil.haneche@doc.umc.edu.dz (Haneche Nabil); el.tayyeb@umc.edu.dz (Hamaizia Tayeb)

Abstract

The spider wasp optimization (SWO) algorithm is a new nature-inspired meta-heuristic optimization algorithm based on the hunting, nesting, and mating behaviors of female spider wasps. This paper aims to apply chaos theory to the steps of the SWO algorithm in order to increase its convergence speed. Four versions of chaotic algorithms are constructed using the traditional spider wasp optimizer. The proposed chaotic spider wasp optimization (CSWO) algorithms select various chaotic maps and adjust the main parameters of the SWO optimizer to ensure the balance between exploration and exploitation stages. Furthermore, the constructed CSWO algorithms are benchmarked on eight well-known test functions divided into unimodal and multimodal problems. The experimental results and statistical analysis are carried out to demonstrate that CSWO algorithms are very suitable for searching optimal solutions for the benchmark functions. Specifically, the implementation of chaotic maps can significantly enhance the performance of the SWO algorithm. As a result, the new algorithm has high flexibility and outstanding robustness, which we can apply to engineering design problems.

Keywords: Meta-heuristic optimizer; chaotic map; spider wasp algorithm; benchmark function

AMS 2020 Classification: 37N40; 68T20; 90C59; 92B20

1 Introduction

Optimization is a structured method used to determine decision variables while adhering to various constraints to either maximize or minimize the cost function. The constraints, cost function, and design variables are the fundamental components of every optimization problem. Optimization approaches have significant applications in engineering, image processing, wireless sensor

➤ **Received:** 22.10.2024 ➤ **Revised:** 17.02.2025 ➤ **Accepted:** 12.03.2025 ➤ **Published:** 31.03.2025

networks, and bioinformatics [1]. A number of real-world problems exhibit high non-convexity and non-linearity, typically due to the presence of several design variables and fundamental constraints. Furthermore, there is no guarantee of achieving the optimal global solution. These practical problems present challenges that motivate scientists to develop new and effective methods for better results. Optimization methods may be classified into two fundamental categories: gradient-based deterministic methods and stochastic non-traditional methods [2]. Deterministic methods have constraints when solving problems that include search spaces that are discontinuous, nonconvex, high-dimensional, and have non-differentiable objective functions. In contrast, stochastic-based algorithms do not depend on gradient-based information. Instead, they rely on stochastic methods inside the search space to reduce these constraints. Meta-heuristic algorithms (MAs) are extensively used in stochastic-based methods due to their wide use over different techniques. Meta-heuristic algorithms provide a significant capacity for fully examining the solution space and effectively adopting what is the optimal solution. As a result, in recent years, many researchers have worked to introduce novel meta-heuristic algorithms and enhance the performance of current methods [3].

Recently, several nature-inspired meta-heuristic algorithms have been developed. These artificial algorithms imitate the behaviors of existing species or natural phenomena. Thus, these algorithms have been proposed and used as effective approaches for solving several optimization problems [4]. However, these MAs often demonstrate higher levels of sensitivity when they involve adjusting user-defined parameters. MAs may not precisely attain the global optimal solution, which is another disadvantage [5]. There are two categories of MAs: single solution-based and population-based [6]. The single-solution approach to optimization includes evaluating one solution. In contrast, with the population-based method, solutions are generated during each optimization step. Population-based meta-heuristic algorithms start the optimization process by generating a set of random individuals. Each of them signifies a possible optimal solution. The population will be gradually replaced by substituting the current population with a new generation using certain stochastic operators.

Considering the wide range of these algorithms, they always share a key characteristic: search processes may be categorized into exactly two stages, namely exploration and exploitation [7]. As a result, in the first stages of the search process, a carefully designed optimizer must show exploration behaviors that are sufficiently mixed with randomness in order to provide a greater number of random solutions. Furthermore, it enhanced multiple elements of the search space. After the exploration stage is completed, the exploitation stage is performed. The optimizer accelerates the search process by emphasizing a particular area instead of the whole search space, emphasizing near-optimal solutions. A successful optimizer must achieve an adequate and accurate balance between the exploration and exploitation stages. On the other hand, the probability of being trapped in local optima and overcoming partial convergence challenges increases. According to the No Free Lunch theorem [8], all the proposed metaheuristic algorithms exhibit similar average performance when solving a possible optimization problem. Meanwhile, no algorithm can be regarded as absolutely efficient. As a result, this theorem encourages the research and enhancement of more effective optimization algorithms.

Chaos theory focuses on the study of unpredictable and irregular system motions that are highly sensitive to initial conditions. A deterministic nonlinear dynamical system is called chaotic if it has at least one positive Lyapunov exponent. Several practical applications of chaos were shown in the literature, including in biology [9–11], ecology [12], infectious diseases [13], control [14], cryptosystems [15], and secure communication [16, 17]. Traditional optimization techniques, such as gradient, Newton, and Hessians methods, may successfully determine global optimum solutions for continuously differentiable functions, demonstrating fast convergence and high

accuracy. However, these classical optimization techniques can become trapped in local optima when solving optimization problems that require various multimodal functions [18].

Motivation

The chaotic spider wasp optimization algorithm is developed to address the limitations of traditional optimization methods, such as getting trapped in local minima and being time-consuming. Inspired by the hunting, nesting, and mating behaviors of female spider wasps, this algorithm offers a novel approach to solving complex optimization problems with improved exploration and exploitation capabilities. By using chaotic maps, the algorithm is better able to avoid local optima and reach faster convergence. This makes it more useful and efficient for many situations.

Contributions

The main contributions of the current paper are summarized as follows:

- An improved optimization algorithm inspired by hunting, nesting, and mating behaviors of female spider wasps is developed based on chaos theory.
- A detailed comparison between the traditional SWO algorithm and the CSWO algorithm is presented.
- The performance analysis and speed convergence of four different counterparts of the CSWO algorithm are analyzed through several unimodal and multimodal benchmark functions.
- The experimental results show that the CSWO algorithm has better performance compared to the SWO counterpart and is more efficient for solving real-world optimization problems.

The remainder of this paper is organized as follows: In Section 2, the literature review is provided. Section 3 reports a short introduction to the chaos theory and some properties of chaotic systems. In addition, a general concept of using chaos in optimization algorithms is presented. Section 4 introduces five well-known 1-D chaotic maps, their chaotic behaviors, and Lyapunov exponents. In Section 5, the traditional SWO algorithm is presented. Section 6 introduces new counterparts of the SWO algorithm that are based on chaos theory. Section 7 deals with experimental analysis and statistical testing, in which the CSWO algorithms are benchmarked on eight test functions. A qualitative analysis is presented in order to compare the traditional SWO and the proposed chaotic methods. Section 8 gives the discussion and conclusion.

2 Literature review

Recently, there has been increasing interest in the study and application of meta-heuristic algorithms for solving optimization problems. In the scientific literature, population-based meta-heuristic algorithms can be divided into four main categories based on their basic concepts: evolutionary algorithms [19], physics-based algorithms [20], human-based algorithms [21], and swarm-based algorithms [22]. Evolutionary algorithms mimic the mechanisms of biological evolution, such as recombination and mutation. The Genetic Algorithm [23], Biogeography-Based Optimizer [24], and Mind Evolutionary Optimizer [25] are all considered the most important evolutionary algorithms. Algorithms inspired by physical phenomena use hypotheses based on scientific concepts, such as gravitation and magnetic attraction. Some examples are the Gravitational Search Algorithm [26] and the Energy Valley Optimizer [27]. Human-based machine agents frequently mimic certain human behaviors. Socio Evolution and Learning Optimization [28], Human Felicity Algorithm [29], and Social Network Search [30] are a few examples of this classification. Swarm-based multi-agent systems imitate the social behaviors shown by animals that live in swarms or groups. Particle Swarm Optimization [31] and Salp Swarm Algorithm [32] are considered the most significant meta-heuristic algorithms in this specific field.

Nowadays, swarm-based multi-agent systems have attracted increased interest due to their various sources of inspiration and efficiency in solving an extensive variety of optimization problems. A new optimization algorithms in this field have been developed, including the Mountain Gazelle Optimizer [33], Spotted Hyena Optimizer [34], Honey Bee Mating Optimization [35], Butterfly Optimization Algorithm [36], Ant Lion Optimizer [37], Harris Hawks Optimizer [38], Bat-Inspired Algorithm [39], Fruit Fly Optimization Algorithm [40], Whale Optimization Algorithm [41], Grasshopper Optimization Algorithm [42], Artificial Gorilla Troops Optimizer [43], Grey Wolf Optimizer [44], Marine Predators Algorithm [45], Hunger Games Search [46], Aquila Optimizer [47], and many others. Because of their stochastic nature, meta-heuristic algorithms have enhanced flexibility for escaping constraint in local optima. These algorithms may be used across numerous fields according to their efficiency, adaptability, and highly effective performance. The main challenge in designing any meta-heuristic algorithm arises from the stochastic nature of the optimization process, requiring sufficient balance between exploration and exploitation stages [48]. The exploration stage allows the optimizer to fully investigate the search space on a global scale. Additionally, the population faces sudden and significant changes during this period. On the other hand, the exploitation stage focuses on improving possible solutions that were discovered in the exploration stage. In this context, the population undergoes small and sudden fluctuations.

The SWO algorithm is a novel meta-heuristic optimizer developed to solve continuous optimization problems. In particular, it can solve complex nonlinear engineering optimization problems by mimicking biological or physical phenomena [49]. The SWO algorithm was created from a mathematical model of the three different behaviors shown by female spider wasps, including nesting, hunting, and mating behaviors.

The literature has extensively studied the application of chaos theory in the development of optimization algorithms. In [50], the authors have enhanced the Chaotic Whale Optimization Algorithm by incorporating various chaotic maps to improve its performance and achieve the global optimum for several test functions. Arora et al. [51] have developed a novel meta-heuristic optimization algorithm called the Grasshopper Optimization Algorithm inspired by grasshoppers' swarming behavior. To enhance global convergence, chaos theory was included in the optimization process, using chaotic maps to balance exploration and exploitation over the optimization process. In [52], the authors have developed an improved meta-heuristic optimization algorithm called the Chaotic Bird Swarm Algorithm. In order to improve this algorithm's exploitation performance, they used different chaotic maps. Kiani et al. [53] have proposed the Chaotic Sand Cat Swarm Optimization, and they introduced chaotic maps to enhance the performance of this algorithm. In addition, they applied the chaotic algorithm to a total of 39 functions and multidisciplinary problems. Arora et al. [54] have introduced chaos into the Butterfly Optimization Algorithm in order to increase its performance and convergence speed. They concluded that using chaos can enhance the optimization process to exploit the algorithm for solving engineering design problems. Shinde et al. [55] have presented a developed counterpart of the meta-heuristic Sine-Cosine Algorithm, which is based on chaos theory. The suggested algorithm is inspired by the sine and cosine classical functions. Using different chaotic maps, they replaced the random parameters in the traditional algorithm with chaotic variables to enhance the performance of the proposed algorithm. Hamaizia and Lozi [56] have developed a novel strategy for global search and multidimensional chaotic attractors using a locally averaged method. In addition, they examined the robustness of the suggested approach using several benchmark functions.

Based on the best knowledge gained from the literature review, there are only a few papers that integrate chaos theory in meta-heuristic optimization algorithms, so it is necessary to develop a new meta-heuristic algorithm based on chaotic systems. However, crucial properties of discrete

chaotic dynamic systems, such as sensitivity to initial conditions, ergodicity, and unpredictability, are prone to designing an optimizer. In the next section, based on the mathematical modeling of female spider wasp behaviors, an improved chaotic meta-heuristic algorithm is developed to handle optimization applications to address this research gap.

3 Chaotic optimization algorithm

In this section, we will describe some properties of chaos phenomena, followed by an optimization algorithm using chaotic maps.

Chaos

Nonlinear systems often exhibit chaotic behavior. It describes an example of irregular motions exhibited by deterministic systems inside a bounded phase space. Chaos theory is explained as the phenomenon known as the "butterfly effect", which was first described by Lorenz in 1963. Lorenz observed that slight variations in initial conditions could result in significantly different outcomes in future scenarios. Chaos is a result of the unpredictability produced by deterministic dynamical systems. Three fundamental properties characterize the chaotic systems: [57]

- ergodicity. Chaos has the ability to go through all possible states within a given range without repetition.
- sensibility. A very common characteristic of chaotic systems is their sensitive dependence on initial conditions. The system's behaviour may rapidly diverge with slightly different conditions, making it unpredictable.
- regularity. Chaos is exhibited by deterministic dynamical systems.

Chaos is a complex and unpredictable phenomenon that exhibits non-linear behavior. The ergodicity of chaos implies that using chaotic variables for optimization may provide an advantage compared to random searches with stochastic variables. It has been able to prevent algorithms from getting trapped in local optima. As a result, it is frequently used for optimization problems.

A general idea of a chaotic optimization algorithm

A random-based optimization algorithm that uses random number sequences obtained from chaotic maps instead of random number generators is called a chaotic optimization algorithm (COA). Its properties include simple integration, quick execution, and effective methods for avoiding local optimization. Consequently, it has enormous potential as a tool for engineering applications [58]. The COA is a highly efficient method for solving the optimization problems of a nonlinear multimodal function with boundary constraints. Chaos, unlike stochastic searches that rely on probabilities, may do comprehensive searches at faster rates due to its lack of repetition.

The COA generally has two main stages: the global stage and the local stage, which are often characterized by chaotic methods. Firstly, in the global stage, chaotic points are selected from the search domain $[L, U]$ based on a specific chaotic model. Next, the objective function is determined at various positions, and the point with the minimum objective function is chosen as the current optimum. Furthermore, it is assumed that during the local stage, the current optimum will be nearly the global optimum after a certain number of iterations. The current optimum is regarded as a center with minimal chaotic disturbances, whereas the global optimum is determined through an extensive search. The chaos phenomenon is characterized by randomness. Usually, a deterministic function can display chaotic behavior for some initial conditions and parameter values. These functions are so-called chaotic maps.

4 Chaotic maps

This section presents five one-dimensional non-invertible chaotic maps that are used to generate chaotic sequences. We use the logistic, Gauss/mouse, sinusoidal, piecewise, and tent chaotic maps in our study [59]. The details of these chaotic maps are shown in Table 1. The chaotic behavior of

Table 1. Chaotic maps

Chaotic map	Equation	Range	Parameter	Initial condition
Logistic	$x_{n+1} = \mu x_n (1 - x_n)$	$[0, 1]$	$\mu = 3.9$	$x_0 = 0.6$
Gauss/mouse	$x_{n+1} = \begin{cases} 0 & x_n = 0, \\ \frac{1}{x_n} - \lfloor \frac{1}{x_n} \rfloor & \text{otherwise} \end{cases}$	$[0, 1]$		$x_0 = 0.7$
Sinusoidal	$x_{n+1} = a x_n^2 \sin(\pi x_n)$	$[0, 1]$	$a = 2.3$	$x_0 = 0.9$
Piecewise	$x_{n+1} = \begin{cases} \frac{x_n}{p} & 0 \le x_n < p, \\ \frac{x_n - p}{0.5 - p} & p \le x_n < \frac{1}{2}, \\ \frac{1 - p - x_n}{0.5 - p} & \frac{1}{2} \le x_n < 1 - p, \\ \frac{1 - x_n}{p} & 1 - p \le x_n < 1 \end{cases}$	$[0, 1]$	$p = 0.4$	$x_0 = 0.8$
Tent	$x_{n+1} = \begin{cases} \frac{x_n}{0.7} & x_n < 0.7, \\ \frac{10}{3}(1 - x_n) & x_n \ge 0.7 \end{cases}$	$[0, 1]$		$x_0 = 0.4$

the proposed maps is depicted in Figure 1.

The rationale behind selecting chaotic maps, such as logistic, Gauss/mouse, sinusoidal, piecewise,

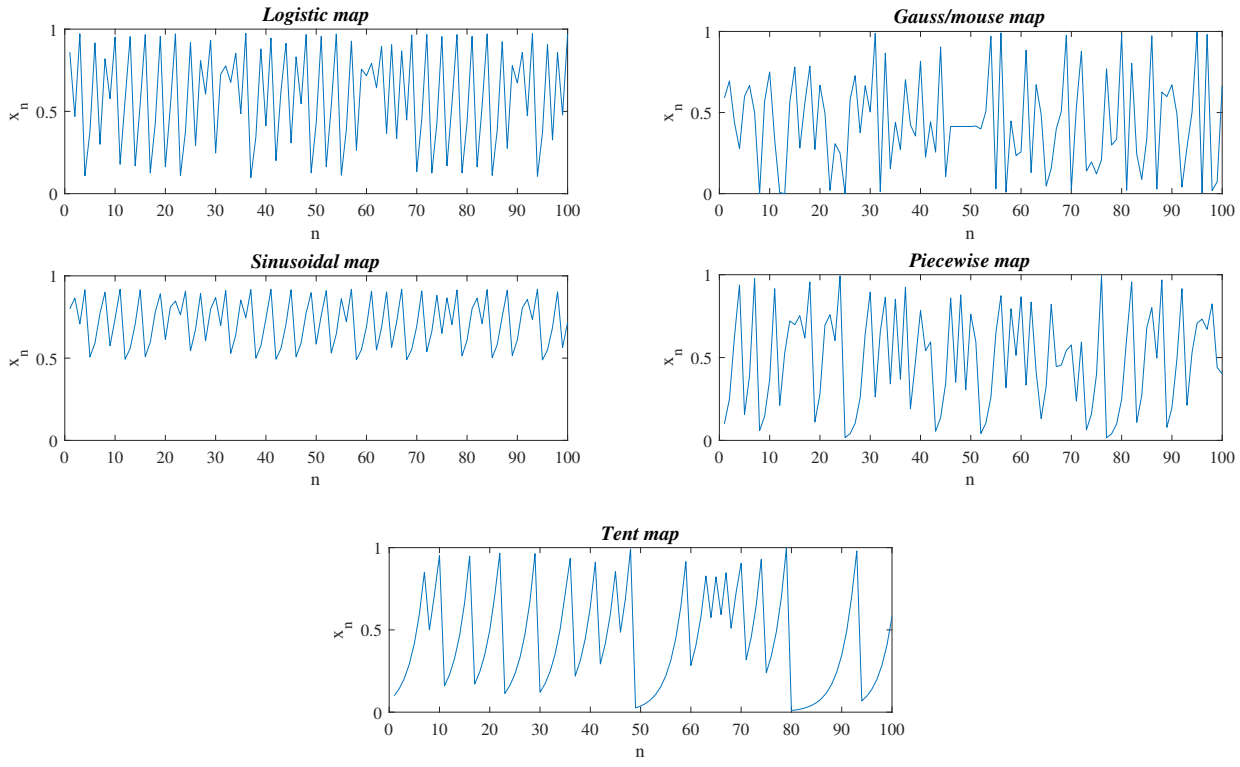

Figure 1. Visualization of chaotic maps

and tent maps, to replace random parameters in the SWO algorithm lies in the following reasons:

1. Chaotic maps provide better exploration and exploitation.
   - Exploration. Chaotic maps generate sequences that are deterministic yet appear random.

These sequences can help the SWO algorithm explore the search space more effectively than purely random numbers, as they avoid premature convergence to local optima.
- Exploitation. Chaotic maps can also provide fine-grained control over the search process, allowing the SWO algorithm to exploit promising regions more efficiently.

2. Avoidance of randomness pitfalls. Traditional random number generators may lead to uneven exploration of the search space, causing the algorithm to get stuck in suboptimal regions. On the other hand, chaotic maps provide a more structured and diverse exploration, reducing the likelihood of stagnation.
3. Diversity in search patterns. Each chaotic map has unique dynamics and properties. By incorporating multiple chaotic maps, the SWO algorithm can leverage different patterns of exploration, ensuring a more robust search process.
4. Improved convergence and stability. Chaotic maps can help the SWO algorithm converge faster to the global optimum by maintaining a balance between exploration and exploitation. They also reduce the risk of premature convergence, which is common in traditional random-based algorithms.

Note that we can use other chaotic maps not listed here to enhance the performance of the traditional SWO algorithm if they generate chaotic numbers in the range $[0, 1]$ with absolute value. In this paper, we select five chaotic maps that generate chaotic numbers in the range $[0, 1]$, which is consistent with the range of random parameters in the SWO algorithm.

Quantitative measure of chaos

In chaos theory, the rate of divergence or convergence of nearby trajectories of a deterministic dynamical system is evaluated by using Lyapunov exponents. In particular, when the maximum Lyapunov exponent (MLE) is positive, the system is chaotic. For a one-dimensional dynamic system, the Lyapunov exponent is defined as [60]

$$\lambda = \lim_{n\to\infty} \frac{1}{n} \sum_{j=0}^{n-1} \ln |f'(x_j)|, \tag{1}$$

where n is the maximum iteration number, $f'(x_j)$ is the derivative of $f(x_j)$.
Based on the above formula, we compute the maximum Lyapunov exponent for the five chaotic maps for 1000 iterations. The average values of MLEs are given in Table 2.

Table 2. Maximum Lyapunov exponent of the ten chaotic maps

Map	Logistic	Gauss/mouse	Sinusoidal	Piecewise	Tent
MLE	0.693	0.721	0.682	1.532	0.693

It can be shown from Table 2 that the maximum Lyapunov exponent is positive for the five maps, meaning that these maps exhibit chaotic behavior. Therefore, they may be used with accuracy in chaotic optimisation algorithms.

5 Spider wasp optimization algorithm

The spider wasp optimization algorithm is a nature-inspired meta-heuristic algorithm that imitates the hunting, nesting, and mating behaviors of female spider wasps used in optimization problems. This work will develop a novel variant of the optimization strategy inspired by the hunting and nesting behaviors of some wasp species, as well as their practice of required brood parasitism,

which involves dropping a single egg into each spider's abdomen. Firstly, female spider wasps investigate the surrounding habitats in search of appropriate spiders. They then immobilize and transport the spiders to pre-prepared nests that are perfect for their needs. This behavior serves as the primary motivation for the SWO algorithm. Once they have located adequate prey and nests, they proceed to pull them into the nests. They then place an egg on the spider's abdomen, closing the nest. The SWO approach randomly distributes a specified number of female wasps over the search space. Each individual will systematically explore the search region in continuous motion, looking for a spider suitable for the gender of its offspring, as determined by the haplodiploid sex-determination system intrinsic to all hymenopterans. The search depends on their predatory and tracking behaviors. After finding suitable spiders, female spider wasps will remove them from the center region of the spider's web and systematically search the ground six times to recover any spiders that have fallen from the web [61]. Next, the female wasps will attack the victim and try to paralyze it for transmission to the selected nest. After putting an egg inside the spider's abdomen, the female wasp next closes the nest.

Figure 2. The female spider wasp in nature engages in hunting behavior

The following is a brief description of the wasp behaviors investigated in this study:

- Searching behavior. This behavior includes an aggressive search of prey during the first stages of optimization to determine a spider appropriate to larval growth.
- Following and escaping behavior: once they locate their prey or spiders, they may make an effort to quickly escape the central area of the spider web. As a result, the female wasp chases them, immobilizing and pulling the most suitable one.
- Nesting behavior. This behavior mimics the way in which prey is dragged to nests that are suitable in size for both the prey and the egg.
- Mating behavior. This behavior emulates the characteristics of the offspring produced by hatching the egg via the uniform crossover operator between male and female wasps, controlled by a certain probability called the crossover rate.

In the following, we will present the mathematical model for these four behaviors.

Hunting and nesting behavior

The female spider wasp initiates a first search, referred to as an "exploration operator", to discover potential prey. Once the target is identified, the entity transmits a signal to its operator responsible for exploiting the situation, initiating the process of approaching and launching an assault. The

mathematical specifics of these two operators are shown here.

Search stage (Exploration operator)

As previously mentioned, the female spider wasp initiates this operation at the onset of its search for its preferred food. This behaviour may be mathematically represented by the following expression:

$$\vec{x}_i^{t+1} = \vec{x}_i^t + \mu_1 * \left(\vec{x}_a^t - \vec{x}_b^t\right), \tag{2}$$

where a and b are two indices being randomly chosen from the current population, which are used to find the direction of investigation by the female wasps, and μ_1 is used to ascertain the consistent movement in this particular direction by means of the following equation:

$$\mu_1 = |r_n| * r_1, \tag{3}$$

where r_1 is a random number in $[0, 1]$ and r_n is a random number that has been picked from a normal distribution. If the female wasps are unable to grab it, prey that falls from the orb may be lost. In order to locate the missing prey, they use an alternative exploration approach, which may be precisely modeled using the following mathematical formula:

$$\vec{x}_i^{t+1} = \vec{x}_c^t + \mu_2 * \left(\overrightarrow{L} + \overrightarrow{r_2} * (\overrightarrow{U} - \overrightarrow{L})\right), \tag{4}$$

$$\mu_2 = B * \cos(2\pi l), \tag{5}$$

$$B = \frac{1}{1 + \exp(l)}, \tag{6}$$

where c, an index that represents the position of the dropped prey, is randomly chosen from the population. $\overrightarrow{L}$ and $\overrightarrow{U}$ represent the lower and upper bounds, respectively. l is a number randomly chosen from the interval $[-2, -1]$, whereas, $\vec{r_2}$ is a random vector in $[0, 1]$. The value of μ_2, which is between the range of -0.8 to 0.8, defines the direction of the search. This helps to prevent any incorrect direction that may be determined by Eq. (2). In order to enhance investigation and identify the most favorable areas, we assume that the following tradeoff between Eq. (2) and Eq. (4) is satisfied.

$$\vec{x}_i^{t+1} = \begin{cases} Eq.\ (2) & r_3 < r_4, \\ Eq.\ (4) & otherwise, \end{cases} \tag{7}$$

where r_3 and r_4 are two random numbers chosen from the range $[0, 1]$.

Following and escaping stage (exploration and exploitation operator)

Upon locating its prey, the wasp initiates pursuit of the spider. This behavior may be mathematically modeled in the following manner:

$$\vec{x}_i^{t+1} = \vec{x}_i^t + C * |2 * \overrightarrow{r_5} * \vec{x}_a^t - \vec{x}_i^t|, \tag{8}$$

$$C = \left(2 - 2 * \left(\frac{t}{t_{max}}\right)\right) * r_6, \tag{9}$$

where a is an index randomly selected from the population. t and t_{max} represent the current and maximum evaluations, respectively. $\overrightarrow{r_5}$ is a random vector in $[0,1]$, and r_6 is a random number in $[0,1]$. C is a parameter that modulates the wasp's speed according to distance, starting at a speed of two and progressively decreasing to zero. As the female wasp chases the spider, the distance between them gradually increases. This time period is mostly defined by exploitation. As the distance expands, exploitation evolves into exploration. This behavior is mimicked using the following formula:

$$\vec{x}_i^{t+1} = \vec{x}_i^t * \overrightarrow{v_c}, \tag{10}$$

where $\overrightarrow{v_c}$ is a vector of numerical values in the range $[-k,k]$ according to the normal distribution. k is given by the following formula:

$$k = 1 - \frac{t}{t_{max}}. \tag{11}$$

The next equation will be used for achieving the tradeoff between Eq. (8) and Eq. (10).

$$\vec{x}_i^{t+1} = \begin{cases} Eq.\ (8) & r_3 < r_4, \\ Eq.\ (10) & otherwise. \end{cases} \tag{12}$$

Further, the tradeoff between searching in Eq. (7) and Eq. (12) is described by the following equation:

$$\vec{x}_i^{t+1} = \begin{cases} Eq.\ (7) & p < k, \\ Eq.\ (12) & otherwise, \end{cases} \tag{13}$$

where p represents a random number in the range $[0,1]$.

Nesting behavior (exploitation operator)

Female wasps retrieve the damaged spider and bring it back to their nest. Spider wasps have the ability to excavate and construct chambers in the ground, build nests using mud on leaves or rocks, and make use of pre-existing nests or holes. Spider wasps exhibit diverse nesting behaviours, and as a result, the SWO algorithm employs two equations to represent these behaviors accurately. The first equation evaluates the spider's attraction to an area that provides the best conditions for nesting with its egg on its abdomen. This equation is given by:

$$\vec{x}_i^{t+1} = \vec{x}_i^t + \cos(2\pi l) * \left(\vec{x}^* - \vec{x}_i^t\right), \tag{14}$$

where $\vec{x}^*$ represents the optimum solution gained so far. The second equation establishes the nest at the position of a female spider, selected randomly from the population. This equation has a supplementary step size to guarantee that no two nests are constructed at the same location. Thus, we have the following equation:

$$\vec{x}_i^{t+1} = \vec{x}_a^t + r_3 * |\delta| * \left(\vec{x}_a^t - \vec{x}_i^t\right) + (1 - r_3) * \overrightarrow{H} * \left(\vec{x}_b^t - \vec{x}_c^t\right), \tag{15}$$

where a, b, and c represent the indices of three solutions randomly selected from the population. δ is a number determined by the Levy flight, and r_3 is a random number in the range $[0,1]$. $\overrightarrow{H}$ is a

binary vector that represents when a step size must be performed to avoid the construction of two nests at the same location. $\overrightarrow{H}$ is given as:

$$\overrightarrow{H} = \begin{cases} 1 & \overrightarrow{r_4} > \overrightarrow{r_5}, \\ 0 & otherwise, \end{cases} \tag{16}$$

where $\overrightarrow{r_4}$ and $\overrightarrow{r_5}$ are two random vectors in $[0, 1]$. In order to update each solution during the optimisation process, a random swap is performed between Eq. (14) and Eq. (20) using the following formula:

$$\vec{x}_i^{t+1} = \begin{cases} Eq.\ (14) & r_3 < r_4, \\ Eq.\ (20) & otherwise. \end{cases} \tag{17}$$

The tradeoff between hunting and nesting behaviors may be expressed using the following equation:

$$\vec{x}_i^{t+1} = \begin{cases} Eq.\ (13) & i < N * k, \\ Eq.\ (17) & otherwise, \end{cases} \tag{18}$$

where N represents the population size.

Mating behavior

At this stage, spider wasps have an important capacity to determine gender. This depends on the size of the egg. Smaller spider wasps imply males, and bigger wasps imply females. In our approach, each spider wasp represents a possible solution in the current generation, while the spider wasp egg signifies the newly generated possible solution in that same generation. The new solutions, also known as spider wasp eggs, are described by the following equation:

$$\vec{x}_i^{t+1} = Crossover\left(\vec{x}_i^t, \vec{x}_m^t, CR\right), \tag{19}$$

where *Crossover* represents the uniform crossover operator applied to the vectors $\vec{x}_i^t$ and $\vec{x}_m^t$ for the female and male spider wasps, respectively, with a probability CR. The male spider wasp is generated using the SWO algorithm to exhibit distinct characteristics from the female wasps, according to the following formula:

$$\vec{x}_i^{t+1} = \vec{x}_i^t + \exp(l) * |\beta| * \vec{v}_1 + (1 - \exp(l)) * |\beta_1| * \vec{v}_2, \tag{20}$$

where β and β_1 are two numbers picked randomly from the normal distribution. $\vec{v}_1$ and $\vec{v}_2$ are two vectors constructed using the following formula:

$$\begin{aligned} \vec{v}_1 &= \begin{cases} \vec{x}_a - \vec{x}_i & f\left(\vec{x}_a\right) < f\left(\vec{x}_i\right), \\ \vec{x}_i - \vec{x}_a & otherwise, \end{cases} \\ \vec{v}_2 &= \begin{cases} \vec{x}_b - \vec{x}_c & f\left(\vec{x}_b\right) < f\left(\vec{x}_c\right), \\ \vec{x}_c - \vec{x}_b & otherwise, \end{cases} \end{aligned} \tag{21}$$

where a, b, and c are distinct indices representing three solutions randomly chosen from the population. $f(\vec{x}_i)$ is the objective function that represents an individual in the population. Finally,

we denote by (TR) the tradeoff rate that determines the compromise between hunting, nesting, and mating behaviors.

Population reduction and conserving memory

After the female spider lays an egg on the host's abdomen, she closes the nest and discreetly vacates the location. This hypothesis suggests that the female's role in the optimization process is almost complete, and transferring the function evaluation to other wasps for the remainder of the process may provide enhanced results. Over the iteration, some wasps in the population will be killed to provide more function evaluations to the surviving wasps. This mechanism reduces population variety, hence accelerating convergence towards the near-optimal solution. In each iteration of the function evaluations, the size of the new population will be adjusted according to the following equation:

$$N = N_{min} + (N - N_{min}) \times k, \tag{22}$$

where N_{min} denotes the minimal population size required to prevent the optimization process from being trapped in local minima. To enhance efficiency, the SWO applies a memory preservation method that transmits the highest rank of each wasp to the next generation. The proposed new location of each wasp is evaluated against its current position, and if it is worse, the next solution is substituted. The pseudo-code of the SWO algorithm is shown in Algorithm 1.

Algorithm 1: Pseudo-code of SWO algorithm

Input: N, N_{min}, CR, TR, t_{max}
Output: $\vec{x}_i^*$

```
Initialize N female wasps, x_i^t (i = 1, 2, ..., N), using Eq. (2)
Compute f(x_i^t) while storing x*
t = 1;
while (t < t_max) do
    r_6: generating a random number in the interval [0, 1]
    if (r_6 < TR) then
        for i = 1 : N do
            Update the position of x_i^t using Eq.(18) to x_i^{t+1}
            Compute f(x_i^{t+1})
            t = t + 1;
        end for
        else
        for i = 1 : N do
            Applying Eq. (19)
            t = t + 1;
        end for
    end if
    Applying Conserving Memory
    Updating N using Eq. (22)
end while
```

6 The improved chaotic spider wasp optimization algorithm

According to Eq. (3) and Eq. (9), the parameters r_1 and r_6 are the main variables of female spider wasps' convergence toward their objective throughout the SWO algorithm iterations. Chaotic maps have the capacity to enhance the performance of optimization methods. In the standard SWO algorithm, there is no need to preserve linearly decreasing values. In fact, using a chaotic variable that changes r_1 and r_2 may be better for the search. According to the SWO, the values obtained through the chaotic map must fall within the range of $[0,1]$. In the current work, the values of r_1 and r_6 highlighted in Algorithm 1 are substituted with the values generated by chaotic maps to give chaotic behavior to the r_1 and r_6 parameters. This may also lead to the approach converging to the optimal value quickly, as explained in the next section. As a result, this study focuses on the task of adjusting the values of r_1 and r_6 using several chaotic maps. Ten different kinds of SWO employ distinct chaotic maps. In the rest, we will construct four variants of the SWO by adopting the following manner:

- Eq. (23) is obtained by substituting the random parameter r_1 in the search stage that initiates the spider wasp optimization algorithm with the sequence obtained from ten different chaotic maps, where $r_1(t)$ represents the value that results from the chaotic map over the t-th iteration.
- Eq. (24) is obtained by substituting the random parameter r_6 in the following and escaping stage found in the spider wasp optimization algorithm with the sequence obtained from ten different chaotic maps, where $r_6(t)$ represents the value that results from the chaotic map over the t-th iteration.

$$CSWOA1 : \mu_1(t) = |r_n| * r_1(t), \tag{23}$$

$$CSWOA2 : C(t) = \left(2 - 2 * \left(\frac{t}{t_{max}}\right)\right) * r_6(t), \tag{24}$$

$$CSWOA3 : \mu_1(t) = |r_n| * r_1(t) \quad \text{and} \quad C(t) = \left(2 - 2 * \left(\frac{t}{t_{max}}\right)\right) * r_6(t). \tag{25}$$

CSWOA3 has been constructed by combining the CSWOA1 and CSWOA2 algorithms. In order to enrich the content of this study, the CSWOA4 is created by substituting the random number p in Eq. (13) in the SWO with chaotic maps. Thus, the parameter p will behave chaotically.

$$CSWOA4 : \vec{x}_i^{t+1} = \begin{cases} Eq.\ (7) & p(t) < k, \\ Eq.\ (12) & otherwise, \end{cases} \tag{26}$$

where $p(t)$ represents the value that results from the chaotic map over the t-th iteration.

The next section presents a comparative analysis using the distinct chaotic parameters mixed with the traditional SWO algorithm. Furthermore, the combination of these parameters (SWO with chaotic r_1, SWO with chaotic r_6, SWO with chaotic r_1 and chaotic r_6, and SWO with chaotic p) has been implemented and tested using several benchmark functions.

The key distinctions between these algorithms lie in the incorporation of chaos theory into their parameters, which enhances their exploration, exploitation, and convergence properties. In CSWOA1, CSWOA2, and CSWOA4, the integration of chaotic maps is applied only in one parameter (r_1, r_6, and p, respectively). However, in CSWOA3, we have incorporated both the parameters r_1 and r_6 with chaotic maps. This makes CSWOA3 more robust and effective for solving complex optimization problems compared to other algorithms. Integrating more than one chaotic map in CSWOA3 can improve its ability to explore the search space thoroughly because

each chaotic map generates more diverse and unpredictable sequences. The chaotic behaviors help the algorithm's convergence, enhancing both speed and precision, particularly in complex and multimodal optimization problems, by avoiding premature convergence. Therefore, by adopting two chaotic parameters in CSWOA3, we obtain a better balance between exploration and exploitation. This results in improved convergence and higher-quality solutions. In conclusion, incorporating chaos theory into CSWOA1, CSWOA2, CSWOA3, and CSWOA4 adds stochasticity and unpredictability, which improves the algorithm's ability to escape local optima and explore the search space more effectively.

In practice, the chaotic spider wasp optimization algorithm avoids local optima by employing several strategies:

- Using chaotic maps allows providing randomness and diversity, where the algorithm can escape local optima by generating diverse solutions that might not be reachable through deterministic methods.
- Balancing exploration and exploitation through a dual population strategy. The algorithm mimics the behavior of spider wasps, which use two populations: spiders (prey) and wasps (predators). The interactions between these two populations ensure a balance between exploration (wasps searching for spiders) and exploitation (spiders trying to escape). This dual strategy helps avoid stagnation in local optima by maintaining diversity in the search process.
- Dynamically adjusting parameters to adapt to the search process. This allows the algorithm to switch between exploration and exploitation stages, reducing the risk of getting trapped in local optima.
- Introducing random perturbations to escape stagnation. These perturbations help the algorithm explore new regions of the search space, even after it has found a promising solution.
- Maintaining population diversity through fitness-based selection in order to prioritize better solutions to contribute to the search process. These mechanisms collectively enable the CSWO algorithm to explore the search space more effectively and avoid getting stuck in suboptimal solutions.

The following objectives may help demonstrate the theoretical efficiency of the suggested chaotic algorithms:

- The chaotic r_1 aids CSWO in dynamically updating the locations of female spider wasps in a chaotic manner, which can improve the exploration process.
- As we mentioned, C in Eq. (9) is a distance-controlling factor that determines the speed of the wasp when it starts chasing the prey (spider). Thus, the chaotic r_6 provides greater speed to CSWO in the exploitation stage than the SWO because the r_6 may have various values.
- Various chaotic maps for r_1, r_6 and p provide better exploration and exploitation behaviors for the CSWO algorithm.
- Chaotic maps aid the CSWO in escaping local optima when confronted with this problem.

The pseudo-code of the CSWO algorithm is shown in Algorithm 2.

For completeness, we provide a comparison of computational complexity between SWO and CSWO algorithms in Table 3.

From Table 3, it is shown that the computational complexity of CSWO is slightly higher than SWO due to the additional chaotic behavior. The complexity for SWO can be considered as $O(t_{max} \cdot N)$, while $O(t_{max} \cdot N \cdot C)$ for CSWO, where N is the population size, t_{max} is the maximum number of iterations, and C is the complexity introduced by the chaotic maps. On the other hand, the time

Algorithm 2: Pseudo-code of CSWO algorithm

Input: N, N_{min}, CR, TR, t_{max}
Output: $\vec{x}_i^*$

```
Initialize N female wasps, x_i^t (i = 1, 2, ..., N), using Eq. (2)
Evaluate each x_i^t and calculate the fitness of each search agent
x* = the best search agent
Initialize the value of the chaotic map x_0 randomly
t = 1;
while (t < t_max) do
    Update the chaotic number using the chaotic map function
    if (r_6 < TR) then
        for i = 1 : N do
            Update the position of x_i^t using Eq. (18) to x_i^{t+1}
            Compute f(x_i^{t+1})
            t = t + 1;
        end for
        else
        for i = 1 : N do
            Applying Eq. (19)
            t = t + 1;
        end for
    end if
    Applying Conserving Memory
    Updating N using Eq. (22)
end while
```

Table 3. Comparison of computational complexity of SWO and CSWO algorithms

Feature	SWO	CSWO
Initialization	Random population of agents	Random population of agents
Evaluation	Objective function	Objective function
Position update	Random and local search	Chaotic maps enhance search
Mating behavior	Information exchange	Information exchange
Selection	Best solution selected	Best solution selected
Computational complexity	$O(t_{max} \cdot N)$	$O(t_{max} \cdot N \cdot C)$
Time complexity	$O(t_{max} \cdot D \cdot N) + O(t_{max} \cdot D \cdot N)$	$O(t_{max} \cdot D \cdot N \cdot C) + O(t_{max} \cdot D \cdot N)$
Exploration capability	Standard	Enhanced by chaotic behavior
Exploitation capability	Standard	Enhanced by chaotic behavior

complexity for the SWO algorithm is designed as:

$$\begin{aligned} T(SWO) &= T(\text{Hunting and Nesting behaviors}) + T(\text{Mating behavior}) \\ &= O(t_{max} \cdot D \cdot N) + O(t_{max} \cdot D \cdot N), \end{aligned} \tag{27}$$

where D is the dimension of the search space. For the CSWO algorithm, the time complexity is designed as:

$$T(CSWO) = O(t_{max} \cdot D \cdot N \cdot C) + O(t_{max} \cdot D \cdot N). \tag{28}$$

Therefore, CSWO generally offers better performance in terms of exploration and exploitation due to the integration of chaotic maps, but at the cost of increased both computational and time complexities compared to the standard SWO algorithm.

7 Experimental setup and result discussions

The accuracy of the proposed meta-heuristic algorithms will be compared to traditional SWO using a set of eight well-known unimodal or multimodal benchmark functions. Unimodal benchmark functions provide only one optima and are very suitable for evaluating and comparing exploitation strategies. In contrast, multimodal benchmark functions include several optima, which renders them more complex than unimodal functions. The term "global optima" means that there exists a single optima, whereas the rest are known as "local optima". The key property of any efficient meta-heuristic algorithm is its capacity to avoid local optima and determine the global optimum. The primary goal of multimodal benchmark functions is to evaluate the exploration's performance in order to avoid trapping in local optima. Table 4 presents a summary of the test functions, including their range of optimization variables, their dimension Dim, and their minima f_{min}. Furthermore, the topologies of benchmark functions are represented in Figure 3. As shown in Table 4, the minima of all the proposed test functions is 0, except for the Schwefel function. Among the proposed benchmark functions, the unimodal functions are F_1, F_2, F_3, F_7 and F_8. In contrast, F_4, F_5 and F_6 are multimodal functions.

Table 4. List of eight benchmark functions

Function name	Formula	Dim	Search space	f_{min}
Sphere	$F_1(x) = \sum_{i=1}^{n} x_i^2$	30	$[-100, 100]$	0
Quartic Noise	$F_2(x) = \sum_{i=1}^{n} ix_i^4 + rand(0,1)$	30	$[-1.28, 1.28]$	0
Rosenbrock	$F_3(x) = \sum_{i=1}^{n-1} \left[100(x_{i+1} - x_i^2)^2 + (x_i - 1)^2\right]$	30	$[-30, 30]$	0
Griewank	$F_4(x) = \frac{1}{4000} \sum_{i=1}^{n} x_i^2 - \prod_{i=1}^{n} \cos(\frac{x_i}{\sqrt{i}}) + 1$	30	$[-600, 600]$	0
Rastrigin	$F_5(x) = \sum_{i=1}^{n} \left[x_i^2 - 10\cos(2\pi x_i + 10)\right]$	30	$[-5.12, 5.12]$	0
Schwefel	$F_6(x) = -\sum_{i=1}^{n} x_i \sin(\sqrt{\lvert x_i \rvert})$	30	$[-500, 500]$	-418.9829$\times D$
Schwefel 2.21	$F_7(x) = \max\{\lvert x_i \rvert, 1 \leq i \leq n\}$	30	$[-100, 100]$	0
Schwefel 2.22	$F_8(x) = \sum_{i=1}^{n} \lvert x_i \rvert + \prod_{i=1}^{n} \lvert x_i \rvert$	30	$[-10, 10]$	0

We can measure each algorithm's performance using three distinct statistical tests: the best, the mean of the fitness function, and the standard deviation (STD).

1. **Statistical mean:** represents the average value of the best fitness function F_* obtained after performing the algorithm T_{max} iterations. It is computed as follows:

$$Mean = \frac{1}{T_{max}} \sum_{i=1}^{T_{max}} F_*^i. \tag{29}$$

2. **Statistical best:** represents the minimum value of the best fitness function F_* obtained after performing the algorithm T_{max} iterations, i.e;

$$Best = \min_{i=1}^{T_{max}} F_*^i. \tag{30}$$

3. **Statistical standard deviation:** is used as a performance test to verify the algorithm's stability

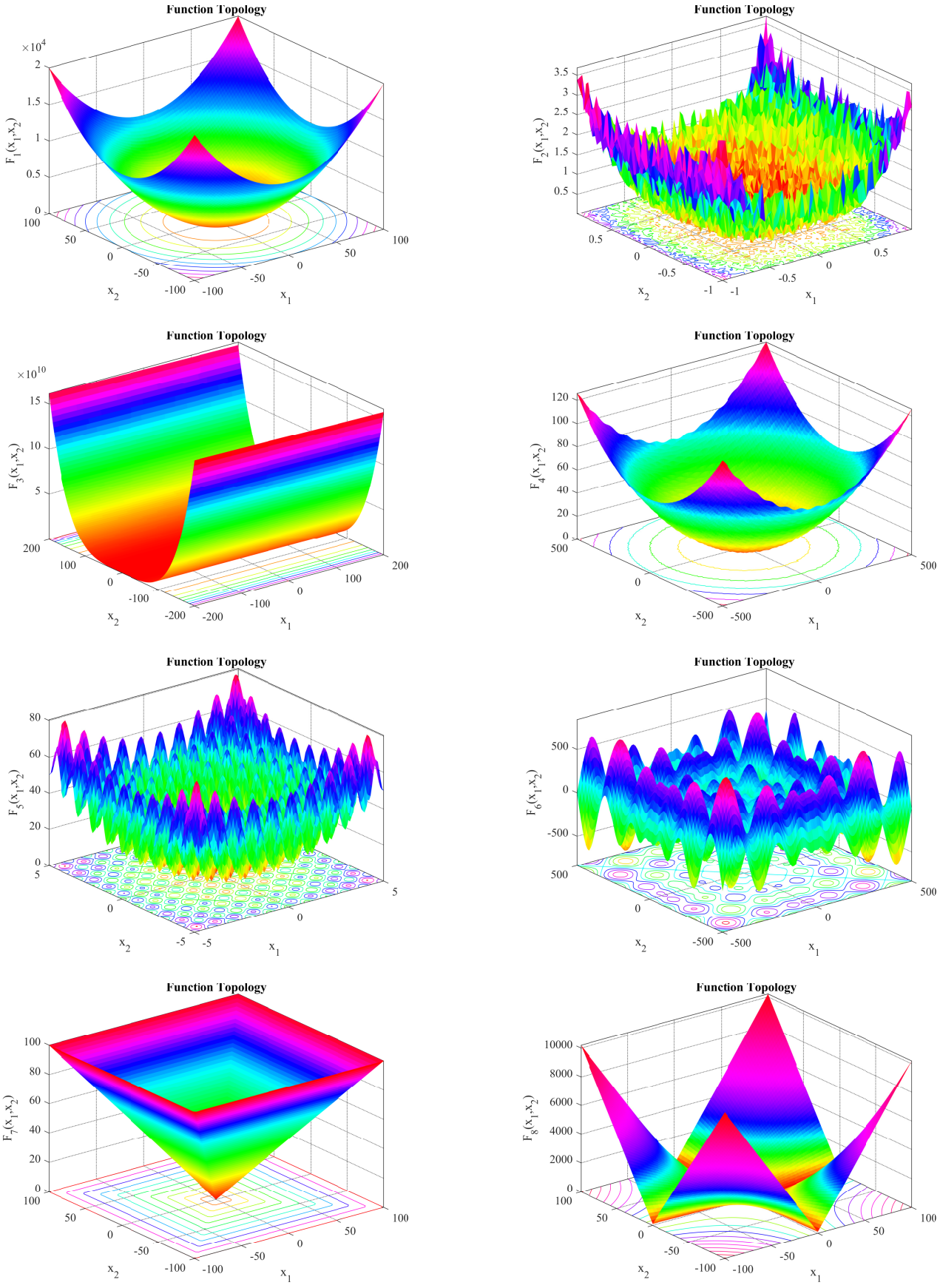

Figure 3. Topologies of the benchmark functions

and robustness. A lower standard deviation in the obtained solutions means that the algorithm accurately finds good solutions. It can be determined as:

$$STD = \sqrt{\frac{1}{T_{max}-1}\sum_{i=1}^{T_{max}}\left(F_*^i - Mean\right)^2}. \tag{31}$$

The performance of CSWO with chaos

All algorithms in the following numerical simulations were implemented using MATLAB software with the Microsoft Windows 10 operating system. All simulations are performed on the same PC with an Intel(R) Core(TM) i5-6300U 2.4 processor and 8GB of RAM. The proposed meta-heuristic algorithms are evaluated on various well-known benchmark functions using different chaotic maps. Their details can be found in Table 4. For all algorithms, the number of population is 30, the number of iterations is 500, and the number of independent runs is 10. The results of five chaotic maps applied from CSWO1 to CSWO4 are displayed in Table 6, where the best, the mean (average), and the STD of the best solutions obtained in the last iteration in simulation are illustrated. Function values showing the most optimal results are emphasized in bold. It can be shown from Table 6 that CSWO algorithms provide better results as compared to SWO algorithm. In particular, Gauss/mouse, piecewise, and tent maps yields better results. In contrast, logistic and sinusoidal maps perform less well when we implement CSWO compared to the SWO algorithm. Therefore, Gauss/mouse, piecewise, and tent maps may effectively improve the performance of SWO algorithm. Table 6 shows that the tent and piecewise-based SWO algorithms consistently generates the best solutions over all test functions. In the following, considering the mean and standard deviation statistical tests, a comparison is conducted between test functions that have been optimized using the spider wasp optimization algorithm (SWO) and test functions that have been optimized using chaotic maps.

- For function F_1, Gauss/mouse map-based CSWO 1, CSWO 2, and CSWO 3 algorithms, along with sinusoidal map-based CSWO 2, CSWO 3, and piecewise map-based CSWO 1, CSWO 2, and CSWO 3 algorithms, yield better results than SWO algorithm.
- For function F_2, all logistic map-based algorithms from CSWO 1 to CSWO 4, Gauss/mouse map-based CSWO 2, CSWO 3, and CSWO 4 algorithms, sinusoidal map-based CSWO 1, and CSWO 2 algorithms, piecewise map-based CSWO 2, CSWO 3, and CSWO 4 algorithms, and all tent map-based algorithms from CSWO 1 to CSWO 4 give better solutions than SWO algorithm.
- For function F_3, logistic map-based CSWO 4 algorithm, Gauss/mouse map-based CSWO 4 algorithm, piecewise map-based CSWO 2 and CSWO 3 algorithms, and tent map-based CSWO 3 and CSWO 4 algorithms yield better results compared to SWO algorithm.
- For functions F_4 and F_5, it has been demonstrated that most chaotic algorithms accurately provide the minima of these functions, which is 0, with the exception of some algorithms such as Gauss/mouse map-based CSWO 3 and CSWO 4 algorithms, and sinusoidal map-based CSWO 1 and CSWO 4 algorithms. As a result, the logsitic, piecewise, and tent maps can accurately improve the SWO algorithm's performance.
- For function F_6, most of the chaotic algorithms using logistic, Gauss/mouse, sinusoidal, piecewise, and tent maps give better results than SWO algorithm. Thus, using chaos can improve the research performance for minima of function F_6.
- For function F_7, logistic map-based CSWO 1, CSWO 2, and CSWO 4 algorithms, Gauss/mouse map-based CSWO 2 algorithm, sinusoidal map-based CSWO 3 algorithm, and tent map-based CSWO 2 algorithm provide better solutions compared to SWO algorithm. Obviously, using

chaotic maps for function F_7 can greatly enhance the optimization process's performance.
- For function F_8, logistic map-based CSWO 1, CSWO 2, and CSWO 4 algorithms, Gauss/mouse map-based CSWO 1 and CSWO 2 algorithms, sinusoidal map-based CSWO 1 and CSWO 3 algorithms, piecewise map-based CSWO 1, CSWO 3, and CSWO 4 algorithms, and all tent map-based algorithms from CSWO 1 to CSWO 4 display better solutions as compared to SWO algorithm.

According to the comparative study, the F_4 and F_5 functions demonstrated higher efficiency compared to the other functions in algorithms based on logistic, Gauss/mouse, sinusoidal, piecewise, and tent chaotic maps.

In the resolution of diverse optimization problems, both runtime and solution accuracy are of crucial importance. Table 5 shows the average runtime of the algorithm using different chaotic maps. From the table, it is shown that the runtime decreases when integrating chaotic maps into

Table 5. Runtime of SWO and CSWO algorithms (Unit: second)

Map	Metrics	SWO	CSWOA1	CSWOA2	CSWOA3	CSWOA4
No map	Time	45.2	N/A	N/A	N/A	N/A
	Rank	N/A	N/A	N/A	N/A	N/A
Logistic	Time	N/A	29.1	29.3	28.67	28.89
	Rank	N/A	3	4	1	2
Gauss/mouse	Time	N/A	27.4	28.32	27.1	28.12
	Rank	N/A	2	4	1	3
Sinusoidal	Time	N/A	28.56	29.94	28.42	28.16
	Rank	N/A	3	4	2	1
Piecewise	Time	N/A	31.62	34.26	30.99	31.44
	Rank	N/A	3	4	1	2
Tent	Time	N/A	31.84	31.72	30.25	30.59
	Rank	N/A	4	3	1	2
	Mean Rank	N/A	3.00	3.80	1.20	2.00
	Final Rank	5	3	4	1	2

the SWO algorithm. From the last row of the table, it can be seen that the average runtime of the CSWOA3 is ranked 1.20, placing it first overall, which is better compared to the SWO, CSWOA1, CSWOA2, CSWOA3, and CSWOA4. Therefore, incorporating chaos theory in the traditional SWO algorithm enhances its convergence speed, which ensures the efficiency of the CSWO algorithm for solving various optimization problems.

Qualitative analysis

A qualitative study has been conducted on several benchmark functions. Figure 4(a)-Figure 4(h) illustrate the convergence of several benchmark functions using the CSWO algorithm. These graphs provide an additional explanation of each algorithm's convergence rate, showing the best optimal solution obtained from 10 iterations of the algorithm using the tent chaotic map.

Figure 4(a) represents the convergence curves obtained using the tent map on the F_1 Sphere function, which has 0 as a global minimum. From Figure 4(a), CSWO 3 has the fastest convergence rate to the global solution. Similarly, CSWO 1 is very close to CSWO 3, which provides a very good convergence rate. On the other hand, SWO yields the slowest convergence rate when it comes to determining the global minimum during the optimization process.

Figure 4(b) depicts the convergence curves obtained using the tent map on the F_2 Quartic noise function, which has 0 as a global minimum. From Figure 4(b), CSWO 3 has the fastest convergence

rate to the global solution. Similarly, CSWO 4 is very close to CSWO 3, which gives a very good convergence rate. On the other hand, SWO yields the slowest convergence rate when it comes to determining the global minimum during the optimization process.

Figure 4(c) illustrates the convergence curves obtained using the tent map on the F_3 Rosenbrock function, which has 0 as a global minimum. As can be shown, CSWO 2 with CSWO 3 and CSWO 1 have the fastest convergence rate to the global solution. In contrast, SWO and CSWO 4 provide the slowest convergence rate over the maximum number of iterations.

Figure 4(d) displays the convergence curves obtained using the tent map on the F_4 Greiwank function. F4 has the property of being slightly easier to solve for dimensions that are higher rather than lower [62]. From Figure 4(d), it is shown that all of the algorithms failed to find the global solution over the maximum number of iterations, and they crashed before the first 60 iterations. Over the search process, CSWO 3 and CSWO 4 have the best convergence rate towards the global optimum.

Figure 4(e) shows the convergence curves obtained using the tent map on the F_5 Rastrigin function. As can be observed, all of the algorithms failed to find the global solution over the maximum number of iterations, and they crashed before the first 50 iterations. During the search process, CSWO 2 and CSWO 4, followed by SCWO 3 and SWO, have the best convergence rate towards the global optimum.

Figure 4(f) illustrates the convergence curves obtained using the tent map on the F_6 Schwefel function. As can be shown, CSWO 1 and CSWO 2, followed by CSWO 3 and CSWO 4, have the fastest convergence rate to the global solution. In contrast, SWO displays the slowest convergence rate over the maximum number of iterations.

Figure 4(g) represents the convergence curves obtained using the tent map on the unimodal F_7 Schwefel 2.21 function, which has 0 as a global minimum. As we can see, CSWO 1 has the fastest convergence rate to the global solution compared to the other algorithms. In particular, SWO provides the slowest convergence rate over the maximum number of iterations. As a result, the meta-heuristic algorithm's performance is improved when using chaotic maps.

Figure 4(h) shows the convergence curves obtained using the tent map on the unimodal F_8 Schwefel 2.22 function, which has 0 as a global minimum. Compared to the other algorithms, CSWO 1 and CSWO 3 exhibit the fastest convergence rate to the global solution. In particular, SWO and CSWO 4 display the slowest convergence rate over the maximum number of iterations. Finally, we can conclude that using chaos in meta-heuristic optimization algorithms provides better performance in the search process for the optimum solution.

8 Discussion and conclusions

This work has presented a novel variant of the SWO algorithm enhanced by chaos theory, developing the CSWO algorithm. Five chaotic maps were selected for improving the traditional SWO algorithm's efficiency by adjusting parameters. Inspired by the behaviors of female spider wasps, the CSWO algorithm imitates searching for a spider, escaping a falling spider, nesting the entrapped spider, and mating behavior during egg-laying. The robustness of the CSWO algorithm was analyzed using eight benchmark functions to evaluate exploitation, exploration, capacity to escape local optima, and convergence speed. The study showed that chaotic maps, particularly the tent and piecewise maps, significantly improved SWO performance. The incorporating of chaos increases the search speed for the best solution by replacing pseudo-random numbers with chaotic variables, enhancing the convergence rate during the optimization process.

Table 6. Statistical tests on benchmark functions using 5 chaotic maps on CSWO

Map	Algorithms		Functions							
			F_1	F_2	F_3	F_4	F_5	F_6	F_7	F_8
No map	SWO	Best	2.26E−154	1.44E−05	8.44E−06	**0.00E+00**	**0.00E+00**	−1.97E+04	9.70E−82	6.02E−79
		Mean	5.14E−111	1.57E−04	1.10E−03	**0.00E+00**	**0.00E+00**	−1.85E+04	2.80E−68	5.16E−56
		STD	1.62E−110	1.40E−04	1.18E−03	**0.00E+00**	**0.00E+00**	1.24E+04	8.85E−68	1.63E−55
Logistic	CSWO 1	Best	8.93E−155	6.27E−06	3.13E−06	**0.00E+00**	**0.00E+00**	**−4.18E+03**	4.59E−77	3.34E−78
		Mean	2.50E−105	1.51E−04	2.09E−03	**0.00E+00**	**0.00E+00**	−3.67E+03	1.14E−71	3.69E−72
		STD	7.91E−105	1.76E−04	2.77E−03	**0.00E+00**	**0.00E+00**	8.32E+02	3.61E−71	7.63E−72
	CSWO 2	Best	3.90E−156	2.23E−05	4.78E−05	**0.00E+00**	**0.00E+00**	**−4.18E+03**	4.51E−81	1.39E−78
		Mean	7.88E−104	1.16E−04	1.43E−03	**0.00E+00**	**0.00E+00**	−3.49E+03	1.11E−71	**4.21E−75**
		STD	2.69E−103	8.84E−05	1.68E−03	**0.00E+00**	**0.00E+00**	8.94E+02	3.46E−71	**1.11E−74**
	CSWO 3	Best	1.51E−158	8.70E−06	5.17E−05	**0.00E+00**	**0.00E+00**	**−4.18E+03**	4.42E−77	9.84E−81
		Mean	5.94E−106	1.03E−04	1.39E−03	**0.00E+00**	**0.00E+00**	−3.54E+03	4.98E−57	2.47E−53
		STD	1.87E−105	1.18E−04	1.26E−03	**0.00E+00**	**0.00E+00**	8.32E+02	1.57E−56	7.81E−53
	CSWO 4	Best	1.90E−150	1.17E−05	5.85E−06	**0.00E+00**	**0.00E+00**	**−4.18E+03**	8.86E−76	3.97E−77
		Mean	5.98E−72	1.52E−04	2.00E−04	**0.00E+00**	**0.00E+00**	−3.50E+03	1.14E−71	1.35E−60
		STD	1.88E−71	1.33E−04	**1.87E−04**	**0.00E+00**	**0.00E+00**	8.86E+02	3.43E−71	4.29E−60
Gauss/mouse	CSWO 1	Best	6.96E−159	6.73E−06	2.03E−05	**0.00E+00**	**0.00E+00**	**−4.18E+03**	3.03E−80	5.66E−81
		Mean	1.41E−127	1.61E−04	2.22E−03	**0.00E+00**	**0.00E+00**	−3.28E+03	1.62E−52	4.23E−58
		STD	4.47E−127	1.57E−04	3.94E−03	**0.00E+00**	**0.00E+00**	8.47E+02	5.12E−52	1.33E−57
	CSWO 2	Best	9.29E−161	1.50E−05	1.62E−06	**0.00E+00**	**0.00E+00**	**−4.18E+03**	4.79E−79	2.05E−78
		Mean	**6.75E−142**	1.54E−04	2.09E−03	**0.00E+00**	**0.00E+00**	−3.34E+03	2.55E−66	1.99E−57
		STD	**2.11E−141**	1.06E−04	3.70E−03	**0.00E+00**	**0.00E+00**	8.99E+02	8.07E−66	6.31E−57
	CSWO 3	Best	8.15E−161	9.89E−06	1.34E−05	1.03E−04	1.34E−05	−4.13E+03	1.42E−78	2.60E−78
		Mean	1.11E−107	1.00E−04	2.09E−03	2.10E−02	1.72E−02	−2.45E+03	3.39E−59	6.41E−54
		STD	3.53E−107	8.44E−05	2.17E−03	2.89E−02	3.70E−02	7.33E+02	1.07E−58	2.02E−53
	CSWO 4	Best	**7.41E−166**	9.05E−06	1.63E−05	1.11E−16	1.42E−14	−2.33E+03	**4.15E−83**	**1.57E−83**
		Mean	8.11E−78	8.83E−05	8.77E−04	2.60E−07	2.77E−11	−2.09E+03	5.93E−40	1.27E−37
		STD	2.54E−77	6.07E−05	1.61E−03	7.76E−07	5.51E−11	1.94E+02	1.87E−39	3.68E−37

Map	Algorithms		Functions							
			F_1	F_2	F_3	F_4	F_5	F_6	F_7	F_8
Sinusoidal	CSWO 1	Best	5.92E−160	1.20E−05	2.87E−05	1.04E−11	5.68E−14	−3.00E+03	2.79E−78	3.09E−79
		Mean	2.33E−105	1.17E−04	2.14E−03	4.21E−09	9.41E−10	−2.31E+03	2.12E−58	9.32E−63
		STD	7.37E−105	9.45E−05	3.08E−03	5.29E−09	9.69E−10	4.12E+02	6.72E−58	2.94E−62
	CSWO 2	Best	9.09E−155	1.12E−05	3.40E−05	**0.00E+00**	**0.00E+00**	**−4.18E+03**	1.41E−80	3.34E−81
		Mean	3.59E−128	1.12E−04	2.03E−03	**0.00E+00**	**0.00E+00**	−3.53E+03	1.72E−62	3.07E−55
		STD	1.13E−127	8.10E−05	3.23E−03	**0.00E+00**	**0.00E+00**	8.71E+02	5.46E−62	9.39E−55
	CSWO 3	Best	7.14E−157	3.41E−05	7.68E−06	3.33E−15	**0.00E+00**	**−4.18E+03**	2.39E−77	4.48E−82
		Mean	4.63E−111	1.79E−04	1.52E−03	4.67E−08	1.74E−10	−3.82E+03	**7.41E−73**	4.73E−70
		STD	1.46E−110	1.24E−04	3.35E−03	1.47E−07	3.31E−10	7.67E+02	**1.73E−72**	1.49E−69
	CSWO 4	Best	5.78E−22	2.25E−05	2.01E−03	**0.00E+00**	**0.00E+00**	−3.88E+03	8.78E−12	6.18E−10
		Mean	4.17E−08	1.79E−04	5.47E−02	9.15E−08	1.00E−12	−2.75E+03	1.35E−05	8.43E−05
		STD	1.32E−07	1.40E−04	5.92E−02	1.16E−07	2.68E−12	4.66E+02	4.23E−05	2.52E−04
Piecewise	CSWO 1	Best	9.29E−161	1.50E−05	**1.62E−06**	**0.00E+00**	**0.00E+00**	**−4.18E+03**	4.79E−79	2.05E−78
		Mean	**6.75E−142**	1.76E−04	2.09E−03	**0.00E+00**	**0.00E+00**	−3.40E+03	2.55E−66	1.99E−57
		STD	**2.11E−141**	1.52E−04	3.70E−03	**0.00E+00**	**0.00E+00**	8.45E+02	8.07E−66	6.31E−57
	CSWO 2	Best	5.85E−159	6.67E−06	3.61E−05	**0.00E+00**	**0.00E+00**	**−4.18E+03**	7.40E−81	1.04E−79
		Mean	2.95E−141	1.12E−04	6.93E−04	**0.00E+00**	**0.00E+00**	−3.66E+03	5.68E−54	4.72E−53
		STD	9.35E−141	9.67E−05	4.95E−04	**0.00E+00**	**0.00E+00**	8.16E+02	1.79E−53	1.49E−52
	CSWO 3	Best	1.07E−154	1.60E−05	1.04E−05	**0.00E+00**	**0.00E+00**	**−4.18E+03**	6.25E−81	6.19E−79
		Mean	3.83E−125	1.21E−04	7.81E−04	**0.00E+00**	**0.00E+00**	−3.89E+03	5.39E−66	6.43E−61
		STD	1.21E−124	9.55E−05	9.79E−04	**0.00E+00**	**0.00E+00**	6.14E+02	1.69E−65	1.84E−60
	CSWO 4	Best	7.21E−160	7.85E−06	2.81E−05	**0.00E+00**	**0.00E+00**	**−4.18E+03**	7.53E−80	1.96E−80
		Mean	9.23E−99	6.79E−05	1.26E−03	**0.00E+00**	9.81E−05	**−4.03E+03**	1.55E−39	4.22E−75
		STD	2.91E−98	7.46E−05	1.40E−03	**0.00E+00**	3.10E−04	**4.74E+02**	3.27E−39	1.31E−74

Map	Algorithms		Functions							
			F_1	F_2	F_3	F_4	F_5	F_6	F_7	F_8
Tent	CSWO 1	Best	1.46E−165	1.33E−05	2.54E−06	**0.00E+00**	**0.00E+00**	**−4.18E+03**	2.58E−78	2.90E−80
		Mean	8.80E−104	1.13E−04	2.11E−03	**0.00E+00**	**0.00E+00**	−3.66E+03	9.15E−56	1.21E−71
		STD	2.78E−103	1.18E−04	4.10E−03	**0.00E+00**	**0.00E+00**	6.89E+02	2.89E−55	3.81E−71
	CSWO 2	Best	1.18E−155	1.22E−06	1.94E−06	**0.00E+00**	**0.00E+00**	**−4.18E+03**	2.35E−76	1.13E−79
		Mean	6.30E−101	1.56E−04	1.70E−03	**0.00E+00**	**0.00E+00**	−3.40E+03	2.55E−68	4.42E−56
		STD	1.80E−100	1.36E−04	3.46E−03	**0.00E+00**	**0.00E+00**	1.00E+03	4.57E−68	1.39E−55
	CSWO 3	Best	4.67E−160	**9.74E−07**	1.55E−05	**0.00E+00**	**0.00E+00**	**−4.18E+03**	5.50E−83	2.23E−80
		Mean	5.26E−106	**3.98E−05**	8.78E−04	**0.00E+00**	1.58E−05	−3.79E+03	1.72E−54	7.21E−73
		STD	1.66E−105	**3.93E−05**	1.68E−03	**0.00E+00**	5.01E−05	8.08E+02	3.91E−54	2.28E−72
	CSWO 4	Best	3.35E−143	1.45E−05	3.01E−06	**0.00E+00**	**0.00E+00**	**−4.18E+03**	6.17E−72	4.01E−73
		Mean	7.16E−65	9.70E−05	**3.94E−04**	**0.00E+00**	**0.00E+00**	−3.70E+03	1.72E−34	2.50E−66
		STD	2.07E−64	6.70E−05	4.95E−04	**0.00E+00**	**0.00E+00**	8.02E+02	5.44E−34	4.91E−66

Chaotic maps can improve the SWO algorithm by enhancing exploration and exploitation, but they come with several challenges. Using chaotic maps increases computational overhead and complexity, which can slow down the algorithm. Performance is sensitive to map selection and parameters, leading to unpredictability. Chaotic behavior can cause excessive exploitation, reducing population diversity and causing premature convergence. Multiple chaotic maps introduce implementation challenges and increase complexity. They can also exhibit noise, potentially destabilizing the optimization process. Careful tuning and empirical validation are needed to effectively integrate chaotic maps and benefit from their behavior.

The CSWO algorithm, inspired by spider wasps and enhanced with chaotic maps, is a powerful metaheuristic optimization method applicable to many real-world scenarios. In engineering, it optimizes structures like bridges, airplane wings, and mechanical systems for efficiency and material use. In energy systems, it improves renewable energy configurations and power grid operations. For transportation, it resolves vehicle routing issues and optimizes traffic signals to reduce congestion. In healthcare, CSWO enhances medical imaging and drug design. Financial firms use it for portfolio optimization and algorithmic trading. In machine learning, it aids feature selection and hyperparameter tuning. Environmental applications include water resource management and crop planning. Telecommunications benefit from improved network design, while robotics and aerospace use it for route planning and system optimization. Chemical engineering leverages CSWO for process and reactor design. In education, it enhances curriculum design and training programs. Overall, CSWO is a versatile tool for solving optimization challenges across

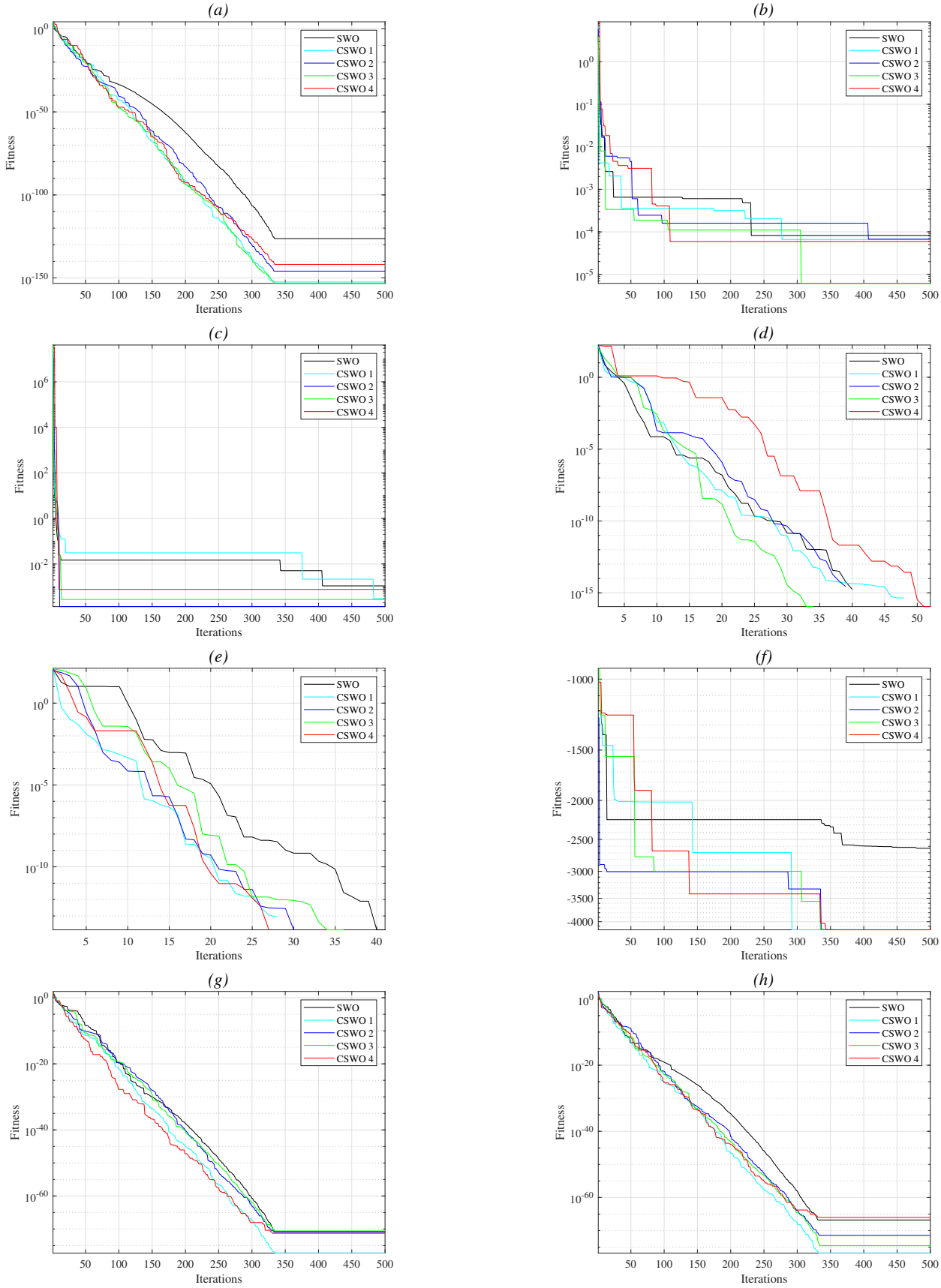

Figure 4. Convergence graph of each algorithm in solving: (a) F_1 Sphere; (b) F_2 Quartic noise; (c) F_3 Rosenbrock; (d) F_4 Griewank; (e) F_5 Rastrigin; (f) F_6 Schwefel; (g) F_7 Schwefel 2.21 and (h) F_8 Schwefel 2.22 benchmark functions

various domains, making it valuable for both researchers and practitioners.

Declarations

Use of AI tools

The authors declare that they have not used Artificial Intelligence (AI) tools in the creation of this article.

Data availability statement

No Data associated with the manuscript.

Ethical approval (optional)

The authors state that this research complies with ethical standards. This research does not involve either human participants or animals.

Consent for publication

Not applicable

Conflicts of interest

The authors declare that they have no conflict of interest.

Funding

No funding was received for this research.

Author's contributions

H.N.: Conceptualization, Methodology, Data Curation, Writing-Original Draft Preparation, Formal Analysis, Investigation, Software, Validation, Visualization. H.T.: Supervision, Conceptualization, Methodology, Investigation, Software, Formal Analysis, Writing Original Draft Preparation, Validation. All authors have read and agreed to the published version of the manuscript.

Acknowledgements

Not applicable

References

[1] Deepa, R. and Venkataraman, R. Enhancing Whale Optimization Algorithm with Levy Flight for coverage optimization in wireless sensor networks. *Computers & Electrical Engineering*, 94, 107359, (2021). [CrossRef]

[2] Kitayama, S., Arakawa, M. and Yamazaki, K. Differential evolution as the global optimization technique and its application to structural optimization. *Applied Soft Computing*, 11(4), 3792-3803, (2011). [CrossRef]

[3] Tomar, V., Bansal, M. and Singh, P. Metaheuristic algorithms for optimization: A brief review. *Engineering Proceedings*, 59(1), 238, (2024). [CrossRef]

[4] Alorf, A. A survey of recently developed metaheuristics and their comparative analysis. *Engineering Applications of Artificial Intelligence*, 117(A), 105622, (2023). [CrossRef]

[5] Rajwar, K., Deep, K. and Das, S. An exhaustive review of the metaheuristic algorithms for

search and optimization: taxonomy, applications, and open challenges. *Artificial Intelligence Review,* 56, 13187-13257, (2023). [CrossRef]

[6] Sowmya, R., Premkumar, M. and Jangir, P. Newton-Raphson-based optimizer: A new population-based metaheuristic algorithm for continuous optimization problems. *Engineering Applications of Artificial Intelligence,* 128, 107532, (2024). [CrossRef]

[7] Črepinšek, M., Liu, S.H. and Mernik, M. Exploration and exploitation in evolutionary algorithms: A survey. *ACM Computing Surveys (CSUR),* 45(3), 1-33, (2013). [CrossRef]

[8] Wolpert, D.H. and Macready, W.G. No free lunch theorems for optimization. *IEEE Transactions on Evolutionary Computation,* 1(1), 67-82, (1997). [CrossRef]

[9] Naik, P.A., Owolabi, K.M., Yavuz, M. and Zu, J. Chaotic dynamics of a fractional order HIV-1 model involving AIDS-related cancer cells. *Chaos, Solitons & Fractals,* 140, 110272, (2020). [CrossRef]

[10] Haneche, N. and Hamaizia, T. A three-dimensional discrete fractional-order HIV-1 model related to cancer cells, dynamical analysis and chaos control. *Mathematical Modelling and Numerical Simulation with Applications,* 4(3), 256-279, (2024). [CrossRef]

[11] Haneche, N. and Hamaizia, T. On the stability analysis for a three-dimensional fractional-order tümor system with obesity and immunosuppression. *Advances in Mathematical Sciences & Applications,* 33(2), p551, (2024). [CrossRef]

[12] Eskandari, Z., Naik, P.A. and Yavuz, M. Dynamical behaviors of a discrete-time prey-predator model with harvesting effect on the predator. *Journal of Applied Analysis and Computation,* 14(1), 283-297, (2024). [CrossRef]

[13] Joshi, H. and Jha, B.K. Chaos of calcium diffusion in Parkinson's infectiousdisease model and treatment mechanism via Hilfer fractional derivative. *Mathematical Modelling and Numerical Simulation with Applications,* 1(2), 84-94, (2021). [CrossRef]

[14] Hammouch, Z., Yavuz, M. and Özdemir, N. Numerical solutions and synchronization of a variable-order fractional chaotic system. *Mathematical Modelling and Numerical Simulation with Applications,* 1(1), 11-23, (2021). [CrossRef]

[15] Shahna, K.U. Novel chaos based cryptosystem using four-dimensional hyper chaotic map with efficient permutation and substitution techniques. *Chaos, Solitons & Fractals,* 170, 113383, (2023). [CrossRef]

[16] Nabil, H. and Tayeb, H. A secure communication scheme based on generalized modified projective synchronization of a new 4-D fractional-order hyperchaotic system. *Physica Scripta,* 99(9), 095203, (2024). [CrossRef]

[17] Nabil, H. and Tayeb, H. A fractional-order chaotic Lorenz-based chemical system: Dynamic investigation, complexity analysis, chaos synchronization, and its application to secure communication. *Chinese Physics B,* 33(12), 120503, (2024). [CrossRef]

[18] Kvasov, D.E. and Mukhametzhanov, M.S. Metaheuristic vs. deterministic global optimization algorithms: The univariate case. *Applied Mathematics and Computation,* 318, 245-259, (2018). [CrossRef]

[19] Radhika, S. and Chaparala, A. Optimization using evolutionary metaheuristic techniques: a brief review. *Brazilian Journal of Operations & Production Management,* 15(1), 44-53, (2018). [CrossRef]

[20] Sridharan, S., Subramanian, R.K. and Srirangan, A.K. Physics based meta heuristics in manufacturing. *Materials Today: Proceedings,* 39(1), 805-811, (2021). [CrossRef]

[21] Trojovskỳ, P. A new human-based metaheuristic algorithm for solving optimization problems based on preschool education. *Scientific Reports,* 13(1), 21472, (2023). [CrossRef]

[22] Xie, L., Han, T., Zhou, H., Zhang, Z.R., Han, B. and Tang, A. Tuna swarm optimization: A novel Swarm-Based metaheuristic algorithm for global optimization. *Computational Intelligence and Neuroscience,* 2021(1), 9210050, (2021). [CrossRef]

[23] Katoch, S., Chauhan, S.S. and Kumar, V. A review on genetic algorithm: past, present, and future. *Multimedia Tools and Applications,* 80, 8091-8126, (2021). [CrossRef]

[24] Santosa, B. and Safitri, A.L. Biogeography-based optimization (BBO) algorithm for single machine total weighted tardiness problem (SMTWTP). *Procedia Manufacturing,* 4, 552-557, (2015). [CrossRef]

[25] Bai, H., Cao, Q. and An, S. Mind evolutionary algorithm optimization in the prediction of satellite clock bias using the back propagation neural network. *Scientific Reports,* 13, 2095, (2023). [CrossRef]

[26] Rashedi, E., Nezamabadi-Pour, H. and Saryazdi, S. GSA: a gravitational search algorithm. *Information Sciences,* 179(13), 2232-2248, (2009). [CrossRef]

[27] Azizi, M., Aickelin, U.A., Khorshidi, H. and Baghalzadeh Shishehgarkhaneh, M. Energy valley optimizer: a novel metaheuristic algorithm for global and engineering optimization. *Scientific Reports,* 13(1), 226, (2023). [CrossRef]

[28] Kumar, M., Kulkarni, A.J. and Satapathy, S.C. Socio evolution & learning optimization algorithm: A socio-inspired optimization methodology. *Future Generation Computer Systems,* 81, 252-272, (2018). [CrossRef]

[29] Kazemi, M.V. and Veysari, E.F. A new optimization algorithm inspired by the quest for the evolution of human society: Human felicity algorithm. *Expert Systems with Applications,* 193, 116468, (2022). [CrossRef]

[30] Bayzidi, H., Talatahari, S., Saraee, M. and Lamarche, C.P. Social network search for solving engineering optimization problems. *Computational Intelligence and Neuroscience,* 2021(1), 8548639, (2021). [CrossRef]

[31] Gad, A.G. Particle swarm optimization algorithm and its applications: a systematic review. *Archives of Computational Methods in Engineering,* 29(5), 2531-2561, (2022). [CrossRef]

[32] Mirjalili, S., Gandomi, A.H., Mirjalili, S.Z., Saremi, S., Faris, H. and Mirjalili, S.M. Salp Swarm Algorithm: A bio-inspired optimizer for engineering design problems. *Advances in Engineering Software,* 114, 163-191, (2017). [CrossRef]

[33] Abdollahzadeh, B., Gharehchopogh, F.S., Khodadadi, N. and Mirjalili, S. Mountain gazelle optimizer: a new nature-inspired metaheuristic algorithm for global optimization problems. *Advances in Engineering Software,* 174, 103282, (2022). [CrossRef]

[34] Dhiman, G. and Kumar, V. Spotted hyena optimizer: a novel bio-inspired based metaheuristic technique for engineering applications. *Advances in Engineering Software,* 114, 48-70, (2017). [CrossRef]

[35] Afshar, A., Haddad, O.B., Marino, M.A. and Adams, B.G. Honey-bee mating optimization (HBMO) algorithm for optimal reservoir operation. *Journal of the Franklin Institute,* 344(5), 452-462, (2007). [CrossRef]

[36] Arora, S. and Singh, S. Butterfly optimization algorithm: a novel approach for global optimization. *Soft Computing,* 23, 715-734, (2019). [CrossRef]

[37] Mirjalili, S. The ant lion optimizer. *Advances in Engineering Software,* 83, 80-98, (2015). [CrossRef]

[38] Heidari, A.A., Mirjalili, S., Faris, H., Aljarah, I., Mafarja, M. and Chen, H. Harris hawks optimization: Algorithm and applications. *Future Generation Computer Systems,* 97, 849-872, (2019). [CrossRef]

[39] Gandomi, A.H., Yang, X.S., Alavi, A.H. and Talatahari, S. Bat algorithm for constrained optimization tasks. *Neural Computing and Applications,* 22, 1239-1255, (2013). [CrossRef]

[40] Pan, W.T. A new fruit fly optimization algorithm: taking the financial distress model as an example. *Knowledge-Based Systems,* 26, 69-74, (2012). [CrossRef]

[41] Mirjalili, S. and Lewis, A. The whale optimization algorithm. *Advances in Engineering Software,* 95, 51-67, (2016). [CrossRef]

[42] Saremi, S., Mirjalili, S. and Lewis, A. Grasshopper optimisation algorithm: theory and application. *Advances in Engineering Software,* 105, 30-47, (2017). [CrossRef]

[43] Abdollahzadeh, B., Soleimanian Gharehchopogh, F. and Mirjalili, S. Artificial gorilla troops optimizer: a new nature-inspired metaheuristic algorithm for global optimization problems. *International Journal of Intelligent Systems,* 36(10), 5887-5958, (2021). [CrossRef]

[44] Mirjalili, S., Mirjalili, S.M. and Lewis, A. Grey wolf optimizer. *Advances in Engineering Software,* 69, 46-61, (2014). [CrossRef]

[45] Faramarzi, A., Heidarinejad, M., Mirjalili, S. and Gandomi, A.H. Marine Predators Algorithm: A nature-inspired metaheuristic. *Expert Systems with Applications,* 152, 113377, (2020). [CrossRef]

[46] Mehta, P., Yildiz, B.S., Sait, S.M. and Yildiz, A.R. Hunger games search algorithm for global optimization of engineering design problems. *Materials Testing,* 64(4), 524-532, (2022). [CrossRef]

[47] Abualigah, L., Yousri, D., Abd Elaziz, M., Ewees, A.A., Al-Qaness, M.A. and Gandomi, A.H. Aquila optimizer: a novel meta-heuristic optimization algorithm. *Computers & Industrial Engineering,* 157, 107250, (2021). [CrossRef]

[48] Morales-Castañeda, B., Zaldivar, D., Cuevas, E., Fausto, F. and Rodríguez, A. A better balance in metaheuristic algorithms: Does it exist? *Swarm and Evolutionary Computation,* 54, 100671, (2020). [CrossRef]

[49] Abdel-Basset, M., Mohamed, R., Jameel, M. and Abouhawwash, M. Spider wasp optimizer: A novel meta-heuristic optimization algorithm. *Artificial Intelligence Review,* 56, 11675-11738, (2023). [CrossRef]

[50] Kaur, G. and Arora, S. Chaotic whale optimization algorithm. *Journal of Computational Design and Engineering,* 5(3), 275-284, (2018). [CrossRef]

[51] Arora, S. and Anand, P. Chaotic grasshopper optimization algorithm for global optimization. *Neural Computing and Applications,* 31, 4385-4405, (2019). [CrossRef]

[52] Ismail, F.H., Houssein, E.H. and Hassanien, A.E. Chaotic bird swarm optimization algorithm. In Proceedings, *of the International Conference on Advanced Intelligent Systems and Informatics (AISI 2018),* pp. 294-303, Cairo, Egypt, (2018, August). [CrossRef]

[53] Kiani, F., Nematzadeh, S., Anka, F.A. and Findikli, M.A. Chaotic sand cat swarm optimization. *Mathematics,* 11(10), 2340, (2023). [CrossRef]

[54] Arora, S. and Singh, S. An improved butterfly optimization algorithm with chaos. *Journal of*

Intelligent & Fuzzy Systems, 32(1), 1079-1088, (2017). [CrossRef]

[55] Shinde, V., Jha, R. and Mishra, D.K. Improved Chaotic Sine Cosine Algorithm (ICSCA) for global optima. *International Journal of Information Technology*, 16, 245-260, (2024). [CrossRef]

[56] Hamaizia, T., Lozi, R. and Hamri, N.E. Fast chaotic optimization algorithm based on locally averaged strategy and multifold chaotic attractor. *Applied Mathematics and Computation*, 219(1), 188-196, (2012). [CrossRef]

[57] Feng, J., Zhang, J., Zhu, X. and Lian, W. A novel chaos optimization algorithm. *Multimedia Tools and Applications*, 76, 17405-17436, (2017). [CrossRef]

[58] Shayeghi, H., Shayanfar, H.A., Jalilzadeh, S. and Safari, A. Multi-machine power system stabilizers design using chaotic optimization algorithm. *Energy Conversion and Management*, 51(7), 1572-1580, (2010). [CrossRef]

[59] Cisternas-Caneo, F., Crawford, B., Soto, R., Giachetti, G., Paz, A. and Peña Fritz, A. Chaotic binarization schemes for solving combinatorial optimization problems using continuous metaheuristics. *Mathematics*, 12(2), 262, (2024). [CrossRef]

[60] Fiedler, R., Hetzler, H. and Bäuerle, S. Efficient numerical calculation of Lyapunov-exponents and stability assessment for quasi-periodic motions in nonlinear systems. *Nonlinear Dynamics*, 112, 8299-8327, (2024). [CrossRef]

[61] Rayor, L.S. Attack strategies of predatory wasps (Hymenoptera: Pompilidae; Sphecidae) on colonial orb web-building spiders (Araneidae: Metepeira incrassata). *Journal of the Kansas Entomological Society*, 69(4), 67-75, (1996).

[62] Liang, J.J., Qin, A.K., Suganthan, P.N. and Baskar, S. Comprehensive learning particle swarm optimizer for global optimization of multimodal functions. *IEEE Transactions on Evolutionary Computation*, 10(3), 281-295, (2006). [CrossRef]

Mathematical Modelling and Numerical Simulation with Applications (MMNSA)
(https://dergipark.org.tr/en/pub/mmnsa)

How to cite this article: Nabil, H. & Tayeb, H. (2025). Effect of chaos on the performance of spider wasp meta-heuristic optimization algorithm for high-dimensional optimization problems. *Mathematical Modelling and Numerical Simulation with Applications*, 5(1), 143-171. https://doi.org/10.53391/mmnsa.1571964

Mathematical Modelling and Numerical Simulation with Applications, 2025, 5(1), 172–197

https://dergipark.org.tr/en/pub/mmnsa

ISSN Online: 2791-8564 / Open Access

https://doi.org/10.53391/mmnsa.1572436

RESEARCH PAPER

Dynamics of a stochastic SEIQR model: stationary distribution and disease extinction with quarantine measures

S. Saravanan [1,‡] and **C. Monica** [1,*,‡]

[1]Department of Mathematics, School of Advanced Sciences, Vellore Institute of Technology, Vellore 632014, Tamil Nadu, India

*Corresponding Author

‡saravanan.s2019b@vitstudent.ac.in (S. Saravanan); monica.c@vit.ac.in (C. Monica)

Abstract

This paper investigates the dynamics of a stochastic $\mathcal{SEIQR}$ epidemic model, which integrates quarantine measures and a saturated incidence rate to more accurately reflect real-world disease transmission. The model is based on the classical $\mathcal{SEIR}$ framework, with the addition of a quarantined compartment, offering insights into the impact of quarantine on epidemic control. The saturated incidence rate accounts for the diminishing rate of new infections as the susceptible population grows, addressing the limitations of traditional bilinear incidence rates in modeling epidemic spread under high disease prevalence. We first establish the basic reproductive number, $\mathcal{R}_0$, for the deterministic model, which serves as a threshold parameter for disease persistence. Through the stochastic Lyapunov function method, we identify the necessary conditions for the existence of a stationary distribution, focusing on the case where $\mathcal{R}_0^* > 1$, signals the potential long-term persistence of the disease in the population. Furthermore, we derive sufficient conditions for disease extinction, particularly when $\mathcal{R}_S^* < 1$, indicating that the disease will eventually die out despite the inherent randomness in disease transmission. Numerical simulations confirm that environmental noise and quarantine rates shape disease dynamics. Simulations show that more noise or higher quarantine rates speed up disease extinction, offering key policy insights. Our results clarify how quarantine, noise intensity, and disease dynamics interact, aiding epidemic modeling in stochastic settings.

Keywords: Stochastic epidemic model; Lyapunov function; stationary ergodic distribution; extinction

AMS 2020 Classification: 37M05; 37N25; 34D08; 60G10

1 Introduction

Mathematical models have been indispensable in understanding infectious disease dynamics since Daniel Bernoulli's pioneering work in 1766 [1]. These models elucidate disease transmission

➤ **Received:** 23.10.2024 ➤ **Revised:** 18.02.2025 ➤ **Accepted:** 12.03.2025 ➤ **Published:** 31.03.2025

dynamics and analyze the behavior of diseases among populations with varying health statuses. Notably, Kermack and McKendrick's research in 1927 [2] explored infectious disease dynamics using mathematical models, paving the way for numerous subsequent models aimed at understanding epidemic behavior and controlling its spread. The development of stochastic epidemic models, stemming from simple deterministic models, has enabled accurate predictions of disease dissemination and facilitated public health awareness campaigns. Such models are instrumental in preventing disease dissemination and reducing infection rates in society.

Stochastic epidemics trace back to the 1920s, with McKendrick developing the first stochastic SIR model in 1926 [2]. Researchers like Anderson, Roy, Daley, and Gani have since contributed to the field by analyzing infectious disease epidemiology through mathematical models [3, 4]. Their work has focused on determining transmission probabilities for infectious agents and examining the effects of interventions such as vaccination and quarantine, offering theoretical and numerical frameworks for disease prevention and control. There has been a significant increase in the application of mathematical models to investigate mechanisms within infectious diseases such as polio, diphtheria, tuberculosis, HIV, COVID-19, and others [5–11]. Quarantine emerges as a crucial method for preventing disease dissemination, as evidenced by its historical efficacy in reducing the spread of various human and animal diseases. Therefore, studying infectious disease models that incorporate quarantine strategies is essential.

The main objective of this study is to develop a stochastic SEIQR epidemic system incorporating temporary immunity, quarantine strategies, and random perturbations. While providing detailed insights into disease persistence, stochastic models may lack positive equilibrium due to environmental noise interference [12, 13]. Understanding ergodicity theory and stationary distributions is crucial for comprehending epidemic transmission patterns and estimating statistical properties essential for effective disease prevention.

Additionally, several mathematical models investigate infectious disease dynamics under quarantine models [14, 15]. For instance, Dieu et al. [16] have developed the threshold of a stochastic SIQS epidemic model with standard isolation, while Zhou et al. [17] have investigated an SQEIAR stochastic epidemic model with media coverage and asymptomatic infection. Zhang et al. [18] proposed the stationary distribution and extinction of a stochastic SEIQ epidemic model with a general incidence function and temporary immunity. Currently, researchers are actively investigating the SIQR model [19–21].

Therefore, many mathematical biologists consider more realistic factors, such as demographic changes, migration, cross-infections, and other practical elements. Every time infectious diseases affect people, people take precautions to minimize their impact. The quarantine method has been used for controlling contagious diseases, which is one of the most effective ways to prevent epidemic disease outbreaks. Mathematicians and biologists are drawn to this area of research.

2 Mathematical model

Vaccinations and quarantines for disease prevention and disease control have become more crucial in modern medicine developments. In recent years, several researchers have examined the effect of vaccination and quarantines on disease [22–25]. Many infectious diseases incubate within a host for a period of time before becoming infectious, so the duration of infection must also be taken into account. In response to the aforementioned research, the following system describes an epidemic model with imperfect quarantine based on the $\mathcal{SEIQR}$ model:

$$\frac{d\mathcal{S}}{d\mathbf{t}} = \Theta - \frac{\beta\mathcal{S}\mathcal{I}}{1+\mathbf{k}\mathcal{I}} - \mu\mathcal{S},$$

$$\begin{aligned}
\frac{d\mathcal{E}}{d\mathbf{t}} &= \frac{\beta\mathcal{S}\mathcal{I}}{1+\mathbf{k}\mathcal{I}} - (\gamma+\mu)\mathcal{E}, \\
\frac{d\mathcal{I}}{d\mathbf{t}} &= \gamma\mathcal{E} - (\xi+\eta+\alpha_1+\mu)\mathcal{I}, \\
\frac{d\mathcal{Q}}{d\mathbf{t}} &= \eta\mathcal{I} - (\delta+\alpha_2+\mu)\mathcal{Q}, \\
\frac{d\mathcal{R}}{d\mathbf{t}} &= \xi\mathcal{I} + \delta\mathcal{Q} - \mu\mathcal{R}.
\end{aligned} \tag{1}$$

In total, the population size is estimated to be $N(\mathbf{t}) = \mathcal{S}(\mathbf{t}) + \mathcal{E}(\mathbf{t}) + \mathcal{I}(\mathbf{t}) + \mathcal{Q}(\mathbf{t}) + \mathcal{R}(\mathbf{t})$. In these epidemic models, the saturated incidence rate is $h(\mathcal{I})\mathcal{S}$ and the model is composed of a $(\mathcal{SEIQR})$ epidemic model. In model (1), the transitions between compartments describe an $\mathcal{SEIQR}$ epidemic model without temporary immunity. The saturation level of $h(\mathcal{I})$ occurs when $\mathcal{I}$ increases in size.

$$h(\mathcal{I})\mathcal{S} = \frac{\beta\mathcal{I}\mathcal{S}}{1+\mathbf{k}\mathcal{I}}.$$

The infection force is represented by $\beta\mathcal{I}$, and when numbers increase, it causes the behavior of susceptible individuals to change. $\frac{1}{1+\mathbf{k}\mathcal{I}}$ represents this inhibition effect. Obviously the region,

$$\mathcal{D} = \{(\mathcal{S},\mathcal{E},\mathcal{I},\mathcal{Q},\mathcal{R})/\mathcal{S}\geq 0,\mathcal{E}\geq 0,\mathcal{I}\geq 0,\mathcal{Q}\geq 0,\mathcal{R}\geq 0,\mathcal{S}+\mathcal{E}+\mathcal{I}+\mathcal{Q}+\mathcal{R}\leq \Theta/\mu\},$$

is a collection of model (1) that is positively invariant. The reproduction number of the model is

$$\mathcal{R}_0 = \frac{\beta\Theta\gamma}{\mu(\gamma+\mu)(\xi+\mu+\alpha_1+\eta)}.$$

Table 1. Model variables and their descriptions

Variables	Descriptions
$\mathcal{S}(\mathbf{t})$	Population of Susceptible
$\mathcal{E}(\mathbf{t})$	Population of Exposed
$\mathcal{I}(\mathbf{t})$	Population of Infected
$\mathcal{Q}(\mathbf{t})$	Population of Quarantined
$\mathcal{R}(\mathbf{t})$	Population of Recovered

Table 2. Model parameters, explanations and units

Parameters	Explanations	Units
Θ	Birth rate	Individual/ day
β	Transmission co-efficient	$(\text{Individual}\times \text{day})^{-1}$
μ	Natural death rate	1/day
γ	Infective individuals of exposed people	1/day
η	Infective individuals of quarantined recovery rate	1/day
ξ	Recovery rate of infective people	1/day
α_1	Rates of disease-induced death among infected individuals	1/day
α_2	Disease induced death rate of quarantined people	1/day
δ	Recovery rate of quarantined individuals	1/day
$\mathbf{k}$	Saturation rate of the inhibition effect rate	1/day

Remark 1 *i. If $\mathcal{R}_0 \leq 1$ holds, then the model (1) will only have an disease-free equilibrium of $\mathbf{E}_0 = (\mathcal{S}_0, 0, 0, 0, 0)$ in which there is global asymptotical stability. Then, only a vulnerable and healthy population remains after the pandemic illnesses have gone away.*
ii. When $\mathcal{R}_0 > 1$ is valid, in positive equilibria, there is an asymptotically stable value $\mathbf{E}^* = (\mathcal{S}^*, \mathcal{E}^*, \mathcal{I}^*, \mathcal{Q}^*, \mathcal{R}^*)$ in the area $\mathcal{D}$ for the model (1), indicating that epidemic diseases will continue to exist.

It is impossible to describe the behavior of species using deterministic models in the natural world. Noise from the environment can sometimes cause disturbance to species. Therefore, there should be a fair amount of stochasticity in some parameters [26–28]. The ecosystem is dominated by this phenomenon without a doubt. Therefore, a substantial amount of research has been conducted on the effects of stochastic perturbations on disease [20, 29, 30]. In many branches of applied sciences, including disease dynamics, stochastic differential equations (SDEs) play an important role because they are capable of predicting the future dynamics of their deterministic counterpart. Until now, very few studies have been conducted on the global dynamics of stochastic $\mathcal{SEIQR}$ epidemic models. The model (1) is made more reasonable and realistic by assuming that $\mathcal{S}(t), \mathcal{E}(t), \mathcal{I}(t), \mathcal{Q}(t)$, and $\mathcal{R}(t)$ are directly proportional to environmental noise. Afterward, in accordance with model (1), a stochastic version may be obtained by

$$\begin{aligned}
d\mathcal{S} &= \left[\Theta - \frac{\beta\mathcal{S}\mathcal{I}}{1+\mathbf{k}\mathcal{I}} - \mu\mathcal{S}\right] d\mathbf{t} + \varrho_1 \mathcal{S} dW_1(\mathbf{t}), \\
d\mathcal{E} &= \left[\frac{\beta\mathcal{S}\mathcal{I}}{1+\mathbf{k}\mathcal{I}} - (\gamma+\mu)\mathcal{E}\right] d\mathbf{t} + \varrho_2 \mathcal{E} dW_2(\mathbf{t}), \\
d\mathcal{I} &= [\gamma\mathcal{E} - (\xi+\eta+\alpha_1+\mu)\mathcal{I}]\, d\mathbf{t} + \varrho_3 \mathcal{I} dW_3(\mathbf{t}), \\
d\mathcal{Q} &= [\eta\mathcal{I} - (\delta+\alpha_2+\mu)\mathcal{Q}]\, d\mathbf{t} + \varrho_4 \mathcal{Q} dW_4(\mathbf{t}), \\
d\mathcal{R} &= [\xi I + \delta\mathcal{Q} - \mu\mathcal{R}]\, d\mathbf{t} + \varrho_5 \mathcal{R} dW_5(\mathbf{t}),
\end{aligned} \tag{2}$$

where, $W_i = B_i = 1, 2, 3, 4, 5$ are independent standard one-dimensional Brownian motion and $\varrho_i(t)$, are the intensity of the white noise, $i = 1, 2, 3, 4, 5$. All other parameters are similar to those in model (1). As a result, the paper has been organized as follows: In Section 3, this model provides a significant unique global solution to the model (2). In Section 4, we prove that model (2) has an ergodic stationary distribution under certain conditions. In Section 5, we establish what conditions must be met for the disease to be wiped out. In the Section 6, numerical simulations are provided to illustrate the theoretical results. A brief summary of the main findings is presented in Section 7.

3 Uniqueness of global solution

An epidemic models dynamic behavior can be studied by determining whether or not the solution exits and remains nonnegative. It is well known that with stochastic differential equations, numerical solutions must satisfy both the local Lipschitz condition and the linear growth condition so that they have an exclusive global solution. Model (2) requires linear growth, despite its Lipschitz continuous coefficients, so a finite-time explosion may occur if the linear growth condition is not met. It is necessary to consider the existence and positivity of solutions to the model (2) before studying population system dynamics.
Firstly, we consider stochastic differential equations in d-dimensions

$$d\mathcal{X} = f(\mathcal{X}(\mathbf{t}), \mathbf{t})d\mathbf{t} + g(\mathcal{X}(\mathbf{t}), \mathbf{t})dB(\mathbf{t}), \quad for \quad \mathrm{t} \geq \mathbf{t}_0,$$

with the initial condition for $\mathcal{X}(0) = \mathcal{X}_0 \in \mathbb{R}^{\mathsf{d}}$. The differential operator $\mathcal{L}$ associated with the equation above can be defined as follows:

$$\mathcal{L} = \frac{\partial}{\partial \mathbf{t}} + \sum_{\mathsf{i}=1}^{d} f_{\mathsf{i}}(\mathcal{X}, \mathbf{t}) \frac{\partial}{\partial \mathcal{X}_{\mathsf{i}}} + \frac{1}{2} \sum_{\mathsf{i},\mathsf{j}=1}^{d} \left[g^T(\mathcal{X}, \mathbf{t}) g(\mathcal{X}, \mathbf{t}) \right]_{\mathsf{ij}} \frac{\partial^2}{\partial \mathcal{X}_{\mathsf{i}} \partial \mathcal{X}_{\mathsf{j}}}.$$

If $\mathcal{L}$ acts on a function $\mathcal{V} \in \mathcal{C}^2 \left(\mathbb{R}^d \times [t_0, \infty; \mathbb{R}_+] \right)$, then

$$\mathcal{L}\mathcal{V}(\mathcal{X}, \mathbf{t}) = \mathcal{V}_{\mathbf{t}}(\mathcal{X}, \mathbf{t}) + \mathcal{V}_{\mathcal{X}}(\mathcal{V}\mathcal{X}, \mathbf{t}) f(\mathcal{X}, \mathbf{t}) + \frac{1}{2} trace \left[g^T(\mathcal{X}, \mathbf{t}) \mathcal{V}_{\mathcal{X}\mathcal{X}}(\mathcal{X}, \mathbf{t}) g(\mathcal{X}, \mathbf{t}) \right],$$

where, $\mathcal{V}_{\mathbf{t}} = \frac{\partial \mathcal{V}}{\partial \mathbf{t}}, \mathcal{V}_{\mathcal{X}} = \left(\frac{\partial \mathcal{V}}{\partial \mathcal{X}_1}, \frac{\partial \mathcal{V}}{\partial \mathcal{X}_2}, ..., \frac{\partial \mathcal{V}}{\partial \mathcal{X}_d} \right), \mathcal{V}_{\mathcal{X}\mathcal{X}} = \left(\frac{\partial^2 \mathcal{V}}{\partial \mathcal{X}_i \partial \mathcal{X}_j} \right)_{d \times d}$. Thus, by Ito's formula, if $\mathcal{X}(\mathbf{t}) \in \mathbb{R}^d$, then

$$d\mathcal{V}(\mathcal{X}(\mathbf{t}), \mathbf{t}) = \mathcal{L}\mathcal{V}(\mathcal{X}(\mathbf{t}), \mathbf{t}) d\mathbf{t} + \mathcal{V}_{\mathcal{X}}(\mathcal{X}(\mathbf{t}), \mathbf{t}) g(\mathcal{X}(\mathbf{t}), \mathbf{t}) d\mathcal{B}(\mathbf{t}).$$

Lemma 1 *As a result of the model (2), we get a positive local and unique solution* $(\mathcal{S}(\mathbf{t}), \mathcal{E}(\mathbf{t}), \mathcal{I}(\mathbf{t}), \mathcal{Q}(\mathbf{t}), \mathcal{R}(\mathbf{t}))$ *for* $\mathbf{t} \in [-\varpi, \mathbf{e})$, *where* $\tau_{\mathbf{e}}$ *is the time of the explosion [31], at any starting value* $(\mathcal{S}(0), \mathcal{E}(0), \mathcal{I}(0), \mathcal{Q}(0), \mathcal{R}(0)) \in \mathbb{R}^5_+$.

Theorem 1 *The model (2) has a unique positive solution* $(\mathcal{S}(t), \mathcal{E}(t), \mathcal{I}(t), \mathcal{Q}(t), \mathcal{R}(t)) \in \mathbb{R}^5_+$ *on* $t \geq 0$ *at any starting value* $(S(0), \mathcal{E}(0), \mathcal{I}(0), \mathcal{Q}(0), \mathcal{R}(0)) \in \mathbb{R}^5_+$.

Proof In the case of model (2), the coefficients are Lipschitz continuous on the region $\mathbb{R}_+$. Two parts are involved in the following proof.
Part − I. According to Lemma 1, In model (2), for any given initial state $(\mathcal{S}(0), \mathcal{E}(0), \mathcal{I}(0), \mathcal{Q}(0), \mathcal{R}(0)) \in \mathbb{R}^5_+$. there is a positive local solution $(\mathcal{S}(\mathbf{t}), \mathcal{E}(\mathbf{t}), \mathcal{I}(\mathbf{t}), \mathcal{Q}(\mathbf{t}), \mathcal{R}(\mathbf{t}))$.
Part − II. Now, we demonstrate that $\tau_{\mathbf{e}} = +\infty$ a.s, there is only one positive solution, and that is a global solution. If $\mathbf{n}_0 \geq 0$ is sufficiently large, then $\mathcal{S}(0), \mathcal{E}(0), \mathcal{I}(0), \mathcal{Q}(0)$, and $\mathcal{R}(0)$ will all lie in the range $\left[\frac{1}{\mathbf{n}_0}, \mathbf{n} \right]$. For every integer $\mathbf{n} \geq \mathbf{n}_0$, as a general rule, stopping times can be defined as follows:

$$\begin{aligned} \tau_{\mathbf{n}} \quad = \quad & \inf \left\{ \mathbf{t} \in [\varpi, \tau_{\mathbf{e}}) : \mathcal{S}(\mathbf{t}) \notin \left(\frac{1}{\mathbf{n}}, \mathbf{n} \right), \mathcal{E}(\mathbf{t}) \notin \left(\frac{1}{\mathbf{n}}, \mathbf{n} \right), \mathcal{I}(\mathbf{t}) \notin \left(\frac{1}{\mathbf{n}}, \mathbf{n} \right), \right. \\ & \left. \mathcal{Q}(\mathbf{t}) \notin \left(\frac{1}{\mathbf{n}}, \mathbf{n} \right) \quad or \quad \mathcal{R}(\mathbf{t}) \notin \left(\frac{1}{\mathbf{n}}, \mathbf{n} \right) \right\}. \end{aligned} \tag{3}$$

In the case of an empty set $\varnothing$, we define here $\inf \varnothing = +\infty$. There is no doubt that $\tau_{\mathbf{n}}$ increases strictly when $\mathbf{n} \to \infty$. Assume $\tau_\infty = \lim_{\mathbf{n} \to \infty} \tau_{\mathbf{n}}$; therefore, $\tau_\infty = \tau_{\mathbf{e}}$. The only thing left to do is prove $\tau_\infty = +\infty$ a.s. If $\tau_\infty = +\infty$ is not true, then there exist a both constants $\mathcal{T} > 0$ and $\zeta \in (0, 1)$ such that $\mathbb{P}\tau_\infty \leq \mathcal{T} > \zeta$. Consequently, there exists $\mathbf{n}_1 \geq \mathbf{n}_0 (\mathbf{n}_1 \in \mathbb{N}_+)$.
Define a $\mathcal{C}^{1,2}-$ function $\widehat{\mathcal{V}} : \mathbb{R}^5_+ \to \mathbb{R}_+$

$$\begin{aligned} \widehat{\mathcal{V}}(\mathcal{S}, \mathcal{E}, \mathcal{I}, \mathcal{Q}, \mathcal{R}) \quad = \quad & \mathcal{S} - 1 - \ln \mathcal{S} + \mathcal{E} - 1 - \ln \mathcal{E} + \mathcal{I} - 1 - \ln \mathcal{I} \\ & + \mathcal{Q} - 1 - \ln \mathcal{Q} + \mathcal{R} - 1 - \ln \mathcal{R}. \end{aligned} \tag{4}$$

By applying Definition in view of model (2), we get

$$\begin{aligned} d\widehat{\mathcal{V}} &= p\widehat{\mathcal{V}}\mathbf{dt} + \varrho_1(\mathcal{S}-1)dW_1(\mathbf{t}) + \varrho_2(\mathcal{E}-1)dW_2(\mathbf{t}) + \varrho_1(\mathcal{I}-1)dW_3(\mathbf{t}) \\ &\quad +\varrho_4(\mathcal{Q}-1)dW_4(\mathbf{t}) + \varrho_5(\mathcal{R}-1)dW_5(\mathbf{t}), \end{aligned} \tag{5}$$

where,

$$\begin{aligned} p\widehat{\mathcal{V}} &= \left(1-\frac{1}{\mathcal{S}}\right)\left[\Theta - \frac{\beta\mathcal{S}\mathcal{I}}{1+\mathbf{k}\mathcal{I}} - \mu\mathcal{S}\right] + \left(1-\frac{1}{\mathcal{E}}\right)\left[\frac{\beta\mathcal{S}\mathcal{I}}{1+\mathbf{k}\mathcal{I}} - (\gamma+\mu)\mathcal{E}\right] \\ &\quad + \left(1-\frac{1}{\mathcal{I}}\right)[\gamma\mathcal{E} - (\xi+\eta+\alpha_1+\mu)\mathcal{I}] + \left(1-\frac{1}{\mathcal{Q}}\right)[\eta\mathcal{I} - (\delta+\alpha_2+\mu)\mathcal{Q}] \\ &\quad + \left(1-\frac{1}{\mathcal{R}}\right)[\xi\mathcal{I} + \delta\mathcal{Q} - \mu\mathcal{R}] \\ \\ &= \Theta - \frac{\Theta}{\mathcal{S}} - \frac{\beta\mathcal{I}}{1+\mathbf{k}\mathcal{I}} - \frac{\beta\mathcal{S}\mathcal{I}}{\mathcal{E}(1+\mathbf{k}\mathcal{I})} + 5\mu - \mu(\mathcal{S}+\mathcal{E}+\mathcal{I}+\mathcal{Q}+\mathcal{R}) \\ &\quad +\gamma+\xi+\eta+\alpha_1+\alpha_2+\delta-\alpha_1\mathcal{I}+\alpha_2\mathcal{Q} - \frac{\gamma\mathcal{E}}{\mathcal{I}} - \frac{\eta\mathcal{I}}{\mathcal{Q}} - \frac{\xi\mathcal{I}}{\mathcal{R}} - \frac{\delta\mathcal{Q}}{\mathcal{R}} \\ &\quad + \frac{\varrho_1^2+\varrho_2^2+\varrho_3^2+\varrho_4^2+\varrho_5^2}{2} \\ &\leq \Theta + 5\mu - \frac{\beta}{\mathbf{k}} + \gamma+\xi+\eta+\delta+\alpha_1+\alpha_2 + \frac{\varrho_1^2+\varrho_2^2+\varrho_3^2+\varrho_4^2+\varrho_5^2}{2} \\ &\leq \mathcal{K}_0 \in R_+. \end{aligned}$$

Hence, $\mathcal{K}_0$ is a positive constant.
Thus,

$$\begin{aligned} d\widehat{\mathcal{V}} &\leq \mathcal{K}_0\mathbf{dt} + \varrho_1(\mathcal{S}-1)dW_1(\mathbf{t}) + \varrho_2(\mathcal{E}-1)dW_2(\mathbf{t}) + \varrho_3(\mathcal{I}-1)dW_3(\mathbf{t}) \\ &\quad +\varrho_4(\mathcal{Q}-1)dW_4(\mathbf{t}) + \varrho_5(\mathcal{R}-1)dW_5(\mathbf{t}). \end{aligned} \tag{6}$$

In order to take the expectation, we integrate both sides of $\tau_{\mathbf{n}} \wedge \mathcal{T}$ to get,

$$\mathbb{E}\left[\widehat{\mathcal{V}}\left(\mathcal{S}(\tau_{\mathbf{n}}\wedge\mathcal{T}), \mathcal{E}(\tau_{\mathbf{n}}\wedge\mathcal{T}), \mathcal{I}(\tau_{\mathbf{n}}\wedge\mathcal{T}), \mathcal{Q}(\tau_{\mathbf{n}}\wedge\mathcal{T}), \mathcal{R}(\tau_{\mathbf{n}}\wedge\mathcal{T})\right)\right]$$

$$\begin{aligned} &\leq \widehat{\mathcal{V}}\left(\mathcal{S}(0), \mathcal{E}(0), \mathcal{I}(0), \mathcal{Q}(0), \mathcal{R}(0)\right) + \mathbb{E}\left[\int_0^{\tau_{\mathbf{n}}\wedge\mathcal{T}} \mathcal{K}_0\mathbf{dt}\right] \\ &\leq \widehat{\mathcal{V}}\left(\mathcal{S}(0), \mathcal{E}(0), \mathcal{I}(0), \mathcal{Q}(0), \mathcal{R}(0)\right) + \mathcal{K}_0\mathcal{T}. \end{aligned} \tag{7}$$

Allow it to set $\Omega_{\mathbf{n}} = (\tau_{\mathbf{n}} \leq T)$ for $\mathbf{n} \geq \mathbf{n}_1$, we have $\mathbb{P}(\Omega_{\mathbf{n}}) \geq \varepsilon$ with $\varepsilon \in (0,1)$. Note not for each $\omega \in \Omega_n$, a minimum of one of these exist $\mathcal{S}(\tau_{\mathbf{n}}, \omega)$ or $\mathcal{E}(\tau_{\mathbf{n}}, \omega)$ or $\mathcal{I}(\tau_{\mathbf{n}}, \omega)$ or $\mathcal{Q}(\tau_{\mathbf{n}}, \omega)$ or $\mathcal{R}(\tau_{\mathbf{n}}, \omega)$ either of these is equal $(\mathbf{n} \quad or \quad 1/\mathbf{n})$.

In that case, $\widehat{\mathcal{V}}(\mathcal{S}(\tau_{\mathsf{n}},\varpi),\mathcal{E}(\tau_{\mathsf{n}},\varpi),\mathcal{I}(\tau_{\mathsf{n}},\varpi),\mathcal{Q}(\tau_{\mathsf{n}},\varpi),\mathcal{R}(\tau_{\mathsf{n}},\varpi))$ cannot be less than either

$$\left(\frac{1}{\mathsf{n}}-1-\ln\frac{1}{\mathsf{n}}\right) \quad or \quad (\mathsf{n}-1-\ln\mathsf{n})=\left(\frac{1}{\mathsf{n}}-1+\ln\mathsf{n}\right).$$

The results are as follows:
$\widehat{\mathcal{V}}(\mathcal{S}(0),\mathcal{E}(0),\mathcal{I}(0),\mathcal{Q}(0),\mathcal{R}(0))+\mathcal{K}_0\mathcal{T}$

$$\begin{aligned}
&\geq \mathbb{E}\left[l_{\Omega_{\mathsf{n}}(\varpi)}\widehat{\mathcal{V}}(\mathcal{S}(\tau_{\mathsf{n}},\varpi),\mathcal{E}(\tau_{\mathsf{n}},\varpi),\mathcal{I}(\tau_{\mathsf{n}},\varpi),\mathcal{Q}(\tau_{\mathsf{n}},\varpi),\mathcal{R}(\tau_{\mathsf{n}},\varpi))\right]\\
&\geq \zeta\left[\frac{1}{\mathsf{n}}-1-\ln\frac{1}{\mathsf{n}}\right]\wedge(\mathsf{n}-1-\ln\mathsf{n}). \qquad (8)
\end{aligned}$$

Using a stochastic differential equation, this may be explained if Ω_{n} is denoted by $l_{\Omega_{\mathsf{n}}(\varpi)}$. Suppose $\mathsf{n}\to+\infty$, this implies

$$+\infty>(\mathcal{S}(0),\mathcal{E}(0),\mathcal{I}(0),\mathcal{Q}(0),\mathcal{R}(0))+\mathcal{K}_0\mathcal{T}=+\infty.$$

Therefore, it is contradictory, and therefore, we have $\tau_\infty=+\infty$. The proof is complete.

An equilibrium solution's asymptotic activities in a disease-free system

There is no doubt that $\mathsf{E}^*(\mathcal{S}_0,0,0,0,0)$ satisfies the condition for the model (1), and is associated with disease-free equilibrium. At some points, the disease will be extinct because the solution E^* is global stochastically asymptotically stable. The idea of disease-free equilibrium as a means of containing infectious diseases has thus gained popularity. In this section, the stochastic Lyapunov function is used primarily to achieve the stability of the disease-free equilibrium solution.

Theorem 2 *The stochastic model* (2) *saddles* $\mathcal{D}$ *in the disease-free equilibrium* $\mathsf{E}^*(\mathcal{S}_0,0,0,0,0)$, *when* $\mathcal{R}_0\leq 1$.

Proof Create a Lyapunov function $\mathcal{C}^2-$ on $\mathcal{V}:\mathbb{R}^5_+\to\mathbb{R}_+$ as follows

$$\mathcal{V}(\mathcal{S},\mathcal{E},\mathcal{I},\mathcal{Q},\mathcal{R})=\ln(\mathcal{S}+\mathcal{E}+\mathcal{I}+\mathcal{Q}+\mathcal{R})^2+\ln\mathcal{E}+\ln\mathcal{I}.$$

Applying the infinitesimal generator $\mathcal{L}$ is applied to $\mathcal{V}$, we obtain

$$\begin{aligned}\mathcal{LV}(\mathcal{S},\mathcal{E},\mathcal{I},\mathcal{Q},\mathcal{R}) &= \left(\Theta-\frac{\beta\mathcal{SI}}{1+\mathsf{k}\mathcal{I}}-\mu\mathcal{S}\right)\left(\frac{2}{\mathcal{S}-1+\mathcal{E}+\mathcal{I}+\mathcal{Q}+\mathcal{R}}\right)\\ &+\left(\frac{\beta\mathcal{SI}}{1+\mathsf{k}\mathcal{I}}-(\gamma+\mu)\mathcal{E}\right)\left(\frac{2}{\mathcal{S}-1+\mathcal{E}+\mathcal{I}+\mathcal{Q}+\mathcal{R}}+\frac{1}{\mathcal{E}}\right)\\ &+(\gamma\mathcal{E}-(\xi+\eta+\alpha_1+\mu)\mathcal{I})\left(\frac{2}{\mathcal{S}-1+\mathcal{E}+\mathcal{I}+\mathcal{Q}+\mathcal{R}}+\frac{1}{\mathcal{I}}\right)\\ &+(\eta\mathcal{I}-(\delta+\alpha_2+\mu)\mathcal{Q})\left(\frac{2}{\mathcal{S}-1+\mathcal{E}+\mathcal{I}+\mathcal{Q}+\mathcal{R}}\right)\\ &+(\xi I+\delta\mathcal{Q}-\mu\mathcal{R})\left(\frac{2}{\mathcal{S}-1+\mathcal{E}+\mathcal{I}+\mathcal{Q}+\mathcal{R}}\right)\\ &-\left(\frac{2}{2(\mathcal{S}-1+\mathcal{E}+\mathcal{I}+\mathcal{Q}+\mathcal{R})^2}\right)\varrho_1^2S^2\\ &+\frac{1}{2}\left(\frac{-2}{(\mathcal{S}-1+\mathcal{E}+\mathcal{I}+\mathcal{Q}+\mathcal{R})^2}-\frac{1}{\mathcal{E}^2}\right)\varrho_2^2E^2\\ &+\frac{1}{2}\left(\frac{-2}{(\mathcal{S}-1+\mathcal{E}+\mathcal{I}+\mathcal{Q}+\mathcal{R})^2}-\frac{1}{\mathcal{I}^2}\right)\varrho_3^2I^2\\ &+\frac{1}{2}\left(\frac{-2}{(\mathcal{S}-1+\mathcal{E}+\mathcal{I}+\mathcal{Q}+\mathcal{R})^2}\right)\varrho_4^2Q^2\\ &-\left(\frac{2}{2(\mathcal{S}-1+\mathcal{E}+\mathcal{I}+\mathcal{Q}+\mathcal{R})^2}\right)\varrho_4^2R^2.\end{aligned} \tag{9}$$

As a result of simplifying $\mathcal{S}+\mathcal{E}+\mathcal{I}+\mathcal{Q}+\mathcal{R}\leq 1$, we get

$$\begin{aligned}\mathcal{LV}(\mathcal{S},\mathcal{E},\mathcal{I},\mathcal{Q},\mathcal{R}) &= \frac{2}{\mathcal{S}-1+\mathcal{E}+\mathcal{I}+\mathcal{Q}+\mathcal{R}}(\Theta-\mu\mathcal{S}-\mu\mathcal{E}-\mu\mathcal{I}-\mu\mathcal{Q}-\mu\mathcal{R})\\ &+(\beta\mathcal{S}-(\gamma+\mu))+(\gamma-(\xi+\eta+\alpha_1+\mu))\\ &-\frac{\varrho_1^2\mathcal{S}^2+\varrho_2^2\mathcal{E}^2+\varrho_3^2\mathcal{I}^2+\varrho_4^2\mathcal{Q}^2+\varrho_5^2\mathcal{R}^2}{(\mathcal{S}-1+\mathcal{E}+\mathcal{I}+\mathcal{Q}+\mathcal{R})^2}-\frac{\varrho_2^2}{2}-\frac{\varrho_3^2}{2}.\end{aligned}$$

It follows that $\mathcal{LV}$ will be negative and definite on $\mathcal{D}$ if $\mathcal{R}_0<1$ holds. A disease-free equilibrium solution $\mathsf{E}^*(\mathcal{S}_0,0,0,0,0)$ in $\mathcal{D}$ is global asymptotically stable for the stochastic model (2).

Remark 2 *The overhead Theorem 2 proves that the disease cases exist if $\mathcal{R}_0<1$ holds. The stability condition of the disease $\mu>\beta\gamma\mathcal{S}-((\gamma+\mu)+(\xi+\eta+\alpha_1+\mu))$ disease will be disappear. Taking the reproductive number $\mathcal{R}_0<1$, as a consequence, $\mathsf{E}^*(\mathcal{S}_0,0,0,0,0)$ is stochastically asymptotically stable in the large in the stochastic system (2). According to Theorem 2, the stochastic model (2) will approach disease-free equilibrium if the intensity of white noise is high enough. Since the intensity of white noise ϱ_i (for $i=1,2,3,4,5$) is small, the solutions of stochastic model (2) will generally fluctuate around the disease-less equilibrium of deterministic model (1).*

4 Ergodicity and stationary distribution

It is not only important to study epidemiological dynamics to determine when a disease will eventually become extinct. It is also to determine how long the disease will persist in the population. The endemic equilibrium does not exist for model (2). Therefore, this section examines whether there is a stationary distribution, which indicates the prevalence of a disease, according

to Hasminskii [32].
Then, let $X(t)$ be a time-homogeneous Markov process in $E_n \subset \mathbb{R}_n$. In order to explain this idea, a stochastic differential equation approach can be used.

$$d\mathcal{X}(t) = f(\mathcal{X})dt + \sum_{k=1}^{n} \sigma_k(\mathcal{X})dB_k(t). \tag{10}$$

In this case, E_n represents an n-dimensional Euclidean space. Following is a description of the diffusion matrix:

$$\widehat{\mathcal{A}}(x) = \left(a_{ij}(x)\right), a_{ij}(x) = \sum_{k=1}^{n} \sigma_k^i(x)\sigma_k^j(x). \tag{11}$$

Assumption 1 *The following properties are satisfied by a bounded domain $U \subset E_n$ with a regular boundary Π, such that $\overline{U} \subset E_n$ ($\overline{U}$ is the closure of U):*

i. The diffusion matrix $\widehat{\mathcal{A}}(x)$ is bounded away from zero in the domain U and some nearby neighborhoods.
ii. The mean time it takes for a path leading from 'x' to reach the set U is finite if $x \in E_n \backslash U$, and this holds true for each compact subset of E_n.

Lemma 2 *[32]. If Assumption 1 hold, then the Markov process $\mathcal{X}(t)$ has a stationary distribution $\widehat{\omega}(.)$. Besides, the measure $\widehat{\omega}$ may be integrated when $f(.)$ is a function, then*

$$\mathbb{P}_x\left\{\lim_{\mathcal{T}\to\infty} \frac{1}{\mathcal{T}} \int_0^{\mathcal{T}} f(\mathcal{X}(t))dt = \int_{E_n} f(x)\widehat{\omega}(dx)\right\} = 1,$$

for all $x \in E_n$.

Remark 3 *The demonstration of Assumption 1 (i) [33] involves showing that a bounded domain H has uniform ellipticity F; here is an example.*

$$\mathcal{F}_u = b(x)u_x \frac{1}{2} trace(\mathcal{A}(x)u_{xx}).$$

In particular, there exists a positive number $\mathfrak{Z}$ such that

$$\sum_{i,j=1}^{n} a_{ji}(x)\xi_i\xi_j \geq \mathfrak{Z}\,|\xi|^2, \quad x \in \overline{\mathcal{H}}, \xi \in \mathbb{R}^n.$$

It is possible to prove Assumption 1 (ii) [34] if there is a certain neighborhood U and some non-negative $\mathcal{C}^{2,1}$-function $\mathcal{V}$ such that for all $x \in E_n \backslash U$,
$\mathcal{L}\mathcal{V}(x) < 0$.
The following main results can be obtained by using Lemma 2.

Theorem 3 *If*

$$\mathcal{R}_0^* = \frac{\beta b\gamma}{(\mu + \frac{\varrho_1^2}{2})(\gamma + \mu + \frac{\varrho_2^2}{2})(\xi + \eta + \mu + \alpha_1 + \frac{\varrho_3^2}{2})} > 1,$$

and for the any initial value given as $(\mathcal{S}(0),\mathcal{E}(0),\mathcal{I}(0),\mathcal{Q}(0),\mathcal{R}(0)) \in \mathbb{R}^5_+$, *then the system has a uniquely stationary distribution* $\widehat{\omega}(.)$ *and it is has a ergodic property.*

Proof Define a function $\mathcal{C}^2$ such that,

$$\widehat{\mathcal{V}} : \mathbb{R}^5_+ \to \mathbb{R}_+,$$

$$\begin{aligned}\widehat{\mathcal{V}}(\mathcal{S},\mathcal{E},\mathcal{I},\mathcal{Q},\mathcal{R}) &= \Gamma\left[(\mathcal{S}+\mathcal{E}+\mathcal{I}+\mathcal{Q}+\mathcal{R}) - c_1\ln\mathcal{S} - c_2\ln\mathcal{E} - c_3\ln\mathcal{I}\right]\\ &\quad + \frac{1}{p+1}(\mathcal{S}+\mathcal{E}+\mathcal{I}+\mathcal{Q}+\mathcal{R})^{\kappa+1} - \ln\mathcal{S} - \ln\mathcal{E} - \ln\mathcal{Q}\\ &\quad - \ln\mathcal{R} + (\mathcal{S}+\mathcal{E}+\mathcal{I}+\mathcal{Q}+\mathcal{R})\\ &= \Gamma\mathcal{V}_1 + \mathcal{V}_2 + \mathcal{V}_3 + \mathcal{V}_4 + \mathcal{V}_5 + \mathcal{V}_6 + \mathcal{V}_7, \end{aligned} \tag{12}$$

here κ and c_i, $(\mathbf{i} = 1,2,3)$ the positive constant satisfying the condition

$$0 < \kappa < 2\mu\left(\frac{1}{\varrho_1^2+\varrho_2^2+\varrho_3^2+\varrho_4^2+\varrho_5^2}\right),$$

$$c_1 = \frac{\Theta}{\mu+\frac{\varrho_1^2}{2}}, \quad c_2 = \frac{\Theta}{\gamma+\mu+\frac{\varrho_2^2}{2}}, \quad c_3 = \frac{\Theta}{\xi+\mu+\eta+\alpha_1+\frac{\varrho_3^2}{2}},$$

we can consider $\Gamma > 0$ and make it large enough, such that

$$\Gamma\phi + \mathcal{M} \leq -2,$$

obviously,

$$\liminf_{\pi\to(\mathcal{S},\mathcal{E},\mathcal{I},\mathcal{Q},\mathcal{R})\in\mathbb{R}^5_+\setminus\mathbb{U}_\pi} \overline{\mathcal{V}}(\mathcal{S},\mathcal{E},\mathcal{I},\mathcal{Q},\mathcal{R}) = +\infty, \tag{13}$$

and here, $\mathbb{U}_\pi = (\frac{1}{\pi},\pi)\times(\frac{1}{\pi},\pi)\times(\frac{1}{\pi},\pi)\times(\frac{1}{\pi},\pi)\times(\frac{1}{\pi},\pi)$.
There exists a point $(\mathcal{S}^*,\mathcal{E}^*,\mathcal{I}^*,\mathcal{Q}^*,\mathcal{R}^*)$ in $\mathbb{R}^5_+$ that is the minimum point of $\widehat{\mathcal{V}}(\mathcal{S},\mathcal{E},\mathcal{I},\mathcal{Q},\mathcal{R})$ because $\widetilde{\mathcal{V}}(\mathcal{S},\mathcal{E},\mathcal{I},\mathcal{Q},\mathcal{R})$ is a continuous function. The positive define $\mathcal{C}^2-$ function $\mathcal{V} : \mathbb{R}^5_+ \to \mathbb{R}_+$ by

$$\mathcal{V}(\mathcal{S},\mathcal{E},\mathcal{I},\mathcal{Q},\mathcal{R}) = \widehat{\mathcal{V}}(\mathcal{S},\mathcal{E},\mathcal{I},\mathcal{Q},\mathcal{R}) - \widehat{\mathcal{V}}(\mathcal{S}^*,\mathcal{E}^*,\mathcal{I}^*,\mathcal{Q}^*,\mathcal{R}^*), \tag{14}$$

from Ito's formula,

$$\begin{aligned}\mathcal{L}\mathcal{V}_1 &= -\mu - \frac{c_1\Theta}{\mathcal{S}} - \frac{c_2\beta\mathcal{S}\mathcal{I}}{\mathcal{E}(1+\mathbf{k}\mathcal{I})} - \frac{c_3\gamma\mathcal{E}}{\mathcal{I}} + \frac{c_1\beta\mathcal{I}}{1+\mathbf{k}\mathcal{I}} + \Theta - \alpha_1\mathcal{I} - \alpha_2\mathcal{Q}\\ &\quad + c_1\left(\mu+\frac{\varrho_1^2}{2}\right) + c_2\left(\gamma+\mu+\frac{\varrho_2^2}{2}\right) + c_3\left(\xi+\mu+\eta+\alpha_1+\frac{\varrho_3^2}{2}\right)\end{aligned}$$

$$
\begin{aligned}
&= -\mu - \frac{c_1\Theta}{\mathcal{S}} - \frac{c_2\beta\mathcal{S}\mathcal{I}}{\mathcal{E}(1+\mathbf{k}\mathcal{I})} - \frac{c_3\gamma\mathcal{E}}{\mathcal{I}} + \frac{c_1\beta\mathcal{I}}{1+\mathbf{k}\mathcal{I}} + \Theta + c_1\left(\mu + \frac{\varrho_1^2}{2}\right) \\
&\quad + c_2\left(\gamma + \mu + \frac{\varrho_2^2}{2}\right) + c_3\left(\xi + \mu + \eta + \alpha_1 + \frac{\varrho_3^2}{2}\right) \\
&\leq -4\left(\frac{\mu c_1 c_2 c_3 b\beta\gamma}{1+\mathbf{k}\mathcal{I}}\right)^{\frac{1}{4}} + \frac{c_1\beta\mathcal{I}}{1+\mathbf{k}\mathcal{I}} + \Theta + c_1\left(\mu + \frac{\varrho_1^2}{2}\right) + c_2\left(\gamma + \mu + \frac{\varrho_2^2}{2}\right) \\
&\quad + c_3\left(\xi + \mu + \eta + \alpha_1 + \frac{\varrho_3^2}{2}\right) \\
&\leq -4\left(\frac{\mu c_1 c_2 c_3 \Theta\beta\gamma}{1+\mathbf{k}\mathcal{I}}\right)^{\frac{1}{4}} + \frac{c_1\beta\mathcal{I}}{1+\mathbf{k}\mathcal{I}} - 4\mu \\
&\leq -4\mu\left[\left(\frac{\Theta\beta\gamma}{(1+\mathbf{k}\mathcal{I})\left(\mu + \frac{\varrho_1^2}{2}\right)\left(\gamma + \mu + \frac{\varrho_2^2}{2}\right)\left(\xi + \mu + \eta + \alpha_1 + \frac{\varrho_3^2}{2}\right)}\right)^{\frac{1}{4}} - 1\right] \\
&\quad + \frac{c_1\beta\mathcal{I}}{1+\mathbf{k}\mathcal{I}} \\
&\leq \frac{-4\mu}{1+\mathbf{k}\mathcal{I}}\left[(\mathcal{R}_0^*)^{\frac{1}{4}} - 1\right] + \frac{c_1\beta\mathcal{I}}{1+\mathbf{k}\mathcal{I}}, \qquad (15)
\end{aligned}
$$

$$
\begin{aligned}
\mathcal{L}\mathcal{V}_2 &= (\mathcal{S}+\mathcal{E}+\mathcal{I}+\mathcal{Q}+\mathcal{R})^{\kappa}\left[\Theta - (\mathcal{S}+\mathcal{E}+\mathcal{I}+\mathcal{Q}+\mathcal{R})\mu - \alpha_1\mathcal{I} - \alpha_2\mathcal{Q}\right] \\
&\quad + \frac{\kappa(\mathcal{S}+\mathcal{E}+\mathcal{I}+\mathcal{Q}+\mathcal{R})^{\kappa+1}}{2}\left(\varrho_1^2\mathcal{S}^2 + \varrho_2^2\mathcal{E}^2 + \varrho_3^2\mathcal{I}^2 + \varrho_4^2\mathcal{Q}^2 + \varrho_5^2\mathcal{R}^2\right) \\
&\leq \Theta(\mathcal{S}+\mathcal{E}+\mathcal{I}+\mathcal{Q}+\mathcal{R})^{\kappa} - \left[\mu - \frac{\kappa}{2}(\varrho_1^2 \vee \varrho_2^2 \vee \varrho_3^2 \vee \varrho_4^2 \vee \varrho_5^2)\right] \\
&\quad \times (\mathcal{S}+\mathcal{E}+\mathcal{I}+\mathcal{Q}+\mathcal{R})^{\kappa+1} \\
&\leq \omega - \frac{1}{2}\left[\mu - \frac{\kappa}{2}(\varrho_1^2 \vee \varrho_2^2 \vee \varrho_3^2 \vee \varrho_4^2 \vee \varrho_5^2)\right](\mathcal{S}+\mathcal{E}+\mathcal{I}+\mathcal{Q}+\mathcal{R})^{\kappa+1} \\
&< \omega - \frac{1}{2}\left[\mu - \frac{\kappa}{2}(\varrho_1^2 \vee \varrho_2^2 \vee \varrho_3^2 \vee \varrho_4^2 \vee \varrho_5^2)\right] \\
&\quad \times (\mathcal{S}^{\kappa+1} + \mathcal{E}^{\kappa+1} + \mathcal{I}^{\kappa+1} + \mathcal{Q}^{\kappa+1} + \mathcal{R}^{\kappa+1}), \qquad (16)
\end{aligned}
$$

where,

$$
\begin{aligned}
\omega &= \sup_{(\mathcal{S},\mathcal{E},\mathcal{I},\mathcal{Q},\mathcal{R})\in\mathbb{R}_+^5}\{\Theta(\mathcal{S}+\mathcal{E}+\mathcal{I}+\mathcal{Q}+\mathcal{R})^{\kappa} \\
&\quad - \left[\mu - \frac{\kappa}{2}(\varrho_1^2 \vee \varrho_2^2 \vee \varrho_3^2 \vee \varrho_4^2 \vee \varrho_5^2)\right] \times (\mathcal{S}+\mathcal{E}+\mathcal{I}+\mathcal{Q}+\mathcal{R})^{\kappa+1}\Big\} \\
&< \infty.
\end{aligned}
$$

Similarly, we get

$$\mathcal{L}\mathcal{V}_3 = -\frac{\Theta}{\mathcal{S}} + \frac{\beta\mathcal{I}}{1+\mathbf{k}\mathcal{I}} + \mu + \frac{\varrho_1^2}{2}, \tag{17}$$

$$\mathcal{L}\mathcal{V}_4 = -\frac{\beta\mathcal{S}\mathcal{I}}{\mathcal{E}(1+\mathbf{k}\mathcal{I})} + (\mu+\gamma) + \frac{\varrho_2^2}{2}, \tag{18}$$

$$\mathcal{L}\mathcal{V}_5 = -\frac{\eta\mathcal{I}}{\mathcal{Q}} + (\xi_\mu + \alpha_2) + \frac{\varrho_4^2}{2}, \tag{19}$$

$$\mathcal{L}\mathcal{V}_6 = -\frac{\xi\mathcal{I}+\delta\mathcal{Q}}{\mathcal{R}} + \mu + \frac{\varrho_5^2}{2}, \tag{20}$$

$$\mathcal{L}\mathcal{V}_7 = \Theta - (\mathcal{S}+\mathcal{E}+\mathcal{I}+\mathcal{Q}+\mathcal{R})\mu. \tag{21}$$

Therefore,

$$\begin{aligned}\mathcal{L}\mathcal{V} = {} & -\varphi\phi + \frac{\varphi c_1\beta\mathcal{I}}{1+\mathbf{k}\mathcal{I}} - \frac{1}{2}\left[\mu - \frac{\kappa}{2}(\varrho_1^2 \vee \varrho_2^2 \vee \varrho_3^2 \vee \varrho_4^2 \vee \varrho_5^2)\right] \\ & (\mathcal{S}^{\kappa+1} + \mathcal{E}^{\kappa+1} + \mathcal{I}^{\kappa+1} + \mathcal{Q}^{\kappa+1} + \mathcal{R}^{\kappa+1}) \\ & -\frac{\Theta}{\mathcal{S}} - \frac{\beta\mathcal{S}\mathcal{I}}{\mathcal{E}(1+\mathbf{k}\mathcal{I})} - \frac{\eta\mathcal{I}}{\mathcal{Q}} - \frac{\xi\mathcal{I}+\delta\mathcal{Q}}{\mathcal{R}} - (\mathcal{S}+\mathcal{E}+\mathcal{I}+\mathcal{Q}+\mathcal{R})\mu \\ & +\Theta + \pi + \xi + \gamma + 4\mu + \alpha_2 + \frac{\varrho_1^2 \vee \varrho_2^2 \vee \varrho_4^2 \vee \varrho_5^2}{2}.\end{aligned} \tag{22}$$

As a next step, let us examine compact subset $\mathcal{D}$

$$\mathcal{D} = \left\{\varepsilon \le \mathcal{S} \le \frac{1}{\epsilon}, \epsilon_4^2 \le \mathcal{E} \le \frac{1}{\epsilon_4^2}, \epsilon_2^2 \le \mathcal{I} \le \frac{1}{\epsilon_2^2}, \epsilon_3^2 \le \mathcal{Q} \le \frac{1}{\epsilon_3^2}, \epsilon_4^2 \le \mathcal{R} \le \frac{1}{\epsilon_4^2}\right\}.$$

The following conditions must be satisfied if ϵ is a sufficiently small constant:

$$\begin{aligned}
& - \quad \frac{\Theta}{\mathcal{S}} + \frac{\Upsilon c_1\beta}{\mathbf{k}} + F \le -1 \\
& - \quad \Upsilon\phi + \Upsilon c_1\beta\epsilon \le -1 \\
& - \quad 2\left(\frac{\mu\beta}{1+\mathbf{k}\mathcal{I}}\right)^{\frac{1}{2}} + \Upsilon\epsilon_1\beta + \mathcal{M} \le -1 \\
& - \quad \frac{\eta}{\epsilon} + \frac{\Upsilon c_1\beta}{1+\mathbf{k}\mathcal{I}} + \mathcal{M} \le -1 \\
& - \quad \frac{\epsilon}{\epsilon^2} - \frac{\delta}{\epsilon} + \Upsilon c_1\beta + \mathcal{M} \le -1 \\
& - \quad \frac{1}{2}\left[\mu - \frac{\kappa}{2}\left(\varrho_1^2 \vee \varrho_2^2 \vee \varrho_3^2 \vee \varrho_4^2 \vee \varrho_5^2\right)\right]\frac{1}{\epsilon^{i(\kappa+1)}} + \Upsilon c_1\beta\mathcal{I} \\
& \quad +\mathcal{M} \le -1.
\end{aligned}$$

Here ϵ is a sufficiently small constant, where $i = 1, 2, 3, 4, 5$. In that case, $\mathbb{R}^5_+ \backslash \mathcal{D} = \mathcal{D}_1 \cup \mathcal{D}_2 \cup \mathcal{D}_3 \cup \mathcal{D}_4 \cup, ..., \cup \mathcal{D}_{10}$ with,

$$\begin{aligned}
\mathcal{D}_1 &= \left\{(\mathcal{S}, \mathcal{E}, \mathcal{I}, \mathcal{Q}, \mathcal{R}) \in \mathbb{R}^5_+ / 0 < \mathcal{S} < \epsilon\right\}, \\
\mathcal{D}_2 &= \left\{(\mathcal{S}, \mathcal{E}, \mathcal{I}, \mathcal{Q}, \mathcal{R}) \in \mathbb{R}^5_+ / \mathcal{S} \geq \epsilon, \mathcal{I} \geq \epsilon_2^2, 0 < \epsilon < \epsilon_4^2\right\}, \\
\mathcal{D}_3 &= \left\{(\mathcal{S}, \mathcal{E}, \mathcal{I}, \mathcal{Q}, \mathcal{R}) \in \mathbb{R}^5_+ / \mathcal{S} \geq \epsilon, 0 < \mathcal{I} < \epsilon_3^2\right\}, \\
\mathcal{D}_4 &= \left\{(\mathcal{S}, \mathcal{E}, \mathcal{I}, \mathcal{Q}, \mathcal{R}) \in \mathbb{R}^5_+ / \mathcal{I} \geq \epsilon_2^2, 0 < \mathcal{Q} < \epsilon_3^2\right\}, \\
\mathcal{D}_5 &= \left\{(\mathcal{S}, \mathcal{E}, \mathcal{I}, \mathcal{Q}, \mathcal{R}) \in \mathbb{R}^5_+ / \mathcal{S} \geq \epsilon, \mathcal{I} \geq \epsilon_2^2, \mathcal{Q} \geq \epsilon_3^2, 0 < \mathcal{R} < \epsilon_4^2\right\}, \\
\mathcal{D}_6 &= \left\{(\mathcal{S}, \mathcal{E}, \mathcal{I}, \mathcal{Q}, \mathcal{R}) \in \mathbb{R}^5_+ / \mathcal{S} > \frac{1}{\epsilon}\right\}, \\
\mathcal{D}_7 &= \left\{(\mathcal{S}, \mathcal{E}, \mathcal{I}, \mathcal{Q}, \mathcal{R}) \in \mathbb{R}^5_+ / \mathcal{E} > \frac{1}{\epsilon_4^2}\right\}, \\
\mathcal{D}_8 &= \left\{(\mathcal{S}, \mathcal{E}, \mathcal{I}, \mathcal{Q}, \mathcal{R}) \in \mathbb{R}^5_+ / \mathcal{I} > \frac{1}{\epsilon_3^2}\right\}, \\
\mathcal{D}_9 &= \left\{(\mathcal{S}, \mathcal{E}, \mathcal{I}, \mathcal{Q}, \mathcal{R}) \in \mathbb{R}^5_+ / \mathcal{Q} > \frac{1}{\epsilon_3^2}\right\}, \\
\mathcal{D}_{10} &= \left\{(\mathcal{S}, \mathcal{E}, \mathcal{I}, \mathcal{Q}, \mathcal{R}) \in \mathbb{R}^5_+ / \mathcal{R} > \frac{1}{\epsilon_4^2}\right\}.
\end{aligned}$$

As a result, we can now calculate the negative $\mathcal{LV}$ value for every $(\mathcal{S}, \mathcal{E}, \mathcal{I}, \mathcal{Q}, \mathcal{R}) \in \mathbb{R}^5_+ \backslash \mathcal{D}$.
Case-1: Suppose $(\mathcal{S}, \mathcal{E}, \mathcal{I}, \mathcal{Q}, \mathcal{R}) \in \mathcal{D}_1$

$$\begin{aligned}
\mathcal{LV} &\leq -\frac{\Theta}{\mathcal{S}} + \frac{\Upsilon c_1 \beta \mathcal{I}}{1 + \mathbf{k}\mathcal{I}} - \frac{1}{2}\left[\mu - \frac{\kappa}{2}(\varrho_1^2 \vee \varrho_2^2 \vee \varrho_3^2 \vee \varrho_4^2 \vee \varrho_5^2)\right] \\
&\quad \times (\mathcal{S}^{\kappa+1} + \mathcal{E}^{\kappa+1} + \mathcal{I}^{\kappa+1} + \mathcal{Q}^{\kappa+1} + \mathcal{R}^{\kappa+1}) + \Theta + \pi + \xi + \gamma + 4\mu + \alpha_2 \\
&\quad + \frac{\varrho_1^2 + \varrho_2^2 + \varrho_3^2 + \varrho_4^2 + \varrho_5^2}{2} \\
&\leq -\frac{\Theta}{\mathcal{S}} + \frac{\Upsilon c_1 \beta}{\mathbf{k}} + F \leq -1.
\end{aligned} \tag{23}$$

Case-2: In this case, $(\mathcal{S}, \mathcal{E}, \mathcal{I}, \mathcal{Q}, \mathcal{R}) \in \mathcal{D}_2$

$$\begin{aligned}
\mathcal{LV} &\leq -\Upsilon\phi + \frac{\Upsilon c_1 \beta \mathcal{S}\mathcal{I}}{1 + \mathbf{k}\mathcal{I}} + \frac{\beta \mathcal{S}\mathcal{I}}{\mathcal{E}(1 + \mathbf{k}\mathcal{I})} - \frac{1}{2}\left[\mu - \frac{\kappa}{2}(\varrho_1^2 \vee \varrho_2^2 \vee \varrho_3^2 \vee \varrho_4^2 \vee \varrho_5^2)\right] \\
&\quad (\mathcal{S}^{\kappa+1} + \mathcal{E}^{\kappa+1} + \mathcal{I}^{\kappa+1} + \mathcal{Q}^{\kappa+1} + \mathcal{R}^{\kappa+1}) + \pi + \xi + \gamma + 4\mu + \alpha_2 \\
&\quad + \frac{\varrho_1^2 + \varrho_2^2 + \varrho_3^2 + \varrho_4^2 + \varrho_5^2}{2} \\
&\leq -\Upsilon\phi + \frac{\Upsilon c_1 \beta}{1 + \mathbf{k}\mathcal{I}} \frac{1}{2}\left[\mu - \frac{\kappa}{2}(\varrho_1^2 \vee \varrho_2^2 \vee \varrho_3^2 \vee \varrho_4^2 \vee \varrho_5^2)\right] \\
&\quad \times (\mathcal{S}^{\kappa+1} + \mathcal{E}^{\kappa+1} + \mathcal{I}^{\kappa+1} + \mathcal{Q}^{\kappa+1} + \mathcal{R}^{\kappa+1}) + \pi + \xi + \gamma + 4\mu + \alpha_2
\end{aligned}$$

$$
\begin{aligned}
&+\frac{\varrho_1^2+\varrho_2^2+\varrho_3^2+\varrho_4^2+\varrho_5^2}{2}\\
&\leq -\Upsilon\phi+\frac{\Upsilon c_1\beta}{\mathbf{k}}+G\\
&\leq -\Upsilon\phi+\Upsilon c_1\beta\epsilon\leq -1.
\end{aligned}
\tag{24}
$$

Case-3: In case of $(\mathcal{S},\mathcal{E},\mathcal{I},\mathcal{Q},\mathcal{R})\in\mathcal{D}_3$

$$
\begin{aligned}
\mathcal{LV} &= -2\left(\frac{\mu\beta\mathcal{S}\mathcal{I}}{\mathcal{E}(1+\mathbf{k}\mathcal{I})}\right)^{\frac{1}{2}}+\frac{\Upsilon c_1\beta\mathcal{S}\mathcal{I}}{1+\mathbf{k}\mathcal{I}}+\pi+\xi+\gamma+4\mu+\alpha_2\\
&\quad+\frac{\varrho_1^2+\varrho_2^2+\varrho_3^2+\varrho_4^2+\varrho_5^2}{2}\\
&\leq -2\left(\frac{\mu\beta}{1+\mathbf{k}}\right)^{\frac{1}{2}}+\frac{\Upsilon\epsilon_1\beta}{1+\mathbf{k}\mathcal{I}}+M\\
&\leq -2\left(\frac{\mu\beta}{1+\mathbf{k}}\right)^{\frac{1}{2}}+\Upsilon\epsilon_1\beta+M\leq -1.
\end{aligned}
\tag{25}
$$

Case-4: In case $(\mathcal{S},\mathcal{E},\mathcal{I},\mathcal{Q},\mathcal{R})\in\mathcal{D}_4$

$$
\begin{aligned}
\mathcal{LV} &\leq -\frac{\eta\mathcal{I}}{\mathcal{Q}}+\frac{\Upsilon c_1\beta\mathcal{I}}{1+\mathbf{k}\mathcal{I}}+b+\pi+\xi+\gamma+4\mu+\alpha_2\\
&\quad+\frac{\varrho_1^2+\varrho_2^2+\varrho_3^2+\varrho_4^2+\varrho_5^2}{2}\\
&\leq -\frac{\eta}{\epsilon}+\frac{\Upsilon c_1\beta}{1+\mathbf{k}\mathcal{I}}+M\leq -1.
\end{aligned}
\tag{26}
$$

Case-5: In this case, $(\mathcal{S},\mathcal{E},\mathcal{I},\mathcal{Q},\mathcal{R})\in\mathcal{D}_5$

$$
\begin{aligned}
\mathcal{LV} &\leq -\frac{\xi\mathcal{I}-\delta\mathcal{Q}}{\mathcal{R}}+\frac{\Upsilon c_1\beta\mathcal{I}}{1+\mathbf{k}\mathcal{I}}+M\\
&\leq -\frac{\epsilon}{\epsilon^2}-\frac{\delta}{\epsilon}+\Upsilon c_1\beta+M\leq -1.
\end{aligned}
\tag{27}
$$

Case-6: Suppose $(\mathcal{S},\mathcal{E},\mathcal{I},\mathcal{Q},\mathcal{R})\in\mathcal{D}_6$

$$
\begin{aligned}
\mathcal{LV} &\leq -\frac{1}{2}\left[\mu-\frac{\kappa}{2}\left(\varrho_1^2\vee\varrho_2^2\vee\varrho_3^2\vee\varrho_4^2\vee\varrho_5^2\right)\right]\mathcal{S}^{\kappa+1}+\frac{\gamma c_1\beta\mathcal{I}}{1+\mathbf{k}\mathcal{I}}+M\\
&\leq -\frac{1}{2}\left[\mu-\frac{\kappa}{2}\left(\varrho_1^2\vee\varrho_2^2\vee\varrho_3^2\vee\varrho_4^2\vee\varrho_5^2\right)\right]\frac{1}{\epsilon^{\kappa+1}}+\gamma c_1\beta\mathcal{I}+M\\
&\leq -1.
\end{aligned}
\tag{28}
$$

Subsequently, providing under requirement (4.19) for $i=1$. We get $\mathcal{LV}\leq -1$ on $\mathcal{D}_6$. Similarly, it follows from the equation (4.19) for $i=2,\ldots,4$, the same procedure can deduced for the compartments $\mathcal{E},\mathcal{I},\mathcal{Q},\mathcal{R}$ on $\mathcal{LV}\leq -1$ and for $\mathcal{D}_i, i=7,\ldots,10$.
Based on the 10 cases mentioned above, it can be concluded that According to the discussion of the above ten cases, it becomes clear that, for a sufficiently small ε,

$$\mathcal{LV} \leq -1 \quad \text{for all} \quad (\mathcal{S}, \mathcal{E}, \mathcal{I}, \mathcal{Q}, \mathcal{R}) \in \mathbb{R}^5_+ \setminus \mathcal{D}. \tag{29}$$

Therefore, Assumption 1 (ii) is satisfied. A diffusion matrix is also presented for model (2) as follows:

$$A = \begin{pmatrix} \varrho_1^2\mathcal{S}^2 & 0 & 0 & 0 & 0 \\ 0 & \varrho_2^2\mathcal{E}^2 & 0 & 0 & 0 \\ 0 & 0 & \varrho_3^2\mathcal{I}^2 & 0 & 0 \\ 0 & 0 & 0 & \varrho_4^2\mathcal{Q}^2 & 0 \\ 0 & 0 & 0 & 0 & \varrho_5^2\mathcal{R}^2 \end{pmatrix}.$$

A positive number exists,

$$\mathcal{X} = \min_{(\mathcal{S},\mathcal{E},\mathcal{I},\mathcal{Q},\mathcal{R})\in\mathbb{D}} \left\{ \varrho_1^2\mathcal{S}^2, \varrho_2^2\mathcal{E}^2, \varrho_3^2\mathcal{I}^2, \varrho_4^2\mathcal{Q}^2, \varrho_5^2\mathcal{R}^2 \right\},$$

such that,

$$\begin{aligned} \sum_{i,j=1}^{5} a_{ij}\xi_i\xi_j &= \varrho_1^2\mathcal{S}^2\xi_1^2 + \varrho_2^2\mathcal{E}^2\xi_2^2 + \varrho_3^2\mathcal{I}^2\xi_3^2 + \varrho_4^2\mathcal{Q}^2\xi_4^2 + \varrho_5^2\mathcal{R}^2\xi_5^2 \\ &\geq \mathcal{X}\,|\xi|^2. \end{aligned} \tag{30}$$

In this case, Assumption 1 (i) is satisfied. Due to this, the model (2) has an ergodic distribution $\widehat{\omega}(.)$ with a uniquely stationary distribution. Proof of the Theorem is complete.

Remark 4 *Theorem 3 indicates that model (2) has an uniquely ergodic stationary distribution if $\mathcal{R}_0^* > 1$. If $\varrho_i = 0 (i = 1, 2, 3, 4, 5)$, the expression of $\mathcal{R}_0^*$ corresponds to the reproduction number $\mathcal{R}_0$ of the model (1). It is clear from this that the results of model (1) can be generalized. Furthermore, this theorem shows that the disease can be resistant to small levels of environmental noise in order to remain persistent.*

5 Extinction

The purpose of this section is to discuss the parameter conditions for the extinction of diseases in the model (2). First, we give a useful lemma before proving our main conclusions:

Lemma 3 *If $(\mathcal{S}(t), \mathcal{E}(t), \mathcal{I}(t), \mathcal{Q}(t), \mathcal{R}(t))$ be a solution of the system for any given initial value $(\mathcal{S}(t), \mathcal{E}(t), \mathcal{I}(t), \mathcal{Q}(t), \mathcal{R}(t)) \in \mathbb{R}^5_+$ has the following properties,*

$$\lim_{t\to\infty} \frac{1}{t} (\mathcal{S}(t), \mathcal{E}(t), \mathcal{I}(t), \mathcal{Q}(t), \mathcal{R}(t)) = 0, \qquad a.s.$$

In addition, when $\mu > \frac{1}{2}\left(\varrho_1^2 \vee \varrho_2^2 \vee \varrho_3^2 \vee \varrho_4^2 \vee \varrho_5^2\right)$ *holds.*

$$\begin{aligned}
\lim_{t\to\infty}\frac{1}{t}\int_0^t \mathcal{S}(x)dB_1(x) &= 0, \lim_{t\to\infty}\frac{1}{t}\int_0^t \mathcal{E}(x)dB_2(x) = 0,\\
\lim_{t\to\infty}\frac{1}{t}\int_0^t \mathcal{I}(x)dB_2(x) &= 0, \lim_{t\to\infty}\frac{1}{t}\int_0^t \mathcal{Q}(x)dB_4(x) = 0,\\
\lim_{t\to\infty}\frac{1}{t}\int_0^t \mathcal{R}(x)dB_5(x) &= 0, \quad a.s.
\end{aligned} \tag{31}$$

Proof The proof of Lemma 3 follows the same way as [35, 36]; therefore, we omit it.

Theorem 4 *Let* $\mu > \frac{1}{2}\left(\varrho_1^2 \vee \varrho_2^2 \vee \varrho_3^2 \vee \varrho_4^2 \vee \varrho_5^2\right)$ *at any given initial value* $(\mathcal{S}(t), \mathcal{E}(t), \mathcal{I}(t), \mathcal{Q}(t), \mathcal{R}(t)) \in \mathbb{R}_+^5$, *if*

$$\mathcal{R}_S^* = \frac{2\gamma\beta(\gamma+\mu)}{\left[(\xi+\mu+\alpha_1+\eta+\frac{\varrho_3^2}{2})(\gamma+\mu)^2\right] \wedge \left(\frac{\gamma^2\varrho_2^2}{2}\right)} < 1.$$

Then

$$\lim_{t\to\infty}\mathcal{E}(t) = \lim_{t\to\infty}\mathcal{I}(t) = \lim_{t\to\infty}\mathcal{Q}(t) = \lim_{t\to\infty}\mathcal{R}(t) = 0, \quad a.s.$$

Furthermore,

$$\lim_{t\to\infty}\langle \mathcal{S}\rangle = \frac{\Theta}{\mu} = \mathcal{S}_0, \quad a.s.$$

Proof In the following equation, define a function V_0 that is differentiable

$$\begin{aligned}
dV_0 &= \left\{\frac{\Upsilon(\beta\mathcal{S}\mathcal{I}/1+\mathbf{k}\mathcal{I}) - (\gamma+\mu)(\xi+\mu+\alpha_1+\eta)\mathcal{I}}{\Upsilon\mathcal{E}+(\gamma+\mu)\mathcal{I}} - \frac{\gamma^2\varrho_2^2\mathcal{E}^2 + (\gamma+\mu)^2\varrho_3^2\mathcal{I}^2}{2\left[\gamma\mathcal{E}+(\gamma+\mu)\mathcal{I}\right]^2}\right\}dt\\
&\quad + \frac{\Upsilon\varrho_2\mathcal{E}}{\Upsilon\mathcal{E}+(\gamma+\mu)\mathcal{I}}dB_2(t) + \frac{(\gamma+\mu)\varrho_3\mathcal{I}}{\Upsilon\mathcal{E}+(\gamma+\mu)}dB_3(t).\\
&\leq \left\{\frac{\Upsilon\beta}{(\gamma+\mu)} - \frac{(\gamma+\mu)^2\mathcal{I}^2(\xi+\mu+\alpha_1+\eta+\frac{\varrho_3^2}{2}) + (\frac{\gamma^2\varrho_2^2}{2})\mathcal{E}^2}{\left[\gamma\mathcal{E}+(\gamma+\mu)\mathcal{I}\right]^2}\right\}\\
&\quad + \frac{\Upsilon\varrho_2\mathcal{E}}{\Upsilon\mathcal{E}+(\gamma+\mu)\mathcal{I}}dB_2(t) + \frac{(\gamma+\mu)\varrho_3\mathcal{I}}{\Upsilon\mathcal{E}+(\gamma+\mu)}dB_3(t)\\
&\leq \left\{\frac{\Upsilon\beta}{\gamma+\mu} - \frac{(\xi+\eta+\alpha_1+\mu+\frac{\varrho_3^2}{2})(\gamma+\mu)^2 \wedge \left(\frac{\gamma^2\varrho_2^2}{2}\right)}{2(\gamma+\mu)^2}\right\}dt\\
&\quad + \frac{\Upsilon\varrho_2\mathcal{E}}{\Upsilon\mathcal{E}+(\gamma+\mu)\mathcal{I}}dB_2(t) + \frac{(\gamma+\mu)\varrho_3\mathcal{I}}{\Upsilon\mathcal{E}+(\gamma+\mu)}dB_3(t).
\end{aligned} \tag{32}$$

The integration from 0 to t and the division by t on both sides of (32) are done as follows:

$$\begin{aligned}\frac{\ln[\gamma\mathcal{E}+\mathcal{I}(\mathbf{t})(\gamma+\mu)]}{\mathbf{t}} \leq\ & \frac{\Upsilon\beta}{\gamma+\mu}-\frac{(\xi+\eta+\alpha_1+\mu+\frac{\varrho_3^2}{2})(\gamma+\mu)^2\wedge\left(\frac{\gamma^2\varrho_2^2}{2}\right)}{2(\gamma+\mu)^2}\\ &+\frac{\ln[\gamma\mathcal{E}(0)+\mathcal{I}(0)(\gamma+\mu)]}{\mathbf{t}}\\ &+\frac{\gamma\varrho_2}{\mathbf{t}}\int_0^{\mathbf{t}}\frac{\mathcal{E}(x)}{\gamma\mathcal{E}(x)+(\gamma+\mu)\mathcal{I}(x)}dB_2(x)\\ &+\frac{(\gamma+\mu)\varrho_3}{\mathbf{t}}\int_0^{\mathbf{t}}\frac{\mathcal{I}(x)}{\gamma\mathcal{E}(x)+(\gamma+\mu)\mathcal{I}(x)}dB_3(x).\end{aligned}$$

By applying Lemma 3, we need to

$$\begin{aligned}\limsup_{\mathbf{t}\to\infty}\frac{\ln[\gamma\mathcal{E}(\mathbf{t})+\mathcal{I}(\mathbf{t})(\gamma+\mu)]}{\mathbf{t}} \leq\ & \frac{\Upsilon\beta}{\gamma+\mu}\\ &-\frac{(\xi+\eta+\alpha_1+\mu+\frac{\varrho_3^2}{2})(\gamma+\mu)^2\wedge\left(\frac{\gamma^2\varrho_2^2}{2}\right)}{2(\gamma+\mu)^2}\\ <\ & 0\quad a.s.\end{aligned}$$

The result of which is

$$\lim_{\mathbf{t}\to\infty}\mathcal{E}(\mathbf{t})=0,\lim_{\mathbf{t}\to\infty}\mathcal{I}(\mathbf{t})=0\quad a.s.$$

The model (2) is easily understood by taking the fourth equation as an example

$$\lim_{\mathbf{t}\to\infty}\mathcal{Q}(\mathrm{t})=0\quad a.s.$$

Furthermore, on both sides of the first equation of model (2), integrating from 0 to t and dividing by t results in the following.

$$\frac{\mathcal{S}(\mathbf{t})-\mathcal{S}(0)}{\mathbf{t}}=\Theta-\frac{\beta}{1+\mathbf{k}\mathcal{I}}\langle\mathcal{S}\mathcal{I}\rangle+\frac{\varrho_1}{\mathbf{t}}\int_0^{\mathbf{t}}\mathcal{S}(x)dB(x),\tag{33}$$

$$\lim_{\mathrm{t}\to\infty}\langle\mathcal{S}\rangle=\frac{\Theta}{\mu}=\mathcal{S}_0\quad a.s.$$

A similar result can be obtained

$$\lim_{\mathbf{t}\to\infty}\langle\mathcal{R}\rangle=0\quad a.s.$$

The proof is validated.

6 Numerical simulations

A numerical simulation was conducted using Matlab software in order to illustrate the results of the above theorems. In order to determine the discretization transformation of the model (2), we use the Milstein method mentioned in [37].

$$\begin{aligned}
\mathcal{S}_{i+1} &= \mathcal{S}_i + \left[\Theta - \frac{\beta \mathcal{S}_i \mathcal{I}_i}{1+\mathbf{k}\mathcal{I}_i} - \mu \mathcal{S}_i\right]\Delta t + \varrho_1 \mathcal{S}_i \sqrt{\Delta t}\zeta_{1,i} + \frac{\varrho_1^2}{2}\mathcal{S}_i(\zeta_{1,i}^2 - 1)\Delta t,\\
\mathcal{E}_{i+1} &= \mathcal{E}_i + \left[\frac{\beta \mathcal{S}_i \mathcal{I}_i}{1+\mathbf{k}\mathcal{I}_i} - (\gamma+\mu)\mathcal{E}_i\right]\Delta t + \varrho_2 \mathcal{E}_i \sqrt{\Delta t}\zeta_{2,i} + \frac{\varrho_2^2}{2}\mathcal{E}_i(\zeta_{2,i}^2 - 1)\Delta t,\\
\mathcal{I}_{i+1} &= \mathcal{I}_i + [\gamma \mathcal{E}_i - (\xi+\eta+\alpha_i+\mu)\mathcal{I}_i]\Delta t + \varrho_3 \mathcal{I}_i \sqrt{\Delta t}\zeta_{3,i} + \frac{\varrho_3^2}{2}\mathcal{I}_i(\zeta_{3,i}^2 - 1)\Delta t,\\
\mathcal{Q}_{i+1} &= \mathcal{Q}_i + [\eta \mathcal{I}_i - (\delta+\alpha_2+\mu)\mathcal{Q}_i]\Delta t + \varrho_4 \mathcal{Q}_i \sqrt{\Delta t}\zeta_{4,i} + \frac{\varrho_4^2}{2}\mathcal{Q}_i(\zeta_{4,i}^2 - 1)\Delta t,\\
\mathcal{R}_{i+1} &= \mathcal{R}_i + [\xi \mathcal{I}_i + \delta \mathcal{Q}_i - \mu \mathcal{R}_i]\Delta t + \varrho_5 \mathcal{R}_i \sqrt{\Delta t}\zeta_{5,i} + \frac{\varrho_5^2}{2}\mathcal{R}_i(\zeta_{5,i}^2 - 1)\Delta t. \qquad (34)
\end{aligned}$$

Suppose $\zeta_{j,i}(j = 1,2,3,4,5; i = 1,2,..,n)$ represent $\mathcal{N}(0,1)$ is independent distributed random variables and Δt is greater than zero.

Example 1 *Assume that model (2) has the following parameters are considered;* $\Theta = 2$, $\mu = 0.4$, $\beta = 1.25, \mathbf{k} = 0.5$, $\gamma = 0.75$, $\alpha_1 = 0.01$, $\alpha_2 = 0.01$, $\eta = 0.5$, $\varrho_i = 0.3, \quad \forall i = 1 to 5$, *as well as the initial condition values* $(\mathcal{S}(0), \mathcal{E}(0), \mathcal{I}(0), \mathcal{Q}(0), \mathcal{R}(0)) = 0.25$, *and* $\Delta \mathbf{t} = 0.1$. *Then*

$$\begin{aligned}
\mathcal{R}_0^* &= \frac{\beta\Theta\gamma}{(\mu+\frac{\varrho_1^2}{2})(\gamma+\mu+\frac{\varrho_2^2}{2})(\xi+\eta+\mu+\alpha_1+\frac{\varrho_3^2}{2})}\\
&= 2.1968 > 1,
\end{aligned}$$

as a result of Theorem 3, model (2) has an ergodic property and a unique stationary distribution $\widehat{\omega}(.)$. This small neighborhood is shown in Figure 1, which shows the ups and downs of the solution of the model (2), as a result, we can see that there is a stationary distribution. In accordance with Theorem 3, Figure 3 and Figure 5a confirms our results.

Example 2 *According to the model (2), the following parameters are considered:* $\Theta = 1.5$, $\mu = 0.5$, $\beta = 1.75$, $\mathbf{k} = 0.25$, $\gamma = 1.5$, $\alpha_1 = 0.2$, $\alpha_2 = 0.2$, $\eta = 0.3$, $\varrho_1 = 0.15$, $\varrho_2 = 1$, $\varrho_3 = 1$, $\varrho_4 = 0.5$, $\varrho_5 = 0.25$, *as well as the initial condition values* $(\mathcal{S}(0), \mathcal{E}(0), \mathcal{I}(0), \mathcal{Q}(0), \mathcal{R}(0)) = 0.25$, *and* $\Delta \mathbf{t} = 0.5$. *Then*

$$\begin{aligned}
\mathcal{R}_S^* &= \frac{2\gamma\beta(\gamma+\mu)}{\left[(\xi+\mu+\alpha_1+\eta+\frac{\varrho_3^2}{2})(\gamma+\mu)^2\right] \wedge \left(\frac{\gamma^2\varrho_2^2}{2}\right)}\\
&= 0.9315 < 1,
\end{aligned}$$

Figure 2, Figure 4, and Figure 5b satisfy the Theorem 4 conditions; the chances of individuals who will become extinct are almost certainly high when they are exposed, infected, and quarantined. In model (2), we see that the permanent disease can die out through stochastic effects after exposed, infected, and quarantined individuals are sent to extinction. It follows that stochastic disturbances are conducive to controlling epidemic diseases. In Figure 6, we represent that Theorem 2 confirms the stability of the disease-free equilibrium E^* when $R_0 \leq 1$. No negative population values were

observed, ensuring that the model remains biologically valid. This demonstrates the effectiveness of the stochastic Lyapunov function in guaranteeing global asymptotic stability.

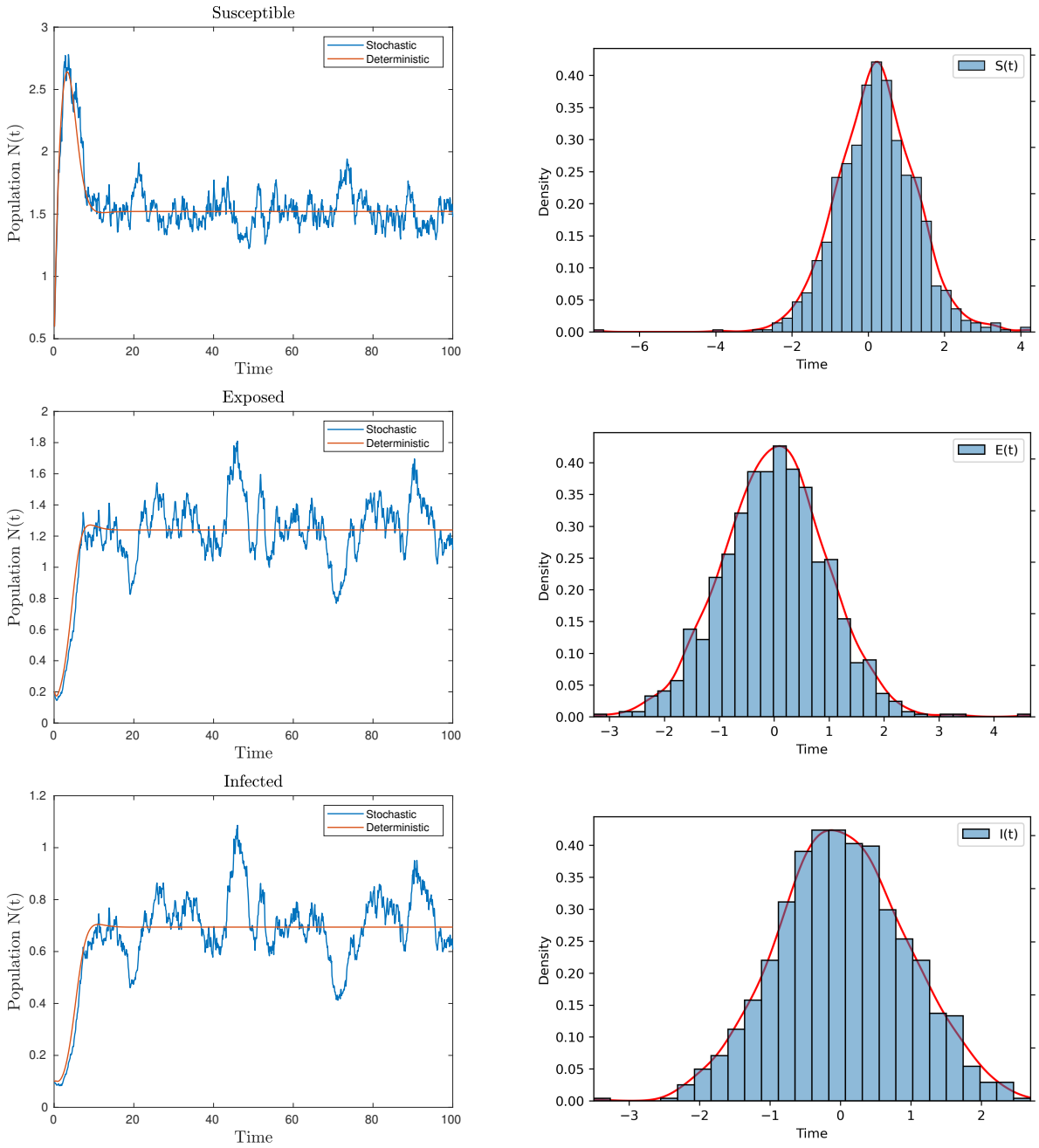

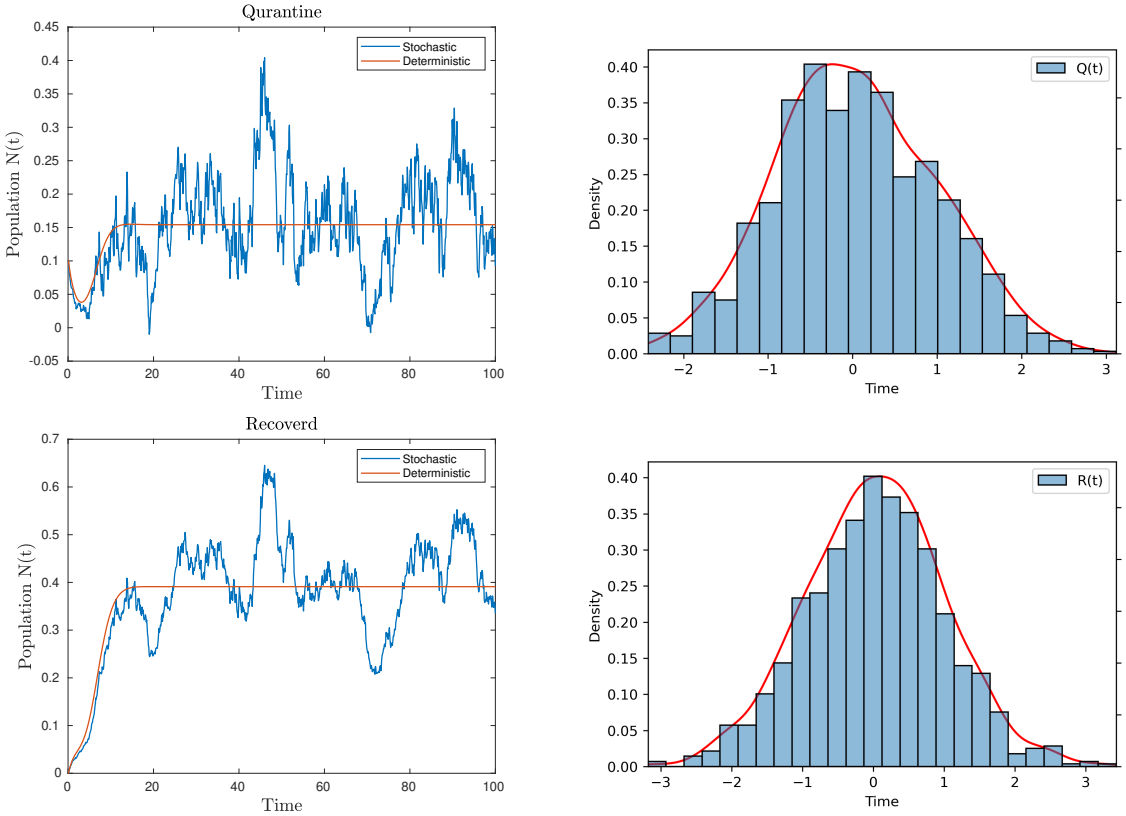

Figure 1. This diagram consists of a time sequence of stochastic persistence and stationary distribution of diseases based on model (2). In the right column, the histogram is represented by the probability density function for $S(\mathbf{t}), E(\mathbf{t}), I(\mathbf{t}), Q(\mathbf{t})$, and $R(\mathbf{t})$

.

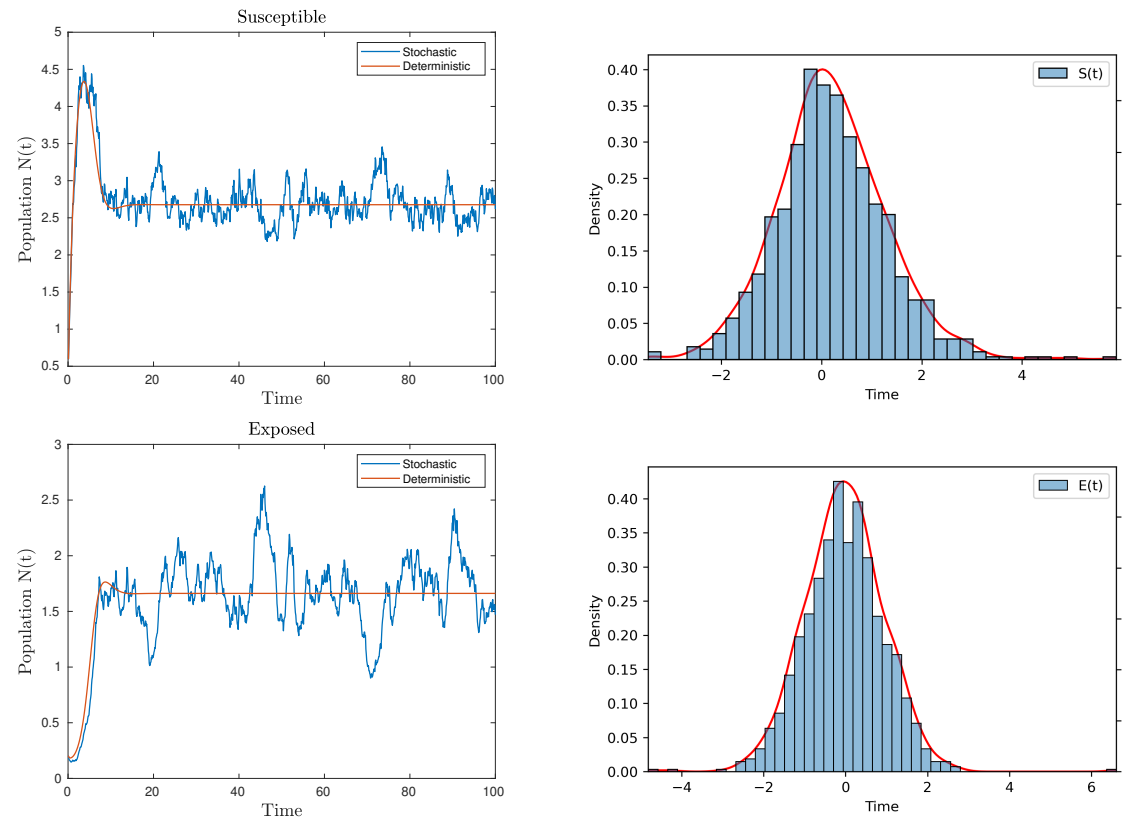

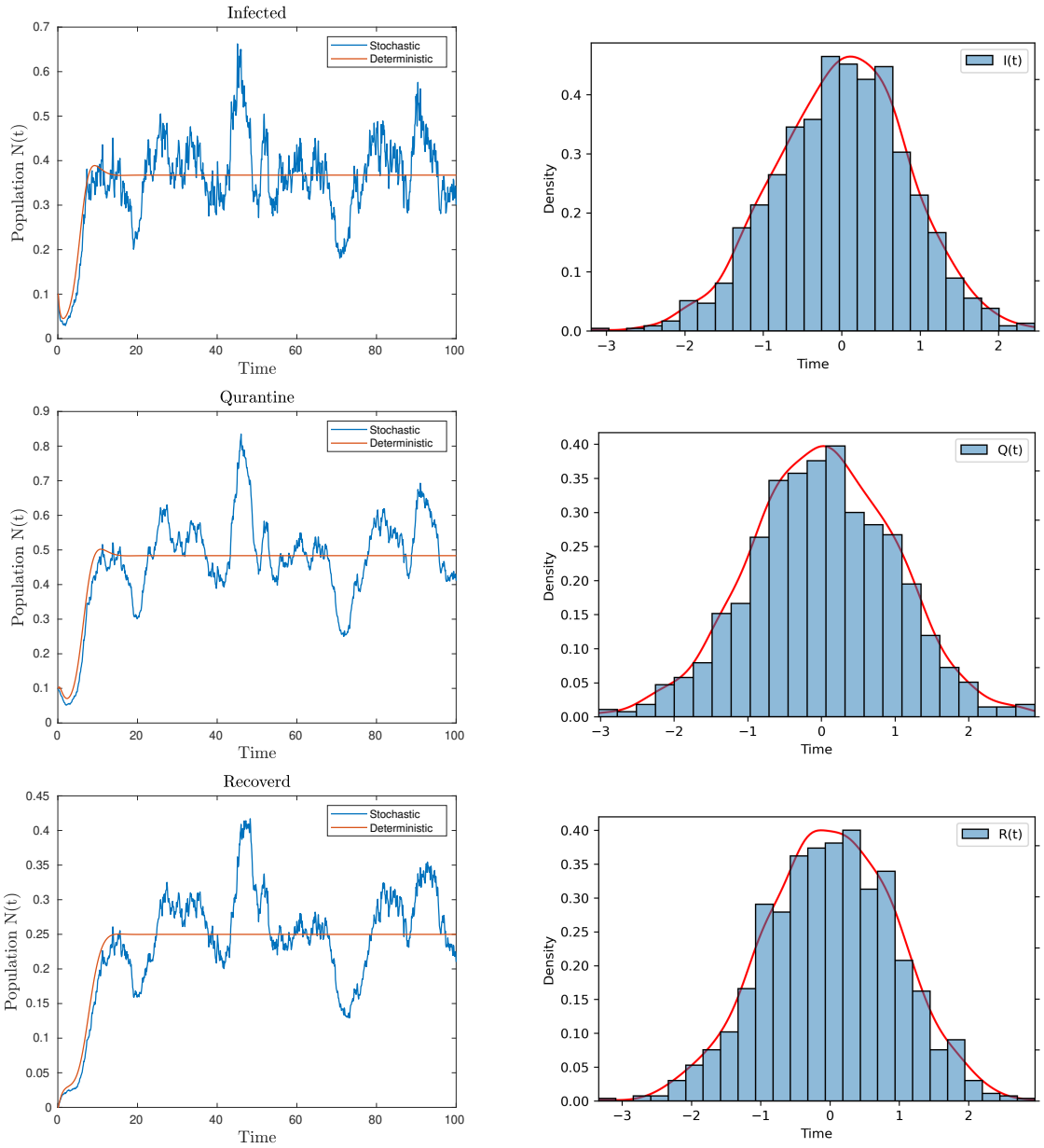

Figure 2. This time sequence diagram illustrates how disease extinction occurs in model (2). In the right column, the histogram is represented by the probability density function for $S(\mathbf{t}), E(\mathbf{t}), I(\mathbf{t}), Q(\mathbf{t})$, and $R(\mathbf{t})$

7 Conclusion

An epidemic model with saturated incidence rates is developed in this paper using a stochastic $\mathcal{SEIQR}$ model. As a result of building a suitable stochastic Lyapunov function, we have found that the positive solutions to the model (2) have a stationary distribution when $\mathcal{R}_0^* > 1$. Furthermore, we established sufficient conditions for disease extinction as well, which means, $\mu > \dfrac{\varrho_1^2 \vee \varrho_2^2 \vee \varrho_3^2 \vee \varrho_4^2 \vee \varrho_5^2}{2}$ and $\mathcal{R}_S^* < 1$. Besides, we found that saturated incidence significantly affected disease spread within a population. Furthermore, we find that when white noise intensity is high, the disease disappears, whereas when white noise intensity is low, the disease persists. During stochastic environmental disturbances, white noise prevents disease. This manifests itself at the exact time epidemics arise, affecting epidemic dynamics. The findings show that virus dynamics-based stochastic epidemic models outperform deterministic models in epidemic prediction. Finally, our findings are validated using numerical simulation.

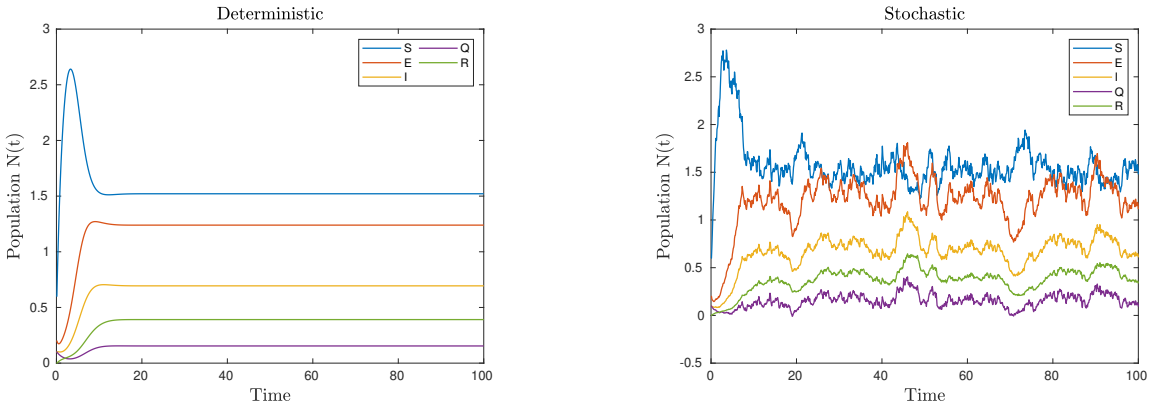

(a) **(b)**

Figure 3. The solution for all class of Deterministic and Stochastic model with $\mathcal{R}_0^*$ greater than 1

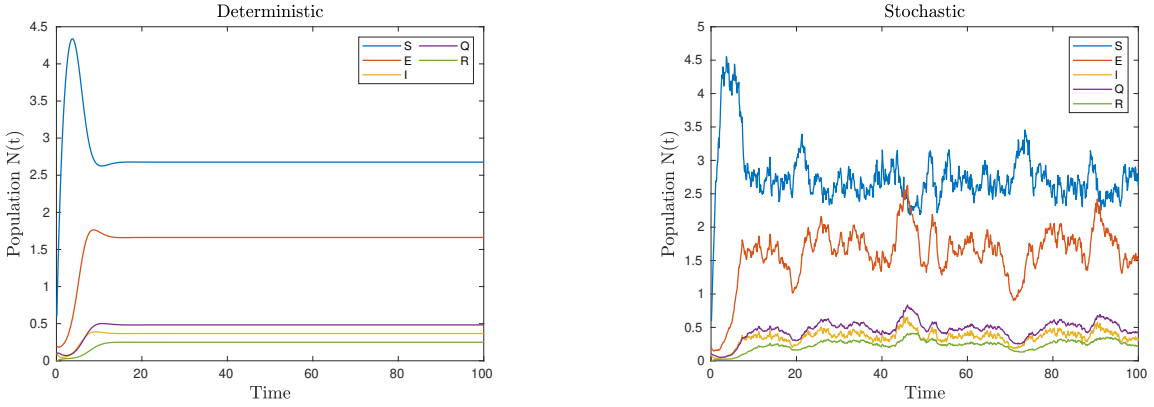

(a) **(b)**

Figure 4. The solution for all class of Deterministic and Stochastic model with $\mathcal{R}_S^*$ less than 1

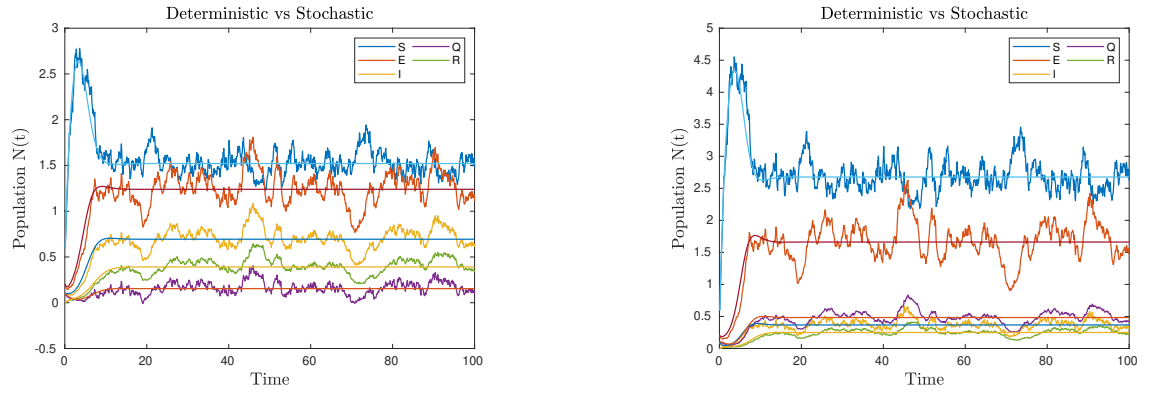

(a) **(b)**

Figure 5. Comparison of solutions on $\mathcal{S}(0), \mathcal{E}(0), \mathcal{I}(0), \mathcal{Q}(0)$, and $\mathcal{R}(0)$: for all class in Deterministic vs Stochastic model with (a) $\mathcal{R}_0^*$ greater than 1 and (b) $\mathcal{R}_S^*$ less than 1

In the future, we will be able to propose practical and complex models, such as models that consider the effects of regime switching on SEIQR epidemics [38] or consider the dynamical characteristics of a stochastic SIR, SEIQR, SEIVQR epidemic model with various incidence and time-based delays [20, 39]. We will continue to investigate these issues in the future.

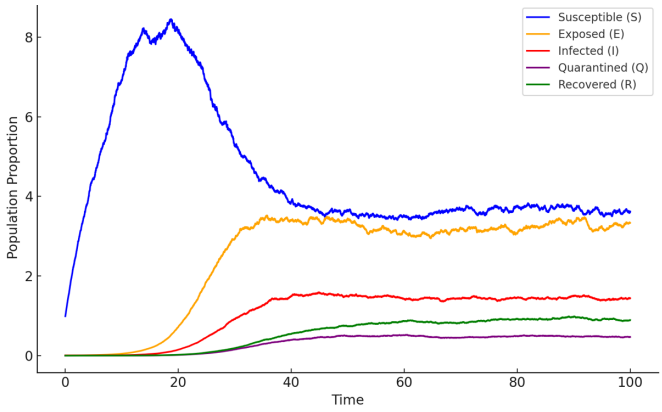

Figure 6. Stochastic SEIQR model simulation in $\mathcal{R}_0 \leq 1$

Declarations

Use of AI tools

The authors declare that they have not used Artificial Intelligence (AI) tools in the creation of this article.

Data availability statement

Data availability is not applicable to this article as no new data were created or analyzed in this study.

Ethical approval (optional)

The authors state that this research complies with ethical standards. This research does not involve either human participants or animals.

Consent for publication

Not applicable

Conflicts of interest

The authors declare that they have no conflict of interest regarding the publication of this manuscript.

Funding

Not applicable.

Author's contributions

S.S.: Conceptualization, Methodology, Software, Validation, Data Curation, Writing - Original Draft. M.C.: Writing - Review & Editing, Supervision. All authors have read and agreed to the published version of the manuscript.

Acknowledgements

The authors would like to thank the anonymous reviewers for taking the time and effort necessary to review the manuscript. They sincerely appreciate all valuable comments and suggestions, which helped them to improve the quality of the manuscript.

References

[1] Bernoullid, D. A new analysis of the mortality caused by smallpox. In *The History of Actuarial Science Vol VIII*, pp.1-38. Paris: Routledge, (1766).

[2] Kermack, W.O. and McKendrick, A.G. Contributions to the mathematical theory of epidemics–I. 1927. *Bulletin of Mathematical Biology*, 53(1-2), 33-55, (1991). [CrossRef]

[3] Abbey, H. An examination of the Reed-Frost theory of epidemics. *Human Biology*, 24(3), 201, (1952).

[4] Bartlett, M.S. Some evolutionary stochastic processes. *Journal of the Royal Statistical Society. Series B (Methodological)*, 11(2), 211-229, (1949). [CrossRef]

[5] Berger, D.W., Herkenhoff, K.F. and Mongey, S. An SEIR infectious disease model with testing and conditional quarantine. *National Bureau of Economic Research*, (2020). [CrossRef]

[6] Panigoro, H.S., Rahmi, E., Nasib, S.K., Gawa, N.P.H. and Peter, O.J. Bifurcations on a discrete–time SIS–epidemic model with saturated infection rate. *Bulletin of Biomathematics*, 2(2), 182–197, (2024). [CrossRef]

[7] Wells, C.R., Townsend, J.P., Pandey, A., Moghadas, S.M., Krieger, G., Singer, B. et al. Optimal COVID-19 quarantine and testing strategies. *Nature Communications*, 12, 356, (2021). [CrossRef]

[8] Naik, P.A., Yeolekar, B.M., Qureshi, S., Yavuz, M., Huang, Z. and Yeolekar, M. Fractional insights in tumor modeling: an interactive study between tumor carcinogenesis and macrophage activation. *Advanced Theory and Simulations*, 2401477, (2025). [CrossRef]

[9] Mustapha, U.T., Ado, A., Yusuf, A., Qureshi, S. and Musa, S.S. Mathematical dynamics for HIV infections with public awareness and viral load detectability. *Mathematical Modelling and Numerical Simulation With Applications*, 3(3), 256-280, (2023). [CrossRef]

[10] Lan, G., Yuan, S. and Song, B. The impact of hospital resources and environmental perturbations to the dynamics of SIRS model. *Journal of the Franklin Institute*, 358(4), 2405-2433, (2021). [CrossRef]

[11] Joshi, H. and Yavuz, M. Chaotic dynamics of a cancer model with singular and non-singular kernel. *Discrete and Continuous Dynamical Systems-S*, 18(5), 1416-1439, (2025). [CrossRef]

[12] Phan, T.A., Tian, J.P. and Wang, B. Dynamics of cholera epidemic models in fluctuating environments. *Stochastics and Dynamics*, 21(02), 2150011, (2021). [CrossRef]

[13] Sabbar, Y., Kiouach, D. and Rajasekar, S.P. Acute threshold dynamics of an epidemic system with quarantine strategy driven by correlated white noises and Levy jumps associated with infinite measure. *International Journal of Dynamics and Control*, 11, 122-135, (2023). [CrossRef]

[14] Rauta, A.K., Rao, Y.S., Behera, J., Dihudi, B. and Panda, T.C. SIQRS epidemic modelling and stability analysis of COVID-19. In *Predictive and Preventive Measures for Covid-19 Pandemic* (pp. 35-50). Springer: Singapore, (2021). [CrossRef]

[15] Wang, K., Fan, H. and Zhu, Y. Dynamics and application of a generalized SIQR epidemic model with vaccination and treatment. *Applied Mathematical Modelling*, 120, 382-399, (2023). [CrossRef]

[16] Daşbaşı, B. Stability analysis of an incommensurate fractional-order SIR model. *Mathematical Modelling and Numerical Simulation with Applications*, 1(1), 44-55, (2021). [CrossRef]

[17] Dieu, N.T., Sam, V.H. and Du, N.H. Threshold of a stochastic SIQS epidemic model with isolation. *Discrete & Continuous Dynamical Systems-Series B*, 27(9), p5009, (2022). [CrossRef]

[18] Zhang, Y., Ma, X. and Din, A. Stationary distribution and extinction of a stochastic SEIQ epidemic model with a general incidence function and temporary immunity. *AIMS Math*, 6(11), 12359-12378, (2021). [CrossRef]

[19] Qi, H., Zhang, S., Meng, X. and Dong, H. Periodic solution and ergodic stationary distribution of two stochastic SIQS epidemic systems. *Physica A: Statistical Mechanics and its Applications*, 508, 223-241, (2018). [CrossRef]

[20] Ma, Y., Cui, Y. and Wang, M. Global stability and control strategies of a SIQRS epidemic model with time delay. *Mathematical Methods in the Applied Sciences*, 45(13), 8269-8293, (2022). [CrossRef]

[21] Wang, M., Hu, Y. and Wu, L. Dynamic analysis of a SIQR epidemic model considering the interaction of environmental differences. *Journal of Applied Mathematics and Computing*, 68, 2533–2549, (2022). [CrossRef]

[22] Pan, Q., Huang, J. and Wang, H. An SIRS model with nonmonotone incidence and saturated treatment in a changing environment. *Journal of Mathematical Biology*, 85, 23, (2022). [CrossRef]

[23] Yang, J., Shi, X., Song, X. and Zhao, Z. Threshold dynamics of a stochastic SIQR epidemic model with imperfect quarantine, *Applied Mathematics Letters*, 136, 108459, (2023). [CrossRef]

[24] Wang, K., Fan, H., & Zhu, Y. Dynamics and application of a generalized SIQR epidemic model with vaccination and treatment, *Applied Mathematical Modeling*, 120, 382-399, (2023). [CrossRef]

[25] Zhang, G., Li, Z. and Din, A. A stochastic SIQR epidemic model with Levy jumps and three-time delays. *Applied Mathematics and Computation*, 431, 127329, (2022). [CrossRef]

[26] Lu, C., Liu, H. and Zhang, D. Dynamics and simulations of a second order stochastically perturbed SEIQV epidemic model with saturated incidence rate. *Chaos, Solitons & Fractals*, 152, 111312, (2021). [CrossRef]

[27] Gao, S., Chen, L., Nieto, J.J. and Torres, A. Analysis of a delayed epidemic model with pulse vaccination and saturation incidence. *Vaccine*, 24(35-36), 6037-6045, (2006). [CrossRef]

[28] Rajasekar, S.P. and Pitchaimani, M. Qualitative analysis of stochastically perturbed SIRS epidemic model with two viruses. *Chaos, Solitons & Fractals*, 118, 207-221, (2019). [CrossRef]

[29] Yang, J., Shi, X., Song, X. and Zhao, Z. Threshold dynamics of a stochastic SIQR epidemic model with imperfect quarantine. *Applied Mathematics Letters*, 136, 108459,(2023). [CrossRef]

[30] Selvan, T.T. and Kumar, M. Dynamics of a deterministic and a stochastic epidemic model combined with two distinct transmission mechanisms and saturated incidence rate. *Physica A: Statistical Mechanics and its Applications*, 619, 128741,(2023). [CrossRef]

[31] Mao, X. *Stochastic Differential Equations and Applications*. Elsevier: Oxford, (2007).

[32] Khasminskii, R. *Stochastic Stability of Differential Equations*. Springer Science & Business Media: New York, (2011). [CrossRef]

[33] Gard, T.C. *Introduction to Stochastic Differential Equations*. Marcel Dekker: New York, (1988).

[34] Zhu, C. and Yin, G. Asymptotic properties of hybrid diffusion systems. *SIAM Journal on Control and Optimization*, 46(4), 1155-1179, (2007). [CrossRef]

[35] Zhao, Y. and Jiang, D. The threshold of a stochastic SIS epidemic model with vaccination. *Applied Mathematics and Computation*, 243, 718-727, (2014). [CrossRef]

[36] Meng, X., Zhao, S., Feng, T. and Zhang, T. Dynamics of a novel nonlinear stochastic SIS epidemic model with double epidemic hypothesis. *Journal of Mathematical Analysis and Appli-*

cations, 433(1), 227-242, (2016). [CrossRef]

[37] Higham, D.J. An algorithmic introduction to numerical simulation of stochastic differential equations. *SIAM Review*, 43(3), 525-546, (2001). [CrossRef]

[38] Wei, W., Xu, W. and Liu, J. A regime-switching stochastic SIR epidemic model with a saturated incidence and limited medical resources. *International Journal of Biomathematics*, 16(07), 2250124, (2023). [CrossRef]

[39] Goel, K. and Nilam. A mathematical and numerical study of a SIR epidemic model with time delay, nonlinear incidence and treatment rates. *Theory in Bio-sciences*, 138, 203-213, (2019). [CrossRef]

Mathematical Modelling and Numerical Simulation with Applications (MMNSA)
(https://dergipark.org.tr/en/pub/mmnsa)

How to cite this article: Saravanan, S. & Monica, C. (2025). Dynamics of a stochastic SEIQR model: stationary distribution and disease extinction with quarantine measures. *Mathematical Modelling and Numerical Simulation with Applications*, 5(1), 172-197. https://doi.org/10.53391/mmnsa.1572436

Mathematical Modelling and Numerical Simulation with Applications, 2025, 5(1), 198–233

https://dergipark.org.tr/en/pub/mmnsa
ISSN Online: 2791-8564 / Open Access
https://doi.org/10.53391/mmnsa.1545744

RESEARCH PAPER

Global dynamics and sensitivity analysis of a diabetic population model with two-time delays

Hanis Nasir [1,‡] and **Auni Aslah Mat Daud** [2,‡]

[1]Department of Mathematical Sciences, Faculty of Science, Universiti Teknologi Malaysia, 81310 Johor Bahru, Johor, Malaysia, [2]Faculty of Computer Science and Mathematics, Universiti Malaysia Terengganu, 21030 Kuala Nerus, Terengganu, Malaysia

*Corresponding Author
‡muhamadhanis@utm.my (Hanis Nasir); auni_aslah@umt.edu.my (Auni Aslah Mat Daud)

Abstract

Diabetes is a chronic disease that can cause various long-term complications. This study revisits a four-state model of type-2 diabetic population with a saturating recovery rate of diabetes complications, and its qualitative properties are further analysed. The non-negativity and boundedness of the solution for delay and non-delay models are proved. However, the non-negativity of the solutions of the delay model can only be guaranteed if the model inputs satisfy certain conditions. The stability analysis of the non-delay model is performed, and the numerical simulation is conducted to illustrate and validate the findings. In the presence of two delay parameters, we discuss the characteristic equation of the delay model under the case of the first time delay equal to zero to obtain the stable region of the second time delay. The critical value corresponding to the delay parameter is derived. There are five conditions to characterize the stability properties of the (unique) equilibrium point (either locally asymptotically stable or unstable) and the occurrence of Hopf bifurcation. The delay values affect the stability of the equilibrium point. A locally asymptotically stable equilibrium point can become unstable under certain conditions, and a periodic orbit can arise from the equilibrium point as the model switches its stability. The sensitivity analysis shows that the overall diabetes cases can be reduced significantly by reducing the rate of developing diabetes, and the diabetics with complications will decrease if the parameter measuring the limited medical resources gets smaller.

Keywords: Diabetes; time-delays; Hopf bifurcation; stability analysis; sensitivity analysis

AMS 2020 Classification: 92B05; 34D32; 35B35

1 Introduction

Diabetes mellitus is a life-long disease caused by hyperglycemia (high blood glucose levels) due to defects in either lack of insulin or cells resisting the insulin or both. In 2021, the International

➤ **Received:** 09.09.2024 ➤ **Revised:** 06.03.2025 ➤ **Accepted:** 17.03.2025 ➤ **Published:** 31.03.2025

Diabetes Federation (IDF) [1] estimated that 6.7 million adults died due to diabetes and its complications. and diabetes and its consequences cost the world economy USD966 billion. In Malaysia, the estimated percentage of diabetics among adults aged 18 and above has increased from 11.6% in 2006 to 18.3% in 2019 [2]. In 2021, Malaysia's total diabetes-related health expenditure was estimated at USD4833.5 million, with USD1090.7 per individual with diabetes [3].
Therefore, there is an urgent need to study the population dynamics of diabetes to address the problem. Several population models of non-communicable diseases, such as diabetes [4, 5], hypertension [6], thyroid disorders [7], and anemia [8], have been developed in the literature. In the study, we will revisit the diabetic model in [9]. Although there are a few similarities between the findings of [9] and the present paper, there are some significant differences too, offering valuable insights and further information that were not provided in [9]. The distinctions between [9] and the present paper are as follows: First, [9] did not discuss the non-negativity and boundedness of the solution. This is an important issue in mathematical modeling because we expect the state variables to be non-negative for all time. Secondly, global stability analysis was not addressed in [9]. Third, [9] did not analyze the sensitivity of the model outputs to changes in the model inputs. This aspect is crucial as it helps identify which parameters may become potential targets for further investigation to control the disease in the population. Fourth, the numerical simulations in the present paper involve five sets of parameter values.
In this paper, Section 2 discusses the assumptions of the mathematical model to study the population dynamics of type-2 diabetes. Section 3 mainly focuses on the corresponding model without time delays. The global asymptotic stability is also established by constructing suitable Lyapunov functions. In Section 4, the dynamics of the delay model are studied. The Hopf bifurcation occurs for some parameter values, making the Lyapunov direct method not work due to the appearance of a periodic orbit. In Section 5, we compute the normalized forward sensitivity indices of the model outputs with respect to the changes in the model inputs. We perform the numerical simulation of the model in Section 6.

2 The mathematical model

The progression of diabetes is slow from the stage of non-diabetics to people with diabetes and from the stage of diabetes to the development of complications [5]. In the present paper, we use the model proposed by Nasir [9]. We extend the work of [9] by revising the local stability analysis and adding the global stability analysis and sensitivity analysis. The model assumptions are:

1. The model is used to study the population of type-2 diabetes. The total population is subdivided into four compartments, namely the non-diabetics, diabetics who never had any complications, diabetics with complications, and diabetics with recovered complications. Figure 1 shows the compartmental diagram under study.

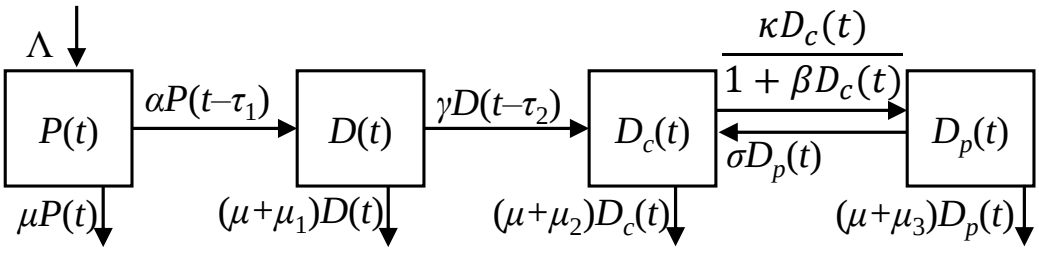

Figure 1. Four-state diabetic population [9]

Table 1. Definition of the symbols in Figure 1

Symbol	Definition	Dimension
$P(t)$	number of non-diabetics at time t	individuals
$D(t)$	number of diabetics who never had any complications at time t	individuals
$D_c(t)$	number of diabetics with complications at time t	individuals
$D_p(t)$	number of diabetics with recovered complications at time t	individuals
Λ	the recruitment rate of non-diabetics	individuals time^{-1}
α	the diabetes incidence rate	time^{-1}
τ_1	the slow progression in developing type-2 diabetes	time
γ	rate of the first incidence of complication	time^{-1}
τ_2	time delay in the first incidence of complication	time
σ	the recurrence rate of complications	time^{-1}
κ	the recovery rate of complications	time^{-1}
β	non-negative parameter measuring the limited medical resources	individuals^{-1}
μ_1	the diabetes-related mortality rate among diabetics without complications	time^{-1}
μ_2	the diabetes-related mortality rate among diabetics with complications	time^{-1}
μ_3	the diabetes-related mortality rate among diabetics with recovered complications	time^{-1}
μ	the mortality rate due to causes other than diabetes	time^{-1}

Every symbol in Figure 1 is defined in Table 1. All parameters are assumed to be positive because they represent human population dynamics.

2. Type 2 diabetes is a slowly progressive disease and degenerative [5]. The type of time delay used in this study is a constant delay. The first delay parameter (τ_1) concerns the stage of non-diabetics to diabetics. This assumption is supported by Khetan and Rajagopalan [10], where nearly all people affected with type 2 diabetes pass through a long phase of pre-diabetes before becoming a full-blown diabetic. The second delay parameter (τ_2) concerns the first incidence of complication after the onset of diabetes. This assumption is introduced by the fact that diabetes is a slowly progressive disease and can be symptomless. After being unrecognized for a long time, people with diabetes may already have complications at the time of diagnosis, such as a foot ulcer, change in vision, or infection that fails to heal [11].

3. The time delays are ignored for the other processes in Figure 1 because they do not require as much time as developing type-2 diabetes and the first incidence of complication. For example, complications related to the small blood vessels may range from 6 to 13 years after developing diabetes [12]. In addition, type-2 diabetes is usually diagnosed at an old age. The average age of diabetes that is diagnosed among Malaysians is 53 [13]. Hence, the delay in the recurrence rate of complications (at rate $\sigma D_p(t)$) is ignored because the diabetics with recovered complications are assumed no longer in the early stage of diabetes and are vulnerable to repeated complications [13].

4. For the treatment of complications, a saturating rate of recovery of complications of the form $h(D_c) = \dfrac{\kappa D_c}{1+\beta D_c}$. In reality, $\dfrac{1}{1+\beta D_c}$ can be described as the reverse effect of the diabetics with complications being postponed for treatment. If $\beta = 0$, this saturating recovery rate reverts to the linear one: $\kappa D_c(t)$, representing the unlimited medical resources [14]. The term

$h(D_c) = \dfrac{\kappa D_c}{1+\beta D_c}$ is also widely known as the Holling type-2 functional response [15]. Note that in our model, we employed different functional responses to represent the dynamics of recovery and recurrence. For recovery (cessation of symptoms), we used a Holling Type 2 functional response between D_c and D_p. This choice is biologically motivated by the fact that recovery rates often exhibit saturation effects observed in diabetes recovery. This saturation can be attributed to factors such as limitations in treatment resources and efficacy, which cause the rate of recovery of individuals with complications to plateau as the population of individuals with complications increases. Such saturation is well captured by a Holling Type 2 response. On the other hand, Holling Type 1 is utilized to model the recurrence of symptoms. This assumes a linear relationship between D_p and $\dfrac{dD_c}{dt}$. The rationale behind this choice is that symptom recurrence often depends primarily on individual risk factors such as lifestyle choices (diet, physical activity), medication adherence, and disease progression, rather than being constrained by saturation mechanisms. While this simplification may not capture all potential influences on recurrence, it provides a reasonable approximation for the purpose of our model. A Holling Type 2 response would be inappropriate in this case because the recurrence of symptoms does not exhibit resource-limited behavior in the same way that recovery does. This distinction ensures that the model accurately captures the underlying mechanisms of disease progression and treatment effects. However, if empirical data suggests otherwise, alternative functional forms could be considered in future extensions of this study.

The dynamics in Figure 1 are governed as follows:

$$\frac{dP(t)}{dt} = \Lambda - \alpha P(t-\tau_1) - \mu P(t), \tag{1a}$$

$$\frac{dD(t)}{dt} = \alpha P(t-\tau_1) - \gamma D(t-\tau_2) - (\mu+\mu_1)D(t), \tag{1b}$$

$$\frac{dD_c(t)}{dt} = \gamma D(t-\tau_2) - \frac{\kappa D_c(t)}{1+\beta D_c(t)} + \sigma D_p(t) - (\mu+\mu_2)D_c(t), \tag{1c}$$

$$\frac{dD_p(t)}{dt} = \frac{\kappa D_c(t)}{1+\beta D_c(t)} - (\sigma+\mu+\mu_3)D_p(t), \tag{1d}$$

where the initial conditions are defined as follows:

$$P(\theta) = \phi_1(\theta) > 0,\ D(\theta) = \phi_2(\theta) > 0,\ \theta \in [-\tau_{\max}, 0],$$
$$\tau_{\max} = \max\{\tau_1, \tau_2\},\ D_c(0) = D_{c0} > 0,\ D_p(0) = D_{p0} > 0,$$

where $\phi_i(\theta)$ $(i = 1, 2)$ are continuous functions on $\theta \in [-\tau_{\max}, 0]$. The total population size with respect to model (1) is denoted as $N(t) = P(t) + D(t) + D_c(t) + D_p(t)$.
Note that the case where $\alpha P(t-\tau_1)$ is assumed to be a constant incidence rate I will be addressed in another paper (see [16]). In [16], three variables will be discussed because the variable $P(t)$ is excluded. Consequently, the model in [16] contains one time-delay parameter only. Nasir et al. [16] also pay special attention to the limited availability of medical resources for the treatment of the complications of diabetes.

3 Qualitative analysis of the corresponding non-delay model

In this section, we study model (1) with no time delays $(\tau_1 = \tau_2 = 0)$. For simplifying the notations, the variables P, D, D_c, D_p, and N_2 are evaluated at time t, unless the argument is

other than t (for example, $D_c(0)$ and $P(t-\tau_1)$). Model (1) under the assumption of instantaneous dynamics is written as:

$$\frac{dP}{dt} = \Lambda - (\alpha + \mu)P, \tag{2a}$$

$$\frac{dD}{dt} = \alpha P - (\gamma + \mu + \mu_1)D, \tag{2b}$$

$$\frac{dD_c}{dt} = \gamma D - \frac{\kappa D_c}{1 + \beta D_c} + \sigma D_p - (\mu + \mu_2)D_c, \tag{2c}$$

$$\frac{dD_p}{dt} = \frac{\kappa D_c}{1 + \beta D_c} - (\sigma + \mu + \mu_3)D_p, \tag{2d}$$

with the initial conditions:

$$P(0) = P_0 > 0,\ D(0) = D_0 > 0,\ D_c(0) = D_{c0} > 0,\ D_p(0) = D_{p0} > 0.$$

In the following sections, we study the non-negativity and boundedness of the solution and the stability properties of the equilibrium point of the non-delay model (2).

Basic properties of non-delay model (2)

Non-negativity and boundedness of the solution of non-delay model (2)

Proposition 1 *The solutions P, D, D_c, and D_p of the non-delay model (2) remain non-negative and bounded for all $t > 0$. Furthermore, the region:*

$$\Omega = \left\{ \left(P, D, D_c, D_p\right) \in \mathbb{R}^4_+ \middle| P + D + D_c + D_p \leq \frac{\Lambda}{\mu} \right\},$$

is a positively-invariant region with respect to the non-delay model (2).

Proof For the non-negativity of the solution P of the non-delay model (2), from Eq. (2a), we obtain:

$$\frac{dP}{dt} + (\alpha + \mu)P = \Lambda. \tag{3}$$

Since $\Lambda \geq 0$, Eq. (3) becomes:

$$\frac{dP}{dt} + (\alpha + \mu)P \geq 0. \tag{4}$$

The integrating factor is given as $e^{(\alpha+\mu)t}$. By multiplying inequality (4) with the integrating factor and changing the variable t to variable ε, we obtain:

$$\frac{d}{d\varepsilon}\left[P(\varepsilon)e^{(\alpha+\mu)\varepsilon}\right] \geq 0. \tag{5}$$

Integrating both sides of inequality (5) from $\varepsilon = 0$ to $\varepsilon = t$ gives:

$$P \geq P(0)e^{-(\alpha+\mu)t}.$$

Therefore, the solution P remains non-negative for all $t > 0$.

For the non-negativity of the solution D of the non-delay model (2), from Eq. (2b), we obtain:

$$\frac{dD}{dt} + (\gamma + \mu + \mu_1)D = \alpha P. \tag{6}$$

Since the term $\alpha P \geq 0$, Eq. (6) becomes:

$$\frac{dD}{dt} + (\gamma + \mu + \mu_1)D \geq 0,$$
$$D \geq D(0)e^{-(\gamma+\mu+\mu_1)t}.$$

Therefore, the solution D remains non-negative for all $t > 0$.
Since the solution is assumed to be a continuous and differentiable function, the functions $D_c(t)$, $D_p(t)$ cannot become negative without crossing the axes $D_c = 0, D_p = 0$. Let $t^* = \min\{t_c, t_p\}$ where $D_c(t_c) = 0, D_p(t_p) = 0$ and $(t_c, t_p) \geq (0, 0)$. If $t^* = t_c$ then $D_c(t_c) = 0$ and the functions $D_p(t_c) > 0$ at $t = t_c$, yields

$$\frac{dD_c}{dt}(t^* = t_c) = \gamma D(t) + \sigma D_p(t) \geq 0.$$

Therefore, when the function $D_c(t)$ touches the axis $D_c = 0$, $\frac{dD_c}{dt}$ is always non-negative, and the function $D_c(t)$ will not decrease and will never cross to the negative part. Using a similar argument, it can be shown that

$$\frac{dD_p}{dt}(t^* = t_p) = \frac{\kappa D_c(t)}{1 + \beta D_c(t)} \geq 0.$$

Thus, all solutions $D_c(t), D_p(t)$ are always non-negative for all $t > 0$.
For the boundedness of the solutions P, D, D_c, and D_p of the non-delay model (2), adding all equations of the non-delay model (2) yields:

$$\frac{dN}{dt} = \Lambda - \mu N - \mu_1 D - \mu_2 D_c - \mu_3 D_p. \tag{7}$$

Since the terms $\mu_1 D \geq 0$, $\mu_2 D_c \geq 0$, and $\mu_3 D_p \geq 0$, Eq. (7) becomes:

$$\frac{dN}{dt} + \mu N \leq \Lambda,$$
$$N(t) \leq \frac{\Lambda}{\mu} + \left(N(0) - \frac{\Lambda}{\mu}\right)e^{-\mu t}.$$

If $N(0) \leq \frac{\Lambda}{\mu}$, then we have $N(t) \leq \frac{\Lambda}{\mu}$. This implies that the upper bound of the total population size is $\frac{\Lambda}{\mu}$. If $N(0) > \frac{\Lambda}{\mu}$, then $N_2(t)$ will decrease to $\frac{\Lambda}{\mu}$ because $\lim_{t\to\infty} N(t) = \frac{\Lambda}{\mu}$.
The region Ω is a positively-invariant region with respect to the non-delay model (2).

Stability of the equilibrium point of non-delay model (2)

Equilibrium point of non-delay model (2)

Let $T^* = (P^*, D^*, D_c^*, D_p^*)$ be the equilibrium point of the non-delay model (2), where $P = P^*$, $D = D^*$, $D_c = D_c^*$, and $D_p = D_p^*$. Substituting these into the right-hand-side equations of the non-delay model (2) and letting them equal to zero yields:

$$\Lambda - (\alpha + \mu)P^* = 0, \tag{8a}$$

$$\alpha P^* - (\gamma + \mu + \mu_1)D^* = 0, \tag{8b}$$

$$\gamma D^* - \frac{\kappa D_c^*}{1 + \beta D_c^*} + \sigma D_p^* - (\mu + \mu_2)D_c^* = 0, \tag{8c}$$

$$\frac{\kappa D_c^*}{1 + \beta D_c^*} - (\sigma + \mu + \mu_3)D_p^* = 0. \tag{8d}$$

From Eq. (8a), we have $P^* = \dfrac{\Lambda}{\alpha + \mu}$. From Eq. (8b), we have $D^* = \dfrac{\alpha P^*}{\gamma + \mu + \mu_1}$. From Eq. (8d), we have $D_p^* = \dfrac{\kappa D_c^*}{(1 + \beta D_c^*)(\sigma + \mu + \mu_3)}$. By substituting the expressions of D^* and D_p^* into Eq. (8c), we obtain:

$$z_1 (D_c^*)^2 + z_2 D_c^* + z_3 = 0, \tag{9}$$

where $z_1 = \beta(\mu + \mu_2)(\sigma + \mu + \mu_3)$, $z_2 = (\mu + \mu_2)(\mu + \mu_3 + \sigma) + \kappa(\mu + \mu_3) - \beta\gamma(\sigma + \mu + \mu_3)D^*$, and $z_3 = -\gamma(\sigma + \mu + \mu_3)D^*$. The roots of Eq. (9) are as follows:

$$\frac{-z_2 + \sqrt{z_2^2 - 4z_1 z_3}}{2z_1}, \tag{10}$$

and

$$\frac{-z_2 - \sqrt{z_2^2 - 4z_1 z_3}}{2z_1}. \tag{11}$$

Notice that z_1 and z_3 are opposite signs. Then, we have $\sqrt{z_2^2 - 4z_1 z_3} > \sqrt{z_2^2} = |z_2|$. This indicates that the root in (10) is positive while the root in (11) is negative.

Since the state variables represent individuals in the population, the only biologically meaningful equilibrium point is as follows:

$$T^* = \left(\frac{\Lambda}{\alpha + \mu}, \frac{\alpha P^*}{\gamma + \mu + \mu_1}, \frac{-z_2 + \sqrt{z_2^2 - 4z_1 z_3}}{2z_1}, \frac{\kappa D_c^*}{(1 + \beta D_c^*)(\sigma + \mu + \mu_3)} \right). \tag{12}$$

Local stability

Theorem 1 *The equilibrium point T^* of the non-delay model (2) is locally asymptotically stable.*

Proof The characteristic equation with respect to the equilibrium point T^* of the non-delay model

(2) is obtained by computing:

$$\det[\lambda_3 \mathbf{I}_4 - \mathbf{B}_1] = 0, \tag{13}$$

where λ_3 represents the eigenvalues, $\mathbf{I}_4$ is an identity matrix of dimension 4,

$$\mathbf{B}_1 = \begin{bmatrix} -(\alpha+\mu) & 0 & 0 & 0 \\ \alpha & -(\gamma+b_1) & 0 & 0 \\ 0 & \gamma & -b_2 & \sigma \\ 0 & 0 & b_3 & -b_4 \end{bmatrix},$$

and

$$b_1 = \mu + \mu_1,\ b_2 = b_3 + \mu + \mu_2,\ b_3 = \frac{\kappa}{(1+\beta D_c^*)^2},\ b_4 = \sigma + \mu + \mu_3. \tag{14}$$

After expanding Eq. (13), we obtain:

$$\chi_1(\lambda_3)(\lambda_3 + \alpha + \mu)(\lambda_3 + \gamma + b_1) = 0, \tag{15}$$

where $\chi_1(\lambda_3) = \lambda_3^2 + (b_2 + b_4)\lambda_3 + b_3(\mu + \mu_3) + b_4(\mu + \mu_2)$. Two of the roots of Eq. (15) are $-(\alpha+\mu)$ and $-(\gamma+b_1)$, which is negative because $\alpha + \mu > 0$ and $\gamma + b_1 > 0$. The other two roots of Eq. (15) are determined by $\chi_1(\lambda_3) = 0$ or:

$$\lambda_3^2 + (b_2 + b_4)\lambda_3 + b_3(\mu + \mu_3) + b_4(\mu + \mu_2) = 0. \tag{16}$$

By the Routh-Hurwitz criteria of a polynomial of degree two [17], all roots of Eq. (16) are negative or have negative real parts because $b_2 + b_4 > 0$ and $b_3(\mu + \mu_3) + b_4(\mu + \mu_2) > 0$. As a result, Theorem 1 is established.

Theorem 1 tells us that the small displacement from the equilibrium point T^* will decrease to zero regardless of the parameter values.

Global stability

In this section, we use the Lyapunov direct method to prove the non-existence of periodic orbits for the non-delay model (2) [18]. Constructing an appropriate Lyapunov function to investigate global stability is known to be a difficult problem in general. In the following, we discuss two remarks, where Remark 1 is an example of an attempt to find a Lyapunov function and Remark 2 is the numerical simulation to indicate the global stability of the equilibrium point T^*.

Remark 1 A function is suggested as follows:

$$\begin{aligned} \tilde{L}(P, D, D_c, D_p) =& (2\mu + \gamma + \mu_1)(D - D^*)^2 + \alpha[(P - P^*) + (D - D^*)]^2 \\ &+ (2\mu + \mu_2 + \mu_3)(D_c - D_c^*)^2 + \sigma[(D_c - D_c^*) + (D_p - D_p^*)]^2, \end{aligned} \tag{17}$$

where $\tilde{L}(P, D, D_c, D_p) \geq 0$ for all $(P, D, D_c, D_p) \geq (0, 0, 0, 0)$ with equality if and only if $(P, D, D_c, D_p) = (P^*, D^*, D_c^*, D_p^*)$. The time derivative of $\tilde{L}$ computed along the solution of non-delay model (2) is

given by:

$$\begin{aligned}\frac{d\tilde{L}}{dt} &= \frac{\partial \tilde{L}}{\partial P}\frac{dP}{dt} + \frac{\partial \tilde{L}}{\partial D}\frac{dD}{dt} + \frac{\partial \tilde{L}}{\partial D_c}\frac{dD_c}{dt} + \frac{\partial \tilde{L}}{\partial D_p}\frac{dD_p}{dt} \\ &= \Big(2\alpha(P-P^*) + 2\alpha(D-D^*)\Big)\Big(\Lambda - (\alpha+\mu)P\Big) \\ &\quad + \Big(2\alpha(P-P^*) + 2(2\mu+\gamma+\mu_1+\alpha)(D-D^*)\Big)\Big(\alpha P - (\gamma+\mu+\mu_1)D\Big) \\ &\quad + \Big(2(2\mu+\mu_2+\mu_3+\sigma)(D_c-D_c^*) + 2\sigma(D_p-D_p^*)\Big)\Big(\gamma D - \frac{\kappa D_c}{1+\beta D_c} + \sigma D_p \\ &\quad - (\mu+\mu_2)D_c\Big) + \Big(2\sigma(D_c-D_c^*) + 2\sigma(D_p-D_p^*)\Big)\Big(\frac{\kappa D_c}{1+\beta D_c} - (\sigma+\mu+\mu_3)D_p\Big). \end{aligned} \tag{18}$$

Note that we have:

$$\begin{aligned}\Lambda &= (\alpha+\mu)P^*, \\ 0 &= -\alpha P^* + (\gamma+\mu+\mu_1)D^*, \\ 0 &= -\gamma D^* + \frac{\kappa D_c^*}{1+\beta D_c^*} - \sigma D_p^* + (\mu+\mu_2)D_c^*, \\ 0 &= -\frac{\kappa D_c^*}{1+\beta D_c^*} + (\sigma+\mu+\mu_3)D_p^*. \end{aligned}$$

Therefore, Eq. (18) becomes:

$$\begin{aligned}\frac{d\tilde{L}}{dt} &= \Big(2\alpha(P-P^*) + 2\alpha(D-D^*)\Big)\Big((\alpha+\mu)P^* - (\alpha+\mu)P\Big) \\ &\quad + \Big(2\alpha(P-P^*) + 2(2\mu+\gamma+\mu_1+\alpha)(D-D^*)\Big)\Big(\alpha P - (\gamma+\mu+\mu_1)D \\ &\quad - \alpha P^* + (\gamma+\mu+\mu_1)D^*\Big) + \Big(2(2\mu+\mu_2+\mu_3+\sigma)(D_c-D_c^*) + 2\sigma(D_p-D_p^*)\Big) \\ &\quad \times \Big(\gamma D - \frac{\kappa D_c}{1+\beta D_c} + \sigma D_p - (\mu+\mu_2)D_c - \gamma D^* + \frac{\kappa D_c^*}{1+\beta D_c^*} - \sigma D_p^* + (\mu+\mu_2)D_c^*\Big) \\ &\quad + \Big(2\sigma(D_c-D_c^*) + 2\sigma(D_p-D_p^*)\Big)\Big(\frac{\kappa D_c}{1+\beta D_c} - (\sigma+\mu+\mu_3)D_p \\ &\quad - \frac{\kappa D_c^*}{1+\beta D_c^*} + (\sigma+\mu+\mu_3)D_p^*\Big) \\ &= -2\alpha\mu(P-P^*)^2 - 2(2\mu+\gamma+\mu_1+\alpha)(\gamma+\mu+\mu_1)(D-D^*)^2 \\ &\quad - \frac{2\kappa(2\mu+\mu_2+\mu_3)(D_c-D_c^*)^2}{(1+\beta D_c)(1+\beta D_c^*)} - 2(2\mu+\mu_2+\mu_3+\sigma)(\mu+\mu_2)(D_c-D_c^*)^2 \\ &\quad - 2\sigma(\mu+\mu_3)(D_p-D_p^*)^2 + 2\gamma(2\mu+\mu_2+\mu_3+\sigma)(D-D^*)(D_c-D_c^*) \\ &\quad + 2\sigma\gamma(D-D^*)(D_p-D_p^*). \end{aligned}$$

The term $\frac{d\tilde{L}}{dt} \leq 0$ for all $(P, D, D_c, D_p) \geq (0,0,0,0)$ is not satisfied because the terms $2\gamma(2\mu+\mu_2+\mu_3+\sigma)(D-D^*)(D_c-D_c^*)$ and $2\sigma\gamma(D-D^*)(D_p-D_p^*)$ are not less than or equal to zero for all $(P, D, D_c, D_p) \geq (0,0,0,0)$. Therefore, Eq. (17) in this Remark 1 is not the Lyapunov function that we are looking for.

Remark 2 As shown in Remark 1, it is difficult to show the global stability by the Lyapunov direct method because we have to go through trial and error and it requires a lot of guessing. We will use numerical simulations to display the global stability of the equilibrium point T^* of the non-delay model (2). Consider the following particular case of the non-delay model (2):

$$\frac{dP}{dt} = 35 - 0.015P, \tag{19a}$$

$$\frac{dD}{dt} = 0.005P - 0.135D, \tag{19b}$$

$$\frac{dD_c}{dt} = 0.05D - \frac{0.5D_c}{1 + 0.0005D_c} + 0.4D_p - 0.26D_c, \tag{19c}$$

$$\frac{dD_p}{dt} = \frac{0.5D_c}{1 + 0.0005D_c} - 0.51D_p. \tag{19d}$$

We obtain the equilibrium point $T^* = (2333.3333, 86.4198, 11.7670, 11.4688)$. Figure 2 shows the numerical simulations of system (19) with four sets of initial conditions $(P_0, D_0, D_{c0}, D_{p0})$: $(3000, 200, 15, 80)$, $(1500, 150, 30, 30)$, $(500, 10, 50, 5)$, and $(100, 100, 5, 50)$. This figure shows the

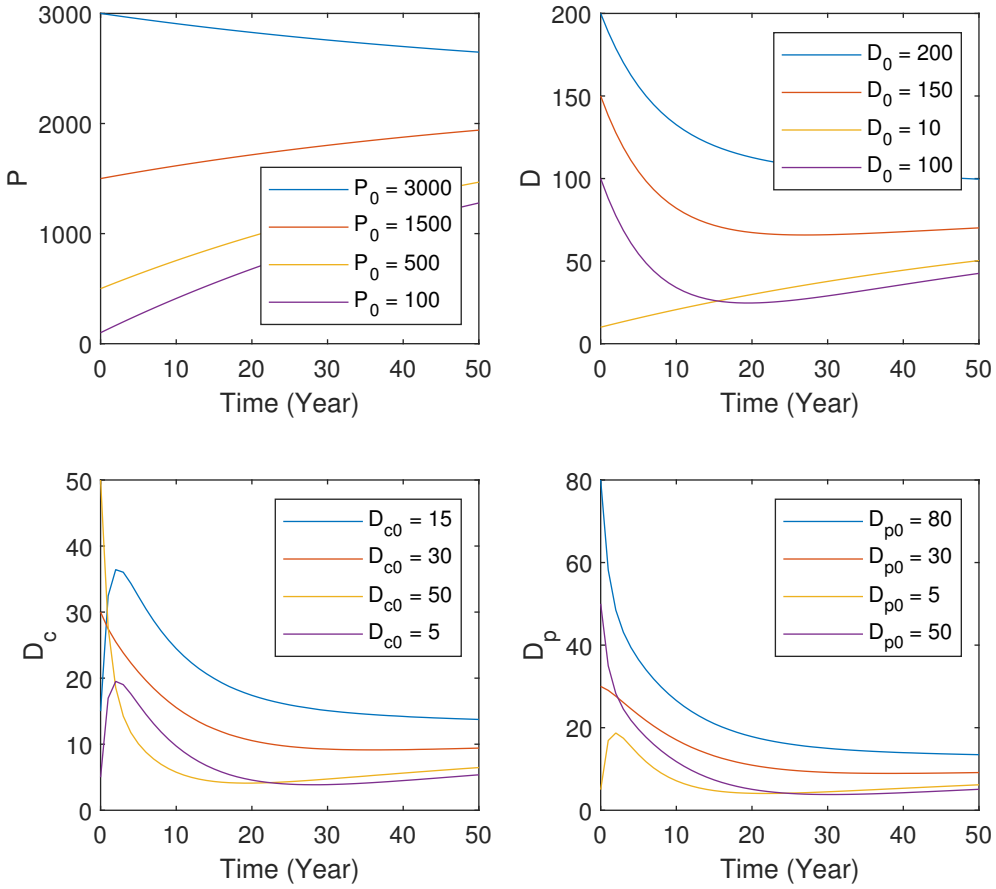

Figure 2. Numerical simulations of system (19)

global stability of T^* where the solutions P, D, D_c, and D_p of model (19) converge to T^* as time t increases, regardless of any positive initial conditions. The numerical simulations indicate that the

equilibrium point T^* of the non-delay model (2) may be globally asymptotically stable.

4 Qualitative analysis of the delay model

In this section, we study the non-negativity and boundedness of the solution, and the stability properties of the equilibrium point of the delay model (1).

Basic properties of delay model (1)

Non-negativity and boundedness of the solution of delay model (1)

Proposition 2 *If conditions:*

(H1) $\Lambda > \alpha P(t_1 - \tau_1)$ *at the boundary* $P(t_1) = 0$ *for any time* t_1,

and

(H2) $\alpha P(t_2 - \tau_1) > \gamma D(t_2 - \tau_2)$ *at the boundary* $D(t_2) = 0$ *for any time* t_2,

are satisfied, then the solutions P, D, D_c, *and* D_p *of the delay model* (1) *remain non-negative and bounded for all* $t > 0$. *Furthermore, the region:*

$$\Omega = \left\{ \left(P, D, D_c, D_p\right) \in \mathbb{R}^4_+ \middle| P + D + D_c + D_p \leq \frac{\Lambda}{\mu} \right\},$$

is a positively-invariant region with respect to the delay model (1).

Condition (H1) means that, in any event, if the number of non-diabetics drops to zero, the number of non-diabetics who will develop diabetes should be less than the number of newly recruited non-diabetics. On the other hand, condition (H2) means that if the number of diabetics who never had any complications drops to zero, the number of diabetics who will develop the first complication should be less than the number of non-diabetics who will develop diabetes. The proof of Proposition 2 is as follows.

Proof We prove the non-negativity of variable P of the delay model (1) as follows. $P(t) > 0$ for all $t > 0$. If this is not the case, suppose that there exists $t_1 > 0$ such that $P(t) > 0$ for $t \in [0, t_1)$, $P(t_1) = 0$, and $\frac{dP(t_1)}{dt} \leq 0$. From Eq. (1a), we obtain:

$$\frac{dP(t_1)}{dt} = \Lambda - \alpha P(t_1 - \tau_1).$$

We have $\frac{dP(t_1)}{dt} \leq 0$ for $\Lambda \leq \alpha P(t_1 - \tau_1)$, which agrees to the supposition that $\frac{dP(t_1)}{dt} \leq 0$. Therefore, if $\Lambda \leq \alpha P(t_1 - \tau_1)$ at the boundary $P(t_1) = 0$ for any time t_1, the solution P may enter the negative region. Condition (H1) indicates that the solution P remains non-negative for all $t > 0$.

Next, we prove the non-negativity of the solution D of the delay model (1) as follows. $D(t) > 0$ for all $t > 0$. If this be not the case, suppose that there exists $t_2 > 0$ such that $D(t) > 0$ for $t \in [0, t_2)$, $D(t_2) = 0$, and $\frac{dD(t_2)}{dt} \leq 0$. From Eq. (1b), we obtain:

$$\frac{dD(t_2)}{dt} = \alpha P(t_2 - \tau_1) - \gamma D(t_2 - \tau_2).$$

We have $\frac{dD(t_2)}{dt} \leq 0$ for $\alpha P(t_2-\tau_1) \leq \gamma D(t_2-\tau_2)$, which agrees to the supposition that $\frac{dD(t_2)}{dt} \leq 0$. Therefore, if $\alpha P(t_2-\tau_1) \leq \gamma D(t_2-\tau_2)$ at the boundary $D(t_2) = 0$ for any time t_2, the solution D may enter the negative region. Condition (H2) indicates that the solution D remains non-negative for all $t > 0$.
In the following, conditions (H1) and (H2) are satisfied.
Since variables D_c and D_p of delay model (1) depend on each other, we prove the non-negativity as follows: $D_c(t) > 0$ for all $t > 0$. If this is not the case, suppose that there exists $t_3 > 0$ such that $D_c(t) > 0$ for $t \in [0, t_3)$, $D_c(t_3) = 0$, and $\frac{dD_c(t_3)}{dt} \leq 0$. We first find the integration of Eq. (1d). From Eq. (1d), we obtain:

$$D_p(t) = D_p(0)e^{-(\sigma+\mu+\mu_3)t} + e^{-(\sigma+\mu+\mu_3)t}\int_0^t \frac{\kappa D_c(\varepsilon)}{1+\beta D_c(\varepsilon)} e^{(\sigma+\mu+\mu_3)\varepsilon}\, d\varepsilon. \tag{20}$$

From Eq. (20), we have $D_p(t) > 0$ for $t \in [0, t_3]$. Then, from Eq. (1c), we have:

$$\frac{dD_c(t_3)}{dt} = \gamma D(t_3-\tau_2) + \sigma D_p(t_3) > 0,$$

but this leads to a contradiction to the supposition that $\frac{dD_c(t_3)}{dt} \leq 0$. We can conclude that the solution D_c remains non-negative for all $t > 0$. Consequently, from Eq. (20), the solution D_p also remains non-negative for all $t > 0$.
For the boundedness of the solutions P, D, D_c, and D_p of the delay model (1), adding all equations of the delay model (1) yields:

$$\frac{dN}{dt} = \Lambda - \mu N_2 - \mu_1 D - \mu_2 D_c - \mu_3 D_p. \tag{21}$$

Since the terms $\mu_1 D \geq 0$, $\mu_2 D_c \geq 0$, and $\mu_3 D_p \geq 0$, Eq. (21) becomes:

$$\frac{dN}{dt} + \mu N \leq \Lambda.$$
$$N(t) \leq \frac{\Lambda}{\mu} + \left(N(0) - \frac{\Lambda}{\mu}\right)e^{-\mu t}.$$

If $N(0) \leq \frac{\Lambda}{\mu}$, then we have $N(t) \leq \frac{\Lambda}{\mu}$. This implies that the upper bound of the total population size is $\frac{\Lambda}{\mu}$. If $N(0) > \frac{\Lambda}{\mu}$, then $N(t)$ will decrease to $\frac{\Lambda}{\mu}$ because $\lim_{t\to\infty} N(t) = \frac{\Lambda}{\mu}$.
As a result, conditions (H1) and (H2) are required to be true so that the region Ω becomes a positively-invariant region with respect to the delay model (1). The proposition is proposed.

Stability of the equilibrium point of delay model (1)

Equilibrium point of delay model (1)

The equilibrium point $T^* = (P^*, D^*, D_c^*, D_p^*)$ given in (12) is also the equilibrium point of the delay model (1) because when the delay model (1) reaches its equilibrium state, we have:

$$P = P(t-\tau_1) = P^*,\ D = D(t-\tau_2) = D^*,\ D_c = D_c^*,\ D_p = D_p^*. \tag{22}$$

Upon substituting (22) into the right-hand-side equations of the delay model (1) and letting them equal to zero, we obtain the same set of equations as given in (8).

Local stability and the occurrence of Hopf bifurcation

In the following sections, we will separate the local stability discussion into two parts. First, in section "Stable region of τ_2 when $\tau_1 = 0$", we identify the stable region of τ_2 when $\tau_1 = 0$. Then, for τ_2 is within its stable region, we identify the critical value for τ_1 in section "$\tau_1 > 0$ and τ_2 is within its stable region".

Stable region of τ_2 when $\tau_1 = 0$

For $\tau_1 = 0$ and $\tau_2 > 0$, we have the following theorem.

Theorem 2 *For the delay model (1) with $\tau_1 = 0$:*

(i) If condition:

(H3) $b_1 \geq \gamma$,

holds, then T^* is locally asymptotically stable for $\tau_2 \geq 0$.

(ii) If condition:

(H4) $b_1 < \gamma$,

holds, then there exists a critical value:

$$\tau_{20} = \frac{1}{\omega_{20}} \cos^{-1}\left\{-\frac{b_1}{\gamma}\right\}, \tag{23}$$

where

$$\omega_{20} = \sqrt{-(b_1+\gamma)(b_1-\gamma)}, \tag{24}$$

such that T^* is locally asymptotically stable for $\tau_2 \in [0, \tau_{20})$ and becomes unstable for $\tau_2 > \tau_{20}$. Furthermore, a Hopf bifurcation occurs at $\tau_2 = \tau_{20}$ and a family of periodic orbits arises from T^*.

Condition (H3) means that the rate of the first incidence of complication does not exceed the total death rate of diabetics who never had any complications. While condition (H4) means that the rate of the first incidence of complication is greater than the total death rate of diabetics who never had any complications. The proof of Theorem 2 is as follows:

Proof The characteristic equation with respect to the equilibrium point T^* of the delay model (1) with $\tau_1 = 0$ is obtained by computing:

$$\det\left[\lambda_4 \mathbf{I}_4 - \mathbf{B}_2 - e^{-\lambda_4 \tau_2}\mathbf{B}_3\right] = 0, \tag{25}$$

where λ_4 represents the eigenvalues, $\mathbf{I}_4$ is an identity matrix of dimension 4,

$$\mathbf{B}_2 = \begin{bmatrix} -(\alpha+\mu) & 0 & 0 & 0 \\ \alpha & -b_1 & 0 & 0 \\ 0 & 0 & -b_2 & \sigma \\ 0 & 0 & b_3 & -b_4 \end{bmatrix}, \ \mathbf{B}_3 = \begin{bmatrix} 0 & 0 & 0 & 0 \\ 0 & -\gamma & 0 & 0 \\ 0 & \gamma & 0 & 0 \\ 0 & 0 & 0 & 0 \end{bmatrix},$$

and b_1, b_2, b_3, and b_4 are as given in Eqs. (14). After expanding Eq. (25), we obtain:

$$(\lambda_4 + \mu + \alpha)\chi_1(\lambda_4)\chi_2(\lambda_4) = 0, \tag{26}$$

where

$$\chi_1(\lambda_4) = \lambda_4^2 + (b_2 + b_4)\lambda_4 + b_3(\mu + \mu_3) + b_4(\mu + \mu_2),$$
$$\chi_2(\lambda_4) = (\lambda_4 + b_1 + e^{-\lambda_4\tau_2}\gamma).$$

One of the roots of Eq. (26) is $-(\mu + \alpha)$, which is negative because $\mu + \alpha > 0$. The other two roots of Eq. (26) are determined by equation $\chi_1(\lambda_4) = 0$ and by the Routh-Hurwitz criteria [17], they are all negative or have negative real parts because $b_2 + b_4 > 0$ and $b_3(\mu + \mu_3) + b_4(\mu + \mu_2) > 0$. Lastly, the other roots of Eq. (26) are determined by equation $\chi_2(\lambda_4) = 0$ or

$$(\lambda_4 + b_1 + e^{-\lambda_4\tau_2}\gamma) = 0. \tag{27}$$

Assume that for some $\tau_2 > 0$, $\lambda_4 = i\omega_2$ ($i = \sqrt{-1}$ and $\omega_2 > 0$) is one of the roots of Eq. (27). Then, we can obtain

$$\omega_2^2 + (b_1 + \gamma)(b_1 - \gamma) = 0. \tag{28}$$

Eq. (28) can be written into a polynomial of degree one in $\varpi_2 = \omega_2^2$, as follows:

$$\varpi_2 + (b_1 + \gamma)(b_1 - \gamma) = 0. \tag{29}$$

The root of Eq. (29) is negative if condition (H3) is satisfied. Condition (H3) implies that $\varpi_2 = \omega_2^2 \leq 0$, which is a contradiction because we initially assumed $\omega_2 > 0$. The characteristic Eq. (27) cannot have $\lambda_4 = i\omega_2$ as one of the roots. Therefore, the equilibrium point T^* is locally asymptotically stable for $\tau_2 \geq 0$ with $\tau_1 = 0$. This proves Theorem 2(i).
For the second proof, suppose that condition (H4) is satisfied. Condition (H4) implies that Eq. (28) has one positive root, that is, Eq. (24). Then, the corresponding critical delays are given by:

$$\tau_2^{(j)} = \frac{1}{\omega_{20}}\cos^{-1}\left\{-\frac{b_1}{\gamma}\right\} + \frac{2j\pi}{\omega_{20}}, \quad j = 0, 1, 2, \ldots.$$

Let $\tau_{20} = \tau_2^{(0)}$ be the first critical value at which Eq. (27) has roots on the imaginary axis and $\lambda_4 = \pm i\omega_{20}$ are the corresponding roots. Then, the equilibrium point T^* is locally asymptotically stable for $\tau_2 \in [0, \tau_{20})$ with $\tau_1 = 0$. Moreover, the transversality condition for the establishment of Hopf bifurcation at $\tau_2 = \tau_{20}$ is satisfied [19], as follows:

$$\text{sign}\left\{\Re\left[\frac{d\lambda_4}{d\tau_2}\right]\Big|_{\lambda_4(\tau_{20})=i\omega_{20}}\right\} = \text{sign}\left\{\Re\left[\frac{d\lambda_4}{d\tau_2}\right]^{-1}\Big|_{\lambda_4(\tau_{20})=i\omega_{20}}\right\} > 0,$$

where

$$\Re\left[\frac{d\lambda_4}{d\tau_2}\right]^{-1}\Big|_{\lambda_4(\tau_{20})=i\omega_{20}} = \frac{1}{\gamma^2}.$$

This completes the proof of Theorem 2(ii).

$\tau_1 > 0$ and τ_2 is within its stable region

For $\tau_1 > 0$ and τ_2 is within its stable region, we have the following theorem.

Theorem 3 *For delay model (1) with $(\tau_1, \tau_2) > (0, 0)$, given τ_2 is within its stable region (τ_2 can be any non-negative value if condition (H3) holds, or $\tau_2 \in [0, \tau_{20})$ if condition (H4) holds). Given an equation with respect to ω_1 as follows:*

$$\begin{aligned}&\omega_1^4 + (b_1^2 + \gamma^2 + \mu^2 - \alpha^2)\omega_1^2 + (b_1^2 + \gamma^2)(\mu^2 - \alpha^2)\\ &+ 2b_1\gamma(\omega_1^2 + \mu^2 - \alpha^2)\cos\omega_1\tau_2 - 2\gamma\omega_1(\omega_1^2 + \mu^2 - \alpha^2)\sin\omega_1\tau_2 = 0.\end{aligned} \tag{30}$$

We have:

(i) If condition:

(H5) *Eq. (30) has no root,*

holds, then the equilibrium point T^* is locally asymptotically stable for $\tau_1 \geq 0$.

(ii) If condition:

(H6) *Eq. (30) has at least one positive root,*

holds, then there exists a critical value:

$$\tau_{10} = \min_{k\in\{1,2,\ldots,n\}}\{\tau_{1k}^{(0)}\}, \tag{31}$$

where

$$\tau_{1k}^{(0)} = \frac{1}{\omega_{1k}}\cos^{-1}\left\{-\frac{\mu}{\alpha}\right\},$$

where ω_{1k} $(k = 1, 2, \ldots, n)$ are any positive roots of Eq. (30), such that the equilibrium point T^* is locally asymptotically stable for $\tau_1 \in [0, \tau_{10})$ and becomes unstable for $\tau_1 > \tau_{10}$. Furthermore, if the following condition is satisfied:

(H7) $V_0V_2 + V_1V_3 > 0$,

where

$$\begin{aligned}V_0 &= (b_1 + \mu) + \alpha\cos\omega_{10}\tau_{10} + (\gamma - \mu\gamma\tau_2)\cos\omega_{10}\tau_2\\ &\quad - \gamma\tau_2\omega_{10}\sin\omega_{10}\tau_2 - \alpha\gamma\tau_2\cos\omega_{10}(\tau_{10} + \tau_2),\end{aligned} \tag{32a}$$

$$\begin{aligned}V_1 &= 2\omega_{10} - \alpha\sin\omega_{10}\tau_{10} - (\gamma - \mu\gamma\tau_2)\sin\omega_{10}\tau_2\\ &\quad - \gamma\tau_2\omega_{10}\cos\omega_{10}\tau_2 + \alpha\gamma\tau_2\sin\omega_{10}(\tau_{10} + \tau_2),\end{aligned} \tag{32b}$$

$$V_2 = b_1\alpha\omega_{10}\sin\omega_{10}\tau_{10} - \alpha\omega_{10}^2\cos\omega_{10}\tau_{10} + \alpha\gamma\omega_{10}\sin\omega_{10}(\tau_{10} + \tau_2), \tag{32c}$$

$$V_3 = \alpha\omega_{10}^2\sin\omega_{10}\tau_{10} + b_1\alpha\omega_{10}\cos\omega_{10}\tau_{10} + \alpha\gamma\omega_{10}\cos\omega_{10}(\tau_{10} + \tau_2), \tag{32d}$$

where ω_{10} is the corresponding positive root of Eq. (30) when $\tau_1 = \tau_{10}$, then a Hopf bifurcation occurs at $\tau_1 = \tau_{10}$ and a family of periodic orbits arises from T^*.

Proof The characteristic equation with respect to the equilibrium point T^* of the delay model (1) is obtained by computing:

$$\det\left[\lambda_5 \mathbf{I}_4 - \mathbf{B}_4 - e^{-\lambda_5\tau_1}\mathbf{B}_5 - e^{-\lambda_5\tau_2}\mathbf{B}_3\right] = 0, \tag{33}$$

where λ_5 represents the eigenvalues, $\mathbf{I}_4$ is an identity matrix of dimension 4,

$$\mathbf{B}_4 = \begin{bmatrix} -\mu & 0 & 0 & 0 \\ 0 & -b_1 & 0 & 0 \\ 0 & 0 & -b_2 & \sigma \\ 0 & 0 & b_3 & -b_4 \end{bmatrix}, \mathbf{B}_5 = \begin{bmatrix} -\alpha & 0 & 0 & 0 \\ \alpha & 0 & 0 & 0 \\ 0 & 0 & 0 & 0 \\ 0 & 0 & 0 & 0 \end{bmatrix}, \mathbf{B}_3 = \begin{bmatrix} 0 & 0 & 0 & 0 \\ 0 & -\gamma & 0 & 0 \\ 0 & \gamma & 0 & 0 \\ 0 & 0 & 0 & 0 \end{bmatrix},$$

and b_1, b_2, b_3, and b_4 are given in Eqs. (14). After expanding Eq. (33), we obtain:

$$\chi_1(\lambda_5)\chi_3(\lambda_5) = 0, \tag{34}$$

where

$$\begin{aligned} \chi_1(\lambda_5) &= \lambda_5^2 + (b_2 + b_4)\lambda_5 + b_3(\mu + \mu_3) + b_4(\mu + \mu_2), \\ \chi_3(\lambda_5) &= (\lambda_5 + \mu + e^{-\lambda_5\tau_1}\alpha)(\lambda_5 + b_1 + e^{-\lambda_5\tau_2}\gamma). \end{aligned}$$

Two of the roots of Eq. (34) are determined by $\chi_1(\lambda_5) = 0$ and by the Routh-Hurwitz criteria [17], they are all negative or have negative real parts because $b_2 + b_4 > 0$ and $b_3(\mu + \mu_3) + b_4(\mu + \mu_2) > 0$. The other roots of Eq. (34) are determined by $\chi_3(\lambda_5) = 0$ or:

$$\lambda_5^2 + (b_1 + \mu)\lambda_5 + b_1\mu + e^{-\lambda_5\tau_1}(\alpha\lambda_5 + b_1\alpha) + e^{-\lambda_5\tau_2}(\gamma\lambda_5 + \mu\gamma) + e^{-\lambda_5(\tau_1+\tau_2)}\alpha\gamma = 0. \tag{35}$$

For τ_2 within its stable region (either condition (H3) or (H4) holds), we assume that for some $\tau_1 > 0$, $\lambda_5 = i\omega_1$ ($i = \sqrt{-1}$ and $\omega_1 > 0$) is one of the roots of Eq. (35). Substituting $\lambda_5 = i\omega_1$ into Eq. (35) and separating the real and imaginary parts yields:

$$\begin{aligned} (b_1\alpha + \alpha\gamma\cos\omega_1\tau_2)\cos\omega_1\tau_1 + (\alpha\omega_1 - \alpha\gamma\sin\omega_1\tau_2)\sin\omega_1\tau_2 & \\ = (\omega_1^2 - b_1\mu) - \gamma\omega_1\sin\omega_1\tau_2 - \mu\gamma\cos\omega_1\tau_2, & \quad (36a) \\ (b_1\alpha + \alpha\gamma\cos\omega_1\tau_2)\sin\omega_1\tau_1 - (\alpha\omega_1 - \alpha\gamma\sin\omega_1\tau_2)\cos\omega_1\tau_2 & \\ = (b_1 + \mu)\sin\omega_1\tau_1 + \gamma\omega_1\cos\omega_1\tau_2 - \mu\gamma\sin\omega_1\tau_2. & \quad (36b) \end{aligned}$$

We eliminate τ_1 by squaring and adding both Eqs. (36). Then, we can obtain Eq. (30). Suppose that condition (H5) is satisfied. Condition (H5) implies that the characteristic Eq. (35) cannot have $\lambda_5 = i\omega_1$ as one of the roots. Therefore, the equilibrium point T^* is locally asymptotically stable for $\tau_1 \geq 0$. This proves Theorem 3(i).

For the second proof, suppose that condition (H6) holds. Without loss of generality, suppose that Eq. (30) has a finite number of positive roots denoted by $\omega_{11}, \omega_{12}, \ldots, \omega_{1n}$. For every ω_{1k} ($k = 1, 2, \ldots, n$) and using the equations in (36), we obtain the corresponding critical delays as follows:

$$\tau_{1k}^{(j)} = \frac{1}{\omega_{1k}}\cos^{-1}\left\{-\frac{\mu}{\alpha}\right\} + \frac{2j\pi}{\omega_{1k}}, \quad j = 0, 1, 2, \ldots.$$

Let $\tau_{10} = \min_{k\in\{1,2,\ldots,n\}} \{\tau_{1k}^{(0)}\}$ be the first critical value for which Eq. (35) has roots on the imaginary axis and $\lambda_5 = \pm i\omega_{10}$ are denoted as the corresponding roots. Then, the equilibrium point T^* is locally asymptotically stable for $\tau_1 \in [0, \tau_{10})$. To establish the occurrence of Hopf bifurcation at $\tau_1 = \tau_{10}$, we need to show that:

$$\text{sign}\left\{\Re\left[\frac{d\lambda_5}{d\tau_1}\right]\Big|_{\lambda_5(\tau_{10})=i\omega_{10}}\right\} > 0.$$

By differentiating Eq. (35) with respect to τ_1, we obtain:

$$\left[\frac{d\lambda_5}{d\tau_1}\right]^{-1} = \frac{2\lambda_5 + b_1 + \mu + \alpha e^{-\lambda_5\tau_1} - (\gamma\tau_2\lambda_5 - \gamma + \mu\gamma\tau_2)e^{-\lambda_5\tau_2} - \alpha\gamma\tau_2 e^{-\lambda_5(\tau_1+\tau_2)}}{(\alpha\lambda_5^2 + b_1\alpha\lambda_5)e^{-\lambda_5\tau_1} + \alpha\gamma\lambda_5 e^{-\lambda_5(\tau_1+\tau_2)}} - \frac{\tau_1}{\lambda_5}. \quad (37)$$

Evaluating Eq. (37) at $\lambda_5(\tau_{10}) = i\omega_{10}$ yields:

$$\left[\frac{d\lambda_5}{d\tau_1}\right]^{-1}\Big|_{\lambda_5(\tau_{10})=i\omega_{10}} = \frac{V_0 + iV_1}{V_2 + iV_3} - \frac{\tau_{10}}{i\omega_{10}}, \quad (38)$$

where V_0, V_1, V_2, and V_3 are as given in Eqs. (32). The real part of Eq. (38) is given by:

$$\Re\left[\frac{d\lambda_5}{d\tau_1}\right]^{-1}\Big|_{\lambda_5(\tau_{10})=i\omega_{10}} = \frac{V_0V_2 + V_1V_3}{V_2^2 + V_3^2}.$$

If condition (H7) is satisfied, then

$$\text{sign}\left\{\Re\left[\frac{d\lambda_5}{d\tau_1}\right]^{-1}\Big|_{\lambda_5(\tau_{10})=i\omega_{10}}\right\} = \text{sign}\left\{\Re\left[\frac{d\lambda_5}{d\tau_1}\right]\Big|_{\lambda_5(\tau_{10})=i\omega_{10}}\right\} > 0.$$

This completes the proof of Theorem 3(ii).

Remark 3 We discussed the criteria implying that there exists a periodic orbit for the delay model (1) for some parameter values. Such results are interesting because the equilibrium point T^* can become unstable and not approach T^*. In this case, T^* of the delay model (1) is not globally asymptotically stable, and the Lyapunov direct method would not work.

5 Sensitivity analysis

Model (1) has four model outputs (state variables) and sixteen model inputs (parameters and initial conditions). The model outputs are denoted as $\mathbf{x} = \{P, D, D_c, D_p\}$, while the model inputs are denoted as $\boldsymbol{\varsigma} = \{\Lambda, \alpha, \gamma, \kappa, \beta, \sigma, \mu, \mu_1, \mu_2, \mu_3, \tau_1, \tau_2, \phi_1(\theta), \phi_2(\theta), D_{c0}, D_{p0}\}$. Following [20, 21], the sensitivity index of an arbitrary model output x_i with respect to an arbitrary model input ς_j is as given by:

$$S_{\varsigma_j}^{x_i}(t) = \frac{\partial x_i(t)}{\partial \varsigma_j}, \quad i = 1, 2, 3, 4, \quad j = 1, \ldots, 16.$$

For simplifying the notations, the variable $S_{\varsigma_j}^{x_i}(t)$ is denoted as $S_{\varsigma_j}^{x_i}$, unless the argument is other than t. Following [21, 22], the system of differential equations for the sensitivity indices of the

outputs P, D, D_c, and D_p with respect to an arbitrary model input ς_j is given by:

$$\begin{aligned}
\begin{bmatrix} \frac{dS^P_{\varsigma_j}}{dt} \\ \frac{dS^D_{\varsigma_j}}{dt} \\ \frac{dS^{D_c}_{\varsigma_j}}{dt} \\ \frac{dS^{D_p}_{\varsigma_j}}{dt} \end{bmatrix} &= \begin{bmatrix} -\mu & 0 & 0 & 0 \\ 0 & -(\mu+\mu_1) & 0 & 0 \\ 0 & 0 & -\left(\frac{\kappa}{(1+\beta D_c)^2}+(\mu+\mu_2)\right) & \sigma \\ 0 & 0 & \frac{\kappa}{(1+\beta D_c)^2} & -(\sigma+\mu+\mu_3) \end{bmatrix} \begin{bmatrix} S^P_{\varsigma_j} \\ S^D_{\varsigma_j} \\ S^{D_c}_{\varsigma_j} \\ S^{D_p}_{\varsigma_j} \end{bmatrix} \\
&+ \begin{bmatrix} -\alpha & 0 & 0 & 0 \\ \alpha & 0 & 0 & 0 \\ 0 & 0 & 0 & 0 \\ 0 & 0 & 0 & 0 \end{bmatrix} \begin{bmatrix} S^P_{\varsigma_j}(t-\tau_1) \\ S^D_{\varsigma_j}(t-\tau_1) \\ S^{D_c}_{\varsigma_j}(t-\tau_1) \\ S^{D_p}_{\varsigma_j}(t-\tau_1) \end{bmatrix} + \begin{bmatrix} 0 & 0 & 0 & 0 \\ 0 & -\gamma & 0 & 0 \\ 0 & \gamma & 0 & 0 \\ 0 & 0 & 0 & 0 \end{bmatrix} \begin{bmatrix} S^P_{\varsigma_j}(t-\tau_2) \\ S^D_{\varsigma_j}(t-\tau_2) \\ S^{D_c}_{\varsigma_j}(t-\tau_2) \\ S^{D_p}_{\varsigma_j}(t-\tau_2) \end{bmatrix} \\
&+ \left[\frac{\partial}{\partial \varsigma_j}\left(\frac{dP}{dt}\right) \quad \frac{\partial}{\partial \varsigma_j}\left(\frac{dD}{dt}\right) \quad \frac{\partial}{\partial \varsigma_j}\left(\frac{dD_c}{dt}\right) \quad \frac{\partial}{\partial \varsigma_j}\left(\frac{dD_p}{dt}\right) \right]^\top,
\end{aligned} \tag{39}$$

with the initial conditions

$$\begin{bmatrix} S^P_{\varsigma_j}(\theta) \\ S^D_{\varsigma_j}(\theta) \\ S^{D_c}_{\varsigma_j}(0) \\ S^{D_p}_{\varsigma_j}(0) \end{bmatrix} = \left[\frac{\partial \phi_1(\theta)}{\partial \varsigma_j} \quad \frac{\partial \phi_2(\theta)}{\partial \varsigma_j} \quad \frac{\partial D_{c0}}{\partial \varsigma_j} \quad \frac{\partial D_{p0}}{\partial \varsigma_j} \right]^\top, \quad \theta \in [-\tau_{\max}, 0].$$

In particular, the system of differential equations for the sensitivity indices of the model outputs P, D, D_c, and D_p with respect to the recruitment rate of non-diabetics (Λ) is given by:

$$\frac{dS^P_\Lambda}{dt} = -\mu S^P_\Lambda - \alpha S^P_\Lambda(t-\tau_1) + 1, \tag{40a}$$

$$\frac{dS^D_\Lambda}{dt} = -(\mu+\mu_1) S^D_\Lambda + \alpha S^P_\Lambda(t-\tau_1) - \gamma S^D_\Lambda(t-\tau_2), \tag{40b}$$

$$\frac{dS^{D_c}_\Lambda}{dt} = -\frac{\kappa S^{D_c}_\Lambda}{(1+\beta D_c)^2} - (\mu+\mu_2) S^{D_c}_\Lambda + \sigma S^{D_p}_\Lambda + \gamma S^D_\Lambda(t-\tau_2), \tag{40c}$$

$$\frac{dS^{D_p}_\Lambda}{dt} = \frac{\kappa S^{D_c}_\Lambda}{(1+\beta D_c)^2} - (\sigma+\mu+\mu_3) S^{D_p}_\Lambda, \tag{40d}$$

with the initial conditions:

$$S^P_\Lambda(\theta) = 0,\ \theta \in [-\tau_{\max}, 0],\ S^D_\Lambda(\theta) = 0,\ S^{D_c}_\Lambda(0) = 0,\ S^{D_p}_\Lambda(0) = 0.$$

The equilibrium solutions of system (40) is given by:

$$S^{P^*}_\Lambda = \frac{1}{\alpha+\mu},$$

$$
\begin{aligned}
S_{\Lambda}^{D^*} &= \frac{\alpha S_{\Lambda}^{P^*}}{\gamma+\mu+\mu_1},\\
S_{\Lambda}^{D_c^*} &= \frac{\gamma S_{\Lambda}^{D^*}(\sigma+\mu+\mu_3)(1+\beta D_c^*)^2}{\kappa(\mu+\mu_3)+(\mu+\mu_2)(\sigma+\mu+\mu_3)(1+\beta D_c^*)^2},\\
S_{\Lambda}^{D_p^*} &= \frac{\kappa S_{\Lambda}^{D_c^*}}{(\sigma+\mu+\mu_3)(1+\beta D_c^*)^2}.
\end{aligned}
$$

The system of differential equations for the sensitivity indices of the model outputs P, D, D_c, and D_p with respect to the time delay parameter (τ_1) is given by:

$$\frac{dS_{\tau_1}^{P}}{dt} = -\mu S_{\tau_1}^{P} - \alpha S_{\tau_1}^{P}(t-\tau_1) + \alpha\frac{dP(t-\tau_1)}{dt}, \tag{41a}$$

$$\frac{dS_{\tau_1}^{D}}{dt} = -(\mu+\mu_1)S_{\tau_1}^{D} + \alpha S_{\tau_1}^{P}(t-\tau_1) - \gamma S_{\tau_1}^{D}(t-\tau_2) - \alpha\frac{dP(t-\tau_1)}{dt}, \tag{41b}$$

$$\frac{dS_{\tau_1}^{D_c}}{dt} = -\frac{\kappa S_{\tau_1}^{D_c}}{(1+\beta D_c)^2} - (\mu+\mu_2)S_{\tau_1}^{D_c} + \sigma S_{\tau_1}^{D_p} + \gamma S_{\tau_1}^{D}(t-\tau_2), \tag{41c}$$

$$\frac{dS_{\tau_1}^{D_p}}{dt} = \frac{\kappa S_{\tau_1}^{D_c}}{(1+\beta D_c)^2} - (\sigma+\mu+\mu_3)S_{\tau_1}^{D_p}, \tag{41d}$$

with the initial conditions:

$$S_{\tau_1}^{P}(\theta) = 0,\ \theta\in[-\tau_{\max},0],\ S_{\tau_1}^{D}(\theta) = 0,\ S_{\tau_1}^{D_c}(0) = 0,\ S_{\tau_1}^{D_p}(0) = 0. \tag{42}$$

The equilibrium solution of system (41) is given by

$$S_{\tau_1}^{P^*} = 0, \quad S_{\tau_1}^{D^*} = 0, \quad S_{\tau_1}^{D_c^*} = 0, \quad S_{\tau_1}^{D_p^*} = 0.$$

Similarly, we can derive the sensitivity indices with respect to the other model inputs using system (39). Then, we compute the normalized forward sensitivity indices by using:

$$\Upsilon_{\varsigma_j}^{x_i} = S_{\varsigma_j}^{x_i}\frac{\varsigma_j}{x_i}, \quad i=1,2,3,4, \quad j=1,\ldots,16.$$

Sensitivity index of equilibrium point T^*

In this section, we compute the normalized forward sensitivity indices of T^* with respect to each model input using the values in Table 2.

The normalized forward sensitivity indices of the equilibrium point $T^* = (P^*, D^*, D_c^*, D_p^*)$ with respect to every model input are presented in Table 3.

From Table 3, changes in the model inputs $\phi_1(\theta)$, $\phi_2(\theta)$, D_{c0}, D_{p0}, τ_1, and τ_2 have no effects on the equilibrium point T^*. Furthermore, we can decrease the total number of diabetics by increasing the death-related model inputs (μ, μ_1, μ_2, and μ_3). However, these actions are impractical and unethical. A similar argument applies to the recruitment rate of non-diabetics (Λ). It is unreasonable to restrict the growth of non-diabetics in order to reduce the equilibrium solution of all diabetic subpopulations. Apart from these model inputs $(\phi_1(\theta), \phi_2(\theta), D_{c0}, D_{p0}, \mu, \mu_1, \mu_2, \mu_3, \Lambda, \tau_1$, and $\tau_2)$, we rank the normalized forward sensitivity indices of D^*, D_c^*, and D_p^* with respect to the other model inputs from the most sensitive to least (see Table 4). The signs and magnitudes of

Table 2. List of values for the model inputs of model (1)

Model input	Value	Dimension	Source
$\phi_1(\theta)$	17375603	individuals	Assumed after [2]
$\phi_2(\theta)$	2558998	individuals	[16]
D_{c0}	666483	individuals	[16]
D_{p0}	666483	individuals	[16]
Λ	274314.75	individuals year^{-1}	Estimated after [2]
α	5.2108×10^{-3}	year^{-1}	Estimated after [2]
γ	0.1	year^{-1}	[16]
σ	0.15	year^{-1}	[16]
μ	0.008678	year^{-1}	[16]
μ_1	5.84×10^{-4}	year^{-1}	[16]
μ_2	0.002336	year^{-1}	[16]
μ_3	0.001752	year^{-1}	[16]
κ	0.988986	year^{-1}	[16]
β	5×10^{-6}	individuals^{-1}	[16]
τ_1	10	years	[10]
τ_2	5	years	[16]

Table 3. Normalized forward sensitivity indices of the equilibrium point T^* of model (1) using the model inputs in Table 2

ς_j	$\Upsilon_{\varsigma_j}^{P^*}$	$\Upsilon_{\varsigma_j}^{D^*}$	$\Upsilon_{\varsigma_j}^{D_c^*}$	$\Upsilon_{\varsigma_j}^{D_p^*}$
Λ	1	1	1.1487	0.0302
α	−0.3752	0.6248	0.7177	0.0188
γ	0	−0.9152	0.0974	0.0026
κ	0	0	−0.1527	0.9960
β	0	0	0.1487	−0.9698
σ	0	0	0.1428	−0.9312
μ	−0.6248	−0.7043	−1.7125	−0.0991
μ_1	0	−0.0053	−0.0061	-1.613×10^{-4}
μ_2	0	0	−0.2112	−0.0055
μ_3	0	0	−0.0240	−0.0116
τ_1	0	0	0	0
τ_2	0	0	0	0
$\phi_1(\theta)$	0	0	0	0
$\phi_2(\theta)$	0	0	0	0
D_{c0}	0	0	0	0
D_{p0}	0	0	0	0

$\Upsilon_{\varsigma}^{P^*}$ are not given because we are only concerned with the diabetic subpopulations.

Reducing the overall diabetes prevalence is the primary concern. Based on the status of individuals with diabetes, we should give extra precautions to reduce diabetics with complications (D_c) as they can affect the availability of the treatment of the complications. From Table 4(B), the diabetes incidence rate (α) is at the highest rank but in the positive direction. Thus, decreasing α will affect the most in reducing the equilibrium solution of diabetics with complications (D_c^*). In addition, the decrease in α will also decrease the equilibrium solution of diabetics who never had any complications (D^*) and diabetics with recovered complications (D_p^*), making α the most

Table 4. Magnitude and sign of the normalized forward sensitivity indices of D^*, D_c^*, and D_p^* with respect to the model inputs α, γ, κ, β, and σ

(A) indices of D^*		
ς	$\lvert\Upsilon_\varsigma^{D^*}\rvert$	sign
γ	0.9152	$-$
α	0.6248	$+$
κ	0	
β		
σ		

(B) indices of D_c^*		
ς	$\lvert\Upsilon_\varsigma^{D_c^*}\rvert$	sign
α	0.7177	$+$
κ	0.1527	$-$
β	0.1487	$+$
σ	0.1428	
γ	0.0974	

(C) indices of D_p^*		
ς	$\lvert\Upsilon_\varsigma^{D_p^*}\rvert$	sign
κ	0.9960	$+$
β	0.9698	$-$
σ	0.9312	
α	0.0188	$+$
γ	0.0026	

important model input to curb the overall diabetes cases.

A 1% increase in the recurrence rate of complications (σ) increases the equilibrium solution of diabetics with complications (D_c^*) by approximately 0.1428%, while a 1% increase in the rate of the first incidence of complication (γ) increases the equilibrium solution of diabetics with complications (D_c^*) by approximately 0.0974%. Thus, decreasing γ and σ are beneficial to lower D_c^*.

From Table 4(C), the recovery rate of complications (κ) is the most sensitive model input in changing the equilibrium solution of diabetics with recovered complications (D_p^*), where a 1% increase in κ increases D_p^* by approximately 0.9960%. However, the value of κ is at maximum because if the inhibition effect $\beta = 0$ individuals^{-1}, $\kappa + \mu + \mu_2 = 1$ year^{-1} (the total rates of individuals leaving the compartment of diabetics with complications (D_c)). The value of κ gets smaller due to the inhibition effect of limited medical resources measured by the term $\dfrac{1}{1+\beta D_c}$. In reality, $\dfrac{1}{1+\beta D_c}$ can be described as the reverse effect of diabetics with complications being postponed for treatment [14]. From Table 4(B, C), a 1% increase in the inhibition effect β results in an approximately 0.1487% increase in the equilibrium solution of diabetics with complications (D_c^*) and an approximately 0.9698% decrease in the equilibrium solution of diabetics with recovered complications (D_p^*). Thus, decreasing β is crucial to decrease D_c^*.

6 Numerical simulation

Stability of equilibrium point T^*

In this section, we give some numerical simulations for several cases of model (1) to validate and illustrate our theoretical results. Five examples are presented, and Table 5 shows the differences between them.

Table 5. Numerical example with respect to model (1)

Example	Theorem					
	1	2		3		
		(H3)	(H4)	(H5)	(H6)	(H7)
1	•					
2		•		•		
3		•			•	•
4			•	•		
5			•		•	•

Example 1 *Consider the model inputs:* $\Lambda = 35$, $\alpha = 0.005$, $\gamma = 0.05$, $\kappa = 0.5$, $\beta = 0.0005$, $\sigma = 0.4$, $\mu = 0.01$, $\mu_1 = 0.075$, $\mu_2 = 0.25$, $\mu_3 = 0.1$, $\tau_1 = 0$, $\tau_2 = 0$, $P_0 = 3000$, $D_0 = 200$, $D_{c0} = 15$, *and* $D_{p0} = 80$, *which give the following particular non-delay case of model* (1)*:*

$$\frac{dP}{dt} = 35 - 0.005P - 0.01P, \tag{43a}$$

$$\frac{dD}{dt} = 0.005P - 0.05D - 0.085D, \tag{43b}$$

$$\frac{dD_c}{dt} = 0.05D - \frac{0.5D_c}{1 + 0.0005D_c} + 0.4D_p - 0.26D_c, \tag{43c}$$

$$\frac{dD_p}{dt} = \frac{0.5D_c}{1 + 0.0005D_c} - 0.51D_p, \tag{43d}$$

with the initial conditions:

$$P(0) = 3000,\ D(0) = 200,\ D_c(0) = 15,\ D_p(0) = 80.$$

We obtain the equilibrium point $T^* = (2333.3333, 86.4198, 11.7670, 11.4688)$. *According to Theorem 1, T^* of system* (43) *is locally asymptotically stable (see Figure 3).*

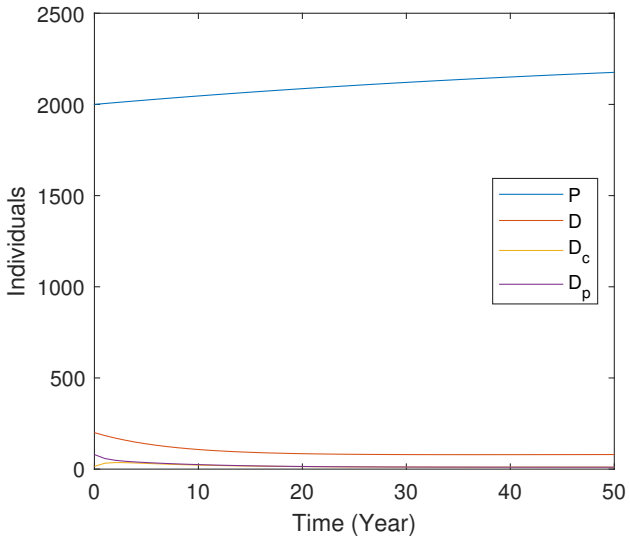

Figure 3. The dynamics of system (43)

Example 2 *Consider the model inputs:* $\Lambda = 35$, $\alpha = 0.005$, $\gamma = 0.05$, $\kappa = 0.5$, $\beta = 0.0005$, $\sigma = 0.4$, $\mu = 0.01$, $\mu_1 = 0.075$, $\mu_2 = 0.25$, $\mu_3 = 0.1$, $\phi_1(\theta) = 3000$, $\phi_2(\theta) = 200$, $D_{c0} = 15$, *and* $D_{p0} = 80$, *which give the following particular case of model* (1)*:*

$$\frac{dP}{dt} = 35 - 0.005P(t - \tau_1) - 0.01P, \tag{44a}$$

$$\frac{dD}{dt} = 0.005P(t - \tau_1) - 0.05D(t - \tau_2) - 0.085D, \tag{44b}$$

$$\frac{dD_c}{dt} = 0.05D(t - \tau_2) - \frac{0.5D_c}{1 + 0.0005D_c} + 0.4D_p - 0.26D_c, \tag{44c}$$

$$\frac{dD_p}{dt} = \frac{0.5D_c}{1 + 0.0005D_c} - 0.51D_p, \tag{44d}$$

with the initial conditions:

$$P(\theta) = 3000,\ \theta \in [-\tau_{\max}, 0],\ D(\theta) = 200,\ D_c(0) = 15,\ D_p(0) = 80.$$

We obtain the equilibrium point $T^* = (2333.3333, 86.4198, 11.7670, 11.4688)$.

We first check the existence of critical value τ_{20} *when* $\tau_1 = 0$. *From Theorem 2, condition (H3) is satisfied because* $b_1 - \gamma = 0.035 \geq 0$. *According to Theorem 2(i), the equilibrium point* T^* *of system (44) with* $\tau_1 = 0$ *is locally asymptotically stable for* $\tau_2 \geq 0$.

Furthermore, for condition (H3) holds, we check the existence of critical value τ_{10} *provided* τ_2 *can be any non-negative value. From Theorem 3 and choosing* $\tau_2 = 13$, *Eq. (30) becomes*

$$\begin{aligned}&\omega_1^4 + 0.0098\omega_1^2 + (7.2938 \times 10^{-7}) + 0.0085(\omega_1^2 + 7.5 \times 10^{-5})\cos 13\omega_1 \\ &- 0.1\omega_1(\omega_1^2 + 7.5 \times 10^{-5})\sin 13\omega_1 = 0.\end{aligned} \tag{45}$$

Eq. (45) has no root, and condition (H5) is satisfied. Thus, from Theorem 3(i), T^* *of system (44) with* τ_2 *can be any non-negative value (in this case,* $\tau_2 = 13$*) is locally asymptotically stable for* $\tau_1 \geq 0$. *Figure 4 shows the dynamics of system (44) with two sets of* τ_1 *and* τ_2*: (i)* $\tau_1 = 15$ *and* $\tau_2 = 13$, *and (ii)* $\tau_1 = 150$ *and* $\tau_2 = 13$.

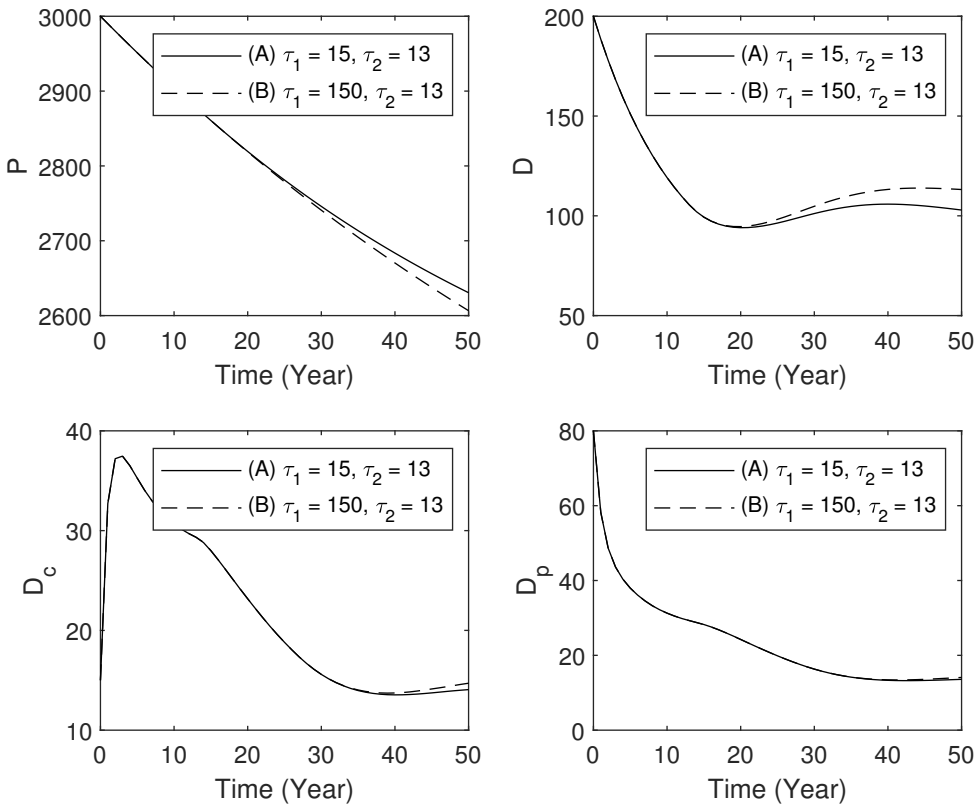

Figure 4. Dynamics of system (44) with: (A) $\tau_1 = 15$ and $\tau_2 = 13$. (B) $\tau_1 = 150$ and $\tau_2 = 13$

When conditions (H3) and (H5) are satisfied, the solution (P, D, D_c, D_p) *converges to* T^* *regardless of the value of* τ_1 *and* τ_2.

Example 3 *Consider the model inputs:* $\Lambda = 35$, $\alpha = 0.125$, $\gamma = 0.05$, $\kappa = 0.5$, $\beta = 0.0005$, $\sigma = 0.4$, $\mu = 0.05$, $\mu_1 = 0.075$, $\mu_2 = 0.25$, $\mu_3 = 0.1$, $\phi_1(\theta) = 300$, $\phi_2(\theta) = 100$, $D_{c0} = 30$, *and* $D_{p0} = 40$, *which give the following particular case of model (1):*

$$\frac{dP}{dt} = 35 - 0.125P(t-\tau_1) - 0.05P, \tag{46a}$$

$$\frac{dD}{dt} = 0.125P(t-\tau_1) - 0.05D(t-\tau_2) - 0.125D, \tag{46b}$$

$$\frac{dD_c}{dt} = 0.05D(t-\tau_2) - \frac{0.5D_c}{1+0.0005D_c} + 0.4D_p - 0.3D_c, \tag{46c}$$

$$\frac{dD_p}{dt} = \frac{0.5D_c}{1+0.0005D_c} - 0.55D_p, \tag{46d}$$

with the initial conditions:

$$P(\theta) = 300,\ \theta \in [-\tau_{\max}, 0],\ D(\theta) = 100,\ D_c(0) = 30,\ D_p(0) = 40.$$

We obtain the equilibrium point $T^* = (200, 142.8571, 16.4108, 14.7975)$.
We first check the existence of critical value τ_{20} *when* $\tau_1 = 0$. *From Theorem 2, condition (H3) is satisfied because* $b_1 - \gamma = 0.075 \geq 0$. *According to Theorem 2(i),* T^* *of system (46) with* $\tau_1 = 0$ *is locally asymptotically stable for* $\tau_2 \geq 0$.
Furthermore, for the condition (H3) holds, we check the existence of critical value τ_{10} *provided* τ_2 *can be any non-negative value. From Theorem 3 and choosing* $\tau_2 = 100$, *Eq. (30) becomes*

$$\begin{aligned}&\omega_1^4 + 0.005\omega_1^2 - (2.3789 \times 10^{-4}) + 0.0125(\omega_1^2 - 0.0131)\cos 100\omega_1 \\ &- 0.1\omega_1(\omega_1^2 - 0.0131)\sin 100\omega_1 = 0.\end{aligned} \tag{47}$$

We obtain one positive root of Eq. (47), which is $\omega_{11} = 0.1146$, *and the condition (H6) is satisfied. Then, we obtain* $\tau_{10} = 17.3030$. *We also satisfy condition (H7), which is* $V_0V_2 + V_1V_3 = 6.1780 \times 10^{-4} > 0$. *From Theorem 3(ii),* T^* *of system (46) with* τ_2 *can be any non-negative value (in this case,* $\tau_2 = 100$*) is locally asymptotically stable when* $\tau_1 \in [0, 17.3030)$, *where the solution* (P, D, D_c, D_p) *converges to* T^* *as time t increases (see Figure 5(A)).*
The equilibrium point T^* *becomes unstable when* $\tau_1 > 17.3030$, *where the solution* (P, D, D_c, D_p) *gets larger and away from* T^* *as time t increases (see Figure 5(B)). System (46) with* τ_2 *can be any non-negative value (in this case,* $\tau_2 = 100$*) undergoes a Hopf bifurcation at* T^* *when* $\tau_1 = 17.3030$, *and a periodic orbit arises from* T^* *(see Figure 5(C)).*

Example 4 *Consider the model inputs:* $\Lambda = 35$, $\alpha = 0.005$, $\gamma = 0.175$, $\kappa = 0.5$, $\beta = 0.0005$, $\sigma = 0.4$, $\mu = 0.05$, $\mu_1 = 0.075$, $\mu_2 = 0.25$, $\mu_3 = 0.1$, $\phi_1(\theta) = 550$, $\phi_2(\theta) = 10$, $D_{c0} = 35$, *and* $D_{p0} = 20$, *which give the following particular case of model (1):*

$$\frac{dP}{dt} = 35 - 0.005P(t-\tau_1) - 0.05P, \tag{48a}$$

$$\frac{dD}{dt} = 0.005P(t-\tau_1) - 0.175D(t-\tau_2) - 0.125D, \tag{48b}$$

$$\frac{dD_c}{dt} = 0.175D(t-\tau_2) - \frac{0.5D_c}{1+0.0005D_c} + 0.4D_p - 0.3D_c, \tag{48c}$$

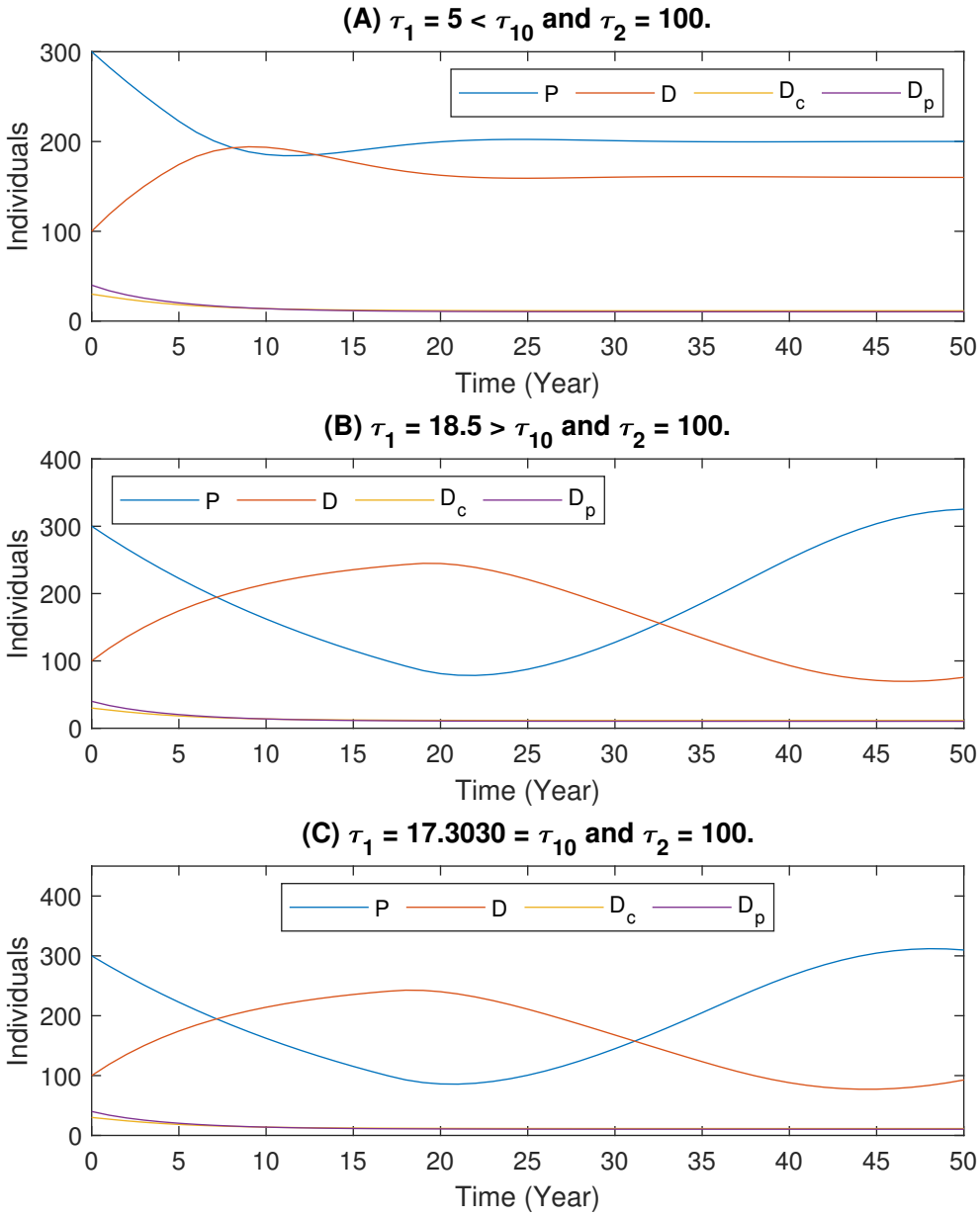

Figure 5. When τ_2 can be any non-negative value (in this case, $\tau_2 = 100$): (A) The equilibrium point T^* of system (46) is locally asymptotically stable for $\tau_1 = 5 < \tau_{10}$. (B) T^* is unstable for $\tau_1 = 18.5 > \tau_{10}$. (C) System (46) undergoes a Hopf bifurcation at $\tau_1 = 17.3030 = \tau_{10}$

$$\frac{dD_p}{dt} = \frac{0.5D_c}{1 + 0.0005D_c} - 0.55D_p, \tag{48d}$$

with the initial conditions:

$$P(\theta) = 550,\ \theta \in [-\tau_{\max}, 0],\ D(\theta) = 10,\ D_c(0) = 35,\ D_p(0) = 20.$$

We obtain the equilibrium point $T^* = (636.3636, 10.6061, 4.2563, 3.8611)$.

We first check the existence of critical value τ_{20} when $\tau_1 = 0$. From Theorem 2, condition (H4) is satisfied because $b_1 - \gamma = -0.05 < 0$. Then, we obtain $\tau_{20} = 19.3216$. By Theorem 2(ii), the equilibrium point T^* of system (48) with $\tau_1 = 0$ is locally asymptotically stable when $\tau_2 \in [0, 19.3216)$, where the solution converges to T^* as time t increases (see Figure 6(A)).

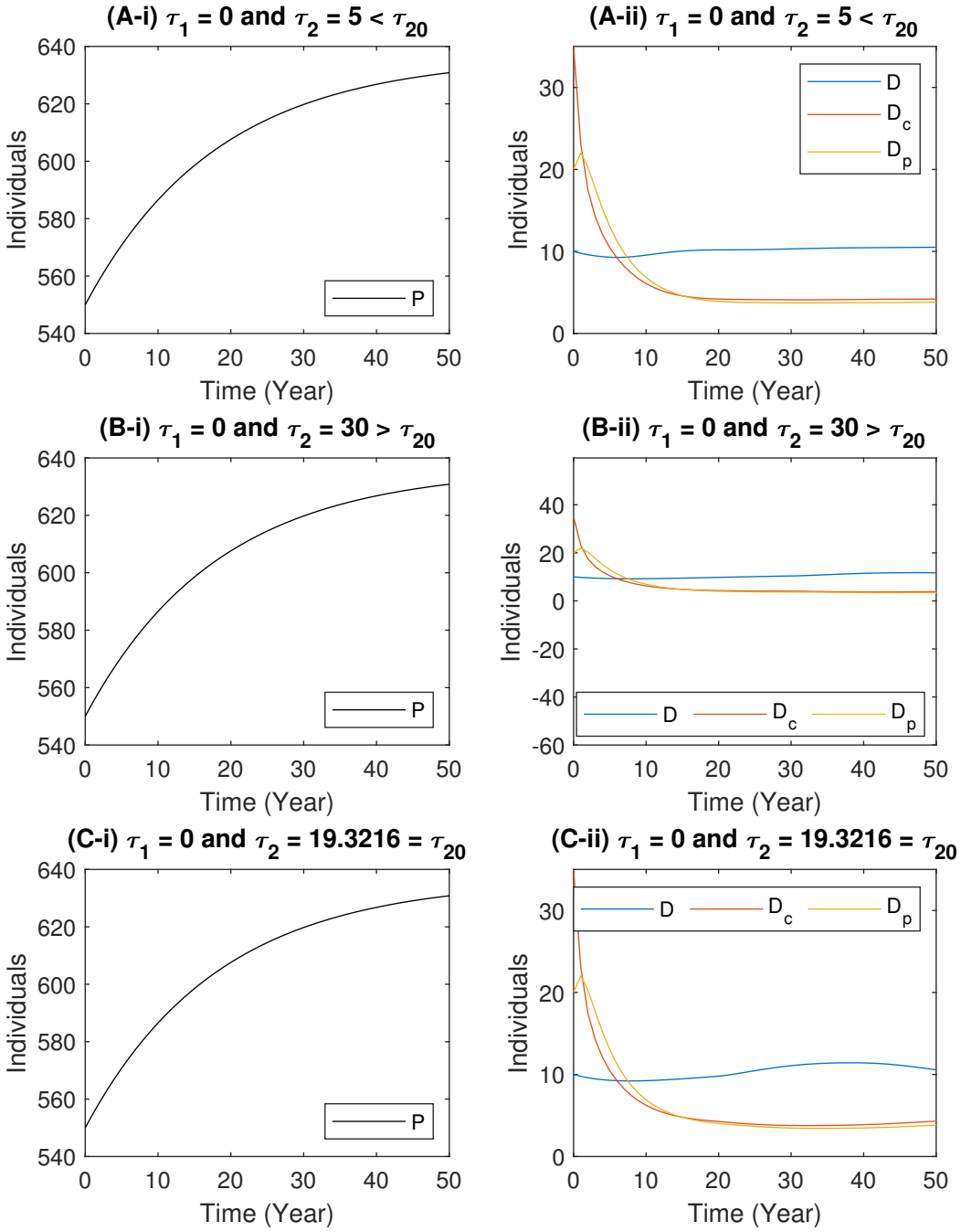

Figure 6. For system (48) with $\tau_1 = 0$: (A) The equilibrium point T^* is locally asymptotically stable for $\tau_2 = 5 < \tau_{20}$. (B) T^* is unstable for $\tau_2 = 30 > \tau_{20}$. (C) System (48) undergoes a Hopf bifurcation when $\tau_2 = 19.3216 = \tau_{20}$

T^* becomes unstable when $\tau_2 > 19.3216$, where the solutions D, D_c, and D_p move away from the equilibrium solutions D^*, D_c^*, and D_p^*, respectively, as time t increases (see Figure 6(B)). System (48) with $\tau_1 = 0$ undergoes a Hopf bifurcation when $\tau_2 = 19.3216$, where the solutions D, D_c, and D_p show periodic behaviors (see Figure 6(C)).
Notice that the solution P for Figure 6(B–C) does not oscillate like the other variables. The differential equation of P (Eq. (1a)) is unaffected by D, D_c, and D_p. Hence, the oscillation of other variables does not affect P since if $\tau_1 = 0$, P is locally asymptotically stable (see Remark 4). On the contrary, if the solution P has an oscillating behavior, the other variables will also oscillate.

Remark 4 Recall Eq. (1a),

$$\frac{dP}{dt} = \Lambda - \alpha P(t-\tau_1) - \mu P. \tag{49}$$

The characteristic equation that associated with the equilibrium solution P^* of Eq. (49) is given by:

$$\lambda_6 + \mu + e^{-\lambda_6 \tau_1}\alpha = 0, \tag{50}$$

where λ_6 represents the eigenvalues. For the case of $\tau_1 = 0$, Eq. (50) has a negative root given by $-(\mu+\alpha)$. Hence, P^* of Eq. (49) with $\tau_1 = 0$ is locally asymptotically stable. This is the reason the solution P in Figure 6(B, C) does not oscillate even though τ_2 is not within its stable region. Apart from this, we discuss the case of $\tau_1 > 0$. Assume that $\lambda_6 = i\hat{\omega}$ ($i = \sqrt{-1}$ and $\hat{\omega} > 0$) is one of the roots of Eq. (50). By substituting $\lambda_6 = i\hat{\omega}$ into Eq. (50) and after some algebraic manipulations, we obtain $\hat{\omega} = \sqrt{(\alpha+\mu)(\alpha-\mu)}$. If $\alpha \leq \mu$, a contradiction occurs because we initially assumed $\hat{\omega} > 0$ and P^* is locally asymptotically stable for $\tau_1 \geq 0$. However, P^* loses its stability for some values of $\tau_1 > 0$ if $\alpha > \mu$.

Next, for the condition (H4) holds, we check the existence of critical value τ_{10} provided τ_2 is within $[0, 19.3216)$. From Theorem 3 and choosing $\tau_2 = 5 \in [0, 19.3216)$, Eq. (30) becomes

$$\begin{aligned}&\omega_1^4 + 0.0487\omega_1^2 + (1.1447 \times 10^{-4}) + 0.0438(\omega_1^2 + 0.0025)\cos 5\omega_1 \\ &- 0.35\omega_1(\omega_1^2 - 0.0025)\sin 5\omega_1 = 0.\end{aligned} \tag{51}$$

Eq. (51) has no root, and condition (H5) is satisfied. From Theorem 3(i), the equilibrium point T^* of system (48) with τ_2 within its stable region (in this case, $\tau_2 = 5 \in [0, 19.3216)$) is locally asymptotically stable for $\tau_1 \geq 0$. Figure 7 shows two simulations of two different values of τ_1 ($\tau_1 = 7$ and $\tau_1 = 87$) with $\tau_2 = 5 \in [0, 19.3216)$. In both figures, the solution (P, D, D_c, D_p) converges to T^* regardless of the value of τ_1.

Example 5 *Consider the model inputs: $\Lambda = 35$, $\alpha = 0.125$, $\gamma = 0.175$, $\kappa = 0.5$, $\beta = 0.0005$, $\sigma = 0.4$, $\mu = 0.05$, $\mu_1 = 0.075$, $\mu_2 = 0.25$, $\mu_3 = 0.1$, $\phi_1(\theta) = 60$, $\phi_2(\theta) = 10$, $D_{c0} = 40$, and $D_{p0} = 20$, which give the following particular case of model (1):*

$$\frac{dP}{dt} = 35 - 0.125P(t-\tau_1) - 0.05P, \tag{52a}$$

$$\frac{dD}{dt} = 0.125P(t-\tau_1) - 0.175D(t-\tau_2) - 0.125D, \tag{52b}$$

$$\frac{dD_c}{dt} = 0.175D(t-\tau_2) - \frac{0.5D_c}{1+0.0005D_c} + 0.4D_p - 0.3D_c, \tag{52c}$$

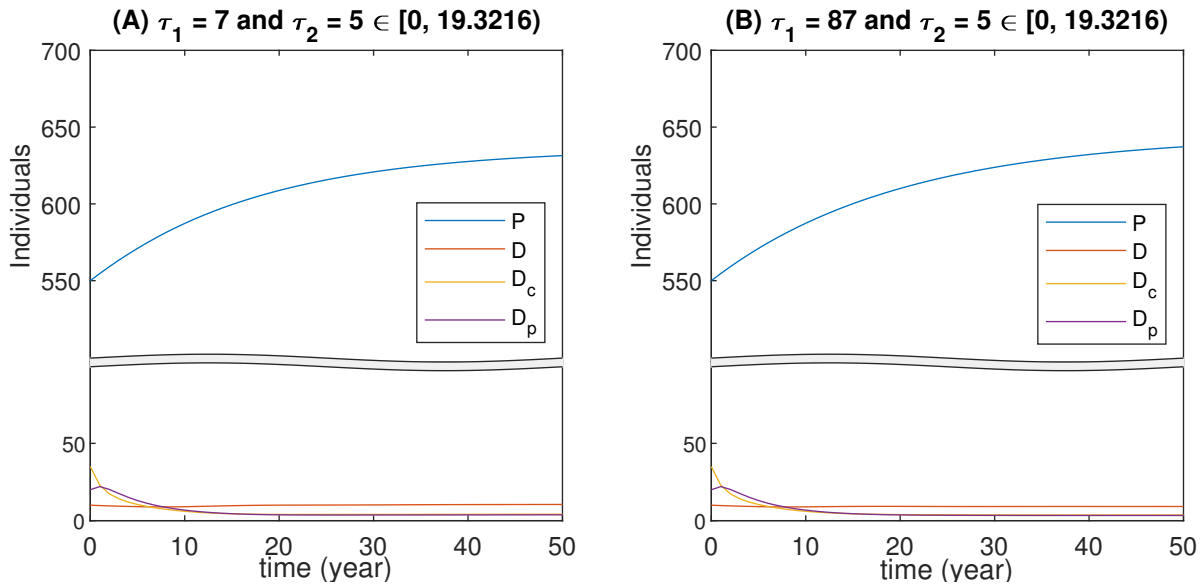

Figure 7. Dynamics of system (48) when τ_2 is within its stable region (in this case, $\tau_2 = 5 \in [0, 19.3216)$): (A) $\tau_1 = 7$. (B) $\tau_1 = 87$

$$\frac{dD_p}{dt} = \frac{0.5D_c}{1 + 0.0005D_c} - 0.55D_p, \tag{52d}$$

with the initial conditions:

$$P(\theta) = 60,\ \theta \in [-\tau_{\max}, 0],\ D(\theta) = 10,\ D_c(0) = 40,\ D_p(0) = 20.$$

We obtain the equilibrium point $T^* = (200, 83.3333, 33.5936, 30.0351)$.
We first check the existence of critical value τ_{20} *when* $\tau_1 = 0$. *From Theorem 2, condition (H4) is satisfied because* $b_1 - \gamma = -0.05 < 0$. *We obtain* $\tau_{20} = 19.3216$. *By Theorem 2(ii), the equilibrium point* T^* *of system (52) with* $\tau_1 = 0$ *is locally asymptotically stable when* $\tau_2 \in [0, 19.3216)$ *and becomes unstable when* $\tau_2 > 19.3216$. *System (52) with* $\tau_1 = 0$ *undergoes a Hopf bifurcation when* $\tau_2 = 19.3216$. *The corresponding plots and trajectories have similar characteristics as in Figure 6.*
Furthermore, for the condition (H4) holds, we check the existence of critical value τ_{10} *provided* τ_2 *is within* $[0, 19.3216)$. *From Theorem 3 and choosing* $\tau_2 = 4 \in [0, 19.3216)$, *Eq. (30) becomes*

$$\begin{aligned}&\omega_1^4 + 0.0331\omega_1^2 - (6.0703 \times 10^{-4}) + 0.0438(\omega_1^2 - 0.0131)\cos 4\omega_1 \\ &- 0.35\omega_1(\omega_1^2 - 0.0131)\sin 4\omega_1 = 0.\end{aligned} \tag{53}$$

The positive root of Eq. (53) is $\omega_{11} = 0.1146$ *and the condition (H6) is satisfied. Then, we obtain* $\tau_{10} = 17.3030$. *We also satisfy the condition (H7), which is* $V_0V_2 + V_1V_3 = 0.0011 > 0$. *From Theorem 3(ii), the equilibrium point* T^* *of system (52) with* τ_2 *within its stable region (in this case,* $\tau_2 = 4 \in [0, 19.3216)$*) is locally asymptotically stable when* $\tau_1 \in [0, 17.3030)$, *where the solution* (P, D, D_c, D_p) *converges to* T^* *as time* t *increases (see Figure 8(A)).* T^* *becomes unstable when* $\tau_1 > 17.3030$, *where the solution* (P, D, D_c, D_p) *gets larger and moves away from* T^* *as time* t *increases (see Figure 8(B)). System (52) with* τ_2 *within its stable region (in this case,* $\tau_2 = 4 \in [0, 19.3216)$*) undergoes a Hopf bifurcation when* $\tau_1 = 17.3030$, *that is, a periodic orbit arises from* T^* *(see Figure 8(C)).*

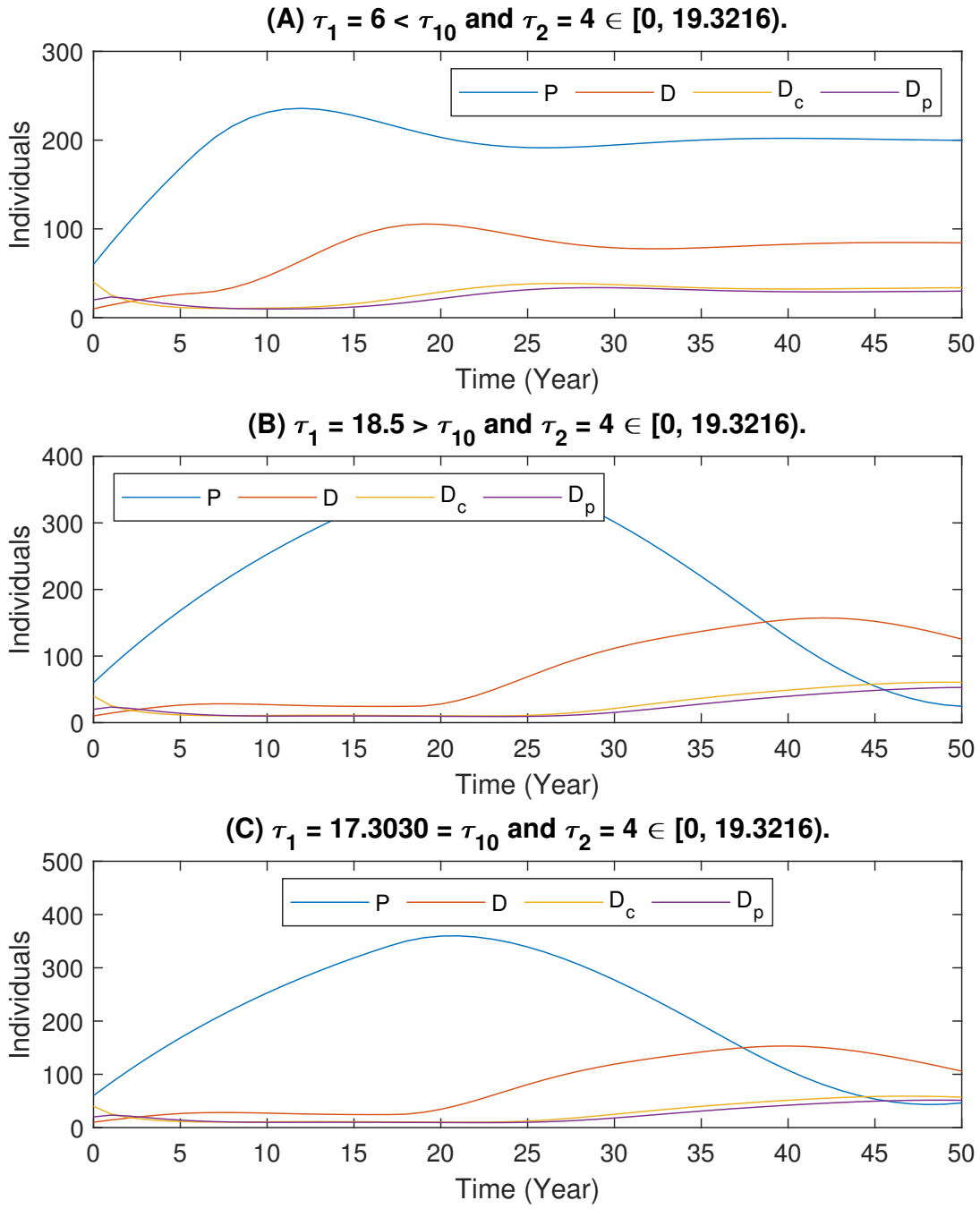

Figure 8. Dynamics of system (52) with τ_2 within its stable region (in this case, $\tau_2 = 4 \in [0, 19.3216)$): (A) The equilibrium point T^* is locally asymptotically stable for $\tau_1 = 6 < \tau_{10}$. (B) T^* is unstable for $\tau_1 = 18.5 > \tau_{10}$. (C) System (52) undergoes a Hopf bifurcation when $\tau_1 = 17.3030 = \tau_{10}$

Simulation with respect to the model inputs in Table 2

Stability of T^*

Based on the values in Table 2, the corresponding equilibrium point of model (1) is $T^* = (1.9751 \times 10^7, 9.4193 \times 10^5, 7.4153 \times 10^6, 1.2005 \times 10^6)$. Accordingly, from the discussion in Section 4, we

first set $\tau_1 = 0$ and look at the range of τ_2 for which T^* remains locally asymptotically stable. Condition (H4) of Theorem 2 is satisfied. We obtain the critical value $\tau_{20} = 16.7073$, where the switching stability occurs at $\tau_2 = \tau_{20}$. Note that from Table 2, we have $\tau_2 = 5$, which is within the stable region. We proceed with finding the critical value for the delay τ_1. Then, we obtain that condition (H5) of Theorem 3 is satisfied. From Theorem 3(i), T^* is locally asymptotically stable (see Figure 9).

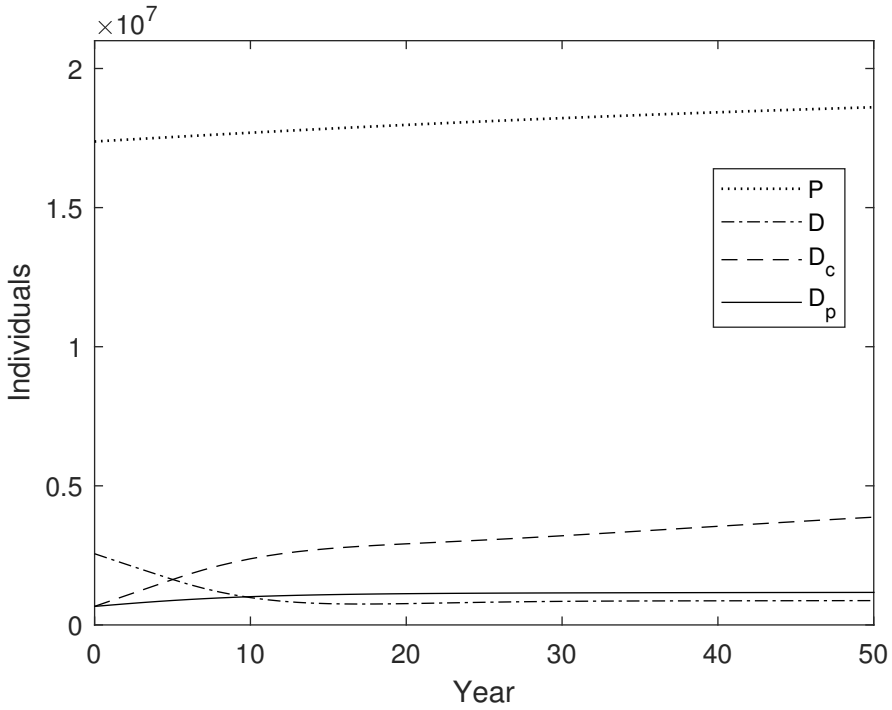

Figure 9. Dynamics of model (1) with the values in Table 2

From Figure 9, we may observe that the solution (P, D, D_c, D_p) approaches T^* as time t gets larger. If this tendency is left untreated, the number of diabetics with complications (D_c) would grow and approach D_c^* at the long-term simulation. This situation should be avoided because a large number of diabetics with complications (D_c) will slow down the recovery rate of complications as many are waiting for their turn to get appropriate treatment. This situation should be avoided because the medical team will be stressed and face some difficulties in handling this overcrowded situation.

Simulation with various α, γ, σ, and β

From the sensitivity analysis results (Section 5), we suggest lowering the diabetes incidence rate (α) to curb the overall diabetes cases. Figure 10 shows that by decreasing α, the number of non-diabetics increases significantly while all the diabetic subpopulations decrease.

The intervention is by increasing the awareness among non-diabetics about the severity of diabetes. Consequently, it may decrease the rate of developing diabetes (α).

Second, we suggest decreasing the rate of the first incidence of complication (γ) and the recurrence rate of complications (σ) in order to decrease the number of diabetics with complications. Figure 11 shows the simulations of decreasing values of γ and σ where the number of diabetics with complications (D_c) decreases to a much lower level.

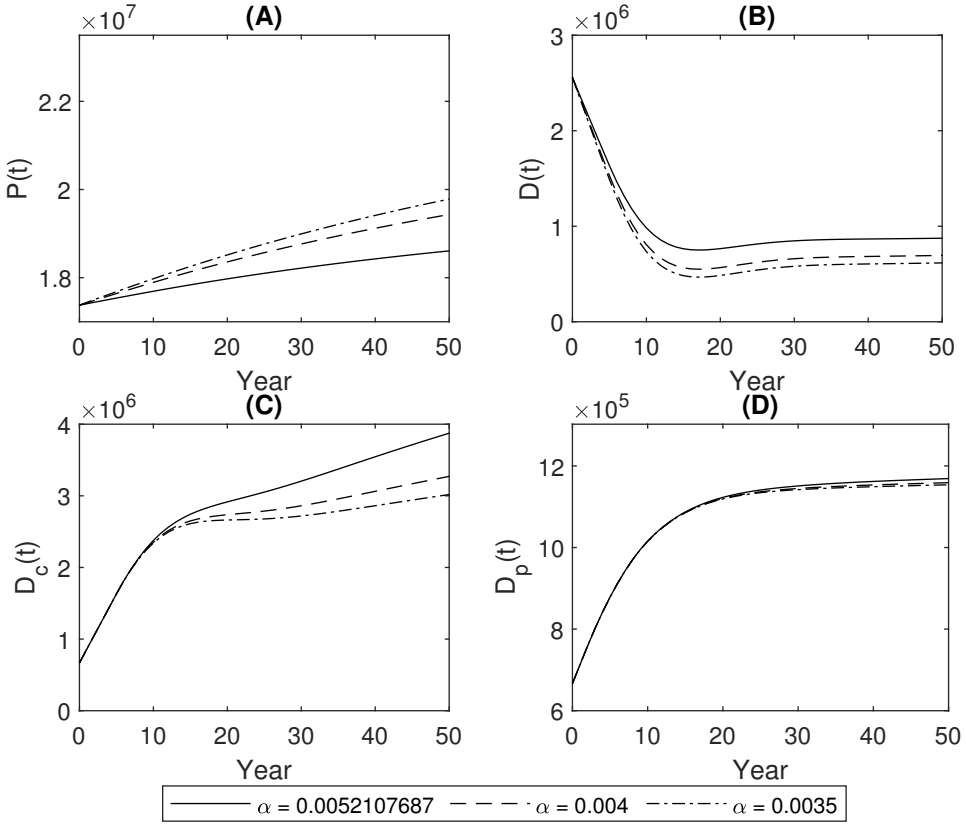

Figure 10. Simulation of model (1) with different rates of developing diabetes (α) ($\alpha = 0.0052108$, $\alpha = 0.004$, and $\alpha = 0.0035$) with the other model inputs in Table 2

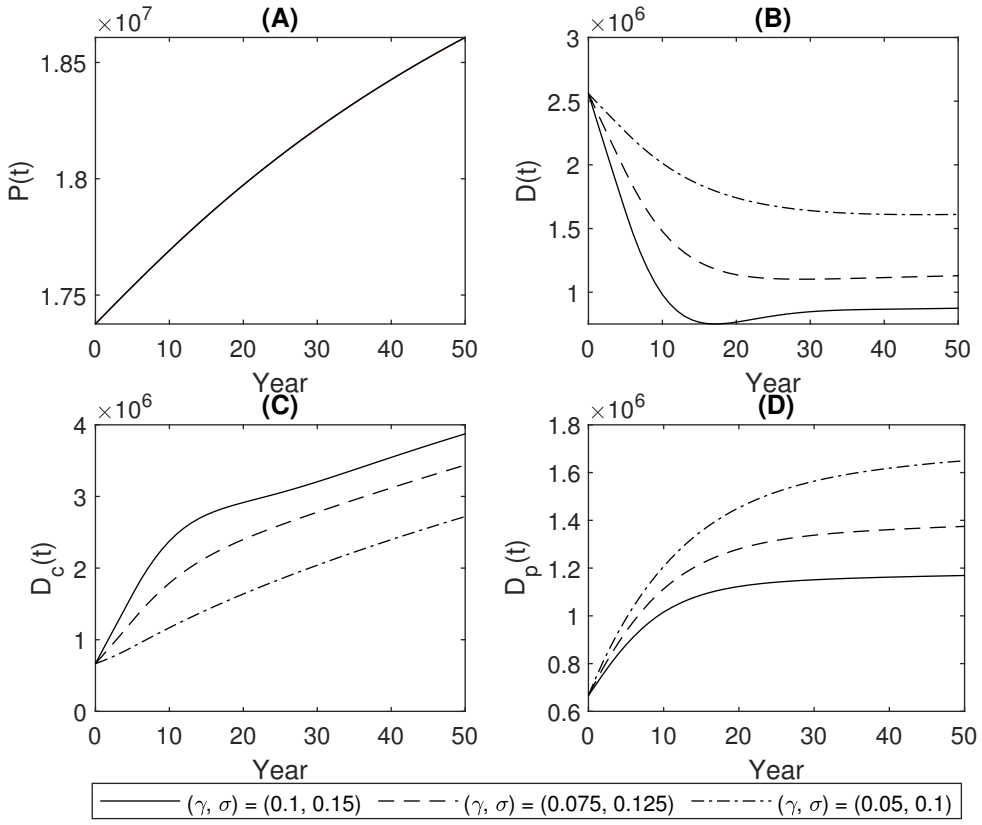

Figure 11. Simulation of model (1) with different values of the first and recurrence incidence of complications (γ,σ) ($(\gamma,\sigma) = (0.1, 0.15)$, $(\gamma,\sigma) = (0.075, 0.125)$, and $(\gamma,\sigma) = (0.05, 0.1)$) with the other model inputs in Table 2

Note that no changes can be observed in Figure 11(A) because the dynamics of non-diabetics (P) are unaffected by γ and σ. The interventions to decrease the rate of developing complications may include early detection of diabetes, education about the complications of diabetes, better self-management of diabetes, lifestyle modifications, and support from family members.

Lastly, we suggest decreasing the effect due to limited medical resources (β). Figure 12 shows the simulation of decreasing value of β.

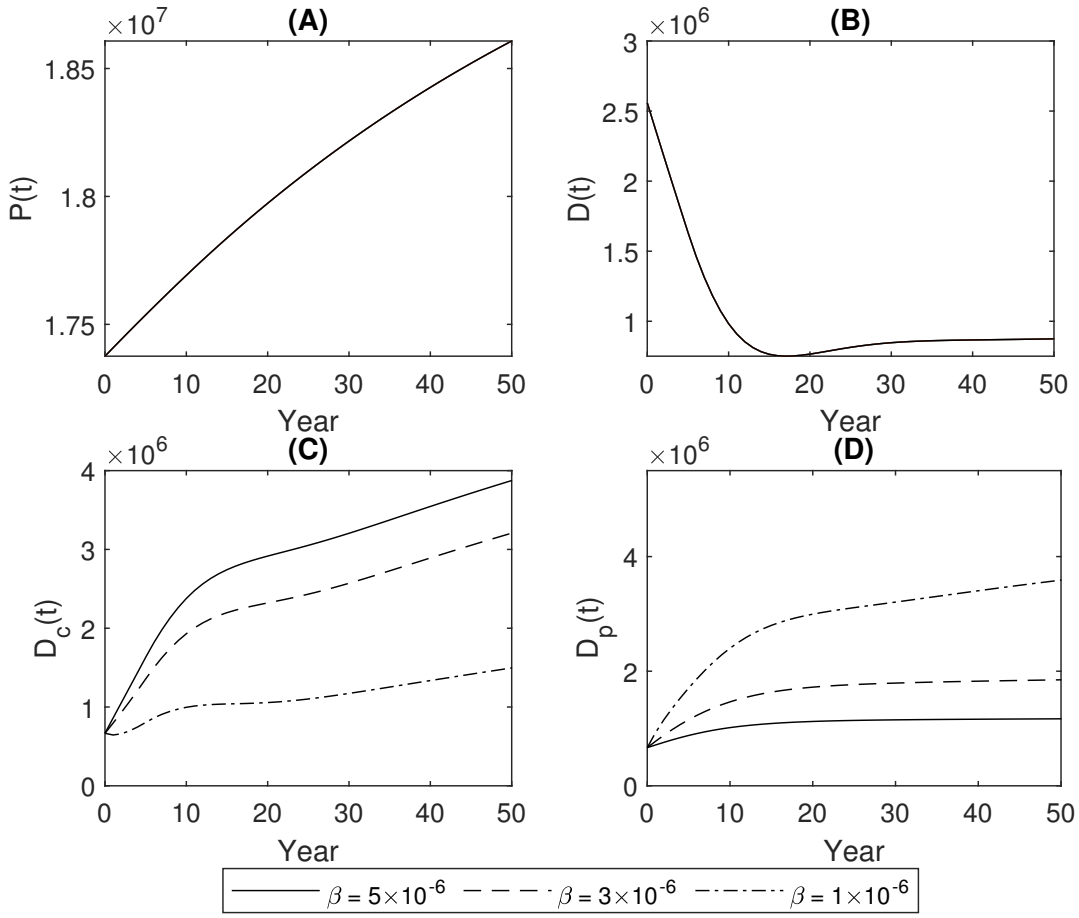

Figure 12. Simulation of model (1) using different values of the inhibition effect (β) ($\beta = 5 \times 10^{-6}$, $\beta = 3 \times 10^{-6}$, and $\beta = 1 \times 10^{-6}$) with the other model inputs in Table 2

Note that no changes can be observed in Figure 12(A–B) because the dynamics of P and D are unaffected by β. As the effect due to limited medical resources (β) decreases, the number of diabetics with complications (D_c) decreases and persists at a much lower level, while the number of diabetics with recovered complications (D_p) increases and persists at a much higher level. To decrease the effect of limited medical resources (β), we recommend providing adequate resources for the treatment of diabetes complications.

Influence of incidence rate of diabetes (α) on Hopf bifurcation corresponds to the time delay τ_1

From Remark 4, the indicator for the equilibrium point T^* of the delay model (1) to lose its stability for some $\tau_1 > 0$ is $\alpha > \mu$. Hence, we investigate the variation of the critical value of time delay τ_{10} (Eq. (31)) with respect to the various rates of incidence of diabetes (α). For the model inputs given in Table 2 and choosing $\alpha \in [0.01, 0.99]$, we plot the stable and unstable regions in Figure 13.

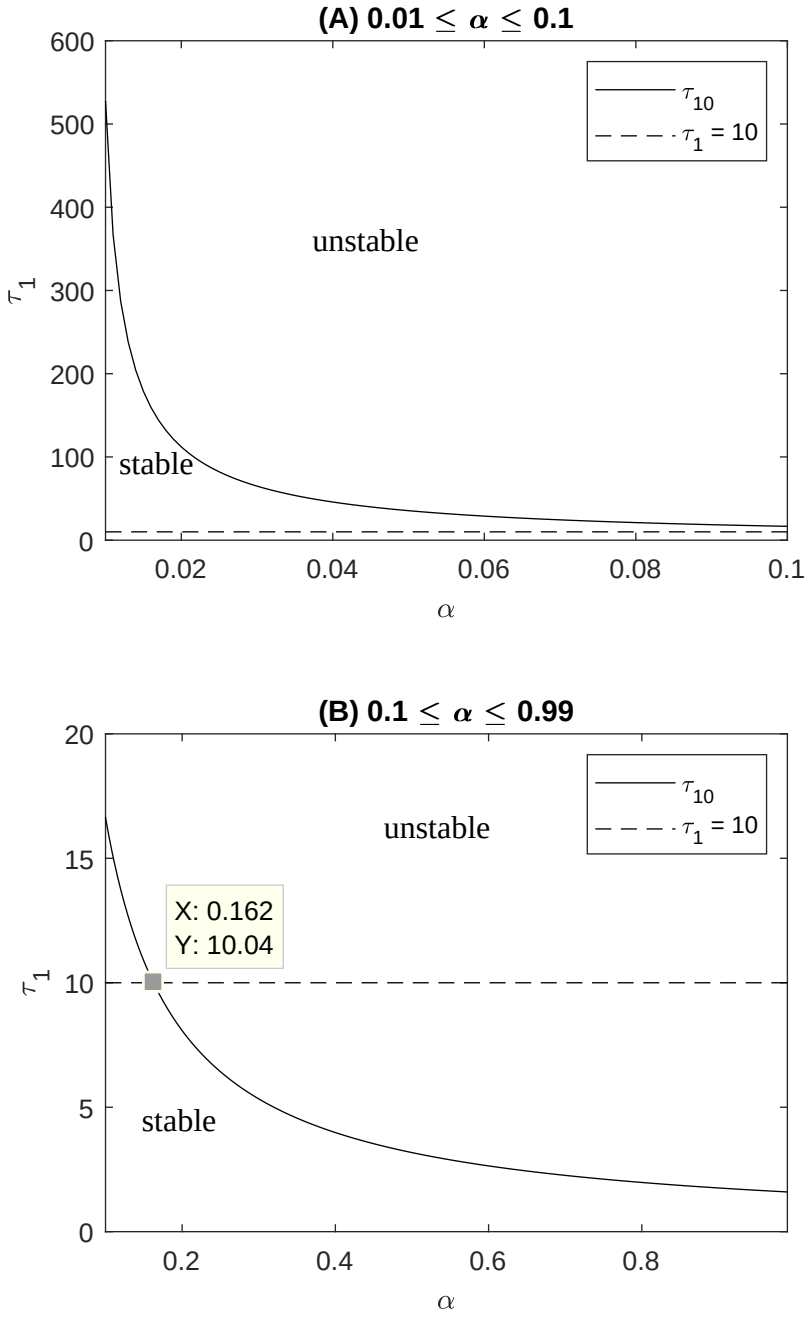

Figure 13. Graph of τ_1 versus α showing the stable and unstable regions of model (1) with the other model inputs in Table 2 (the dashed line represents the line $\tau_1 = 10$)

This figure shows the minimum value of α so that the equilibrium point T^* of model (1) remains locally asymptotically stable. This variation shows that the higher incidence rate of diabetes (α) results in a lower critical value τ_{10}. If the rate $\alpha > 0.162$ year^{-1}, then the solution (P, D, D_c, D_p) of model (1) will show unstable behaviors because $\tau_1 = 10 > \tau_{10}$ (see Figure 13(B)). Sometimes the number of diabetics is high and sometimes low. In this case, it may be difficult to predict the size of every subpopulation. Consequently, implementing control measures to lower diabetes cases will be difficult. If we wish to predict the number of diabetics, the incidence rate of diabetes (α) should be no more than 0.162 year^{-1} for the other model inputs in Table 2.

7 Conclusion

In this paper, we studied a four-state model of a type-2 diabetic population with a saturating recovery rate of diabetes complications. We first investigated the non-negativity and boundedness of the solution for delay and non-delay cases. However, the non-negativity of the solutions P, D, D_c, and D_p of the delay model (1) can only be guaranteed if the model inputs satisfy the conditions stated in Proposition 2.
In the absence of time delay, we discussed the local and global stability analysis. Numerical simulation to indicate the global stability of the non-delay model was given. In the presence of two delay parameters, we discussed the characteristic equation of delay model (1) under the case of $\tau_1 = 0$ to obtain the stable region of τ_2. After that, we derived the critical value corresponding to the delay parameter τ_1. Overall, we have five conditions (H3)-(H7) to characterize the stability properties of T^* (either locally asymptotically stable or unstable) and the manifestation of Hopf bifurcation. The delay values affect the stability of the equilibrium point T^*. A locally asymptotically stable equilibrium point T^* can become unstable under certain conditions. We have shown examples of a periodic orbit that arises from T^* as the model switches its stability.
From the sensitivity analysis, we give three conclusions as follows:

1. We may significantly reduce the overall diabetes cases by decreasing the rate of developing diabetes (α). This includes education on diabetes and the implementation of awareness programs.

2. Diabetes screening should continue so that the status of diabetes can be known earlier. Consequently, medications assist individuals with diabetes in controlling their glucose levels, and the rate of the first incidence of complication (γ) may decrease.

3. We may increase the availability of the treatment of complications for the diabetics with complications, as our sensitivity indices suggested that the diabetics with complications will decrease if the parameter (β) measuring the limited medical resources gets smaller. This concerns diabetics with complications receiving better treatment of the complications such as the improvement or shortening of waiting time for elective cases such as renal or heart transplant.

Declarations

Use of AI tools

The authors declare that they have not used Artificial Intelligence (AI) tools in the creation of this article.

Data availability statement

No Data associated with the manuscript.

Ethical approval (optional)

The authors state that this research complies with ethical standards. This research does not involve either human participants or animals.

Consent for publication

Not applicable

Conflicts of interest

The authors declare that they have no conflict of interest.

Funding

The research was supported by the Ministry of Higher Education, Malaysia, through Fundamental Research Grant Scheme 59523 (FRGS/1/2018/STG06/UMT/02/2).

Author's contributions

H.N.: Conceptualization, Methodology, Software, Formal Analysis, Investigation, Writing - Original Draft, Writing - Review & Editing, Visualization. A.A.M.D.: Conceptualization, Methodology, Formal Analysis, Investigation, Resources, Writing - Original Draft, Writing - Review & Editing, Supervision, Project Administration, Funding Acquisition. All authors have read and agreed to the published version of the manuscript.

Acknowledgements

Not applicable

References

[1] IDF Diabetes Atlas, IDF Diabetes Atlas 2021, (2021). https://diabetesatlas.org/atlas/tenth-edition/

[2] National Health and Morbidity Survey 2019, NCDs–Non-Communicable Diseases: Risk Factors and other Health Problems, (2011). https://iku.gov.my/images/IKU/Document/REPORT/NHMS2019/Report_NHMS2019-NCD_v2.pdf

[3] IDF Diabetes Atlas, Malaysia Diabetes Report 2000-2045, (2021). https://www.diabetesatlas.org/data/en/country/120/my.html

[4] Mat Daud, A.A., Toh, C.Q. and Saidun, S. Development and analysis of a mathematical model for the population dynamics of Diabetes Mellitus during pregnancy. *Mathematical Models and Computer Simulations*, 12, 620-630, (2020). [CrossRef]

[5] Nasir, H. and Mat Daud, A.A. Population models of diabetes mellitus by ordinary differential equations: a review. *Mathematical Population Studies*, 29(3), 95-127, (2022). [CrossRef]

[6] Mat Daud, A.A., Toh, C.Q. and Saidun, S. A mathematical model to study the population dynamics of hypertensive disorders during pregnancy. *Journal of Interdisciplinary Mathematics*, 22(4), 433-450, (2019). [CrossRef]

[7] Mat Daud, A.A. Mathematical modeling and stability analysis of population dynamics. In Proceedings, *Dynamical Systems, Bifurcation Analysis and Applications (DySBA 2018)*, pp. 3-13, Penang, Malaysia, (2018, August). [CrossRef]

[8] Mat Daud, A.A., Toh, C.Q. and Saidun, S. Mathematical modeling and analysis of anemia during pregnancy and postpartum. *Theory in Biosciences*, 140, 87-95, (2021). [CrossRef]

[9] Nasir, H. Hopf bifurcation analysis for a diabetic population model with two delays and saturated treatment. *Physica Scripta*, 96, 125013, (2021). [CrossRef]

[10] Khetan, A.K. and Rajagopalan, S. Prediabetes. *Canadian Journal of Cardiology*, 34(5), 615-623, (2018). [CrossRef]

[11] IDF Diabetes Atlas, Diabetes around the world in 2021, (2021). https://www.diabetesatlas.org/en/

[12] Gómez-Peralta, F., Abreu, C., Cos, X. and Gómez-Huelgas, R. When does diabetes start? Early detection and intervention in type 2 diabetes mellitus. *Revista Clínica Española (English Edition)*, 220(5), 305-314, (2020). [CrossRef]

[13] National Diabetes Registry, National Diabetes Registry Report 2013-2019, (2020). https://www.moh.gov.my/moh/resources/Penerbitan/Rujukan/NCD/Diabetes/National_Diabetes_Registry_Report_2013-2019_26082021.pdf

[14] Zhang, X. and Liu, X. Backward bifurcation of an epidemic model with saturated treatment function. *Journal of Mathematical Analysis and Applications*, 348(1), 433-443, (2008). [CrossRef]

[15] Krebs, C.J. Some historical thoughts on the functional responses of predators to prey density. *Frontiers in Ecology and Evolution*, 10, 1052289, (2022). [CrossRef]

[16] Nasir, H. and Mat Daud, A.A. Dynamics of a three-state diabetic population model with a time delay and limited medical resources. *Submitted*.

[17] Allen, L.J.S. *An Introduction to Mathematical Biology*. Pearson/Prentice Hall: Italy, (2007).

[18] Tan, K.P. and Mat Daud, A.A. Modelling and qualitative analysis of an illicit drugs model with saturated incidence rate and relapse. *Journal of Mathematics and Computer Science*, 28(4), 373-392, (2023). [CrossRef]

[19] Smith, H. *An Introduction to Delay Differential Equations with Applications to the Life Sciences* (Vol. 57). Springer: New York, (2011).

[20] Zi, Z. Sensitivity analysis approaches applied to systems biology models. *IET Systems Biology*, 5(6), 336-346, (2011). [CrossRef]

[21] Nasir, H. and Mat Daud, A.A. Sensitivity analysis based on the direct differential method for dynamical systems with discrete delays. *AIP Conference Proceedings*, 2905(1), 030016, (2024). [CrossRef]

[22] Rihan, F.A. Sensitivity analysis for dynamic systems with time-lags. *Journal of Computational and Applied Mathematics*, 151(2), 445-462, (2003). [CrossRef]

Mathematical Modelling and Numerical Simulation with Applications (MMNSA)
(https://dergipark.org.tr/en/pub/mmnsa)

How to cite this article: Nasir, H. & Mat Daud, A.A. (2025). Global dynamics and sensitivity analysis of a diabetic population model with two-time delays. *Mathematical Modelling and Numerical Simulation with Applications*, 5(1), 198-233. https://doi.org/10.53391/mmnsa.1545744

Mathematical Modelling and Numerical Simulation with Applications, 2025, 5(1), 234–256

https://dergipark.org.tr/en/pub/mmnsa

ISSN Online: 2791-8564 / Open Access

https://doi.org/10.53391/mmnsa.1540240

RESEARCH PAPER

Economic resilience in the face of pandemic: a holistic mathematical analysis of the pandemic in India

Amit Thakuria [1,‡], **Anshuman Mridul Sharma** [1,‡], **Nainvi Chothwani** [1,‡], **Arkaprovo Chakraborty** [1,‡] **and Pundikala Veeresha** [1,*,‡]

[1]Department of Mathematics, CHRIST University, 560029 Bengaluru, India

*Corresponding Author

‡amit.thakuria@ems.christuniversity.in (Amit Thakuria); anshuman.sharma@ems.christuniversity.in (Anshuman Mridul Sharma); nainvi.chothwani@ems.christuniversity.in (Nainvi Chothwani); arkaprovo.chakraborty@res.christuniversity.in (Arkaprovo Chakraborty); pundikala.veeresha@christuniversity.in (Pundikala Veeresha)

Abstract

COVID-19 was initiated in 2020 and caused an immediate threat to global countries in terms of both economic and health influences. In this present work, we extend the Susceptible-Infected-Recovered (SIR) model by considering two new variables, gross domestic product or GDP (G) and unemployment (U), to study the impact of this epidemic on the Indian economy during the 2020–2023 period. Since our extended SIR model includes two novel compartments, which are GDP and unemployment rate, we can now explore in more detail the sophisticated relationship between health and economic matters. The framework allows us to investigate the following consequences: how changes in the infection rate affect the economy and how changes in GDP and unemployment translate into the spread of this contagion. These visualizations are based on real-time quarterly data and provide full knowledge of the interaction between health and economic dynamics during the COVID-19 crisis in India. Government initiatives and regulations are also reviewed for their efficiency to contain the virus while taming the economic cost. Real-world results are contrasted with the care to find the strengths and weaknesses of the policies that come out with the underlying assumptions in the model. This paper, in other words, deploys an in-depth analysis of the convoluted links between economics, policy, and public health in the face of a pandemic with a geographic focus in India.

Keywords: GDP; COVID-19; unemployment; epidemic model; stability analysis

AMS 2020 Classification: 65L05; 92-10; 97M10; 97M40

1 Introduction

The economic blow caused by the pandemic was not limited to formal sectors but equally aggravated the informal economy, which employs the majority of the Indian workforce. The lockdown

➤ **Received:** 29.08.2024 ➤ **Revised:** 14.02.2025 ➤ **Accepted:** 20.02.2025 ➤ **Published:** 31.03.2025

measures, though helpful in reducing the spread of the virus, led to a significant loss of income for many informal workers, pushing them towards poverty [1]. The pandemic also highlighted the importance of digitization, as those who could access digital platforms were able to continue working, while others faced severe livelihood challenges [2]. In response, the Indian government implemented various measures, including direct cash transfers, food security initiatives, and credit guarantees, to support the economy. However, the effectiveness of these measures in mitigating the economic downturn remains a subject of ongoing analysis [3].

Epidemiological and economic models have been studied for the multifaceted impacts of pandemics [4–7]. For example, Chakraborty and Maity (2020) [8] investigated the economic implications of lockdowns and highlighted that health and economic variables must be modeled simultaneously in order to formulate effective policy interventions [9]. Mishra et al. (2021) [10] pointed out the importance of nonlinear dynamics in such models by applying advanced mathematical methods to explore the long-term interplay between public health crises and economic stability [11]. Moreover, a recent study by Singh et al. (2023) [12] offered empirical evidence regarding the effectiveness of government measures in reducing economic shocks during pandemics, especially in informal economies [13]. The role of numerical methods such as RK-4 in solving complex epidemiological-economic models has also been emphasized, as it allows for the precise simulation of the nonlinear interdependencies. Based on these fundamentals, the current research contributes to the field by formulating a new SIRUG model, integrating unemployment and GDP dynamics in an epidemiological context, utilizing RK-4 and least-square methods to predict and analyze economic consequences of pandemics more holistically.

In this study, we use the Runge-Kutta 4th order method (RK-4) [14] to solve our equations. This method helps us get more accurate results than basic calculation methods because it looks at multiple points when solving each step. RK-4 is especially good at handling sudden changes, like when a pandemic quickly impacts jobs and the economy, and the algorithm of the considered method directly as compared to the complexity of the algorithm of other methods [15]. By using this method, we can better predict both immediate and long-term changes in employment and economic growth.

The key objective of this research is to develop a mathematically sophisticated model that combines the SIR model with unemployment and GDP components, considering Okun's Law to analyze the relationship between GDP and unemployment [16]. The RK-4 method will be applied to simulate and predict the dynamic behaviors of unemployment and GDP, capturing both short-term fluctuations and long-term consequences [17]. This ambitious undertaking aims to unravel the complex linkages among health, labor markets, and economic performance during a time of unprecedented shocks.

The year-on-year unemployment rate in urban India surged from 8.8% in April to June 2019 to 20.8% in April to June 2020, highlighting the heavy toll on the labor force due to the pandemic [18]. This metric underscores the urgency of understanding and addressing the economic repercussions of public health crises.

The choice of the RK-4 method is based on its efficiency in solving differential equations and its suitability for capturing the nonlinear interactions inherent in economic and epidemiological models [19]. The classical SIR model is modified to include parameters characterizing unemployment and GDP, enhancing the model's ability to capture the complexity of real-world economic systems, especially during crises.

This research fills a striking gap in the literature by integrating health-related and economic variables within a common framework. While previous studies have often focused on health or economic aspects alone, this work combines them into an integrated model. Furthermore, the study extends the scope by incorporating the RK-4 method to predict the potential impact of

future pandemics and adds a least square method to provide a forward-looking dimension to our understanding [20].

This study is crucial in providing actionable insights for policymakers and researchers to make informed decisions amid dynamic economic conditions influenced by public health crises. By filling this gap in the literature, the research contributes to mathematical modeling, epidemiology, and economic forecasting, laying the foundation for future studies to build on this integrated framework [21].

Our SIRUG model presents a unified framework to explore the relationship between disease spread and economic changes during public health crises. By combining traditional disease modeling with economic indicators like unemployment and GDP through Okun's Law and employing the RK-4 method to analyze their interactions, this research provides valuable insights into both immediate and future economic impacts of pandemics. The addition of least square analysis enhances our ability to make accurate predictions, making this work particularly valuable for policymakers and researchers. This study establishes a foundation for future research in this field, offering new ways to understand and address the economic challenges that arise during public health emergencies.

2 Basic results

The following results played a crucial role in the comprehensive analysis and validation of our model, significantly contributing to its efficacy and reliability.

Theorem 1 *[22] The autonomous system* $x'(t) = Ax(t), \quad x(0) = x_0$ *is asymptotically stable iff* $|arg(\lambda(A))| > \frac{\pi}{2}$. *Stable if and only if either it is asymptotically stable, or those critical eigenvalues which satisfy* $|arg(\lambda(A))| = \frac{\pi}{2}$ *have geometric multiplicity one. Here,* $arg(\lambda(A))$ *denotes the argument of the eigenvalues of the square matrix* A.

Theorem 2 *[23] Let* $f(t)$ *be a continuous function on* $[0, \infty)$ *and satisfies*

$$\frac{df}{dt} \leq -\Phi f(t) + \gamma_1, f(t_0) = f_{t_0},$$

where $\Phi, \gamma_1 \in \mathbb{R}$ *and* $\Phi \neq 0$, *then*

$$f(t) \leq \left(f_{t_0} - \frac{\gamma_1}{\Phi}\right) e^{-\Phi(t-t_0)} + \frac{\gamma_1}{\Phi}.$$

Definition 1 *The function* $f : E \to \mathbb{R}^n$ *is said to admit the Lipschitz condition on the open subset* E *of* $\mathbb{R}^n$ *if there is a positive constant* K *such that*

$$|f(x) - f(y)| \leq K|x - y|, \quad \forall x, y \in E.$$

3 Model construction

In this section, we introduce the model that we consider for the present study. The following statement contains a simplified explanation of the SIRUG model. The explanation has been primarily based on assuming there would be no future uncertainties.

Key components of the model

i. **Susceptible (*S*)**: This group represents individuals who are not infected but are susceptible to the disease. Over time, some of them may become infected if they come into contact with

infectious individuals.

ii. **Infected (I)**: This group includes individuals who are currently infected and capable of spreading the disease to susceptible individuals. The number of infected individuals typically increases initially.

iii. **Recovered (R)**: The "Recovered" category represents individuals who have recovered from the disease and are no longer infectious. These individuals may have developed immunity to the disease, depending on the disease in question.

iv. **Unemployed Population (U)**: This represents the number of individuals who are currently unemployed and seeking employment.

v. **Gross Domestic Product (G)**: It represents the total value of goods and services produced within a country, serving as a measure of its economic performance.

The SIR model

SIR [24] is a system of ordinary differential equations showing the dynamics of infectious spread. The following equations outline how, over time, the number of people in each category varies:

$$\begin{aligned} \frac{dS}{dt} &= -\beta SI, \\ \frac{dI}{dt} &= \beta SI - \gamma I, \\ \frac{dR}{dt} &= \gamma I. \end{aligned} \tag{1}$$

Uses and practicality in real life:

The SIR model has several important uses and practical applications in real life:

(i) **Epidemic modeling:** SIR is one of the most used models for studying and predicting the dynamics of infectious diseases. It is often used in the simulation of different scenarios by adjusting various parameters like transmission rate and recovery rate. It can assess how interventions like vaccination or social distancing affect the outcome.

(ii) **Public health planning [25]**: Health authorities and policymakers use the SIR model to aid in making decisions concerning disease control strategies, planning resource allocation during an outbreak, and healthcare system readiness. These models aid in the calculation of projections of cases that may occur and identify the critical times in an outbreak and health system needs.

(iii) **Parameter estimation:** Through the SIR model, parameters for the disease can be estimated, including, but not limited to, the basic reproduction number, R_0, which can be described as the average number of secondary infections generated by one infectious individual in an entirely susceptible population. The calibration of these parameters is essential for the design of suitable public health policies.

(iv) **Vaccination campaigns [26]:** The SIR model is utilized in the layout and analysis of vaccination policies. They calculate ideal vaccine coverage levels to achieve the idea of herd immunity, which refers to the idea of a high enough percentage of the population becoming immune to prevent large-scale outbreaks.

(v) **Early warning systems [27]:** Continuous monitoring of the data and the SIR model allows for the development of early warning systems that might help limit the spread of the disease while it is still at its beginning stages.

Thus, SIR models are very helpful in understanding infectious disease transmission dynamics

and are an important tool for epidemiologists, public health experts, and policymakers. These models help Inform decisions that can eventually save lives and reduce the impact of epidemics on society.

The SIRUG model

The traditional SIR model categorizes all people into three classes: Susceptible, Infected, and Recovered. This model has been very useful in understanding the basic trends by which infectious diseases spread through a population. It mostly overlooks the bidirectional and nuanced interaction between health and economic stability. Motivated by this important gap in our understanding, we introduce a new holistic modified SIR model. Added to this adaptation are two more compartments, such as the Unemployed and GDP, which will allow for a critical look into the multi-dimensional reality of disease spread and further-reaching implications in society.
This is a modified version of the SIR model, which accounted for an epidemic process and was used to describe and predict the dynamics of infectious diseases within a population. This modified model adds extra compartments defined to include the economic factors influencing the dynamics of the epidemic as follows:

$$\begin{cases} \frac{dS}{dt} = -\beta_1 SI + \alpha S + \omega G, \\ \frac{dI}{dt} = \beta_2 SI - \gamma_1 I + \eta I, \\ \frac{dR}{dt} = \gamma_2 I - \delta R, \\ \frac{dU}{dt} = \lambda S - \mu U, \\ \frac{dG}{dt} = \phi G - \kappa UG. \end{cases} \tag{2}$$

Explanation of each compartment:

In this adapted SIR model, various factors are taken into consideration that might have an influence on the dynamics of the epidemic and the economy. Following is a detailed explanation of the modifications and what each compartment stands for:

I. **Susceptible dynamics** $(\frac{dS}{dt})$**:**

i) (-β_1SI): This term is the rate at which the susceptible S entered the infected I state. It thus depends upon the infection rate, β_1 and on the product of the number of people susceptible, S, and infectious, I.

ii) (αS): This term is the birth rate, and it provides the number of people that are added to the susceptible population at any given time. It, therefore, increases the susceptible population.

iii) (ωG): This term is how the Gross Domestic Product, GDP, affects the susceptible population. This shows the way in which the economic characteristics influence the birth rate and, consequently, cause an increase or a decline in the susceptible population.

II. **Infected dynamics** $(\frac{dI}{dt})$**:**

i) (β_2SI): The expression gives the rate of conversion of Susceptible, S, into Infectious, I, due to COVID-19. In that, it is affected by the conversion rate, β_2, with the product of the number of Susceptible, S and the Infectious, I.

ii) (-γ_1I): This term reflects the rate at which the number of infections is reduced. It accounts for factors like recovery or medical interventions that reduce the number of infectious

individuals.

iii) (ηI): This term denotes the disease-induced death rate among the infected population. It represents the mortality associated with the disease.

III. **Recovered dynamics** $(\frac{dR}{dt})$**:**

i) (γ_2I): This term signifies the rate at which individuals move from the infectious (I) to the recovered (R) compartment. It represents recovery from the disease.

ii) (-δR): This term denotes the natural death rate among the recovered population. It reflects the mortality rate of individuals who have recovered from the disease.

IV. **Unemployed dynamics** $(\frac{dU}{dt})$**:**

i) (λS): This term represents the increase in unemployment due to the pandemic. It reflects how the susceptible population contributes to the rise in unemployment.

ii) (-μU): This term represents the re-employment rate, indicating the rate at which individuals move from unemployment to employment. It reflects the recovery of the job market.

V. **GDP dynamics** $(\frac{dG}{dt})$**:**

i) (ϕG): This term represents the GDP growth rate. It indicates the natural growth or expansion of the economy.

ii) (-κUG): This term represents the GDP decay rate due to unemployment. It reflects the negative impact of unemployment on GDP, capturing how economic downturns affect the overall economic output.

4 Parameter estimation

Parameter estimation is one of the most important elements in mathematical modeling and data analysis and, therefore, in our attempt to appreciate the intricate inner workings of complex systems, whether in physics, biology, economics, engineering, or generally in scientific and engineering fields. The main aim of the parameter estimation process is to provide an exact numerical value for parameters underlying a given mathematical model and bring clarity to many of the otherwise elusive behaviors manifested by real-world systems.

Accurate parameter estimation plays a crucial role as a bridge between theoretical concepts and tangible empirical reality. This essential bridge guides scientific investigations grounded in evidence-based, data-driven approaches, providing researchers with a roadmap to navigate the complexities of complex systems.

Using the least square method, we got the best-fitted parameter values, which are presented in Table 1.

5 Stability of equilibrium points

The equilibrium points of system (2) for the parameter values as in Table 1 are

i. $E_1 = (1.67 \times 10^9, 40, 155556, 9.61538, 0)$,
ii. $E_2 = (1.48417 \times 10^9, 0, 0, 8.5625, -296.833)$,
iii. $E_3 = (0, 0, 0, 0, 0)$.

Theorem 3 *System* (2) *is stable at* E_1*, but unstable at* E_2 *and* E_3*.*

Proof Following are the eigenvalues of system (2) at the three equilibrium points:

i. The Eigenvalues corresponding to equilibrium point E_1 can be stated as follows:

$$\lambda_{1,1} = -1.3, \quad \lambda_{1,2} = -0.1688462, \quad \lambda_{1,3} = -0.009, \quad \lambda_{1,4} = 0.001i, \quad \lambda_{1,5} = -0.001i.$$

ii. The Eigenvalues corresponding to equilibrium point E_2 can be stated as follows:

$$\lambda_{2,1} = -1.3, \quad \lambda_{2,2} = -0.1095, \quad \lambda_{2,3} = -0.009, \quad \lambda_{2,4} = -0.0011705, \quad \lambda_{2,5} = 0.00117044.$$

iii. The Eigenvalues corresponding to equilibrium point E_3 can be stated as follows:

$$\lambda_{3,1} = 1.37, \quad \lambda_{3,2} = -1.3, \quad \lambda_{3,3} = -1, \quad \lambda_{3,4} = -0.009, \quad \lambda_{3,5} = 1 \times 10^{-6}.$$

Table 1. Value of parameters associated with system (2)

Parameter	Description	Value
β_1	Infection rate	2.5×10^{-8}
β_2	Conversion rate of Susceptible people into infected by COVID-19	6×10^{-10}
α	Birth Rate	1×10^{-6}
ω	Influence of GDP on susceptible population	5
γ_1	Rate at which number of infections are reduced	3
γ_2	Rate at which people move from I to R	35
η	Disease induced death rate	2
δ	Natural death rate	0.009
λ	Unemployment rate	7.5×10^{-9}
μ	Re-employment rate	1.3
ϕ	GDP growth rate	1.37
κ	GDP decay rate due to unemployment	0.16

Table 2. Comparison of argument with $\frac{\pi}{2}$

Eigenvalue	Argument Value	Comparison with $\pi/2$
$\lambda_{1,1}$	π	$\pi > \frac{\pi}{2}$
$\lambda_{1,2}$	π	$\pi > \frac{\pi}{2}$
$\lambda_{1,3}$	π	$\pi > \frac{\pi}{2}$
$\lambda_{1,4}$	$\frac{\pi}{2}$	$\frac{\pi}{2} = \frac{\pi}{2}$
$\lambda_{1,5}$	$\frac{\pi}{2}$	$\frac{\pi}{2} = \frac{\pi}{2}$
$\lambda_{2,1}$	π	$\pi > \frac{\pi}{2}$
$\lambda_{2,2}$	π	$\pi > \frac{\pi}{2}$
$\lambda_{2,3}$	π	$\pi > \frac{\pi}{2}$
$\lambda_{2,4}$	π	$\pi > \frac{\pi}{2}$
$\lambda_{2,5}$	0	$0 < \frac{\pi}{2}$
$\lambda_{3,1}$	0	$0 < \frac{\pi}{2}$
$\lambda_{3,2}$	π	$\pi > \frac{\pi}{2}$
$\lambda_{3,3}$	π	$\pi > \frac{\pi}{2}$

Table 2. Comparison of argument with $\frac{\pi}{2}$ - continued

Eigenvalue	Argument Value	Comparison with $\pi/2$
$\lambda_{3,4}$	π	$\pi > \frac{\pi}{2}$
$\lambda_{3,5}$	0	$0 < \frac{\pi}{2}$

The arguments of the above eigenvalues are presented in Table 2. As it can be seen from those values,

- The equilibrium point E_1 is stable.
- The equilibrium point E_2 is unstable as $\lambda_{2,5} < \frac{\pi}{2}$.
- The equilibrium point E_3 exhibits instability, since $\lambda_{3,1}, \lambda_{3,5} < \frac{\pi}{2}$.

6 Existence and uniqueness of solutions

Theorem 4 *The kernels F_1, F_2, F_3, F_4, F_5 admit the Lipschitz condition and contraction when*

$$0 < K_1, K_2, K_3, K_4, K_5 \leq 1,$$

where $K_1 = \beta_1\epsilon_2 + \alpha$, $K_2 = \beta_2\epsilon_1 - \gamma_1 + \eta$, $K_3 = \delta$, $K_4 = \mu$, and $K_5 = \phi + \kappa\epsilon_4$.

Proof We assume that $\|S\| \leq \lambda_1$, $\|I\| \leq \lambda_2$, $\|R\| \leq \lambda_3$, $\|U\| \leq \lambda_4$, $\|G\| \leq \lambda_5$ and

$$\frac{dS}{dt} = F_1(t, S, I, R, U, G), \tag{3}$$
$$\frac{dI}{dt} = F_2(t, S, I, R, U, G), \tag{4}$$
$$\frac{dR}{dt} = F_3(t, S, I, R, U, G), \tag{5}$$
$$\frac{dU}{dt} = F_4(t, S, I, R, U, G), \tag{6}$$
$$\frac{dG}{dt} = F_5(t, S, I, R, U, G). \tag{7}$$

For Eq. (3), we show

$$\|F_1(t, S, I, R, U, G) - F_1(t, S^*, I, R, U, G)\| \leq K_1\|S - S^*\|,$$

where $K_1 \in [0, 1)$. Now,

$$\begin{aligned}\|-\beta_1 SI + \alpha S + \omega G + \beta_1 S^* I - \alpha S^* - \omega G\| &= \|-\beta_1 I(S - S^*) + \alpha(S - S^*)\| \\ &\leq \|\beta_1 I(S - S^*)\| + \|\alpha(S - S^*)\| \\ &\leq |\beta_1|\|I\|\|S - S^*\| + |\alpha|\|S - S^*\| \\ &\leq \beta_1\epsilon_2\|S - S^*\| + \alpha\|S - S^*\| \\ &\leq (\beta_1\epsilon_2 + \alpha)\|S - S^*\|.\end{aligned}$$

Therefore $K_1 = (\beta_1\epsilon_2 + \alpha)$. For Eq. (4), we need to provide

$$\|F_2(t, S, I, R, U, G) - F_2(t, S, I^*, R, U, G)\| \leq K_2\|I - I^*\|,$$

where $K_2 \in [0,1)$. Now,

$$\begin{aligned}\|F_2(t,S,I,R,U,G) - F_2(t,S,I^*,R,U,G)\| &= \|\beta_2 SI - \gamma_1 I + \eta I - \beta_2 SI^* + \gamma_1 I^* - \eta I^*\| \\ &= \|\beta_2 S(I-I^*) - \gamma_1(I-I^*) + \eta(I-I^*)\| \\ &\leq |\beta_2|\|S\|\|I-I^*\| - |\gamma_1|\|I-I^*\| + |\eta|\|I-I^*\| \\ &\leq (|\beta_2|\|S\| - |\gamma_1| + |\eta|)\|I-I^*\| \\ &\leq (\beta_2\epsilon_1 - \gamma_1 + \eta)\|I-I^*\|.\end{aligned}$$

Therefore $K_2 = (\beta_2\epsilon_1 - \gamma_1 + \eta)$. For Eq. (5), we need to show

$$\|F_3(t,S,I,R,U,G) - F_3(t,S,I,R^*,U,G)\| \leq K_3\|R-R^*\|,$$

where $K_3 \in [0,1)$. Then

$$\begin{aligned}\|F_3(t,S,I,R,U,G) - F_3(t,S,I,R^*,U,G)\| &= \|\gamma_2 I - \delta R - \gamma_2 I + \delta R^*\| \\ &= \|-\delta(R-R^*)\| \leq |\delta|\|R-R^*\| \\ &\leq \delta\|R-R^*\|.\end{aligned}$$

Therefore $K_3 = \delta$. For Eq. (6), we need to obtain

$$\|F_4(t,S,I,R,U,G) - F_4(t,S,I,R,U^*,G)\| \leq K_4\|U-U^*\|,$$

where $K_4 \in [0,1)$. Now, we have

$$\begin{aligned}\|F_4(t,S,I,R,U,G) - F_4(t,S,I,R,U^*,G)\| &= \|\alpha G - \mu U - \alpha S + \mu U^*\| \\ &= \|-\mu(U-U^*)\| \leq |\mu|\|U-U^*\| \\ &\leq \mu\|U-U^*\|.\end{aligned}$$

Therefore $K_4 = \mu$. For Eq. (7), we need to show

$$\|F_5(t,S,I,R,U,G) - F_5(t,S,I,R,U,G^*)\| \leq K_5\|G-G^*\|,$$

where $K_5 \in [0,1)$. Then

$$\begin{aligned}\|\phi G - \kappa UG - \phi G^* + \kappa UG^*\| &\leq \|\phi(G-G^*) - \kappa U(G-G^*)\| \\ &\leq |\phi|\|G-G^*\| + \kappa\epsilon_4\|G-G^*\| \\ &\leq (\phi + \kappa\epsilon_4)\|G-G^*\|.\end{aligned}$$

Therefore $K_5 = (\phi + \kappa\epsilon_4)$.
Here, K_1, K_2, K_3, K_4, K_5 are the Lipschitz constants for the functions F_1, F_2, F_3, F_4 and F_5, respectively.
Now that we have proved the existence of Lipschitz constants K_1, K_2, K_3, K_4, K_5, the existence of a unique solution to system (2) is also ensured following the methodology shown in [28].

7 Boundedness

Theorem 5 *The proposed S-I-R-U-G model Eq. (2) is bounded by Theorem 2.*

Proof Let $X(t) = S(t) + I(t) + R(t) + U(t) + G(t)$.
On differentiating $X(t)$, we have

$$\frac{dX}{dt} + \Phi X = \frac{d(S + I + R + U + G)}{dt} + \Phi(S + I + R + U + G).$$

Simplifying, we have

$$\begin{aligned}\frac{dX}{dt} + \Phi X = &-\beta_1 SI + \alpha S + \omega G + \beta_2 SI - \gamma_1 I + \eta I + \gamma_2 I - \delta R \\ &+ \lambda S - \mu U + \phi G - \kappa UG + \Phi S + \Phi I + \Phi R + \Phi U + \Phi G.\end{aligned}$$

Removing the negative terms, we get

$$\frac{dX}{dt} + \Phi X \leq \alpha S + \omega G + \beta_2 SI + \eta I + \gamma_2 I + \lambda S + \phi G + \Phi S + \Phi I + \Phi R + \Phi U + \Phi G.$$

Now, the solution of system (2) exists uniquely in

$$\{(S, I, R, U, G) : max(|S|, |I|, |R|, |U|, |G|) \leq M\},$$

where M is a positive constant. Therefore, we can write

$$\frac{dX}{dt} + \Phi X \leq (\alpha + \omega + \beta_2 M + \eta + \gamma_2 + \lambda + \phi)M + 5\Phi M = \gamma_1.$$

Using Theorem 1, we get

$$X(t) \leq \left(X_{t_0} - \frac{\gamma_1}{\Phi}\right) e^{-\Phi(t-t_0)} + \frac{\gamma_1}{\Phi}.$$

Therefore, system (2) is bounded.

8 Numerical method

The Runge-Kutta 4th order (RK4) method occupies a pivotal position in the arsenal of numerical techniques applied to SIR (Susceptible-Infectious-Recovered) modeling within epidemiology. Renowned for its adept balance between accuracy and computational efficiency, RK4 is widely embraced for its reliability and ease of implementation. Its enduring popularity stems from its ability to deliver precise solutions while remaining relatively straightforward to employ, robust in the face of diverse scenarios, and stable across a range of conditions. As a consequence, RK4 has emerged as a cornerstone in epidemiological simulations, serving as a linchpin for researchers seeking to unravel the complexities of disease dynamics.

At its core, RK4 functions by breaking down the differential equations governing infectious disease transmission into discrete steps, allowing for the meticulous exploration of various epidemiological scenarios. By leveraging RK4, researchers can simulate and analyze the impact of different interventions, ranging from vaccination campaigns to social distancing measures, thereby informing evidence-based public health strategies and policy decisions.

In practical terms, RK4 enables epidemiologists to simulate disease outbreaks with a high degree of fidelity, providing invaluable insights into the progression and containment of infectious diseases. Its versatility extends beyond simple SIR models, as RK4 can be adapted to explore

more complex dynamics, such as spatial spread, heterogeneous populations, and the interplay of multiple infectious agents. Moreover, RK4's computational efficiency makes it well-suited for real-time epidemic forecasting and scenario planning, empowering public health officials to anticipate and respond effectively to emerging threats.
To solve system (2) using the classical Runge-Kutta method of 4th order, we define the system as

$$\begin{aligned} f_1(S,I,R,U,G) &= -\beta_1 SI + \alpha S + \omega G, \\ f_2(S,I,R,U,G) &= \beta_2 SI - \gamma_1 I + \eta I, \\ f_3(S,I,R,U,G) &= \gamma_2 I - \delta R, \\ f_4(S,I,R,U,G) &= \lambda S - \mu U, \\ f_5(S,I,R,U,G) &= \phi G - \kappa UG. \end{aligned} \tag{8}$$

Using the RK4 method, we compute the intermediate values as follows

$$\begin{aligned} k_1^{(i)} &= hf_i(S_n, I_n, R_n, U_n, G_n), \\ k_2^{(i)} &= hf_i\left(S_n + \frac{k_1^{(1)}}{2}, I_n + \frac{k_1^{(2)}}{2}, R_n + \frac{k_1^{(3)}}{2}, U_n + \frac{k_1^{(4)}}{2}, G_n + \frac{k_1^{(5)}}{2}\right), \\ k_3^{(i)} &= hf_i\left(S_n + \frac{k_2^{(1)}}{2}, I_n + \frac{k_2^{(2)}}{2}, R_n + \frac{k_2^{(3)}}{2}, U_n + \frac{k_2^{(4)}}{2}, G_n + \frac{k_2^{(5)}}{2}\right), \\ k_4^{(i)} &= hf_i\left(S_n + k_3^{(1)}, I_n + k_3^{(2)}, R_n + k_3^{(3)}, U_n + k_3^{(4)}, G_n + k_3^{(5)}\right). \end{aligned} \tag{9}$$

The values at the next time step are computed as

$$\begin{aligned} S_{n+1} &= S_n + \frac{1}{6}\left(k_1^{(1)} + 2k_2^{(1)} + 2k_3^{(1)} + k_4^{(1)}\right), \\ I_{n+1} &= I_n + \frac{1}{6}\left(k_1^{(2)} + 2k_2^{(2)} + 2k_3^{(2)} + k_4^{(2)}\right), \\ R_{n+1} &= R_n + \frac{1}{6}\left(k_1^{(3)} + 2k_2^{(3)} + 2k_3^{(3)} + k_4^{(3)}\right), \\ U_{n+1} &= U_n + \frac{1}{6}\left(k_1^{(4)} + 2k_2^{(4)} + 2k_3^{(4)} + k_4^{(4)}\right), \\ G_{n+1} &= G_n + \frac{1}{6}\left(k_1^{(5)} + 2k_2^{(5)} + 2k_3^{(5)} + k_4^{(5)}\right). \end{aligned} \tag{10}$$

To generate the simulation results presented in this study, the RK4 method was implemented using Python. Python's rich ecosystem of libraries, including NumPy and Matplotlib, was utilized to ensure precision in numerical computations and clarity in visualizing the results. The implementation in Python further underscores the accessibility and reproducibility of the simulation process, enabling researchers to replicate and extend the findings with ease.

Model simulations

The following are the graphs obtained using the Runge-Kutta 4th-order method. The red points showcase the real data value points, and the blue line showcases our model.

Inferences on the different compartments based on the numerical simulations for system (2):

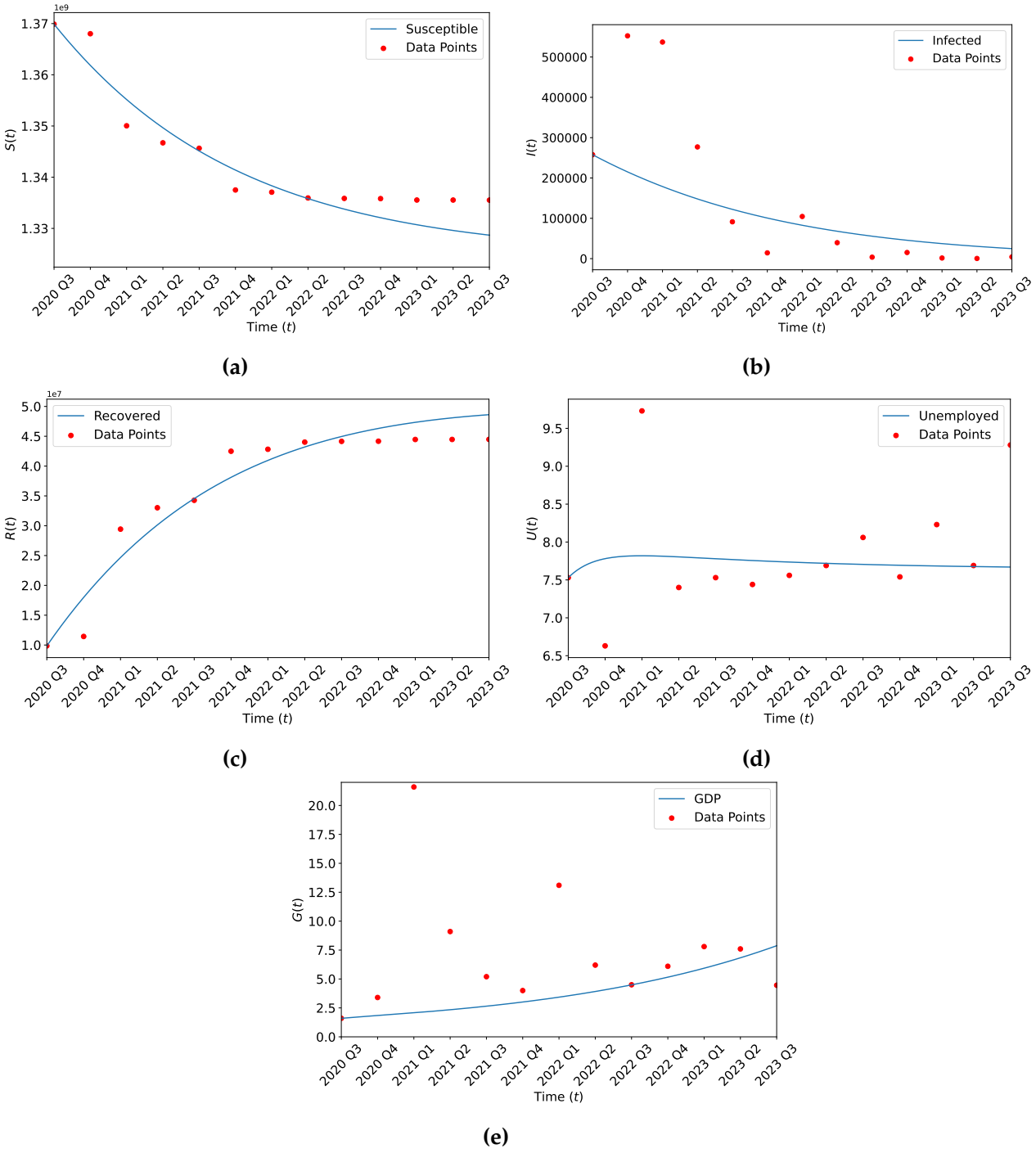

Figure 1. Subplot showing numerical results for (a) Susceptible, (b) Infection, (c) Recovered, (d) Unemployment and (e) GDP at parameters given in Table 1

Susceptible population: In Figure 1a, the susceptible population ($S(t)$) exhibits a decreasing trend over time, indicating potential exposure and infection in the population. The red data points, representing observed values, align closely with the simulated results, underscoring the accuracy of the model.

Infected population: In Figure 1b, the infected population ($I(t)$) displays fluctuations over time, possibly reflecting the impact of interventions or variations in disease spread. The close alignment of the data points with the model's predictions suggests that the model effectively captures ob-

served infection trends.

Recovered population: In Figure 1c, the recovered population ($R(t)$) demonstrates a consistent increase over time, illustrating the cumulative number of individuals who have successfully overcome the infection. The model's trajectory closely follows the provided data points, affirming its reliability in simulating recovery dynamics.

Unemployed population: In Figure 1d, the unemployed population ($U(t)$) experiences fluctuations, possibly influenced by economic factors or external events. The observed data points exhibit variations, and the model successfully captures the general trend, indicating its ability to simulate the dynamics of unemployment in response to changing conditions.

GDP: In Figure 1e, GDP, denoted as ($G(t)$), displays a consistent increase over time, suggesting economic growth. The observed data points align well with the model's predictions, indicating that the simulated economic dynamics accurately represent the growth trends in GDP.

9 Results and discussion

The following sections demonstrate the influence of various parameters like ϕ and κ on GDP and of λ and μ on the unemployment rate.

Influence of ϕ and κ on GDP

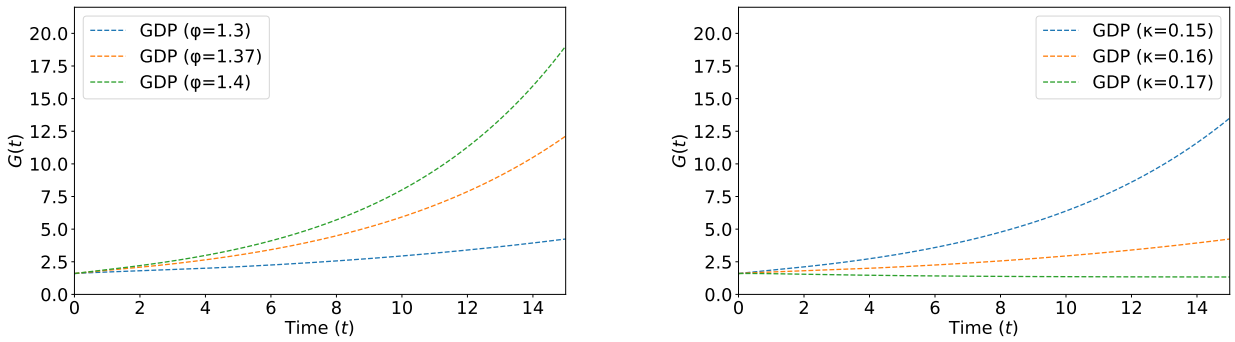

(a) **(b)**

Figure 2. (a) GDP with decreased and increased ϕ value, (b) GDP with decreased and increased κ value at parameters given in Table 1

Influence of ϕ (gross domestic product growth rate) on GDP dynamics:
The parameter ϕ plays a key role in shaping the economy's path. It represents the natural rate at which the Gross Domestic Product grows. In economic terms, ϕ shows how much room an economy has to grow and come up with new ideas. Looking at Figure 2a, we can see that when ϕ drops to 1.3, the GDP growth curve moves to the right. This shift means the economy is growing more. When growth slows down like this, it often leads to other changes. Companies might not want to invest as much money. Workers might not produce as much. And the country might fall behind in developing new tech and building new infrastructure. On the other hand, when ϕ goes up (1.4), it pushes the GDP growth curve to the left, showing faster economic growth. A higher intrinsic growth rate points to a more energetic and ever-changing economy. This means

that a setting that supports new ideas, business creation, and good economic conditions can help overcome the problems caused by disease outbreaks and job losses, leading to a quicker bounce back.

Influence of κ (GDP decay rate due to unemployment) on GDP dynamics:
The κ parameter captures how unemployment hurts GDP, showing the cost to the economy when people can't work. Looking at Figure 2b, we see that a lower κ (0.15) pushes the GDP growth curve to the left, which is good news. This move hints that steps to soften the unemployment's blow can speed up economic growth. A smaller κ points to a tougher job market, less economic decay, and more room for GDP to grow. On the flip side, a higher κ (0.17) pushes the GDP growth curve to the right, meaning unemployment hits economic growth harder. A faster GDP decay rate due to joblessness suggests a job market that's slower to change and respond, which could slow down the whole process of getting the economy back on track.

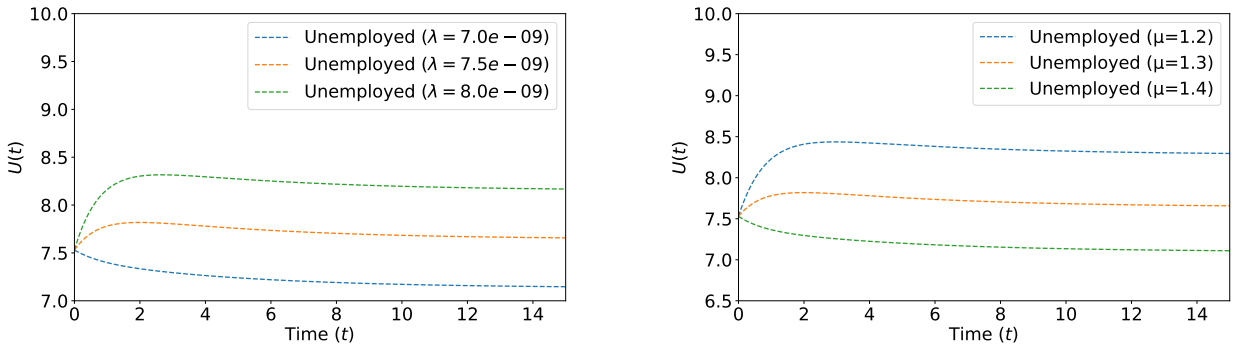

(a) **(b)**

Figure 3. (a) Unemployment with decreased and increased λ value, (b) Unemployment with decreased and increased μ value at parameters given in Table 1

Influence of unemployment rate (λ) on unemployment dynamics:
The unemployment rate, symbolized by λ, plays a key role in shaping how unemployment changes over time. Looking at Figure 3a, we see that when λ goes down (7×10^{-9}), the unemployment curve moves to the right. This shift shows that a lower jobless rate causes unemployment to grow more as time passes. We can link this to things like fewer people quitting their jobs or less job loss in the economy. On the other hand, when λ goes up (8×10^{-9}), it pushes the unemployment curve to the left. This means unemployment grows faster as time passes. This might happen because more people quit their jobs or because jobs disappear quicker in the economy. When unemployment rates go up, it makes the job market tougher. This can put more stress on the economy.

Influence of re-employment rate (μ) on unemployment dynamics:
The re-employment rate, symbolized by μ, plays a key role in the dynamics of unemployment, showing how well the labor market supports job transitions. As seen in Figure 3b, when μ decreases, the unemployment curve shifts to the left. This shift indicates that a lower re-employment rate causes unemployment to rise more quickly over time. This could happen due to a lack of job opportunities or slower job creation in the economy.

In contrast, when μ increases, the unemployment curve moves to the right, indicating a slower rise in unemployment over time. This could be because of more job opportunities or faster job creation in the economy. A higher re-employment rate reflects a more effective labor market, which can help reduce unemployment and promote economic stability.

Influence of infection rate (β_1) on gross domestic product

The influence of infection rates, denoted by β_1, on GDP is important. Figure 4 demonstrates how different infection rates affect GDP growth. Increased speeds will reduce the life of the pandemic, which will mean faster accelerated rates that will foster economic recovery, whereas decelerated rates would only lengthen the downturn. This underlines the delicate balance between public health and economic stability, emphasizing the need for effective strategies to manage infection rates while promoting sustainable growth.

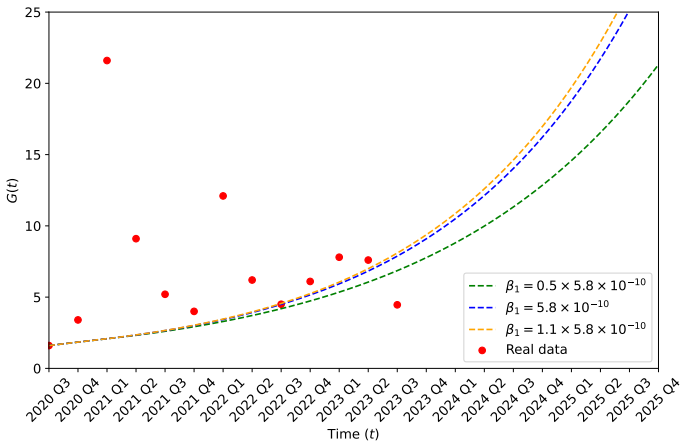

Figure 4. Influence of infection rate on GDP

Accelerated infection rate and economic recovery

An increased infection rate implies a rapid spread of the disease, leading to a quicker rise in the number of infected individuals within a shorter timeframe. A shorter duration of the pandemic may prompt an earlier commencement of the economic recovery phase. The accelerated completion of the pandemic might lead to a more immediate resurgence in economic activities, potentially resulting in a swifter rebound in GDP.

Decelerated infection rate and prolonged economic downturn

A slower infection rate extends the timeline of the pandemic, resulting in a more prolonged period of disease transmission. A longer pandemic timeline might lead to a more prolonged economic downturn.

Economic implications of infection rates on diverse sectors

Healthcare outlays stimulating economic sectors

Elevated infection rates increase healthcare spending, leading to a surge in resource allocation toward healthcare infrastructure, medical supplies, and research. This intensifies during health crises. Heightened healthcare expenditure catalyzes economic activity within specific sectors, fostering favorable growth in GDP. Amid the pandemic, India's public health spending increased from 1.5 percent to 1.8 percent of the GDP [29]. The PM Ayushman Bharat Health Infrastructure Mission scheme intends to enhance infrastructure, funded by the central government [29].

Labor market fluctuations in response to infection rates

Rapid escalations can initially lead to a transient reduction in the labor force. The reintegration of workers into the workforce can contribute to a resurgence in economic productivity.

Innovative resilience and industrial adaptation

Heightened infection rates often spur an incentive for innovation and adaptability within industries. This incentive leads to pivots in production to accommodate the manufacturing of essential goods or services requisite during crises, raising the need for the emergence of novel business models or technological advancements. This adaptive shift can give rise to growth in specific sectors, exerting a positive influence on aggregate GDP.

Dynamic consumer behavioral shifts

Varied infection rates may cause shifts in consumer behavior patterns during pandemics. These shifts lead to alterations in expenditure distributions, with some sectors witnessing a downturn while others experience increased demand. The surge in demand for essential commodities or the accelerated adoption of online services can invigorate specific sectors, thereby bolstering overall GDP growth. There has been a surge of over 100 percent in the demand for essential commodities like rice, wheat, and pulses [30]. Additionally, other food categories such as confectioneries, sweets, organic processed food, and spices have also experienced a notable increase of 15-20 percent [30].

Governmental fiscal interventions and stimuli

Governmental responses to pandemics often include fiscal policies and stimuli aimed at buttressing businesses and individuals impacted by the crisis. Such interventions, spanning financial aid, tax concessions, or infrastructure investment, are designed to stabilize the economy and wield a positive influence on GDP growth trajectories. India's government introduced a COVID-19 social aid package worth INR 1.7 lakh crore (equivalent to 25 billion US dollars) through the Pradhan Mantri Garib Kalyan Yojana (PM-GKY) [31] to offer prompt assistance to those in need.

Research and development investments for long-term economic impacts

Escalating infection rates frequently prompt heightened investments in research and development endeavors, particularly toward vaccines, treatments, or preventive measures. The resultant scientific breakthroughs engendered by such investments manifest long-term positive repercussions across various industries, nurturing innovation and consequent economic growth.

Prospective revival of tourism and hospitality sectors

Subsequent to periods of elevated infection rates and constrained travel, pent-up demand often surfaces for travel and related hospitality services upon the amelioration of the situation. This prospective resurgence in the tourism and hospitality sectors holds the potential to significantly contribute to the resurgence of GDP growth. The recovery of the tourism sector will hinge on enhancing trust in travel and reducing the perceived risks associated with it [32]. The impact of COVID-19 influences consumers' perceptions of tourism products and services [33].

Okun's law

Okun's law originates from the study between unemployment and economic growth by Okun (1962) [34] on the United States economy, where he observed that there was an inverse relationship between the two variables. Okun (1962) observed that a percentage increase in economic growth would result in a 0.3 percent decline in unemployment.

The SIRUG model incorporating Okun's Law provides a comprehensive framework for understanding the complex interplay between epidemiological dynamics and economic factors during the COVID-19 pandemic. It facilitates informed decision-making and policy formulation [35] to mitigate the health and economic impacts of the crisis.

The graph Figure 5 plots the unemployment rate on the y-axis and GDP on the x-axis. The data points show a negative correlation between the two variables, consistent with Okun's Law. In other words, as the unemployment rate increases, GDP decreases, and vice versa. However, the data points also deviate from a straight line, indicating that the relationship between the unemployment rate and GDP is not perfectly linear. The data points in the graph represent the percent change in value with the previous value as the base. A negative value indicates a negative percent change, while a positive value indicates a positive percent change.

Observations

Outliers, such as the sharp decline in GDP accompanied by a high unemployment rate in 2020 Q2, can be understood within the framework of Okun's Law. Such an event could be associated with an economic downturn or recession, where a significant drop in GDP leads to an increase in unemployment. This could be due to factors like reduced consumer spending, investment, and overall economic activity due to the surge of the pandemic.

The period of economic recovery observed in 2021 and 2022, where GDP increases and unemployment decreases, aligns well with Okun's Law. As the economy begins to recover, increased economic output (reflected in rising GDP) typically leads to job creation and a decline in unemployment rates. This can be attributed to factors like increased consumer confidence, government stimulus measures, and business investments.

The increase in unemployment and decrease in GDP observed in 2023 Q4 is again consistent with Okun's Law but in the reverse direction. Such a scenario could signal another economic downturn or slowdown, where a decrease in GDP leads to layoffs and rising unemployment rates. Factors contributing to this could include external shocks, changes in government policies, or shifts in global economic conditions.

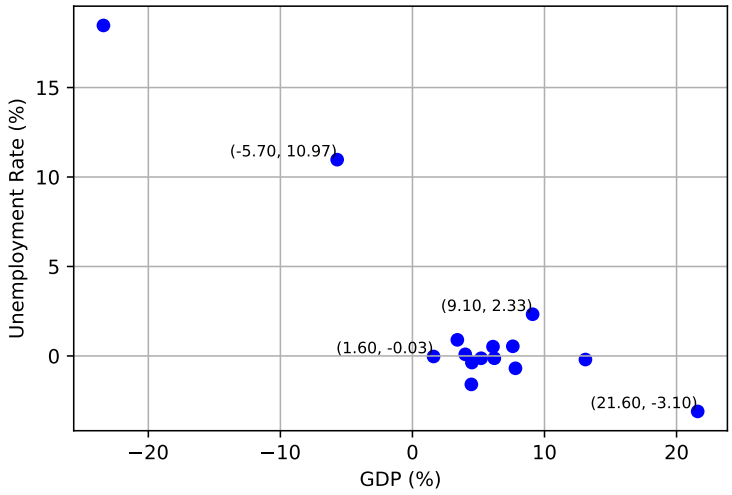

Figure 5. Change in GDP with change in unemployment - demonstration of Okun's Law

Long-term economic implications and policy recommendations

The analysis of the SIRUG model, incorporating epidemiological and economic dynamics, reveals several crucial implications for long-term economic planning and policy formulation. The model's findings demonstrate significant relationships between health metrics, economic indicators, and social outcomes, providing valuable insights for policy development.

Labor market dynamics and economic growth

The examination of unemployment (λ) and re-employment (μ) rates reveals crucial patterns in labor market behavior. The model demonstrates that decreased re-employment rates shift unemployment curves leftward, indicating accelerated unemployment growth. When the natural growth rate (ϕ) increases to *1.4*, the economy exhibits faster growth patterns, highlighting the importance of supporting innovation and entrepreneurship. Additionally, lower GDP decay rates ($\kappa = 0.15$) correlate with enhanced economic resilience, suggesting that robust unemployment protection mechanisms significantly contribute to economic stability.

Healthcare infrastructure and sectoral adaptations

The study establishes a clear correlation between infection rates (β_1) and economic performance. Analysis reveals that while accelerated infection rates may shorten pandemic duration, they can trigger severe economic shocks. This finding is supported by India's strategic increase in health spending from *1.5%* to *1.8%* of GDP [29]. The model further indicates substantial shifts in consumer behavior during crisis periods, with essential commodities experiencing demand surges exceeding *100%* [36]. These patterns emphasize the necessity for sector-specific adaptation strategies and modernized healthcare infrastructure.

Economic stabilization and future preparedness

The relationship between unemployment and GDP, as demonstrated through the model's application of Okun's Law, provides crucial insights for economic stabilization mechanisms. The implementation of support programs, exemplified by India's PM-GKY scheme providing INR *1.7 lakh crore* in aid [37], demonstrates the effectiveness of timely governmental intervention. The study indicates that anticipatory policy frameworks, encompassing both immediate response capabilities and long-term resilience mechanisms, are essential for future crisis management.

Research investment and policy integration

The model's findings emphasize the critical role of research and development in crisis resilience. Analysis suggests that integrated approaches combining healthcare research, technological advancement, and economic adaptation yield optimal outcomes. This necessitates sustained investment in research infrastructure and the development of flexible policy frameworks capable of responding to evolving challenges. The study demonstrates that successful economic recovery requires coordinated efforts across healthcare, employment, and fiscal policy domains.

The findings support a comprehensive approach to policy development, integrating health infrastructure investment, labor market flexibility, and research advancement. These elements, working in concert, provide the foundation for robust economic recovery and long-term resilience against future crises. The model's insights suggest that policy effectiveness depends on the ability to implement coordinated responses across multiple sectors while maintaining flexibility for rapid adaptation to changing circumstances..

10 Future directions

The SIRUG model opens up several exciting avenues for future research in understanding how diseases affect economies. Future studies could enhance the model by exploring the complex ways that health crises and economic factors influence each other, going beyond the current straightforward relationships. An important area for development would be incorporating the effects of different government policies, such as economic support packages and healthcare initiatives, to better predict their impact on recovery. Additionally, future research could break

down the analysis by different economic sectors, as studying how various industries respond uniquely to health crises could provide more targeted policy recommendations.

The model's framework could be further enriched by exploring regional variations and demographic factors, as health crises often affect communities differently. This could lead to more tailored intervention strategies based on local conditions and population characteristics. Furthermore, incorporating international factors such as global supply chains and trade relationships would make the model more comprehensive and applicable to our interconnected world economy. These enhancements would build upon the current SIRUG model's foundation, making it an even more powerful tool for understanding and responding to future health and economic challenges..

11 Conclusion

The paper provides an overall analysis of the complex relationship between health variables and economic variables during the COVID-19 pandemic period in India from 2020 to 2023. In a bid to understand the impact of the pandemic on public health and the economy, this research modified the classic SIR model by adding the components of Gross Domestic Product and rate of unemployment. Anchoring on SIRUG, we have combined Okun's Law aspect with epidemiological dynamics and relevant economic factors in our model. Our results suggest, as expected, that on average, unemployment is negatively correlated with GDP. In keeping with Okun's Law, changes in one variable do seem to influence another. We also showed deviations from a perfect linear relationship, which further proves the multifaceted nature of this relationship of variables.

The trends that came out were the steep fall of GDP followed by a surge in unemployment in 2020 Q2, commensurate with the economic downturns attributed to the pandemic. Similarly, the economic recoveries during 2021 and 2022, accompanied by rising GDP and decreased unemployment, are not only in conformity with Okun's Law but also represent the strong bounce-back ability of the economy after crisis periods. On the other hand, challenges have been found in the research, like increasing reduction in GDP observed in 2023 Q4, indicating the likelihood of economic slowdowns or recessions.

These findings highlight how aggressive policy measures at both ends can dampen the adverse impacts of health shocks on the economy and vice versa. This paper opens the pathway to future and deep research into this complex interaction of epidemics and economic variables for India in several possible ways. First, the SIRUG model could be fine-tuned to enhance policy decisions during pandemics, its parameters can be calibrated with India-specific data, effectuating an equilibrium between GDP growth rate, unemployment level, and disease diffusion. This model could also be extended to incorporate behavior changes in order to speed up the program impact on the transmission and recovery rates, respectively. This will help fight any negative repercussions arising from educating the population on proper health measures that aim at reducing morbidity and mortality in general. Thirdly, incorporating variables like viral mutation patterns and healthcare delivery capacity will future-proof it for other pandemics while capturing regional differences across India. Fourthly, in the pursuit of long-term resilience, strategies such as health sector development or supporting a diversity of industries are necessary to sustain them over time. Further, it will be able to assess government programs for the control of unemployment and various other health issues that they confront today. Lastly, sensitivity analyses, real-time forecasting, and the use of present values data would enhance the model's accuracy and relevance. In summary, the effort put into this research creates an in-depth insight into the interactive dynamics at play during pandemics and becomes very resourceful to policymakers and researchers. We establish a platform for an informed decision– by combining health and economic variables in

a unified model, making provision for policy formulation that will help to address the challenges that may be triggered by future health and economic crises.

Declarations

Use of AI tools

The authors declare that they have not used Artificial Intelligence (AI) tools in the creation of this article.

Data availability statement

The data used in this study can be accessed through the following links:
https://dge.gov.in/dge/sites/default/files/2023-05/Employment_and_Unemployment_scenario_of_India_May_2023.pdf
https://www.mospi.gov.in/dataviz-quarterly-gdp-growth-rates
https://www.thehindu.com/business/Economy/gdp-surges-76-per-cent-in-2023-july-to-september-quarter-goes-past-rbi-forecast/article67591434.ece

Ethical approval (optional)

The authors state that this research complies with ethical standards. This research does not involve either human participants or animals.

Consent for publication

Not applicable

Conflicts of interest

The authors declare that they have no conflict of interest.

Funding

No funding was received for this research.

Author's contributions

A.T.: Conceptualization, Methodology, Investigation, Formal analysis, Writing – original draft. A.M.S.: Conceptualization, Methodology, Investigation, Formal analysis, Writing – original draft. N.C.: Conceptualization, Methodology, Investigation, Formal analysis, Writing – original draft. A.C.: Supervision, Formal analysis, Writing – Reviewing and editing. P.V.: Investigation, Supervision, Formal analysis, Writing – Reviewing and editing. All authors discussed the results and agreed to publish the manuscript.

Acknowledgements

Not applicable

References

[1] Unni, J. Impact of COVID-19 on informal economy: The revival. *The Indian Journal of Labour Economics*, 63, 113-118, (2020). [CrossRef]

[2] Gururaja, B.L. and Ranjitha, N. Socio-economic impact of COVID-19 on the informal sector in India. *Contemporary Social Science*, 17(2), 173-190, (2022). [CrossRef]

[3] Wikipedia, Economic impact of the COVID-19 pandemic in India, (2020). https://en.wikipedia.org/wiki/Economic_impact_of_the_COVID-19_pandemic_in_India#:~:text=The%20Indian%20economy%20was%20expected,declared%20following%20the%20coronavirus%20outbreak.

[4] Ouaziz, S.I. and El Khomssi, M. Mathematical approaches to controlling COVID-19: optimal control and financial benefits. *Mathematical Modelling and Numerical Simulation with Applications*, 4(1), 1-36, (2024). [CrossRef]

[5] Boulaaras, S., Yavuz, M., Alrashedi, Y., Bahramand, S. and Jan, R. Modeling the co-dynamics of vector-borne infections with the application of optimal control theory. *Discrete and Continuous Dynamical Systems-S*, 18(5), 1331-1352, (2025). [CrossRef]

[6] Mani, D.N.P., Shanmugam, M., Yavuz, M. and Muthuradhinam, S. Dynamic behaviour of an eco-epidemiological model of fractional-order with a fear effect. *Journal of Applied Mathematics and Computing*, 1-25, (2025). [CrossRef]

[7] Işık, E. and Daşbaşı, B. A compartmental fractional-order mobbing model and the determination of its parameters. *Bulletin of Biomathematics*, 1(2), 153-176, (2023). [CrossRef]

[8] Chakraborty, I. and Maity, P. COVID-19 outbreak: Migration, effects on society, global environment and prevention. *Science of the Total Environment*, 728, 138882, (2020). [CrossRef]

[9] Gunerhan, H., Rezazadeh, H., Adel, W., Hatami, M., Sagayam, K.M., Emadifar, H. et al. Analytical approximate solution of fractional order smoking epidemic model. *Advances in Mechanical Engineering*, 14(9), 1-11, (2022). [CrossRef]

[10] Singh, A.K. and Misra, A. Impact of COVID-19 and comorbidities on health and economics: Focus on developing countries and India. *Diabetes & Metabolic Syndrome: Clinical Research & Reviews*, 14(6), 1625-1630, (2020). [CrossRef]

[11] Srivastava, H.M. and Günerhan, H. Analytical and approximate solutions of fractional-order susceptible-infected-recovered epidemic model of childhood disease. *Mathematical Methods in the Applied Sciences*, 42(3), 935-941, (2019). [CrossRef]

[12] Jha, S., Pandey, B.K., Pandey, D., Singh, R., Jha, B., Jha, S. et al. Impact of corona virus, preventive government policies and public awareness strategies: an Indian perspective. *Biochemical & Cellular Archives*, 23(1), 1-24, (2023). [CrossRef]

[13] Adel, W., Günerhan, H., Nisar, K.S., Agarwal, P. and El-Mesady, A. Designing a novel fractional order mathematical model for COVID-19 incorporating lockdown measures. *Scientific Reports*, 14, 2926, (2024). [CrossRef]

[14] Iskandar, D. and Tiong, O.C. The application of the Runge-Kutta Fourth Order Method in SIR Model for simulation of COVID-19 Cases. *Proceedings of Science and Mathematics*, 10, 61-70, (2022).

[15] Veeresha, P. A numerical approach to the coupled atmospheric ocean model using a fractional operator. *Mathematical Modelling and Numerical Simulation with Applications*, 1(1), 1-10, (2021). [CrossRef]

[16] Katz, L. *Long-term Unemployment in the Great Recession*. EPRN: Ruanda, (2015).

[17] Press, W.H. *Numerical Recipes 3rd Edition: The Art of Scientific Computing*. Cambridge University Press: Cambridge, (2007).

[18] Centre for Monitoring Indian Economy, Unemployment Rate in Urban India, (2020).

[19] Dormand, J.R. and Prince, P.J. A family of embedded Runge-Kutta formulae. *Journal of*

Computational and Applied Mathematics, 6(1), 19-26, (1980). [CrossRef]

[20] Atkeson, A. What will be the economic impact of COVID-19 in the US? Rough estimates of disease scenarios. *National Bureau of Economic Research*, 26867, (2020). [CrossRef]

[21] Van Bergeijk, P.A. *Pandemic Economics*. Edward Elgar Publishing: England, (2021).

[22] Matignon, D. Stability results for fractional differential equations with applications to control processing. In *Computational Engineering in Systems Applications* (pp. 963-968). Paris, France: (1996).

[23] Li, H.L., Zhang, L., Hu, C., Jiang, Y.L. and Teng, Z. Dynamical analysis of a fractional-order predator-prey model incorporating a prey refuge. *Journal of Applied Mathematics and Computing*, 54, 435-449, (2017). [CrossRef]

[24] Kudryashov, N.A., Chmykhov, M.A. and Vigdorowitsch, M. Analytical features of the SIR model and their applications to COVID-19. *Applied Mathematical Modelling*, 90, 466-473, (2021). [CrossRef]

[25] Liu, T., Huang, J., He, Z., Zhang, Y., Yan, N., Zhang, C.J. and Ming, W.K. A real-world data validation of the value of early-stage SIR modelling to public health. *Scientific Reports*, 13, 9164, (2023). [CrossRef]

[26] Nakamura, G., Grammaticos, B. and Badoual, M. Vaccination strategies for a seasonal epidemic: a simple SIR model. *Open Communications in Nonlinear Mathematical Physics*, 1, 20-40, (2021). [CrossRef]

[27] O'Regan, S.M. and Drake, J.M. Theory of early warning signals of disease emergence and leading indicators of elimination. *Theoretical Ecology*, 6, 333-357, (2013). [CrossRef]

[28] Priyadarshini, P. and Veeresha, P. Analysis of models describing thermocline depth-ocean temperature and dissolved oxygen concentration in the ocean-plankton community. *Waves in Random and Complex Media*, 1-25, (2023). [CrossRef]

[29] DWIH New Delhi, Healthcare in India - Status, Challenges and Opportunities, (2021). https://pib.gov.in/PressNoteDetails.aspx?ModuleId=3&NoteId=153237&utm=&reg=3&lang=1

[30] Trade Promotion Council of India, Ephemeral Spike in Demand in India's Food Sector Owing to Covid-19: TPCI, (2020). https://www.tpci.in/press_release/ephemeral-spike-in-demand-in-indias-food-sector-owing-to-covid-19-tpci/

[31] Varshney, D., Kumar, A., Mishra, A.K., Rashid, S. and Joshi, P.K. India's COVID-19 social assistance package and its impact on the agriculture sector. *Agricultural Systems*, 189, 103049, (2021). [CrossRef]

[32] Assaf, A. and Scuderi, R. COVID-19 and the recovery of the tourism industry. *Tourism Economics*, 26(5), 731-733, (2020). [CrossRef]

[33] Yu, F., Du, L., Ojcius, D.M., Pan, C. and Jiang, S. Measures for diagnosing and treating infections by a novel coronavirus responsible for a pneumonia outbreak originating in Wuhan, China. *Microbes and Infection*, 22(2), 74-79, (2020). [CrossRef]

[34] Prachowny, M.F. Okun's law: theoretical foundations and revised estimates. *The Review of Economics and Statistics*, 75(2), 331-336, (1993). [CrossRef]

[35] Wen, Y. and Chen, M. Okun's law: a meaningful guide for monetary policy? *Economic Synopses*, 2012(15), (2012).

[36] Press Information Bureau, Government of India Ministry of Commerce & Industry, (2021). https://pib.gov.in/Pressreleaseshare.aspx?PRID=1684674&utm

[37] Economic and Political Weekly, India's COVID-19 Social Assistance Package, (2021). https://www.india.gov.in/pm-garib-kalyan-yojana-pmgky?utm

Mathematical Modelling and Numerical Simulation with Applications (MMNSA)
(https://dergipark.org.tr/en/pub/mmnsa)

How to cite this article: Thakuria, A., Sharma, A.M., Chothwani, N., Chakraborty, A. & Veeresha, P. (2025). Economic resilience in the face of pandemic: a holistic mathematical analysis of the pandemic in India. *Mathematical Modelling and Numerical Simulation with Applications*, 5(1), 234-256. https://doi.org/10.53391/mmnsa.1540240